

BULGARIAN CHEMICAL COMMUNICATIONS

2017 Volume 49 / Special Issue H

*Journal of the Chemical Institutes
of the Bulgarian Academy of Sciences
and of the Union of Chemists in Bulgaria*

BULGARIAN CHEMICAL COMMUNICATIONS

A quarterly published by

THE BULGARIAN ACADEMY OF SCIENCES

and

THE UNION OF CHEMISTS IN BULGARIA

Volume 49, Special issue H

ИЗВЕСТИЯ ПО ХИМИЯ

Тримесечно издание на

БЪЛГАРСКА АКАДЕМИЯ НА НАУКИТЕ

и

СЪЮЗ НА ХИМИЦИТЕ В БЪЛГАРИЯ

Том 49, Книга H

2017

Editor-in-Chief:

V. Beschkov

Visiting editor:

Abdol Ghaffar Ebadi

EDITORIAL BOARD

Ch. Bonev, L. Boyadzhiev, I. Gutzow, I. Havezov, E. Ivanova, K. Petkov, K. Petrov, L. Petrov, I. Pojarlieff, S. Rakovsky, D. Stoychev, P. Petrov, D. Tsalev, D. Vladikova, D. Yankov, V. Kurteva

Members from abroad:

J. M. Albella (Spain), S. Berger (Germany), J. C. Breakman (Belgium), J. Etourneau (France), M. Farina (Italy), K. Friedrich (Germany), J. Gyenis (Hungary), A. J. Kirby (United Kingdom), T. Kowalska (Poland), K. Kutchitsu (Japan), A. Lasia (Canada), O. V. Mazurin (Russia), B. Mutaftshiev (France), E. Peter Kündig (Switzerland), S. De Rosa (Italy), T. F. Tadros (United Kingdom), K. Valko (Hungary)

The annual subscription (for 4 issues) for vol. 48 (2017) is € 160. – including postage, handling and packaging charge.

Payments should be delivered to:

*Editorial Board of Bulgarian Chemical Communications, Institute of Chemical Engineering,
UniCredit Bulbank, IBAN: BG65 UNCR 7630 3400 0017 48; SWIFT/BIC - UNCRBGSF (for Euro €).*

UniCredit Bulbank, IBAN: BG18 UNCR 9660 3119 9033 12; SWIFT/BIC - UNCRBGSF (for local currency BGN).

Research on infrared interference performance of carbon smoke

T. Shen, X.J. Li*, D.P. Wang, M.L. Yao

Xi'an Research Institute of High Technology, shannxi China 710025

Received May 24, 2017, Revised July 20, 2017

Abstract: Using Lambert-Beer law, the interference characteristics of smoke composed by spheroid and spherical particles of carbon black is analyzed respectively in 10.64 μm band based on the T matrix theory and Mie scattering theory in this paper. Analysis shows that whether it is spherical or non-spherical there is an optimum size (about 1.51 μm) to make the interference effects of smoke best. The interference effects of smoke composed of spheroid particles are better than those composed of spherical particles. More obvious non-spherical features of spheroid is, then more better the interference effect is. When the particle size is constant, along with the thickness and concentration of smoke become larger, the interference effect becomes better.

Keywords: carbon smoke; T- matrix theory; Mie theory; infrared interference

INTRODUCTION

Smoke is a simple and effectual means of laser passive interference. It played very important role in the nearly wars. The smoke particles can absorb or scatter the incident light effectively and decay the incident light energy. The infrared smoke materials take on the better infrared extinction capability. Its interference effect depends on the smoke composition, smoke particle dimension and the incident light wavelength. The carbon black particles can absorb infrared radiation effectively and can be used to smoke material[1]. Based on the T matrix theory and Mie scattering theory[2], Lambert-Beer law was used. The interference performance of smoke composed by spheroid and spherical particles of carbon black was analyzed respectively in 10.64 μm band.

BASIC THEORY

T-Matrix Theory

T-Matrix method can also call zero field method or extended boundary condition method. It is suitable for non-spheroid particle extinction parameter calculation. Its main thought is that the expansion coefficient of scattered field vector ball harmonic function is expressed by incident field. The conversion matrix is a T-matrix [1]. Under the incident light irradiation, the particle surface produces electric current and the current forms scattered field by agitation [3]. Adopting vector spherical wave function to express the scattered field $E_{\text{inc}}(r)$ and incident field $E_{\text{sca}}(r)$:

$$E_{\text{inc}}(r) = \sum_{n=1}^{\infty} \sum_{m=-n}^n [a_{mn} RgM_{mn}(kr) + b_{mn} RgN_{mn}(kr)] \quad (1)$$

$$E_{\text{sca}}(r) = \sum_{n=1}^{\infty} \sum_{m=-n}^n [p_{mn} M_{mn}(kr) + q_{mn} N_{mn}(kr)], |r| > r_0 \quad (2)$$

In the formula: $k = 2\pi / \lambda$ is wave number of ambient medium; r_0 is the external tangent spherical radius of the scattered particle. $RgM_{mn}(kr)$ and $RgN_{mn}(kr)$ are vector function.

According to the linear relationship of Maxwell equations set, the scattered field expansion coefficient p_{mn} , q_{mn} and the incident field expansion coefficient a_{mn} , b_{mn} are expressed by T-matrix as followed:

$$p_{mn} = \sum_{n'=1}^{\infty} \sum_{m'=-n'}^{n'} (T_{mm'n'}^{11} a_{m'n'} + T_{mm'n'}^{12} b_{m'n'}) \quad (3)$$

$$q_{mn} = \sum_{n'=1}^{\infty} \sum_{m'=-n'}^{n'} (T_{mm'n'}^{21} a_{m'n'} + T_{mm'n'}^{22} b_{m'n'}) \quad (4)$$

This linear relationship can be changed as following form.

$$\begin{bmatrix} p \\ q \end{bmatrix} = T \begin{bmatrix} a \\ b \end{bmatrix} = \begin{bmatrix} T^{11} & T^{12} \\ T^{21} & T^{22} \end{bmatrix} \begin{bmatrix} a \\ b \end{bmatrix} \quad (5)$$

From the relational expression above, the incident field expansion coefficient a_{mn} and b_{mn} can be obtained by known incident light electric field vector. So, as long as the conversion coefficient of T-matrix can be get, the scattered field expansion coefficient p_{mn} and q_{mn} can also be get accordingly.

In this paper, the gyration ellipsoid model is used to calculate the extinction parameter of the carbon ellipsoid particle. Its equation is:

$$r(\theta, \phi) = b \left[\sin^2 \theta + \frac{b^2}{a^2} \cos^2 \theta \right]^{\frac{1}{2}} \quad (6)$$

In the equation, a is half axial length of gyration

* To whom all correspondence should be sent:
E-mail: luckyschentao@163.com

shaft; b is radius length of revolution. As $a/b < 1$, it is flat ellipsoid. As $a/b > 1$, it is prolate ellipsoid. As $a/b = 1$, it is sphere. In this paper, the isopyknic radius of sphere and a/b express the size and shape of the gyration ellipsoid accordingly. The isopyknic radius of sphere is $r_v = a^{1/3}b^{2/3}$. To random orientation revolving solid particle, its extinction cross section and scattered cross section are following:

$$C_{ext} = -\frac{2\pi}{k^2} \text{Re} \sum_{n=1}^{\infty} \sum_{m=-n}^n (T_{mm'n'}^{11} + T_{mm'n'}^{22}) \quad (7)$$

$$C_{sca} = \frac{2\pi}{k^2} \sum_{n=1}^{\infty} \sum_{m=-n}^n \sum_{n'=1}^{\infty} \sum_{m'=-n'}^n (|T_{mm'n'}^{11}|^2 + |T_{mm'n'}^{12}|^2 + |T_{mm'n'}^{21}|^2 + |T_{mm'n'}^{22}|^2) \quad (8)$$

Mie theory

To regular spheric scatterer, when the incident electromagnetic field wavelength is nearly to the scatterer length, the Mie Thoery can express the scattering process of the scatterer to electromagnetic field^[5]. Its extinction cross section and scattered cross section are following:

$$C_{ext} = \frac{\lambda^2}{2\pi} \sum_{n=1}^{\infty} (2n+1) \text{Re}(a_n + b_n) \quad (9)$$

$$C_{sca} = \frac{\lambda^2}{2\pi} \sum_{n=1}^{\infty} (2n+1) (|a_n|^2 + |b_n|^2) \quad (10)$$

$$C_{abs} = C_{ext} - C_{sca} \quad (11)$$

In the equation, a_n and b_n are Mie coefficient, λ is radiation wavelength.

Lambert-Beer law

Infrared smoke transmissivity can express the interfere degree of infrared smoke to image-forming system. According to the Lambert-Beer law, the transmissivity is:

$$T = \frac{I}{I_0} = \exp[-C_{ext}NL] \quad (12)$$

In the equation, I is incident intensity, I_0 is transmitted intensity, N is the smoke particle density, L is smoke thickness.

Spheric particle extinction cross section C_{ext} can be calculated by Mie Thoery and gyration ellipsoid particle extinction cross section C_{ext} can be calculated by T-matrix. Smoke particle concentration $N = c/(\rho V)$, c is smoke concentration; ρ is smoke particle mass density; V is the particle capacity; The smoke transmissivity can express as following:

$$T_{sphere} = \exp(-C_{ext}NL) = \exp(-3cC_{ext}L/4\pi r^3 \rho) \quad (13)$$

$$T_{ellipsoid} = \exp(-C_{ext}NL) = \exp(-3cC_{ext}L/4\pi r_v^3 \rho) \quad (14)$$

Carbon particle smoke infrared interfere characteristics

Suppose smoke is single uniform dispersion system^[6]. Under the condition that incident wavelength $\lambda=1.06\mu\text{m}$, carbon particle complex refractive index $n = 3.1020 + 1.3010i$, the smoke is compesed by gyration ellipsoid and spheric scatterer particle accordingly. The smoke transmissivity is compared.

When the particle size changed, the other parameters are set as following: smoke concentration is $c=0.0005\text{kg/m}^3$; smoke thickness is $L=10\text{m}$; smoke particle mass density $\rho=1500\text{kg/m}^3$; gyration ellipsoid axial length ratio is $a/b=1/4$, $a/b=1/2$, $a/b=2$, $a/b=4$ accordingly. The calculation results are Fig.1.

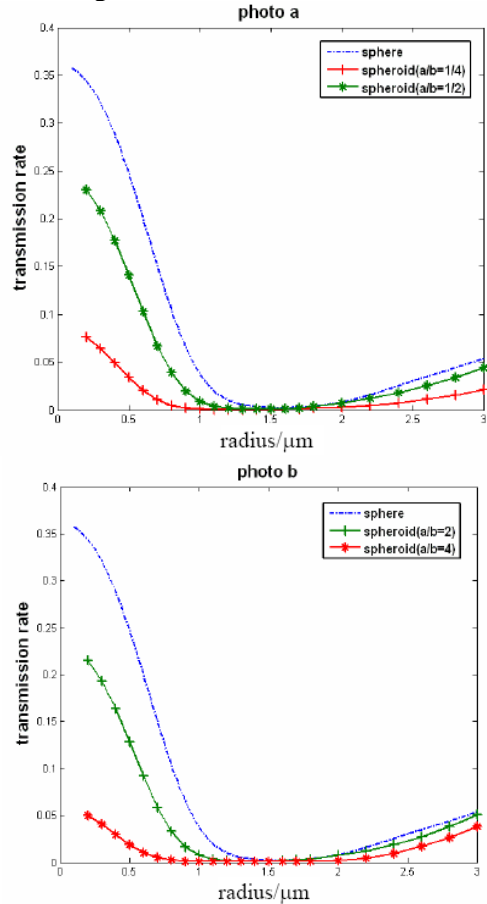


Fig. 1. The influence on transmissivity of carbon black smoke screen with particle radius change

From Fig.1 above, whatever gyration ellipsoid or spheric scatterer, the smoke transmissivity changes with particle radius. The interference effect is best when the particle radius in the 1-2 μm . In Fig.1 photo(a), The interference effect of gyration

ellipsoid axial length ratio $a/b=1/4$ is better than $a/b=1/2$ and they are both better than spheric scatterer. In Fig.1 photo (b), The interference effect of gyration ellipsoid axial length ratio $a/b=4$ is better than $a/b=2$ and they are both better than spheric scatterer.

To compare the gyration ellipsoid interference effect in different axial length directly, put axial length ratio $a/b=4$ and $a/b=1/4$ curve in one figure and axial length ratio $a/b=2$ and $a/b=1/2$ curve in the other figure. The results are Fig.2.

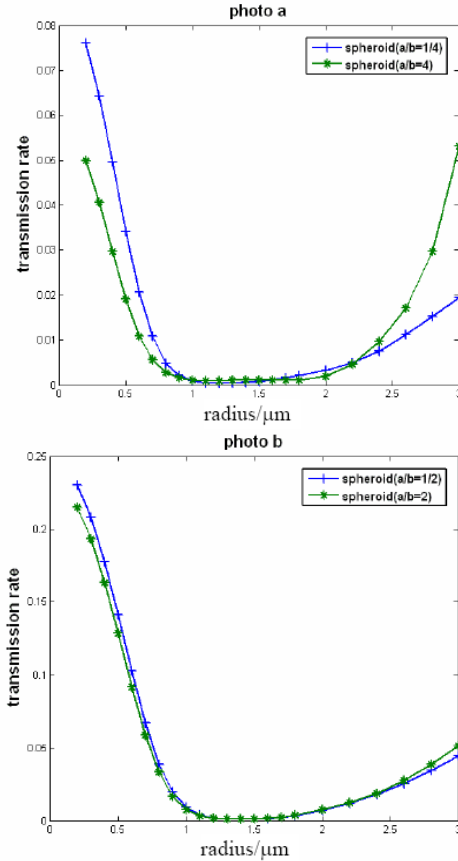


Fig. 2. The comparison of transmission rate for different a/b of spheroid

From Fig.2, the difference of interference effect is very small. To gyration ellipsoid, when its axial length ratios are reciprocal each other, the interference effect is nearly similar.

When the smoke concentration changed, the other parameters are set as following: particle radius is $r=r_v=1.5\mu m$; smoke thickness is $L=15m$; smoke particle mass density $\rho=1550kg/m^3$; gyration ellipsoid axial length ratio is $a/b=1/4$, $a/b=1/2$, $a/b=2$, $a/b=4$ accordingly. The calculation results are Fig.3.

From Fig.3 above, whatever gyration ellipsoid or spheric scatterer, the smoke transmissivity changes with particle radius. The interference effect of gyration ellipsoid particle smoke is better than the spheric scatterer particle smoke.

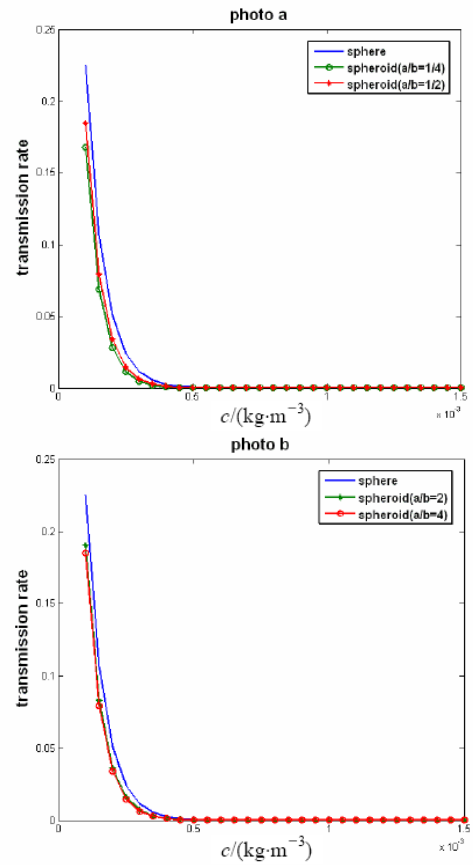


Fig. 3. The influence on transmission rate of carbon black screen with smoke concentration change

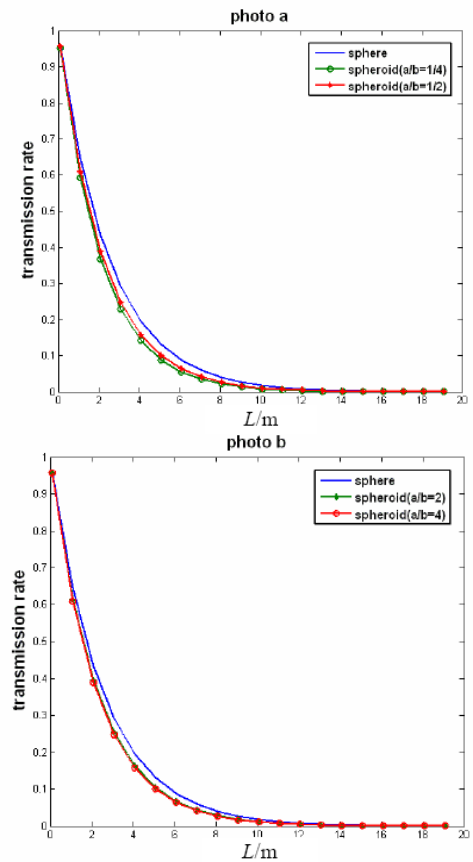


Fig. 4. The influence on transmission rate of carbon black screen with smoke thickness change.

The gyration ellipsoid axial length ratio is different, but the interference effect is similar. The interference effect of gyration ellipsoid axial length ratio $a/b=1/4$ is better than $a/b=1/2$ and $a/b=4$ is better than $a/b=2$.

When the smoke thickness changed, the other parameters are set as following: particle radius is $r=r_v=1.5\mu\text{m}$; smoke particle mass density $\rho=1550\text{kg/m}^3$; smoke concentration is $c=0.0004\text{kg/m}^3$; gyration ellipsoid axial length ratio is $a/b=1/4$, $a/b=1/2$, $a/b=2$, $a/b=4$ accordingly. The calculation results are Fig.4.

From Fig.4 above, the smoke transmissivity reduces with smoke thickness increasing. The interference effect of gyration ellipsoid particle smoke is better than the spheric scatterer particle smoke. The gyration ellipsoid axial length ratio is different, but the interference effect is similar. The interference effect of gyration ellipsoid axial length ratio $a/b=1/4$ is better than $a/b=1/2$ and $a/b=4$ is better than $a/b=2$.

CONCLUSION

Based on the T-Matrix Theory and Mie Theory, the smoke interference effect of gyration ellipsoid and spheric scatterer are calculated by Lambert-Beer law. The conclusion is that there is

an optimal particle size (about $1.5\mu\text{m}$), the smoke interference effect is best. To gyration ellipsoid, under axial length ratio $a/b<1$, the more small the axial length ratio is, the better the interference effect is. Under axial length ratio $a/b>1$, the more large the axial length ratio is, the better the interference effect is. The interference effect of gyration ellipsoid particle smoke is better than the spheric scatterer particle smoke under the condition of this paper. When the particle size is invariant, the better the smoke interference effect is, the larger smoke density and thickness is.

REFERENCES

1. L. Liu, M.I. Mishchenko, W.P. Arnott, *JQSRT*, **109**, 2656 (2008).
2. M.I. Mishchenko, G. Videenb, V.A. Babenko, *JQSRT*, **88**, 357 (2004).
3. B.O. Lee, W.J. Woo, H.S. Park, *J Mater Sci*, **37**, 1839 (2012).
4. X.C. Nie, L.W. Li, *Micro Opt Tech Lett*, **38**(1), 30 (2008).
5. C. Resende, F.J.S. Moreira, O.M.C.P. Filho, *J Micro Opt*, **16**(1), 220 (2007).
6. J.-H. Du, C. Sun, S. Bai, *J Mater Res*, **17**(5), 1232 (2008).

The factor analysis of environment changes on groundwater

A.J. Shao^{1*}, Z.G. Li¹, S.W. Wang¹

Hebei GEO University, Shijiazhuang, China

Received May 25 2017, Revised June 20 2017

Environmental variations and the influences on water resources are complicated. According to a great number of the statistical data of Hebei province in Northern China since the 1950s, the analyzing indicated that the water resources volume in Hebei province trended towards decreasing during the recent 50 years as the variations of natural environment and human activities increasing. Precipitation reducing and air temperature rising are the basic cause of leading to the water resources decreasing. The continual lowering of groundwater level, which was created by the excess development of groundwater, not only caused surface runoff decreasing but also made groundwater recharge lessening. The level increase of crop output directly consumed a great lot of water resources, simultaneously had farmland evapotranspiration strengthened, and also brought about surface runoff and groundwater recharge decrease.

Keywords: Water resources; Climate change; Surface runoff; Groundwater recharge; Crop water requirements

INTRODUCTION

Hebei is one of the provinces of the most serious shortage of water in China. Water resource occupancy per person only accounts one sixth in the country per person level. The contradictions of water resource supplying and demanding highlight seriously. The shortage of water resource has become a bottle-neck which limits to the high speed economical development and improve people life level. In recent 50 years, the impact on the water resource quantity and water environment quality is larger and larger because of the change of the global climate changing and the large extent of human economical activity. The article primarily discusses the impact of the environment change on the term of water resource quantity in Hebei province.

Impact Of Climate Change On Resource

Impact of temperature change on water resource

Climate change is one of the main reasons that created the shortage of water resources in Hebei province. According to a great number of statistical and survey from 42 observatories of the province in the 20th century[1]: the rising of year average temperature was 0.1-0.6°C at the most of observatories in 50-60s'; 0.1-0.7°C in 60-70s'; 0.1-0.6°C in 70-80s'; 0.2-1.2°C in 80-90s', and the biggest one. During recent 50 years, in 1950-90s', the year average temperature in Hebei province increased by 0.2-2.1, and the average ascended by 1.0°C.

If not thinking the other climate change factors, the impact of the temperature change on the water resources mainly embodies that evaporation and intensity enlarges with temperature up. The elevating of temperature can bring about increasing the consumed water and lessening water resources which can be used by the public whether it is water surface evaporation, leaf evaporation, soil evaporation or groundwater evaporation. Since 1950s', the temperature of Hebei elevated gradually by age. The rate of elevation was quickest during 1980s'. Generally, high temperature and drought turned up at the same time. High temperature picked drought up and made the farmland water requirement rise, high temperature also caused the consumed water of town increasing. So, the water resource contradictions of demanding and supplying highlight.

Impact of precipitation change on water resource

According to the statistical data from 112 hydrological stations in Hebei[1], the average precipitation gradually lessened in 1950-80s', the range of decreasing was 79.7mm, the average decreased 26.6mm every 10 years. The range of decreasing in mountains was bigger than in plain; after 1990s' it turned to rise again but still be less 62.1mm than in 1950s'. The statistical data showed that during 1950-90s', the average precipitation decreased by decade in most of stations (table 1).

Generally, water resources of an area are the reparable and newborn surface water resource and groundwater resource. Surface water re-

* To whom all correspondence should be sent:
E-mail: shaoaijun@sohu.com

source is multi-year average runoff of river and is computed by drainage area. Groundwater resource is multi-year average fresh water recharged and evaluated by groundwater aquifer system. The river runoff comes from the air precipitation, groundwater in mountainous area. Groundwater recharge comes from the air precipitation, surface water and over stream from other aquifer. Whether surface water or groundwater. Therefore, the decreasing of the air precipitation is the basic cause of leading to the shortage of water resource in Hebei.

Table 1. Changes of average precipitation in Hebei (mm).

| Age | 1950s' | 1960s' | 1970s' | 1980s' | 1990s' |
|---------------|--------|--------|--------|--------|--------|
| Mountain area | 590.8 | 541.9 | 530.0 | 497.6 | 532.5 |
| Plain area | 569.3 | 579.2 | 550.3 | 510.8 | 501.2 |
| Average | 582.4 | 556.5 | 538.1 | 502.7 | 520.3 |

Impact Of Development Of Groundwater On Water Resource

The Condition of Groundwater Development

Hebei province mainly develops and uses groundwater. During recent years, groundwater development was over $160 \times 10^8 \text{ m}^3/\text{a}$, the practical usage of groundwater accounted the usage of water resource in the province for 75%-80%. 85% of the total groundwater put use into the farmland irrigation. There are over 70×10^4 exploitation wells.

According to some data statistic, in 1950s'[2], the groundwater exploited of the whole province was focused around pore phreatic water, the well depth was 10-15m and the exploitation quantity was over $30 \times 10^8 \text{ m}^3/\text{a}$, and well irrigation area was $67 \times 10^4 \text{ hm}^2$, so groundwater was in the balance situation. In 1960', groundwater was exploited still as pore phreatic water, the well depth was 20-40m, and the exploitation quantity was over $50 \times 10^8 \text{ m}^3/\text{a}$, and well irrigation area was $133 \times 10^4 \text{ hm}^2$, so groundwater was still in the balance state. In 1970s', groundwater was exploited as the mixed of phreatic water and confined water in the plain before mountains, the depth reached 60-80m. In the plain, people started to exploit a lot of deeper confined water, the depth was

200-250m. Groundwater development was about $110 \times 10^8 \text{ m}^3/\text{a}$ in this period, and the exploitation in Hebei plain was about $100 \times 10^8 \text{ m}^3/\text{a}$, and the well irrigation area was $233 \times 10^4 \text{ hm}^2$. In the period, groundwater level began to go down territorially and developed several groundwater decreasing funnels. In 1980s', the exploitation in the whole province was $130 \times 10^8 \text{ m}^3/\text{a}$, the exploitation in Hebei plain reached $120 \times 10^8 \text{ m}^3/\text{a}$, the number of well was 60×10^4 and the irrigation area reached $287 \times 10^4 \text{ hm}^2$, the well depth was 170-350m. In 1990s', groundwater exploitation in the whole province reached $160 \times 10^8 \text{ m}^3/\text{a}$, the exploitation in Hebei plain was about $135 \times 10^8 \text{ m}^3/\text{a}$. The exploited well reached 70×10^4 , and the irrigation area was $280 \times 10^4 \text{ hm}^2$ and the depth was 250-380 m (table 2).

Impact of Excess Development of Groundwater on Water Resource

Since 1980s', groundwater exploitation has been about $140\text{-}150 \times 10^8 \text{ m}^3/\text{a}$. The Hebei plain exploitation has been about $120 \times 10^8\text{-}130 \times 10^8 \text{ m}^3/\text{a}$. Generally the excess development has reached $15 \times 10^8\text{-}23 \times 10^8 \text{ m}^3/\text{a}$ each year and the highest has been about $30 \times 10^8\text{-}40 \times 10^8 \text{ m}^3/\text{a}$. According to the groundwater exploitation data from 1985 to 1995, the excess development of the low groundwater was $15.6 \times 10^8 \text{ m}^3/\text{a}$; and the deep groundwater was $8.9 \times 10^8 \text{ m}^3/\text{a}$. The total excess development was $24.5 \text{ m}^3/\text{a}$. The groundwater level has gone down in a large range, and the low groundwater level in Hebei plain generally has gone down 5-15m, the deeper is 20-30m; the deep groundwater level generally has gone down 20-40m, the deeper is 40-50m.

Table 2. Decade changes of groundwater exploitation in Hebei

| Age | 1950s' | 1960s' | 1970s' | 1980s' | 1990s' |
|--|--------|--------|--------|--------|--------|
| Development of groundwater $/ \times 10^8 \text{ m}^3/\text{a}$ | 3 | 5 | 11 | 13 | 16 |
| Well irrigation area $/ \times 10^4 \text{ hm}^2$ | 67 | 133 | 233 | 287 | 280 |

It resulted in that groundwater level continued to go down in a large range and there was some groundwater level decreasing funnels in

some cities that exploited a lot of water and consumed much water. The Hebei plain has appeared groundwater level decreasing funnels since the beginning of 1970s' and they gradually turned to perennial funnels. Over 20 years until the end of 1995, there was over 20 funnels of groundwater level decreasing. The low funnels located mainly in the Hebei plain before mountain and nearby some cities that connected to the middle of the plain. At the end of 1995 there was 10 perennial funnels; the deep groundwater decreasing funnels located mainly in the middle of Hebei plain and coastal area and there was 12 perennial funnels. According to data, the bigger funnels were Shijiazhuang, Jizaoheng and Cangzhou[3] (table 3).

The recharge of groundwater in Hebei plain is mainly atmospheric precipitation. The supplying of the atmospheric precipitation nearly accounts for 70% of the total ground water supplying quantity. Since 1970s', as a result of ground water massive exploitation, in the Hebei plain great scope, the groundwater level has continued to drop, the water level depth large scale increased. Unsaturated zone largely changes thick. According to the pertinent data, above 70% of total precipitation in Hebei plain approximately all transforms as soil water, another small part turns to the deep aquifer, and transforms as the ground water. Atmospheric precipitation military supplies ground water quantity except with the air precipitation, unsaturated zone, the vegetation cover situation, the preliminary soil water content related outside, but also concerns with the thickness of the unsaturated zone. Under the same condition, the bigger thickness of the unsaturated zone is, then the more the atmospheric precipitation which the unsaturated zone absorbs and detains are, the less the quantity of the atmospheric precipitation which supplies ground water is. Therefore, the dropping of the region groundwater level and the increasing of the unsaturated zone thickness are one of the main reasons that create the groundwater recharge reducing. On the other hand, the increasing of the unsaturated zone thickness, can cause the more atmospheric precipitation to be absorbed by the zone, causes surface water volume reducing, then, and causes the reduction of the surface water resource.

Table 3. Changes of groundwater depression cones in Hebei Plain

| Year | Shijiazhuang funnel | | Jizaoheng funnel | | Cangzhou funnel |
|------|----------------------|---------|-----------------------|----------|-----------------|
| | Area/km ² | Depth/m | Area /km ² | Depth /m | Depth /m |
| 1965 | 58 | 7.57 | | | 0.00 |
| 1970 | 154 | 10.37 | | 12.06 | |
| 1975 | 187 | 15.29 | 3476 | 32.68 | 50.28 |
| 1980 | 189 | 20.39 | 3588 | 50.31 | 69.99 |
| 1985 | 259 | 31.32 | 4698 | 56.10 | 75.65 |
| 1990 | 338 | 37.22 | 4023 | 56.84 | 82.08 |

Impact of The Change of Surface Runoff on Water Resource

Change of Surface Runoff

In Shijiazhuang Plain, the agricultural irrigation water occupies about 80% of total exploited groundwater quantity. The figure. 1 shows that, the buried depth of groundwater (h) is closely related with exploited agricultural groundwater quantity (Q) and will be increased with ever growing exploitation. Generally, the two elements show a positive correlation which can be summarized as

$$h = 1.4558e^{0.0929Q}, \quad R^2 = 0.7455.$$

The rivers of Hebei distribute four water systems: Hai river, Luan river, Liao river and Inland river. The total area of the basin is 18.77×10^4 km². According to the data from Hebei Bureau of Water Resources, in 1950s', surface runoff of the whole province was 199×10^8 m³/a and water which goes into the sea was 86.4×10^8 m³/a; in 1980s', surface runoff of the whole province was 81.3×10^8 m³/a, and water into the sea was 13.2×10^8 m³/a. Comparing with 1950s', at present the river runoff of the whole province and water which goes into the sea has decreased at a large range (table 4).

In the hydraulic engineering, after the founding of the nation, Hebei carried out the big scale hydraulic engineering construction. At present, the mountainous area has completed 18 large-scale reservoirs, 38 medium reservoirs and 1086 small reservoirs. The total storage capacity is 112.9×10^8 m³. These reservoirs control 85% of the mountainous area, and control 90% of water that comes from the moun-

tainous area. These hydraulic projects mostly completed in 1960s'. In 1970s' they tended to the normal operation. The surface water usage rate of the entire provinces reached 70% in 1980- 90s', the partial area reached above 90%. The degree of surface water development and utility is higher, has surpassed the convention, and created the serious ecological environment problem.

Table 4. Changes of surface runoff and runoff into the sea in Hebei

| Age | 1950s' | 1960s' | 1970s' | 1980s' | 1990s' | Average |
|---|--------|--------|--------|--------|--------|---------|
| Surface runoff/ $\times 10^8$ m ³ /a | 19.9 | 13.7 | 12.6 | 8.13 | 12.8 | 12.5 |
| Runoff into the sea / 10^8 m ³ /a | 8.64 | 5.89 | 6.08 | 1.32 | 3.37 | 4.63 |

Impact of change of surface runoff on water resource

River runoff stands for surface water resource. As the decreasing of surface runoff since 1970s', it caused the decreasing of surface water resource directly.

Groundwater has to be developed and used as the serious lack of surface water resource. During 1970s', because of the excess development of groundwater, the continual decline of groundwater level and the increasing of the unsaturated zone, they have made surface runoff and groundwater recharge decrease. And the environment problem is more and more serious.

Impace of Change of Grain Output on Water Resource

Hebei is a big agricultural province[4]. At the end of 1998, the area of farmland in Hebei is 648.46×10^4 hm². Since 1970s', the total grain output of Hebei has always been the tendency of increasing. The grain output was 1272.5×10^4 t in 1970 and 1522.4×10^4 t in 1980 respectively. And the grain output in 1998 reached 2917.5×10^4 t, which was 2.3 times higher than that in 1970 (figure 1).

Generally the higher the crop output level is, the more the crop water requirement and the more the soil water consumes[5].

Under the same rainy condition, the higher the crop output level is, the less the surface

runoff and the recharge of groundwater is. Therefore, the improvement of grain output level is one of the reasons for the decreasing of water resource.

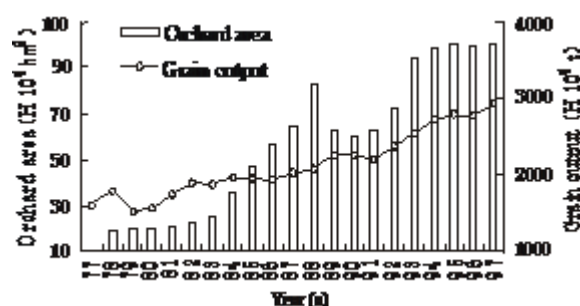


Fig. 1. Grain output and orchard area in Hebei

CONCLUSIONS

(1) The impact of the change of environment on water resource was complex. The climate factors: the precipitation reducing, air temperature rising and so on results in the decreasing of surface runoff and groundwater recharge, the enhancing of farm evaporation. They are the basic cause of leading to the water resources decreasing. The continual lowering of groundwater level which is created by the excess development of groundwater not only causes surface runoff decreasing but also makes groundwater recharge lessening. It is a major man-made factor of decreasing the water resources.

(2) In the use of water resources, agriculture is a big consumer of water[6]. The quantity of farmland irrigation is about 85% of the whole quantity of using groundwater of Hebei province. Especially for the increase of crop output of Hebei plain, it consumed a great lot of water resources and had farm evaporation strengthened, and also brought about surface runoff and groundwater recharge decrease.

Acknowledgements: LiZhiGuang, 1978.10, The Han nationality, Associate professor of Hebei GEO University, Mainly engaged in engineering geology, environmental geology research work. The National Natural Science Foundation of China: Study on The Relationship between Urban Architecture Planning and Land Subsidence in North China by Model Simulation Experiment: Taking Cangzhou as Example (Grant No.41301015) .

REFERENCES

1. C. Wanghe. *Seismological Press*, **1-8**, 492 (1999).
2. G. Yingchun, Z. Guanglu, R. Xin, Z. Yubin, *Geography and Territorial Research*, **17**(2), 67 (2001).
3. S. Zhenrong, *China Science and Technology Press*, **136**, 239 (1992).
4. W. Daolong, *Resources and Environment*, **11**(3), 31 (2001).
5. X. Yueqing, L. Xiubin, *Resources Science*, **23**(5), 28 (2001).
6. Z. Zonghu, S. Zhaoli, X. Yuqun, R. Fuhong, S. Dehong, Y. Zhengzhou, Z. Zuoye, S. Xinghe., Evolution of groundwater environment in North China Plain. – Beijing: Geological Publishing House, 2000, p. 3

Distribution and magnetic features of igneous rocks in the Gaize-Nima area of Tibet plateau based on magnetic data

C.G. Zhang^{1*}, G.L. Zhang², M.H. Zhang³, J.G. Chen⁴

¹School of Earth Sciences and Engineering, Xi'an Shiyu University, No. 18 Dianzi 2 Road, Xi'an, Shaanxi, China

²Tianjin Geological Survey Center, China Geological Survey, No. 4 Dazhigu 8 Road, Tianjin, China

³Development and Research Center, China Geological Survey, No. 45 Fuwai Street, Beijing, China

⁴Huabei Department, BGP Inc. of CNPC, Middle Section, North Station East Road, Renqiu, Hebei, China

Received June 16, 2017; Revised July 20, 2017

Gaize-Nima, a part of the Qinghai-Tibet Plateau, has magnetic characteristics and a distribution of temporal and spatial development of igneous rock which are closely associated with Qinghai-Tibet plateau tectonic movement. This research aims to lay a foundation for ore-prospecting prognosis and regional tectonic zonation by investigating the magnetic characteristics and distribution of temporal and spatial development for igneous rock in the Gaize-Nima area of the Qinghai-Tibet Plateau, China. In this research, the aeromagnetic anomaly by reduction to the pole was calculated based on the aeromagnetic total intensity anomaly data at a scale of 1:200,000. Besides, the aeromagnetic anomaly data was subjected to anomaly decomposition using the regularization filtering method to obtain data about the local magnetic anomaly (LMA) and regional magnetic anomaly (RMA) in the Gaize-Nima area. Besides, based on existing research in geology and geophysics, the characteristics of the aeromagnetic anomaly, LMA and RMA were analysed. Moreover, the corresponding relationship between the igneous rock exposed on the surface, and the magnetic anomaly, was studied. In addition, the magnetic characteristics of the igneous rock exposed on the surface in Gaize-Nima were demonstrated. Moreover, this research explored the temporal and spatial distributions of igneous rock and inferred the distribution characteristics of concealed igneous rocks therein. Results show that the ophiolite and ultrabasic rock in the area were characterised by strong magnetism; while, basic, and intermediate rocks generally exhibited weak magnetic characteristics; acidic rock was characterised by medium-strong magnetism. In this area, the acidic rocks (Neogene and Jurassic), the intermediate rocks (Cretaceous and Jurassic), as well as the basic rocks (Cretaceous and Permian), showed weak magnetism. The acidic rocks (Palaeogene and Cretaceous), and the dolerite (Neogene and Jurassic) both presented stronger magnetism. The magnetism of the ultrabasic rocks and ophiolite (Jurassic) was strongest. The distribution characteristics of magnetic anomaly and igneous rock exposed revealed that there were two concealed ophiolite belts (Jurassic) in Gaize-Laiduoqangma and Songqin, respectively. Moreover, there were three groups of concealed ultrabasic rocks belts (Jurassic) in South Baiqing, Gaize, and Emule, and there were large areas of concealed acidic rocks in Duoba, Bangduo, North Cuoqin, Chachangle, west Nale, and west Kangqiongle.

Keywords: Igneous rock, magnetic features, magnetic anomaly, Gaize-Nima, Tibet plateau

INTRODUCTION

The Qinghai-Tibet Plateau is bordered to the North by the Altun Mountains and Qilian Mountain, to the south by the Himalayan range, to the west by the Karakorum Mountains, and to the east by the Hengduan Mountains. It covers an area of 2.6×10^6 km² with an average elevation of 4000 m above sea level. It is located in the Tarim basin, Gansu corridor, Sichuan basin, and the low plain of Indus river (the Ganges), and is known as "The roof of the world". As a part of the Qinghai-Tibet plateau, the magnetic characteristics, and the temporal and spatial development of igneous rock in the Gaize-Nima area are shown to be closely related to the tectonic movement of the Qinghai-Tibet Plateau. Existing studies have achieved many favourable

results by investigating this area using geological information [1, 2, 3, 4], and performing inversion and explanation of the physical properties of crustal structures in this area, based on geophysical materials [5, 6, 7]. Furthermore, previous research has conducted analysis of the geochemical characteristics of ophiolite, the temporal and spatial distribution of granite [8, 9, 10], and also explored the relationship between tectonics and igneous rock in this area [11, 12]. It is known that aeromagnetic data play an essential role in research into the temporal and spatial distribution behaviour of igneous rock. Existing studies mainly adopted data from the aeromagnetic survey of the midwest Qinghai-Tibet plateau at a scale of 1:1,000,000 collected by China's Aero Geophysical Survey and Remote Sensing Centre for Land and Resources, Beijing, China from September, 1998 to April, 1999. The complex magnetic anomaly characteristics of the midwest Qinghai-Tibet plateau are attributed to

* To whom all correspondence should be sent:
E-mail: chunguan-zhang@163.com

the complex fault tectonics in this area [13, 14, 15, 16, 17]. Based on the aforementioned aeromagnetic data, Yao et al. [18] analysed the relationship between aeromagnetic anomalies and the presence of ophiolite. Xiong et al. [19] also explored the distribution of igneous rock in the Midwest Qinghai-Tibet plateau.

To discuss the magnetic characteristics of igneous rock in Gaize-Nima, this research collected the ΔT anomaly data based on the aeromagnetic survey at a scale of 1:200,000 undertaken by the Airborne Survey and Remote Sensing Centre for the Nuclear Industry in response to the consignment of China's National Petroleum Committee from 1994 to 1995. This research analysed the characteristics of the aeromagnetic anomalies, LMA and RMA, by separation of the magnetic anomaly data. Besides, it researched the relationship between the igneous rock exposed on the surface, and magnetic anomaly, so as to reveal the magnetic characteristics and the temporal and spatial development of igneous rock.

Geological setting

The Gaize-Nima area is located between 82° to 90° E and 31° to 33° N and covers an area of 175,000 km². The research areas included: the Gangdise block, the Bangongcuo-Nujiang suture zone, and the Qiangtang block [20, 21].

Based on the geological map of the Qinghai-Tibet plateau, and adjacent areas, published by Chengdu Institute of Geology and Mineral Resources, China in July, 2004, the authors drew a geological map of the Gaize-Nima area (see Fig. 1).

The igneous rock exposed on the surface in this area revealed that acidic rock is widely distributed in the Gangdise block, and sparsely distributed across the Qiangtang block and Bangongcuo-Nujiang suture zone. Intermediate rock is primarily distributed in the Gangdise block, and sparsely distributed in the Qiangtang block around Baiqing, there is no intermediate rock found in the Bangongcuo-Nujiang suture zone; basic rocks are dispersed across Nale-Chalicao and Yanhu in the Gangdise block, Gaize in the Bangongcuo-Nujiang suture zone, and the surrounding areas of Yagencuo, Baiqing in the Qiangtang block, and in areas near Changshanliang; while ultrabasic rocks are mainly distributed in South Gaize in the Gangdise block and Emule belt; it shows small areas of distribution in south Baiqing in Qiangtang block and no distribution in the Bangongcuo-Nujiang suture zone; ophiolite was found to be mainly distributed in Gaize-Laiduoqiangma and Songqin of the Bangongcuo-Nujiang suture zone, and present but not distributed in the Gangdise block and Qiangtang block. Acidic rocks consisted of: Neogene granite, Paleogene adamellite, Cretaceous adamellite, Cretaceous granodiorite, Cretaceous granite, Cretaceous granite-porphry, Cretaceous granodiorite porphyry, Jurassic granite; while intermediate rocks included: Cretaceous diorite-porphryrite, Cretaceous quartz diorite, Cretaceous monzodiorite, Jurassic quartz diorite, and Jurassic diorite; basic rocks consisted of: Neogene dolerite, Cretaceous gabbro, Jurassic dolerite, and Permian gabbro. Ultrabasic rocks and ophiolite were Jurassic.

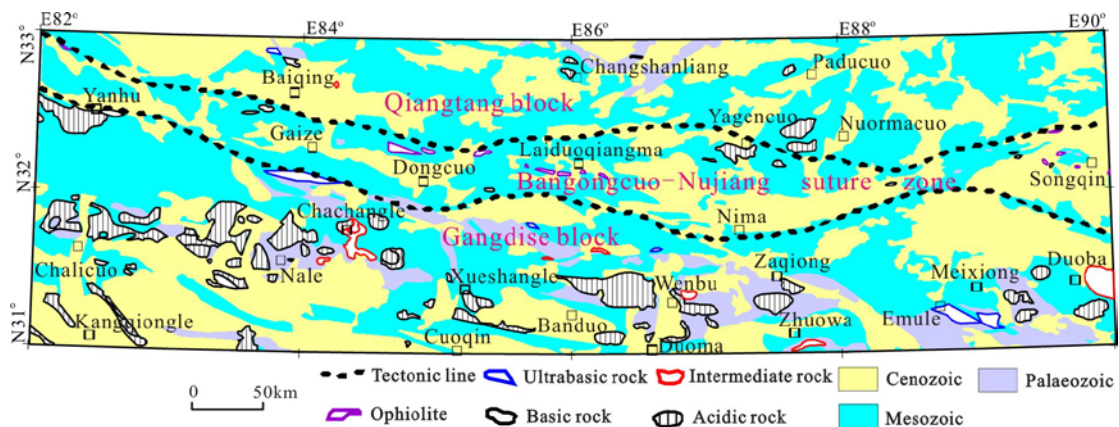


Fig. 1. Geologic sketch map of Gaize-Nima Area in Qinghai-Tibet plateau (modified after Geng et al., 2011 [21]).

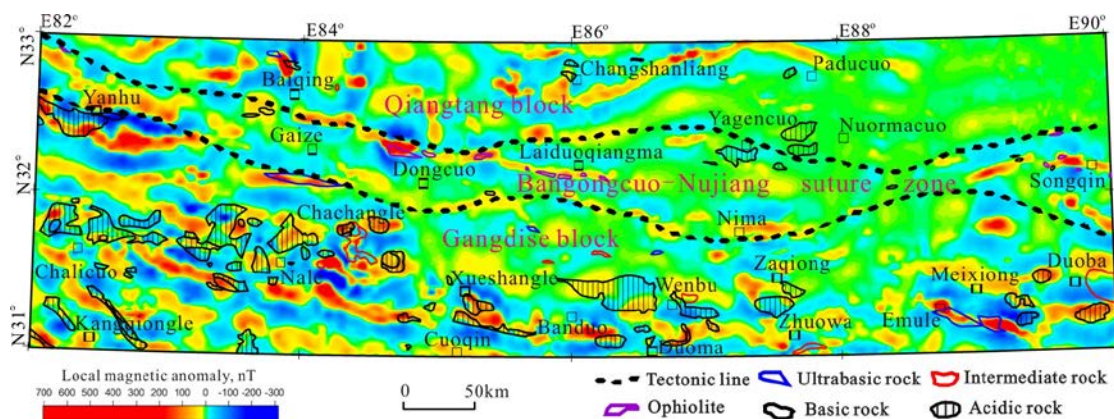


Fig. 2. Local magnetic anomaly map of Gaize-Nima Area in Qinghai-Tibet plateau.

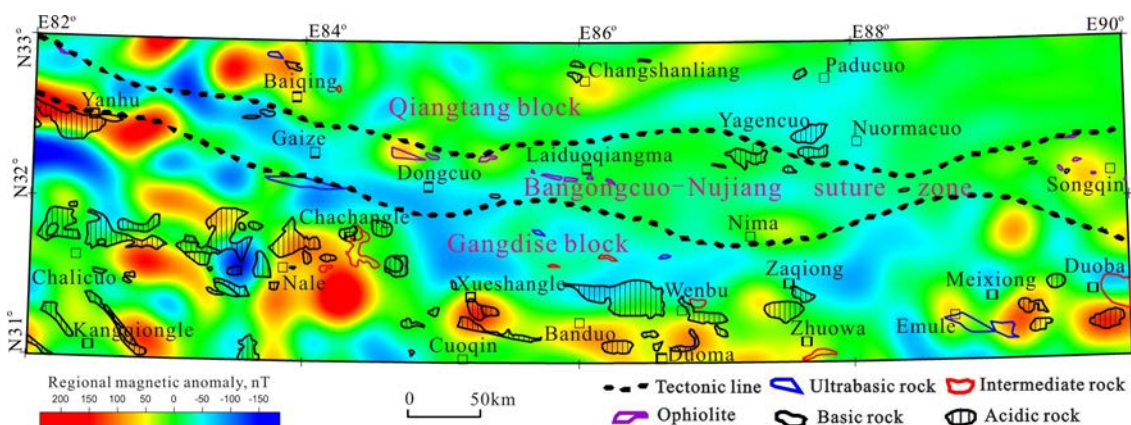


Fig. 3. Regional magnetic anomaly map of Gaize-Nima Area in Qinghai-Tibet plateau.

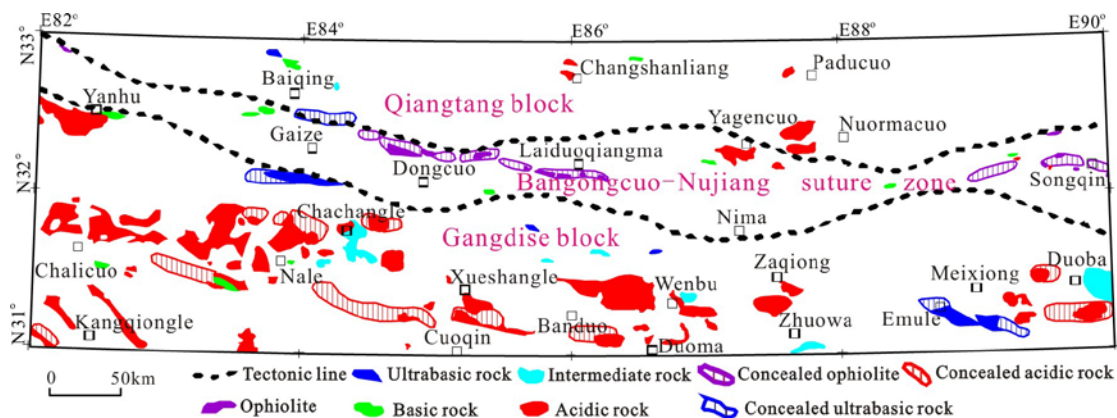


Fig. 4. The distribution map of igneous rocks of Gaize-Nima Area in Qinghai-Tibet plateau.

CHARACTERISTICS OF THE MAGNETIC FIELD

The magnetic inclination technique for the reduction to the Pole of magnetic anomalies was used to conduct the reduction to the pole of ΔT data and obtain aeromagnetic anomaly values. The time for calculating geomagnetic inclination and geomagnetism declination is 1995.00a. The mean height (4900 m) of this area was taken as the topographic height. The longitude to be calculated used the latitude of 86° for the central meridian of this area; the latitude interval for the reduction to the pole was 0.5° . LMA is able to reflect, primarily,

the effects of magnetic field induced by the local geological body; while RMA can present the effects of magnetic force and magnetic field resulting from large scale geological bodies. In this study, the mature filter regularization technique [22] was used to separate the aeromagnetic anomaly to obtain LMA and RMA. By processing the results obtained by repeated analysis and comparison through varying filter windows, the filter window for 40 km, which was in agreement with that of the ophiolite and ultrabasic rocks in this area, was chosen as the basic reference Figures for LMA and RMA.

As shown in the LMA (Fig. 2), LMA presented apparent zonation characteristics. Similar to the aeromagnetic anomaly, the LMA in the Qiangtang block was distributed into east and west blocks: the LMA in the former was moderate; while the that in the latter was well-developed. The high LMA in the Bangongcuo-Nujiang suture zone showed a zonal distribution, in particular it indicated a tenuous distribution in the Songqin and Laiduoqiangma; the LMA in the Gangdise block was high and developed in large areas in the Chalicuo-Cuoqin-Zhuowa-Duoba area. The LMA in the Qiangtang block did not agree well with the distribution trend of the aeromagnetic anomaly: the high LMA in the zone adjacent to the north boundary of the Bangongcuo-Nujiang suture zone was generally distributed in agreement with the fault, and this showed that it was influenced by the fault. The high LMA in the Qiangtang block in East Baiqing was shown to be distributed in a South-North trend. The LMA in the Changshanliang-Paducuo zone presented a strip distribution owing to the effect of the magnetic materials in the formation. In addition, much the same as the characteristics of the aeromagnetic anomaly, the high LMA distribution in the Bangongcuo-Nujiang suture zone was subject to the faulting on its south and north boundaries. The LMA in the Gangdise block is shown in the east, middle, and west zones respectively. Its distribution in the west zone, involving Chalicuo-Nale-Duoma, generally showed a NWW tendency; while the Zaqiong-Emule area exhibited a North-West trend. This phenomenon differed from that of the LMA in the east and west sides. Besides, East Duoba showed an East-West tendency.

As shown in the RMA (Fig. 3), the zonal distribution in a North-South trend was obvious. The areas in the Qiangtang block (Baiqing and Changshanliang) showed a high RMA; while that in the Baiqing-Changshanliang, and Nuormacuo, zones was low; the RMA in the Bangongcuo-Nujiang suture zone was low from a macro-perspective; however Dongcuo, Nima, and Songqin showed a high RMA; in the Gangdise block, the RMA was shown in northern and southern areas: the high RMA in the former zones were shown in Chalicuo-Nale-Duoma-Duoba; while the low RMA in the northern zone was distributed in Chachangle-Dangqiong-Nouth Xiongmei.

Distribution and magnetic features of igneous rocks

In this research area, the relationship between the igneous rock exposed on the surface and the magnetic anomaly is shown in Fig. 2 and Fig. 3. As shown in Fig. 2, regardless of the influence of

RMA, the Jurassic ophiolite in the Bangongcuo-Nujiang suture zone, and the Jurassic ultrabasic rocks in the Gangdise block showed better correlation with the aeromagnetic anomaly compared with LMA. The igneous rocks exposed on the surface in many other zones agreed well with LMA, such as; the Cretaceous adamellite and Paleogene adamellite in the Duoba, the Cretaceous adamellite in Xueshangle, the Paleogene adamellite in Duoma, the Cretaceous granodiorite in Chachangle, the Cretaceous granodiorite and Neogene granite and Neogene dolerite in Nale, and the Jurassic quartz diorite in Wenbu. The igneous rocks exposed on the surface in some areas were uncorrelated with the trend in LMA, these included: the Cretaceous adamellite, Cretaceous granodiorite, and Cretaceous granite porphyry in the Kangqiongle, and the Jurassic granite in Changshanliang. As seen in Fig. 3, the igneous rocks exposed on the surface were usually found in the belt zones with high RMA, and were even exposed in large areas such as: the Yanhu, Chalicuo-Duoma, Emule-Duoba, Baiqing, Changshanliang, Songqin, and Dongcuo. Only in south Xiongmei, were the igneous rocks with high RMA not exposed on the surface, which suggested that the RMA in the area was influenced by magmatic activity.

There were 102 zones with exposed igneous rocks in the research area, among which, acidic rock occurred in 62 zones, intermediate rock in nine zones, basic rock in 12 zones, ultrabasic rocks in six zones, and ophiolite in 13 zones. The corresponding relationship between the igneous rock and magnetic anomaly suggested that: the Jurassic ophiolite and Jurassic ultrabasic rocks were both distributed in zones with high LMA, and coincided well therewith. This indicated that the ophiolite and ultrabasic rocks in the area showed stronger magnetism. Among the 12 zones with basic rock, five zones were found to be in locations with a high LMA; while there were only two zones showing good coincidence with high LMA, which revealed that the overall magnetism of the basic rock was relatively weak; for the nine zones with intermediate rock, there were two zones found in locations with high LMA, and only one zone indicating good correlation therewith. This phenomenon showed that the intermediate rock exhibited weak magnetism; in the 62 zones with acidic rock, there were 23 zones in places with a high LMA, and 18 zones coinciding well with a high LMA. These results indicated that the acidic rock had, in general, strong magnetism. In temporal sequence, the magnetism in the acidic rocks of the

Neogene and Jurassic was weak, while the acidic rocks of the Paleogene and Cretaceous were slightly stronger; the intermediate rocks of the Cretaceous and Jurassic both showed weak magnetism; the dolerite of the Neogene and Jurassic had strong magnetism; the magnetism of the gabbro from the Cretaceous and Permian was weak. The ultrabasic rocks, and ophiolite showed strong magnetic characteristics.

On the basis of the corresponding relationship of the igneous rock exposed on the surface in this area and the magnetic anomaly, this research speculated that the concealed igneous rocks and results were as shown in Fig. 4: the concealed Jurassic ophiolite belt (7 km wide and 177 km long) was discovered in the Gaize-Laiduoqiangma zone; while the concealed Jurassic ophiolite belt (8 km wide and 100 km long) was found in Songqin; in south Baiqing, the concealed Jurassic ultrabasic rocks (8 km wide and 42 km long) were discovered; moreover, the concealed Jurassic ultrabasic rocks (8 km wide and 66 km long), and the Jurassic ultrabasic rock belt (10 km wide and 82 km long) were found in south Gaize and Emule respectively. In addition, the concealed acidic rocks which were developed in different areas were discovered in areas such as: Duoba, Bangduo, North Cuoqin, Chachangle, West Nale, and West Kangqiongle.

CONCLUSIONS

(1) In the research area, ophiolite and ultrabasic rocks were characterised by strong magnetism; while basic, and intermediate, rocks were generally shown to have weak magnetism. Acidic rock primarily showed medium-strong magnetism.

(2) The rocks developed in this area involved acidic rocks from the Neogene and Jurassic, the intermediate rock was Cretaceous and Jurassic, the basic rock of the Cretaceous and Permian presented weak magnetism; while the acidic rocks of the Paleogene and Cretaceous, and the dolerite of the Neogene and Jurassic, both showed stronger magnetism. Among them, the ultrabasic rocks and ophiolite of the Jurassic indicated the highest magnetism.

(3) In this area, there were two concealed Jurassic ophiolite belt zones: Gaize-Laiduoqiangma and Songqin; meanwhile, there were three groups of concealed belt zones of Jurassic ultrabasic rocks in South Baiqing, South Gaize, and Emule. Moreover, large areas of acidic rocks were found in other areas including: Duoba, Bangduo, North Cuoqin, Chachangle, West Nale, and West Kangqiongle.

Acknowledgements: This work is supported by Natural Science Basic Research Plan in Shaanxi Province of China (Program No. 2017JM4007). We are also grateful for the valuable comments of referees for improving the original manuscript.

REFERENCES

1. J. Yu, H. Lei, Q. Wang, C. Liu, *Xinjiang Petroleum Geology*, **24**, 509 (2003).
2. G. Pan, X. Mo, Z. Hou, D. Zhu, L. Wang, G. Li, Z. Zhao, Q. Geng, Z. Liao, *Acta Petrologica Sinica*, **22**, 521 (2006).
3. S. Cao, X. Luo, F. Tang, L. Chen, *Geology in China*, **31**, 51 (2004).
4. Z. Wu, P. Ye, C. Yin, *Geoscientia Sinica*, **34**, 31 (2013).
5. Z. Zhang, D. Liu, Q. Fan, Y. Duan, *Plateau Earthquake Research*, **20**, 54 (2008).
6. S. Jin, W. Wei, G. Ye, M. Deng, H. Tang, U. Martyn, *Chinese Journal of Geophysics*, **52**, 2666 (2009).
7. Q. Zhong, H. Fang, C. Liu, X. Li, J. Lu, B. Gao, *Geological Bulletin of China*, **29**, 870 (2010).
8. X. Mo, G. Dong, Z. Zhao, S. Zhou, L. Wang, R. Qiu, F. Zhang, *Geological Journal of China Universities*, **11**, 281 (2005).
9. B. Wang, J. Xu, Q. Zeng, Z. Kang, J. Chen, Y. Dong, *Acta Petrologica Sinica*, **23**, 1521 (2007).
10. S. Fan, R. Shi, L. Ding, D. Liu, Q. Huang, H. Wang, *Acta Petrologica et Mineralogica*, **29**, 467 (2010).
11. Y. Jiang, T. Xu, Y. Zhao, *Journal of Geomechanics*, **15**, 336 (2009).
12. S. Cao, Z. Wang, F. Luo, J. Huang, W. Xiong, *Acta Geologica Sinica*, **88**, 2018 (2014).
13. M. Jiang, H. Wang, *Geological Science and Technology Information*, **20**, 95 (2001).
14. F. Zhou, Z. Yao, Z. Liu, Y. Zhang, *Geophysical & Geochemical Exploration*, **26**, 12 (2002).
15. D. Xue, M. Jiang, L. Wu, Q. Li, X. Wang, *Geology in China*, **33**, 912 (2006).
16. R. He, R. Gao, H. Zheng, J. Zhang, *Chinese Journal of Geophysics*, **50**, 1131 (2007).
17. S. Xiong, Y. Ding, Z. Li, *Geological Review*, **58**, 201 (2012).
18. Z. Yao, F. Zhou, D. Xue, Z. Liu, Y. Zhang, *Geophysical & Geochemical Exploration*, **26**, 165 (2002).
19. S. Xiong, F. Zhou, Z. Yao, D. Xue, *Geophysical & Geochemical Exploration*, **31**, 404 (2007).
20. J. Lu, M. He, H. Fang, Y. Ye, Q. Zhong, B. Gao, *Geophysical & Geochemical Exploration*, **34**, 787 (2010).
21. Q. Geng, G. Fan, L. Wang, Z. Peng, Z. Zhang, *Geological Bulletin of China*, **30**, 1261 (2011).
22. Y. An, Z. Guan, *Computing Techniques for Geophysical and Geochemical Exploration*, **7**, 13 (1985).

Thermally induced pore pressure and consolidation volumetric strain for saturated soils

B. Bai^{1*}, S. Jiang¹

¹ School of Civil Engineering, Beijing Jiaotong University, Beijing 100044, PR China

Received June 19 2017, Revised July 20 2017

The aim of this paper is to experimentally investigate thermally induced pore pressure and subsequent consolidation volumetric strain. Studies show that normalized pore pressure tends to decrease with an increase in confining pressure and repeated thermal loading cycles. Test results from three typical soils all show that there are approximately linear relationships between consolidation volumetric strain and thermally induced pore pressure, which is influenced by the specimens' water content, confining pressure, and amplitude, and the number of thermal loading cycles applied. An equation for describing the pore pressure induced by temperature and confining pressures is proposed. Additionally, the relationship between consolidation volumetric strain and thermally induced pore pressure is established.

Key words: Thermal energy, Induced pore pressure, saturated soil, repeated thermal loading, Geo-environmental influence.

INTRODUCTION

Soil thermal properties are encountered in many engineering fields dealing with high-level nuclear waste isolation, waste containment facilities, gas pipelines, energy piles, electric transmission lines, thermal ground improvement techniques, etc. [1, 2]. Much effort has been made to model heat transfer through geomaterials with the help of experimental, analytical or numerical models [3]. Hüpers and Kopf [4] have discussed thermal influence on the consolidation state of oceanic sediments and its implications for excess pore pressure, with increasing temperature leading to an enhanced reduction in pore space. Due to the need for a barrier material in nuclear waste disposal repositories, Villar et al [5] experimentally investigated the dependence of the swelling strains of bentonite on temperature, the increase in permeability of water-saturated bentonite with increased temperature, water retention curves of bentonite compacted at different dry densities, among other effects. Bai and Chen [6] have discussed the degradation effect of saturated clay subjected to cyclic thermal loading using a temperature-controlled triaxial apparatus.

The temperature increases in saturated porous materials under undrained conditions may lead to thermal pressurization of the pore fluid. This increase in the pore fluid pressure induces a reduction of the effective mean stress, and can lead to shear failure or hydraulic fracturing. Khalili et al [7] have presented a non-isothermal constitutive relation for a saturated porous material, derived a

closed-form solution for the heat-induced pore pressure, and examined the validity of the theoretical assertions through a targeted program of laboratory testing as well as data from the literature. Ghabezloo and Sulem [8] believe that the thermally induced pore pressure is determined by the discrepancy between the thermal expansion of the pore fluid and of the solid phase, the stress-dependency of the compressibility and the non-elastic volume changes of the porous material. Monfared et al [9] have discussed the thermal pore pressure of low-permeability argillites using a hollow cylinder triaxial cell. Yilmaz [10] has investigated the thermal impact on particle size, water content, specific gravity, plasticity, activity index, swelling characteristics, compression index and strength properties, specifically for kaolinite and bentonite.

The thermal behavior of soils, including pore pressure and thermal deformation, is a function of mineralogical composition, porosity, pore fluid, degree of saturation, water content, range of temperature change, state of stress, and other factors [11]. Laloui and Cekerevac [12] have discussed the combined effects of some factors in both drained and undrained conditions. Ouhadi et al [13] have investigated the impact of temperature on the re-structuring of the soil microstructure, as well as its geotechnical and geo-environmental influences on smectite behavior. However, the thermal behaviors of soils are not yet completely understood in extant literatures. For instance, the undrained thermal pressurization coefficient differs by two orders of magnitude in some studies [14, 15].

* To whom all correspondence should be sent:

E-mail: baibing66@263.net

At present, reliable assessment methods for pore pressure induced by heating and subsequent consolidation deformation due to dissipation of the pore pressure are scarce. In this study, thermally induced pore pressure and subsequent consolidation volumetric strain is experimentally investigated using three typical soils, and the influence factors such as specimens' water content, confining pressure, amplitude, and number of thermal loading cycles are discussed. Finally, methods for describing the pore pressure and consolidation volumetric strain with pore pressure are proposed.

TEST DESCRIPTIONS

Test soils

This test includes three types of soils. The physical properties are as follows: soil 1 is a silty clay, with specific gravity $G_s=2.71$, plastic limit $w_p=17.6\%$, liquid limit $w_L=31.4\%$, and plasticity index $I_p=13.8$; soil 2 is a clay, with $G_s=2.71$, $w_p=15.8\%$, $w_L=34.9\%$, and $I_p=19.1$; soil 3 is a red clay, with $G_s=2.74$, $w_p=39.2\%$, $w_L=71.8\%$, $I_p=32.6$. These soils were chosen for analysis because they have very distinct plasticity indexes. Soil 1 (silty clay) and soil 2 (clay) were taken from Beijing, China, and soil 3 (red clay; i.e., laterite) was taken from Guangxi, China. To obtain uniform samples, air-dried sediments were ground to soil fines that could pass through a 0.5 mm sieve. The soils were mixed to predetermined initial water contents and stored in a plastic container. After at least 24 hours, the sample was taken out and poured into a cylindrical specimen mold. The prepared specimens were 3.91 cm in diameter and 8 cm in height. Next, the molds, together with the specimens, were placed in a large vessel for saturation by vacuum pump for at least 6 hours, and finally were immersed in distilled water for testing.

In all of the tests, vertical strips of filter paper were placed on the sides of the specimen to speed up the consolidation. Additionally, filter paper discs were positioned on the top and bottom of the soil specimens to prevent particles from being forced into the pores of the porous stones placed on the specimen ends. Before this, the porous stones were kept in distilled water and then boiled for sufficient time to reach saturation.

Test apparatus

Tests were performed using a triaxial shear device modified for the thermal loading application, which was described in reference [6]. The temperature inside the pressure chamber can vary in the 20 °C-100 °C range, controlled by an electro-

thermal belt inside the metallic hollow sleeve of the chamber, which is connected to a thermocouple. The precision of the thermo-controller system is ± 0.1 °C. The pore pressure was measured through a porous stone at the bottom center of the specimens, using a pore pressure transducer (measuring range: 0-1 MPa) connected to a digital monitoring apparatus. Pore pressure measurement was resolved to 0.1 kPa. The confining pressure was also monitored and controlled using a pressure transducer (measuring range: 0-1 MPa) attached to the bottom of the pressure chamber by another digital monitoring apparatus.

Test methods

Table 1 gives the test schemes (cases 1, 2, 3 and 4), the brief descriptions of which are as follows:

Case 1 and 2

For soil 1 (the remolded saturated silty clay), several undrained heating tests are conducted. This scheme includes two water content levels ($w=25.1\%$ and 22.1% ; Case 1 and 2 in Table 1, respectively), three confining pressures ($\sigma'_3=50$, 100, and 150 kPa), six heating-cooling cycles and two thermal loading amplitudes ($\theta=25$ °C and 50 °C). The thermal loading amplitude is expressed here as $\theta=T-T_0$, where T and T_0 are the current and initial temperatures, respectively.

The specimens were isotropically consolidated under different effective confining pressures at a primary temperature of $T_0=25$ °C. With the completion of the isotropical consolidation, the specimens were then subjected to six heating-cooling cycles, with each cycle ($N=1, 2, 3, 4, 5, 6$) consisting of undrained heating from the primary temperature of 25 °C to a higher temperature of 50 °C, isothermal consolidation at the elevated temperature of 50 °C, undrained cooling from 50 °C to 25 °C, and isothermal consolidation (a drainage or water-absorbing process) at the original temperature of 25 °C. This composed a single cycle of the heating-cooling process. Next, the heating-cooling process was repeated.

Case 3

For soil 2 (i.e., the remolded saturated clay), specimens were isotropically consolidated under various effective confining pressures σ'_3 ($\sigma'_3=50$, 100, and 150 kPa) at a primary temperature of $T_0=20$ °C, and then heated to a higher temperature in two steps (20 °C→50 °C→80 °C) under undrained conditions. The specimen temperature is then lowered again in two steps (80 °C→50 °C→20 °C). During heating and cooling, the

specimens are not allowed to dissipate; the specimens are heated to a given higher temperature (50 °C or 80 °C), and then allowed to consolidate (a drainage or water-absorbing process). After this, the heating-cooling process was repeated a second and third time.

Case 4

For soil 3 (the remolded red clay), specimens were isotropically consolidated under the effective confining pressure of $\sigma'_3=50$ kPa and primary temperature $T_0=20$ °C, and then heated to a different higher temperature ($T=40, 50, 60, 80, 90$ °C; see Table 1) under undrained conditions. The specimens were then allowed to consolidate.

THERMALLY INDUCED PORE PRESSURES

Pore pressure during repeated undrained heating

Figure 1 gives the relationship between normalized pore pressure u/σ'_3 and temperature T for three confining pressures ($\sigma'_3=50, 100,$ and 150 kPa) during repeated undrained heating and cooling when $\theta=25$ °C and $\theta=50$ °C, respectively. Test results show that the normalized pore pressure increases as the temperature of the specimen increases during undrained heating. Generally, the normalized pore pressure decreases with the increase in confining pressure, which can be seen in comparisons between Fig. 1(a), (b), and (c) or Fig. 1(d), (e), and (f). Additionally, the pore pressure appears to degrade with increasing temperature cycles ($N=1, 2, 3, 4, 5$ and 6). With the increase in confining pressure and repeated thermal loading cycles, the ranges of variation of pore pressure

narrow during subsequent heating and cooling processes, which reflects an “aging effect” of saturated soils due to heating. At this time, the soils will show an over-consolidated state. In other words, the specimens initially exhibit an obvious un-recovered thermo-mechanical process at a normally consolidated or lightly over-consolidated state, and eventually transition to a recovered thermo-elastic response at a heavily over-consolidated state with cyclic thermal loading.

It should be noted that with increasing temperature, the thermal pore pressure takes on a complicated non-linear evolution process, which is closely related to the physical properties of the soil, confining pressure, number of thermal loading cycles, and the overconsolidation ratio of the soil. When the specimen temperature is lower ($T<50$ °C; see Fig. 1(a), (b), (c)), the undrained thermal pressurization coefficient, defined as the pore pressure variation due to a unit temperature variation in the undrained condition, increases with the increase in temperature; however, under a higher temperature and a lower confining pressure ($T>60$ °C and $\sigma'_3=50$ kPa; see Fig. 1(d)), the undrained thermal pressurization coefficient initially increases and then gradually begins to decrease.

On the other hand, the pore pressure decreases during undrained cooling processes ($50\rightarrow25$ °C in Fig. 1), and the undrained thermal pressurization coefficient also decreases. The shape of the temperature evolution is similar to the following heating processes.

Table 1. Test schemes

| Case | Soil | Water content $w(\%)$ | Dry unit weight γ_d (kN/m ³) | Void ratio e | Degree of saturation S_r (%) | Primary temperature T_0 (°C) | Confining pressure σ'_3 (kPa) | Repeated number N | Temperature variation (°C) | Temperature variation of the second step(°C) |
|------|---------------|-----------------------|---|----------------|--------------------------------|--------------------------------|--------------------------------------|---------------------|----------------------------|--|
| 1 | 1, silty clay | 25.1 | 15.5 | 0.70 | 96.9 | 25 | 50 | 6 | 25→50 | |
| | | | | | | | 100 | 6 | 25→50 | |
| | | | | | | | 150 | 6 | 25→50 | |
| 2 | 1, silty clay | 22.1 | 16.5 | 0.61 | 97.8 | 25 | 50 | 6 | 25→75 | |
| | | | | | | | 100 | 6 | 25→75 | |
| | | | | | | | 150 | 6 | 25→75 | |
| 3 | 2, clay | 29.7 | 15.1 | 0.85 | 95.1 | 20 | 50 | 3 | 20→50 | 50→80 |
| | | | | | | | 100 | 2 | 20→50 | 50→80 |
| | | | | | | | 150 | 2 | 20→50 | 50→80 |
| | | | | | | | 50 | 1 | 20→40 | |
| | | | | | | | 50 | 1 | 20→50 | |
| 4 | 3, red clay | 47.0 | 11.9 | 1.25 | 99.2 | 20 | 50 | 1 | 20→60 | |
| | | | | | | | 50 | 1 | 20→80 | |
| | | | | | | | 50 | 1 | 20→90 | |
| | | | | | | | 50 | 1 | 20→90 | |

Pore pressure during two steps of undrained heating

The relationship of normalized pore pressure u/σ'_3 with the temperature of the clay (soil 2 in Table 1) for three confining pressures ($\sigma'_3=50, 100,$ and 150 kPa) during two steps of undrained heating is also analyzed, and exhibits a pattern similar to that of the silty clay under repeated undrained heating (case 1 and case 2). In reality, the pore pressure induced by the second process of heating ($50 \rightarrow 80$ °C) still reaches a higher temperature (e.g., when $\sigma'_3=50$ kPa, $u/\sigma'_3=0.84$) although the specimens take on a slightly over-consolidated state due to having undergone a step of heating ($20 \rightarrow 50$ °C) and corresponding isothermal consolidation. The maximum pore pressure induced by the two steps of heating with isothermal consolidation between steps is lower than that induced by a single heating step ($20 \rightarrow 80$ °C) without the consolidation process.

Pore pressure of a red clay during undrained heating

For the red clay (soil 3 in Table 1), the pore pressure induced by heating also initially increases rapidly, subsequently reaching a higher value, and gradually assumes a steady state. Finally, the maximum normalized pore pressure reaches $u/\sigma'_3=0.94$ at a temperature of $T=90$ °C, which means that the shear strength of the specimen nearly fails. It appears that the undrained thermal pressurization coefficient of the red clay (soil 3) is greater than that of the silty clay (soil 1) due to higher water content ($w=47.0\%$ and 22.1% , respectively, for soil 3 and soil 1). For example, when $\sigma'_3=50$ kPa and $T=50$ °C, the normalized pore pressure of the red clay and the silty clay are $u/\sigma'_3=0.65$ and $u/\sigma'_3=0.48$, respectively.

Relationship between thermally induced pore pressures and temperature

The test results of the three soils show that the relationship between normalized pore pressure and temperature can be described by the following equation:

$$\frac{u}{\sigma'_3} = 1 - \frac{1}{1 + \exp^{(T-\alpha)/\beta}} \quad (1)$$

where T is the current temperature, and α and β are fitting parameters which determine the shape of the fitting curve.

The relationship given by Eq. (1) can be obtained using Matlabsoftware, a mathematical optimization analysis software package.

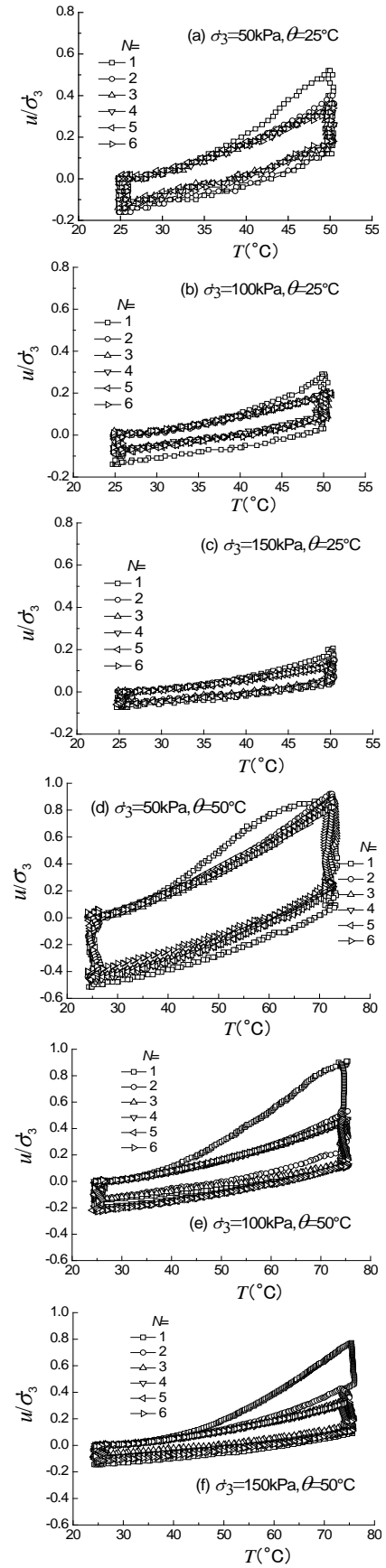


Fig. 1. Normalized pore pressure vs. temperature for various confining pressures and various temperature amplitudes.

Generally, optimization analysis is performed using the least squares method. Figure 2(a) illustrates the fitting relationship of the silty clay (soil 1) for case 2 when $N=1$, which shows that the evaluated results are in good agreement with the test data.

Here, when $\sigma'_3=50, 100, \text{ and } 150 \text{ kPa}$, then $\alpha=50.59, 58.15, \text{ and } 64.39$; $\beta=8.20, 8.84, \text{ and } 9.63$; and the coefficient of determination is $R^2=0.994, 0.997, \text{ and } 0.999$, respectively.

Parameters α and β are both linear with confining pressure, and can be written as

$$\alpha = a\sigma'_3 + b \quad (2)$$

$$\beta = c\sigma'_3 + d \quad (3)$$

where a, b, c and d are the parameters of soil properties.

Here, $a=0.138, b=43.910, c=0.014$ and $d=7.461$. The coefficients of determination are $R^2=0.997$ and 0.996 , respectively, for α and β .

Figure 2(b) illustrates the fitting curve for the red clay (soil 3), which also shows that the evaluated results agree with the test data. Here, $\alpha=44.59$ and $\beta=8.87$, and the coefficient of determination $R^2=0.982$.

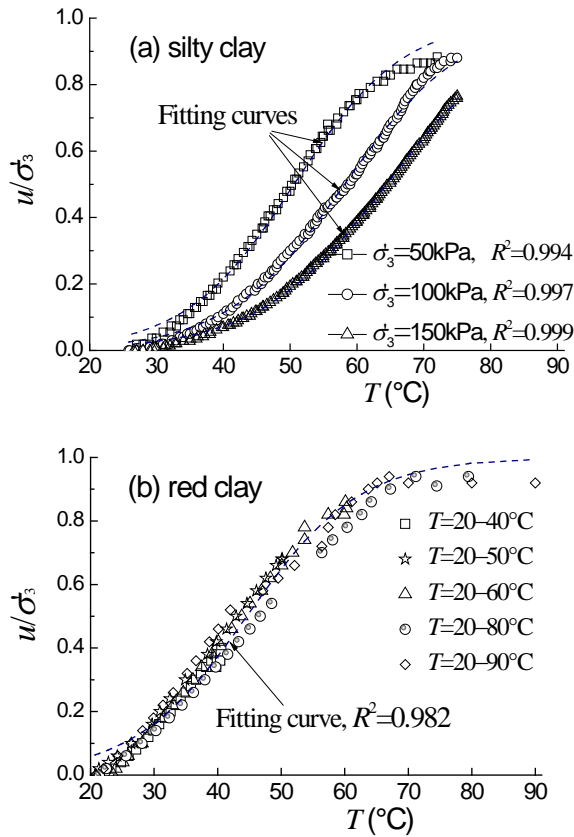


Fig. 2. Comparisons of evaluated pore pressure with measured values

Thermal consolidation volumetric strain

Figure 3 gives the fitting relationship between consolidation volumetric strain and thermally induced pore pressure for soils 1, 2 and 3 (see Table 1). Here, the consolidation volumetric strain is defined by $\varepsilon_v = \Delta V/V_0$, expressed as a percentage, with V_0 and ΔV being the specimen volume before consolidation and the amount of outflow pore water (both measured at primary temperature T_0), respectively.

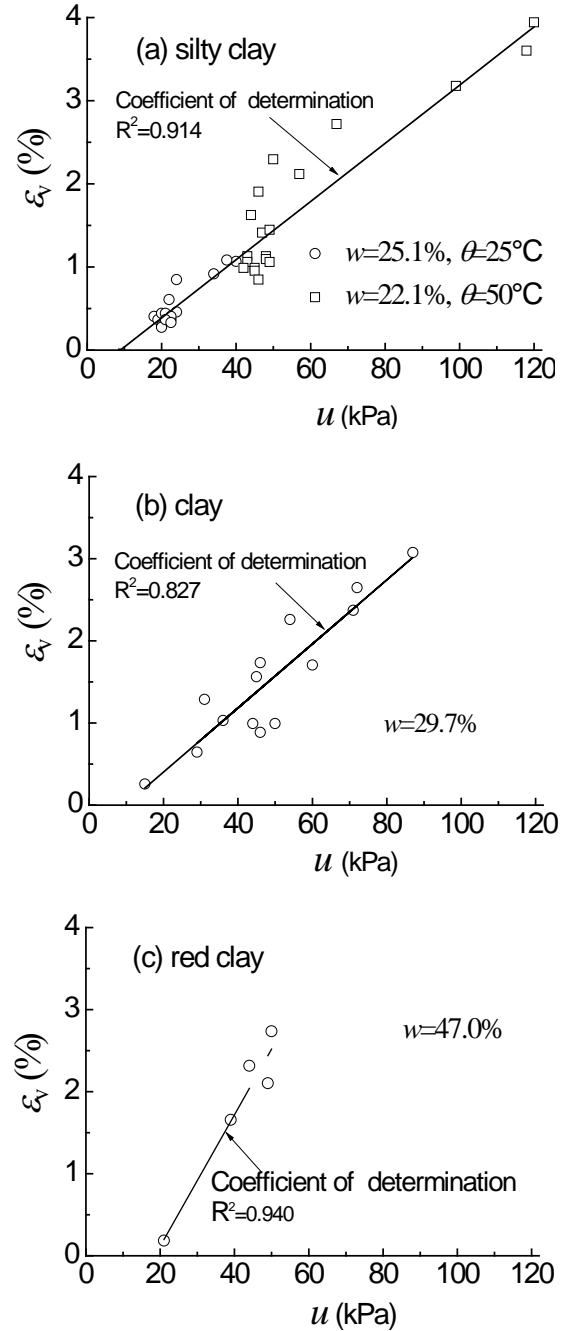


Fig. 3. Relationship between consolidation volumetric strains and pore pressure

Figure 3 shows that there are approximately linear relationships between volumetric strain and pore pressure, which is influenced by the specimens' water content, confining pressure, amplitude, and number of applied thermal loading cycles. The relationship is expressed as

$$\varepsilon_v = k(u - u_0) \quad (4)$$

where ε_v is the consolidation volumetric strain; u is the pore pressure induced by heating; and k and u_0 are fitting parameters.

For the silty clay, the obtained fitting parameters are $k=0.035$, $u_0=8.91$ and the coefficient of determination $R^2=0.914$ (Fig. 3(a)); for the clay, $k=0.039$, $u_0=9.67$ and $R^2=0.827$ (Fig. 3(b)); and for the red clay, $k=0.080$, $u_0=18.51$ and $R^2=0.940$ (Fig. 3(c)). In fact, the parameter k reflects the degree of variation in the amount of thermally induced volumetric strain. On the other hand, the parameter u_0 in Eq. (4) indicates an initial pore pressure. Figure 3 appears to show that the soils with a higher plasticity index or higher water content (for soil 3, $I_p=32.6$, $w=47.0\%$) have greater thermal consolidation volumetric strain (i.e., a greater parameter k) than the soils with a lower plasticity index (e.g., for soil 1 and 2, $I_p=13.8$ and 19.1 , respectively; $w=22.1-25.1\%$ and $w=29.7\%$).

CONCLUSION

(1) Generally, the normalized pore pressure increases as temperature increases, and decreases with the increase in confining pressure and repeated thermal loading cycles.

(2) Test results show that there are approximately linear relationships between consolidation volumetric strain and thermally induced pore pressure, which is influenced by the specimens' water content, confining pressure, amplitude and number of applied thermal loading cycles.

(3) An equation for describing the pore pressure induced by temperature and confining pressures is

proposed. Additionally, the relationship between consolidation volumetric strain and thermally induced pore pressure is established

Acknowledgements: This work is financially supported by the National Natural Science Foundation of China (51678043; 51478034), to which the authors are very grateful.

REFERENCES

1. R.B. Hetnarski, J. Ignaczak, *Journal of Thermal Stresses*, **16**, 473 (1993).
2. H.R.Thomas, H.T. Yang, Y. He, P.J. Cleall, *International Journal for Numerical and Analytical Methods in Geomechanics*, **27**, 951 (2003).
3. H. Brandl, *Geotechnique*, **56**(2), **81**, 122 (2006).
4. A. Hüpers, A.J. Kopf, *Earth and Planetary Science Letters*, **286**, 324 (2009).
5. M.V. Villar, R. Gomez-Espina, A. Lloret, *Journal of Rock Mechanics and Geotechnical Engineering*, **2**(1), 71 (2010).
6. B. Bai, X. Chen, *Journal of Geotechnical Engineering*, **33**(10), 1 (2011).
7. N. Khalili, A. Uchaipichat, A.A. Javadi, *Mechanics of Materials*, **42**, 593 (2010).
8. S. Ghabezloo, J. Sulem, *Italian Geotechnical Journal*, **1**, 29 (2010).
9. M. Monfared, P. Delage, J. Sulem, M. Mohajerani, A.M. Tang, E. De Laure, *International Journal of Rock Mechanics and Mining Sciences*, **48**, 637 (2011).
10. G. Yilmaz, *Scientific Research and Essays*, **6**(9): 1928 (2011).
11. H.M. Abuel-Naga, D.T. Bergado, A. Bouazza, *International Journal of Geomechanics*, **8**(2), 114 (2008).
12. L. Laloui, C. Cekerevac, *Computers and Geotechnics* **30**, 649 (2003).
13. V.R. Ouhadi, R.N. Yong, A.R. Goodarzi, M. Safari-Zanjani, *Applied Clay Science*, **47**, 2 (2010).
14. R.G. Campanella, J.K. Mitchell, *Journal of Soil Mechanics and Foundation Engineering Division*, **94**(3), 709 (1968).
15. V.V. Palciauskas, P.A. Domenico, *Water Resources Research*, **18**(2), 281 (1982).

The water storage capability and hydraulic conductivity of different expansive soils

Z.J. Dai*, S.X. Chen, J. Li

State Key Laboratory of Geomechanics and Geotechnical Engineering, Institute of Rock and Soil Mechanics, Chinese Academy of Sciences, Wuhan, China

Received June 26 2017, Revised July 20 2017

For the strong and medium expansive soils of the middle-route of South-to-North Water Transfer Project, pressure plate tests and double-ring infiltration tests were carried out. The water storage capability, its influence factors and the evolution of hydraulic conductivity was comparative studied on different expansive soils. The results show, the soil with stronger expansion potential, higher fine grain content and higher dry density has better water retention capability. Saturated permeability coefficient of strong expansive soil is low, and it decreases with the increase of dry density. Unsaturated hydraulic conductivity, which has power function relationship with matrix suction, decreases with the decrease of the moisture content.

Key words: Expansive soil, Water storage capability, Unsaturated soil, Hydraulic conductivity.

INTRODUCTION

Unsaturated expansive soil is a special soil, which contains a large number of hydrophilic clay minerals. The change in moisture content of expansive soil is the factor determining its deformation and reduction in strength, and it is also an important factor for geological disasters. So, expansive soil is particularly a major problem faced by engineering geologist in the construction of water conservancy projects.

Soil-water characteristic curve (SWCC) is an important method used in describing unsaturated soil water retention characteristics, many hydraulic parameters showing the relationship between matric suction and the water storage state of unsaturated soil can be obtained using SWCC [1-2]. Currently, there are a variety of models to describe the soil-water characteristic curve, such as Garden model [3], Brook and Corey model [4] with characterization of effective saturation, the Van Genuchten models [5] and Fredlund and Xing model [6] with characterization of volumetric water content. For the expansive soil water storage properties, studies were carried out from different angles, and achieved certain results [7-10]. At present, the research on the soil water storage are mainly concentrated on clayey soil, loess, silt and, weak and medium expansive soil, but very little for strong expansive soil.

In this paper, for the different expansive soil of the middle route of South-to-North Water Transfer Project, pressure plate tests and double-ring infiltration tests were carried out, and the same tests for medium expansive soil were taken for

comparative study. According SWCC, the water storage capability and its influence factors, including physical properties, mineral composition and structure characteristics for different expansive soils were studied. Water volume change coefficient and variation characteristics of the hydraulic conductivity were discussed, and the regularity of the penetration characteristics was studied. It can provided the calculation parameters for disaster prevention and control.

EXPERIMENTAL

Materials

The soil samples were taken from the channel of the middle route of South-to-North Water Transfer Project. Strong and medium expansive soils were selected from TS95 channel bottom yellow-green clay and TS106 channel slope tan clay.

Table 1. Physical properties of expansive soil

| Expansive soil | Moisture content (%) | Density (g/cm ³) | Liquid limit (%) | Plastic limit (%) | Free expansion ration (%) |
|----------------|----------------------|------------------------------|------------------|-------------------|---------------------------|
| Strong | 27.77 | 1.94 | 89.03 | 29.30 | 109 |
| Medium | 25.85 | 1.94 | 59.54 | 27.12 | 69 |

Table 2. Mineral composition

| Expansive soil | Mineral composition (%) | | | | |
|----------------|-------------------------|--------|-----------|------------------------|---------------------------|
| | Montmorillonite | Illite | Kaolinite | Illite-montmorillonite | Kaolinite-montmorillonite |
| Strong | 19.62 | 9.63 | - | 13.55 | 1.73 |
| Medium | 8.23 | 7.25 | 1.66 | 1.24 | 1.91 |

Table 1 shows the results of basic physical properties of each sample based on laboratory soil tests. Table 2 shows the results of the identification of the mineral composition of each sample by X-

* To whom all correspondence should be sent:
E-mail: daij0078@163.com

ray diffraction test using D8 Advance X-ray diffractometer.

Test methods

Soil-water characteristic curves of soil samples are obtained from the pressure plate test. The pressure plate apparatus are made in the United States Soil Moisture company (see Fig.1), and the clay plate intake is 15 bar. The test environment is a room temperature of 20 °C, and the test plan is shown in Table 3.

Each sample is saturated and weighed by vacuum saturation method at first, and then the sample is placed on clay board in a pressure cooker before installing and connecting the instrument and adjusting the sample chamber pressure. Sample should be weighed every 12 to 24 hours until the mass change less than 0.01 g within 24 h, which can be considered to achieve balance, then the next pressure level measurement can be continued. The test pressure series is 0.2, 0.5, 1, 2, 4, 7, 10, 13 bar. When the final pressure equilibrium, the samples should be placed in environment with 105 °C for drying to constant weight before weighing the mass of dry soil.



Fig. 1. Pressure plate test device

Table 3. Test plan of pressure plate test

| Soil type | Dry density (g/cm ³) | Number of tests |
|-----------------------|----------------------------------|-----------------|
| Strong expansive soil | 1.51 | 1 |
| | 1.53 | 1 |
| Medium expansive soil | 1.49 | 1 |
| | 1.53 | 1 |

Double-ring infiltration test is commonly used to determine the stable water infiltration rate of the soil. The test devices are primarily stylus, the inner and outer ring with 30cm in height, 26.2 cm and 47 cm in diameter (see Fig.2).

According to the situation, graduated cylinder is used to replace the flow bottle to put water to the two rings. During the test, it must to maintain the inner and outer ring water level. When the water surface drops after the needle tip during infiltration, a certain amount of water (100 to 200 mL) should

be put into the inner ring before recording the time until infiltration speed is stable.

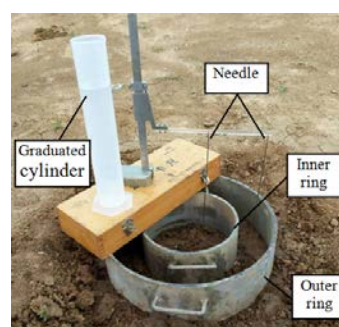


Fig. 2. Double-ring infiltration test device

Field test site is located in Nanyang segment of the main canal. Mainly Quaternary reddish brown - brick red, brown clay and silty clay, containing Calcareous and Ferromanganese concretions in the formation of leaching by groundwater. The reddish brown - brick red clay contains many vertical fissures, filled with the gray clay with strong expansion, such a clay overall is strong - medium expansive soil. However, the brown clay and silty clay contain extensive internal irregular meshed fracture, the soils always are weak - medium expansive soils. Engineering geological conditions of typical test points are shown in Table 4.

Table 4. Engineering geological conditions of typical test points

| Location | Depth (m) | Density (g/cm ³) | Moisture content (%) | Free expansion ration (%) | Swelling potential * |
|----------|-----------|------------------------------|----------------------|---------------------------|----------------------|
| TS102 | 10 | 1.96 | 19.82 | 63 | W |
| TS102 | 6 | 1.96 | 16.09 | 70 | M- |
| TS102 | 6 | 1.91 | 17.94 | 73 | M |
| TS105 | 4 | 2.04 | 20.95 | 71 | M |
| TS105 | 15 | 2.08 | 16.72 | 86 | M+ |
| TS105 | 15 | 2.05 | 18.54 | 90 | S |
| TS105 | 5 | 2.03 | 19.37 | 77 | M |
| TS105 | 3 | 2.05 | 18 | 85 | M+ |
| TS95 | 9 | 2.03 | 21 | 93 | S |

* W/M-/M/M+/S are respectively weak / weak-medium / medium / medium-strong / strong.

RESULTS AND DISCUSSION

SWCC characteristics and its influencing factors

Fig. 3 shows the soil water characteristic curve of expansive soils. SWCC of strong expansive soil is located above that of the medium expansive soil, with matric suction increasing, the saturation of strong expansion soil changes slower.

Analyzing from the physical properties of soil, the sample with stronger swelling potential and higher plasticity index contents more fine particles

and it has larger specific surface area and bound water content, and the slower rate of dehydration.

Analyzing from the mineral composition of soil, Table 2 shows that clay mineral (montmorillonite, illite, etc.) content of the strong expansive soil is greater than 30%, and no amount of water molecules can be absorbed between montmorillonite unit cells, therefore, strong expansive soil has better water retention capacity and slower dehydration rate.

For the samples with the same swelling potential, SWCC of the one with greater dry density is located in the top. With the increasing of matric suction, saturation of expansive soil with greater dry density changes slower and also the rate of dehydration. This is because soil samples with greater dry density has higher density and smaller internal pore structure, the drainage channel of which is limited when matric suction increases.

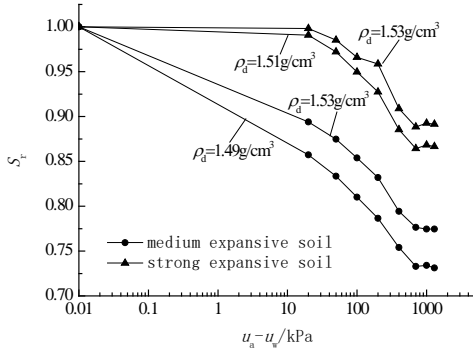


Fig. 3. SWCC of expansive soil with different dry densities

SWCC mathematical model

The result of soil moisture content in different matric suction obtained by the pressure plate test is a series of discrete data points. SWCC model can be used to fit the points into a continuous function, which can be taken to calculate the parameters of the non-saturated water movement.

Van Genuchten model has the following expression [5]:

$$\theta(h) = \begin{cases} \theta_r + \frac{\theta_s - \theta_r}{[1 + |\alpha h_u|^n]^m} & (h < 0) \\ \theta_s & (h > 0) \end{cases} \quad (1)$$

Where θ_s and θ_r are saturated and residual moisture content (%), h_u is pressure head (mm), m and n are the empirical parameters, $m=1-1/n$.

Williams proposed model expression [11] is:

$$\ln s = a_1 + b_1 \ln \theta \quad (2)$$

Fredlund based on soil pore size distribution and statistical analysis theory, drawn Fredlund and Xing model [6], which is applicable to the whole suction range of various soils:

$$\begin{cases} \theta = \frac{C(s)\theta_s}{\{\ln[e + (s/a)^n]\}^m} \\ C(s) = \frac{1 - \ln(1 + s/s_r)}{\ln[1 + (10^6/s_r)]} \end{cases} \quad (3)$$

Based on the soil mass distribution and the fractal characteristics of pores, the researchers obtained the SWCC fractal model establishing on the fractal relationship between pore volume and pore size and Young-Laplace equation [12]:

$$\frac{\theta - \theta_r}{\theta_s - \theta_r} = (\varphi / \varphi_b)^{D_v - 3} \quad (4)$$

Through research and division of vapor form for the unsaturated soil, researchers found that the points of intake values and residual water content in Fredlund curve are approximately linear relationship [13], based on this, SWCC of the logarithmic equation form was proposed:

$$\frac{\theta - \theta_r}{\theta_s - \theta_r} = F(\varphi) = \frac{\lg \varphi_r - \lg \varphi}{\lg \varphi_r - \lg \varphi_b} \quad (5)$$

SWCC model fitting

In this paper, using Van Genuchten model, soil-water characteristic curves of expansive soils are fitted by the method of least squares, and fitting results and parameters are shown in Fig. 4 and Table 5. The saturated moisture content θ_s and the residual moisture content θ_r are measured by tests.

α is a scale parameter related to the average pore radius, it is about the reciprocal of air intake values. With the expansion potential enhancing, intake value increases, α is significantly reduced. Air intake value can be influenced by soil physical properties and mineral content, which has linear relationships with the plasticity index and the free expansion ratio (see Fig. 5).

Table 5. The fitting parameters of SWCC model

| Soil type | Fitting parameters | | | | |
|-----------------------|--------------------|----------------|-------------------------|--------|--------|
| | θ_s (%) | θ_r (%) | a (mm ⁻¹) | n | m |
| Strong expansive soil | 44.25 | 16.31 | 0.000213 | 1.0785 | 0.0728 |
| Medium expansive soil | 44.27 | 11.93 | 0.012852 | 1.0637 | 0.0599 |

The water volume change coefficient

In the dehumidifying process, the water volume change coefficient m_2^w reflects the dehydration rate changes. m_2^w is the rate of change of the volumetric moisture content with the matric suction changing, which can be used the following formula to determine [6].

$$m_2^w = -d\theta / d(u_a - u_w) \quad (6)$$

Pressure head h_u can be calculated by the equation 3.

$$h_u = (u_a - u_w) / (\rho_w g) \quad (7)$$

Where u_a and u_w are pore air pressure (kPa) and pore water pressure (kPa), ρ_w is the density of water (kg/m^3). Substituting equation 7 into equation 6

$$m_2^w = -d\theta / (\rho_w g dh_u) \quad (8)$$

m_2^w can be determined by SWCC model through substituting the Van Genuchten model equation 1 into equation 8

$$m_2^w = mna(\theta_s - \theta_r) |ah_u|^{n-1} / [\rho_w g (1 + |ah_u|^n)^{m+1}] \quad (9)$$

Water volume variation coefficients of different expansive soils can be calculated by equation 9, its relationship with the moisture content is shown in Fig. 6.

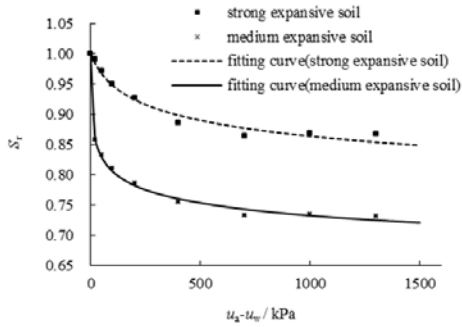


Fig. 4. Curve of SWCC model of expansive soil

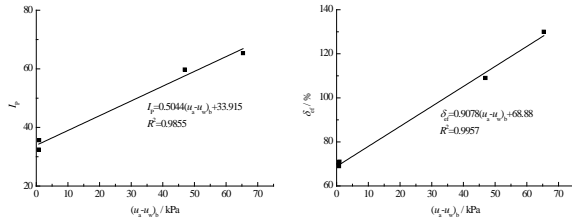


Fig. 5. Correlation between intake values and physical indicators

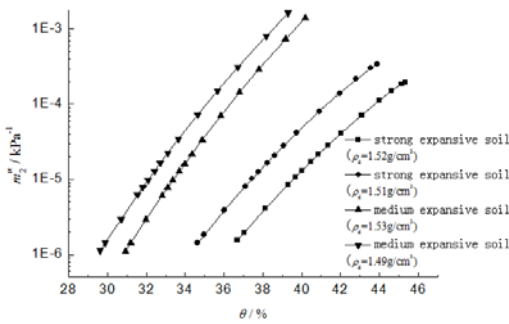


Fig. 6. Curve between m_2^w and water content

m_2^w of unsaturated expansive soil decreases with the decreasing of moisture content during the dewatering process. Strong expansive soil has gentle curve of m_2^w , which changes slowly with moisture content. The m_2^w of samples with greater dry density has smaller range of variation in the wet removal process.

Obtained by calculating, the water volume change coefficient of expansive soil has power function relationship with matrix suction.

Permeability coefficient calculation method

Unsaturated hydraulic conductivity is one of the key parameters during non-saturated soil water movement quantitative analysis. Under isothermal conditions, specific water capacity C_w reflects the quantitative relationship between matric potential and volumetric water content. C_w is the product of the water volume variation coefficient and water weight

$$C_w = m_2^w \rho_w g \quad (10)$$

Soil water diffusivity $D(\theta)$ is a necessary parameters to study water movement in soil, it is controlled by the physical and chemical properties of soil and other factors.

$$D(\theta) = k(\theta) \frac{-\partial(u_a - u_w)}{\partial \theta} \quad (11)$$

Based on the test results of a large number of studies, it is found that $D(\theta) = ae^{b\theta}$ can better describe the relationship between moisture content and $D(\theta)$ [14]. For expansive soil, $D(\theta)$ can be determined by equation 12 obtained by fitting the test results

$$D(\theta) = 7.67 \times 10^{-9} e^{14.493\theta} \quad (12)$$

Unsaturated hydraulic conductivity of expansive soil is the product of specific water capacity and soil water diffusivity

$$k_w = C_w D(\theta) = m_2^w \rho_w g D(\theta) \quad (13)$$

Saturated hydraulic conductivity characteristics

Fig. 7 shows the stable infiltration rates of different expansive soils testing by the double-ring infiltration test.

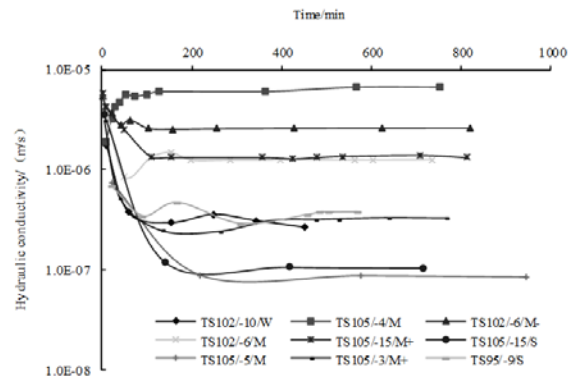


Fig. 7. Penetration time curve ('TS102/-10/W' represents 'Location/ Depth/ Swelling potential')

Infiltration of different types expansive soil is similar, it experiences constant penetration - deceleration penetration - steady penetration. Permeability is related to the swelling and fissured of expansive soils. Hydraulic conductivity decreases with the increase of the swelling potential. Fissures accelerate the water infiltration at the beginning.

Generally, Fig. 8 shows the infiltration rate of expansive soil tested by double-ring infiltration test. It requires a long time to achieve the steady infiltration for stronger swelling potential soil, which has smaller saturated permeability coefficient. k_s of medium expansive soil is the 10^{-7} m/s order of magnitude, and it is 10^{-8} m/s order of magnitude for strong expansive soil.

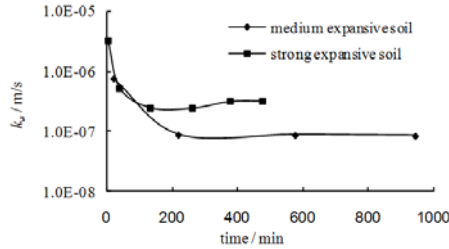


Fig. 8. Permeability coefficient change with time

Combined with the SWCC fitting formula and the water volume variation coefficient, Table 6 shows the saturated permeability coefficient of expansive soil with different dry density when saturation $S_r = 1$, which is calculated by the equation 13.

Table 6. Saturated permeability coefficient

| Expansive soil | Dry density (g/cm ³) | saturated permeability coefficient (m/s) |
|----------------|----------------------------------|--|
| Strong | 1.51 | 1.125×10^{-8} |
| | 1.53 | 7.072×10^{-9} |
| Medium | 1.49 | 9.290×10^{-7} |
| | 1.53 | 3.185×10^{-7} |

The calculation result is consistent with the in-situ test results. Saturated permeability coefficient of expansive soil is generally 10^{-7} - 10^{-9} m/s. The saturated permeability coefficient is smaller when the swelling potential is stronger. Influence of dry density is more significant, soil with greater dry density has smaller saturated permeability coefficient, and it often exhibits differences on the order of magnitude.

Unsaturated hydraulic conductivity characteristics

Fig. 9 shows the curve between unsaturated hydraulic conductivity and degree of saturation for typical expansive soil. It can be seen that the expansive soil saturated hydraulic conductivity decreases with the decrease of soil moisture content.

Fig. 10 shows the fitting curve of strong and medium expansive soils unsaturated hydraulic conductivity and matric suction, which shows a good fit power function. The empirical relationship and correlation coefficients are shown in Table 8. Unsaturated hydraulic conductivity decreases and its rate of change slow down with the increase of the matric suction. Known matric suction,

unsaturated hydraulic conductivity of typical expansive soil of South-to-North Water Transfer Project can be calculated, which provides the basic parameters for the simulation of seepage for moisture in the soil.

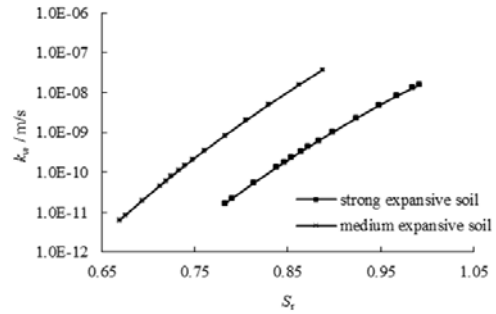


Fig. 9. Curve between unsaturated hydraulic conductivity and degree of saturation

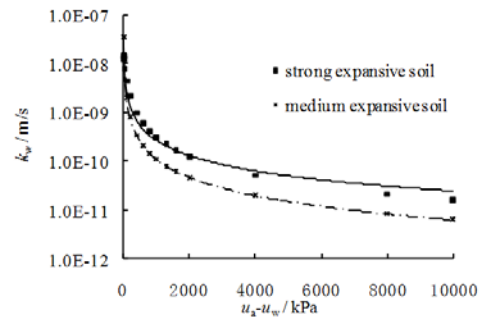


Fig. 10. Curve between unsaturated permeability coefficient and matric suction

CONCLUSION

Water storage capability of expansive soil is influenced by the physical properties, mineral composition and structure characteristics. The sample with stronger swelling contents more fine particles, it has slower dehydration rate, higher intake value and smaller storage coefficient. Soil samples with greater dry density have smaller internal pore structure, which exhibits stronger water storage capacity.

Water volume variation coefficients m_2^w of the unsaturated expansive soil decreases with the decreasing of moisture content. m_2^w of Strong expansive soil changes slowly with moisture content. The m_2^w of samples with greater dry density has smaller range of variation in the wet removal process.

Saturated permeability coefficient of expansive soil is generally 10^{-7} - 10^{-9} m/s. The saturated permeability coefficient is smaller when the swelling potential is stronger and dry density is greater. Unsaturated hydraulic conductivity, which has power function relationship with matrix suction, decreases with the decrease of the moisture content, and the rate of hydraulic conductivity

change decreases with the increase of matrix suction.

Acknowledgements: The research was supported by the National Natural Science Foundation of China (51579236).

REFERENCES

1. Z.Q. Li, R.L. Hu, L.C. Wang, Z.X. Li. *Rock and Soil Mechanics*, **27**(5), 730 (2006).
2. B. Bai, D.P. Liu. *Rock and Soil Mechanics* **27**(12), 2085 (2006).
3. W.R. Gardner, *Soil Science*, **85**(4), 228 (1958).
4. R.H. Brooks, A.T. Corey, Hydraulic Properties of Porous medium, Hydrology Paper, No.3, Civ. Engineering. Dept., Colorado State Univ., Fort Collins. 1964.
5. M.T. Van Genuchten, *Soil Science Society of America Journal*, **44**(5), 892 (1980).
6. D.G. Fredlund, A. Xing, *Canadian Geotechnical Journal*, **31**, 521 (1994).
7. L.T. Zhan, P. Chen, C.W.W. Ng, *Journal of Zhejiang University-Science A*, **8**(5), 699 (2007).
8. L.W. Kong, X.W. Li, A.G. Guo, Y. Zhang. *Chinese Journal of Geotechnical Engineering* **31**(3): 335 (2009).
9. B.C. Zhou, L.W. Kong, W. Chen, H. Bai, X.W. Li. *Chinese Journal of Rock Mechanics and Engineering*, **29**(5), 1052 (2010).
10. J.Y. Zhai, G.X. Wei, *Rock and Soil Mechanics*, **30**(11), 3337 (2009).
11. P.J. Williams, *The surface of the earth: an introduction to geotechnical science*. Addison Wesley Longman Ltd, London, 1982.
12. Y.F. Xu, P. Dong, *Rock and Soil Mechanics*, **4**, 400 (2002).
13. J. Gan, D.G. Fredlund, H. Rahardjo, *Canadian Geotechnical Journal*, **25**(3), 500 (1988).
14. X.Y. Yang, X.F. Chen, J.L. Ding, Y. Li, L.J. Kou, Y.J. Wang. *Journal of Irrigation and Drainage*, **23**(3), 45 (2004).

Financial crisis early-warning model for listed company in China energy industry based on logistic regression

Q.W. Yu, L. Zhang*

School of Humanities & Economic Management, China University of Geosciences (Beijing), Haidian District, Beijing, 100083

Received July 13, 2017; Revised July 21, 2017

Energy industry plays an important role on the economic development in China, so their financial position has become the focus study problems for many scholars. According to China energy industry's financial statements and sustainable development, how to find their financial crisis is one of the directions of energy industry's finance. This paper describes the energy industry financial crisis management, constructs the financial crisis early-warning indicator system and describes all indicators, takes ST shares and non-ST shares of China A-share energy industry listed companies as a sample, filters out a series of financial indicators by the normality and the factor analysis, and constructs the Logistic regression early-warning model, and proves the validity of the proposed model by the predictive tests of training samples and testing samples. Finally, the results show that the Logistic model can give an ideal warning for energy industry listed companies' financial position, can give the judgment before listed companies meet financial crisis.

Key words: Energy industry listed company; Early-warning model; Logistic regression.

INTRODUCTION

In China, the capital market is greatly develop; the market economic system is gradually perfect; competition between enterprises is increasingly fierce under this situation, and some enterprises will inevitably fall into financial crisis, or even go bankrupt. If enterprises fall into crisis, they will threaten many aspects of economic life, and create the tremendous impact. Energy industry play an important role on the economic development in China, and help to fasten the development of China's capital market, so their financial position has become the focus study problems for many scholars. At present, many energy industry listed companies in china meet the problem of Special Treatment, one of the main reasons is that they fall into financial crisis. If we can make timely and effective measures before those companies appear financial crisis, it is possible to avoid greater losses.

The main reason of financial crisis is enterprise's various financial and operational risks. Financial crisis early-warning system can monitor and detect all activities in the course of company business, and can identify, evaluate and analyse the unstable operation status and the financial unusual phenomenon caused by expanding financial crisis, the early-warning system can warn the company manager when the financial crisis gets the soften

warning limits, help the managers to find the source of financial crisis, take timely measures of effective regulation, then financial crisis can be reduced to be a relatively safe level.

Based on this consideration and financial crisis early-warning's study situation and methods, this paper puts the identification of financial crisis factor and the construction of financial crisis evaluation indicators into the study frame of energy industry financial crisis early-warning system, so that energy industry managers can fully identify enterprise financial crisis factors and evaluate enterprises' financial situation to construct effective financial crisis early-warning model. According to financial crisis and early-warning theory, this paper takes the special treatment of energy industry in China A-share listed companies as the study objects, screens a series of financial indicators by the normality test and the factor analysis, establishes the Logistic regression early-warning model, and proves the validity of the proposed model through the predictive testing of training samples and testing samples..

LOGISTIC REGRESSION MODEL

Logistic regression is mainly used in the binary response variable or orderly response variable, its goal is to seek the conditional probability of the observed object, and judge the observed object's financial position and operating risks. It is built on the basis of the cumulative probability function, and the independent variables do not need to obey

* To whom all correspondence should be sent:
E-mail: zhanglongdragon@hotmail.com

the multivariate normal distribution and equal between the two groups covariance assumptions. The model estimates the parameter values by using the maximum likelihood estimation method according to the sample data, obtains the probability of response variables' value by certain mathematical operations. If the calculated probability is greater than the setting point, it is determined that the company is in financial crisis. Specific mathematical principles are as follows

Assuming that X_i is a variable of the i -th financial crisis early-warning indicators, then there are the regression relationship between financial crises probability P_i and X_i :

$$P_i = \frac{\exp(Y_i)}{1 + \exp(Y_i)} \quad (1)$$

The concrete operational process is

$$Y_i = \alpha + \beta_1 X_1 + \beta_2 X_2 + \dots + \beta_i X_i = \alpha + \sum \beta_i X_i \quad (2)$$

The value Y_i is the total discrimination, it reflects the i -th characteristics; β_i is the weight and the degree of the relevant independent variables X_i ; α is the financial crisis early-warning indicator variables; is a constant.

The formula (3) can be obtained by the formula (1):

$$Y_i = \ln\left(\frac{P_i}{1 - P_i}\right) \quad (3)$$

Y_i is the total discrimination value, P_i calculated by the linear regression model is the probability of financial crisis.

$$\text{Thus } \alpha + \sum \beta_i X_i = \ln\left(\frac{P_i}{1 - P_i}\right)$$

$$\text{Calculate it, gets } P_i = \frac{\exp(\alpha + \sum \beta_i X_i)}{1 + \exp(\alpha + \sum \beta_i X_i)}$$

$$\text{So } P_i = \frac{\exp(Y_i)}{1 + \exp(Y_i)}$$

The value of $Y_i = \ln\left(\frac{P_i}{1 - P_i}\right)$ can be obtained by substituting the selected variables into the regression equation, thus P_i -value can be calculated. Setting the thresholds as a criterion of the incident, if the P_i value is greater than the

threshold value, it is determined that the event occurs, otherwise, it is determined that the event does not occur. Thus, each sample category can be determined. The curve of the logistic regression model is the type S , and its early-warning maximum value approaches 1, the minimum value approaches 0.

The logistic regression has not specific requirements for the distribution of the variable, the scope of application is more extensive, and the value is a probability value, it is simple and convenient. Therefore, this paper studies the financial crisis early-warning model by the Logistic regression method.

INDICATOR SYSTEM CONSTRUCTION

The financial data by which this paper builds the financial crisis early-warning model is from energy industry of China Shanghai and Shenzhen A-share listed company's true financial data. This paper takes the ST companies of China energy industry listed companies as the financial crisis enterprises, and selects the non-ST as the normal company according to the principle of the same industry and similar asset size, determines the financial anomalies first birthday as the reference day, chooses the financial statements date in two years before the reference day.

Thirty ST companies selected from energy industry of Chinese A-share listed companies at 2011 is the study samples, according to the principle of the same industry and similar asset size, thirty non-ST companies is the paired samples that form the training samples, financial data of those sixty companies are the training samples' financial data. In order to test the model's predictive ability, sixty energy industry listed companies at the same period are selected to be the testing samples, including thirty ST companies and thirty non-ST companies. The built early-warning model is tested by the training sample inspection and the test sample inspection to analyse their respective accuracy and false positive rate.

For the selection of financial indicators, experts and scholars at home and abroad have done a lot of exploration and research, we can learn from outstanding achievements.

According to the files of the National Safety Supervision Bureau and references, the paper builds the China energy industry listed companies' financial crisis warning indicator system (Table 1).

CHINA ENERGY INDUSTRY LISTED COMPANIES' FINANCIAL CRISIS EARLY-WARNING MODEL

Table 1. China energy industry listed companies' financial crisis warning indicator system

| Target layer | Level indicators | Secondary indicators |
|---|-------------------------|---------------------------------------|
| China energy industry listed companies' financial crisis early-warning indicator system A | Profitability B1 | ROA X1 |
| | | ROE X2 |
| | | OPE X3 |
| | Solvency B2 | liquidity ratio X4 |
| | | Current liabilities ratio X5 |
| | | Asset-liability ratio X6 |
| | | Total asset turnover X7 |
| | Operating capacity B3 | Accounts receivable turnover ratio X8 |
| | | Inventory Turnover X9 |
| | | Main business revenue growth X10 |
| | The ability to grow B4 | Net profit growth X11 |
| | | The growth rate of total assets X12 |
| | | The mail profit growth X13 |
| | Cash flow indicators B5 | Sales-to-cash ratio X14 |
| | | Asset cash Recovery X15 |
| | | Cash gearing ratio X16 |

Table 3. The eigenvalues and the contribution rate

| Component | Total Variance Explained | | | | | | | | |
|-----------|--------------------------|---------------|--------------|-------------------------------------|---------------|--------------|-----------------------------------|---------------|--------------|
| | Initial Eigenvalues | | | Extraction Sums of Squared Loadings | | | Rotation Sums of Squared Loadings | | |
| | Total | % of Variance | Cumulative % | Total | % of Variance | Cumulative % | Total | % of Variance | Cumulative % |
| 1 | 3.41 | 21.317 | 21.32 | 3.411 | 21.317 | 21.317 | 3.104 | 19.397 | 19.397 |
| 2 | 2.55 | 15.946 | 37.26 | 2.551 | 15.946 | 37.263 | 2.074 | 12.960 | 32.357 |
| 3 | 2.08 | 13.028 | 50.29 | 2.084 | 13.028 | 50.291 | 1.931 | 12.066 | 44.423 |
| 4 | 1.74 | 10.867 | 61.16 | 1.739 | 10.867 | 61.157 | 1.785 | 11.158 | 55.581 |
| 5 | 1.18 | 7.365 | 68.52 | 1.178 | 7.365 | 68.522 | 1.753 | 10.958 | 66.539 |
| 6 | 1.07 | 6.674 | 75.2 | 1.068 | 6.674 | 75.196 | 1.248 | 7.801 | 74.340 |
| 7 | 1.01 | 6.294 | 81.490 | 1.007 | 6.294 | 81.490 | 1.144 | 7.150 | 81.490 |
| 8 | .731 | 4.571 | 86.061 | | | | | | |
| 9 | .562 | 3.515 | 89.577 | | | | | | |
| 10 | .487 | 3.046 | 92.623 | | | | | | |
| 11 | .417 | 2.603 | 95.226 | | | | | | |
| 12 | .326 | 2.038 | 97.264 | | | | | | |
| 13 | .214 | 1.340 | 98.604 | | | | | | |
| 14 | .111 | .692 | 99.296 | | | | | | |
| 15 | .085 | .531 | 99.827 | | | | | | |
| 16 | .028 | .173 | 100.000 | | | | | | |

Note: The data of this study comes from the CCER economic and financial research database in China.

This paper makes the normality test, factor analysis and logistic regression analysis on the financial indicators by the statistical software SPSS17.0, builds the early-warning model.

Data Factor Analysis

Making the factor analysis on sixty samples in 2009 by the SPSS Version 17 statistical software.

Factor Analysis Test

In order to determine the suitability of the factor analysis, this paper makes the KMO test and Bartlett test on the sample data, the results are shown in Table 2:

By inspection, the KMO sampling moderate determination is 0.520 which is bigger than 0.5, and the Bartlett test's χ^2 statistic significance probability value is 0.000, which is far less than the significance level 0.05, all that indicate that the sample data suits for the factor analysis.

Table 2. KMO test and Bartlett test

| KMO and Bartlett's Test | | |
|---|--------------------|---------|
| Kaiser-Meyer-Olkin Measure of Sampling Adequacy | | 520 |
| Bartlett's Test of Sphericity | Approx. Chi-Square | 513.026 |
| | df | 120 |
| | Sig. | 0 |

The Eigenvalues and the Contribution Rate

After completing factor analysis on the sixteen financial indicators of sample data, we can get sixteen eigenvalues. This paper extracts seven factor variables whose eigenvalues is bigger than 1 as the variables at the next step, and the cumulative contribution rate of the seven factors variable reaches 81.490% shown in table 3, they contain 81.490% information of the original sixteen financial indicators, so that, these seven factors variable basically reflects the difference of the original financial indicators.

Factors Explain

To make it easier to explain the initial factor, this paper uses the variance maximum method of the orthogonal rotation method for conversion. Because it can not only find a suitable explanation for each factor, but also avoid multicollinearity between variables. Factor loading matrix as shown in Table 4:

Table 4. Orthogonal rotation of factor loadings matrix.

| | Rotated Component Matrixa | | | | | | |
|-----|---------------------------|-------|-------|-------|-------|-------|-------|
| | Component | | | | | | |
| | 1 | 2 | 3 | 4 | 5 | 6 | 7 |
| X1 | .228 | .583 | -.012 | .444 | -.119 | -.335 | .173 |
| X2 | .020 | .049 | .018 | .075 | -.011 | .854 | .040 |
| X3 | -.498 | .018 | .145 | .387 | -.189 | -.486 | -.124 |
| X4 | .174 | .132 | .034 | .855 | -.123 | .126 | -.044 |
| X5 | .101 | .402 | .156 | -.109 | -.697 | -.276 | .100 |
| X6 | -.157 | -.365 | .083 | -.709 | -.157 | .075 | -.242 |
| X7 | -.031 | .814 | -.032 | .067 | .106 | .216 | -.141 |
| X8 | .055 | .081 | -.961 | -.015 | .097 | .040 | -.023 |
| X9 | .155 | .261 | .020 | -.221 | .736 | -.123 | .208 |
| X10 | -.105 | -.093 | .027 | .095 | -.118 | .065 | .918 |
| X11 | .046 | .024 | .972 | -.021 | .063 | .023 | .000 |
| X12 | -.109 | .809 | -.031 | .216 | -.020 | -.055 | -.034 |
| X13 | -.214 | .041 | .044 | .037 | .761 | .002 | -.334 |
| X14 | .935 | -.098 | -.043 | .011 | -.122 | .000 | -.001 |
| X15 | .953 | .080 | .033 | .133 | .009 | -.005 | -.035 |
| X16 | .925 | -.016 | .031 | .240 | -.050 | .041 | -.072 |

Table 4 shows that the contribution rate of ROE X2 reflecting the profitability indicators is up to 0.854, the contribution rate of liquidity ratio X4 reflecting solvency indicators is up to 0.855, the contribution rate of total asset turnover X7 reflecting the entrepreneurial capacity indicators is up to 0.814, reflecting business growth capacity indicators the greatest contribution to net profit growth rate X11 is 0.972, reflecting cash flow indicators, the greatest contribution to the recovery

of cash assets X15 is 0.953. Therefore, the final ROE X2, liquidity ratio X4, total asset turnover X7, net profit growth rate X11 and asset cash recovery rate X15 can be the initial variable to build financial crisis early warning model.

Logistic Regression Early-Warning Model

Select the Critical Point

Before building the logistic regression model, we must firstly determine the model discriminate critical point. The logistic regression model has not the optimal split point, so the split point is selected depending on the specific objectives of the model user. In fact, for any critical point, all models will make two types of errors: the class I error and class II error. The class I error is that ST is usually mistaken as non-ST companies. Class II error is that non-ST is usually mistaken as ST. When class I error reduces, class II error increases, and the cost of two types of errors is the same. Most research ships 0.5 as the critical point, i.e., if the probability of an event calculated by the model is greater than or equal to 0.5, then it is determined that the event occurs, otherwise it is judged that the event does not occur. Selected sample in this article is paired, so, selecting 0.5 to be the critical point.

Logistic Regression Early-Warning Model

Using the version SPSS17 statistical analysis software, this paper makes the logistic regression analysis on the selected five variables and their sample data of the previous two years. By forward stepwise selection variable method, the results are shown in Table 5:

Table 5. Model Coefficients Test

| | | Chi-square | df | Sig. |
|--------|-------|------------|----|------|
| Step 1 | Step | 14.812 | 1 | .000 |
| | Block | 14.812 | 1 | .000 |
| | Model | 14.812 | 1 | .000 |
| Step 2 | Step | 10.209 | 1 | .001 |
| | Block | 25.020 | 2 | .000 |
| | Model | 25.020 | 2 | .000 |

Note: Chi-square is the chi-square value, df is freedom degrees, Sig is the p-value

The model corresponding p-value is 0.000, and is less than 0.05, therefore, the overall model is significant.

Table 6 shows that the statistics Cox & Snell R Square and Nagelkerke R Square are 0.341 and 0.455, respectively, that means that the model explains about 60% of the explained variable, the model fitting degree is higher.

Table 6. Model Summary

| Step | -2 Log likelihood | Cox & Snell R Square | Nagelkerke R Square |
|------|-------------------|----------------------|---------------------|
| 1 | 68.366a | .219 | .292 |
| 2 | 58.157a | .341 | .455 |

a. Estimation terminated at iteration number 5 because parameter estimates changed by less than .001

Table 7. Variables in the Equation

| | B | S.E. | Wald | df | Sig. | Exp(B) | |
|----------|----------|-------|------|--------|------|--------|--------|
| Step 1 a | X4 | -.015 | .005 | 8.682 | 1 | .003 | .985 |
| | Constant | 1.669 | .594 | 7.884 | 1 | .005 | 5.305 |
| Step 2 b | X4 | -.013 | .005 | 6.272 | 1 | .012 | .987 |
| | X7 | -.026 | .010 | 7.151 | 1 | .007 | .974 |
| | Constant | 3.053 | .854 | 12.788 | 1 | .000 | 21.172 |

a. Variable(s) entered on step 1: X4

b. Variable(s) entered on step 2: X7

Table 7 shows that two factor variables are through the significance test whose significance level is 0.05 and enter the final model, while the other three variables fail to pass the test, the final logistic early-warning model will be only two variables, respectively, X_4 and X_7 .

According to the formula (2):

$$Y_i = \alpha + \beta_1 X_1 + \beta_2 X_2 + \dots + \beta_i X_i = \alpha + \sum \beta_i X_i$$

Substituting the above results into the above formula, we can get the listed companies' financial crisis early warning model:

$$Y_i = 3.053 - 0.026X_4 - 0.013X_7 \quad (4)$$

Substitute into equation (1): $P_i = \frac{\exp(Y_i)}{1 + \exp(Y_i)}$

We can get the financial crisis early warning model of energy industry listed companies:

$$P_i = \frac{\exp(3.053 - 0.026X_4 - 0.013X_7)}{1 + \exp(3.053 - 0.026X_4 - 0.013X_7)} \quad (5)$$

X_4 represents the current ratio, reflects the company's solvency indicators;

X_7 represents the total asset turnover, reflects the company's entrepreneurial capacity indicators.

Table 8 shows that the financial crisis Logistic early-warning model obtains a better discriminate accuracy rate before two years. The overall accuracy rate is 75.0%; the accuracy of non-financial crisis is 70.0%, the error rate is 30.0%; the

accuracy rate of financial crisis company is 80.0%, the error rate is 20.0%.

Table 8. Classification Table

| | Observed | Predicted | | Percentage Correct |
|---------------------|----------|-----------------------|----|--------------------|
| | | crisis occur or not 0 | 1 | |
| crisis occur or not | 0 | 21 | 9 | 70.0 |
| Step 1 | 1 | 9 | 21 | 70.0 |
| Overall Percentage | | | | 70.0 |
| crisis occur or not | 0 | 21 | 9 | 70.0 |
| Step 2 | 1 | 6 | 24 | 80.0 |
| Overall Percentage | | | | 75.0 |

a. The cut value is .500

Financial Crisis Early-Warning Model Test

Training Sample Test Results

Using the built early-warning model to test sixty training samples, if P-value is bigger than or equal to 0.5, we can judge that the company falls into financial crisis, if less than 0.5, the company does not fall into financial crisis.

Sixty training samples are used to test the accuracy of the built early-warning model, the results show in Table 9:

Table 9. Training samples' test results

| | Whether the crisis | Predictive value | | accuracy rate |
|----------------|--------------------|------------------|-----|---------------|
| | | No | Yes | |
| | | No | 25 | |
| Whether crisis | Yes | 4 | 26 | 86.67 |
| Total | | 29 | 31 | 85.00 |

There are five non-financial crisis companies judged to be financial crisis by Logistic early-warning model, the error rate is about 16.67%; Four financial crisis companies are judged to be non-financial crisis, the error rate is about 13.33%. The total error rate both is 15%, the general warning accuracy rate is 85%.

The Test Results of Samples

The early-warning model is derived from the training sample data, so the training sample test results will overestimate its early-warning capacity. To further test the early-warning capability of the model, sixty samples which were not used in the

modeling process test the model, 0.5 is the critical point, the results are shown in Table 10:

Table 10. Test results of the testing samples

| | | Predictive value | | | accuracy rate |
|---------------------|-----|---------------------|-----|-------|---------------|
| | | Crisis occur or not | | | |
| | | No | Yes | | |
| Crisis occur or not | No | 22 | 8 | 73.33 | |
| | Yes | 7 | 23 | 76.67 | |
| Total | | 29 | 31 | 75.00 | |

The test results are that the general warning accuracy rate of the model is 75%, so the built logistic regression early-warning model has also a good prediction in practical applications.

CONCLUSION

This paper firstly defines the study object of the early-warning model, and selects sixty energy industry listed companies as the financial indicators data and then makes the normal distribution test on the financial indicators data and determines that they are suitable for factor analysis or not. Then, the logistic early-warning model is constructed based on the principal component factors screened by the forward stepwise variable selection method. Finally, this paper gets a good prediction of the

model checking through the training and testing samples.

Acknowledgement: The paper is supported by “the Fundamental Research Funds for the Central Universities” (No. 2652015014).

REFERENCES

1. J.Z. Li, T.M. Wu, *J. Harbin Univ. Commerce*, **5**, 89. (2010).
2. X.W. Liu, P. Tao, *J. Eng. Management*, **25**(4), (2011).
3. Y.L. Wang, H.B. Wang, *Zhongguo Jiti Jingji*, **24**, 72. (2011).
4. L. Yang. *Modern Economic Information*, **14**, 221. (2012).
5. H. Han, *China Chief Financial. Officer*, **7**, 126. (2012).
6. N.X. Chen, *Times Finance*, **12**, 70. (2010).
7. H.P. Wu, *Friends of Accounting*, **35**, 100. (2012).
8. R. Ye, X.H. Hui, C.H. Xun, *Advanced Materials Research*, **361-363**, 1651. (2011).
9. M. Hao, *Applied Mechanics and Materials*, **291-294**, 28. (2013).
10. C.Y. Liu, *Special Zone Economy*, **1**, (2012).
11. S. Enzo, *Int. Business Research*, **5**(2), (2012).
12. M. Adam, T. Paul, *Public Administration*, **90**(3), 759. (2012).
13. W.S. Cathy, *J. Forecasting*, **31**(8), 661. (2012).
14. Y. Wang, *Sys. Eng. Procedis*, **3**, 153. (2012).
15. C. Bertrand, D. Elena-Ivona, H. Christophe, *IMF Economic Review*, **4**, 60. (2012).

Effect of polymer compounds on base ions of salinized soil

L.L. Tan[#], X.M. Tian[#], H. Fan, F. H. Zhang, H.J. Wang, Y.B. Li, C. Fei, K.Y. Wang^{*}

The Agriculture of Shihezi University, Xinjiang Shihezi, 832003, China

Received June 26, 2017; Revised July 21, 2017

Secondary soil salinization will result in soil structure degradation. At present, soil salinization has become one of the main factors impeding the improvement of soil fertility. This study is targeted at salinized soil, and in the study, the effect of polymer compounds on the base ions of salinized soil is analyzed through an indoor pot experiment. The results indicate that polymer compounds, including polyacrylate (M1), cellulose (M3), polyacrylate + cellulose (M4), and polyacrylamide + cellulose (M5), are able to reduce the water-soluble base ion content and electrical conductivity of severely salinized soil. The main factors of polymer compounds that can significantly affect the properties of severely salinized soil are EC, Na⁺, Cl⁻, SO₄²⁻, and Mg²⁺ ions, and the main factors that significantly affect the soil EC value are Na⁺, Cl⁻, SO₄²⁻, and Mg²⁺.

Keywords: Polymer compound; Base ion; Salt content; Main component analysis

INTRODUCTION

Soil salinization is a critical factor impeding the sustainable development of oasis agriculture in draught and semi-draught areas, and it poses a tremendous threat to the stability of the oasis ecological system [1]. The secondary soil salinization of agricultural fields in oasis-irrigated areas has caused a serious deterioration of soil structure, and salt content has become one of the main factors impeding the improvement of soil fertility [2]. The damage caused by soil salinization results in restricted irrigation in draught and semi-draught areas. When the irrigating water contains salt, the salt content in soil accumulates gradually, leading to an excessively high concentration in the soil solution and resulting in physiological drought, yield reduction, or crop death [3, 4]. Currently, the soil of 32.07% of the agricultural fields in Xinjiang has been damaged by salt and alkali, resulting in decreased soil quality. The total area of farmland that has been abandoned due to soil salinization in the entire Xinjiang region is up to 133 thousand hm² [5, 6].

The degree of soil salinization mainly depends on the base ion content in the soil solution [7]. In general, the total salt content in soil equals the sum of various base ions in the soil solution and is used to express the magnitude of the salt content of the soil and the level of soil salinization [8]. Polymer compounds are able to effectively improve the salt-containing condition of the soil [9]. Furthermore, researches demonstrate that polymer compounds can

effectively reduce the salt content and pH value of salinized soil [10, 11].

Numerous studies have been conducted on the effect of polymer compounds on improving soil quality, maintaining water and soil, increasing crop yields, and improving the environment, and there have already been some achievements [12, 13, 14, 15, 16]. However, less research has been conducted on the effect of polymer compounds on the base ions of salinized soil. In this paper, the effect of polymer compounds on the base ions of salinized soil is studied through improving the soil with a number of polymer compounds, which provides reference for the study of the draught and salt resistance of salinized soil.

MATERIALS AND METHODS

Test materials

The soil used for testing was severely salinized soil, and its basic physical/chemical properties were summarized in Table 1. The wheat used for the tests was Xinchun No. 6. Table 2 details the classification criteria of salinized soil. For the relationship between electrical conductivity (EC) and total salt content for Xinjiang soil, refer to the Total salt content = $3.51 \times EC_{1.5} + 0.38$ ($R^2=0.95$, $P<0.01$) [17]. Table 3 gives the treatments of the pot experiment of the polymer compounds used for the tests.

Test design

Potted plant (top diameter 8 cm, bottom diameter 5cm, height 12 cm) was used for the tests. The wheat seedlings were planted in soil treated with different polymers and cultivated indoors.

[#] These authors contributed equally to this study and share first authorship

^{*} To whom all correspondence should be sent:

E-mail: wky20@163.com

Table 1. Basic Physical and Chemical Properties of Soil Used for Testing

| pH | EC (dS.m ⁻¹) | K ⁺ (g.kg ⁻¹) | Na ⁺ (g.kg ⁻¹) | Ca ²⁺ (g.kg ⁻¹) | Mg ²⁺ (g.kg ⁻¹) | SO ₄ ²⁻ (g.kg ⁻¹) | Cl ⁻ (g.kg ⁻¹) | HCO ₃ ⁻ (g.kg ⁻¹) | CO ₃ ²⁻ (g.kg ⁻¹) |
|-----|-----------------------------|---|--|---|---|--|--|--|--|
| 8.8 | 5.039 | 0.125 | 2.574 | 0.659 | 1.112 | 0.320 | 0.208 | 0.041 | 0.000 |

Table 2. Classification Criteria of Salinized Soil.

| Salt content (dry soil weight %) | Degree of salinization |
|-------------------------------------|------------------------|
| <0.3 | Non-salinized soil |
| 0.3-0.5 | Slight salinization |
| 0.5-1.0 | Moderate salinization |
| 1.0-2.2 | Severe salinization |
| > 2.2 | Saline soil |

Table 3. Pot Experiment Treatments.

| Treatments | Polymer compound |
|------------|---------------------------------------|
| CK | Polymer compound not used. |
| M1 | 0.2% polyacrylate |
| M2 | 0.2% polyacrylamide |
| M3 | 0.2% cellulose |
| M4 | 0.1% polyacrylic acid+0.1% cellulose |
| M5 | 0.1% polyacrylamide +0.1% cellulose |
| M6 | 0.1% polyacrylic acid +0.1% cellulose |

Table 4. Main Index Measuring Method

| Items | Measuring method |
|---|------------------------------------|
| Moisture content | Oven drying |
| pH value | 2.5:1 Water-soil ratio electrode |
| Electrical conductivity | 5:1 Conductivity meter |
| K ⁺ and Na ⁺ | Flame photometry |
| Ca ²⁺ and Mg ²⁺ | EDTA titration |
| SO ₄ ²⁻ measurement | EDTA titration |
| Cl ⁻ measurement | Silver nitrate titration |
| CO ₃ ²⁻ and HCO ₃ ⁻ | Double indicator-neutral titration |

Three types of polymer compounds were selected and used for the test, and seven treatments were designed, including CK (blank), M1 (polyacrylate), M2 (polyacrylamide), M3 (cellulose), M4 (polyacrylate and cellulose), M5 (polyacrylamide and cellulose), and M6 (polyacrylate and polyacrylamide).

Each treatment was repeated three times, and 10 wheat grains are planted for each treatment. Prior to the experiment, the collected soil was dried naturally. Next, the soil was ground and evenly mixed, and then, the soil was sieved with a 2.5 mm sieve. A pot was filled with 10cm soil in layers at 1.2 g.cm⁻³ bulk density so that the soil in each pot weighs 0.5 kg.

Then, the polymer compound was mixed evenly with the soil at the specified mix ratio (polymer

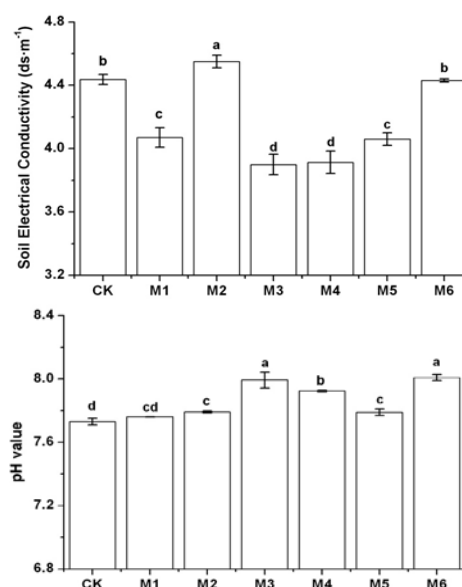
compound/salinized soil mass ratio was 0.2%, and the mass ratio of each two polymer materials mixed together was 0.1%).

Finally, nitrogen, phosphate, and potassium fertilizers were applied one time during soil filling at a 1:0.9:0.5 ratio to serve as the basal dressing. The test method was shown in Table 4.

RESULTS AND DISCUSSION

Effect of polymer compound on salt content and pH value of salinized soil

As shown in Fig. 1, organic polymer compounds significantly affect the electrical conductivity of saline-alkaline soil. As compared with soil treated with SK, the electrical conductivity of the soil treated with M2 increases significantly, and the changes of the electrical conductivity of the soil treated with M6 are not significant. As compared with CK, the soil electrical conductivities of M1, M3, M4, and M5 are significantly ($P<0.05$) reduced by 8.3%, 12.1%, 11.8%, and 8.5%, respectively. These results indicate that the polymers increase the water retention capacity of the soil as well as reduce the loss of water evaporation, which weakens the accumulation of soil salt.

**Fig. 1.** Effect of polymer compound on soil electrical conductivity and pH

Note: A lower-case letter denotes significant

difference ($P < 0.05$), and the same below.

Polymer compounds can increase the soil pH value significantly to a range of 7.7~8.0 with a small amplitude of change (Fig. 1). As compared with soil treated with CK, the soils treated with M1, M2, M3, M4, M5, and M6 have pH value rate increases of 0.4%, 0.8%, 3.4%, 2.5%, 0.8%, and 3.6%, respectively. For M1, the difference is not significant. This indicates that the carboxyl group at the end of the hydrophobic association monomer increases the solution viscosity under the alkaline condition, thus increasing the soil pH value.

Effect of polymer compounds on base ion of salinized soil

The effect of different polymer compounds on the cations of severely salinized soil is significant ($P < 0.05$) (Fig. 2). The water soluble cation content in severely salinized soil can be reduced by treating the soil with polymer compounds. As shown in Fig. 2, as compared with the CK treatment, the M1, M2, M3, M4, M5, and M6 treatments reduce the content of water soluble K^+ in the soil by 34.0%, 21.5%, 21.5%, 21.5%, 8.7%, and 23.3%, respectively.

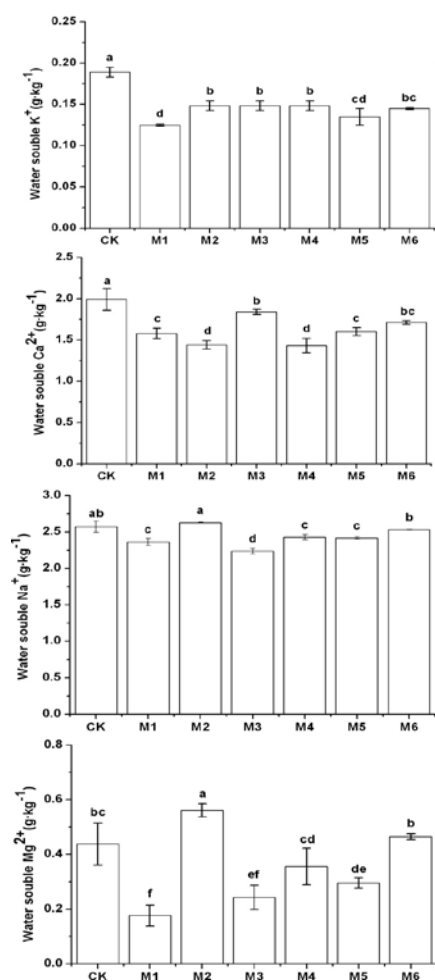


Fig. 2. Effect of different treatments on cationsthe

effect of different polymer compounds on the anions of severely salinized soil is significant ($P < 0.05$).

Furthermore, the M1, M3, M4, and M5 treatments significantly reduce the content of water soluble Na^+ in the soil by 8.2%, 13.1%, 5.7%, and 6.1%, respectively. The M2 and M6 treatments do not significantly affect the water soluble Na^+ content in the soil. Additionally, the M1, M2, M3, M4, M5, and M6 treatments significantly reduce the content of water soluble Ca^{2+} in the soil by 20.7%, 27.6%, 7.6%, 28.16%, 19.7%, and 14.0%, respectively. Finally, the M1, M3, M4, and M5 treatments reduce the content of water soluble Mg^{2+} in the soil by 59.81%, 44.50%, 18.66%, and 32.54%, respectively. The effects of the M1, M3, and M5 treatments are significant. The M6 treatment does not significantly affect the water soluble Mg^{2+} content; however, the M2 treatment does significantly increase the water soluble Mg^{2+} content in soil.

These results indicate that the M1, M3, M4, and M5 treatments better reduce the base ion content in soil. The Ca^{2+} and Mg^{2+} exchange adsorption is activated by soil colloids Na^+ , which indicates that the polymer compounds disperse $CaCO_3$ and $MgCO_3$. It can easily be washed out of the soil in the pot experiment because the Na^+ in the soil has a strong mobility, which results in a decrease in the soil water-soluble Ca^{2+} , Mg^{2+} , and Na^+ contents. The original sodium hydrophilic colloid becomes a loose calcium colloid, which enhances the salinization of soil structure and permeability and can significantly promote soil desalination and inhibit soil desalination [18].

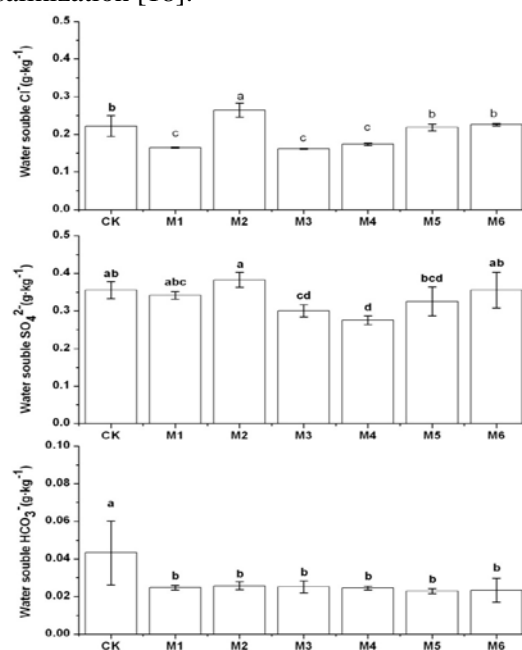


Fig. 3. Effect of different treatments on anions

However, polyacrylamides dissolve to form

carboxylate ions, and due to the higher Na content, the carboxylate ions are shielded. Molecular clusters occur, and there is a corresponding reduction in apparent size, which results in lower viscosity, and polyacrylamides on soil Na^+ and Mg^{2+} adsorption capacity decrease.

The content of water soluble anions in severely salinized soil can be reduced by treating the soil with polymer compounds. As shown in Fig. 3, as compared with the CK treatment, the M1, M3, M4 and M5 treatments reduce the content of water soluble SO_4^{2-} in the soil by 4.1%, 15.6%, 22.8%, and 8.7%, respectively, and the M3 and M4 treatments had significant effects. Furthermore, the M1, M3, M4, M5, and M6 treatments reduce the Cl^- content in the soil by 26.0%, 27.2%, 21.7%, 1.6%, and 1.7% respectively, and the M1, M3 and M4 treatments had significant effects. Finally, the M1, M2, M3, M4, M5, and M6 treatments reduce the content of water soluble HCO_3^- in the soil by 42.63%, 40.40%, 41.81%, 43.31%, 46.96%, and 45.95%, respectively. These results indicate that the M1, M3, M4, and M5 treatments better reduce the base ion content in soil. Additionally, these results demonstrate that the carboxyl group, the hydroxyl group, and the other active groups of these polymers can chelate with the salt ions in the soil and reduce the harm of the salt to the plant [19]. At the same time, the salt concentration of the soil solution can be diluted by maintaining the moisture.

Principal component analysis of salt content in salinized soil treated with different polymer compounds

Principal component analysis was performed for the base ion content, EC values, and pH values of severely salinized soil. The analysis related to main component factor loading is summarized in Table 5. For severely salinized soil, the variance contribution rate of principle component 1 (PC1) is 54.38%, and that of principle component 2 is 24.23%, i.e., the total variance contribution rate of PC1 and PC2 is 78.61%, which can basically reflect most information of the saline/alkaline factors of the soil. The positive correlations between PC1 and soil Na^+ , Cl^- , and EC are very significant ($P < 0.01$), and the correlation factors are 0.94, 0.88, and 0.95, respectively. Additionally, the positive correlations between PC1 and soil Mg^{2+} and SO_4^{2-} are significant ($P < 0.05$). These five indicators are closely related to soil salinization, and they further indicate that the soil salinization is mainly caused by chloride and sulfate, which is probably due to the formation of parent material and water source salt ion composition.

The negative correlations between PC2 and soil Ca^{2+} and HCO_3^- are significant, and the correlation factors are 0.85 and 0.78, respectively. This indicates that HCO_3^- and Ca^{2+} also affect the soil salinization in the region to a certain extent, and they mainly affect the soil alkalinity.

Table 5. Factor Loading Matrix of Soil

| Index | PC1 | PC2 | EC |
|--------------------|--------|-------|--------|
| K^+ | 0.61 | 0.70 | 0.43 |
| Na^+ | 0.94** | -0.23 | 0.90** |
| Ca^{2+} | 0.19 | 0.85* | 0.13 |
| Mg^{2+} | 0.85* | -0.27 | 0.83* |
| SO_4^{2-} | 0.82* | -0.22 | 0.91** |
| Cl^- | 0.88** | -0.36 | 0.88** |
| HCO_3^- | 0.58 | 0.78* | 0.39 |
| EC | 0.95** | -0.17 | 1 |
| pH | -0.42 | -0.16 | -0.29 |

Note: * means the correlation between the factor and the main component is significant on 0.05 level; ** means the correlation between the factor and the main component is very significant on 0.01 level, and the same below.

The positive correlations between EC and soil Na^+ and SO_4^{2-} and Cl^- are very significant ($P < 0.01$), and the correlation factors are 0.90, 0.91, and 0.88, respectively. Additionally, the positive correlation between EC and soil Mg^{2+} is significant ($P < 0.05$). The positive correlations between EC and soil Na^+ , SO_4^{2-} , and Cl^- are very significant ($P < 0.01$), and the correlation factors are 0.90, 0.91, and 0.88, respectively. The positive correlation between EC and soil Mg^{2+} is significant ($P < 0.05$). This further illustrates that the conductivity value can more accurately reflect the situation in the soil salinization area.

The effect of treatments with different polymer compounds on the salt/alkali content in severely salinized soil varies significantly. In Fig.4, the apparent difference between the polymer compound treatment and the CK treatment is indicated by the PC axis. The scores of the CK treatment and the M2 treatment on the PC1 axis are higher than those of the M1, M3, M4, M5, and M6 treatments. This indicates that the M1, M3, M4, M5, and M6 treatments significantly reduce the Na^+ , Cl^- , EC, Mg^{2+} , and SO_4^{2-} contents in the soil and that the M1, M3, and M4 treatments contribute more to the reduction of ions. The score of the CK treatment on the PC2 axis is higher than those of the M1, M2, M3, M4, M5 and M6 treatments, which indicates that, on the basis of PC1, the M1, M3, M4, M5, and M6 treatments can further reduce the Ca^{2+} and HCO_3^- contents in the soil.

These results indicate that the carboxyl groups and other anionic functional groups are present in some polymer structures. These functional groups have strong ion exchange ability, activated soil

calcium carbonate, complex metal ions, and so on [20], which changed the composition of the soil salts and salt-based ions. At the same time, for the same electrolyte, different polymers have very different holding capacities, so different polymers have quite different effects on base cations [18]. In this paper, the three polymers in the study were obtained using two mutual copolymerization methods, and the copolymer has a higher salt tolerance than the original monomer polymer because some of the groups in the copolymer are less sensitive to salt [21]. Meanwhile, the carboxyl and amide groups contained in the copolymer easily form hydrogen bonds with water, and the carboxylate ionizes with water, and the skeleton of the anionic repulsion between the negative pressures improves water absorption [11]; therefore, it has a better resistance to salt.

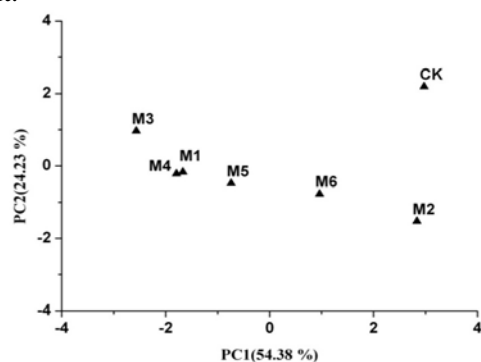


Fig. 4. Analysis of Main Saline/alkaline Components in the Soil Treated with Different Polymer Compounds

CONCLUSION

Polymer compounds can reduce the content of base ions in salinized soil. As compared with CK, polymer compounds, including polyacrylate (M1), cellulose (M3), polyacrylate + cellulose (M4), and polyacrylamide + cellulose (M5), are able to reduce the water-soluble base ion content and electrical conductivity of severely salinized soil.

The main factors of polymer compounds that can significantly affect the properties of severely salinized soil are EC, Na⁺, Cl⁻, SO₄²⁻, and Mg²⁺ ions, and the main factors that significantly affect the EC value of the soil are Na⁺, Cl⁻, SO₄²⁻, and Mg²⁺.

Acknowledgements. This research was supported by the national key research and

development Program of China (2016YFC0501406), the International Science & Technology Cooperation Program of China (2015DFA11660), the National Key Technology R&D Program of China (2014BAC14B0302), the National Natural Science Foundation of China (31560169), and Shihezi University level project (ZZZC201619, RCZX201314).

REFERENCES

1. W.J. Wang, H.S. He, Y.G. Zu, Y. Guan, Z.G. Liu, Z.H. Zhang, H.N. Xu, X.Y. Yu, *Plant Soil*, **339**, 177 (2011).
2. Y. Wang, D. Xiao, Y. Li, X. Li, *China Environ. Monitoring Assessment*, **140**, 291 (2008).
3. H. Boyko, E. Boyko, *Salinity Aridity*. Springer, 1966.
4. L.K. Smedema, K. Shiati, *Irrigation Drainage Sys.*, **16**, 161 (2002).
5. Y. Cui, J. Shao, *Groundwater*, **43**, 471 (2005).
6. Y. Shen, H. Lein, *Norsk Geografisk Tidsskrift-Norwegian J. Geography*, **59**, 237 (2005).
7. Z.Y. Xue, D.Y. Zhi, G.P. Xue, H. Zhang, Y.X. Zhao, G.M. Xia, *Plant Sci.*, **167**, 849 (2004).
8. H.L. Bohn, R.A. Myer, G.A. O'Connor, John Wiley Sons, 2002.
9. T. Robinson, G. McMullan, R. Marchant, P. Nigam, *Bioresource Tech.*, **77**, 247 (2001).
10. A.M. Mahdy, *Soil Water Res*, **6**, 205 (2011).
11. J.Q. Luo, L.L. Wang, Q.S. Li, Q.K. Zhang, B.Y. He, Y. Wang, L.P. Qin, S.S. Li, *Soil Tillage Research*, **149**, 12 (2015).
12. M.R. Islam, Y. Hu, S. Mao, P. Jia, A.E. Eneji, X. Xue, *J. Sci. Food Agricul.*, **91**, 1998 (2011).
13. V. Abrol, I. Shainberg, M. Lado, M. Ben-Hur, *European J. Soil Sci.*, **64**, 699 (2013).
14. X. Li, J.Z. He, J.M. Hughes, Y.R. Liu, Y.M. Zheng, *Applied Soil Ecology*, **73**, 58 (2014).
15. A. Inbar, M. Ben-Hur, M. Sternberg, M. Lado, *Geoderma*, **239**, 107 (2015).
16. S. Xu, L. Zhang, N.B. McLaughlin, J. Mi, Q. Chen, J. Liu, *Soil Tillage Research*, **148**, 31 (2015).
17. H. Wang, J. Shi, H. Zhang, J. Sheng, X. Ma, H. Wu, S. Ren, Q. Zuo, B. Li, *Transactions Chinese Society Agricul. Engin.*, **30**, 102 (2014).
18. S. Ahmad, A. Ghafoor, M.E. Akhtar, *Land Degradation & Development*, **24**(2), 170 (2013).
19. X. Ma, Z.M. Wei, K. Zhang, J. Zhang, *Soils*, **46**(3), 2014.
20. R.A. Ruehrwein, D.W. Ward, *Soil Science*, **73**(6), 485 (1952).
21. R.D. Archibald, R.J. Harper, J.E.D Fox, *Agroforestry Sys.*, **66**(3), 191 (2006).

Application of the bootstrap panel method an empirical study of the granger causality between carbon dioxide emissions and economic growth in emerging countries

M.-Y. Chen*, Y.-S. Perng

¹ Department of Environmental Engineering Dayeh University 168 University Rd. Dacun Changhua 51591 Taiwan.

Received June 26, 2017; Revised August 25, 2017

This study discusses the dilemma countries face when implementing energy conservation policies to protect environmental resources. Implementation of such policies has reduced carbon dioxide CO₂ emissions and decreased industrial production momentum along with economic growth. This study employs the bootstrap panel Granger-causality method to address the conditions of heterogeneity and cross-sectional dependence to allow consideration of cross-country correlations. This study analyzes the link between economic growth and CO₂ emissions in 22 emerging countries from 1993 to 2011. The empirical results show that in a few countries positive and negative bidirectional causality exists between economic growth and CO₂ emissions while many countries surveyed exhibited a positive unidirectional relationship between CO₂ emissions and economic growth. A few countries showed other relationship patterns. These results imply that to pursue economic growth a country should adopt more environmentally-friendly sources of energy in addition to using those that produce CO₂ emissions. **Keywords:** economic growth carbon dioxide CO₂ emission bootstrap panel Granger-causality test emerging country countries.

INTRODUCTION

Purpose

The main purpose of this study is to investigate the 22 emerging countries in four continents by geographic location namely Africa Asia Europe and America and discuss them respectively to explore the possible causal relationship between CO₂ emissions and economic growth. Under this aspect the study further explores when there is a unidirectional causal relationship from CO₂ emissions to economic growth whether the reduction of CO₂ emissions will impede economic growth or when there is unidirectional causal relationship from economic growth to the CO₂ emissions whether the reduction of CO₂ emissions will have a negative impact on economic growth.

In this study the bootstrap panel Granger-causality measurement method proposed by Konya 2006 is used to re-examine the nexus between CO₂ emissions and economic growth.

METHODOLOGY

Panel Causality Tests

Based on the proposal of Granger 1969 the Granger causality indicates that the past historical data of variable X can improve the ability of predicting another variable Y. Given the situation

that cross-sectional dependence and heterogeneity exist between countries this method can illustrate this feature. Although different panel causality methods have been proposed the bootstrap panel causality method proposed by Konya 2006 is able to take into account both cross-sectional dependence and country-specific heterogeneity. The causal relationship can be tested through the bootstrap panel causality approach by estimating and Wald testing the country-specific critical values based on the SUR. The stability of variables under this system is not necessarily required indicating that there is no need to test the nature of the variables in advance through ADF and co-integration.

The utilization of the bootstrap panel causality method to estimate the system is described as follows

$$\begin{aligned}
 y_{1,t} &= \alpha_{1,1} + \sum_{i=1}^{ly_1} \beta_{1,1,i} y_{1,t-i} + \sum_{i=1}^{lx_1} \delta_{1,1,i} x_{1,t-i} + \varepsilon_{1,1,t} \\
 y_{2,t} &= \alpha_{1,2} + \sum_{i=1}^{ly_1} \beta_{1,2,i} y_{2,t-i} + \sum_{i=1}^{lx_1} \delta_{1,2,i} x_{2,t-i} + \varepsilon_{1,2,t} \\
 &\vdots \\
 y_{N,t} &= \alpha_{1,N} + \sum_{i=1}^{ly_1} \beta_{1,N,i} y_{N,t-i} + \sum_{i=1}^{lx_1} \delta_{1,N,i} x_{1,N,t-i} + \varepsilon_{1,N,t}
 \end{aligned}$$

and

* To whom all correspondence should be sent:
E-mail: yung.po@msa.hinet.net

$$\begin{aligned}
 x_{1,t} &= \alpha_{2,1} + \sum_{i=1}^{ly_2} \beta_{2,1,i} y_{1,t-i} + \sum_{i=1}^{lx_2} \delta_{2,1,i} x_{1,t-i} + \varepsilon_{2,1,t} \\
 x_{2,t} &= \alpha_{2,2} + \sum_{i=1}^{ly_2} \beta_{2,2,i} y_{2,t-i} + \sum_{i=1}^{lx_2} \delta_{2,2,i} x_{2,t-i} + \varepsilon_{2,2,t} \\
 &\vdots \\
 x_{N,t} &= \alpha_{2,N} + \sum_{i=1}^{ly_2} \beta_{2,N,i} y_{N,t-i} + \sum_{i=1}^{lx_2} \delta_{2,N,i} x_{N,t-i} + \varepsilon_{2,N,t}
 \end{aligned}$$

where y denotes the economic growth x is the CO₂ emissions and l is the length of time delayed. Because each equation under the system has different predetermined variables as long as the error terms may contemporaneously have correlations i.e. cross-sectional dependencies such an equation set is regarded as the SUR system.

To test Granger-causality on the system the causal relationship can be divided into four categories 1 if estimated parameters $\delta_{1,i}$ are not all zero and $\beta_{2,i}$ are all zero there is a unidirectional causal relationship from variable X to variable Y 2 If estimated parameters $\delta_{1,i}$ are all zero and $\beta_{2,i}$ are not all zero there is a unidirectional causal relationship from variable Y to variable X 3 If neither estimated parameters $\delta_{1,i}$ nor $\beta_{2,i}$ are zero there is bidirectional leading-lagging Granger causality between variables X and variables Y. 4 If both estimated parameters $\delta_{1,i}$ and $\beta_{2,i}$ are zero there is no any Granger causality between variables X and variables Y.

Because the causality test is resulted from the selection of a lag structure the choice of the optimal lag number is very important. Therefore the number of lag periods should be described and determined prior to estimation. For the large panel data the equation the variables and the lag structure may lead to a computational burden. To solve this problem Konya 2006 proposed to take into account the maximum lag period between different variables rather than between the same equations. If a lag periods is assumed as 1-4 to estimate the potential pair combinations of ly_1 , lx_1 , ly_2 and lx_2 under the system in accordance to the Schwarz Bayesian criterion SBC the minimum SBC value will be selected to determine the number of the optimal lag periods.

RESULTS AND DISCUSSIONS

Results and Discussions of the Bootstrap Panel Causality Tests

The determination of the cross-sectional dependence existence and slope heterogeneity in all the countries of four continents can support the empirical results of the bootstrap panel Granger-causality approach. The empirical results of Granger causality between economic growth GDP and CO₂ emissions in the four continents are shown in Table 4.4 – 4.11.

The results of Table 4.3 show that there exists no nexus from economic growth to CO₂ emissions. The results of Table 4.4 show that for the five countries located in Africa, at the 5% significance level the Wald statistics of Egypt and Morocco are greater than the bootstrap critical value and are against the null hypothesis that economic growth will not outpace CO₂ emissions and present a unidirectional relationship from economic growth to CO₂ emissions. However there are no significant relationships between South Africa Zambia and Namibia according to the statistical results.

As we learned from the results in Table 4.5 and 4.6 for the seven countries in Asia there is a bidirectional causal relationship between the economic growth and CO₂ emissions in Korea whereas there is a unidirectional causal relationship from the economic growth to CO₂ emissions in India the Philippines and Malaysia. In China Thailand and Indonesia on the other hand there is no relationship between economic growth and CO₂ emissions.

The results from Table 4.7 and 4.8 show that for the five countries in Europe there is a unidirectional relationship from economic growth to CO₂ emissions in Poland but there is a unidirectional relationship from CO₂ emissions to economic growth in Hungary. In Turkey the Czech Republic and Russia on the other hand there is no relationship between economic growth and CO₂ emissions.

As we learned from the results in Table 4.9 and 4.10 for the five countries of America there is a bidirectional relationship between economic growth and CO₂ emissions in Mexico but there is a unidirectional relationship from economic growth to CO₂ emissions in Brazil Colombia and Chile. In Peru however there is no relationship between economic growth and CO₂ emissions.

The causal relationships between economic growth and CO₂ emissions in the above 22 emerging countries of the four continents are shown in Table 4.11.

CONCLUSIONS

The present study analyzes the causal relationships between the economic growth and CO₂ emissions in 22 emerging countries for the period from 1993 to 2011. For the five countries located in Africa there are unidirectional relationships from economic growth to CO₂ emissions in Egypt and Morocco. For the seven countries located in Asia there is a bidirectional relationship between economic growth and CO₂ emissions in Korea whereas in India the Philippines and Malaysia there are unidirectional relationships from economic growth to CO₂ emissions. For the five European countries there is a unidirectional relationship from economic growth to CO₂ emissions in Poland whereas in Hungary there exists a unidirectional relationship from CO₂ emissions to economic growth. For the five American countries there are bidirectional relationships between economic growth and CO₂ emissions in Mexico whereas in Brazil Colombia and Chile there are unidirectional relationships from economic growth to CO₂ emissions.

In addition to the positive and negative bidirectional causality between economic growth and CO₂ emissions respectively in Mexico and Korea there is a positive and unidirectional relationship from CO₂ emissions to economic growth in Egypt Morocco India Malaysia and Poland whereas the results of the Philippines are on the opposite. At last we observe the negative and unidirectional relationship from CO₂ emissions to economic growth only in Hungary.

RECOMMENDATIONS

Based on the discussion of the causal relationship between economic growth and CO₂ emissions of the above 22 emerging countries we have learnt the dilemma faced by the countries on the implementation of energy conservation policies for the protection of environmental resources because the implementation of energy conservation policies has not only reduced the CO₂ emissions but also driven down the industrial production momentum along with their economic growth. However for the two countries of Korea and the Philippines in this study the former has negative and the bidirectional causal relationship between economic growth and CO₂ emissions and the latter has a negative and unidirectional causal relationship from economic growth to CO₂ emissions. That is to say to pursue the positive economic growth of a country in addition to the use of energy that produces CO₂ emissions policy

makers can adopt alternative energy that is more environment friendly as the energy for corporate expansion to promote the economic growth of the country.

Table 4.1. Cross-sectional Dependence Tests

| Continent | Variable | CD _{bp} | CD _{lm} | CD |
|-----------|-----------------|------------------|------------------|-----------|
| Africa | Economic | 12.989*** | 0.549*** | 6.945*** |
| Asian | growth/ | 37.028*** | 3.244*** | 15.869*** |
| Europe | CO ₂ | 20.958*** | 1.431*** | 8.811*** |
| America | emissions | 8.156*** | 1.754*** | 4.347*** |

Note *** at the 1% significance level the null hypothesis of invalid cross-sectional dependence is rejected.

Table 4.2. Slope Homogeneity Tests

| Continent | Variable | SH |
|-----------|----------------------------------|-----------|
| Africa | | 226.9*** |
| Asian | Economic growth/ CO ₂ | 245.23*** |
| Europe | emissions | 150.97*** |
| America | | 114.47*** |

Note *** at the 1% significance level the null hypothesis of slope homogeneity is rejected.

Table 4.3. H₀ CO₂ Emissions Will Not Outpace Economic Growth

| Country | Wald Statistic | Bootstrap Critical Values | | |
|--------------|----------------|---------------------------|--------|-------|
| | | 1% | 5% | 10% |
| Egypt | 2.716 | 17.416 | 9.333 | 6.199 |
| Morocco | 0.009 | 17.371 | 8.284 | 5.514 |
| South Africa | 0.816 | 18.855 | 10.034 | 6.502 |
| Zambia | 4.767 | 19.038 | 10.392 | 6.966 |
| Namibia | 2.170 | 24.534 | 11.481 | 7.626 |

Note 1. Bootstrap critical values are obtained from 10,000 replications.

Table 4.4. H₀ Economic Growth Will Not Outpace CO₂ Emissions

| Country | Wald Statistic | Bootstrap Critical Values | | |
|--------------|----------------|---------------------------|--------|-------|
| | | 1% | 5% | 10% |
| Egypt | 37.022*** | 15.162 | 7.530 | 5.102 |
| Morocco | 17.234*** | 16.695 | 8.368 | 5.596 |
| South Africa | 1.804 | 14.432 | 7.394 | 5.060 |
| Zambia | 8.132 | 23.775 | 12.550 | 8.931 |
| Namibia | 2.528 | 21.725 | 10.924 | 7.414 |

Note 1. Bootstrap critical values are obtained from 10,000 replications.

Table 4.5. H₀ CO₂ Emissions Will Not Outpace Economic Growth

| Country | Wald Statistic | Bootstrap Critical Values | | |
|-----------------|----------------|---------------------------|--------|--------|
| | | 1% | 5% | 10% |
| India | 1.676 | 29.190 | 15.878 | 10.751 |
| The Philippines | 0.283 | 22.697 | 11.148 | 7.355 |
| Indonesia | 1.431 | 30.468 | 16.205 | 11.081 |
| Malaysia | 3.288 | 26.511 | 13.671 | 8.966 |
| Thailand | 0.000 | 27.848 | 12.640 | 8.242 |
| Korea | 12.339** | 21.163 | 10.573 | 7.083 |
| China | 9.147 | 29.003 | 13.350 | 9.164 |

Note 1. Bootstrap critical values are obtained from 10,000 replications.

Table 4.6. H₀ Economic Growth Will Not Outpace CO₂ Emissions

| Country | Wald Statistic | Bootstrap Critical Values | | |
|-----------------|----------------|---------------------------|--------|-------|
| | | 1% | 5% | 10% |
| India | 15.449** * | 15.100 | 8.270 | 5.518 |
| The Philippines | 6.051* | 15.112 | 7.926 | 5.363 |
| Indonesia | 0.485 | 15.836 | 7.258 | 5.007 |
| Malaysia | 11.229** | 14.116 | 7.410 | 5.058 |
| Thailand | 0.974 | 17.794 | 8.502 | 5.692 |
| Korea | 16.853** | 17.697 | 9.337 | 6.271 |
| China | 0.725 | 25.273 | 13.020 | 8.752 |

Note 1. Bootstrap critical values are obtained from 10,000 replications.

Table 4.7. H₀ CO₂ Emissions Will Not Outpace Economic Growth

| Country | Wald Statistic | Bootstrap Critical Values | | |
|--------------------|----------------|---------------------------|-------|-------|
| | | 1% | 5% | 10% |
| Hungary | 22.071*** | 17.139 | 8.727 | 5.666 |
| Poland | 0.282 | 16.421 | 8.489 | 5.527 |
| Russia | 2.050 | 19.335 | 8.854 | 5.771 |
| Turkey | 1.055 | 17.692 | 8.733 | 5.514 |
| The Czech Republic | 0.427 | 17.343 | 8.252 | 5.567 |

Note 1. Bootstrap critical values are obtained from 10,000 replications.

Table 4.8. H₀ Economic Growth Will Not Outpace CO₂ Emissions

| Country | Wald Statistic | Bootstrap Critical Values | | |
|--------------------|----------------|---------------------------|-------|-------|
| | | 1% | 5% | 10% |
| Hungary | 0.212 | 15.054 | 7.544 | 4.944 |
| Poland | 15.824** * | 15.542 | 8.283 | 5.701 |
| Russia | 1.878 | 14.139 | 7.539 | 5.011 |
| Turkey | 0.512 | 14.595 | 7.679 | 5.035 |
| The Czech Republic | 0.008 | 12.864 | 7.033 | 4.769 |

Note 1. Bootstrap critical values are obtained from 10,000 replications.

Table 4.9. H₀ CO₂ Emissions Will Not Outpace Economic Growth

| Country | Wald Statistic | Bootstrap Critical Values | | |
|----------|----------------|---------------------------|--------|-------|
| | | 1% | 5% | 10% |
| Brazil | 0.836 | 19.311 | 10.081 | 6.774 |
| Mexico | 8.388** | 14.854 | 8.178 | 5.812 |
| Colombia | 1.548 | 15.134 | 7.560 | 4.976 |
| Chile | 2.974 | 15.904 | 7.950 | 5.273 |
| Peru | 0.285 | 15.941 | 8.064 | 5.492 |

Note 1. Bootstrap critical values are obtained from 10,000 replications.

Table 4.10. H₀ Economic Growth Will Not Outpace CO₂ Emissions

| Country | Wald Statistic | Bootstrap Critical Values | | |
|----------|----------------|---------------------------|-------|-------|
| | | 1% | 5% | 10% |
| Brazil | 20.285*** | 14.528 | 6.966 | 4.608 |
| Mexico | 14.058** | 18.615 | 8.775 | 5.574 |
| Colombia | 5.466* | 13.874 | 7.339 | 4.870 |
| Chile | 30.269*** | 13.079 | 7.180 | 4.956 |
| Peru | 4.009 | 15.344 | 7.582 | 4.995 |

Note 1. Bootstrap critical values are obtained from 10,000 replications.

Table 4.11. The Leading–Lagging Relationships between Economic Growth and CO₂ Emissions

| Africa | |
|-----------------|--|
| Egypt | GDP→CO ₂ |
| Morocco | GDP→CO ₂ |
| South Africa | No leading–lagging relationship between economic growth and carbon emissions |
| Zambia | No leading–lagging relationship between economic growth and carbon emissions |
| Namibia | No leading–lagging relationship between economic growth and carbon emissions |
| Asia | |
| India | GDP→CO ₂ |
| The Philippines | GDP→CO ₂ |
| Indonesia | No leading–lagging relationship between economic growth and carbon emissions |
| Malaysia | GDP→CO ₂ |
| Thailand | No causal relationship between economic growth and carbon emissions |
| Korea | CO ₂ ↔ GDP |
| China | No causal relationship between economic growth and carbon emissions |

Table 4.11. Continued

| Europe | |
|--------------------|--|
| Hungary | CO ₂ →GDP |
| Poland | GDP→CO ₂ |
| Russia | No causal relationship between economic growth and carbon emissions |
| Turkey | No any causal relationship between economic growth and CO ₂ emissions |
| The Czech Republic | No causal relationship between economic growth and carbon emissions |
| America | |
| Brazil | GDP→CO ₂ |
| Mexico | CO ₂ ↔ GDP |
| Colombia | GDP→CO ₂ |
| Chile | GDP→CO ₂ |
| Peru | No causal relationship between economic growth and carbon emissions |

Note 1. → Unidirectional causal relationship

2. ↔ Bidirectional causal relationship

REFERENCES

- M.J.I.A. Alama, B.J. Buysse, G.V. Huylenbroeck, *Energy Policy*, **45**, 217 (2012).
- N. Apergis, J.E. Payne, *Energy Economics*, **31**, 641 (2009).
- M.E.H.A.B. Arouri, Y.H. M'henni, C. Rault, *Energy Policy*, **45**, 342 (2012).
- N.B. Behmiri, J.R.P. Manso, *Energy Policy*, **45**, 628 (2012).
- G.H. Erdal, K. Esengün, *Energy Policy*, **36**, 3838 (2008).
- F. Halicioglu, *Energy Policy*, **37**, 1156 (2009).
- G.E. Halkos, N.G. Tzeremes, *Ecological Economics*, **70**, 1354 (2011).
- E.H. Polatidis, D. Haralambopoulos, *Applied Energy*, **88**(4), 1377 (2011).
- Md.S. Hossain, *Energy Policy*, **39**, 6991 (2011).
- V.C. Jaunky, *Energy Policy*, **39**, 1228 (2011).
- K.S.W.K. Lee, K. Nam, *Energy Policy*, **38**, 5938 (2010).
- F.S. Li, X. Donga, L.Q. Liang, W. Yang, *Energy Policy*, **39**(2), 568 (2012).
- M.R. Lotfalipour, M.A. Falahi, M. Ashena, *Energy*, **35**, 5115 (2010).
- R.J.M. Asafu-Adjaye, *Energy Policy*, **35**, 481 (2007).
- O.I.A. Aslan, H. Kalyoncu, *Energy Policy*, **38**, 4422 (2010).
- H.T. Pao, C.M. Tsai, *Energy*, **36**, 685 (2011).
- S.S. Sharma, *Applied Energy*, **87**, 3565 (2010).
- U. Soytaş, R. Sari, *Ecological Economics*, **68**, 1667 (2009).
- K.M. Wang, *Economic Modelling*, **29**, 1537 (2012).
- X.P. Zhang, X.M. Cheng, *Ecological Economics*, **68**, 2706 (2009).
- G. Zou, K. W. Chau, *Energy Policy*, **34**, 3644 (2006).

Evaluating air quality through aerial demand function and an application evaluating air quality

Z.Z. Li*^{1,2}, J.Q. Su¹

¹Faculty of Management and Economics, Dalian University of Technology, Dalian, China, 116023

²Management School, Tianjin Polytechnic University, Tianjin, China, 300387

Received June 26, 2017; Revised July 20, 2017

This paper primarily explores a methodological framework to analyze demand of an omnipresent public good, the concrete instantiation of setting up an aerial demand function to describe its application of influencing on air quality change, for the purpose of compensating the air pollution impairing environmental quality and human health negatively and chronically, and conducing to avoiding cognitive complexity of air quality variety. Bottom-up approach of acquiring individual state preference sampling, and top-down technique of attaining the related air quality variables' sampling, are jointly adopted to support the empirical survey. Due to the former data, contingent valuation method is used to calculate Hicks' consumer surplus; owing to the latter data and the foregoing result, air demand functions is computed to explain the predictor variables' marginal effects. The findings are that the decreased 10 units AQI to improve air quality leads to the average individual willingness to pay in 2 to 4 Yuan, and PM10 concentration engenders the larger effect on human health.

Keywords: Air quality index (AQI); air demand function (ADF); contingent valuation method (CVM); air economic value; marginal effect

AIMS AND BACKGROUND

The air pollution in urban areas has been chronically negatively impaired human health. At the moment, particulate matter (PM), volatile organic compound (VOC) and aerosol pollutants are widely discussed. Simultaneously, TSP (Total Suspended Particulate, of diameter greater than 10 micrometers), PM_{2.5} (Particulate matter with diameter of 2.5 micrometers or less), and PM₁₀ (Particulate matter less than 10 micrometers diameter), are attracted increasing attention [1, 2]. Those are regarded as the chief culprit of the air pollutions and concealed in the morphologies of dust, smoke, powder or fog. The chemist, environmentalist, and meteorologist et al agree on the pollutant components of oxides of nitrogen (NO_x, the oxidized No readily forms No₂, nitrogen dioxide), monoxide (Co), sulfur dioxide (So₂), ozone (O₃), methane (CH₄), metals or metalloid. Naturally, the chemical ingredients involved water soluble ions, such as anions No³⁻ and So₄²⁻ formed mainly from oxidation of So₂ and NO_x, and arsenic, cadmium, nickel, mercury and lead etc. Those play a key role to produce PM currently [3]. Those chemical ingredients impair our organs and tissues, many studies have indicated that exposure to air pollution can increase risks of developing cancer, respiratory and allergy diseases, and aggravate the condition of people suffering from respiratory or

heart diseases [1,4].

Within our limited atmosphere, the high-quality air attracts a variety of profits, even has a therapeutic effect on human health, and also brings on much social welfare enjoying ourselves of outdoor interests and activities on recreation and leisure in the free high-quality air. On the one hand, people present a high demand for various beautiful natural environments included inhalational absorbable fresh air, and many tremendous economic values on extraordinary sight of tourism sites. On the other hand, devastating of the human economic activities not only counteracts our health, but also sometimes erodes environment. The air possesses the characteristic of non-market resource, under many situations, the marketable prices of non-market resources may not exist. Nevertheless, the non-existence of price does not mean zero economic value to be accrued to those non-market resources, neither are their values very low. The value assessment of those environmental goods is comprehensively proposed, which contributes to compensating for the reduction of the fresh air and boosting the conservation of the high-quality air.

For the nonmarket public good non-evaluated by mean of market price, the total economics value (TEV) included use and nonuse value (existence, bequest, and option), is preferred to scholar's research on the environmental economic values [5]. One instrument which is commonly used to measure economic value on non-market resource is the consumer surplus hypothetically acted as a price or value. Furthermore, the related literatures have long

* To whom all correspondence should be sent:

E-mail: LZ200603@hotmail.com

spatiotemporal spans and have been prosperous till now, and the value is frequently measured through Contingent Valuation Method (CVM) and Choice Experiment Model (CEM), which have been used in many research fields such as healthy, risk, waste, environment etc [5-7].

At present, the atmospheric modeling can solve some complex environmental problems aiming at forecasting [8] what are statuses of No₂, Co, So₂, O₃, CH₄, metals or metalloid toxins in order to improving air quality. Furthermore, which can help fostering a more informed and creative environmental programming and respond to the challenges to science practice with other stakeholders such as politics, governance, media, etc [9]. Additionally, econometric approaches are used to analyze the air pollution trend through time series or conventional statistic analysis [10]. The purpose of this research is to measure the marginal effect of air quality diversity to help decision-making environment, and the study is an update and extension of current research on air quality. The new methodology holds three-stage sequential procedures consisted of assessing economic value through CVM after surveying individual state preference, achieving demand function by regression analysis of the partial factors mentioned above, and exploring marginal effect and analyzing finally.

EXPERIMENTAL PART

Hicks summarized important findings in his paper "The Four Consumer's Surpluses" published at journal of The Review of Economic Studies (Vol. 11, No. 1, Winter, 1943, pp.31-41), and explored the distinct relations between the corrected measures of consumer surplus and Marshallian measure. CV (Compensating variation), EV (Equivalent variation), CS (Compensating surplus) and ES (Equivalent surplus) were primarily systematically introduced and argued in the content, which benchmarked Hicks consumer surplus.

According to environmental microeconomic foundation, the four consumer surpluses can be used to explain Willingness to Pay (WTP) or Willingness to Accept (WTA). WTP, the maximum expected value by an individual, is worthy of procuring a good (CV or CS) or avoid something with low quality (EV or ES). WTA is the minimum monetary amount to be worth accepting to a low quality or undesirable good (CV or CS), or abandoning the good (EV or ES). When not directly consuming by participants in the experiment, the consumers determine to acquire a good's value through their WTP, for example, WTP for the air is the expected value of a high-

quality air. CV expresses the effect of a price change on an agent's net welfare at the context of new prices and the initial utility level, which is widely used to measure mean WTP per capita and the consumer surplus.

When thinking about the indifference curves of two goods, let price vector $\mathbf{P} = \{p_1^1, p_1^2, p_2^1, p_2^2\}$, where $\mathbf{P}^1 = \{p_1^1, p_1^2\}$ & $\mathbf{P}^2 = \{p_2^1, p_2^2\}$, $p_2 = p_2^1 = p_2^2$ is constant variable respectively, the wealth level is M , and an expenditure function is $e(\mathbf{P}, u)$. Adopted the traditional method in virtue of the expenditure function of utility u and price \mathbf{P} , the derivative through Shephard Lemma is calculated to get Hicks demand function $h_1(\mathbf{P}, u_0)$. Thereupon then, consumer surpluses are achieved through the function's integrals, shown at Equ1.

$$CV = e(p_1^2, u_0) - e(p_1^1, u_0) = \int_{p_1^2}^{p_1^1} h_1(\mathbf{P}, u_0) dp_1 = \int_{p_1^2}^{p_1^1} \frac{\partial e(\mathbf{P}, u_0)}{\partial p_1} dp_1 \quad (1)$$

Hypothetical, the utility functions of the air good are $u_0(\mathbf{P}^1, M)$ before improving and $u_1(\mathbf{P}^2, M - CV)$ in the high-quality condition to ensure getting the consistency utility, that is, $u_0(\mathbf{P}^1, M) = u_1(\mathbf{P}^2, M - CV)$. Through indirect utility function, $v(p, y) = \max u(x) = [x^*(p, y)]$ s.t. $p \cdot x \leq y$, get $u_0(\mathbf{P}^1, y) = u_1(\mathbf{P}^2, y - WTP_{\max})$ for maximized willingness to pay, while $u_1(\mathbf{P}^2, y - WTP) > u_0(\mathbf{P}^1, y)$ for individual willingness to pay variable.

Any good expression on demand elasticity like the air can be written as follows:

$$E_D = (\Delta Q / Q) / (\Delta P / P) = (\Delta Q / \Delta P) \cdot (P / Q) \quad \text{or} \\ E_D = (dQ / dP) \cdot (P / Q) \quad (2)$$

An ordinary good or service is suitable for use of the law of diminishing returns, a fundamental principle of economics. Marginal utility can be used to analyze the utility change of increasing or decreasing in unit consumption of the good or service. Nevertheless utilization of demand function is ineffectiveness on disposing of the marginal utility, but marginal effect equal to the reciprocal of the coefficient is adequate for solving the change of any explanatory variable owing to increasing or decreasing in unit good consumption, and brings on indirect explanation of the utility change. The marginal effect can be defined as the following equation.

$$ME = \Delta P / \Delta Q = 1 / (\Delta Q / \Delta P) \quad \text{or} \quad ME = 1 / (\partial Q / \partial P) \quad (3)$$

RESULTS AND DISCUSSION

Sampling and survey

The dichotomous choice (DC) empirical survey is easier on the respondents, though it statistically requires a larger sample to attain a given level of precision. The background explanation is one of the crucial steps to get the credible data, and the paper explores a new state preference survey mode through the actual air quality apperception.

In the light of Technical Regulation on Ambient Air Quality Index, there are six AQI levels promulgated by Environmental Protection Ministry of China. Each level is a clustering of many integrated AQIs in the series, and every AQI is the maximization of calculated individual AQI of So₂, No₂, CO, O₃ etc. The first four AQI levels are grouped according to four aggregations every other 50 AQIs of sort ascending. The level 5 is an aggregation of AQIs equal to 201-300, and the level 6 is collected AQIs more than 300. Based on the classifying AQI levels, the choice date of the surveyed layout is fixed on the date of AQI level 3, 4 and 5, helping to respondent apperception and perceived comparison with high-quality air. Meanwhile, the greatly high-quality air is also disclosed and introduced.

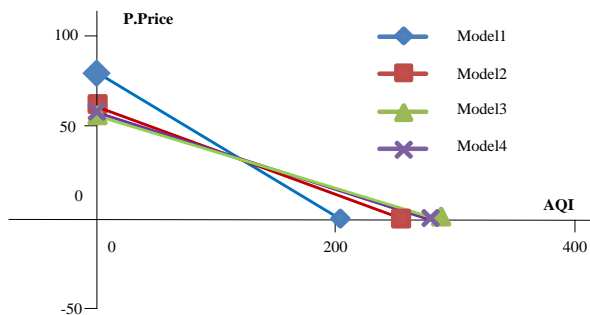


Fig. 1. Air demand function curves of three state preference survey scenarios

The questionnaires are simplification with double/single bounded DC (DBDC/SBDC) items (biding and optioning items) and several socio-economic variables of sex, age, income, education and occupation, for the purpose of acquiring samplings rapidly and largely. The biding value variable is named as *BIDV*. To sum up the empirical survey, three scenarios are respectively chosen to achieve surveys on March, May or June in Tianjin, and each investigation is implemented 3 days per capita.

The paper also necessarily employs an empirical sampling of top-down approach to obtain the data. Base on clustering data from the official websites,

China Meteorological administration, Ministry of Environmental Protection of People's Republic of China, Tianjin Environmental Protection Bureau, and Tianjin Meteorological Bureau, 245 samplings are gained. The descriptive statistics can be browsed at Tab. 1.

Estimating Hicks' consumer surplus

The paper adopts an empirical sampling of bottom-up approach to obtain the data. Two CVMs included SBDC and DBDC is used to calculate Hicks' Compensating variation (CV) which is a deputy of the consumer surplus or the mean WTP per capita, equal to the existence value to be used to similarly reflect TEV per capita, named pseudo price (P. Price) of the air or the other ubiquitous type of public goods. The marginal value (mean WTP per capita) represents the hypothetical price of the public good (air) on several dozens of AQI amount. The computing results are shown at Tab. 2.

In the maximum likelihood estimation, measures of goodness-of-fit and joint significance of the coefficient are often estimated by McFadden's R^2 and the likelihood ratio, while McFadden's R^2 cannot be used to calculate the double-bounded Logit model. Through comparison among the three asymptotically equivalent tests including the likelihood ratio statistic, the Wald statistic, and the Lagrange multiplier statistic, Wald statistic can be exploited in the context of the double-bounded DC model because of its utilization based solely upon the value of the unrestricted likelihood function. For the six models at tab. 2, the variable coefficient is statistically significant: SBDC is tested by LR-ratio and McFadden pseudo R^2 , and DBDC through LR-ratio and Wald test.

Calculating air demand function

The interesting factors comprise of the three chemical (Co, No₂, and So₂) and four atmospheric (temperature, dew, humidity, and wind speed) factors, AQI and AQI's levels (the classification of AQIs). According to the definition of the chemist, environmentalist, and meteorologist et al, the AQI's levels embody the compositive explanation of many factors (pm_{2.5}, pm₁₀, So₂, No₂, O₃, and Co etc). Assumptions in the paper is: (i) the AQI firstly is taken as the supposed demand quantities of the ubiquitous air, and (ii) individual economic value represents the hypothetical price of the air quality reckoned with the process above. The early analysis and research of the author (Li, in publishing) shows that, although the influences of the atmospheric factors are synchronously occurred and statistically significant, if their cross-influences are not

considered better, the evident impact will contort their truly acted results. In this paper, the regressed consequence emerges the disordered situation of regression involved with the atmospheric factors; therefore the air demand function ignores their influences. According to classification of the three scenarios mentioned above, the author utilizes the trend extrapolation approach to acquire the other Mean (WTP) at different AQI level. And then pseudo price is respectively computed through an equably transformation of Mean (WTP). Thereupon then, a new variable is created to exhibit the air value assimilated top-down data.

The ordinary least square method (Model1 and Model2) and the two stages least squares (Model3 and Model4) are used to achieve the regression equation of air demand function, the solution and statistic test shown at Tab.3&4, which presents the strictly statistic significance at each model, except that the regressed coefficients or marginal effects of No2 and So2 are not commonsensible apperception at Model 1 of Tab. 3. Their reversed deflection seems to be influenced by AQI's definition, that is to say, squeezing out a maximization of many individual contamination's AQIs cannot imply the associated factors or independents' regression relationship in existence, and thus the paper develops Model 2-4 of Tab. 4. The explanatory variables, PM2.5, PM10 and CO, express the acceptable correlation, and get the indicative marginal effects of scarce elasticity.

Based upon the estimation results of the air demand functions, their air demand function curves are drawn at Fig. 1, which depicts an instinctive

illustration on demand characteristics of the air good to rely on the individual state preference survey. Certainly, the newly designed survey mode can clearly perceive the survey background, adding up short-term survey can reduce the error, whereas a cognized attention span of AQI amount can hardly aim at an individual state preference WTP at the limited scenarios. The hypothesis is there are approximately the exclusive correspondence between a large number of AQI and a small quantity of WTPs.

Analyzing marginal effect

At model 1 from Tab. 5, the new increase of unit AQI arouses the marginal effect of PM10 reached 16.7 times, and 2.3 times PM2.5. According to Model 3&4, the air good's pseudo price represents the approximate unit elasticity, while at Model 1&2, PM10, PM2.5 Co, No2, So2 etc impact on the pseudo price to an insufficient elasticity, which demonstrates that the air pollution can bring about a calamitous influence of human health and environmental safety.

In this paper, the marginal effect resultings present that the increased unit AQI will give rise to the average individual WTP decreased in 0.2 to 0.4 Yuan, raising 0.1 Co concentration can induce the AQI at one unit high, and the PM2.5's or PM10's concentration respectively goes up 2.3 and 16.8 to lead to the air quality impaired one index. Which expresses that PM10 concentration engenders the larger effect on human health.

Table 1. Descriptive Statistics on the relative factors of air quality

| | Mean | Std. E. | Median | Variance | Skewness | Kurtosis | Min | Max |
|----------|--------|---------|--------|----------|----------|----------|------|------|
| AQI | 131.10 | 4.21 | 112 | 4341.23 | 1.060 | 0.603 | 30 | 361 |
| Level | 3.02 | 0.07 | 3 | 1.30 | 0.496 | -0.792 | 1 | 5 |
| PM2.5 | 94.03 | 3.88 | 77 | 3682.22 | 1.286 | 1.670 | 12 | 330 |
| PM10 | 154.76 | 5.38 | 139 | 7097.35 | 1.108 | 1.478 | 21 | 476 |
| Co | 1.91 | 0.06 | 1.67 | 0.76 | 1.286 | 1.721 | 0.45 | 5.57 |
| No2 | 60.61 | 1.49 | 57 | 541.47 | 0.659 | 0.117 | 16 | 129 |
| So2 | 70.56 | 3.22 | 55 | 2540.22 | 1.022 | 0.576 | 4 | 261 |
| Tem | 9.77 | 0.66 | 8 | 108.28 | 0.275 | -1.219 | -8 | 31 |
| Dew | -1.22 | 0.66 | -3 | 107.67 | 0.165 | -0.803 | -25 | 19 |
| Hum | 52.84 | 1.15 | 52 | 325.95 | 0.058 | -0.797 | 15 | 95 |
| Spd | 11.27 | 0.34 | 10 | 27.98 | 1.307 | 2.083 | 3 | 32 |
| P. Price | 30.55 | 0.93 | | | | | 7 | 58 |

Table 2. Evaluating air quality through two modles under three scenarios

| | Scenario1 | | | | Scenario2 | | | | Scenario3 | | | |
|---------------|-----------|--------|---------|--------|-----------|--------|---------|--------|-----------|--------|---------|--------|
| | SBDC | | DBDC | | SBDC | | DBDC | | SBDC | | DBDC | |
| Variables | Const | BIDV | Const | BIDV | Const | BIDV | Const | BIDV | Const | BIDV | Const | BIDV |
| Coefficient | 0.043 | -0.012 | 0.882 | -0.015 | 0.018 | -0.010 | 0.803 | -0.012 | 0.430 | -0.009 | 0.672 | -0.011 |
| t-statistic | 0.153 | -3.114 | 4.183 | -7.551 | 0.066 | -2.695 | 4.074 | -7.500 | 1.573 | -2.944 | 3.424 | -7.732 |
| t-probability | 0.878 | 0.002 | 0.000 | 0.000 | 0.947 | 0.007 | 0.000 | 0.000 | 0.116 | 0.003 | 0.001 | 0.000 |
| Mean | 108.472 | | 115.00 | | 114.622 | | 108.34 | | 120.991 | | 151.78 | |
| Observations | 106 | | | | 111 | | | | 115 | | | |
| LR-ratio | 18.765 | | 205.306 | | 15.762 | | 187.934 | | 17.548 | | 193.515 | |
| McFadden | 0.141 | | | | 0.110 | | | | 0.116 | | | |
| Wald test | | | 57.013 | | | | 56.251 | | | | 59.787 | |
| Mean(WTP) | 81.080 | | 68.395 | | 96.485 | | 81.533 | | 114.575 | | 90.058 | |

Table 3. Air demand function estimation (Model 1)

| | (Constant) | P. Price | PM2.5 | PM10 | CO | No2 | So2 |
|------------|------------|----------|-------|-------|-------|--------|--------|
| Coeff. | 159.669 | -2.451 | 0.429 | 0.060 | 8.010 | -0.225 | -0.070 |
| S.E. | 8.926 | 0.156 | 0.070 | 0.044 | 3.276 | 0.111 | 0.045 |
| t | 17.888 | -15.755 | 6.137 | 1.341 | 2.445 | -2.023 | -1.561 |
| Sig. | 0.000 | 0.000 | 0.000 | 0.181 | 0.015 | 0.044 | 0.120 |
| Adj. R Sq. | | | | 0.923 | | | |

Table 4. Air demand function estimation (Model 2-4)

| Variable | Model 2 | | Model 3 | | Model 4 | |
|--------------|------------|----------|------------|----------|-----------------------------|----------|
| | (Constant) | P. Price | (Constant) | P. Price | (Constant) | P. Price |
| Coefficient | 259.839 | -4.214 | 280.212 | -4.881 | 279.617 | -4.861 |
| S.E. | 3.611 | 0.107 | 4.466 | 0.136 | 4.417 | 0.134 |
| t | 71.957 | -39.470 | 62.743 | -35.997 | 63.305 | -36.294 |
| Sig. | 0.000 | 0.000 | 0.000 | 0.000 | 0.000 | 0.000 |
| Adj. R Sq. | 0.865 | | 0.841 | | 0.844 | |
| instrumental | | | PM10,PM2.5 | | PM10, PM2.5 Co, No2, So2 | |

Table 5. Price elasticity and marginal effect of demand function

| | Mode1 | Mode | Mode | Mode | Mode1 | | | | |
|----------------------------|-------|----------|-------|-------|--------|---------|--------|-------|--------|
| | | 2 | 3 | 4 | | | | | |
| | | P. Price | | | | PM2.5 | PM10 | CO | No2 |
| $-\partial Q / \partial P$ | 2.451 | 4.214 | 4.881 | 4.861 | -0.429 | -0.060 | -8.010 | 0.225 | 0.070 |
| $-E_p$ | 0.571 | 0.982 | 1.137 | 1.133 | -0.308 | -0.070 | -0.117 | 0.104 | 0.038 |
| $-ME$ | 0.408 | 0.237 | 0.205 | 0.206 | -2.330 | -16.780 | -0.125 | 4.452 | 14.292 |

CONCLUSIONS

This paper mainly gropes for the economic value and marginal effect of air quality change through creating the demand function of air attributed an omnipresent public good. The key contributions are (i) providing an analytical framework of ubiquitous public good's demand, (ii) predicting air economic value based on Hicks consumer surplus, (iii) defining and analyzing the marginal effect of the independents based upon the air demand function. As well as, the surveys comply with two approaches of bottom-up and top-down technique, and samplings of the field investigation on individual state preference and the official websites' data clustering are combined organically.

The marginal value (mean WTP per capita) is measured; meaning that newly increasing dozens of AQI amount can arouse WTP with 68.4 Yuan at the scenario of AQI level 3, 81.5 Yuan at the scenario of AQI level 4, and 90.1 Yuan at the scenario of AQI level 5. Meanwhile, according to analysis of marginal effect, the decreased one unit AQI (to improve air quality) leads to the average individual willingness to pay in 0.2 to 0.4 Yuan, and Co's, PM_{2.5}'s and PM₁₀' marginal effect respectively is 0.1, 2.3 and 16.8, which indicates that PM₁₀ emerges a bigger change during improving air quality at one AQI reduced, that is to say, PM₁₀ concentration brings about the larger effect on human health.

Acknowledgements: This study was funded through Tianjin Philosophy Social Science Fund , China (No.TJGL13-018).

REFERENCES

1. <http://www.epa.gov/airtrends/2011/>.
2. A.B. Vicente, T. Sanfeliu, M.M. Jordan, *Journal of Environmental Management*, 108, 92 (2012).
3. A. M. Taiwo, D.C.S. Beddows, Z Shi, *Science of the Total Environment*, **475**, 29 (2014).
4. <http://www.sciencedaily.com/releases/2010/05/100510161244.htm>.
5. I.J. Bateman: Valid Value Estimates and Value Estimate Validation: Better Methods and Better Testing for Stated Preference Research. In: Bennett, J. (Ed.). *The International Handbook on Non-Market Environmental Valuation*. Edward Elgar Publishing, Cheltenham UK. 2011.
6. J. Armbrrecht: *Tourism Management*, **42**, 141 (2014).
7. G. Marella, R. Raga, *Waste Management*, **34**(7), 1199 (2014).
8. X. Luo, H. Cao, *Procedia Environmental Sciences*, **12**, 159(2012).
9. M. Vedrenne, R.Borge J. Lumbreras, M.E. Rodríguez: *Environmental Modelling & Software*, **57**, 177 (2014).
10. S. Mehta, H. Sbihi, T.N. Dinh, D.V. Xuan, L.L.T. Thanh, C.T. Thanh, G.L. Truong, A. Cohen, M. Brauer, *Atmospheric Environment*, **95**, 571 (2014).

The evaluation of the sustainability of land consolidation and remediation in Funing County

H.G. Zheng^{1,2*}, F.R. Qiao¹, Y.Q. Li³, J.S. Zhang^{1,2}, L.J. Liao^{1,2}, D.J. Wang⁴, J.X. Yu^{1,2},

¹Water Resources and Building, Yunnan Agricultural University, Kunming 650201, China

²Engineering Research Center of Science and Technology of Land and Resources, Yunnan Agricultural University, Kunming 650201, China

³Yunnan Agricultural University Library, Kunming 650201, China

⁴College of Resources and Environment, Yunnan Agricultural University, Kunming 650201, China

Received June 26, 2017; Revised July 21, 2017

Land consolidation and reclamation is an important measure to increase the quantity and quality of arable land. Because the land consolidation and remediation covers a long construction period, the sustainability of the project has become the subject of controversy and suspicion. Combining the characteristics and the theory of sustainable land consolidation and rehabilitation management by building a sustainable evaluation system, the implementation and sustainability of land remediation effect was evaluated. In this paper, the Land consolidation and rehabilitation project of Ban Lun town, Mu yang town, Gui chao town, Li da town, Hua jia town in Funing County as an example, on the basis of investigation and study on the use of Delphi method, Analytic Hierarchy Process (AHP), index summation method other methods, by 18 index. The results show that the effect of the implementation of Funing County land remediation and sustainability is good.

Keywords: land consolidation and rehabilitation; sustainability; evaluation

INTRODUCTION

At present, China is facing a severe shortage of land resources, and land consolidation and remediation is an important measure to increase the amount of arable land, improve the quality of cultivated land and maintain the dynamic balance of farmland. In 1999, the promulgation of *The Law of Land Administration of the People's Republic of China* ushered the prelude of large-scale land consolidation and remediation. Through more than ten years of development, land consolidation and remediation have made a series of achievements, developed and consolidated a lot of land, increased the effective agricultural acreage, and made a positive contribution to the dynamic equilibrium of total cultivated land area as well as macro strategies of food security. The launch of land consolidation and remediation alleviated the tense situation of arable land to some extent, but it outweighed the economic value and functions of land over the ecological functions of land, with relatively weak awareness of ecological environment protection. For instance, it still lays too much emphasis on the increase of quantity regarding the benefit evaluation index system of measuring the land consolidation and remediation project, with the lack of mandatory

indexes that measure quality, environment and other aspects. Besides, land consolidation and remediation has broad construction contents, long duration, difficult supervision of construction quality and other characteristics, the project effect and post-implementation sustainability have received controversy and suspicion[1-8]. In November 2009, "Land Consolidation Project for Border Development" Farmland Consolidation and Remediation Key Project in the Western Ecological Construction Region Yunnan Province declared by Yunnan was approved by the joint review of the Ministry of Land and Resources and Ministry of Finance, and was commenced in 2010. This key project involves 210,000 hectares of land consolidation and remediation in 25 border counties (cities) of the border areas in Yunnan Province, with a construction period of 5 years and a total project budget of 8.62 billion yuan. Being one of the 25 border counties, Funing County is located in the southwest fragile ecological environment, with large differences in vertical elevation, complex topography and landforms, diverse land use patterns, frequent natural disasters and numerous ethnic minorities, hence it has strong representativeness in the evaluation of the effect and sustainability of land consolidation and remediation.

In this paper, the land consolidation and rehabilitation project of Banlun Town, Muyang

* To whom all correspondence should be sent:

E-mail: ynhg61@126.com

Town, Guichao Town, Lida Town, Huajia Town in Funing County was taken as an example to analyze and study the project sustainability after land consolidation and remediation, the results can provide a certain reference for similar studies and land administrative departments.

Overview of the Study Area

Located in southeastern Yunnan Province and the east of Wenshan Zhuang and Miao Autonomous Prefecture, Funing County is the channel connecting Southeast Asia and Yunnan. Its geographical coordinates are about east longitude 105°13'-106°12' and north latitude 23°11'-24°09', with the Tropic of Cancer crossing the south border. The county has an altitude of 684m, with the highest and lowest altitudes of 1,851.8m and 142m, respectively. Land area covers 5,352 km², wherein mountainous and semi-mountainous areas cover 5,067.84km², accounting for 96% of the total county area, the county has 69,300 hectares of arable land and is very rich in water resources, with an average annual rainfall of 1,103mm. Funing County is located in the low latitude hot region, with vast mountainous areas and undulating terrains, forming a monsoon climate that are mainly southern sub-tropical and tropical with distinct dry and wet seasons. Funing is a multi-ethnic settlement, the territory is inhabited by six ethnic groups--Zhuang, Han, Miao, Yao, Yi, Gelao, and the county has a total of 95,000 households and 418,300 people.

METHODS

Construction of evaluation index system

In this paper, the screening of evaluation index is mainly based on the existing benefit evaluation index of land department, while referring to the relevant existing evaluation index of the financial department and the relevant departments, combined with the evaluation characteristics, evaluation contents and purpose, research results at home and abroad[5-8]. The sustainability of land consolidation and remediation evaluation is divided into: comprehensive index, evaluation factors and evaluation index, evaluation factors are divided into cultivated land utilization factor, economic factors, social factors and ecological factors, including 18 evaluation indexes.

Determination of evaluation index weight

In this paper, Delphi method is adopted to determine the evaluation index weight. It generally takes several rounds of expert scoring, and the experts modify their views according to the weight mean values and variances gained in the previous round, thus achieving closer mean values and smaller variances until meeting the requirement. Specific requirements of the experts in scoring process are:

a) Experts carry out independent scoring based on their own theoretical knowledge and practical work experience, and no discussions among each other; b) the sum of selection factor weights is 1.00, otherwise invalid; c) the final classification factors and the determination of their weights must meet certain mathematical statistics requirements, otherwise the next round of scoring must be conducted. On the basis of preliminary indexes selection and project evaluation needs of "land consolidation project for border development" farmland consolidation and remediation key project in the western ecological construction region Yunnan Province, the research group invited 22 experts who are familiar with Yunnan land consolidation and remediation and agricultural production, and made final determination of evaluation index weights by using Delphi method to carry out several rounds of expert consultation and weight scoring until the expert opinions are close to each other. Refer to the evaluation index system of sustainable land consolidation and rehabilitation and evaluation index weight in Tab.1.

Classification of the sustainability of land consolidation and remediation

In this paper, comprehensive index of the sustainability of land consolidation and remediation is adopted to measure the sustainable level of land consolidation and remediation, the comprehensive index of the sustainability of land consolidation and remediation can be calculated by using index sum method, calculation formula is as follows:

$$SLC = \sum_{i=1}^n W_i C_i$$

Where, W_i is the comprehensive index of weights, C_i is the index's score, n is the total number of indexes.

Table 1. Evaluation index system of sustainable land consolidation and rehabilitation and evaluation index weight table

| composite Index | evaluation Factors | relative weights | evaluation index and weight | | |
|--|------------------------------------|------------------|---|-----------------|----------------------|
| | | | evaluation index | relative weight | comprehensive weight |
| Comprehensive index of sustainable land consolidation and rehabilitation | Cultivated land utilization factor | 0.24 | irrigation guarantee rate C1 | 0.21 | 0.05 |
| | | | irrigation and drainage ditches density C2 | 0.17 | 0.04 |
| | | | road density in the field C3 | 0.13 | 0.03 |
| | | | cultivated land quality level C4 | 0.25 | 0.06 |
| | | | raise the level of grain output C5 | 0.25 | 0.06 |
| | | | area ratio of cultivated land C6 | 0.29 | 0.08 |
| | economic factors | 0.27 | the increasing rate of income per mu C7 | 0.22 | 0.06 |
| | | | mu cost reduction rate C8 | 0.19 | 0.05 |
| | | | production improvement factor C9 | 0.19 | 0.05 |
| | | | per capita GDP growth rate C10 | 0.11 | 0.03 |
| | | | per capita annual net income increased C11 | 0.34 | 0.10 |
| | | | poor people out of poverty rate C12 | 0.28 | 0.08 |
| | social factors | 0.29 | public satisfaction rate C13 | 0.17 | 0.05 |
| | | | the rate of increase in agricultural productivity C14 | 0.21 | 0.06 |
| | | | land reclamation rate increment C15 | 0.15 | 0.03 |
| | | | drought and flood disaster reduction rate C16 | 0.3 | 0.06 |
| | | | green vegetation cover increment C17 | 0.2 | 0.04 |
| | | | soil and water loss control rate C18 | 0.35 | 0.07 |
| ecological factor | 0.20 | | | | |
| | | | | | |
| | | | | | |
| | | | | | |
| | | | | | |
| | | | | | |

Table 2. Funing County land consolidation and rehabilitation sustainability post evaluation the calculation data

| evaluation index | No1 consolidation before | | | | | No2 consolidation after | | | | | No3 amount of change | | | | |
|---|--------------------------|------|------|------|------|-------------------------|------|------|------|------|----------------------|------|------|------|------|
| | No1 | No2 | No3 | No4 | No5 | No1 | No2 | No3 | No4 | No5 | No1 | No2 | No3 | No4 | No5 |
| irrigation guarantee rate | 78 | 70 | 75 | 73 | 64 | 80 | 75 | 80 | 85 | 75 | 2 | 5 | 5 | 12 | 11 |
| irrigation and drainage ditches density | 0.09 | 0.02 | 0.01 | 0.02 | 0.07 | 0.1 | 0.0 | 0.0 | 0.08 | 0.13 | 0.07 | 0.03 | 0.03 | 0.06 | 0.05 |
| road density in the field | 0.06 | 0.04 | 0.02 | 0.03 | 0.02 | 0.1 | 0.0 | 0.0 | 0.07 | 0.08 | 0.05 | 0.03 | 0.03 | 0.04 | 0.05 |
| cultivated land quality level | 3 | 3 | 4 | 3 | 3 | 4 | 5 | 6 | 5 | 4 | 1 | 2 | 2 | 2 | 1 |
| the level of grain output | 0.45 | 0.68 | 0.91 | 0.55 | 0.61 | 0.7 | 1.0 | 1.2 | 0.86 | 0.90 | 0.3 | 0.39 | 0.37 | 0.30 | 0.28 |
| area ratio of cultivated land | 78.6 | 74.1 | 75.4 | 79.1 | 80.3 | 92.7 | 77.8 | 81.8 | 85.4 | 94.3 | 13.7 | 3.2 | 6.2 | 6.2 | 13.9 |
| income per mu | 692 | 979 | 673 | 785 | 518 | 809 | 104 | 805 | 931 | 703 | 117 | 66 | 132 | 146 | 185 |
| the cost per mu | 375 | 587 | 403 | 479 | 411 | 425 | 654 | 473 | 567 | 458 | 50 | 67 | 70 | 88 | 47 |
| production improvement factor | 0.47 | 0.79 | 0.80 | 0.53 | 0.50 | 1.0 | 1.2 | 1.1 | 0.80 | 0.95 | 0.55 | 0.46 | 0.33 | 0.26 | 0.45 |
| GDP per capita GDP | 687 | 564 | 495 | 712 | 788 | 978 | 845 | 769 | 102 | 100 | 2911 | 280 | 274 | 308 | 215 |
| per capita annual net income | 152 | 126 | 106 | 165 | 186 | 408 | 365 | 386 | 419 | 395 | 256 | 238 | 280 | 254 | 208 |
| poor people out of poverty rate | 3.4 | 2.8 | 2.6 | 4.8 | 2.2 | 15 | 13 | 9.2 | 18.0 | 9.09 | 11.5 | 12.9 | 7.22 | 13.2 | 7.84 |
| public satisfaction rate | 66 | 58 | 54 | 42 | 40 | 82 | 84 | 86 | 85 | 82 | 16 | 26 | 32 | 43 | 42 |
| agricultural labor productivity | 36 | 12 | 33 | 24 | 35 | 75 | 70 | 82 | 66 | 78 | 39 | 58 | 49 | 42 | 43 |
| land reclamation rate | 81.0 | 74.1 | 75.4 | 86.7 | 79.7 | 84.7 | 77.8 | 81.8 | 89.4 | 81.7 | 3.22 | 3.2 | 6.2 | 2.69 | 2.02 |
| drought and flood rate | 56.7 | 62.4 | 56.4 | 73.5 | 49.7 | 19 | 20 | 18 | 21.6 | 19.5 | - | - | - | - | - |
| green vegetation cover | 82.5 | 75.2 | 76.3 | 87.4 | 80.9 | 85 | 78 | 82 | 89.9 | 82.6 | 2.59 | 2.99 | 5.98 | 2.51 | 1.66 |
| soil and water loss control rate | 8.0 | 11.7 | 9.8 | 12.4 | 7.6 | 26 | 36 | 64 | 44.5 | 37.9 | 18.5 | 25.9 | 55.0 | 32.1 | 30.2 |

Note: No1 instead Ban Lun town, No2 instead Mu Yang town, No3 instead Gui Chao town, No4 instead Li Da town, No5 instead Hua Jia town.

Table 3. Funing County land consolidation and rehabilitation sustainability post evaluation index scores Standard

score

| evaluation index | 0~40 | 40~70 | 70~85 | 85~100 |
|----------------------------------|-------|-----------|------------|----------|
| irrigation guarantee rate | <40 | 40~70 | 70~80 | 85~100 |
| irrigation and drainage ditches | <0.05 | 0.05~0.1 | 0.1~0.15 | 0.15~0.3 |
| road density in the field | <0.05 | 0.05~0.75 | 0.75~0.1 | 0.1~0.2 |
| cultivated land quality level | <3 | 3~5 | 6~10 | 10~16 |
| the level of grain output | <0.5 | 0.5~1 | 1~1.5 | >1.5 |
| area ratio of cultivated land | <50 | 50~70 | 70~90 | 90~100 |
| income per mu | <600 | 600~800 | 800~1000 | >1000 |
| the cost per mu | >600 | 600~400 | 400~300 | <300 |
| production improvement factor | <0.5 | 0.5~1 | 1~1.5 | >1.5 |
| GDP per capita GDP | <5000 | 5000~8000 | 8000~10000 | >10000 |
| per capita annual net income | <2000 | 2000~4000 | 4000~8000 | >8000 |
| poor people out of poverty rate | <10 | 10~30 | 30~50 | 50~100 |
| public satisfaction rate | <40 | 40~70 | 70~80 | 85~100 |
| agricultural labor productivity | <40 | 40~70 | 70~80 | 85~100 |
| land reclamation rate | <40 | 40~70 | 70~80 | 85~100 |
| drought and flood rate | >50 | 50~40 | 40~20 | <20 |
| green vegetation cover | <40 | 40~70 | 70~80 | 85~100 |
| soil and water loss control rate | <20 | 20~50 | 50~80 | 80~100 |

Upon calculating the comprehensive index of the sustainability of land consolidation and remediation, classify the sustainability level of land consolidation and remediation on this basis. This paper divides the sustainability of land consolidation and remediation into four levels based on comparative analysis, expert consultation, reference to relevant literature[9-16], specifically: SLC value is not sustainable between 0-35; SLC value is barely sustainable between 35-70; SLC value is moderately sustainable between 70-85; SLC value is highly sustainable between 85-100.

Finishing of data acquisition

To ensure the comprehensiveness, representativeness and scientific rationality of the study results, method of correspondence survey, literature search, questionnaire, field observation and interview combined together for data acquisition.

Collate data of the five project areas collected via the above methods, calculate the comprehensive index of the sustainability of land consolidation and remediation based on the sustainability of land consolidation and remediation evaluation index system, evaluation index weight, standard for evaluation, etc., and classify and evaluate the sustainability of land consolidation and remediation in Funing County as per the classification standard of the sustainability of land consolidation and remediation. Specific evaluation process is shown in Tab. 2-3.

A comprehensive evaluation analysis of the sustainability of land consolidation and remediation project in the 5 project areas in Funing County has been carried out, the results are shown in Tab. 4:

(1) After land consolidation and remediation, the infrastructure of the five project areas in Funing County have been perfected, a certain improvement have been made in the quality of cultivated land, sustainability of arable land has been enhanced, and the comprehensive indexes value of sustainability by the increased from 12.22, 11.24, 12.14, 10.76 and 11.24 before consolidation and remediation to 17.85, 16.84, 17.33, 17.92 and 16.88 after consolidation and remediation.

(2) After land consolidation and remediation, rural income of the five project areas in Funing County and social stability both increased, social, economic and ecological benefits increase significantly, as for the comprehensive index values of sustainability, socially sustainable comprehensive indexes increased from 10.85, 6.86, 8.27, 8.48 and 9.18 before consolidation and remediation to 19.91, 18.5, 19.01, 20.37 and 18.94 after consolidation and remediation; economically sustainable comprehensive indexes increased from 17.04, 16.9, 16.9, 17.16 and 15.84 before consolidation and remediation to 20.8, 20.47, 20.28, 20.94 and 20.7 after consolidation and remediation; ecologically sustainable indexes increased from 8.43, 7.48, 8.21, 8.33 and 8.43 before consolidation and remediation to 14.47, 14.39, 16.29, 15.38 and 14.81 after

RESULTS AND DISCUSSION

consolidation and remediation;

(3) After land consolidation and remediation, the comprehensive index values of sustainability of Banlun Town, Muyang Town, Guichao Town, Lida Town, Huajia Town in Funing County before land consolidation and remediation were 48.53, 42.47, 44.51, 44.72 and 44.68, respectively, and became 73.04, 70.21, 72.90, 74.62 and 71.33 after land consolidation and remediation, with increments of 24.51, 27.73, 27.38, 29.90 and 26.65, and the classification of the sustainability of land consolidation and remediation of the five project areas is promoted to moderately sustainable from barely sustainable.

CONCLUSION

Through a comprehensive evaluation analysis of the sustainability of land consolidation and remediation project in the five project areas in Funing County, the main conclusions are as follows:

(1) After land consolidation and remediation, rural income of the five project areas in Funing County and social stability both increased, social, economic and ecological benefits increase significantly. After land consolidation and remediation, the intensity of the sustainability of land consolidation and remediation of the five project areas is promoted to moderately sustainable from barely sustainable. The results show that the effect and sustainability of land consolidation and remediation in Funing County are favorable.

Table 4. Funing County land consolidation and rehabilitation sustainability post evaluation index comprehensive index

| evaluation index | No.1 | No.2 | No.3 | No.4 | No.5 | No.1 | No.2 | No.3 | No.4 | No.5 |
|---|------------------------------|-------|-------|-------|-------|-------------------------|-------|-------|-------|-------|
| | SLC consolidation before SLC | | | | | SLC consolidation after | | | | |
| irrigation guarantee rate C1 | 4.08 | 3.36 | 3.84 | 3.60 | 3.12 | 4.32 | 3.84 | 4.32 | 4.80 | 3.84 |
| irrigation and drainage ditches density C2 | 2.81 | 1.30 | 0.86 | 1.51 | 2.16 | 3.67 | 2.59 | 1.73 | 3.02 | 3.02 |
| road density in the field C3 | 1.25 | 1.25 | 0.94 | 0.94 | 0.94 | 2.81 | 1.87 | 1.87 | 2.18 | 2.34 |
| cultivated land quality level C4 | 2.21 | 2.21 | 2.76 | 2.21 | 2.21 | 3.31 | 3.86 | 4.42 | 3.86 | 3.31 |
| raise the level of grain output C5 | 1.87 | 3.12 | 3.74 | 2.50 | 2.81 | 3.74 | 4.68 | 4.99 | 4.06 | 4.37 |
| subtotal | 12.22 | 11.24 | 12.14 | 10.76 | 11.24 | 17.85 | 16.84 | 17.33 | 17.92 | 16.88 |
| area ratio of cultivated land C6 | 5.83 | 5.47 | 5.47 | 5.83 | 5.83 | 6.20 | 5.83 | 5.83 | 6.20 | 6.56 |
| the increasing rate of income per mu C7 | 3.42 | 4.66 | 3.42 | 4.04 | 2.17 | 4.35 | 5.28 | 4.35 | 4.97 | 3.73 |
| mu cost reduction rate C8 | 3.85 | 2.05 | 3.59 | 3.08 | 3.59 | 4.10 | 3.08 | 3.85 | 3.59 | 4.10 |
| production improvement factor C9 | 2.16 | 3.24 | 3.24 | 2.43 | 2.16 | 3.78 | 4.05 | 4.32 | 3.51 | 3.78 |
| per capita GDP growth rate C10 | 1.78 | 1.49 | 1.19 | 1.78 | 2.08 | 2.38 | 2.23 | 1.93 | 2.67 | 2.52 |
| subtotal | 17.04 | 16.90 | 16.90 | 17.16 | 15.84 | 20.80 | 20.47 | 20.28 | 20.94 | 20.70 |
| per capita annual net income increased C11 | 2.70 | 2.25 | 1.80 | 2.70 | 3.60 | 6.74 | 5.39 | 5.84 | 6.74 | 6.29 |
| poor people out of poverty rate C12 | 2.52 | 0.84 | 1.68 | 2.10 | 1.26 | 4.21 | 4.21 | 3.36 | 5.05 | 3.36 |
| public satisfaction rate C13 | 3.39 | 3.13 | 2.87 | 2.09 | 2.09 | 4.18 | 4.44 | 4.70 | 4.44 | 4.18 |
| the rate of increase in agricultural productivity C14 | 2.23 | 0.64 | 1.91 | 1.60 | 2.23 | 4.79 | 4.47 | 5.10 | 4.15 | 5.10 |
| subtotal | 10.85 | 6.86 | 8.27 | 8.48 | 9.18 | 19.91 | 18.50 | 19.01 | 20.37 | 18.94 |
| land reclamation rate increment C15 | 2.40 | 2.10 | 2.25 | 2.55 | 2.40 | 2.55 | 2.40 | 2.40 | 2.70 | 2.40 |
| drought and flood disaster reduction rate C16 | 2.32 | 1.74 | 2.32 | 1.16 | 2.32 | 4.64 | 4.64 | 4.93 | 4.35 | 4.64 |
| green vegetation cover increment C17 | 3.36 | 2.94 | 2.94 | 3.57 | 3.36 | 3.78 | 3.15 | 3.36 | 3.78 | 3.57 |
| soil and water loss control rate C18 | 0.35 | 0.70 | 0.70 | 1.05 | 0.35 | 3.50 | 4.20 | 5.60 | 4.55 | 4.20 |
| subtotal | 8.43 | 7.48 | 8.21 | 8.33 | 8.43 | 14.47 | 14.39 | 16.29 | 15.38 | 14.81 |
| total | 48.53 | 42.47 | 45.52 | 44.72 | 44.68 | 73.04 | 70.21 | 72.90 | 74.62 | 71.33 |

Note: No.1 instead Ban Lun town, No.2 instead Mu Yang town, No.3 instead Gui Chao town, No.4 instead Li Da town, No.5 instead Hua Jia town.

(2) The study gives a comprehensive analysis of the various factors that affect the sustainability of land consolidation and remediation, but the screening index of Delphi method has a certain

degree of subjectivity, the 18 indexes selected in the evaluation index system and their weights have certain limitations.

(3) In future studies, multiple regions in Yunnan

Province can be selected as the study object, finding the similarities and differences between districts through a comparative analysis, and building a project evaluation index system that can be applied to the sustainability of land consolidation and remediation in Yunnan Province and even a wider range, providing reference to the sustainability of land consolidation and remediation project evaluation in Yunnan Province and even the country.

REFERENCES

1. Y. Jianxin, W. Wei, L. Xiaohong, P. Yun, L. Lijun, Z. Yongli, *Transactions of the Chinese Society of Agricultural Engineering*, **29**(10), 234 (2013).
2. B. Zhenxing, W. Bing, Y. Miao, D. Xiuru, S. Fujun, H. Chunlan, Q. Fengkun, *Transactions of the Chinese Society of Agricultural Engineering*, **24**(2), 95 (2008).
3. Y. Xiaoyan, Z. Deju, Y. Wenju, C. Feng, *Transactions of the Chinese Society of Agricultural Engineering*, **21**(9), 67 (2005).
4. Y. Liping, S. Xiazhen, W. Cifang, *Journal of Agricultural Mechanization Research*, **12**(12), 48 (2006).
5. Y. Yang, H. Chunyang, L. Xiaobing, *Journal of Beijing Forestry University*, **32**(3), 33 (2010).
6. S. Nan, Evaluation of Sustainable Development of Forestry in Shaanxi County Region. North West Agriculture and Forestry University, 2012.
7. L. Wenli, Comprehensive Benefit Evaluation of Land Consolidation, Yunnan Agricultural University, 2012.
8. Z. Junfeng, H. Sheng, L. Youzhao, M. Zhan, *Resources and Environment in the Yangtze Basin*, **02**, 153 (2014).
9. Y. Jing, G. Minhua, C. Lijun, *Chinese Agricultural Science Bulletin*, **14**, 211 (2014).
10. Z. Zhengfeng, *Transactions of the Chinese Society of Agricultural Engineering*, **28**(7), 1 (2012).
11. Q. Pengfei, W. Wenke, D. Lei, W. Guangchao, C. Li, *China Sciencepaper*, **10**(3), 348 (2015).
12. X. Kang, J. Xiaobin, W. Dingguo, Z. Yinkang, *Transactions of the Chinese Society of Agricultural Engineering*, **31**(7), 247 (2015).
13. L. Shuyi, Y. Qingyuan, H. Chunyan, W. Xue, H. Pei, *Chinese Agricultural Science Bulletin*, **29**(26), 54 (2013).
14. W. Junmin, H. Baoqing, *Resources Science*, **35**(7), 1407 (2013).
15. H. Huiling, W. Cifang, Z. Shouzhong, *Transactions of the Chinese Society of Agricultural Engineering*, **28**(6), 240 (2012).
16. Y. Jun, W. Zhanqi, J. Gui, C. Bingyin, H. Xianhui, *Resources and Environment in the Yangtze Basin*, **22**(8), 1036 (2013).

CO₂ emissions and economic growth nexus in China: A cointegration analysis of the four-stage environmental Kuznets Curve

H.D. Wen, J. Dai*

Qianjiang College, Hangzhou Normal University, Zhejiang Hangzhou, China

Received May 25, 2017, Revised July 21, 2017

This research puts forward four-stage EKC hypothesis based on the traditional EKC theory (two stages), and also checks the hypothesis by investigating the relationships among CO₂ emissions, energy consumption and economic growth with a cubic model in logarithm form based on the panel data for 29 provinces in China over the period 1995–2010. The empirical tests find some evidences for the existence of the four-stage EKC for CO₂ emissions in China. The long-run cointegrated relationships among the three variables have been found in our empirical results. The regression results find a maxima turning point of the four-stage EKC between economic growth and CO₂ emissions. The causality results show that there exist two bidirectional causalities between energy consumption and CO₂ emissions, and also between economic growth and energy consumption. Moreover, there is a Granger causality running from CO₂ emissions to economic growth. Some policy implications of the theoretical and empirical analysis results are proposed at last.

Key words: CO₂ emissions; economic growth; energy consumption

INTRODUCTION

The increasing threat of global warming has called for more and more discussions all over the world. The major greenhouse gas (GHG) is CO₂ emissions which are considered to be the main gas leading to global warming [1]. But CO₂ emissions have the nature of the "tragedy of the commons" and damage indirectly, so countries may be not interested in reducing CO₂ emissions during its rapid economic development period. So, CO₂ emissions problem has increasingly become the focus of academic research.

The relationship between economic growth and environmental pollution is described usually by the hypothesis of Environmental Kuznets Curve (EKC) in which, environmental pollution increases with economic growth first, and then decreases when the per capita income reaches a certain critical level [2]. Ever since, the EKC hypothesis has become an important research issue which has led to a large number of theoretical and empirical literature. There is also vigorous discussion on the applicability of EKC for CO₂ emissions [3; 4; 5; 6; 7; 8; and so on).

Some researchers claimed the EKC for CO₂ emissions was non-existent. Selden and Song performed a study on the EKC in both RE and FE models, and found no turning point for CO₂ emissions [9]. Gangadharan and Valenzuela adopted data from the World Development Indicators (WDI) 1998 and found an upward

straight line for CO₂ emissions [10]. Lindmark performed a study on the EKC for CO₂ emissions just in Sweden, using dynamic structural model [11]. And he didn't find any turning point for CO₂ emissions and no evidences for inverted U-shape EKC. Richmond and Kaufman tested the EKC for CO₂ emissions and energy use with a panel data of 36 countries [12]. For OECD nations, there is limited support for a turning point in the relationship between income and CO₂ emissions. For non-OECD nations, there is no turning point in the relationship between income and CO₂ emissions. Miah et al studied the EKC for greenhouse gases (GHG) including CO₂, SO_x and NO_x which showed that EKC for CO₂ emissions was following a monotonous straight line in most cases [13]. Ajmi et al. tested EKC for CO₂ emissions in the G7 countries, the finding of inverted N-shaped curves in Italy and Japan lends no support to the traditional EKC hypothesis [14]. Kang et al. tested EKC for CO₂ emissions in China using a spatial panel data model, and found that the relationship between economic growth and CO₂ emissions shapes as an inverted-N trajectory [15]. Dogan and Turkekul tested EKC for CO₂ emissions, and did not support the validity of the environmental Kuznets curve (EKC) hypothesis for the USA because real output leads to environmental improvements while GDP² increases the levels of gas emissions [16].

Other researchers considered the EKC for CO₂ emissions was existent. Holtz-Eakin and Selden tested the EKC for CO₂ emissions [3]. They used a quadratic model for data estimation, and obtained some support of EKC for CO₂ emissions. However, their estimated turning point occurs at a very high

* To whom all correspondence should be sent:

level of per capita income (\$35,428 in per capita 1986 price). Agras and Chapman examined data from 34 countries including developed and developing country, and found a turning point of per capita GDP for CO₂ emissions at \$13,630 [17]. Maradan and Vassiliev examined a number of countries, and they found a turning point of per capita GDP for CO₂ emissions at \$5,924 [18]. Their minimum per capita GDP for turning point was \$325 and maximum was \$17,508 in 1985 price (expressed in PPP). Saboori et al. studied the EKC for CO₂ emissions in Malaysia, and they found the turning point of per capita real income for CO₂ emissions was \$4700 [7]. Apergis found that the EKC hypothesis holds in 12 out of the 15 countries [8]. Bilgili et al. studied the EKC for CO₂ emissions with a panel data of 17 OECD countries, the findings supported the EKC hypothesis, and they found the turning point was from \$10400 to \$88890, so they believed EKC hypothesis was independent of income level [19].

Some recent studies added other potential determinants of CO₂ emissions such as energy consumption by Ang [20], Menyah and Wolde-Rufael [21], Ajmi et al. [14]; foreign trade by Halicioglu [22], Nasir and Rehman [23]; urbanization by Zhang and Cheng [24], Iwata et al. [6] and Hossain [25]; employment by Sari and Soytas [26], Ghosh [27]; population, industry energy intensity and share of nonfossil fuels in primary energy by Liddle [28]; trade openness and financial development by Dogan and Seker [29]; trade openness, energy structure, urbanization and population density by Kang et al. [15]. But still, their conclusions cannot be unified.

The affirmative results of EKC show that there is a turning point of per capita GDP for CO₂ emissions, but the turning point is not unified. Some negative studies show there is no evidence of inverted U-shape EKC for CO₂ emissions, and some other authors even found upward straight line for many countries. It is of course a warning for developing countries that waiting for the CO₂ emissions reduction automatically is dangerous.

Our study extends EKC hypothesis and provides a new empirical analysis on the EKC for CO₂ emissions in China.

FOUR-STAGE EKC

We analyze in the circumstances of an open economy, and assume that the economy can always maintain growth. We propose another possible form of EKC theory that may exist in four-stage EKC.

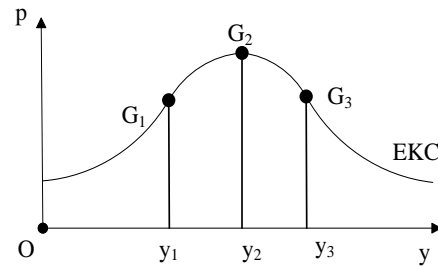


Fig. 1. Four-stage EKC curve

Subject to space, we simplified the analysis. The process can be reflected in figure 1, the curve slope is negative. The per capita environmental pollution increases with per capita output, and the growth rate is changing gradually from increasing to decreasing at the inflection point G1 where the convex function converts to concave function. Define y is per capita output, p is per capita environmental pollution. Then the left of G_1 is $\partial y/\partial p > 0$, $\partial^2 y/\partial p^2 > 0$; on the right of G_1 is $\partial y/\partial p > 0$, $\partial^2 y/\partial p^2 < 0$. The left of G_3 is $\partial y/\partial p < 0$, $\partial^2 y/\partial p^2 < 0$; on the right of G_3 is $\partial y/\partial p < 0$, $\partial^2 y/\partial p^2 > 0$.

DATA AND MODEL

Based on the four-stage EKC hypothesis we can build a per capita quadratic equation model as follows:

$$\ln(c_{it}) = \alpha_{it} + \beta_{1i} \ln(E_{it}) + \beta_{2i} \ln(y_{it}) + \beta_{3i} \ln(y_{it}^2) + \varepsilon_{it} \quad (1)$$

Where c is per capita CO₂ emissions; y is per capita GDP; E is per capita energy consumption; i denotes the provinces in China; t denotes the time period; ε is the standard error term. But based on our research in section 2, the model may not be a quadratic function. As the study in Grossman and Krueger [2], cubic curve may also occur. So we can build the estimation model as follows:

$$\ln(c_{it}) = \alpha_{it} + \beta_{1i} \ln(E_{it}) + \beta_{2i} \ln(y_{it}) + \beta_{3i} \ln(y_{it}^2) + \beta_{4i} (y_{it}^3) + \varepsilon_{it} \quad (2)$$

This study uses annual panel data from 1995 to 2014 in 29 provinces. The province of Tibet is excluded in the empirical analysis because of the lack of data. And the data for Chongqing municipality is merged into Sichuan province for maintaining the consistency throughout the whole study period. The data of energy consumption and GDP for each province comes from "China Energy Statistical Yearbook" (EDNBSC, various years) and "China Statistical Yearbook" (NBSC, various years). China's provinces did not release the CO₂

emissions data, but release the fossil energy consumption breakdown by each fuel category, and the data also comes from “China Energy Statistical Yearbook” (EDNBSC, various years). According to the chapter sixth volume two in national greenhouse gas inventory guide formulated by the IPCC (2006) which provides the reference method, total CO₂ emissions can be estimated according to all kinds of fossil energy consumption. On this basis, Chen estimated the CO₂ emission coefficient of coal, crude oil and natural gas and so on. This paper will draw on this CO₂ emission coefficient [30]. Per capita CO₂ emissions and per capita energy consumption are measured in metric tons, and real per capita GDP is measured in constant 1985 Chinese Yuan. Table 1 above shows the summary statistics of the three variables (in nature logarithm) for the selected years.

Table 1. Summary statistics of 29 provinces for selected years in China

| Variable | Statistics | 1995 | 1999 | 2003 | 2006 | 2010 | 2014 |
|----------|------------|-------|-------|-------|-------|-------|-------|
| c (Ton) | Mean | 1.048 | 1.081 | 1.378 | 1.746 | 2.007 | 2.136 |
| | S.D. | 0.526 | 0.514 | 0.464 | 0.445 | 0.408 | 0.416 |
| E (Ton) | Mean | 0.132 | 0.165 | 0.463 | 0.830 | 1.092 | 1.220 |
| | S.D. | 0.513 | 0.511 | 0.487 | 0.473 | 0.456 | 0.440 |
| y (Yuan) | Mean | 7.545 | 7.889 | 8.238 | 8.587 | 9.030 | 9.391 |
| | S.D. | 0.538 | 0.563 | 0.548 | 0.542 | 0.502 | 0.136 |

And then we make the curve between per capita CO₂ emissions and real per capita GDP as Fig. 2.

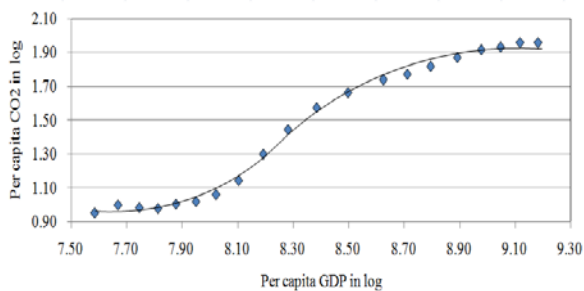


Fig 2. Long-run EKC relationship

The graphical representation of the relationship between per capita CO₂ emissions and real per capita GDP in log levels in Fig. 2 does not accord with an inverted-U shape of EKC like other studies. The curve may have an inflection point (cut-off point of the concave curve and convex curve) except the extremum, just like the left part of figure 1. So model 3 may pass the testing. Under the analyses above, it is expected that $\beta_2 < 0$, $\beta_3 > 0$ and $\beta_4 < 0$. And It is expected that $\beta_1 > 0$ as an

increase in energy consumption will probably cause an increase in CO₂ emissions.

ESTIMATION METHODOLOGY AND RESULTS

Panel unit root tests

The null hypothesis of the unit root tests is that there exists unit root (i.e. the variables are non-stationary), and the alternative hypothesis is that no unit root exists in the series (i.e. the variables are stationary). Table 2 shows the results of the panel unit root tests for variables.

Table 2. Results of IPS panel unit root tests 1995-2014

| Variables | Level | First-order differential |
|---------------------|----------------|--------------------------|
| ln(c) | 1.8275(0.9662) | -4.3426(0.0000)*** |
| ln(E) | 1.8560(0.9765) | -4.6563(0.0000)*** |
| ln(y) | 2.0902(0.9830) | -3.5462(0.0002)*** |
| ln(y ²) | 2.0901(0.9829) | -3.5462(0.0002)*** |
| ln(y ³) | 2.0901(0.9829) | -3.5461(0.0002)*** |

Notes: All panel unit root tests were performed with restricted intercept and trend for all variables. * Represent significance at 10%. ** Represent significance at 5%. *** Represent significance at 1%.

It can be seen from Table 2 that the variables ln(c), ln(E), ln(y), ln(y²) and ln(y³) are statistically insignificant in level form due to the IPS test. However, all the variables with first-order differential form become stationary. Therefore, we may conclude that each variable is integrated of order one.

Panel cointegration tests

Since all the variables with first-order differential form are stationary, so we can do the panel cointegration tests. If panel and group statistics reject the null hypothesis, then there exist cointegration relationships among variables. Table 3 shows the results of panel cointegration test.

Table 3. Results of panel cointegration tests 1995-2014

| Panel (within dimension) | | Group (between dimension) | |
|--------------------------|-------------------|---------------------------|-------------------|
| Statistics | Value(Prob) | Statistics | Value(Prob) |
| Panel v-Statistic | 4.569 (0.000)*** | Group rho-Statistic | 0.309 (0.621) |
| Panel rho-Statistic | -2.573 (0.005)*** | Group PP-Statistic | -4.510 (0.000)*** |
| Panel PP-Statistic | -3.660 (0.000)*** | Group PDF-Statistic | -6.174 (0.000)*** |
| Panel ADF-Statistic | -4.521 (0.000)*** | - | - |

It can be seen from Table 3 that there are four panel statistics reject the null hypothesis, two groups of statistics reject the null hypothesis, and one group statistics admits it. Considering the rho-statistics has lower power than the PP-statistics, and all other statistics support the existence of cointegration relationship, so it may be reasonable to accept the existence of cointegration relationship.

Then we can obtain the following long-run cointegrating equation by estimating Eq. (2):

$$\ln(c) = 13.67 + 1.14\ln(E) - 6.19\ln(y) + 0.83\ln(y^2) - 0.03\ln(y^3) \quad (3)$$

(11.73)^{***} (7.45)^{***} (-2.77) ^{***}(2.18)^{**} (-3.21)^{***}

Using fixed effects model we get estimation results above. The system estimated AR²=0.966, and F=875. Due to Eq. (3), we find that the sign of the coefficients are just as the expected: ln(E) has a positive promotion to ln(c); ln(c) is negatively related to ln(y), positively related to ln(y²), and negatively related to ln(y³).

Let $\partial \ln(c) / \partial \ln(y) = 0$, we get ln(y)=5.4860 and ln(y)= 10.6334 approximately. So we get a very low minimum value about 241 Chinese Yuan in 1985 price (in our analysis after section 1, all the price is in year 1985), and get a maximum value about 41500 Chinese Yuan which has not yet occurred.

Let $\partial^2 \ln(c) / \partial \ln(y)^2 = 0$, we get ln(y)= 8.2587. If ln(y) > 8.2587, $\partial^2 \ln(c) / \partial \ln(y)^2 < 0$, and if ln(y) <

8.2587, $\partial^2 \ln(c) / \partial \ln(y)^2 > 0$. So we get an inflection point (cut-off point of the concave and convex curve). Value of ln(y) = 8.2587, means inflection point is about 3861 Chinese Yuan which has happened in all provinces. So the growth rate of CO₂ emissions may be declined after that. The trend of factor price equalization seems to appear in China already, especially the labor price. So the estimations may fit for China's facts. Now, China has got through the first stage of four-stage EKC, and is in the second stage of four-stage EKC. We do not get a traditional inverted U-shaped curve, but the results provide some evidences for the four-stage curve presented in fig 1.

Granger causality tests

The panel cointegration test results in table 3 suggest that cointegrating relationships exist among CO₂ emissions, energy consumption and economic growth. So it is reasonable to test the Granger causality relationships among the variables. The dynamic error correction model can be expressed as follows:

$$\Delta \ln(c_{it}) = a_{1j} + \sum_{k=1}^q \delta_{1ik} \Delta \ln(c_{it-k}) + \sum_{k=1}^q \varepsilon_{1ik} \Delta \ln(E_{it-k}) + \sum_{k=1}^q \phi_{1ik} \Delta \ln(y_{it-k}) + \sum_{k=1}^q \varphi_{1ik} \Delta \ln(y_{it-k}^2) + \sum_{k=1}^q \gamma_{1ik} \Delta \ln(y_{it-k}^3) + \alpha_{1i} ECM_{it-1} + e_{1it} \quad (4)$$

$$\Delta \ln(E_{it}) = a_{2j} + \sum_{k=1}^q \delta_{2ik} \Delta \ln(c_{it-k}) + \sum_{k=1}^q \varepsilon_{2ik} \Delta \ln(E_{it-k}) + \sum_{k=1}^q \phi_{2ik} \Delta \ln(y_{it-k}) + \sum_{k=1}^q \varphi_{2ik} \Delta \ln(y_{it-k}^2) + \sum_{k=1}^q \gamma_{2ik} \Delta \ln(y_{it-k}^3) + \alpha_{2i} ECM_{it-1} + e_{2it} \quad (5)$$

$$\Delta \ln(y_{it}) = a_{3j} + \sum_{k=1}^q \delta_{3ik} \Delta \ln(c_{it-k}) + \sum_{k=1}^q \varepsilon_{3ik} \Delta \ln(E_{it-k}) + \sum_{k=1}^q \phi_{3ik} \Delta \ln(y_{it-k}) + \sum_{k=1}^q \varphi_{3ik} \Delta \ln(y_{it-k}^2) + \sum_{k=1}^q \gamma_{3ik} \Delta \ln(y_{it-k}^3) + \alpha_{3i} ECM_{it-1} + e_{3it} \quad (6)$$

$$\Delta \ln(y_{it}^2) = a_{4j} + \sum_{k=1}^q \delta_{4ik} \Delta \ln(c_{it-k}) + \sum_{k=1}^q \varepsilon_{4ik} \Delta \ln(E_{it-k}) + \sum_{k=1}^q \phi_{4ik} \Delta \ln(y_{it-k}) + \sum_{k=1}^q \varphi_{4ik} \Delta \ln(y_{it-k}^2) + \sum_{k=1}^q \gamma_{4ik} \Delta \ln(y_{it-k}^3) + \alpha_{4i} ECM_{it-1} + e_{4it} \quad (7)$$

$$\Delta \ln(y_{it}^3) = a_{5j} + \sum_{k=1}^q \delta_{5ik} \Delta \ln(c_{it-k}) + \sum_{k=1}^q \varepsilon_{5ik} \Delta \ln(E_{it-k}) + \sum_{k=1}^q \phi_{5ik} \Delta \ln(y_{it-k}) + \sum_{k=1}^q \varphi_{5ik} \Delta \ln(y_{it-k}^2) + \sum_{k=1}^q \gamma_{5ik} \Delta \ln(y_{it-k}^3) + \alpha_{5i} ECM_{it-1} + e_{5it} \quad (8)$$

Where q is the lag length for the differenced variables, and it can be obtained by the Engle-Granger approach. The dynamic error correction modles in Eqs. (4)–(8) can be derived from the long-run equilibrium Eq. (9) as follows:

$$ECM_{it} = \ln(c_{it}) - \hat{\alpha}_{it} - \hat{\beta}_{1i} \ln(E_{it}) - \hat{\beta}_{2i} \ln(y_{it}) - \hat{\beta}_{3i} \ln(y_{it}^2) - \hat{\beta}_{4i} \ln(y_{it}^3) \quad (9)$$

Table 4. Results of panel Granger causality tests 1995-2014

| Dependent Variables | Independent Coefficient | | | |
|-----------------------------------|-------------------------|-----------------------|---|------------------------|
| | $\Delta \ln(c)$ | $\Delta \ln(E)$ | $\frac{\Delta \ln(y) \Delta \ln(y^2)}{\Delta \ln(y^3)}$ | EMC |
| $\Delta \ln(c)$ | - | 9.6201 ^{***} | 15.4563 ^{***} | 32.7993 ^{***} |
| $\Delta \ln(E)$ | 9.5632 ^{***} | - | 13.7422 ^{***} | 17.7645 ^{***} |
| $\Delta \ln(y)$ | 1.2025 | 8.8364 ^{***} | - | 1.5122 |
| $\Delta \ln(y^2) \Delta \ln(y^3)$ | | | | |

Table 4 summarizes the results of panel short-run and long-run Granger causality tests. In the short run, there is bidirectional causality between CO₂ emissions and energy consumption in China. It indicates that an increase in energy consumption will lead to an increase in CO₂ emissions and an increase in CO₂ emissions also means more energy use. One reason is that fossil energy accounts for a large proportion in total energy consumption. There is also bidirectional causality between energy consumption and economic growth. It means that energy plays an important role in forcing economic growth, and Chinese economic development also means more energy use. Furthermore, it can be found that there

is a Granger causality running from CO₂ emissions to economic growth. So it's to say CO₂ emissions are the cost to promote Chinese economic development.

In the long-run tests, there exist bidirectional causality between energy consumption and CO₂ emissions as shown in Table 4. However, economic growth doesn't respond to deviations from long-run equilibrium.

CONCLUSION

Our research put forward the four-stage EKC hypothesis based on but expands the application of the traditional EKC theory. Chinese data of CO₂ emissions and economic growth provided some evidences for the existence of the four-stage EKC. The four-stage EKC has three turning point. So we believe that CO₂ reduction along with economic growth after a turning point is not certain, it depends on which stage the country is in.

Acknowledgements: The author thanked the National Social Science Foundation in China "Study on green development strategy based on the advantage of backwardness in less developed areas" (Project Number: 16CJL050)

REFERENCES

1. The World Bank, Growth and CO₂ emissions: how do different countries fare. Environment Department, Washington, DC., 2007.
2. G.M., Grossman, A.B. Kruger, *Quarterly Journal of Economics*, **110**(2), 353 (1995).
3. D. Holtz-Eakin, T.M. Selden, *Journal of Public Economics*, **57**, 85 (1995).
4. J.T. Robers, P.E. Grimes, *World Development*, **25**, 191 (1997).
5. S. Dinda, A note on global EKC in case of CO₂ emission. Economic Research Unit, Indian Statistical Institute, Kolkata, Mimeo, 2001.
6. H. Iwata, K. Okada, S. Samreth, *Energy Policy*, **38**, 4057 (2010).
7. B. Saboori, J. Sulaiman, S. Mohd, *Energy Policy*, **51**, 184 (2012).
8. N. Apergis, *Energy Economics*, **54**, 263 (2016).
9. T.M. Selden, D. Song, *Journal of Environmental Economics and Management*, **27**, 147 (1994).
10. L. Gangadharan, Ma.R. Valenzuela, *Ecological Economics*, **36**, 513 (3)(2001).
11. M. Lindmark, *Ecological Economics*, **42**, 333 (2002).
12. A.K. Richmond, R.K. Kaufman, *Ecological Economics*, **56**, 176 (2006).
13. Md.D. Miah, Md.F.H. Masum, M. Koike, *Energy Policy*, **38**, 4643 (2010).
14. A.N. Ajmi, S. Hammoudeh, D.K. Nguyen, J.R. Sato, *Energy Economics*, **49**, 629 (2015).
15. Y.Q. Kang, T. Zhao, Y.Y. Yang, *Ecological Indicators*, **63**, 231 (2016).
16. E. Dogan, F. Seker, *Renewable and Sustainable Energy Reviews*, **60**, 1074 (2016).
17. J. Agras, D. Chapman, *Ecological Economics*, **28**, 267 (1999).
18. D. Maradan, A. Vassiliev, *Swiss Journal of Economics and Statistics*, **141**, 377 (2005).
19. F. Bilgilia, E. Koçakb, Ü. Bulut, *Renewable and Sustainable Energy Reviews*, **54**, 838 (2016).
20. J. Ang, *Energy Policy*, **35**, 4772 (2007).
21. K. Menyah, Y. Wolde-Rufael, *Energy Economics*, **32**, 1374 (2010).
22. F. Halicioglu, *Energy Policy*, **37**, 1156 (2009).
23. M. Nasir, F. Rehman, *Energy Policy*, **39**, 1857 (2011).
24. X.P. Zhang, X.M. Cheng, *Ecological Economics*, **68**, 2706 (2009).
25. S.M. Hossain, *Energy Policy*, **39**, 6991 (2011).
26. U. Soytas, R. Sari, *Ecological Economics*, **68**, 1667 (2009).
27. S. Ghosh, *Energy Policy*, **38**, 2613 (2010).
28. B. Liddle, *Global Environmental Change*, **31**, 62 (2015).
29. E. Dogan, B. Turkecul, *Environmental Science And Pollution Research International*, **23**, 1203 (2016).
30. S.Y. Chen, *Economic Research*, **4**, 41 (2009).

Extraction and tracking method of drop zone of storm cells based on modified SCIT algorithms

X. Yu¹, X. Rui^{2*}, D. Zhang³, S. Yao¹, Y. Song¹, W. Sun⁴, L. Zhu⁵, L. Wu⁶

¹ School of Traffic and Transportation, Shijiazhuang Tiedao University, Shijiazhuang, China

² College of Resources and Environment, University of Chinese Academy of Sciences, Beijing, China

³ Baotou Meteorological Bureau, Baotou, China

⁴ The Third Institute of Surveying and Mapping of Hebei Province, Shijiazhuang, China

⁵ School of Geography Science, Nanjing Normal University, Nanjing, China

⁶ Anhui Weather Modification Office, Hefei, China

Received May 25, 2017; Revised July 20, 2017

In order to extract and to track the drop zone of storm cells under severe convection weather, a modified SCIT (Storm Cell Identification and Tracking) algorithm is proposed, and then, the coordinates (including longitude and latitude) of starting and ending positions of all segments in modified SCIT algorithm are calculated, based on these, the extraction and tracking methods of drop zones of storm cells on the ground are proposed to track and to simulate the precipitation processes. By using the raw weather radar data of CINRAD/CB type at Ordos city of China, one precipitation process in Central Region of Inner Mongolia on 31st July, 2014 afternoon are simulated and replayed, and the tracking results show that the proposed methods can locate and extract the probable precipitation belts precisely which play an important role in making out the precipitation forecast and precipitation assessment more accurately.

Key words: Modified SCIT algorithm, Drop zone of storm cells, Precipitation belts.

INTRODUCTION

If the accurate drop zones of active storm cells are obtained, the activity region of severe convection weather like hails can be accurately located too, and it can also meet the need of fine weather forecast in high resolution. The most well-known of storm cell identification and tracking algorithms include TITAN [1-3]. These algorithms attempt to decrease the dimensionality of the problem by first finding contiguous reflectivity values above a specific threshold along one-dimensional segments, grouping those segments to form two-dimensional components, and then grouping these two dimensional components to identify storm cells. Storm cells are then stored and identified by a centroid position or an ellipse with a shape, size, and orientation similar to that of the identified storm [1-2, 4]. But the exact shape of storm cell's drop zone cannot be fixed by these algorithms. Matthews and Trostel proposed an improved cell identification and tracking algorithm based on DBSCAN (short for Density-Based Spatial Clustering of Applications with Noise) clustering and JPDA (short for Joint Probabilistic Data Association) tracking methods, but they did not introduce the extraction methods of exact shape and the application of these in detail [4]. The occurrence of severe hail in China is not often, but

these are significant meteorological phenomena from the point of view of damage to agriculture, transportation and property. Hail events are limited in time and space, and the ground observation network can only provide partial information about the hail spatial distribution [5]. In order to solve these problem, an extraction and tracking method of drop zone of storm cells which can locate the exact drop zone of storm cells and track the storm cells for acquiring the movement direction was proposed, in the end, it was tested by raw data of CINRAD/CB radar in Ordos of city China.

PRINCIPLE OF THE MODIFIED SCIT ALGORITHMS

The storm cell is taken as a three-dimensional shape in SCIT algorithms, and the identification process of storm cell can be divided into three stages: (1) Searching the one-dimensional storm segments; (2) Combining the two-dimensional storm components; (3) Associating two or more components into three-dimensional storm cells vertically. It searches the storm segments which meet some certain conditions with 7 threshold values (The default values are 30, 35, 40, 45, 50, 55, 60 dBZ) on all radials of all cuts of raw data in the first stages. If neighboring segments at the same cuts are close to one another azimuthally and overlap in a range with a threshold value, then the segments are combined into storm components in

* To whom all correspondence should be sent:
E-mail: ruixpsz@163.com

the second stages. Feature core extraction is employed to isolate the cells from surrounding areas of lower reflectivity. If the centroid of a higher-reflectivity thresholded component falls within the area of a lower-reflectivity thresholded component, the latter component is discarded. In the third stage, the storm components are sorted by decreasing mass from the great to the little firstly, and then two or more components are associated into 3D storm cells vertically. (For further details, see [2].

The storms identified by the above methods, are really the core of storms, and are not the external outline. In order to identify the external outline of storm cells accurately, the SCIT algorithms are modified in this paper. We search the segments by one reflectivity threshold value like 35dBZ and 40dBZ firstly, and then combine the components and associate the three-dimensional storm cells vertically. So the contour surface of reflectivity of storms can be obtained by the modified SCIT algorithm. If the different reflectivity threshold values are adopted, the internal structure of 3D storm cells can be acquired. The diagram is shown by Fig. 1.



Fig. 1. Extracted internal structure of 3D storm cells

EXTRACTION AND TRACKING METHOD OF DROP ZONE OF STORM CELLS

Extraction Method of Drop Zone of Storm Cells

The outline of 3D storm cells can be obtained by the above algorithm, while the drop zone of storms cannot be acquired. In fact, the drop zone of storms is more useful. In this section, the extraction methods of drop zones by the modified SCIT algorithm will be introduced.

After searching all the segments in the modified SCIT algorithm, we calculate and save the angle of elevation (marked by El), azimuth (marked by AZ), starting distance (marked by RS_{beg}), ending distance (marked by RS_{end}) and length of segments (marked by Len_{seg}). The calculation formulas of starting distance and ending distance are shown by formula (1) and (2).

$$RS_{beg} = SV_{beg} \times SVL - SVL / 2 \quad (1)$$

$$RS_{end} = SV_{end} \times SVL + SVL / 2 \quad (2)$$

In the above formulas, SV_{beg} is the first range bin of one segment and SV_{end} is the last, and SVL is the length of one range bin. Its value is 500 meters for CINRAD/CB-type C-band all coherent Doppler radar.

If the coordinates of weather radar (including the longitude, latitude and elevation) are known, the starting and ending coordinates of storm segments can be calculated out. In the following paragraphs, the calculation methods will be introduced in detail.

Because of the atmospheric influence, pulsed electromagnetic waves sent by weather radar are bent from the rectilinear propagation path. Generally, the electromagnetic waves bend down, which increases the maximum detecting distance. In that case, we introduce the concept of equivalent earth radius, R_m , and we assume straight propagation of the electromagnetic waves on the surface of the "earth." The equivalent earth radius is usually larger than the real earth radius, R_e . The relative curvature between electromagnetic waves and the surface of the earth does not change; it does not matter if they are transmitted on the real earth or on the equivalent earth. On that condition, and assuming standard atmospheric refraction, we can calculate R_m using equation (3) [6, 7].

$$R_m = \frac{R_e}{1 + \frac{dn}{dh} R_e} \quad (3)$$

Where the change in refractivity with height, $\frac{dn}{dh}$, is $-4 \times 10^{-8} \text{m}^{-1}$ and the known radius of the earth, R_e , is $6.378137 \times 10^6 \text{m}$, then R_m becomes $8.5627 \times 10^6 \text{m}$.

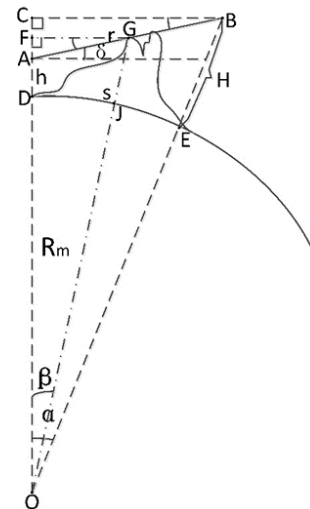


Fig. 2. Diagram for calculating the height value, H, where the unit of angle is $^\circ$

As shown in Fig. 2, a radar station is located at Point A, with height h . Assuming the earth is a standard sphere, when a radar scanning ray with length r , and an elevation angle δ is sent from Point A to Point B, the length of BC is equal to $r \cos \delta$, and the length of OC is equal to $r \sin \delta + h + R_m$. Using the right angle $\angle OCB$, we can calculate the standard height, H , of Point B using Equation (4).

$$H = \sqrt{r^2 \cos^2 \delta + (r \sin \delta + h + R_m)^2} - R_m \quad (4)$$

Angle α and the arc length s from Fig. 2 can also be calculated as shown in equation (5) and equation (6):

$$\alpha = \arctan \frac{r \cos \delta}{r \sin \delta + h + R_m} \quad (5)$$

$$s = \frac{\alpha \pi R_m}{180} \quad (6)$$

In Fig. 2, if we know the longitude and latitude of Point A, the azimuth, and the spherical distance from Point A to Point B, the longitude and latitude of Point B can be calculated using the sine formula of spherical triangle and the cosine formula of spherical triangle [8].

In Fig. 2, longitude and latitude of point A are (λ_A, φ_A) , the longitude and latitude of Point B are (λ_B, φ_B) , and the azimuth from Point A to Point B is θ . Then the longitude and latitude of Points D and E are also (λ_A, φ_A) and (λ_B, φ_B) , and the azimuth from Point D to Point E is equal to θ in Fig. 3. Note that Point D and Point E are equivalent on Fig. 2 and Fig. 3. The North Pole is designated N, and the spherical distance from Point D to Point E is shown as s . We also save the spherical distance per 1° on the equator, and mark it by ΔS , its calculating formula is shown by equation (7).

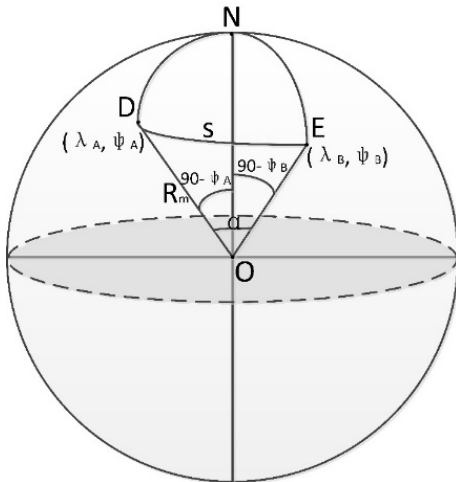


Fig. 3. Diagram for calculating longitude and latitude.

$$\Delta S = \frac{\pi R_m}{180} \quad (7)$$

Then angle $\angle DON$ is equal to $(90 - \varphi_A)$, and the spherical distance from Point D to Point N is equal to $(90 - \varphi_A) \times \Delta S$. While the angle $\angle NOE$ is equal to $(90 - \varphi_B)$, and the spherical distance from Point E to Point N is equal to $(90 - \varphi_B) \times \Delta S$. Since the spherical distance from Point D to Point E is equal to s , and the angle $\angle DOE$ is marked by α , then the three points D, N and E form a spherical triangle on the surface of the earth. According to the cosine formula of spherical triangle shown in equation (8):

$$\cos \angle NOE = \cos \angle NOD \cos \angle DOE + \sin \angle NOD \sin \angle DOE \cos \angle NDE \quad (8)$$

which corresponds to equation (9) and Equation (10):

$$\cos(90 - \varphi_B) = \cos(90 - \varphi_A) \cos \alpha + \sin(90 - \varphi_A) \sin \alpha \cos \theta \quad (9)$$

$$\sin \varphi_B = \sin \varphi_A \cos \alpha + \cos \varphi_A \sin \alpha \cos \theta \quad (10)$$

Which transforms to calculate the latitude of Point B, φ_B , as shown in equation (11).

$$\varphi_B = \arcsin(\sin \varphi_A \cos \alpha + \cos \varphi_A \sin \alpha \cos \theta) \quad (11)$$

According to the sine formula of spherical triangle, shown in equation (12):

$$\frac{\sin \angle DNE}{\sin \alpha} = \frac{\sin \angle NDE}{\sin(90 - \varphi_B)} = \frac{\sin \angle NED}{\sin(90 - \varphi_A)} \quad (12)$$

which transforms to equation (13):

$$\frac{\sin(\lambda_B - \lambda_A)}{\sin \alpha} = \frac{\sin \theta}{\sin(90 - \varphi_B)} = \frac{\sin \angle NED}{\sin(90 - \varphi_A)} \quad (13)$$

The longitude of Point B can be calculated after transforming to equation (14):

$$\lambda_B = \arcsin\left(\frac{\sin \alpha \sin \theta}{\sin(90 - \varphi_B)}\right) + \lambda_A \quad (14)$$

In Fig. 2, Point G is the blocking point during the visibility analysis between Point A and Point B. The GetLineofSight method of IGeoDatabaseBridge2 interface in ArcGIS Engine was used to calculate the longitude and latitude of Point G, which is equal to the longitude and latitude of Point J. This allows the angle $\angle DOJ$, β , to be calculated. From triangle $\triangle AFG$ and $\triangle OFG$, the length of AG can be derived from trigonometric functions and calculated using equation (15):

$$AG = \frac{\tan \beta \tan \delta (h + R_m)}{\sin \theta (1 - \tan \beta \tan \delta)} \quad (15)$$

We can calculate the coordinates (including longitude and latitude) of starting and ending positions of all segments by the above formulas.

After combining the segments into storm components by using the modified SCIT algorithms, one component will contain certain numbers of segments which are sorted by azimuth, and it is shown in Fig. 4. In this figure, we connect the starting points of segments to a line (marked by Line1) in a clockwise direction. In the same way,

we connect the ending points of segments to another line (marked by Line2). Then we connect the two lines to form a closed region which can be taken as the outline of this storm component.

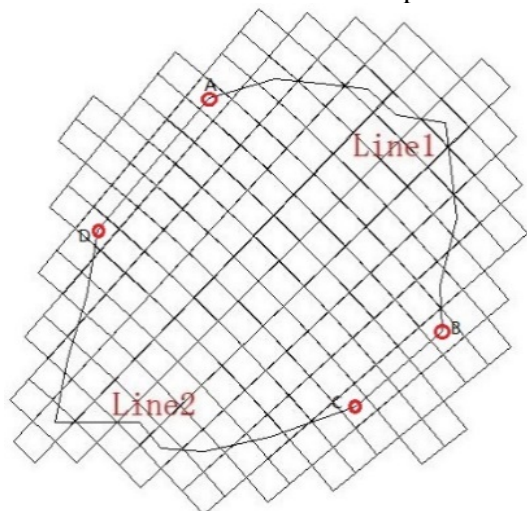


Fig. 4. Extraction of the outline of one component

During the connection, we create a List type of data structure which can save the starting point sets (marked by LstStartPnts) and the ending point sets (marked by LstEndPnts) of storm segments. If the points are saved into the list in a clockwise direction, we add the points in List LstEndPnts into the List LstStartPnts. After that, all the points of one closed storm components can be obtained. As the coordinates of these points saved in the list only include the longitude and latitude, the closed regions formed by these points are really the projection of storm components on the ground. By using this method, we can get all the projections on all cuts which can be used to form the drop zone of storm cells.

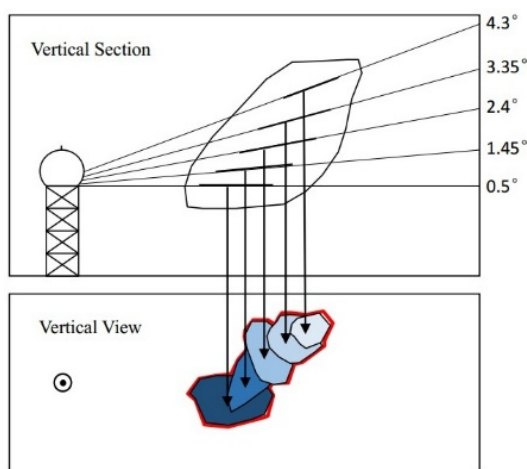


Fig. 5. Union operation of some components in one storm cell

As one storm cell contains two or more storm components which are relative in the vertical

direction, we can get the same number of projections of storm components which are saved in lists. Then we can unite the projections of storm components by using the Union operation of polygon-on-polygon-overlay tools in ArcGIS software. The final result of this operation will be the projections of storm cells on the ground, and it is also the drop zone of storm cells on the ground at this time, and it is shown in Fig. 5 marked by red line. At last, we extract the drop zones of all storm cells, and all the drop zones of storm cells scanned by the weather radar at this time can be obtained.

Tracking Method of Drop Zone of Storm Cells

As the storm cells are always moving on the echo maps at different scanning time, after the identification of storm cells, we need to track the storm cells according to the radar data at different time. This operation can be realized by using the modified SCIT algorithms further. As the storm cells move, the drop zones of storm cells move too, we need to track the drop zone for acquiring the accurate probable precipitation belts.

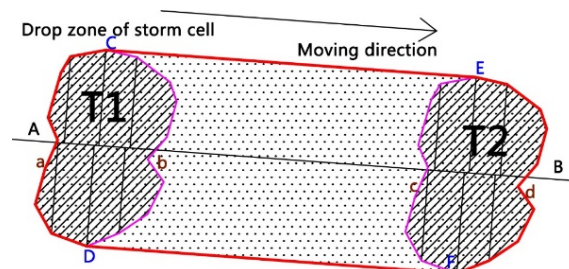


Fig. 6. Tracking method of Drop Zone of Storm Cells

In the above section, the drop zones of storm cells have been calculated accurately. In this section, we will introduce the tracking method of drop zones. In Fig. 6, we mark the drop zone of storm cells at the first observation time, whose color is carmine, by T1, and the drop zone at the second observation time is marked by T2. Supposing that the moving direction, which can be taken as the connection of centroid between polygon T1 and T2, is from A to B (marked by line AB), we draw the vertical lines from all the vertices of polygon T1 and T2 to line AB. The vertices (marked by C and E) corresponding to the two longest vertical lines above the line AB will be the vertices of the precipitation belts, in the same way, we can get the vertices D and F. The curve a is the left part of polygon T1 divided by vertices C and D, and curve d is the right part of polygon T2 divided by vertices E and F. Then the closed region formed by Line CE, Curve d, Line FD and Curve a will be the accurate probable precipitation belts between the observation time from T1 to T2.

By using the above method, the accurate probable precipitation belts for all the observation times can be acquired, based on this, and then we can make out the precipitation forecast and precipitation assessment more accurately.

TEST AND VERIFICATION OF THIS METHODS

Based on the above methods, we track and simulate one precipitation process in Central Region of Inner Mongolia on July 31, 2014 afternoon (Beijing Time, similarly hereinafter) by using the raw radar data scanned at 18:56. The identified storm cells by using the modified SCIT algorithms at different threshold values (including 35dBZ, 40dBZ and 45dBZ) are shown in Fig. 7, 8 and 9.

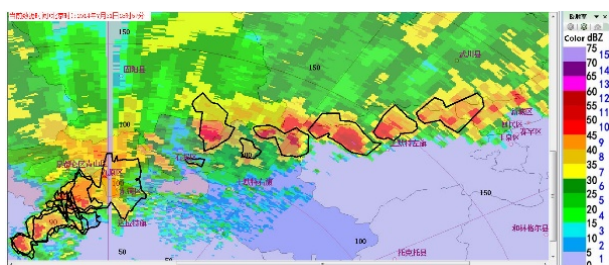


Fig. 7. Identified storm cells by using the modified SCIT algorithms at 35dBZ

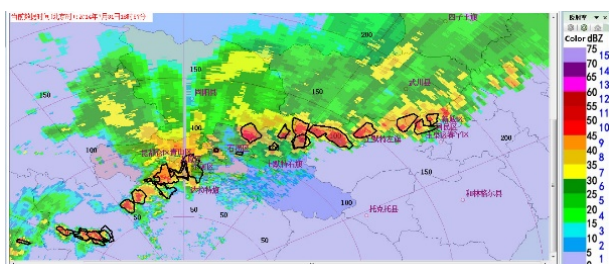


Fig. 8. Identified storm cells by using the modified SCIT algorithms at 40dBZ



Fig. 9. Identified storm cells by using the modified SCIT algorithms at 45dBZ

The identification results of storm cells at different observation time are shown in one map, and it is shown in Fig. 10. From this figure, we can know that the storm cells are moving to east-southeast direction. Then the storm cell identification and tracking results are analyzed. From this results, we can locate the drop zone and the passing region of storm cells, besides, the

results have certain instructive effect on forecasting and estimating the amount of precipitation and the precipitation intensity.

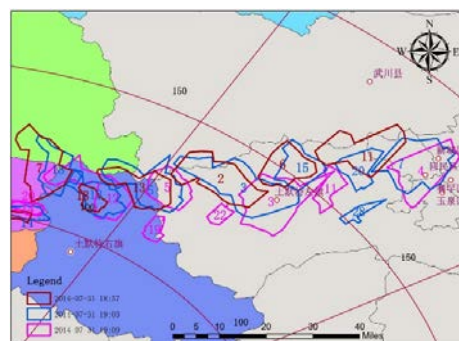


Fig. 10. Tracking results of storm cells at different observation time

CONCLUSIONS AND DISCUSSIONS

A modified SCIT algorithms proposed by the authors is introduced firstly in this paper, based on the algorithms, and then the extraction and tracking methods of drop zones of storm cells on the ground are proposed to track and to simulate the precipitation processes. By using the raw weather radar data of CINRAD/CB type at Ordos city of China, one precipitation process in Central Region of Inner Mongolia on July 31, 2014 afternoon are simulated and replayed, and the tracking results show that the proposed methods can locate and extract the probable precipitation belts precisely which play an important role in making out the precipitation forecast and precipitation assessment more accurately. In this paper, we just tracked and simulated the precipitation belts, not including the hail-fall area. If the hail detection algorithms are added into these methods and the hail-fall area can be calculated out in the future, it will have more significance for forecasting the hail-fall area and appraising the damage caused by hailstorms more accurately.

Acknowledgements: The research reported herein was sponsored by the National Science and Technology Major Project of China (Grant No. 2011ZX05039-004), the National Science and Technology Support Program of China (Grant No. 2012BAC25B01), the National Natural Science Foundation of China (Grant No. 51308358), the Hebei Province Natural Science Fund (Grant No. D2016210008) and the Social Science Foundation Project of Hebei Province (Grant No. HB15SH015).

REFERENCES

1. M. Dixon, G. Wiener, *Journal of Atmospheric and Oceanic Technology*, **10**(6), 785 (1993).
2. J.T. Johnson, P.L. MacKeen, A. Witt, E.D.W. Mitchell, G.J. Stumpf, M.D. Eilts, K. W. Thomas, *Weather and Forecasting*, **13**(2), 263 (1998).
3. L. Han, S. Fu, L. Zhao, Y. Zheng, H. Wang, Y. Lin, *Journal of Atmospheric and Oceanic Technology*, **26**(4), 719 (2009).
4. J. Matthews, J. Trostel, in: An Improved Storm Cell Identification and Tracking (SCIT) Algorithm based on DBSCAN and JPDA Tracking Methods (Proc. 26th Conference on Interactive Information and Processing Systems (IIPS) for Meteorology, Oceanography, and Hydrology, Orlando, 2010), Orlando, 2010, p. 1.
5. K. Skripniková, D. Řezáčová, *Atmospheric Research*, **144**(0), 175 (2014).
6. J. Bech, B. Codina, J. Lorente, D. Bebbington, in: Anomalous Propagation Effects on Weather Radar Beam Blockage Corrections (Proc. 30th International Conference on Radar Meteorology, Munich, 2001), Munich, 2001, p. 267.
7. J. Bech, B. Codina, J. Lorente, D. Bebbington, *Journal of Atmospheric and Oceanic Technology*, **20**(6), 845 (2003).
8. Y. Wan, , H. Yang, Y. Xiao, C. Wu, X. Xu, *Quarterly Journal of Applied Meteorology*, **11**(4), 440 (2000).

Potential dietary toxicity assessment of alum-processed jellyfish

S.L. Lin^{1#}, J.M. Hu^{2#}, R.Guo¹, Y. Lin¹, L.L. Liu¹, B.K. Tan^{2,3}, S.X. Zeng^{1*}

¹College of Food Science, Fujian Agriculture and Forestry University, Fuzhou 350002, PR China

²Warwick Medical School, University of Warwick, Coventry, CV2 2DX, United Kingdom

³Birmingham Heartlands and Solihull Hospitals, Heart of England National Health Service Foundation Trust, Birmingham, B9 5SS, United Kingdom

Received January 4, 2017; Revised August 25, 2017

As a fishery commodity for more than a thousand years, edible jellyfish is an important seafood worldwide. In order to form the crunchy and crispy texture, jellyfish is traditionally processed by curing with salt and hydrated aluminum potassium sulfate. Therefore, potential bioaccumulation of aluminum after dietary consumption of alum-processed jellyfish has received great attention. Here, the concentration of Al in alum-processed jellyfish was measured by inductively coupled plasma mass spectrometry. Furthermore, the safety assessment of alum-processed jellyfish, especially its effects on Al accumulation in different organs were evaluated in mouse. The results indicated alum-processed jellyfish contain high concentrations of Al (549.90 ± 4.66 mg/kg), which could be released into the in vitro human gastric digestion fluid achieving a concentration of 50.92 ± 4.26 μ g Al/L. Although no significant changes in the mortality rate, body weight, behavioral patterns, and neurotoxicity signs were observed after 30 days with intragastric administration of jellyfish slurry (up to 34.7 g/kg.bw), consumption of desalted jellyfish slurry significantly increased the Al accumulation in liver when given at medium (17.4 g/kg.bw) and high (34.7 g/kg.bw) doses. Moreover, the relative liver weights in the medium and high dose consumption group were lower than that in the control group. Furthermore, we show for the first time that organic acids such as citric acid may be a useful way to lower the Al concentration in jellyfish.

Keywords: Aluminums, jellyfish, hepatotoxicity, simulated gastric fluid.

INTRODUCTION

Edible jellyfish is a popular seafood consumed in the world. The global catch of edible jellyfish is estimated to be more than 300,000 tons annually [1] and is valued as a multi-million dollar business with an increasing demand [2]. However, traditional processing of jellyfish involves the use of alum, which raises a food safety concern due to the possible bioaccumulation of aluminum in humans. Furthermore, marine food resources can accumulate high levels of trace elements and heavy metals in their edible tissues, such as mercury (Hg), cadmium (Cd), plumbum (Pb), arsenic (As), zinc (Zn), magnesium (Mg), iron (Fe), copper (Cu), manganese (Mn), nickel (Ni) and stannum (Sn) [3], which could interfere with human physiology, leading to a negative impact on renal, endocrine, gastrointestinal, cardiovascular and nervous systems [4].

Edible jellyfish belong to the order *Rhizostomeae*, in the class of *Scyphomedusae*, with symmetrical soft bodies consisting of a gelatinous umbrella-shaped bell and trailing tentacles.[5]. Jellyfish has been commercially exploited for food consumption

worldwide for more than a thousand years, especially in Asian countries including China, Japan, Philippines, Vietnam, Thailand, Malaysia, Indonesia, Singapore and Myanmar [6-8]. Jellyfish is often served as a salad or appetizer in these countries due to its firm texture. A range of studies have reported that jellyfish possesses immuno-stimulatory, anti-fatigue, anti-oxidation properties and promotes weight loss and skin beauty [9-12]. Jellyfish has positive effects on hypertension, asthma and gastric ulcer[13].

Owing to its perishability, jellyfish is traditionally treated with a dehydration processing using a mixture of salt (NaCl) and alum ($KAl(SO_4)_2 \cdot 12H_2O$) to reduce the water content and decrease the pH [14]. This traditional processing procedure can extend the shelf life to up to 6-12 months at ambient temperature. Meanwhile, alum treatment also creates a crunchy texture as aluminum is a firming agent interacting with the carboxyl groups on the side chains of collagen [15], which constitutes more than 60% of tissue protein in jellyfish[16].

Although alum treatment has its merits for improving the durability and texture of jellyfish, it was also demonstrated to increase aluminum levels in processed jellyfish [7]. Therefore, possible bioaccumulation of aluminum after consumption of alum-processed jellyfish has become a food safety concern. Indeed, the Centre for Food Safety (CFS),

These authors contributed equally to this work

* To whom all correspondence should be sent:
E-mail: zsxfst@163.com

the food safety authority of the Hong Kong government, has issued an advice to the public to limit the consumption of jellyfish due to confirmed reproductive toxicity and developmental toxicity of aluminum compounds in experimental animals. A number of studies also suggested that long-term exposure of aluminum shows toxicity to plants, animals and humans [17-19]. For example, aluminum can evoke several changes in neurons, which are similar to degenerative lesions observed in patients suffering from Alzheimer's disease [20].

Here we examined the Al content in alum-processed jellyfish and its release in an *in vitro* human gastric digestion system. Furthermore, the accumulation of Al and other trace elements and heavy metals (including Co, Mn, Zn, Cu, Pb, Mg, As, Hg, Fe, Cd, Sn and Ni) in different organs *in vivo* after consumption of alum-processed jellyfish was also determined using inductively coupled plasma mass spectrometry (ICP-MS). In addition, a possible economic and rapid processing technology to lower the Al residues in jellyfish was investigated.

MATERIAL AND METHODS

Materials

Male SPF KM mice, weighed 33 g to 36 g (aged 8 to 10 weeks), were purchased from Xiamen University Laboratory, Xiamen, PR China. The animals were group housed in polysulfonate cages (five animals per sex). The rooms are controlled for temperature (20-22 °C), relative humidity (45-65 %) and lighting (12 h light/dark cycle). The animals were allowed to acclimatize for one week before the initiation of experiments with food and water available *ad libitum*. All of the animal experiments were performed according to the ethics rules approved by the Xiamen University Ethics Committee (Xiamen, China) (Permit Number: XMUMC2012-12-9).

The alum-processed jellyfish was purchased from the aquatic products market of Mawei in Fuzhou, PR China and immediately stored at -20 °C until use.

Ethylenediamine tetraacetic acid solution, acetic acid, citric acid, and peroxide of hydrogen were analytical grade and purchased from Sigma Chemicals (St. Louis, MO, USA). Nitric acid and perchloric acid were ultrapure grade and purchased from Sigma Chemicals (St. Louis, MO, USA). Studied elements including Co, Zn, Cu, Pb, Mg, As, Hg, Fe, Cr, Mn, Sn, Ni and Hg were purchased from Sigma Chemicals (St. Louis, MO, USA). Standard stock solutions (1 g/L) were prepared by dissolution of corresponding spectrum metal and inorganic compounds with 1.2 mol/L HNO₃. Working solutions were obtained by diluting of these standard solutions with 1.2 mol/L HNO₃. Milli-Q ultrapure

(Elix UV5 and MilliQ, Millipore, USA) water was used in the whole experiment.

Methods

Preparation of jellyfish slurry

Jellyfish was prepared according to a traditional method as previously reported [7]. Briefly, alum-processed jellyfish, 15 cm in diameter for the part of the umbrella, were split into 5 equal wedges from the center and then were soaked in tap water (material: water ratio is 1:20) for 8 hours. During the procedure, the water was changed every two hours. Then, they were wiped with a paper towel for several seconds, cut into strips and ground into slurry by a miller. The slurry was sealed in zip-lock bags and stored in a 4 °C refrigerator.

Chemical composition analysis

Content of the total carbohydrate and total protein in the jellyfish slurry were determined calorimetrically using phenol-sulfuric acid [21] and bicinchoninic acid protein assay [22] as described previously. Standard methods published by the Association of the Official Analytical Chemists (1995) were used to measure the content of moisture, crude fat and ash [23].

In vitro human gastric digestion model

The experimental setup of the *in vitro* human gastric digestion model used was modified from the previous report [24]. The components of gastric juices used were prepared as follows: 2 g of NaCl and 7 mL of HCl (Merck, 37%), with the addition of 3.33 g of pepsin (Sigma, P7125) were diluted to 1 L and the pH was adjusted to 1.2 using 1.0 M HCl. 0.1 g of jellyfish slurry was digested under simulated 40 mL gastric juices with continuous shaking at approximately 60 rpm at 37 °C for 2 h to mimic the conditions in the stomach. After the digestion, the mixtures were centrifuged at 10,000 g for 10 min at 4 °C in order to separate the digestion fluids (aqueous phase) from the particulate residue. The quantification of Al in samples was performed through the ICP-MS before/after digestion. The concentration of Al solubilized in gastric juices was calculated as the Al (mg) released from jellyfish slurry (kg).

Intragastric administration of jellyfish slurry

The animal experiments were performed according to the ethics rules approved by the Xiamen University Ethics Committee (Xiamen, China) (Permit Number: XMUMC2012-12-9). Forty mice (7-week-old male) were randomly divided into four groups. Group A: Control mice received injections of saline (10 mL/kg.bw·d); group B: positive control mice received 34 mg (Al)/kg.bw by the means of AlCl₃ solutions; group C (low dose): mice treated

with jellyfish slurry at 1.74 g/kg.bw; group D (mid dose): mice treated with jellyfish slurry at 3.47 g/kg.bw; group E (high dose): mice treated with jellyfish slurry at 34.7 g/kg.bw. Jellyfish slurry was administered to the mice by intragastric administration. All mice were allowed free access to diets and water throughout the test period. Signs of toxicity (general status and behavioral characteristics) were observed daily. Mice were weighed every five days. After 30 days, blood was collected from the eyeballs of mice before executed using cervical dislocation, and then the brains, liver, kidney and brain were dissected and weighed. Samples of organs were quickly frozen in liquid nitrogen, and then stored at -80 °C to perform the measurements of trace elements and metal concentrations.

Trace element and heavy metals quantification by ICP-MS

Inductively coupled plasma mass spectrometry (ICP-MS, Agilent 7700) with external calibration approach was applied to quantify Al in mouse diet, jellyfish slurry and gastric juices. The sample digestion method performed, was as described in the previous report [10, 25]. For solid samples (mouse diet, jellyfish slurry), a portion of sample was accurately weighed and digested on a block heater with 500 µL of nitric acid 3 % and 500 µL of hydrogen peroxide at 120 °C for 3 min followed by 150 °C for 3 min, then increased the digestion temperature to 180 °C for 18 min. After partial evaporation, samples were cooled down and diluted to 5 or 10 mL with ultrapure water. For liquid sample (gastric juices and blood), 50 µL of gastric juices were wet digested with 500 µL of concentrated nitric acid at 65 °C for 1 h in a plastic digestion vessel on a block heater. Reagent blanks were prepared in the same manner. The sample solutions were stored in polyethylene vials below 8 °C and analyzed within 5 days.

Similarly, the presence and content of the following metals in mice blood and tissue including Al, Co, Mn, Zn, Cu, Pb, Mg, As, Hg, Fe, Cd, Sn and Ni were determined by ICP-MS (Agilent 7700) with an external calibration approach. Concentrations were expressed in µg or mg per wet weight of tissue samples (µg/kg or mg/kg). Calibration and verification of instrument performance were realized using multi-element solutions, respectively tune F and tune A (Thermo®). The internal standard used was rhodium (Agilent Technologies, USA) to correct for matrix effects and instrumental drift. Calibration ranges preparation was carried out using a multi-element calibrator solution (SCP Science® Plasma Cal).

The limits of detection (LOD) and quantification (LOQ) of each analyte were calculated through the

analyte concentration that corresponded to three and ten times the standard deviation of ten independent blank measurements respectively. The correlation coefficient of the standard curves ranged from $R^2=0.9994$ to $R^2=0.9999$, with the calibration curves displaying great linearity in the concentration range from 1 to 100 ng/g. The result is then divided by the slope of the calibration curve run on the same day of the experiment. Recovery (%), were in accordance with the performance criteria required by the European Commission (EC, 401/2006).

Organic acids treatment on alum-treated jellyfish

Different organic acids used to remove the Al in jellyfish was based on the protocol reported previously [26]. 10 g alum-treated jellyfish were soaked in 200 mL organic acids solutions, including ethylenediamine tetraacetic acid (EDTA) solution (0.01-0.2 g/L), acetic acid (AA) solution (0.1-2 g/L) and citric acid (CA) solution (0.1-2 g/L), for 100 min, and during the procedure, the solution was changed every 40 min. Jellyfish soaked in tap water was used as control.

After equilibration, the solutions were removed and jellyfish slurry was prepared as described above. The Al content was measured using ICP-MS as described above.

Statistical analysis

All experiments were performed in triplicate. All data were presented as means \pm SD and all statistics were performed using GraphPad Prism 5.0 software. Differences between means were analyzed by student's t-test or one-way ANOVA followed by Dunnett's multiple comparison. Differences were considered to be statistical significant at $p < 0.05$.

RESULTS

Chemical compositions

Edible jellyfish has been considered as natural diet food for its low calories and richness in protein and minerals for a long time. Consistent with previous results[7, 27], nutritional composition analysis of alum-processed jellyfish demonstrated samples mainly consists of water and protein. The jellyfish samples had very high moisture content(82.7-86.8 %) and protein content (14.3-15.8%), but low crude fat content (0.38-1.5 %). Besides, the ash content and the carbohydrate content of jellyfish sample were $0.71 \pm 0.34\%$ and $0.82 \pm 0.21\%$, respectively. These results suggested jellyfish may be a good source of protein content.

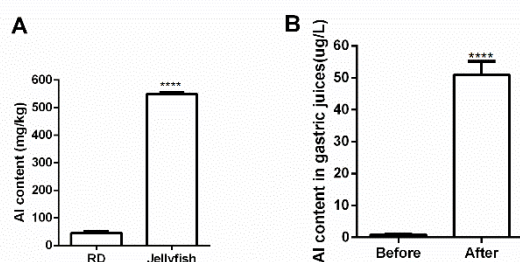


Fig. 1. (A) Aluminum content (mg/kg) in normal laboratory rodent diet (RD) and jellyfish measured by ICP-MS. (B) Aluminum content ($\mu\text{g/L}$) in gastric juices before and after digested measured by ICP-MS. Data are represented as mean \pm SD ($n=3$), statistical significance was assessed by student's t-test. **** $P < 0.01$ compared with the aluminum content in normal laboratory rodent diet.

Al residue in alum-processed jellyfish is released in simulated gastric juices in vitro

Next, we analyzed Al content in alum-processed jellyfish by ICP-MS and compared with normal laboratory rodent diet. The results showed that alum-processed jellyfish contain significantly higher (~ 10 -fold) amount of aluminum than normal laboratory rodent diet ($549.90 \pm 4.66 \text{ mg/kg}$ and $45.90 \pm 5.46 \text{ mg/kg}$, respectively) (Figure 1.A), suggesting alum-processed jellyfish is a Al-rich food, which is consistent to a previous report [10]. Moreover, after 2 hours digestion in the *in vitro* human gastric juices, Al content in gastric juices was significantly increased to $50.92 \pm 4.26 \mu\text{g Al/L}$ (Figure 1.B), indicating that Al in jellyfish slurry might be released after human gastric digestion and absorbed by the digestive system.

Alum-processed jellyfish affect liver-to-body weight index (%) of mice

The appearance and general behavioral patterns of mice were observed daily after jellyfish administration. No toxic symptoms or mortality were observed in all groups. All tested mice lived up to 30 days after the administration of jellyfish slurry at a dose of 34.7 g/kg.bw (Table. 1). Furthermore, the

animals in both control group and jellyfish slurry-treated groups displayed no significant changes in behavior, skin appearance, hair loss, breathing, neurotoxicity signs, and postural abnormalities.

The effect of jellyfish slurry on the body weight was determined by recording the body weight at the beginning of the experiment (day 0) and after feeding for 30 d. As summarized in table 1, the control animals gained a mean of approximately 3.51 ± 0.98 g over the four-week experimental period. Over the same period, the weight gains for jellyfish slurry treated mice was 3.76 ± 0.97 , 4.16 ± 0.71 and 4.68 ± 0.93 for animals receiving 1.74 g/kg.bw , 3.47 g/kg.bw and 34.7 g/kg.bw of jellyfish slurry, respectively. These values did not differ significantly from the control group.

Although no significant changes in body weight were found, the analysis of organ-to-body weight index (%) of several organs including brain, kidney and liver showed an interesting result. The organ-to-body weight index of liver in mice receiving medium-dose and high-dose of jellyfish slurry significantly lower from the control group (Figure 2), indicating alum-processed jellyfish may affect the functions of liver [7].

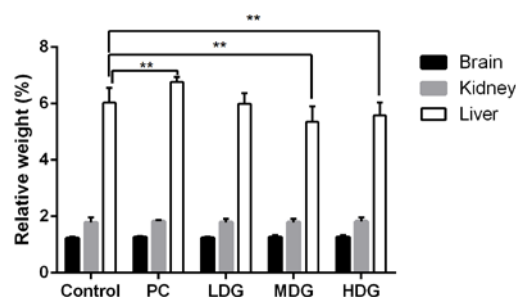


Fig. 2. Organ-to-body weight index (%) of mice exposed to different doses of jellyfish slurry. Organ body index (%) was calculated as (organ weight/body weight) $\times 100$. PC: AlCl_3 -treated positive control group; LDG: low dose group; MDG: medium dose group; HDG: high dose group. Each value is represented as mean \pm SD ($n=10$), statistical significance was assessed by one-way ANOVA (Dunnnett's multiple comparison test). ** $P < 0.01$ compared with control group.

Table 1. The effects of jellyfish slurry on mice survive and body weights

| | Number of mice (day 1) | Number of mice (day 30) | Body weight day 1 (g) | Body weight gain (g) |
|------------------------|---------------------------|----------------------------|--------------------------|-------------------------|
| Control | 10 | 10 | 34.52 ± 4.66 | 3.51 ± 0.98 |
| Positive control group | 10 | 10 | 35.14 ± 2.23 | $-1.27 \pm 2.40^*$ |
| Low dose group | 10 | 10 | 34.31 ± 5.24 | 3.76 ± 0.97 |
| Mid dose group | 10 | 10 | 36.65 ± 2.94 | 4.16 ± 0.71 |
| High dose group | 10 | 10 | 34.56 ± 4.35 | 4.68 ± 0.93 |

All values are presented as mean \pm SD.

Alum-processed jellyfish up-regulates aluminum accumulation in liver and kidney

We next investigated the effects of alum-processed jellyfish on Al accumulation in blood,

liver, kidney, brain and bone of mice. Accumulation of Al was found to be increased in all tested organs in AlCl_3 treated mice compared to the control group. Meanwhile, around 2-fold and 3-fold increase in Al accumulation in the liver were observed in mice after receiving intragastric administration of jellyfish slurry at medium- and high-doses, respectively, while a significant increase of Al accumulation was also found in the kidney. The Al concentrations in the liver and the kidney were positively correlated to the amount of jellyfish consumption, suggesting the direct contribution of jellyfish to hepatic and renal Al accumulation.

We also quantified several other trace elements and heavy metals including Co, Mn, Zn, Cu, Pb, Mg, As, Hg, Fe, Cr, Sn and Ni, in blood, liver, kidney, brain and bone of mice by ICP-MS. Values obtained are summarized in table 2. The results demonstrated that only Zn and Cu accumulation were found to increase upon medium-dose and high-dose jellyfish slurry consumption. However, compared to the dramatic change of Al accumulation in the liver (~2 folds in medium-dose group and ~3 folds in high-dose group), the changes of Zn and Cu in all other organs were relatively smaller, suggesting Al should be the major concern with regards to the food safety of alum-processed jellyfish. Interestingly, several heavy metals such as Pb, As and Hg showed a significant decrease in the organs, indicating that the jellyfish may also affect the metabolism of other heavy metals. Finally, metals such as Cd, Mn, Sn and Ni were found to be present at very low levels, beyond detection limits.

Effect of organic acids treatment on removal of Al in jellyfish

To test the effects of organic acids on lowering Al in jellyfish, EDTA, citric acid, and acetate acid solutions were used to soak jellyfish. As shown in Figure 3, the amount of Al existing in the jellyfish decreased significantly after treatment with all these three organic acids. Among the three organic acids, citric acid and acetate acid demonstrated stronger abilities in lowering the Al residues in jellyfish. Treatment with a 0.5 g/L citric acid solution significantly decreased (~80 %) the Al content in jellyfish compared to controls, while a higher concentration of citric acid (up to 2 g/L) can lower the amount of Al further (Figure 3.B).

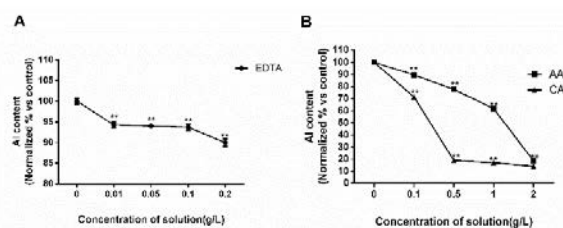


Fig. 3. Effect of different concentration (g/L) of A. EDTA, B. acetic acid (AA) and citric acid (CA) on Al content in jellyfish normalized (%) compared with the content in control. Data are represented as mean \pm SD ($n=3$), statistical significance was assessed by one-way ANOVA (Dunnett's multiple comparison test). ** $P < 0.01$ compared with control group.

DISCUSSION

The determination of harmful trace elements and heavy metals accumulation is an important part in health risk assessment in the food industry [28]. This could provide important information and help formulate guidelines for food consumption to authorities, industry and consumers. To date, the systematic study of the bioaccumulations of Al, Co, Mn, Zn, Cu, Pb, Mg, As, Hg, Fe, Cr, Sn and Ni after jellyfish consumption are lacking.

Previous studies have shown that alum-processed jellyfish contain a significantly higher amount of aluminum than fresh jellyfish, suggesting that the curing of jellyfish with alum leads to high concentrations of alum in jellyfish [7, 10]. Our results support these findings - alum-processed jellyfish contains higher amount of Al (549.90 ± 4.66 mg/kg) than regular rodent diet (45.90 ± 5.46 mg/kg). Furthermore, it was demonstrated that the Al in alum-processed jellyfish could be released into the gastric digestive liquids after 2 hours digestion through the *in vitro* human digestion model. The *in vitro* human digestion model has been demonstrated to offer an appealing alternative to human and animal studies [29], which can mimic the human gastrointestinal conditions to study the structural changes, digestibility, and release of food components [30]. Therefore, the results here highlights and provide compelling data that the Al in alum-processed jellyfish is available for absorption in the intestinal epithelium, and the consumption of these jellyfish may possess a risk for Al accumulation in human.

Notably, chronic exposure to Al has been linked with several pathological processes, including neurodegenerative diseases [31, 32], microcytic anaemia [33] osteoporosis [34] and liver damage [35].

Table 2. Mean concentrations (W./W.) and standard deviations (Mean \pm SD) of trace elements and heavy metals in the matrices of mouse from different groups.

| Elements | Matrix | Control group | Positive control group | Low dose group | Mid dose group | High dose group | Recovery (%) |
|-----------------------------------|--------|------------------------|------------------------|-------------------------|-------------------------|------------------------|--------------|
| Al ($\mu\text{g}/\text{kg}$) | Blood | 831.59 \pm 46.13 | 868.37 \pm 46.22** | 601.82 \pm 49.84* | 540.75 \pm 39.55** | 511.89 \pm 19.58** | 97.9 |
| | Liver | 985.94 \pm 47.76 | 4284.40 \pm 52.24** | 1058.94 \pm 53.02 | 2009.46 \pm 22.62** | 3073.53 \pm 20.35** | |
| | Kidney | 1191.40 \pm 66.97 | 2332.59 \pm 18.61** | 896.69 \pm 31.66** | 1201.32 \pm 59.13 | 2068.56 \pm 81.97** | |
| | Brain | 909.72 \pm 13.76 | 1323.48 \pm 34.65** | 946.92 \pm 40.62 | 872.60 \pm 34.65 | 736.61 \pm 52.68** | |
| Mg (mg/kg) | Blood | 37.37 \pm 2.42 | 38.98 \pm 2.95 | 39.16 \pm 1.70 | 41.24 \pm 2.10 | 37.58 \pm 5.28 | 93.4 |
| | Liver | 244.80 \pm 13.38 | 250.76 \pm 20.28 | 247.02 \pm 7.56 | 260.11 \pm 13.32 | 243.51 \pm 15.25 | |
| | Kidney | 202.30 \pm 6.57 | 224.06 \pm 14.28 | 223.34 \pm 21.11 | 207.39 \pm 9.84 | 212.07 \pm 9.43 | |
| | Brain | 181.03 \pm 1.22 | 189.83 \pm 9.28 | 184.46 \pm 4.22 | 185.25 \pm 3.13 | 184.67 \pm 5.21 | |
| Fe (mg/kg) | Blood | 47.32 \pm 17.78 | 42.46 \pm 15.58 | 48.99 \pm 18.86 | 46.55 \pm 14.57 | 46.89 \pm 11.88 | 94.5 |
| | Liver | 159.53 \pm 93.24 | 148.05 \pm 46.20 | 110.04 \pm 14.27 | 122.50 \pm 16.67 | 103.76 \pm 9.02* | |
| | Kidney | 80.84 \pm 10.46 | 89.52 \pm 15.58 | 73.31 \pm 12.16 | 73.32 \pm 7.67 | 80.10 \pm 36.62 | |
| Zn ($\mu\text{g}/\text{kg}$) | Blood | 4837.76 \pm 460.82 | 4677.46 \pm 200.28 | 4387.48 \pm 468.90 | 4397.00 \pm 193.60 | 5974.27 \pm 174.44** | 88.9 |
| | Liver | 25007.68 \pm 1368.17 | 28800.45 \pm 891.55 | 25363.65 \pm 574.35 | 26849.24 \pm 1722.90* | 24531.27 \pm 1650.36 | |
| | Kidney | 17275.69 \pm 741.20 | 18855.75 \pm 198.08 | 19164.63 \pm 1672.67* | 17564.32 \pm 912.47 | 18633.05 \pm 778.22 | |
| | Brain | 15274.10 \pm 120.98 | 15733.63 \pm 131.51 | 15722.63 \pm 284.35 | 15681.93 \pm 316.17 | 16306.40 \pm 621.46 | |
| Pb ($\mu\text{g}/\text{kg}$) | Blood | 4.358 \pm 0.61 | 4.26 \pm 0.61 | 4.835 \pm 0.83 | 4.413 \pm 0.39 | 4.653 \pm 0.55 | 92.1 |
| | Liver | 6.589 \pm 0.84 | 6.68 \pm 0.64 | 5.729 \pm 0.97 | 6.130 \pm 0.50 | 6.643 \pm 0.23 | |
| | Kidney | 22.021 \pm 7.51 | 21.17 \pm 8.83 | 18.408 \pm 5.61 | 15.975 \pm 3.87* | 13.980 \pm 7.47** | |
| As ($\mu\text{g}/\text{kg}$) | Blood | 44.62 \pm 6.97 | 42.76 \pm 1.68 | 39.50 \pm 4.66 | 34.81 \pm 2.05 | 40.33 \pm 4.76 | 91.0 |
| | Liver | 339.97 \pm 43.07 | 384.05 \pm 36.20** | 357.08 \pm 23.59 | 341.53 \pm 40.32 | 368.92 \pm 30.69 | |
| | Kidney | 194.00 \pm 3.54 | 189.12 \pm 4.58 | 192.96 \pm 7.98 | 184.89 \pm 9.54 | 175.31 \pm 1.74* | |
| Cu ($\mu\text{g}/\text{kg}$) | Blood | 701.35 \pm 43.00 | 796.56 \pm 12.22 | 625.01 \pm 33.46 | 746.56 \pm 147.49 | 756.29 \pm 45.59 | 92.9 |
| | Liver | 3578.38 \pm 483.30 | 3661.91 \pm 488.61 | 3702.30 \pm 165.16 | 3722.70 \pm 463.12 | 4031.51 \pm 158.04* | |
| | Kidney | 3702.83 \pm 26.59 | 3671.53 \pm 55.84 | 3878.53 \pm 90.11 | 3861.42 \pm 92.01 | 3854.05 \pm 80.55 | |
| | Brain | 4019.69 \pm 119.58 | 4045.11 \pm 78.34 | 4199.50 \pm 349.95 | 4078.69 \pm 256.51 | 3798.73 \pm 121.23 | |
| Hg ($\mu\text{g}/\text{kg}$) | Blood | 0.47 \pm 0.05 | 0.45 \pm 0.44 | 0.370 \pm 0.13 | 0.163 \pm 0.03 | 0.126 \pm 0.03 | 91.7 |
| | Liver | 2.62 \pm 0.15 | 2.79 \pm 0.52 | 3.675 \pm 0.23 | 3.805 \pm 0.17 | 3.830 \pm 0.03 | |
| | Kidney | 31.40 \pm 2.43 | 32.52 \pm 2.35 | 30.712 \pm 1.61 | 21.483 \pm 1.37** | 22.019 \pm 1.41** | |
| | Brain | 0.76 \pm 0.06 | 0.82 \pm 0.026 | 0.52 \pm 0.03** | 0.49 \pm 0.02 | 0.25 \pm 0.03 | |

The values are presented as Mean \pm SD. Statistically significant differences are analyzed by one-way ANOVA. * P < 0.05; ** P < 0.01; n = 10.

Although current evidence suggests that dietary exposure to aluminum may not pose a risk for developing Alzheimer's disease, the food safety authorities of some countries have listed aluminum residues in alum-processed jellyfish as a significant food safety concern, and have encouraged the public to limit their consumption of jellyfish.

Our *in vivo* studies found that the medium- and high-dose consumptions of jellyfish significantly lowered the relative liver weights and increased the hepatic Al accumulation in mice. There has been numerous reports on the adverse effects of Al on the liver [17, 36]. For example, it has been reported that the treatment with AlCl_3 solutions (25-36 mg $\text{Al}^{3+}/\text{kg}\cdot\text{bw}$) in mice or rats resulted in liver damage by cell death or apoptosis of hepatocytes [37, 38]. Therefore, our results indicate that the liver functions may be impaired due to the Al accumulation after consumption of traditional alum-processed jellyfish.

Previous studies also found that the bone, brain and kidney are important accumulation sites of Al in the body [17]. Our results are also consistent with these findings. Among tested organs, the highest Al accumulation is found in the kidney, followed by the

bone. Furthermore, after jellyfish slurry treatment, a significant increase in Al accumulation was also found in the kidney. It was also found that Al concentration in these organs was positive-correlated to the amount of jellyfish consumption, indicating a possible direct link between the jellyfish consumption and Al accumulation.

Furthermore, it is widely known that seafood consumption possess a higher risk of bioaccumulation of heavy metals, such as Hg, Cd, Pb, As, Zn, Mg, Fe, Cu, Pb, Mn, Ni and Sn [3]. Among all the analyzed metals, Cd and Ni are recognized as human carcinogens [39]. Despite being weak mutagens, these metals also have the ability to enhance the mutagenicity and carcinogenicity of directly acting genotoxic agents such as ultraviolet or ionizing radiation [39]. Although it has been reported that jellyfish contained abundant inorganic and organic constituents including Zn, Mg, Ca, Al, Sr, Si and alkali metals [10], our data indicated that jellyfish consumption had little influence on the accumulation of these ions in mice compared to Al. Heavy metal contamination also appears not to be a major concern in the safety evaluation of jellyfish since the concentration of

several heavy metals even show a significant decrease after jellyfish consumption. Our data support the hypothesis that the excessive consumption of alum-processed jellyfish will increase the risk of Al poisoning for the consumers. The recommended dietary allowance of jellyfish should be considered based on the Al metabolism *in vivo*.

Several studies have documented that chelating agents such as EDTA and citric acid (CA) can effectively extract heavy metals from waste water and soil [33, 40]. We also applied these organic acids in the desalination process in order to decrease the Al concentration in jellyfish. The results indicate that organic acids would be effective chelators to reduce the content of Al in jellyfish. Future research should focus on the cost, toxicity and degradability of these chelators in the development of novel jellyfish food processing technologies[41].

CONCLUSION

Consumption of jellyfish slurry worsens the Al accumulation in liver and affects the relative liver weights at medium-dose (17.4 g/kg.bw) and high-dose (34.7 g/kg.bw) in mice, indicating a possible toxic effect of over-dose consumption of alum-processed jellyfish. Although no significant changes in mortality rates were observed after 30 days feeding with processed jellyfish, however, considering the adverse effects on liver reported here, the long-term effects of aluminum-rich jellyfish consumption warrants further investigation. Citric acid solutions may reduce Al in alum-processed jellyfish and increase its safety.

The present study provides novel and important data on the safety assessment of alum-processed jellyfish consumption, consistent with the recommendations of food authorities in some countries to reduce the consumption of alum-processed jellyfish. Moreover, this study highlights the urgent need to develop novel processing food technologies of jellyfish, which lowers the aluminum bioaccumulation in jellyfish.

Acknowledgements: *The authors are thankful to Dr. Peng Meng and his team for assistance during organic elements quantification. This study was supported by grants from Natural Science Foundation of Fujian Province (2016J05067) and High-level University Construction Project (612014042).*

ABBREVIATIONS

Al- Aluminums; As- Arsenic; Cd- Cadmium; Co- Cobalt; Cu- Copper; Cr- Chromium; Fe- Iron; Hg- Mercury; Mg- Magnesium; Mn- Manganese; Ni –

Nickel; Pb- Plumbum; Sn- Stannum; Zn- Zinc; ICP-MS - inductively coupled plasma-mass spectroscopy system

REFERENCES

1. M. Omori, E. Nakano, *Hydrobiologia*, **451**,19 (2001).
2. Y.P. Hsieh, F.M. Leong, J. Rudloe, *Hydrobiologia*, **451**, 11 (2001).
3. G. Dugo, L. L. Pera, A. Bruzzese, T. M. Pellicanò, V. L. Turco. *Food Control*, **17**, 146, 2006.
4. R.A. Goyer. *Am J Clin Nutr*, **61**, 646, (1995).
5. D. Gibson, B. Barnes, *Journal of Reviews*, **31**, 101 (2000).
6. Y. Huang. *Cannonball jellyfish (Stomolophus meleagris) as a food resource*. *Journal of food science*, **53**,341 (1988).
7. Y.H.P. Hsieh, F.M. Leong, K.W. Barnes, *J.agric.food Chem*, **44**, 3117(1996)
8. N. M.Khong, F. M Yusoff, B.Jamilah, Basri, M., I. Maznah, K. W. Chan, *Food Chemistry*, **196**, 953 (2016).
9. Z.B. Morais, A.M. Pintão, I.M. Costa, M.T. Calejo, N.M. Bandarra, *Journal of Aquatic Food Product Technology*, **18**, 90 (2009).
10. X. Liu, L. Guo, H. Yu, P. Li. *Food Analytical Methods*, **5**, 301 (2012).
11. J.F. Ding, Y.Y. Li, J.J. Xu, X.R. Su, X. Gao. *Food Hydrocolloids*, **25**, 1350 (2011).
12. H. Morishige, T. Sugahara, S. Nishimoto, A. Muranaka, F. Ohno. *Cytotechnology*, **63**, 481 (2011).
13. S. Addad, J.Y. Exposito, C. Faye, S. Ricard-Blum, C. Lethias. *Marine Drugs*, **9**, 967 (2011).
14. J.R. Li, Y.H. Hsieh, *Asia Pacific Journal of Clinical Nutrition*, **13**, 147 (2004).
15. L. He, S. Cai, B. Wu, C. Mu, G. Zhang. *Journal of Inorganic Biochemistry*, **117**, 124 (2012).
16. S. Miura, S. Kimura, *J Biol Chem*, **260**,15352 (1985).
17. P.O. Ganrot, *Environ Health Perspect*, **65**, 363 (1986).
18. P. Nayak, A.K. Chatterjee, *Food & Chemical Toxicology*, **39**, 587(2001).
19. M.A. Piñeros, L.V. Kochian, *Plant Physiology*, **125**, 292 (2001).
20. M. Kawahara, M. Kato, Y. Kuroda, *Brain research bulletin*, **55**, 211 (2001).
21. L. Chen, W. Xu, S. Lin, Pck Cheung. *Food Hydrocolloids*, **36**, 189 (2014).
22. J. Hu, I. Kyrou, B.K. Tan, G.K. Dimitriadis, M. Ramanjaneya. *Endocrinology*, **157**, 1881 (2016).
23. M. Oh, E.K. Kim, B.T. Jeon, Y. Tang, M.S. Kim. *Meat Science*, **119**, 16(2016).
24. A. Sarkar, K.K.T. Goh, R.P. Singh, H. Singh. *Food Hydrocolloids*, **23**, 1563(2009).
25. J. Lourenço, R. Pereira, F. Gonçalves, S. Mendo. *Sci Total Environ*, **443**, 673(2013).
26. O.K. Borggaard, S.S. Jdrghensen, J.P. Moberg, B. Raben-Lange. *European Journal of Soil Science*, **41**, 443(2006).
27. N.M. Khong, F.M. Yusoff, B. Jamilah, M. Basri. *Food Chem*, **196**, 953 (2016).
28. M. Metian, P. Bustamante, L. Hédouin, M. Warnau. *Environ Pollut*, **152**, 543 (2008).
29. L.G. Danielsson, A. Sparen, A.W. Glynn, *Analyst*,

- 120,713 (1995).
30. M.A. Azenha, M.T. Vasconcelos, *Food Chem Toxicol*, **38**,899 (2000).
31. A. Campbell, A. Becaria, D.K. Lahiri, K. Sharman, S.C. Bondy. *J Neurosci Res*, **75**, 565 (2004).
32. M. Kawahara. *J Alzheimers Dis*, **8**, 171 (2005).
33. C. Turgut, M.K. Pepe, T.J. Cutright, *Environmental Pollution*, **131**, 147(2004).
34. A.M. Pérez-Granados, M.P. Vaquero, *Journal of Nutrition Health and Aging*, **6**, 154 (2002).
35. S. Yumoto, H. Ohashi, H. Nagai, S. Kakimi, A. Ishikawa. *Nuclear Instruments and Methods in Physics Research Section B: Beam Interactions with Materials and Atoms*, **75**,188 (1993).
36. Y. Zhu, Y. Han, H. Zhao, J. Li, C. Hu. *Food Chem Toxicol*, **51**,210 (2013).
37. D. Vitezeliene, E. Jansen, H. Rodovicius, A. Kasauskas, L. Ivanov. *Environ Toxicol Pharmacol*, **31**, 302 (2011).
38. H. Turkez, M.I. Yousef, F. Geyikoglu, *Food Chem Toxicol*, **48**, 2741 (2010).
39. D. Beyersmann. *Toxicol Lett*, **127**,63(2002).
40. Z. Wu, Z. Gu, X. Wang, L. Evans, H. Guo. *Environmental Pollution*, **121**, 469 (2003).
41. S.A. Wasay, S.F. Barrington, S. Tokunaga, *Environmental Technology*, **19**, 369 (1998).

A new formula of loess earth pressures based on the joint strength theory

P. Sun¹, R.-J. Li^{2,*}, O. Igwe³, H. Luo²

¹ Institute of Geomechanics, Chinese Academy of Geological Sciences, Beijing 100081, China

² Shaanxi provincial key laboratory of loess mechanics and engineering, Xi'an University of Technology, Xi'an 710048, China

³ Department of Geology, University of Nigeria, Nsukka, Nigeria

Received May 25, 2017; Revised July 20, 2017

Because the effect of tensile strength on the calculation of the earth pressure of loess is worthy of further evaluation, based on the joint strength theory that fully considers tensile and shear properties of loess, this paper first analyzes active and passive limit stress equilibrium, then derives new calculation formulae for active and passive earth pressures, and finally verifies these new formulae and compares them with Rankine's classical formulae for active and passive earth pressures. The results show that the active earth pressure of loess based on the joint strength theory is larger than the Rankine's active earth pressure; the passive earth pressure of loess based on the joint strength theory is smaller than the Rankine's passive earth pressure.

Keywords: loess, tensile strength, joint strength formula, active earth pressure, passive earth pressure

INTRODUCTION

Classical earth pressure theories derived from the Mohr-Coulomb strength theory, mainly include Rankine's earth pressure theory and Coulomb's earth pressure theory [1].

The concept of earth pressure calculation was put forward in 1773. Coulomb's earth pressure theory [2] and Rankine's earth pressure theory [3] are two classical earth pressure theories proposed in 1776 and 1857 respectively. These studies have laid the preliminary foundation for the research on earth pressures.

Xie et al. [4] and Gao et al. [5] derived formulae to calculate active earth pressures and passive earth pressures. Zhang et al. [6] obtained formulae to calculate active and passive earth pressures. The above studies promoted the calculation of earth pressures on the retaining wall.

To expand the research fields of earth pressures, Nakai et al. [7] introduced the FEM into the calculation of earth pressures on the retaining wall. Zhu et al. [8] set up unified expressions of earth pressures on the inclined retaining wall. Hu et al. [9] studied active earth pressures on a retaining wall in a non-limit state via the thin-layer element method. Zhao et al. [10] established a unified solution to Coulomb's active earth pressures of unsaturated earth. And Ma et al. [11] introduced the concept of structurality of loess to the calculation of earth pressures. The above studies have promoted the development of earth pressure. However, all these studies failed to discuss or evaluate the tensile

strength of structural loess.

In order to consider the tensile strength of structural loess reasonably, Li et al. [12-14] introduced structural parameters into the joint strength theory for structural loess, and put forward a simplified hyperbolic strength formula for structural loess. In addition, based on the hyperbolic strength formula for structural loess, Song et al. [15] introduced structural parameters to the hyperbolic strength formula for structural loess. The above results have fully considered the tensile strength and the shear strength of structural loess.

Therefore, based on the joint strength theory that fully considers tensile and shear properties of loess and through analyzing active and passive limit stress equilibrium, new calculation formulae for active and passive earth pressures will be derived, verified and compared with Rankine's classical formulae in the present study.

METHODS

The joint strength theory

To evaluate the tensile strength effect of structural loess reasonably, the curvilinear relation between tensile strength σ_t and cohesion force c obtained by tests, as shown in Fig.1. Formula (1) is the fitting formula.

$$\sigma_t = 10^{-6} c^3 - 0.0011c^2 + 0.7081c - 1.8913 \quad (1)$$

Via tensile tests and triaxial shear tests, Li et al. [12] obtained strength failure stress circles as shown in Fig.2. Via analyzing Fig.2, the tensile strength values based on the reverse extension lines of Mohr-Coulomb strength lines are 2~3 times significantly higher than the corresponding actual test values.

* To whom all correspondence should be sent:
E-mail: lirongjian@xaut.edu.cn

Results indicate that the Mohr-Coulomb failure criterion overestimate the tensile strength of loess.

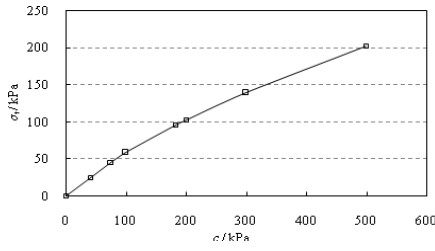


Fig. 1. The correlation between the tensile strength and the cohesive force of structural loess

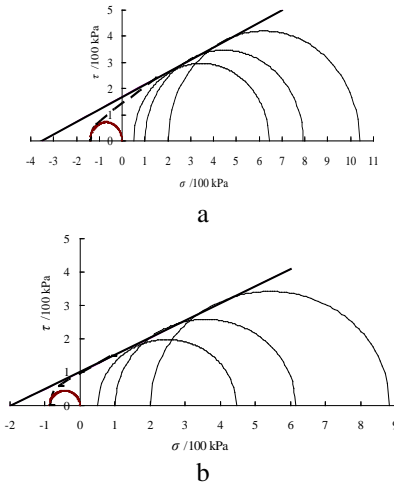


Fig.2 The strength failure lines based on their tensile and shear properties: a) Intact loess; b) Remolded loess.

In Fig.2, Mohr-Coulomb strength lines in the tension-shear region are represented by smooth curves. Apparently, one strength line can be obtained after curve-fitting with a smooth curve used in the tension-shear zone and pressure-shear zone respectively. As a result, the strength line can reflect the tension-shear and pressure-shear failure.

In plane σ - τ , the joint strength formula can be shown as follow:

$$\tau^2 = (c + \sigma \tan \varphi)^2 - (c + \sigma_t \tan \varphi)^2 \quad (2)$$

Among them, φ is the internal friction angle of the backfill behind the wall.

Derivation premise and hypothesis on loess earth pressures based on the joint strength theory

The basic assumption is adopted in the Rankine's earth pressure theory. As shown in Fig.3, σ_h stands for the horizontal stress, and σ_v stands for the vertical stress.

For the convenient description, the joint strength line is divided into three sections: section I indicates the strength line with the horizontal stress in the tensile-shear region, section II indicates the strength

curve with the horizontal stress in the pressure-shear region, and section III indicates the strength straight line with the horizontal stress in the pressure-shear region, as shown in Fig.4.

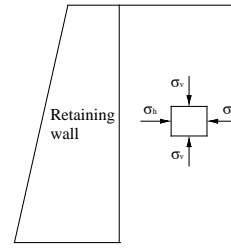


Fig. 3 The stress state of soil in slope.

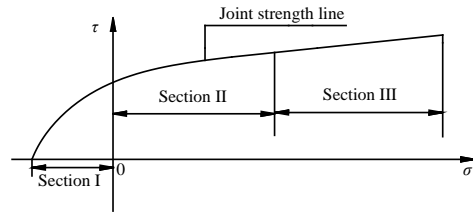


Fig. 4. The segmentation of a joint strength line.

RESULTS

Derivation and analysis of active earth pressures of loess based on the joint strength theory

Analysis of limit equilibrium state in active earth pressure

When the horizontal force σ_h decreases to a certain extent, the Mohr's stress circle is right tangent to the joint strength line. At this point, the horizontal force σ_h is the active earth pressure p_a .

The active limit equilibrium state of soil can be analyzed in three cases (Fig.4). In the first case, the horizontal stress decreases to the extent that the Mohr's circle is tangent to section III; in the second case, the horizontal stress decreases to the extent that the Mohr's circle is tangent to section II; and in the third case, the horizontal stress decreases to the extent that the Mohr's circle is tangent to section I. When the soil is in a state corresponding to the first case:

$$p_a = \gamma z \tan^2 \left(45^\circ - \frac{\varphi}{2} \right) - 2c \tan \left(45^\circ - \frac{\varphi}{2} \right) \quad (3)$$

When the soil is in a state corresponding to the second or third case, active earth pressures on the retaining wall can be derived based on the joint strength.

(2) Derivation of new loess active earth pressure

When the Mohr's stress circle is in an active limit equilibrium state(as shown in Fig.5). Assume that point G is the tangent point, point E is the center of

the Mohr's stress circle, and line segment GF is perpendicular to axis σ with point F as the pedal point.

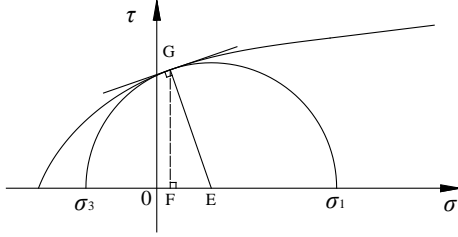


Fig. 5. The active limit equilibrium state

According to formula(2), the ordinate of point G can be obtained. So G (σ_G , $\sqrt{(c + \sigma_G \tan \varphi)^2 - (c + \sigma_i \tan \varphi)^2}$). The slope k_t of the tangent point G can be calculated as:

$$k_t = \frac{d\tau}{d\sigma} = \frac{(c + \sigma_G \tan \varphi) \tan \varphi}{\sqrt{(c + \sigma_G \tan \varphi)^2 - (c + \sigma_i \tan \varphi)^2}} \quad (4)$$

Accordingly, the equation for the normal line at point G can be calculated as:

$$\tau - \tau_G = -\frac{1}{k_t}(\sigma - \sigma_G) \quad (5)$$

Based on formula(5) and equation $\tau=0$, the abscissas of E can be acquired as:

$$\sigma_E = \frac{1}{\cos^2 \varphi} \sigma_G + c \tan \varphi \quad (6)$$

Therefore, center point E ($\frac{1}{\cos^2 \varphi} \sigma_G + c \tan \varphi$, 0).

In ΔGFE , $|GF| = \tau_G$ and $|FE| = k_t \tau_G$. The radius of the Mohr's stress circle can be expressed:

$$|EG| = \sqrt{(k_t \tau_G)^2 + \tau_G^2} \quad (7)$$

The equation for the corresponding Mohr's stress circle can be determined as:

$$\left[\sigma - \left(\frac{1}{\cos^2 \varphi} \sigma_G + c \tan \varphi \right) \right]^2 + \tau^2 = \tau_G^2 (1 + k_t^2) \quad (8)$$

When $\tau=0$ in equation(8), the major principal stress (σ_1) and the minor principal stress (σ_3) can be calculated respectively as:

$$\sigma_1 = \frac{1}{\cos^2 \varphi} \sigma_G + c \tan \varphi + \sqrt{\tau_G^2 + \tau_G^2 k_t^2} \quad (9)$$

$$\sigma_3 = \frac{1}{\cos^2 \varphi} \sigma_G + c \tan \varphi - \sqrt{\tau_G^2 + \tau_G^2 k_t^2} \quad (10)$$

Put formula (4) and τ_G into formula(9) and formula(10), then:

$$\sigma_1 = \frac{1}{\cos^2 \varphi} \sigma_G + c \tan \varphi + \sqrt{(c + \sigma_G \tan \varphi)^2 \cdot \frac{1}{\cos^2 \varphi} - (c + \sigma_i \tan \varphi)^2} \quad (11)$$

$$\sigma_3 = \frac{1}{\cos^2 \varphi} \sigma_G + c \tan \varphi - \sqrt{(c + \sigma_G \tan \varphi)^2 \cdot \frac{1}{\cos^2 \varphi} - (c + \sigma_i \tan \varphi)^2} \quad (12)$$

According to formula(11), an inverse solution can be made as:

$$\sigma_G = -\sqrt{\sin^2 \varphi \cdot \sigma_i^2 + 2c \sin \varphi \cdot \cos \varphi \cdot \sigma_i - \cos^2 \varphi (\sigma_i^2 \tan^2 \varphi + 2c \cdot \sigma_i \tan \varphi)} + \sigma_i \quad (13)$$

To simplify formulae, let:

$$\begin{cases} A = -\cos^2 \varphi (\sigma_i^2 \tan^2 \varphi + 2c \cdot \sigma_i \tan \varphi) \\ B = 2c \sin \varphi \cdot \cos \varphi \\ D = \sin^2 \varphi \end{cases} \quad (14)$$

Then formula(13) can be simplified as:

$$\sigma_G = -\sqrt{D \cdot \sigma_i^2 + B \cdot \sigma_i + A} + \sigma_i \quad (15)$$

In the same vein, formula(12) can be simplified as:

$$\sigma_G = -\sqrt{D \cdot \sigma_3^2 + B \cdot \sigma_3 + A} + \sigma_3 \quad (16)$$

Formula(15) and formula(16) are equal:

$$\sqrt{D \cdot \sigma_3^2 + B \cdot \sigma_3 + A} + \sigma_3 = -\sqrt{D \cdot \sigma_i^2 + B \cdot \sigma_i + A} + \sigma_i \quad (17)$$

After transforming formula(17), σ_3 can be calculated as follows:

$$\sigma_3 = \frac{-\sqrt{4 \cos^2 \varphi (2 \sigma_i \sqrt{D \cdot \sigma_i^2 + B \cdot \sigma_i + A} - D \cdot \sigma_i^2 - B \cdot \sigma_i - \sigma_i^2) + (2 \sigma_i + B - 2 \sqrt{D \cdot \sigma_i^2 + B \cdot \sigma_i + A})^2}}{2 \cos^2 \varphi} + \frac{2 \sigma_i + B - 2 \sqrt{D \cdot \sigma_i^2 + B \cdot \sigma_i + A}}{2 \cos^2 \varphi} \quad (18)$$

When the soil is in an active limit equilibrium state, $\sigma_1 = \gamma z$, and $\sigma_3 = p_a$. Then it can be inferred from formula(18) that:

$$p_a = \frac{-\sqrt{4 \cos^2 \varphi (2 \gamma z \sqrt{D (\gamma z)^2 + B \gamma z + A} - D \cdot (\gamma z)^2 - B \cdot \gamma z - (\gamma z)^2) + (2 \gamma z + B - 2 \sqrt{D (\gamma z)^2 + B \cdot \gamma z + A})^2}}{2 \cos^2 \varphi} + \frac{2 \gamma z + B - 2 \sqrt{D (\gamma z)^2 + B \cdot \gamma z + A}}{2 \cos^2 \varphi} \quad (19)$$

where γ refers to the weight of the backfill behind the wall, and z refers to the depth of the backfill behind the wall.

(3) Verification of the new method of calculating active earth pressures

To verify the joint strength method, active earth pressures on a retaining wall (Fig.3) at the height of 25m are calculated. The calculation conditions are as follows:

In condition C1-1: cohesive force $c=20\text{kPa}$, internal friction angle $\varphi=20^\circ$, and tensile strength σ_t of soil $=-12\text{kPa}$.

In condition C1-2: cohesive force $c=40\text{kPa}$, internal friction angle $\varphi=20^\circ$, and tensile strength σ_t of soil $=-25\text{kPa}$.

In condition C1-3: cohesive force $c=60\text{kPa}$, internal friction angle $\varphi=20^\circ$, and tensile strength σ_t of soil $=-37\text{kPa}$.

After putting the parameters into formula(3) and formula(19), two distribution curves can be obtained, as shown in Fig. 6.

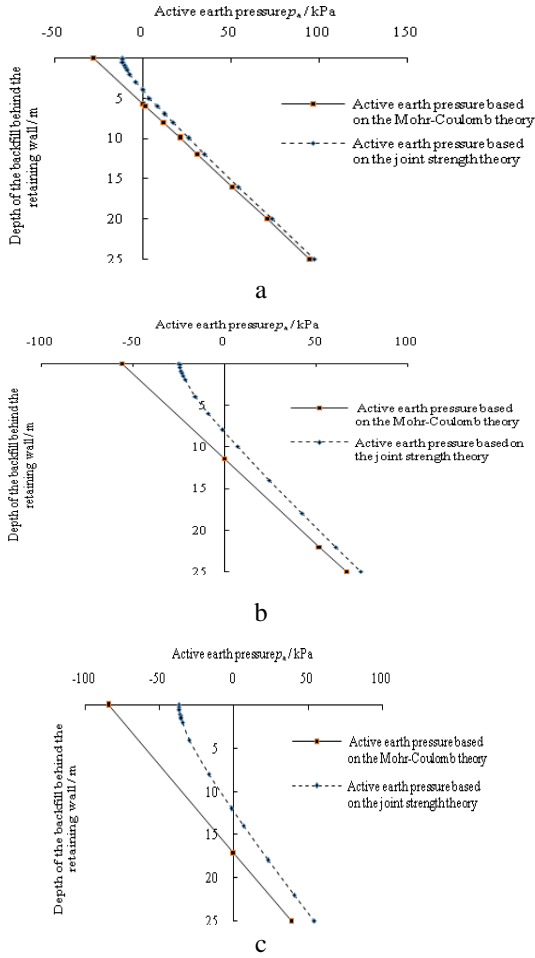


Fig. 6. The distribution curves of active earth pressure: (a) Calculation condition C1-1; (b) Calculation condition C1-2; (c) Calculation condition C1-3

It can be known from Fig.6: active earth pressure values of loess based on the joint strength theory are nonlinearly distributed and larger than Rankine's active earth pressure values; the tensile crack depth of the backfill behind the wall based on the joint strength theory is smaller than that based on the Mohr-Coulomb theory.

The above results show that the Mohr-Coulomb strength theory overestimates the tensile strength of loess.

Derivation and analysis of passive earth pressures of loess based on the joint strength theory

(1) Analysis of limit equilibrium state in passive earth pressure

When the horizontal force σ_h increases to a certain extent, the Mohr's stress circle is right tangent to the strength line. At this point, the horizontal force σ_h is the passive earth pressure p_p . The passive limit equilibrium state of soil can be analyzed in two cases (Fig.4). In the first case, the horizontal stress increases to the extent that the

Mohr's circle is tangent to section II; in the second case, the horizontal stress increases to the extent that the Mohr's circle is tangent to section III. When the soil is in a state corresponding to the second case:

$$p_p = \gamma z \tan^2 \left(45^\circ + \frac{\varphi}{2} \right) + 2c \tan \left(45^\circ + \frac{\varphi}{2} \right) \quad (20)$$

When the soil is in a state corresponding to the first case, passive earth pressures of loess can be derived based on the joint strength.

(2) Derivation of new loess passive earth pressure

When the Mohr's stress circle is in a passive limit equilibrium state (Fig.7). Assume that point N is the tangent point, point M is the center of the Mohr's stress circle, and line segment NQ is perpendicular to axis σ with point Q as the pedal point.

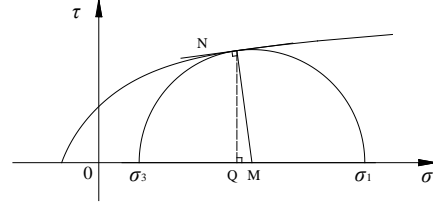


Fig. 7. The passive limit equilibrium state.

According to the method of Section 3.1.2. It can be inferred that:

$$\sigma_N = \sqrt{D \cdot \sigma_1^2 + B \cdot \sigma_1 + A} + \sigma_1 \quad (21)$$

$$\sigma_N = \sqrt{D \cdot \sigma_3^2 + B \cdot \sigma_3 + A} + \sigma_3 \quad (22)$$

Formula(21) and formula(22) are equal. After transforming formula, σ_1 can be calculated, and $\sigma_3 = \gamma z$, and $\sigma_1 = p_p$, therefore:

$$p_p = \frac{\sqrt{-4 \cos^2 \varphi (2\gamma z \sqrt{D(\gamma z)^2 + B\gamma z + A} + D \cdot (\gamma z)^2 + B \cdot \gamma z + (\gamma z)^2) + (2\gamma z + B + 2\sqrt{D(\gamma z)^2 + B \cdot \gamma z + A})^2}}{2 \cos^2 \varphi} + \frac{2\gamma z + B + 2\sqrt{D \cdot (\gamma z)^2 + B \cdot \gamma z + A}}{2 \cos^2 \varphi} \quad (23)$$

(3) Calculating verification of passive earth pressures

To verify the joint strength theory, passive earth pressures on a retaining wall (Fig.3) at the height of 25m are calculated and analyzed. The adopted groups of parameters are identical to those in Section 3.1.3.

After putting these different condition parameters into formula(20) and formula(23) respectively, two distribution curves of passive earth pressures can be obtained, as shown in Fig.8.

It can be obtained from Figure 8: passive earth pressure values of loess based on the joint strength theory are approximately linear distribution and smaller than Rankine's passive earth pressure values; with increasing backfill depths, passive earth

pressure values of loess based on the joint strength theory and Rankine's passive earth pressure values gradually approach.

The above results show that the Mohr-Coulomb strength theory overestimates the tensile strength of loess.

and passive earth pressures of loess can be reasonably evaluated by the joint strength theory.

Acknowledgments: This research was supported by the NSFC (41472296), China Geological Survey Project (DD20160271) and Scientific Research Program of Shaanxi Provincial Education Department (14JS064). The authors' special appreciation goes to the reviewers of this manuscript for their useful comments.

REFERENCES

1. R. Nova, L. Gabrieli, Soil Mechanics, Wiley-Iste, American, 2010.
2. C.A. Coulomb, Essais sur une application des regles des maximis et minimis a quelques problems de statique relatifs a l'architecture. Mem. Acad. Roy. Pres. Drivers, save, Paris, 1776.
3. W.J.M. Rankine, *Philosophical Transactions of the Royal Society of London*, **147**, 9 (1857).
4. Q.-D. Xie, J. He, J. Liu, J.-Y. Youyang, *Chinese Journal of Geotechnical Engineering*, **25**, 343 (2003).
5. J.-P. Gao, Y.-L. Liu, M.-H. Yu, *Journal of Xi'an Jiaotong University*, **40**, 357 (2006).
6. J. Zhang, R.-L. Hu, H.-B. Liu, S.-S. Wang, *Chinese Journal of Rock Mechanics and Engineering*, **29**, 3169 (2010).
7. T. Nakai, *Soils and Foundations*, **3**, 99 (1985).
8. J.-M. Zhu, Q. Zhao, *Rock and Soil Mechanics*, **35**, 2501 (2014).
9. J.-Q. Hu, Y.-H. Zhang, L. Chen, J.-G. Chen, *Chinese Journal of Geotechnical Engineering*, **35**, 381 (2013).
10. J.-H. Zhao, W.-B. Liang Wen, C. G. Zhang, Y. Li, *Rock and Soil Mechanics*, **34**, 609 (2013).
11. L. Ma, S.-J. Shao, C.-L. Chen, *Chinese Journal of Underground Space and Engineering*, **9**, 596 (2013).
12. R.-J. Li, J.-D. Liu, R. Yan, W. Zheng, S.-J. Shao, *Water Science and Engineering*, **7**, 319 (2014).
13. R.-J. Li, J.-D. Liu, R. Yan, W. Zheng, S.-J. Shao, *Disaster Advances*, **6**, 316 (2013).
14. R.-J. Li, J.-D. Liu, W. Zheng, R. Yan, S.-J. Shao, *Chinese Journal of Geotechnical Engineering*, **35**, 247 (2013).
15. Y.-X. Song, R.-J. Li, J.-D. Liu, H.-Y. Gao, *Rock and Soil Mechanics*, **35**(6), 1534 (2014).

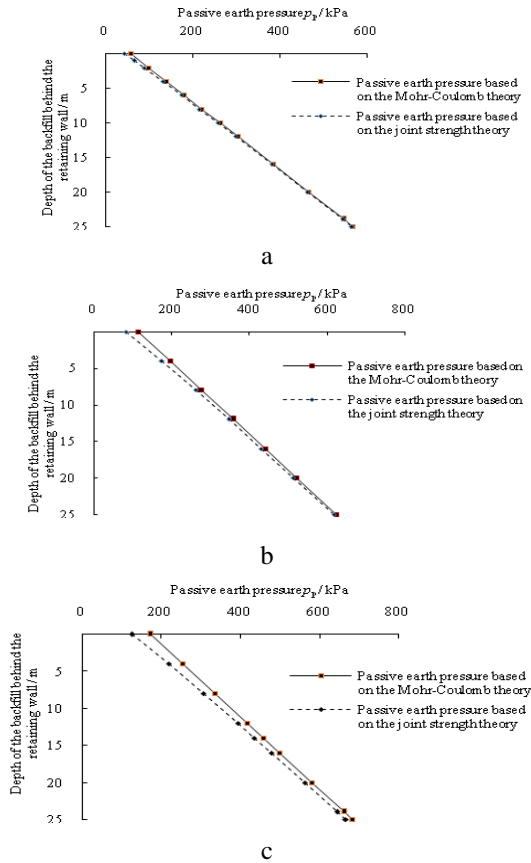


Fig. 8. The distribution curves of passive earth pressures: (a) Calculation condition C2-1; (b) Calculation condition C2-2; (c) Calculation condition C2-3.

DISCUSSION

The Mohr-Coulomb strength theory overestimates the tensile strength of loess, ultimately leading to small Rankine's active earth pressures and large Rankine's passive earth pressures in the calculation. In contrast, due to the proper consideration of the tensile strength of loess, active

Influence of Cu-Fe alloy on the transient thermal characteristics of IMCCR under two special operating conditions

J.C. Cao^{1*}, H. Zhou¹, S. Chen², L. Shi³, J. Zhou³

¹School of Electrical engineering, Beijing Jiaotong University, Beijing, 100044 China

²School of Mechanical Engineering, Harbin University of Science and Technology, Heilongjiang, 150080 China

³Shenzhen Shineng Supernova Inc., Guangdong, 518104 China

Received June 26, 2017; Revised July 20, 2017

A novel Induction Motor with Compound Cage Rotor (IMCCR) is proposed in this paper, in which rotor bars are composed of upper parts made of Cu-Fe alloy (conductor for electric and magnetic) and lower parts made of cast aluminum. By using time-stepping Finite Element Method (FEM), the electro-thermal fields coupling analyses of IMCCR are implemented. Firstly, the electromagnetic and thermal fields of the motor under locked rotor condition are analyzed, and the transient thermal process of motor is also studied, the calculated results are validated by the experimental results. Then, the electromagnetic and thermal fields of the motor excited by impulse current are studied, and the influence on transient heat transfer process in IMCCR are analyzed, especially for the effects on stator windings insulation. The obtained results are compared with that of machine operating under locked rotor condition, which may provide references for the studies on thermal performances of machine operating with impulse current and the heat transfer characteristics of the stator winding insulation.

Keywords: Cu-Fe alloy, compound cage rotor, transient thermal field, locked rotor, inrush current.

INTRODUCTION

The novel alloy materials are widely applied to the motor. By replacing the rotor bars and the end rings of the motor, the electromagnetic parameters and the mechanical parameters are improved, thus the motor can get better performances and safer than it before. A novel alloy material, composed of copper, iron and the other elements, is developed to fabricate the rotor bars of the motor. It is conductor both for current and the magnetic field. Taking advantages of the novel Cu-Fe alloy, a novel induction motor with compound cage rotor, which is very different with the conventional motor, is developed in the paper [1,2].

In practical applications, especially in the occasion of starting with heavy load and the large voltage drop of the long wire, the motor would operate at very low speed or even under locked condition; the auto-reclosure would work. Due to the existence of residual voltage, while power is supplied again, the winding terminal voltage would exceed the rated value and the instantaneous current may ten times more than the rated ones. During the instantaneous process, the current turbulence would occur, and the harm is complicated, for example the local temperature of the motor rise sharply in such a very short time that may cause the damage of motor insulation, or even the burnt-out of the motor itself [3,4,5,6,7,8,9,10].

Thus, the novel induction motor with compound cage rotor, having high performance during starting process, is researched in the paper. The electromagnetic characteristics of the motor under locked rotor condition and operated with impulse current (2.5 times of the locked current) are analyzed. The transient thermal process of the motor under the two special conditions during 10s is also calculated. The transient temperature varies process of the stator winding insulation is detailed in the paper, which would provide reference for fault analysis about insulation in motor.

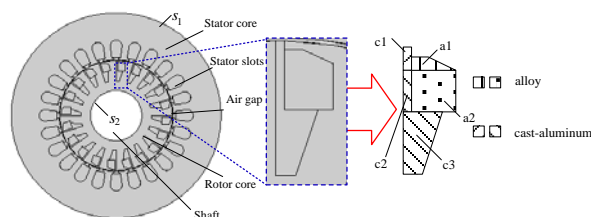


Fig.1. Structure of IMCCR and the heat equivalent diagram of the cage bar

DESIGN OF IMCCR

In this paper, the main element of the Cu-Fe alloy material is industrial pure iron (81.7% in weight) and electrolytic copper (17% in weight). Before smelting, magnesium (0.25% in weight) is put in the bottom of the mould and during the smelting process, ferromanganese (0.7% in weight),

* To whom all correspondence should be sent:
E-mail: scjcs@sina.com

copper phosphorus (0.05% in weight), ferrosilicon (0.2% in weight) and aluminum (0.3% in weight) are added in the raw materials. From associate tests, the permeability of the alloy is about 20 times than that of air and its electric conductivity is about 1.5 times than that of iron. By using the alloy material, a novel induction motor with compound cage rotor is developed. The upper part of rotor bar is made of alloy material and the lower part is made of cast aluminum. The structure of the novel IMCCR and the heat equivalent diagram of the cage bar are shown in Figure1.

ELECTRO-THERMAL ANALYSIS

Electromagnetic Analysis

To simplify the calculation of the electromagnetic field, the following assumptions the made [11]:

1)For there is no skew slot in motor and air-gap length is so small compared with motor polar pitch, the flux distribution in motor core would be 2-D perpendicular to axial direction.

2)Kelvin effect in stator core and windings is ignored.

3)Flux density, magnetic intensity, and magnetic vector potential are sinusoidal waves with time.

Based on the aforementioned assumptions, the whole cross-sectional region of motor core perpendicular to the axial direction (z-axial) is selected as the 2-D analysis model, as shown in Figure 1. The boundary of stator outer periphery s_1 and rotor inner periphery s_2 $\dot{A}_z = 0$. Thus the electromagnetic equations would be

$$\left. \begin{aligned} \frac{\partial}{\partial x} \left(\frac{1}{\mu_e} \frac{\partial \dot{A}_z}{\partial x} \right) + \frac{\partial}{\partial y} \left(\frac{1}{\mu_e} \frac{\partial \dot{A}_z}{\partial y} \right) &= js\omega\sigma\dot{A}_z - \dot{J}_z \\ \dot{A}_z |_{s=s_1+s_2} &= 0 \end{aligned} \right\} (1)$$

where \dot{A}_z and \dot{J}_z are magnetic vector potential and the source current density exclude the eddy current in the z-axial component (in A/m²) respectively, σ is the conductivity (in S/m), s is slip, μ_e is effective permeability.

In the electromagnetic analysis under locked rotor and inrush current operating condition, the stator currents are iterated calculated, in which (2) is selected as the convergence conditions.

$$\left. \begin{aligned} \dot{U} &= \dot{I}(R_1 + jx_{1e}) - \dot{E} \\ I_m^{(k)} &= I_m^{(k-1)} \frac{U}{U^{(k-1)}} \end{aligned} \right\} (2)$$

where \dot{U} is the terminal voltage(in V), \dot{E} is stator phase electromotive force(in V), I_m is winding current (in A), R_1 and x_{1e} are the windings

resistance and end leakage reactance, respectively(in ohm).

A 3kW prototype of IMCCR is produced and tested, and Table I shows the comparisons of the prototype starting performance with that of same power IM , from which the good starting performance of IMCCR could be clearly.

Table 1. Comparison of motor starting performance.

| | IMCCR | | Normal induction motors |
|----------------------|------------|------|-------------------------|
| | calculated | Test | Test |
| Starting current(A) | 33.69 | 34.1 | 38.9 |
| Starting torque(N·m) | 23.68 | 23.7 | 21.6 |

Figure 2 shows the distributions of eddy current density in rotor bars while motor operating with locked rotor and inrush current. Comparing with that in locked rotor operating, the maximum value of induced rotor eddy current density increases about 86.3% in inrush current operating. However, the distributions tendencies have no obvious difference.

Transient Thermal Analysis

To consider the eddy loss (heat sources) distributions in rotor bars comprehensively, and make the thermal analysis model more accurately, the layered equivalent model for rotor bars is developed as shown in Figure1.

The IMCCR adopts totally-enclosed outer fan cooling system. To simplify the calculation, the 3D temperature field problem is converted into 2D situation and the solve model and temperature measured positions are shown in Figure3.

In the figure, l_1 is the inner surface of rotor core, l_2 is terminal box on the shell and the tooth ends of cooling fin, l_3 is other part on the shell. Test points S_1 and S_2 locate at stator wedges, and test points d_1 locates at stator windings, whereas test points R_1 and R_2 at casting aluminum bar and alloy bar, respectively.

According to [10], the mathematical model for 2D transient temperature field could be (3), in which the second equation is the condition of initial temperature, and the third one is the heat transmission boundary conditions, and the last equation is the adiabatic boundary conditions for shaft.

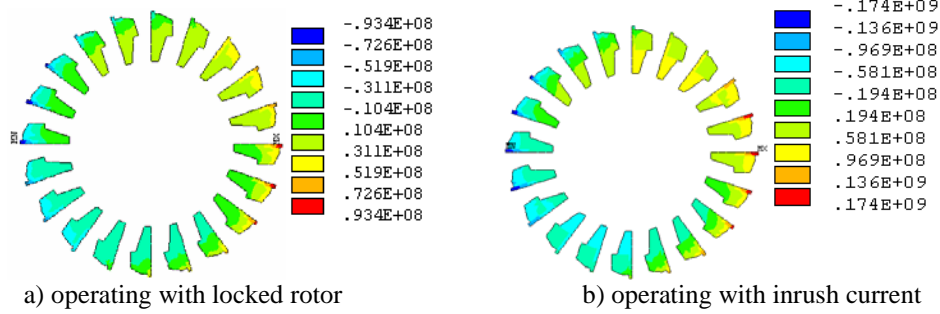


Fig.. 2. Eddy current density distribution in rotor bars (A/m²).

$$\begin{cases} \frac{\partial T}{\partial t} = \frac{1}{\rho C} \left(\lambda \frac{\partial^2 T}{\partial x^2} + \lambda \frac{\partial^2 T}{\partial y^2} \right) + \frac{q_v}{\rho C} \\ t = 0, T = \varphi(x, y) \\ -\lambda \frac{\partial T}{\partial n} \Big|_{l_2, l_3} = \alpha(T - T_0) \\ \frac{\partial T}{\partial n} \Big|_{l_1} = 0 \end{cases} \quad (3)$$

where, T is temperature (in $^{\circ}\text{C}$), λ is the thermal conductivity coefficient (in $\text{W}/(\text{m}\cdot^{\circ}\text{C})$), q_v is the heat source density(in W/m^2), ρ is the density (kg/m^3), C is mass heat capacity (in $\text{J}/(\text{kg}\cdot^{\circ}\text{C})$), t is time(in s), n is unit normal vector on the surface, α is heat transfer coefficient(in $\text{W}/\text{m}^2\cdot^{\circ}\text{C}$), T_f is the ambient air temperature (in $^{\circ}\text{C}$), $\varphi(x, y)$ is the temperature at each node when $t = 0$.

From the electromagnetic analysis, the stator copper loss and rotor eddy loss are obtained, and the corresponding heat generation rates are shown in Figure4. In the figure, d1 is for stator windings heat generation, which is determined by stator current. However, for the induced eddy current distributes unevenly in a rotor bar, the heat generation is different between parts (shown in Figure2), among which casting aluminum at rotor notch (c1) has the highest heat generation density in the motor.

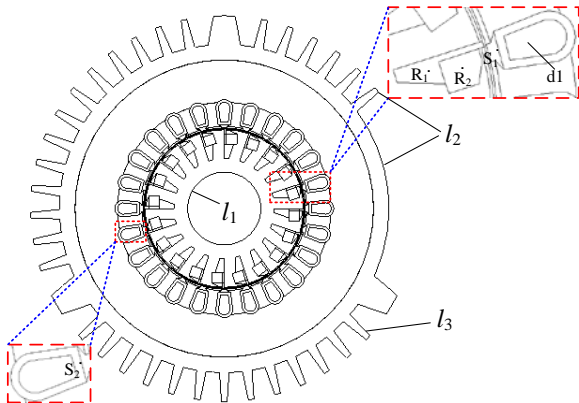


Fig. 3. Thermal analysis model and temperature test positions for IMCCR

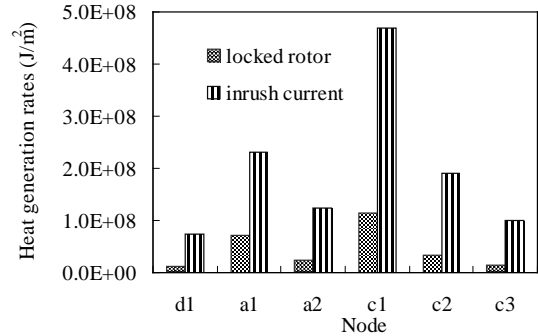


Fig. 4. Heat generation densities in IMCCR different parts under different operating

TRANSIENT TEMPERATURE ANALYSIS OF IMCCR

In this study, temperature of motor operating with short time locked rotor had been tested. The experiment equipments are shown in Figure5. Here, magnetic powder brake is selected as the simulation load. The temperature on the shell was tested by infrared thermos cope, and the temperatures inside motor are tested by heat sensitive resistance with precision of $0.1\text{ }^{\circ}\text{C}$.

Table 2. Comparison of calculated temperatures with the measured data in locked rotor operating at 10^{TH} second.

| positions | calculated($^{\circ}\text{C}$) | test($^{\circ}\text{C}$) |
|----------------|----------------------------------|----------------------------|
| S ₁ | 21.39 | 16.76 |
| S ₂ | 21.40 | 17.16 |
| R ₁ | 41.44 | 38.34 |
| R ₂ | 44.72 | 40.52 |

The comparisons of test temperature with the calculated values are shown in Table. II. For equivalent model could not simulate motor actual situation completely and transient temperature measurement also have certain deviation, the calculated temperature is higher than that of measured.



Fig. 5. Experimental equipments of temperature rise

Temperature Distribution in IMCCR Stator

During the locked rotor operating and inrush current operating, the isothermals in stator slots at time of 10ths are shown in Figure 6. In locked rotor operating the highest temperature is 42.4°C, and temperature rise up about 2.9°C per second. Whereas in inrush operating, the highest temperature is about 195.5°C temperature rise rate is about 18.2°C per second, which is 6.28 times than that in locked rotor.

The temperature drop in insulation layer in locked operating is 10-25°C, whereas it is about 90-150°C in inrush operating. The highest temperature is over the extreme temperatures of insulation already, which would reduce the life of insulation.

Variation of Transient Temperature in Stator Windings

Figure7 shows the variation of temperature along the inner boundary of stator insulation layer with time. At 1st second, temperature distribution curves are nearly straight lines, and the temperature difference of insulation in locked rotor operating is only 0.8 °C, which is about 5°C in operating with inrush current. While operating for 5 second, generated heat in stator windings increase obviously, which made temperature rise significantly. The average temperature in insulation inner boundary reaches up to 89.6°C in operating with inrush current, which about 3.53 times than that in locked rotor operating. While to 10s, the average temperature reaches to 160.5°C, and the temperature difference is about 35°C, which are 36.8°C and 5.6°C for motor operating with locked rotor.

Figure8. shows the variation curves of temperature along the insulation layer outer boundary with time. Due to the poor heat transfer ability of insulation material, the heat generated in stator windings could not be delivered timely, so temperatures at these positions are comparatively lower than that in inner boundary shown in Figure7. The highest temperatures here in motors operating with locked rotor and inrush current are 15°C and 23.4°C respectively. Comparing to teeth, the heat

transfer conditions of yoke is better due to its larger area, so the temperature of insulation connect to yoke is lower than that to teeth. Thus, in Figure7 and Figure8, it is relatively lower in middle of temperature distribution curves.

From the analysis above, in the short time special operating, the temperature difference between two boundaries of insulation is so big that the temperature distribution along the radial direction is extremely uneven. Thus, radial thermal analysis for insulation layer is significantly to associate thermal stress study.

Considering the structure symmetry, only one side of insulation layer is analyzed here. From above analysis, the high temperature region of insulation includes positions at node 1, 2, 3, and 4. Thus, in following analysis, the temperature on line through node 2 and node 3 along the radial direction is studied, and temperature radial distribution in insulation layer at different time are shown in Figure9. The temperature difference in insulation layer along the radial direction is rising sharply, and the temperature changes from 1.6°C to 141.7°C in 10 second operating with inrush current, which is about 6.3 times than that of locked rotor operating, which would lead to aging or damaged for insulation.

In addition to above analysis, the thermal process of motor for the next 600 second natural cooling is also studied, as shown in Figure10. In this stage, temperature of insulation layer next to stator windings is dropping quickly, whereas for that close to stator teeth the temperature is still increasing. In the inrush current operating, temperature of insulation reaches its maximums values after 50s, and then begins to decrease, but it begins to rise after 170s due to the influence of the heat transfer from rotor. The same process of locked rotor operating is studied in [12] already.

Transient Temperature Variation in Rotor

Figure11 shows the temperature distribution of rotor in the inrush current operating. From the isotherm when $t=1s$ and $t=10s$, it can be indicated that temperature in the rotor bar increased more quickly than other parts for higher heat density here. Temperature at the notch is the highest since the higher heat flux density and bad heat transfer conditions. The temperature in rotor is decreasing gradually along the radial directing to shaft, which is similar to that in locked rotor operating studied in [12].

The highest temperatures at stator windings center (node d1) and rotor notch (node c1) are studied next, and temperature time variation curves

in locked rotor and inrush current operations are shown in Figure 12. Because the heat transfer condition at rotor notch is much better than that of stator insulation layer, temperature at rotor notch is always lower than that in windings center in locked rotor operation, although heat generation at rotor notch is

comparatively bigger. Whereas in the inrush current operation, stator windings temperature is higher than that of the rotor notch in the initial period, but temperature of rotor notch is becoming higher than that of stator windings gradually due to the high heat generation.

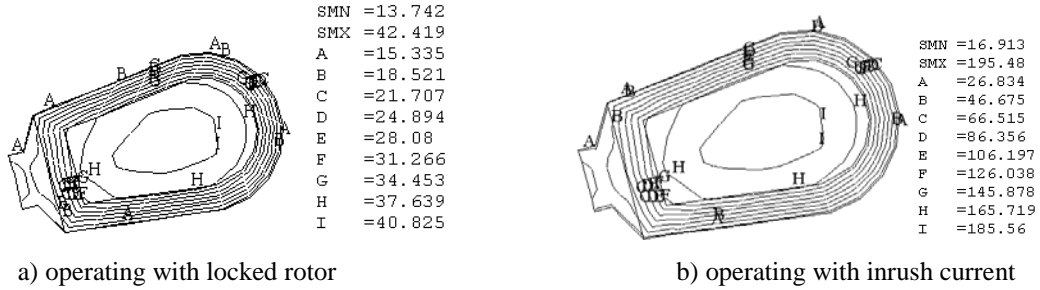


Fig. 6. Isotherm of the stator slots in IMCCR under different operating (°C).

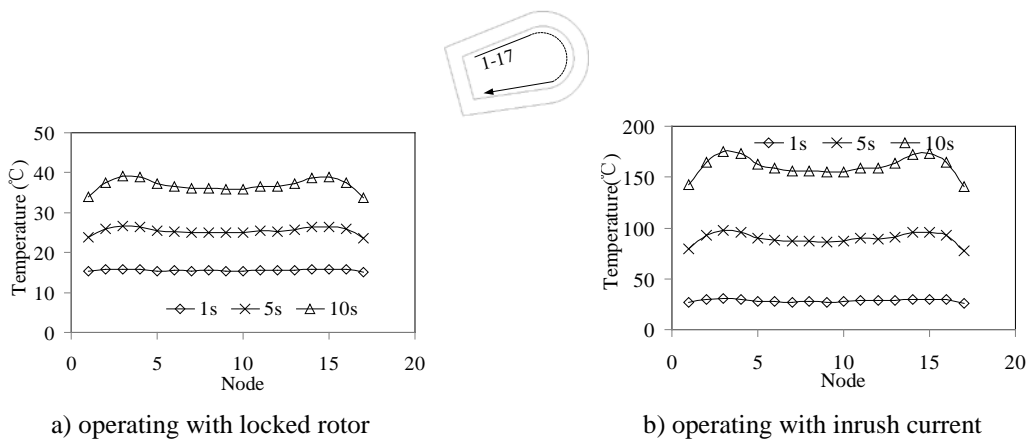


Fig. 7. Variations of temperature at insulation inner boundary with time

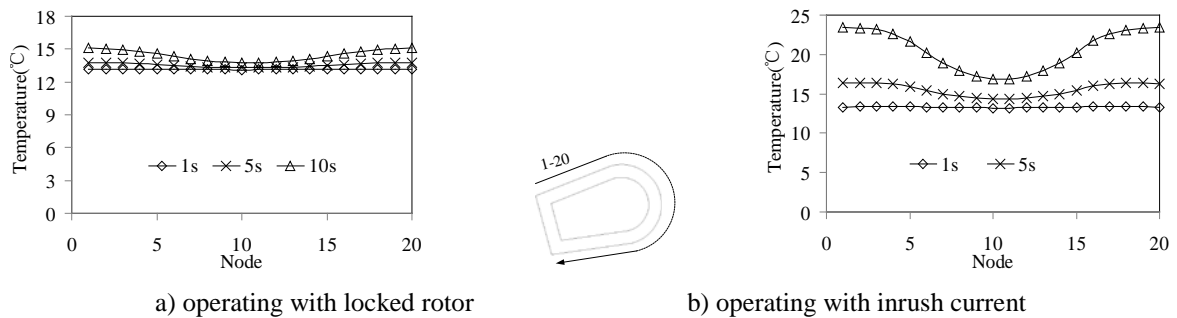


Fig. 8. Variations of temperature at insulation outer boundary with time

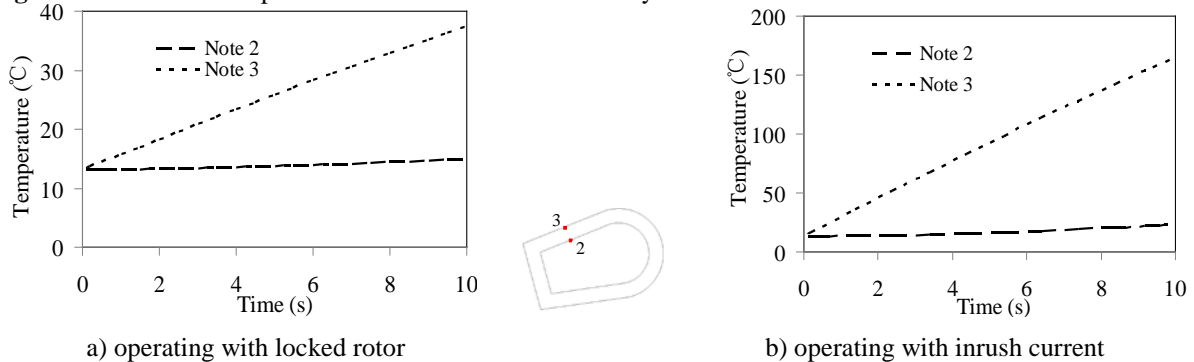


Fig. 9. Radial temperature distribution in insulation layer with time

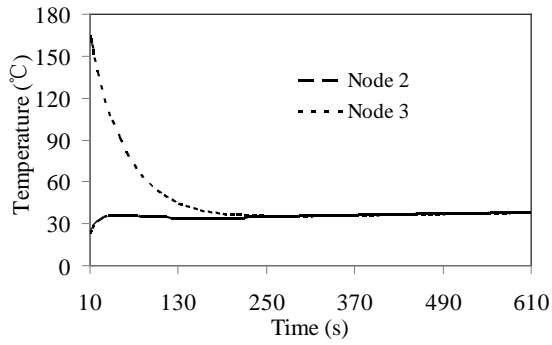


Fig. 10. Variation of radial temperature difference in insulation with time in IMCCR operating with inrush current

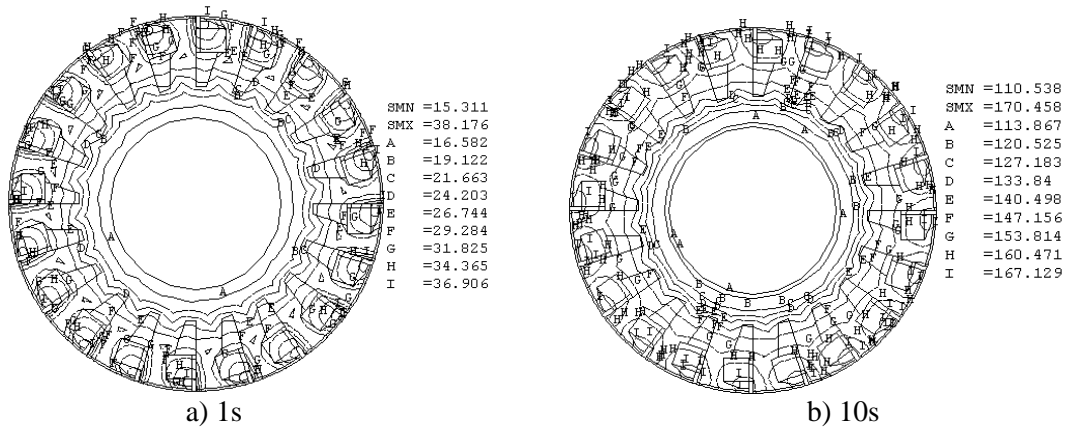


Fig. 11. Isothermal of rotor at different time in operating with inrush current

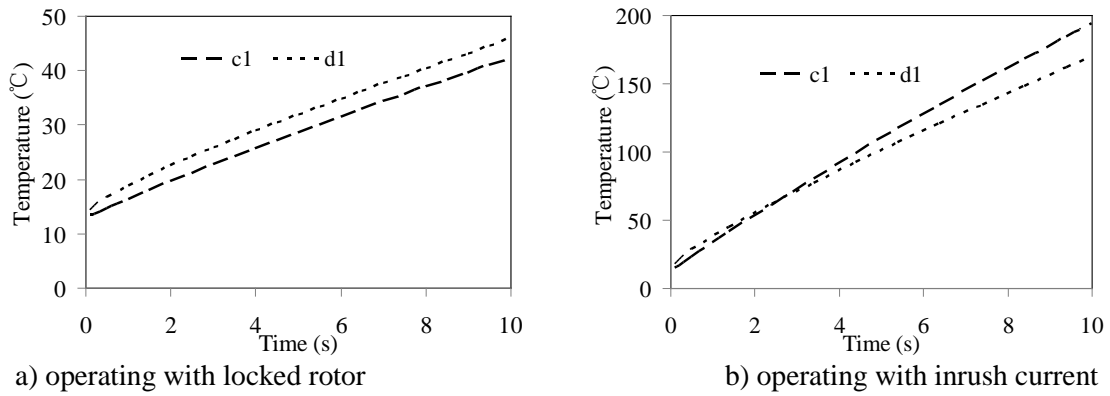


Fig.12. Variation of the highest temperature with time in IMCCR

CONCLUSIONS

1) Comparing with that in motor operating with locked rotor, the highest temperature in motor operating with inrush current appears at different position and becomes higher.

2) The temperature distributes unevenly along the inner boundary of windings insulation layer, the temperature difference is 5.6°C after locked rotor operating for 10 seconds, whereas for operating with inrush current it is about 35°C.

3) The temperature difference in insulation layer along the radial direction is rising sharply in these two operating, which changes from 1.6°C to 141.7°C in 10 second operating with inrush current, and this would lead to aging or damaged for insulation.

Acknowledgements: This work was supported in NSFC (51577007), Supported by Beijing Natural Science Foundation(3162023), Fundamental Research Funds for the Central Universities (2015RC016)

REFERENCES

1. W.L. Li, J.C. Cao, X.C. Zhang, *IEEE Trans. Ind. Electron*, **57**, 660 (2010).
2. Y.P. Zhang, *Proc. CSEE*, **21**, 89 (2001).
3. J. Faiz, M. Ghaneei, A. Keyhani, *IEEE Trans. Energy Con.*, **14**, 101 (1999).
4. W.L. Wei, C. Sina, J. Juri, *Proc. IEEE Electric Power Conf.*, **10**, 1 (2008).
5. Y.C. Chou, A.O. Nabeel, *IEEE Trans. Energy Con.*, **24**, 848 (2009).
6. S.G. Gursharan, P. Stephen, M.H. Makhlof, *IEEE Trans. Indu. Appl.*, **3**, 967 (1999).
7. R.C. Zowarka, T.J. Hotz, J.R. Uglum, H.E. Jordan, *IEEE. Trans. Magn.*, **43**, 275 (2007).
8. M.H. Zhong, H.Q. Sheng, Z.L. Min, H.J. Dong, *Electric machines & control application*, **32**, 3 (2005).
9. J. Faiz, B. Ganji, C.E. Carstensen, *IEEE. Trans. Magn.*, **45**, 2927 (2009).
10. J. Xypteras, V. Hatzianthassiou, *IEEE Trans. Energy Con.*, **14**, 996 (1999).
11. Y.Q. Tang, *Electromagnetic Field in Electric Machine*. Beijing, China: Science Press, 1998.
12. J.C. Cao, W.L. Li, F.Y. Huo, P. Cheng, J.F. Shen, *Proc. EUROCON '09*, **8**, 696 (2009).

Empirical study of effect of financial capital on sustainable economic development in western rural China

T.R. Zhao *

School of Economics & Management Chongqing Normal University, Huxi Campus, Chongqing, 401331, China

Received June 26, 2017; Revised July 20, 2017

It will be conducive to promote sustainable development of the western rural economy by breaking financial restraints on rural economic development and fully playing the catalyst role of financial capital in improving rural production efficiency. Based on the endogenous economic growth theory, this paper analyzed the decisive relationships between variables such as economic growth in western rural China and capital marginal output rate, transformation rate of rural saving to investment and rural savings rate, analyzed the factors affecting changing of these variables, tested the factors by Johansen co-integration test method in the vector auto-regressive model by taking the relevant data of western rural economic development and rural finance from 1985-2012 in China as sample.

Keywords: Western Rural Areas, Sustainable Economic Development, Financial Capital

INTRODUCTION

After years of rapid growth, the economy in western rural China has made considerable development, while integrally still in a state of small-scale peasant economy or of natural economy production with low efficiency of agricultural production. The growth of western rural economy and increasing of farmers' income mainly rely on the inputs of land and labor force instead of total factor productivity. The development pattern of western rural economy is still characterized in extensive growth. Under the constraints of domestic and international market competition intensifying, production factors outflow increasing and ecological environment deteriorating, the western rural economic development is unsustainable. In order to solve the above problems, a fundamental transformation of western rural economy development pattern is required which means transformation from extensive pattern to intensive pattern. And the intensification of production factor inputs is the premise and foundation of realizing transformation from extensive growth to intensive economic growth in western rural economy. The important features of western rural economy, intensification and sustainable development, is extensive inputs of resources and labor replacing by the intensive input of capital and technology especially. The current status of development in western rural China is that supply of labor and land are sufficient and of capital and technology are scarce. Under the condition of fixed rural production

technical level, the capital element, especially the rural financial capital, has significant restraint effects on intensification and sustainable development of western rural economy. Consequently, it will be conducive to promote sustainable development of the western rural economy by breaking financial restraints on rural economic development and fully playing the catalyst role of financial capital in improving rural production efficiency. For this reason, it is necessary to study the relationship between rural economy sustainable development in western China and the financial capital so as to explore deeply how to promote transformation of western rural economy development pattern.

Literature reviews

Regarding the effect of financial capital on rural economy development, the effect of finance on economy growth has been emphasized in foreign early classical literatures made by Bagehot, Schumpeter, Gurley, Shaw, Goldsmith and McKinnon etc [1]. While according to Robinson[2] and Lucas[3], finance has no substantial contribution to economy growth. Till now, foreign academic circles still pay close attention to the study of the effect of finance on economy growth. It has been found by Alessandra[4], August etc[5], Ferda[6], Hsu etc[7], Kar etc[8], Ikonen[9], James[10] and so on that finance, in the way of private savings and investment, can promote economy growth, through theoretical research and empirical analysis both. Levine[11], who has further broken up the functions of financial system into five areas, i.e. mobilizing savings, resource configuration, convenient for risk management,

* To whom all correspondence should be sent:

E-mail: ztr006@126.com

supervising administrators as well as convenient for goods and service exchanging, also thought that finance, through capital accumulation and technical progress, can promote economy growth. Finance, which leads capital from low-efficiency department to high-efficiency department, finally realizes improving of the integral economy efficiency through optimizing capital allocation. In recent years, the effect of technological innovation on economy development is getting greater; the endogenous financial development theory is getting deeper; the finance innovation efficiency is paid close attention[12].

Generally speaking, there are very less literatures about the effects of financial capital on sustainable development of western rural economy. Most of the literatures are concerned on the relationship between finance development and rural economy growth, while no consistent conclusion has been made. And the study of the effects of financial capital on sustainable development of western rural economy, in particular, is scarce. Based on the endogenous economic growth theory frame and taking the relevant data of western rural economic development and rural finance from 1985-2012 as sample, this paper analyzed the restrictive factors of financial capital on western rural economy, and gave answer for whether financial capital can effectively promote transformation of economy development pattern in western rural China.

SPECIFICATION AND PARAMETER SETTING OF THE MODEL

Capital moderate over expansion or through promotion of government direct investment or financial capital, increasing capital investment to western rural economy is proper. While for western rural sustainable economy development, the crucial point is to stimulate economic endogenous growth by financial capital. In order to analyze the effects of financial capital on sustainable economic development in western rural area, we suppose that the western rural economy is a closed economy without government, only produce one kind of product, which can be used for consumption or investment, and suppose that the labor force input scale remains constant, thereby the gross output function can be simplified as:

$$Y_t = AK_t \quad (1)$$

In which A is the capital marginal output rate, K is the total capital stock. In case the product is used for investment and be depreciated at a certain rate terminally, given the capital depreciation rate δ as a

constant, it can be conclude

$$I_t = K_{t+1} - (1 - \delta)K_t \quad (2)$$

Make g_t as the western rural economy growth rate of term t, from (1) knows that $g_{t+1} = \Delta Y_{t+1} / Y_t = (AK_{t+1} - AK_t) / Y_t$. It is obtained by substitution of (2):

$$g_{t+1} = A \frac{I_t}{Y_t} - \delta \quad (3)$$

In a western rural economy system with government involvement, the effects of financial capital mainly reflect in accumulating fund and transforming into capital more efficiently. The capital market reaches equilibrium when the gross saving S_t equals to gross investment I_t . With profit-seeking nature and high transaction cost, the financial capital will have leakage in the process of rural saving transforming into rural investment. Suppose the leakage rate is $(1-\theta)$, then equilibrium is achieved if $I_t = \theta S_t$, in which θ is saving to investment transformation rate. In this way the economy growth rate under equilibrium is:

$$g = A\theta s - \delta \quad (4)$$

In which $s = S/Y$ is saving rate. It is observed from (4) that capital marginal output rate A, saving to investment transformation rate θ and saving rate s are decisive variables for western rural economy growth. Any factors which affecting these three variables will affect the endogenous growth of western rural economy. The expansion of financial capital scale and efficiency improving will increase saving and improve transformation rate of saving to investment which will transform more savings into investment and further increase capital accumulating; ultimately, the output is increased by increasing the scale effect of capital accumulating and technological progress.

RESULTS AND DISCUSSION

Variable selection and data source

It is known from the above that the decisive variables for economy growth in western rural area g are capital marginal output rate A, saving to investment transformation rate θ and saving rate s, and any factors which affecting A, θ and s three variables will affect western rural economy growth. Normally, western rural economy growth g is measured by rural income. Due to lacking of complete statistics data, this paper indicated western rural economy growth index by variation of the sum of primary industry added value (GDP) and township enterprise added value. Capital expansion supports innovation activities of research

department, promotes technological progress which brings output scale increasing return that makes up the defect of capital marginal return diminishing and realizes western rural economy sustainable growth. Therefore, capital marginal output rate is affected by investment ratio. Under the assumption of a clearing western rural market and no stock for producer, the gross investment equals to the fixed capital investment; and capital marginal output rate can be indicated by the ratio of western rural economy growth to fixed capital investment TZ. Saving to investment transformation rate θ is subject to the level and efficiency of western rural financial development. According to financial development theory, western rural financial development level FIR is indicated by the ratio of western rural financial assets to western rural economy growth, in which western rural financial total asset is indicated by the sum of western rural deposits and loans. Western rural financial development efficiency XL, which is the efficiency of deposits transforming into loans by western rural financial system, reflects allocation capability of western rural financial system on rural financial resource and is indicated by the ratio of loans to deposits in this paper. The saving ratio s reflects integral rural saving condition. The western rural savings are affected more by the actual rural disposable assets balance, which is taken up mostly by rural savings. For this reason, the western rural saving ratio is indicated by western rural deposits ratio CB in this paper.

Considering the effects of factors such as data availability and statistical caliber etc, the statistical data of relevant provinces and cities in west part from 1985-2012 were adopted in the paper. Primary industry Gross Domestic Product (gross output of agriculture, forestry, animal husbandry and fishery), township enterprise added value as well as fixed assets investment data were from statistical yearbook of relevant provinces and cities. The rural deposits were the sum of farmers' savings and deposits and agricultural deposits; the rural loans were the sum of loans of agriculture, forestry, animal husbandry and fishery as well as of township enterprise, of which data were from each issue of Almanac of China's Finance.

Model specification

Based on the above mentioned theoretical analysis, the measurement model of this article was established with consideration of variable selection and data source:

$$g = \beta_0 + \beta_1 TZ + \beta_2 FIR + \beta_3 XL + \beta_4 CB + \mu \quad (5)$$

In the above equation, β_0 is a constant term, and $\beta_1, \beta_2, \beta_3, \beta_4$ are western rural investment ratio TZ, western rural financial development level FIR, western rural financial development efficiency XL, coefficient of western rural deposits ratio CB respectively. μ is a random error term.

Empirical analysis

In order to judge the stationeriness of the above variables, Eviews8.0 was adopted to ADF test all variables. The result (see table 1) showed that g, TZ, XL, FIR, CB were all non-stationary variables and all data sequences which have been first difference treated were all stationary and integrated of order one under 1% significance level. In which $\Delta g, \Delta TZ, \Delta XL, \Delta FIR, \Delta CB$ indicated integrated of order one of corresponding variables.

It was known from the ADF test that g, TZ, XL, FIR, CB were all I (1) process. According to the cointegration theory, there may exist co-integration relationship, namely long-term stable relationship in case the variables were the same order single whole (Table 1).

According to the AIC and SC criterion, it was determined that the optimum lag phase of VAR model of g, TZ, XL, FIR, CB was phase II. The whole test process was realized by Eviews8.0 of which cointegration result was shown in Table 2.

From Table 2, it could be seen that co-integration relationship, namely long-term stable relationship existed between the five variables g, TZ, XL, FIR, CB under 1% significance level within sample range of 1985-2012. The equilibrium vector was as follows:

$$\beta' = (1.00, 0.405870, -0.012720, -0.887561, 0.137883, 0.140613) \quad (6)$$

The cointegration equation of the five variables was as follows:

$$\ln g = -0.405870 + 0.012720 \times \ln TZ + 0.887561 \times \ln XL - 0.137883 \times \ln FIR - 0.140613 \times \ln CB$$

| | | | | |
|------------|-----------|-----------|------------|------------|
| (0.04681) | (0.00093) | (0.08333) | (0.02132) | (0.04086) |
| [-8.67086] | [13.7476] | [10.6518] | [-6.46768] | [-3.44114] |

Table 1. The original sequence of unit root test results

| Data Name | Type | ADF Value | ADF critical value | conclusion |
|--------------|-----------|-----------|--------------------|---------------|
| g | (C, T, 3) | -2.453265 | 10% (-3.238) | No Stationary |
| Δ g | (0, 0, 1) | -12.6655 | 1% (-2.660720) | Stationary |
| TZ | (0, 0, 2) | -2.168632 | 10% (-3.243079) | No Stationary |
| Δ TZ | (0, 0, 1) | -5.691089 | 1% (-4.374307) | Stationary |
| XL | (C, T, 3) | -0.400193 | 10% (-3.233456) | No Stationary |
| Δ XL | (0, 0, 0) | -3.805632 | 1% (-2.660720) | Stationary |
| FIR | (C, T, 1) | -2.794157 | 10% (-3.233456) | No Stationary |
| Δ FIR | (0, 0, 1) | -6.043114 | 1% (-2.660720) | Stationary |
| CB | (C, T, 1) | -2.42833 | 10% (-4.356068) | No Stationary |
| Δ CB | (0, 0, 1) | -3.030852 | 1% (-2.660720) | Stationary |

Table 2. Cointegration Test

| The null hypothesis | Characteristic value | Trace statistics | The critical value of 1% significant level | P value |
|---------------------|----------------------|------------------|--|---------|
| 0** | 0.950294 | 140.0853 | 76.97277 | 0 |
| Up to 1** | 0.792754 | 68.04609 | 54.07904 | 0.0018 |
| Up to 2 | 0.499426 | 30.27367 | 35.19275 | 0.1541 |
| Up to 3 | 0.395401 | 13.66565 | 20.26184 | 0.3131 |
| Up to 4 | 0.064067 | 1.589083 | 9.164546 | 0.8572 |

Note: ** said to reject the null hypothesis at the 1% level of significance.

The cointegration equation shows that long-term equilibrium relationship existed between the five variables during 1985-2012 and positive relationship exists between western rural investment ratios (TZ), western rural financial development efficiency (XL) and rural economy growth (g). The contribution degree of western rural investment ratios to economic growth was only 0.013%, and of western rural financial development efficiency was 0.888%. The relationship between western rural financial development level (FIR), western rural deposits ratio (CB) and rural economy growth (g) was negative. The contribution degree of western rural financial development level was -0.138%, of western rural deposits ratio was -0.141%. In general, western rural investment ratios and western rural financial efficiency were favorable factors for western rural economy growth; while western rural financial development level and western rural deposits ratio were unfavorable factors for western rural economy growth during 1985-2012.

CONCLUSION AND POLICY

According to the endogenous growth theory, we know that the output scale return of technological innovation is incremental, which is an important theoretical basis for realizing sustainable economy growth which is driven by technology progress. Capital, one of the important factors for technological progress, being able to expand at a

speed faster than that of economy growth is an necessary condition for western rural sustainable economic development. Capital moderate over expansion or through promotion of government direct investment or financial capital, increasing capital investment to western rural economy is proper. While for western rural sustainable economy development, the crucial point is to stimulate economic endogenous growth by financial capital. Capital marginal output rate, saving to investment transformation rate and saving rate are decisive variables for western rural economy growth. Any factors which affecting these three variables will affect the endogenous growth of western rural economy. The increasing of transformation rate will transform more savings into investment and further increase capital accumulating; ultimately the output is increased by increasing scale effect of capital accumulating and technological progress.

The western rural economy is still small-scale peasant economy or in natural economy production state integrally. Due to small capital scale and outdated production technology, the contribution degree of western rural investment ratios to economic growth was low. The economy growth in western rural area are greatly restricted by the low western rural marginal production rate which is unable to motivate investment will in western rural area as well as excessive saving rate leading to continuous reducing of investment requirements. After financial reform in rural China, the

phenomenon of western rural capital flowing to city was not relieved, but severer. The western rural financial capital neither be gathered for capital expansion, nor be transformed into investment as there are no motivations. Meanwhile, government invested capital is less and scattered. Consequently, the capital supply in western rural China is in serious shortage and capital accumulation is slow, which restrains science and technology innovation and spreading which further delays western rural economy growth. Moreover, the slow-growth western rural economy restricts increasing of saving ratio, which again affects economy growth in western rural area. In this case, the western rural economy will fall into a recurring simple reproduction state. It is thus clear that weakening of western rural financial capital function has severely affected endogenous growth motivation of western rural economy and sustainable economic development is restrained by outdated rural finance.

Changing rural financial system is vital for breaking financial restraints on western rural sustainable economy development. The reason is western rural sustainable economy development is distinguishingly characterized in production factors and technology intensification. Strong and high-efficient rural financial capital is required for supporting and promotion of fixed assets inputting as well as science and technology innovation and spreading both, which is unable to be achieved by existing western rural financial system. For this purpose, it is supposed to overall promote western rural financial system innovation, organizational mechanism innovation, product innovation, credit guarantee mechanism innovation, increase western

rural financial capital efficiency, strengthen western rural financial market construction so as to reproduce financial capital function, improve its catalyst effect on improving rural production efficiency and strive for western rural sustainable economic development.

Acknowledgements: Supported for this paper by National Social Science Fund Project "Research on the development problems of small financial organizations in rural areas" (12BJY097), the Chongqing Municipal Association of Social Sciences (2014BS032) and Chongqing Normal University (16XYY26).

REFERENCE

1. Y. Min, *J.Economics(Ji Kan)*, **497**, 2 (2010).
2. J. Robinson, *London Mac Millan*, **25**, 30 (1952).
3. R.E. Lucas, *Journal of Monetary conomics*, **4**, 22 (1988).
4. D.C. Alessandra, *J.Empirical Economics, Springer*, **131**, 41 (2011).
5. A. August, B. James *J. Economic Modelling, Elsevier*, **40**, 25 (2008).
6. H. Ferda, *Mpra Paper*, **45**, 97 (2007).
7. S. Hsu, L. Jianjun, *MPRA*, **39**, 3 (2012).
8. M. Kar, S. Nazlioglu, H. AgIr *J Economic Modelling, Elsevier*, **689**, 12 (2011).
9. P. Ikonen, *Research Discussion Papers*, **20**, 1 (2010).
10. B. James *Southern Economic Journal*, **745**, 3 (2010).
11. R. Levine, *Journal of Economic Literature*, **692**, 35 (1997).
12. M. Bittencourt, *Journal of Policy Modeling* **346**, 3 (2012).

On coordinated development of BTH urban agglomeration subjected to atmospheric environmental capacity

L.J. Li¹, Y.L. Li^{2*}, X.Y. Li³

¹School of economic & management, Shijiazhuang Tiedao University, Shijiazhuang, China

²School of economic & management, Shijiazhuang Tiedao University, Shijiazhuang, China

³School of Business, East China University of Science and Technology, Shanghai, China

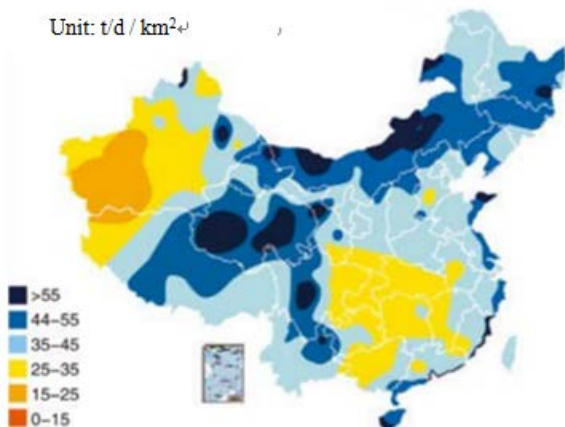
Received May 25, 2017, Revised July 21, 2017

The social economy of Beijing-Tianjin-Hebei (abbreviated BTH) region is experiencing the bottleneck of atmospheric environmental capacity resource. The development of urban community is the basic experience to break through this bottleneck. This paper analyzes the influence of traditional urban and economic development model on the regional atmospheric environment, reveals the interaction between urban agglomeration and atmospheric environment, and studies the optimal layout of the satellite city from the perspective of the influence of the atmospheric cover and tail plume. This paper puts forward some suggestions for mitigating and rebuilding the atmospheric environment capacity of the central city and reasonably allocating the regional atmospheric environmental capacity resources to the overall development of the regional economy.

Key words: BTH urban agglomeration, Atmospheric environmental capacity, Urban microclimate, Satellite city

INTRODUCTION

According to the National Meteorological Administration, the National Climate Center and the Environmental Planning Institute of the Ministry of Environmental Protection, the annual average atmospheric environmental capacity of Beijing, Tianjin and Hebei in 2015 is about 40 tons per day per square kilometer. The northwestern part of Hebei is close to Inner Mongolia, Can reach 50 t/d/km², Hebei, Henan, near the south of the smaller, about 30 t/d/km², see Figure 1.



Source: Central Meteorological Bureau, "2015 China Meteorological Bulletin"

Fig.1 2015 atmospheric environmental capacity mean nationwide

The precipitation in the BTH area is more abundant in summer than that in the summer (April-October). The atmospheric precipitation is obviously self-purifying and the ventilation is also good. The atmospheric environmental capacity is

about 120% of the annual average.), And the atmospheric environmental capacity is reduced by about 80% of the annual mean value. It is estimated that in the winter and winter of the BTH region in 2015, Atmospheric environmental capacity of 27 t/d/km² [1].

THE BTH REGION SHOWED BOTTLENECKS OF ATMOSPHERIC ENVIRONMENTAL CAPACITY

According to the data of China Meteorological Administration, the annual atmospheric environmental capacity of BTH area fluctuates greatly in the winter, and there is a phenomenon of repeated fluctuation in the short term, but the overall trend is obvious decrease. During the 25 years from 1970 to 1985, There are obvious volatility regressions in the interannual variation of atmospheric environmental capacity in the first half of the year, although there is still fluctuation in the period from 1985 to 2015, the overall decrease trend is obvious. See Table 1 and Fig 2.

According to the data of China Meteorological Administration, the annual atmospheric environmental capacity of BTH area fluctuates greatly in the winter, and there is a phenomenon of repeated fluctuation in the short term, but the overall trend is obvious decrease.

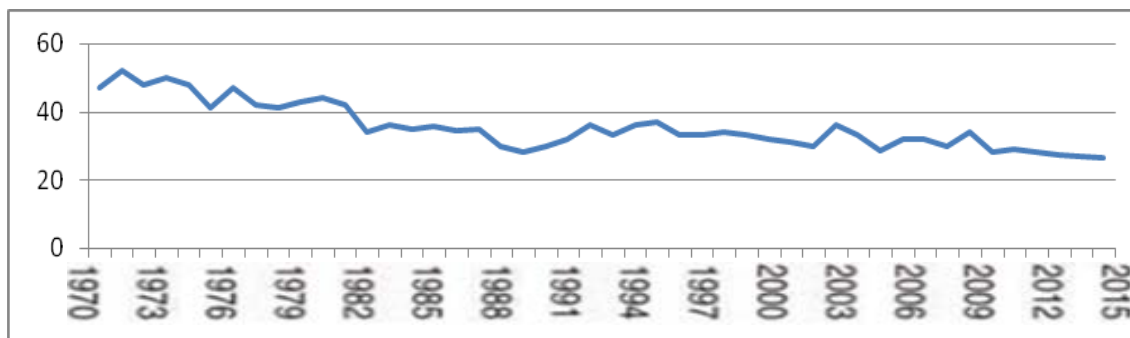
From 1970 to 1985, There are obvious volatility regressions in the interannual variation of atmospheric environmental capacity in the first half of the year, although there is still fluctuation in the period from 1985 to 2015, the overall decrease trend is obvious. See Table 1 and Fig 2.

* To whom all correspondence should be sent:
E-mail: llj56857@163.com

Table 1. Perennial average and 2015 annual mean atmospheric environmental capacity in BTH region

| | perennial average (1961-2015) | annual average 2015 | perennial winter average(1961-2015) | winter average 2015 |
|--|----------------------------------|------------------------|--|------------------------|
| atmospheric environment capacity (t/d/km ²) | 43 | 40 | 36 | 27 |

Source: Central Meteorological Bureau, "2015 China Meteorological Bulletin"



Source: Central Meteorological Bureau, "2015 China Meteorological Bulletin" Unit: t/d / km²

Fig. 2. Variation of atmospheric environmental capacity mean of the winter 1970-2015 in BTH region

According to the research of Wang Jinnan, the environmental planner of the Ministry of Environmental Protection, the atmospheric environmental capacity overload of Beijing, Tianjin and Hebei is serious, that is, the emission of air pollutants far exceeds the allowable limit of environmental capacity. Data show that SO₂ atmospheric environmental capacity overload rate of 300% in 2012, NO_x atmospheric environmental capacity overload rate of 300%, smoke dust atmospheric environmental capacity overload rate of 500% [2], leading to the atmosphere of SO₂, NO_x, smoke dust And other pollutants seriously exceed the safety limits, showing air pollution. As we all know, the BTH regional population is increasing, the vehicle is increasing, the industry is increasing, that is to say, the pollution emission is increasing, and the atmospheric environmental capacity is decreasing. In 2013 and 2014, the air pollution in Beijing, Tianjin, The overload rate is not lower than this value. Such a high rate of atmospheric environmental capacity overload, seriously troubled the BTH region's industrial production growth, affecting the region's comprehensive social development, regional economic and social progress has become a serious bottleneck.

TO DEVELOP URBAN COMMUNITY TO ALLEVIATE THE ENVIRONMENTAL CAPACITY BOTTLENECK

Small-scale high-intensity continuous pollution emissions is very easy to break through a place of

atmospheric environmental capacity limits, Beijing and Tianjin there are a number of such emissions points, that is, the city. The BTH region accounts for 2% of the country's total land area, but its population accounts for 8% of the national total. The GDP of the whole country accounts for 10.9%, the urbanization rate of population is more than 50% and the urban resident population is over 6 million. One, of which 10 million population of the mega-cities 2, Beijing urban resident population reached 20 million. This excessive urbanization affects the atmospheric environment at two levels, one is the small-scale high-intensity living and production emissions consume atmospheric environmental capacity, the other is to change the local natural landscape Lake City Lake artificial lake construction affect the regional wind and rain climate, The atmospheric environmental capacity.

Single city to multi-level group-style cluster development is the international development trend. In the modern sense, the urban agglomeration is a relatively independent urban agglomeration, which is the sum of the urban inter-city relations in the region. It is the result that the developed countries have experienced the rapid development of the industrial cities, and the result of rethinking, repositioning, re-planning and re-constructing the urban development to solve the "big city disease" of production, life, resources, environment and ecology. , Which is characterized by "reverse urbanization" and the rise of the satellite city. It is the advanced structural organization form of the urban development to the mature stage, which is characterized by the strengthening of the inter-city

inner contact and the rural space. Western urban agglomeration development experience "individual urban development and growth - central industry and population spillovers - transport and facilities distribution network - center and peripheral multi-dimensional integration - urban groups mutual benefit" five stages. Environmental capacity and other ecological environment and resource constraints are individual urban spillovers and then integrated the formation of urban agglomeration of the underlying motivation. In the first stage, most of them belong to the ignorant and wanton destruction. After the two stages, they belong to the avoidance behavior after understanding environmental pollution. However, because of the continuing construction and prevention of environmental pollution, Control awareness and measures are not in place, the atmospheric environmental capacity of the damage is still in the rising stage. Industry, resources, ecology, environment, management and other factors in the metropolitan area, the ecological environment in the continuous improvement of effective remediation measures gradually turn for the better under the metropolitan area within the scope of the function of the city, The fifth stage to achieve the coordinated development of urban agglomeration and ecological environment. US economists Grossman and Krueger (1992) summarize the early high-growth, high pollution in developed countries, the latter part of the environmental quality of economic growth has improved data, the relationship between environmental and economic development described as environmental Kuz The EKC (environment Kuznets curve) hypothesis [3], see Figure 3.

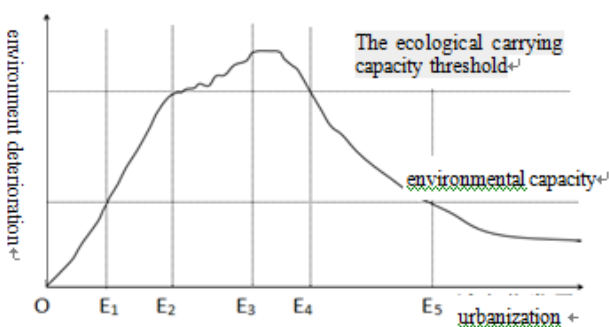


Fig.3 EKC-Urbanization and the ecological environment interaction

EKC curve indicates that the new bright future of the construction of the urban agglomerations of the BTH region, however, it should be noted that the EKC curve from the summit of the mountain began to decline is not naturally appear out of thin air, is to want from ideology, coordinated action and management measures to the technology and equipment of systemic activity combination can

emerge as a result, the urban agglomeration is a reasonable layout, the functional satellite cities to realize reasonable collocation $1 + 1 > 2$ effect. Change of enclosed booth pie development mode, press the counter urbanization, community, road, mutual symbiotic satellite city construction level type, relieving metropolitan population and industry, on the basis of atmospheric environmental capacity, optimize the urban layout and intercity relations, is a traditional urban agglomeration to the new urban agglomeration of BTH region basic direction.

BTH URBAN AGGLOMERATION DEVELOPMENT CAN BREAK THE ENVIRONMENTAL CAPACITY CONSTRAINT

City community development is the starting point to solve the problem of lack of atmospheric environmental capacity from the point of the original city emissions, atmospheric capacity cost point, into a regional city face more emissions, cost a large area of atmospheric environmental capacity, similar to the relationship between pressure and the pressure in physics. If outside the city center to relief functions and industries, and construction of satellite receiving functional industrial base and at the same time, more moderate structure adjustment and technology upgrade, cut down the emissions is moderate, the effect will be better. Problems far more than these, however, need to stress is that due to the strong liquidity diffusivity atmospheric environment, urban agglomeration within urban atmospheric environment influence each other between the obvious, regardless of the atmospheric environmental characteristics and the simple relief and blindly accept industry do not necessarily can rise to alleviate the effect of the atmospheric environmental resource constraints.

The basic principles of urban atmospheric pollution of the environment

Atmospheric pollution of the environment is the external performance of atmospheric environmental capacity has been broken. Atmospheric environment of the city there are two kinds of extreme cases, one is in good condition, under the circumstance of high winds and precipitation is high intensity inversion are the present state of extreme lower environmental capacity, in addition, urban atmospheric environment obvious stratification structure, covering layer, boundary layer and the tail of level. Urban air from the ground to the buildings on the top of the part is called the city layer, BTH region has broken through four city's tallest building is 500 meters, the

majority of more than 300 meters, the normal construction above 150 meters, covering layer of the atmosphere by the "solid" sticky chain construction, liquidity affected by a lot, its composition by building density, height, shape, street width, the density of vehicles, coating materials, pavement emission effect is apparent, such as life and production is often in the pollution state, form the urban dust cover or dust cap.

Top up to the middle of cumulus height of the part by building known as the urban boundary layer, it is covering layer of the atmosphere and wide scope of city street connection layer of the atmosphere, more than the average height between 600-1000 meters, and the city of matter and energy exchange in layer exists, and the urban terrain, surroundings, and the effects of regional climate. Atmospheric pollution is serious, boundary layer will also appear obvious pollution condition, thus the dust cap brim overhanging obviously, huddling with neighboring city overlap, in urban agglomeration of regional pollution. Under normal weather, the city of the wind direction wind will form a city tail layer, also known as the city of tail gas layer, the "tail", as if full of atmospheric pollutants on the influence of wind direction generally up to 30-100 km. Means downwind tail layer within the scope of the big cities, even without pollution, air quality will be affected by the obvious, or rather, the city not only consume their covering layer of atmospheric environmental capacity, and consumption of atmospheric environmental capacity of a few tens of kilometers of wind. This is must be fully considered in the construction of urban agglomeration.

Urban agglomeration economy layout must be based on environmental capacity distributio

According to the principle of urban agglomeration in the economic development, urban atmospheric environment between individuals are closely linked together, not with the transfer of human activities, with the coal transport oil resources such as iron ore to transfer, it requires must be comprehensively considered from the perspective of regional groups, based on urban area atmospheric environment capacity distribution, avoid tail layer, to avoid the dust cap. Otherwise, urban agglomeration would be a wider range of big city, regional economy will fall into irreparable atmospheric environmental capacity resources trap. Langfang in this city, for example, about 40 kilometers in Beijing downwind, in the extreme temperature inversion of secondary pollution

situation in Beijing, in Beijing under the tail feather coat, never may possess.

From meteorological data can be realized, the BTH region urban wind frequency distribution is different, see figure 4. Beijing under the auspices of the wind cover area is about 30 degrees 30 degrees south things area and west of due north direction, tianjin has spread around the average characteristics of the northwest to southeast bidirectional effect is greater than the other direction, shijiazhuang to south to southeast area 45 degrees and the northwest, handan two-way cover for the south north, tangshan basic for north and south, east area and west 25 degrees south direction, baoding is the southwest and northeast bidirectional approximate average distribution. Considering the BTH regional atmospheric environmental capacity during summer and winter seasons influence factors, the difference between the summer rainfall is relatively abundant, can effective rinse clean air, environmental capacity is superior to the winter, so the BTH region city winter under the prevailing wind direction, most of the south by east direction (tangshan east) as about 40 km area, affected by the central city of tail layer is relatively obvious, the atmosphere environmental capacity supply nervous, not suited to encourage and support the satellite city economic development.

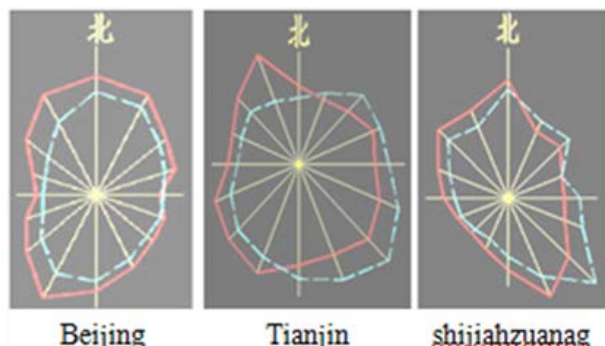


Fig. 4. Major cities of the BTH region perennial average wind rose.

Big city suburb area, the city along the outside layer and nearly cover atmospheric turbulence of boundary layer, the dust cap cap hat type city along the extending outward, even without industrial emissions, air quality is poor, so, suburban doesn't suit the migration resettlement of core city communication industry, clustering set industrial zone is a kind of practice against law of atmospheric environmental capacity resource allocation.

Out set the town, due to the old thinking

BTH urban agglomeration in the process of economic development, is a kind of typical for

satellite city status, for relief industry situation, big cities divided into districts have participated, city, county, town its self advantages are substantially listed resource, population, labor, industry, urban construction, which have no access to place out of the atmospheric environmental capacity resources to compare with other regions. This is already on a path that is not correctly understand and use of BTH resources environment seriously overloaded the "new normal".

Accompanied with the competition form, is a kind of mean type, everybody on a piece of sound, ring all counties and cities of Beijing for Beijing satellite city development direction, ring all the counties and cities of tianjin, with the aim to develop tianjin satellite city ring all facility of city divided into districts and counties to change a city divided into districts, a satellite city as the construction goal, completely because the original is a county town, because the city is close or belong to a city, because of what you've got some kind of industrial base or urban construction conditions. On April 30, 2015, with the highest standard of the political bureau of the CPC central committee meeting examined and approved the program for the coordinated development of the BTH region, put forward "build in Beijing as the core of world class urban agglomeration and the modernized new capital circle", and stressed that "must be based on the capacity of regional resources and environment" [4][5]. If ignore the atmospheric environmental capacity resources, is considered in the traditional sense of the allocation of resources such as land, labor, capital, management, but not to deviate from the prescribed in the central documents, more can make the previous phase of atmospheric environmental capacity resources by super serious fog haze, improvement of BTH urban agglomeration construction ways and measures of social and economic development.

MUTUALLY BENEFICIAL SYMBIOTIC COMMUNITY COMMUNITY RELATIONSHIP BUILDING

At close range is not a group of urban agglomeration in collectively, but emphasize the connection between the city and the relationship, is a community of similar biological community concept. Group of individuals within each other through various channels interact and influence each other, a provides the conditions for another, the survival of a dependent on another's assistance. Urban agglomeration is based on central city, between central city and satellite city and satellite cities between each other, each other, using each

other, each other service organisms, any city, should not be complete in functions and division of labor, and is just one part of the whole urban agglomeration devotion chain, otherwise, he can independence from the group, it is not necessary to become a member of the group.

Alienation from the city center building, building a green belt hose wind belt segregation of mutually beneficial symbiotic community and functional areas. BTH urban development went west in the early industrial revolution "industrial urbanization" of the old road, and urban industrialization go further than the west, formed a strict separation of workers and peasants, between rural and urban areas in recent 30 years, has created industrial country, but the farmland has failed to keep a point in the city. Equivalent to industrial and commercial city, reject planting, exclusion of Lin was development, this model soon brought itself into an ecological disaster and environmental hazards. In the west in the early 20th century had noticed this problem, and began to take industrial area separated from the living quarters. Late last century, this mode also began to show defects: centralized layout of industrial emissions intensity per unit area is too large, the coating pollution concentration is high, the boundary layer sending clear, tail feather layer affects tens of kilometers, 1 km to the original design of the isolation you never even effect the green gallery, and caused a huge traffic industrial area and living area.

The end of last century, the new city layout concept began to appear, the industrial, commercial, residential, auxiliary function mixed layout into urban community, a number of community combined into cities, the small area has a green belt between the hose space, each community has the wide green belt between the hose or natural landscape space, community green belt between the hose throughout the whole city, green belt is not only grass, also can be a farmland or woodland, both guarantee the creature through the city, and safeguard the city supply of fruits and vegetables, can also act as ventilated corridor, formed the workers and peasants, workers live business mix, the urban regional space pattern. Germany, Canada, Australia, the United States, Japan and other countries some cities have taken the analog of the original city layout is reformed[6][7][8]. BTH center city is an urgent need to tear the city from a piece of pie became a number of relatively independent, interval field, forest, slope, river, lake city of loose combination. Center city headquarters economy, science and technology development of economy, finance,

economy, culture, economy, comprehensive service economy to obtain the atmospheric environment on a nest.

Satellite to cooperate with each other, small towns construction functions of obvious characteristics. Function of Beijing in the communication industry and, in fact, according to the urban agglomeration is a symbiotic community relations, that other 12 districts, also should adjust their function, and on the basis of industry and the function of relieving, no relief from the city center, the satellite towns (level 2) from the city center can not be effective as the center city services, by the same token, the secondary industry and functions of the center city relief not bottom go to, the secondary satellite can provide effective services for center city. Center city are made to satellite city do? Center city if it is not a massive transformation and industry transformation, and its environmental capacity can't accommodate the new industry, construction and population. Similarly, satellite, between industry must prevent repetition, to cooperate with each other, common meets the needs of the center city function, choose the right industry and the function, docking with the center city, work, business, culture, education, tourism and leisure, but also can fish farmers.

CONCLUSION

BTH urban agglomeration economy, the direction of the regional economic development is the economic development of urban agglomeration typical of atmospheric environmental capacity constraints. Mutualism first within the urban agglomeration of atmospheric environmental capacity resources mutually beneficial symbiosis, in industrial distribution, industrial adjustment and satellite city layout, the function of satellite positioning, satellite industry development, should fully consider the atmospheric environmental

capacity resource problems. At present, this kind of resource supply and demand changes directly contact the local air quality is not enough, the marketability is not obvious, the configuration is not enough timely and flexible, easily ignored by enterprises and relevant departments, but don't forget that this resource is the coordinated development of BTH, and BTH urban agglomeration of national strategy, is the basic reason for the transformation of the regional economic development. Which is blind to this point, urban agglomeration economic development may be again in the near future in the resource bottleneck.

Acknowledgements: Supported by Hebei Province Department of Education Science and Technology Key Project: Study on the Disposal Technology of Emission Permits Based on Card Measurement in the Control of Atmospheric Haze in Hebei Province (ZD2014070).

REFERENCES

1. <http://news.sina.com.cn/c/nd/2016-01-12/doc-ixnkkuv4442889.shtml>.
2. W. Jinna, C. Xiao, J.L. Yu, in: China's coal consumption under the restriction of atmospheric environmental capacity of total amount control. (Proc. Int. symp. on coal consumption control and energy transformation, China, November 17, 2014), China, 2014.
3. G. Grossman, A. Krueger, *Quarterly Journal of Economic*, **110**, 353 (1995).
4. http://news.xinhuanet.com/fortune/2015-04/30/c_1115147507.htm. 2015-04/30.
5. http://news.xinhuanet.com/politics/2015-04/08/c_1114893758.htm. 2015-04/08.
6. L. Shuyu, F.X. Lei, *Journal of architecture*, **8**, 20 (2010).
7. E. Ren, *Journal of international urban planning*, **28**, 99 (2013).
8. C. Red, Y. Qing, *Journal of international urban planning*, **29**, 114 (2014).

Study and application of repeated mining with paste backfill to recover remaining strip pillars

Q.L. Chang, W.J. Tang, H.Q. Zhou*, J.B. Bai

Key Laboratory of Deep Coal Resource Mining, Ministry of Education of China; School of Mines; China University of Mining & Technology, Xuzhou, 221116, China

Received May 25, 2017; Revised July 20, 2017

In order to thoroughly recover coal resources under buildings, repeated mining with paste backfill to recover remaining strip pillars was proposed. Based on surrounding strata control theories, variation characteristics of surrounding strata structures after repeated mined with paste backfill was discussed. Also, the feasibility was analyzed. Through triangle structure of surrounding strata control, theoretical formula of remaining pillar width in repeated mining with paste backfill was studied. Relational expression of backfill material strength was ensured under conditions of paste backfill repeated mining with traditional limit analysis method. From the point of limited thickness mining, under paste backfill mining conditions, the controlling impact of paste backfill ratio on ground subsidence was analyzed and reasonable index was proposed. The roadway layout pattern and mining methods in mines were proposed. Also, parameters including paste backfill material strength, width of segregating coal pillars, backfill ratio were ascertained. According to field practice, after paste backfill reached full mining in the testing mine, the maximum subsidence of ground was 220 mm and the subsidence ratio was 0.076. The experiment results proved the rationality of this technology which had wide promotional value and practical significance.

Key words: Strip mining, Surrounding strata control, Remaining pillars, Paste backfill, Ground subsidence.

INTRODUCTION

China is a big country in coal producing and consuming. In 2011, the coal consumption accounts for 72.8% of the whole non-renewable energy consumption. Meantime, due to the dense population and wide distribution of buildings, vast coal resources exist under buildings. In order to protect constructions, those coal resources are always excavated by strip mining. But the excavation ratio of this method is less than 50%, a mass of permanent remaining resources were left [1,2]. With the rapid development of town constructions, more precious resources will be wasted seriously. What's more, joint fissures in coal pillars are developed. In this case, coal pillars are easily pressed softly, even broken to pieces. This damaging range will extend to internal pillars gradually, which will cause the instability of coal pillars suddenly and be a threat to safe mining [3-5]. Therefore, realization of repeated mining of strip coal pillars has extreme significance not only in safe mining but also in improving the excavation ratios of coal resources.

Gangues are associated waste during mine production process. In the same time, at present, they are one of major emission solid wastes in China. Fly ash is the maximum discharge powder waste produced by powder plants. The treatment of those

two kinds of wastes in underground has arisen people's attention and application has been conducted in some coal mines [6-8]. Therefore, ground subsidence control, improving mining ratio of coal resources and underground treatment of wastes including gauges, fly ash are combined together. Furthermore, new repeated mining with gauge solid waste as aggregates to recover strip coal pillars was proposed.

Project profile: Ground villages in the range of Dai village Coal Mine which belongs to Zibo Coal Mine Company with Limited Liability in Shandong Province are pretty dense. There are 78 natural villages, 13 thousands households and 50 thousand people in total. Coal resources under villages accounts for 73.6% of the mine total storage. In order to realize the safe mining of coal resources under buildings, strip mining to excavate coal resources under buildings was always adopted in Dai Village Coal Mine and succeeds. But with the extending of mining range, remaining coal pillars increased gradually. According to statistics, up to the end of 2011, the coal pillars under buildings accounted for 94.6% of the total storage. The recoverable reserves of this mine declined to 21.044 million ton and the mine service lift could only maintain to 7.5a. In order to protect ground constructions, repeated mining with paste backfill to recover remaining coal pillars was adopted, which is beneficial to improve mining ratio of resources and expand service life of coal mines.

230 panel was the first mining area in this mine.

* To whom all correspondence should be sent:
E-mail: zkdcql@163.com

Strip mining was used in this whole area and the excavation ratio was merely 37%. Remaining pillar resources rose up to more than 9 million ton. The mining depth in this area was 470 m. 3_{up} coal seam was mined and this seam was stable. The minimum thickness is 2.5 m and the maximum thickness is 3.2 m. The average thickness is 2.9 m. The dip angle ranges from 3 to 12 degrees, with an average angle of 6 degrees. The density of this coal seam is 1.35 t/m³. The roof is medium stable.

EXPERIMENTAL

Repeated mining with paste backfill to recover strip pillars

Technology procedures

The technology procedures were stated as follows. Firstly, mining roadways were excavated in segment coal pillars. After the strip was mined, roadways were tunnelled in narrow pillars remained in coal pillars surrounding the gob area (Fig.1 (a)). Secondly, paste backfill mining was adopted to recover remaining pillars. After the producing system of working face was formed, with the advancement of the working face, paste isolation strip was constructed in the back in order to form backfilling space after certain steps. During the backfill process, roadways and gobs were fully backfilled. The backfill strip could provide support to the overlying strata, preventing them from failure. In this way, the purpose of controlling ground subsidence and protecting buildings is achieved. Furthermore, safe mining of coal pillars is realized (Fig. 1 (b)).

Structural characteristics of surrounding strata

(1) Basic features of strata behaviours in the mining stope

Under general conditions, with the conduct of

coal mining, combined movement in the form of panel will occur in roof upon the working face. It is always controlled by rigid strata which have better mechanics in the roof. From down to up, the area declines. Therefore, “Big structure” forms at a depth in main roof. The upper load on this stable structure is transferred to two sides of the mining stope through bearing points on coal and rock rather than applied directly to the stope [9].

(2) Stability of critical blocks

When strip working face is conducting, with the advancement of the working face, immediate roof close to remaining pillars will collapse. But the main roof will rupture at the depth of coal seam. The bearing point will always situate in remaining coal pillars. Therefore, arc triangle panel (the critical block) will occur. Based on key strata theory of overlying strata in the stope, mechanical model of paste backfill to rover remaining pillars was established, which is shown in Fig. 2.

After the key strata collapse, the key block of B subsides and rotates. Then it contacts with gauges in the stope. For certain deformations, it will be subjected to support from broken gauges and pillars. In the same time, it will suffer gripping impact from the key block of C and key block B. Furthermore, it will also receive horizontal force effect from surrounding blocks shown in Fig.2. Therefore, this key block of B is in the “small structure”. The stress state is relatively balanced and the stability is good. Furthermore, it obeys to the stability theory of S-R (sliding-rotation). As this structure is affected by repeated mining, the suffered load increases continuously. The stress status between blocks will change. However, as long as the technological parameters of paste backfill are reasonable, the dynamic balance can still remain. Also, the main roof on the working face will not rupture [10, 11].

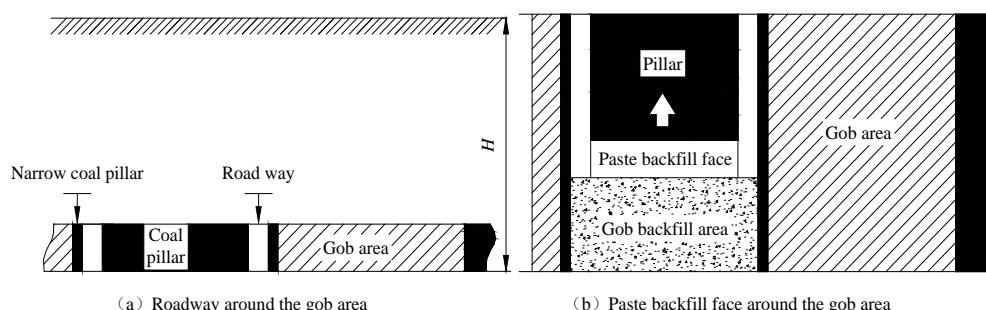


Fig. 1. Diagram of paste backfill mining to recover remaining pillars. (a) Layout diagram of gob-side entry driving; (b) Schematic plot of paste backfill mining.

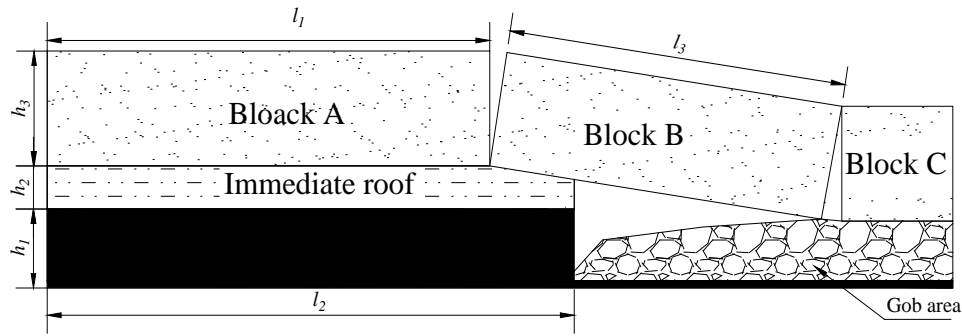


Fig. 2. Schematic diagram for mechanical structure of paste backfill to recover remaining pillars

(3) Stability analysis of surrounding strata with paste backfill to recover remaining pillars

After the working face is conducted, the “big structure” in the main roof will bear partial surrounding strata weight in the stope. The bearing point is located upon remaining coal pillars on two sides in the stope. “Small structure” mainly bears the collapsed rock weight under “big structure”. Under general conditions, the strength of backfill body is large (around 5 MPa). The paste backfill step only ranges from 2 to 4 m. The process of paste backfill mining is actually equivalent to a moving open-off cut, which has relatively small impact on “the big structure” as well as “the small structure” in the stope and has no effect on the stability of the whole structure [12-14]. Therefore, it is theoretically feasible to conduct paste backfill mining technology to recover remaining pillars.

After paste backfill is conducted, the paste body can backfill the gob in time and congeal rapidly to supporting body with certain strength. In the same time, the backfill body has the strain strengthening characteristics, which is beneficial to prevent main roof from subsiding excessively and control movement as well as deformation of overlying strata. This can effectively ensure the stability of paste backfill body and surrounding rock including the main roof in the stope, achieving the purpose of controlling ground subsidence and protecting the safety of surface buildings.

Key of repeated mining with paste backfill to recover remaining pillars

According to Fig.1, the key technology is the stable and reasonable strength of paste backfill body and backfill ratio. The stability of surrounding rock becomes bad when the mining roadways of the working face get more close to peak value of lateral abutment pressure. Furthermore, the waste of resources becomes larger. The smaller the pillar width is, the worse the stability is. And this is not beneficial to construct roadways and roadway

support. That the strength of paste backfill body gets larger is more beneficial to control the main roof and keep it stable. But this will give rise to more paste backfill cost and waste of material strength, which has a relatively worse economic benefit. However, if the paste backfill body has a smaller strength, it will cause the movement and deformation of overlying strata, which is not beneficial to control surface subsidence and protection of surface buildings. What’s more, the purport of paste backfill may lose. Reasonable backfill ratio will reduce the consuming of backfilling materials, lessening backfill cost, which has an optimal combination between usage of backfill materials and surface subsidence control.

Determination of pillar width

After the strip working face is mined, the arc triangle block will occur within the main roof in the stope, which produces stress declining area, stress improving area and original stress area in remaining coal pillars. In order to minimize the impact of surrounding strata stress, roadways should be arranged in the stress declining area near coal pillars, which is most beneficial to control surrounding strata and keep pillars stable. In order to improve profits of mines and excavation ratio of coal resources, narrow fringe coal pillars should be remained to most extent. However, if coal pillars are too narrow, they will deform and damage rapidly and easily, which determine the decline of anchoring force of supporting structures and reduce the supporting strength of surrounding strata. In the same time, cluster winds may easily happen, which has potential safety accidents.

Reasonable coal pillar width B can be calculated as $B = B_1 + B_2 + B_3$ according to Fig.3. To be more specific, B_1 is pillar width in plastic area, while B_2 is stability coefficient of coal pillars and generally calculated as $(B_1 + B_3) \times 40\%$. As for B_3 , it is the length of rock bolts and picked as 1.6 m.

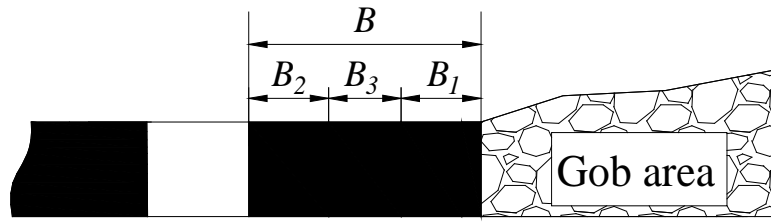


Fig. 3. Schematic diagram of calculating pillar width

The value of B_1 is calculated as the following formula.

$$B_1 = \frac{mA}{2 \tan \varphi_0} \ln \left(\frac{K\gamma H + \frac{C_0}{\tan \varphi_0}}{\frac{C_0}{\tan \varphi_0} + \frac{P_z}{A}} \right)$$

Where, m is coal seam thickness, 2.9 m; A is coefficient of lateral pressure, $A=V/(1-V)$, and $\nu=0.22$; φ_0 is the internal frictional angle and calculated as 27. C_0 is cohesive force, 2.3 MPa; K is the stress concentration coefficient, 2.2; γ is unit weight of rock mass, 25 kN/m³; H is the mining depth, 470 m; P_z is the resistance of supports, 0.

According to mining conditions of practical mines, it can be calculated that $B_1=1.69$ and $B_2=1.0\sim 1.7$ m. Therefore, it can be obtained that $B=4.3\sim 5.0$ m. In order to keep the anchoring effect of rock bolts, the ultimate reasonable width of coal pillars is 5.0 m.

Determination of paste backfill body

After paste backfill is conducted, the paste backfill body situates the unidirectional stress status. Theoretically, the tolerate strength of paste backfill body under unidirectional stress status can be calculated in the following four formulas: Obert-Kwvall/Wang expression (suitable for pillars whose aspect ratio ranging from 1 to 8), Holland expression (suitable for pillars whose aspect ratio ranging from 2 to 8), expression of Salamon-Mnuro and Bieniawski formula. Due to the fact that the field working face is 96 m and mining height is 2.9 m, therefore, the aspect ratio is 33. It is apparent that only the latter two formulas can be selected to calculate the tolerate strength of backfilling body.

Generally speaking, the joints and fractures in coal seams develop and the whole integrity is bad. The deformation destruction has typical plastic and brittleness material features. The fine plastic features of paste backfill body are beneficial to keep backfilling body stable, which has been confirmed in practice. In sum, after paste is backfilled in Dai Village Coal Mine, the later strength of paste backfill body should be calculated according to Bieniawski expression, which is more reasonable and safer.

It can be known from Bieniawski expression that after remaining coal pillars are mined, the tolerate strength $[\sigma]$ of paste backfill body can be calculated as:

$$\sigma_c = \frac{k * \gamma H (1 + We/Wp)}{\sqrt{D/0.9} * (0.64 + 0.36 * w/h)^{1.4}}$$

Where, k is the safety coefficient; γ is the unit weight of rock strata, 25 kN/m³; H is the mining depth, 470 m; D is the diameter of the specimen, mm; We is the width of mining strip, m; Wp is the width of coal pillars, m; W is the width of paste backfill working face, m; h is the mining height, m.

Based on the calculating formula, safety coefficient was 1.5-2.0. According to practical mining conditions of mines, single axial compressive strength of paste backfill body could be determined. Under the standard conditions in the laboratory, when the width of mining coal pillars is less than 50 m, the compressive strength of paste body after 28d should not be less than 5.0 MPa; while when the width of mining coal pillars is less than 100 m, the compressive strength of paste body after 28d should not be less than 2.6 MPa.

Determination of backfill ratio

The research analysis shows that the major factors that affect the surface subsidence induced by backfill mining includes compressive ratio of the paste body, the roof subsidence value before backfill and yawning contacting value. In order to analyse simply, all these parameters were uniformly transferred into backfilling ratio (the specific value of backfill material volume versus volume of gob). As key parameters that reflect backfill effect, the value of backfill ratio is directly related to the degree of surface subsidence control. Under same conditions, the larger the backfill ratio is, the bigger the space where backfill materials occupy in the gob is. And the movement space of strata becomes smaller. In addition to that, the controlling effect of surface subsidence is better. On the contrary, the surface subsidence controlling effect becomes bad.

However, in the same time, the consuming of backfill materials becomes large if the backfill ratio is high. And the amount of backfill work becomes large. Also, the cost of backfill goes high. However, if the backfill ratio is too small, the ground subsidence controlling effect cannot be guaranteed. Therefore, it is really important to select an appropriate backfill ratio. On the basis of limited thickness mining, the backfill ratio of calculating formula can be obtained [15]:

$$\eta \geq 1 - \frac{[\varepsilon]H}{1.52mbq \tan \beta \cos \alpha}$$

Where, η is the backfill ratio; m is the coal seam thickness, 2.9 m; H is the depth of coal seam, 470 m; $[\varepsilon]$ is the maximal tolerate horizontal deformation value of surface constructions, 2 mm/m; b is the horizontal movement ratio, 0.29; q is the subsidence ratio, 0.91; β is tangent of major affecting angle, 2.71; α is the dip angle of coal seam, 6 degree.

Therefore, the backfill ratio can be calculated as:

$$\eta \geq 1 - \frac{2 \times 470}{1.52 \times 2.9 \times 1000 \times 0.29 \times 0.91 \times 2.71 \times \cos 6} = 0.7$$

RESULTS AND DISCUSSION

1 Roadway layout and mining techniques

The roadway layout scheme of the working face was shown as follows: The position and size of backfill working face: it was arranged in the middle of strip pillars and the length of the working face was 95 m. The position and size of roadways that belong to backfill working face: There were two roadways which were the orbit roadway and haulage roadway. To be more specific, the roadway width was 4.0 m

(the roadway height equaled to coal seam thickness) and supported by bolt-mesh-anchor. Considering the impact that the gob has on both two sides of coal pillars, the width of coal pillar that was used to protect roadways should be selected as 5.0 m, which is shown in Fig.4.

The fully mechanized paste backfill mining technique was adopted. And the backfill step ranged from 2 to 4 m. On the basis of fully mechanized process, coal cutting, support movement and scraper conveyer motivation was operated. When the backfill step was reached, the paste backfill was conducted.

Analysis of application effect

Those four adjacent coal pillars have been repeated mined with backfill in Dai Village Coal Mine. From the deformation status of roadway surrounding strata, only slight fissures occurred on the top of one coal pillar. The other remaining strata surrounding roadways were controlled well, which completely satisfied the normal safety requirements.

Measurements of mine pressure indicated that no strata behaviour occurred in backfill working faces. The average compressive strength of backfill body was 3.2 MPa, satisfying the strength requirement. The pressure that backfill body in the gob tolerated was about 12 MPa, basically reaching original rock stress. In the same time, the measurements showed that after full mining, the surface maximum subsidence was 220 mm and the subsidence ratio was 0.076, ensuring the safety of surface buildings. The field practices certified that the repeated mining with backfill to recover coal pillars succeeded.

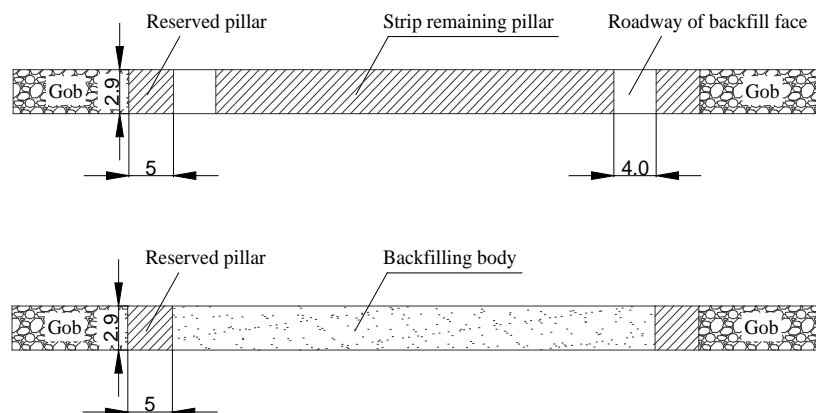


Fig. 4. Schematic diagram of paste backfill mining to recover remaining pillars

CONCLUSION

1) In order to repeated recover remaining coal pillars produced by strip mining and improve the

excavation ratio of coal resources, new paste backfill technology to replace remaining coal pillars produced by strip mining with aggregates of gangues was proposed in this paper. The field practice showed that this technology was feasible completely, which provided reliable new technology for recovering remaining coal pillars under surface buildings generated by strip mining.

2) In order to analyze the stability characteristics of remaining coal pillars by strip mining, the main technology process and procedures during paste backfill mining to recover remaining coal pillars were stated. Furthermore, the mechanical analyzing structural model was discussed. Also, parameters including the coal pillar width, backfill body strength and backfill ratio during paste backfill mining in practice mines were analyzed and determined.

3) The field practice results indicated that after remaining coal pillars produced by strip mining was recovered in this technology, no strata behavior occurred in the backfill working face. When full mining was reached, the maximum surface subsidence was 220 mm and the subsidence ratio was 0.076. The damaging level of surface buildings was in the range of Level I, indicating that no repair was need.

The repeated mining technology with gauge-paste backfill to recover strip coal pillars can not only achieve safe mining of permanent remaining coal pillars but also provides reliable new technology for mining under buildings. In the same time, solid wastes including gauges and fly ash are fully utilized, which promotes the resource utilization of industry wastes and has marked economic and social benefic. In sum, this technology has wide popularization and application values.

Acknowledgements: *The present research work*

was supported by the National key basic research development program sub-project (973 Program: 2015CB251600) ; A Project Funded by the Priority Academic Program Development of Jiangsu Higher Education Institutions (PAPD) ; the Fundamental Research Funds for the Central Universities (NO. 2014XT01); the National Natural Science Foundation of China (No.51574227).

REFERENCES

- 1.M.G. Qian, X.X. Miao, J.L. Xu, China University of Mining and Technology Press, Xuzhou, 2003.
- 2.H.Q.Zhou, C.J. Hou, X.Q. Sun, Q.D. Qu, D.J. Chen, *J CHINA U MIN TECHNO*, **33**(2), 155 (2004).
- 3.J.B. Bai, China University of Mining and Technology Press, Xuzhou, 2006.
- 4.Y.G. Chen, S.L. Lu, China University of Mining and Technology Press, Xuzhou, 1994.
- 5.X.H. Li, Q.L. Yao, N. Zhang, D.Y. Wang, X.G. Zheng, X.L. Ding, *J CHINA COAL SOC*, **25**(4), 420 (2008).
- 6.Q.L. Chang, H.Q. Zhou, J.B. Bai, *J MIN SAF ENG*, **28**(2), 279 (2011).
- 7.D.S. Zhang, H.S. Wang, L.Q. Ma, *J CHINA COAL SOC*, **35**(10), 1549 (2010).
- 8.H.Q. Zhou, C.J. Hou, X.Q. Sun, Q.D. Qu, D.J. Chen, *J CHINA U MIN TECHNO*, **33**(2), 155 (2004).
- 9.X.H. Li, N. Zhang, C.J. Hou, *J CHINA U MIN TECHNO*, **29**(2), 186 (2000).
10. C.J. Hou, X.H. Li, *J CHINA COAL SOC*, **26**(1), 1 (2001).
11. M.G. Qian, X.X. Miao, F.L. He, *J CHINA COAL SOC*, **19**(6), 557 (1994).
12. L.Q. Ma, D.Zhang, H. Wang, Y.S. Li, *CHIN J ROCK MECH ENG*, **29**(4), 674 (2010).
13. M.G. Qian, X.X. Miao, J.L. Xu, *J CHINA COAL SOC*, **32**(1), 1 (2007).
14. J.X. Zhang, X.X. Miao, *J CHINA U MIN TECHNO*, **35**(2), 197 (2006).
15. J.P. Du, L.Q. Wang, China University of Mining and Technology Press, Xuzhou, 2003.
- 16.

An evaluation system of ecology-safe and environment-friendly society - green production system

J.K. Li¹, J. Zhang^{2*}, Z. H. Gao³, Q. Chen⁴, Z. X. Liu¹

¹*Collaborative Innovation Center for Urban-Rural Coordinated , Zhengzhou, China*

²*Xinlian College, Henan Normal University, Zhengzhou, China*

³*Guanghua School of Management, Peking University, Beijing, China*

⁴*International School of Zhengzhou University, Zhengzhou, China*

Received June 27, 2017; Revised July 21, 2017

To build the Green Production System is a practice of green development in China, which is an important way to transform the economic development mode and to complete ecological civilization construction. This study defined the meaning of Green Production System, constructed the green production evaluation index system and made empirical evaluations on green production situation of several advanced areas in China by using Analytic Hierarchy Process (AHP) and Factor Analysis method. The author also measured advantages in the green production system of these regions. The research showed that, as the first National Independent Innovating Demonstration Zone, Haidian District took the lead in all of indicators among developed areas. The reason lies in Haidian District has been focusing on the construction of green production system during the economic and social development in the past several years.

Key words: Green production evaluation system, Analytic Hierarchy Process, Factor analysis

INTRODUCTION

Green production, as a sustainable mode of production, develops in dealing with the problems of increasingly serious environmental pollution and energy resource constraints. Currently, many countries and regions around the world are actively exploring green production models. This paper, is part of a delegated task from the administration of Haidian District in Beijing, China. Although exploring the connotation of green development is complex, an ecology-safe and environment-friendly evaluation system should be the first step of such an exploration.

Current academic studies haven't carried out any specific researches on green production system, most of which now are focusing on the green economy or green manufacturing. It is Hall Who released green environmental quality indexes of the U.S states 1991-1992 and explained what green index is earliest [1]. The American National Geographic Society studied in terms of consumer's behavior of environmental protection and published the '2009 Global Consumer Green Indexes' report (The American National Geographic Society, 2009). To take the development level of green manufacturing system as target layer, SHEN De-cong and RUAN Ping-nan conducted a primary study on the evaluation index system of green manufacturing system of China [3]. By estimating the three first-grade indexes, degree of green economic growth, carrying capacity

of resources and environment and supports of government, Li Xiaoxi, etc. released the 2010 Annual Report of China Green Index, which studied green development indexes of the all the provinces and cities in China[4]. Beijing Haidian District Government made a low-carbon economy index system from the perspective of the transformation of economic growth in 2009 [5].

In 2010, Beijing municipal party committee and municipal government formally promulgated 'Green Beijing' action plan (2010-2012) which put forward the city to developing the low carbon economy and creating green production system. But in that plan, it only included two guide indicators and four binding targets of the green production system, which didn't make a statement of questions like what green production system is and what complete framework should green production system include or something about.

Based on the above, this paper carried out a research on issues related to green production system, studied on the evaluation and structure of green production systems, and calculated and compared the competitiveness of green production of Beijing and several related economically developed areas. This paper will contribute to the development of low-carbon economy and the building of green production system, which is full of significant application value to 'Green China' construction and forward-looking meaning to theoretical innovation.

EXPERIMENTAL

* To whom all correspondence should be sent:
E-mail: echozhang0817@foxmail.com

Green production is a general term for nuisance-free and pollution-free production. Establishing an indicator evaluation system for green production can help us to evaluate the green production development condition in a certain area.

Synthesizing the connotation of green production system, referencing the research to related indicators of green economy and low-carbon economy and under the guidance of principles above, we design the green production indicator system for three-tier structure, that is target layer, criteria layer and indicator layer. Table 1 shows the indicator framework.

Green production indicator system is composed of a whole group of interrelated indicators. It is used to reflect all aspects of the relationship which is interdependence and mutual restraint among socio-economic, natural resources and ecological

environment in green production activities. The system structure is constructed by the use of socioeconomic and natural resources, environment and sustainable development.

Evaluation method

T.L.Saty, an America operational research expert, put forward the Analytic Hierarchy Process (AHP) method in 1970's. This method is based on the principle of arrangement of elements in system to divide a complex problem into multi-level structures which the first level is related to the next level. And factors among all the levels can be compared and calculated to get the weights of those factors which can be ranked, to lay down the solid foundation of research. .

Table 1. Green production index evaluation system.

| Target layer | Criterion layer | Indicator layer |
|-------------------------------|------------------------------------|---|
| Green production index system | Socio-economic indicators | Annual per capita GDP (ten thousand Yuan) |
| | | Residents average years of education(years) |
| | | The number of scientific and technical personnel within a region |
| | | The number of ecological demonstration zones |
| | | The number of patent applications per year |
| | | The total production of new energy and energy-saving environmental protection industry |
| | | R & D expenditure accounts for GDP |
| | | Value loss by pollution per year |
| | | The tertiary industry output value accounts for GDP |
| | | Renewable energy consumption accounts for total energy consumption |
| | Resource utilization indicators | Coal consumption accounts for total energy consumption |
| | | The sales of new energy and energy-saving environmental protection industry in the proportion of total output value |
| | | Ten thousand Yuan GDP energy consumption (kWh / ten thousand Yuan) |
| | | Energy consumption per unit of GDP (Tce / ten thousand Yuan) |
| | | Water consumption per unit of GDP (cubic meters / ten thousand Yuan) |
| | | Sulfur dioxide emissions per unit of GDP (tons / ten thousand Yuan) |
| | | Carbon dioxide emissions per unit of GDP (tons / ten thousand Yuan) |
| | | Compliance rate of city greening |
| | Eco-environmental indicators | The number of enterprises through the ISO14000 certification |
| | | Investment in environmental protection |
| | | Rate of urban sewage treatment |
| | | Recovery rate of electronics, electrical product |
| | | Growth rate of per capita GDP |
| | Sustainable development indicators | Reduction rate of ten thousand Yuan GDP energy consumption |
| | | Reduction rate of ten thousand Yuan GDP water consumption |
| | | Reduction rate of occupational disease and public nuisance disease |
| | | The growth rate of overall labor productivity |

By using Haidian District as an access, this paper selects Guangdong, Jiangsu, Beijing, Shanghai, Henan, Fangshan district of Beijing and Binhai district of Tianjin such developed areas to conduct a research of green production system. All the data comes from 2010 Statistics Yearbook of each province (City) or district, related annual National economic and social development bulletin, and the 2009 China energy Statistical Yearbook.

Because of Haidian District, Tianjin Binhai New Area have great differences with all the provinces, the absolute value of the index cannot represent the real competitiveness. Therefore, this article selects the corresponding index for analysis. Because there are no new energy or energy-saving industries data, some provinces as Jiangsu, Shandong and Henan, this paper uses the high-tech industrial indicators to replace with. For those indicators that have negatively impacts on competitiveness, as per GDP (10,000 yuan) energy consumption, sulfur dioxide emissions per unit of GDP, they were gave a relative treatment as follows:

$$k_{ij} = \frac{X_{ij}}{\max(X_{ij})}, p_{ij} = 1/k_{ij} * 100$$

X_{ij} is the observed value of j indicator in i region; k_{ij} represents the j entropy index of the i region; p_{ij} shows the j index values of i region after conversion. According to previously established indicator system and regional data, this paper selects 19 indicators to be assessed

Table 3. Weights of Index layer.

| C layer | C1 | C2 | C3 | C4 | C5 | C6 | C7 | C8 | C9 | C10 |
|---------|-------|-------|-------|-------|-------|-------|-------|-------|-------|-------|
| Weight | 0.027 | 0.054 | 0.039 | 0.108 | 0.042 | 0.032 | 0.049 | 0.074 | 0.069 | 0.094 |
| C layer | C11 | C12 | C13 | C14 | C15 | C16 | C17 | C18 | C19 | |
| Weight | 0.031 | 0.061 | 0.055 | 0.067 | 0.031 | 0.061 | 0.043 | 0.067 | 0.040 | |

*The above four indicators through the consistency test

Table 4. Scores of the Green production competitiveness

| Region | socio-economic development | | Resource use efficiency | | Eco-environment construction | | Sustainable development | | Comprehensive competitiveness | |
|------------|----------------------------|------|-------------------------|------|------------------------------|------|-------------------------|------|-------------------------------|------|
| | scores | rank | scores | rank | scores | rank | scores | rank | scores | rank |
| Handian | 41.476 | 1 | 40.680 | 1 | 19.246 | 1 | 10.377 | 3 | 132.532 | 1 |
| Fangshan | 9.886 | 5 | 2.954 | 10 | 13.270 | 10 | 9.323 | 5 | 54.080 | 8 |
| Beijing | 15.086 | 2 | 12.161 | 2 | 16.486 | 7 | 9.119 | 6 | 71.090 | 4 |
| Shanghai | 13.120 | 3 | 10.513 | 4 | 18.984 | 2 | 10.778 | 2 | 74.951 | 3 |
| Jiangsu | 5.734 | 8 | 11.219 | 3 | 16.805 | 5 | 8.610 | 7 | 59.590 | 5 |
| Guangdong | 5.464 | 7 | 5.940 | 7 | 14.815 | 9 | 7.920 | 10 | 49.979 | 9 |
| Henan | 2.463 | 10 | 3.698 | 9 | 14.865 | 8 | 8.063 | 9 | 45.214 | 10 |
| Binhai N.A | 11.270 | 4 | 8.743 | 5 | 17.339 | 6 | 18.574 | 1 | 93.074 | 2 |
| Shandong | 3.529 | 9 | 4.978 | 8 | 18.434 | 3 | 10.098 | 4 | 57.233 | 7 |
| Zhejiang | 7.894 | 6 | 6.969 | 6 | 17.565 | 4 | 8.400 | 8 | 57.627 | 6 |

RESULTS AND DISCUSSION

Outcome of AHP

By AHP analysis, each weight of indicators in criterion layer and the index layer is shown in Table 2 and Table 3:

Table 2. Weights of Criteria layer.

| Criterion layer | B1 | B2 | B3 | B4 |
|-----------------|--------|--------|--------|--------|
| Weight | 0.3025 | 0.2857 | 0.2134 | 0.1984 |

* The above four indicators went through the consistency test.

Based on weight of each index above, it is easy to score the green production competitiveness of each region, which is shown in Table 4.

From Table 4, Haidian District, in terms of overall competitiveness, scored 132.532 points and ranked first, which are 39.458 points more than the second Binhai New Area whose score was 93.074 - The both regions had strong competitiveness of green manufacturing. With a score of 45.214, Henan Province ranked in the last place.

From the socio-economic development indicators, Haidian District with a score 41.476 points ranked first. It was 26.39 points more than Beijing which scored 15.086 points and ranked second. Haidian District has more than half amount of the science and technology persons in Beijing. The number of patents per capita and research investment costs are much higher than in other regions, which make Haidian District become one of the most powerful places for scientific research. This also provides a strong support for the social and economic development in Haidian District.

Table 5. Green production index system.

| X | Index |
|-----|---|
| X1 | Annual per capita GDP (ten thousand Yuan) |
| X2 | The number of scientific and technical personnel within a region(Units per ten thousand people) |
| X3 | The number of patent applications per year |
| X4 | R & D expenditure accounts for GDP |
| X5 | The tertiary industry output value accounts for GDP |
| X6 | Energy-saving and environmental protection industry |
| X7 | Ten thousand Yuan GDP power consumption (kWh / ten thousand Yuan) |
| X8 | Energy consumption per unit of GDP (Tce / ten thousand Yuan) |
| X9 | Water consumption per unit of GDP (cubic meters / ten thousand Yuan) |
| X10 | Sulfur dioxide emissions per unit of GDP (tons / ten thousand Yuan) |
| X11 | Compliance rate of city greening |
| X12 | Rate of urban sewage treatment |
| X13 | Industrial dust removal rate |
| X14 | The utilization rate of industrial solid waste |
| X15 | Growth rate of per capita GDP |
| X16 | Reduction rate of ten thousand Yuan GDP energy consumption |
| X17 | Reduction rate of ten thousand Yuan GDP water consumption |
| X18 | The rate of overall labor productivity |
| X19 | The growth rate of new energy and energy-saving environmental protection industry |

Table 6. Characteristic value of factor loading and contribution rate.

| Factor | Characteristic value | Rate of Contribution(%) | The cumulative contribution rate(%) |
|--------|----------------------|-------------------------|-------------------------------------|
| 1 | 8.248 | 45.823 | 45.823 |
| 2 | 3.240 | 17.997 | 63.820 |
| 3 | 2.382 | 13.231 | 77.051 |
| 4 | 1.465 | 8.141 | 85.192 |
| 5 | 1.051 | 5.841 | 91.033 |
| 6 | 0.695 | 3.862 | 94.895 |
| 7 | 0.440 | 2.444 | 97.339 |
| 8 | 0.295 | 1.638 | 98.977 |

Table 7. Orthogonal factor table.

| Index | F_1 | F_2 | F_3 | F_4 | F_5 |
|-------|--------|--------|--------|--------|--------|
| X1 | 0.132 | 0.096 | 0.006 | 0.963 | 0.148 |
| X2 | 0.958 | -0.218 | -0.010 | 0.158 | -0.007 |
| X3 | 0.876 | 0.090 | 0.366 | 0.161 | 0.026 |
| X4 | 0.895 | -0.404 | 0.014 | 0.022 | -0.077 |
| X5 | 0.829 | -0.166 | 0.295 | -0.025 | 0.235 |
| X6 | 0.944 | 0.005 | 0.129 | 0.151 | 0.237 |
| X7 | 0.806 | 0.111 | 0.243 | 0.485 | -0.016 |
| X8 | 0.937 | 0.138 | 0.217 | 0.007 | 0.111 |
| X9 | 0.758 | 0.243 | -0.074 | 0.166 | 0.500 |
| X10 | 0.231 | -0.088 | 0.004 | 0.621 | -0.127 |
| X11 | 0.278 | -0.877 | 0.372 | 0.135 | -0.037 |
| X12 | 0.563 | -0.001 | 0.549 | 0.156 | 0.173 |
| X13 | 0.362 | 0.801 | 0.162 | -0.201 | -0.088 |
| X14 | 0.392 | 0.728 | 0.279 | 0.289 | 0.074 |
| X15 | -0.441 | -0.607 | -0.488 | 0.064 | 0.130 |
| X16 | 0.232 | 0.844 | -0.039 | 0.121 | -0.091 |
| X17 | -0.196 | 0.070 | 0.935 | -0.017 | 0.186 |
| X18 | 0.101 | -0.087 | -0.143 | 0.970 | 0.060 |
| X19 | -0.620 | 0.019 | 0.138 | 0.075 | 0.755 |

From energy efficiency, as water and other resources, Haidian District scored 40.680 points. It was 28.519 points more than Beijing which scored 12.161 points and ranked second. From the individual indicators, various energy indicators in Haidian District are lower than Beijing, which shows that the economic development of Haidian District has entered the low-power stage.

From the ecological environment construction, Haidian District scored 19.246 points and ranked first. It was 0.262 points higher than the second Shanghai with a score 18.984 points. Beijing scored 16.486 and ranked seventh. Due to all the areas have paid attention to environmental protection, the gap of each regional ecological environment construction is not so great. Take Haidian District as an example, its urban sewage treatment rate reached 94.3% and disposal rate of solid waste utilization reached nearly 100%, which showed the Haidian District emphasized much about ecological environment development.

From a sustainable development perspective, Haidian District scored 10.377 points and ranked third, which is behind the Binhai New Area and Shanghai. Binhai New Area with a score 18.574 ranked first. Shanghai scored 10.788 points and ranked second. The sustainable development of Haidian District is behind the Binhai New Area and Shanghai. On one hand, this shows that the economic development in Haidian District has reached advanced level under the current technology conditions and it has limited tap potentials in further developing. On the other hand, it is vital to break the constraints of existing land and other resources for the future economic development of the Haidian District. How to promote the use of technology and expand the use of various elements and resources are essential.

Outcome of Factor Analysis

Obviously, these 28 indices above explained green production system from different angles, but in different regions the contribution of these 28 indices is different. Therefore, it is of significance to analyze the competition of green production in different regions. This paper use factor analysis to go on the next research. Based on the results of AHP, all the selected indexes are shown in Table 5.

By using SPSS 13 statistical software, we got the factor analysis characteristic value, contribution rate and the accumulative contribution rate which are shown in Table 6. As the KMO value is 0.795, so it is suitable to use factor analysis. According to the information of original data reflected by the contribution rate of each factor, the top 5 factors have already contained more than 91.033% of the information of original variables, which satisfy all

the requirements of factor analysis ($\geq 85\%$).

In order to make the right and reasonable roots of load factor is polarized to 0 or 1. The 19 explanation for the main factor, each of square factor loading matrix is rotated by varimax method. Results are shown in table 7.

From table 7, the first main factor has greatest ability to explain the green production and its rate is 45.825%. In the first mainfactors, x_2 、 x_3 、 x_4 、 x_5 、 x_6 、 x_7 、 x_8 、 x_9 the load factors have the larger coefficient. x_2 represents the technical personnel quantity in every million people in different region. x_3 represents the numbers of patents granted per million people. x_4 represents the R &D expenditure accounts for GDP. x_5 represents the third industries accounted for the proportion of GDP. x_6 represents the new energy and energy-saving environmental protection industry added value accounted for the proportion of GDP. x_7 represents Ten thousand Yuan GDP power consumption. x_8 represents the energy consumption per unit of GDP. x_9 represents the water consumption per unit of GDP. The Eight indicators reflect three aspects of local condition, which include science and technology level, advanced industrial structure and energy efficiency.

The stronger the regional green production ability is, the more developed the region is. Therefore, the region like Haidian District, the third industrial output has reached 80% of total output value. Those regions must be able to continue to increase investment in science and technology. So they can promote the development of new technology, new products. And the combination of Produces, study and grinds will increase the utilization rate or circular utilization of renewable energy resources. And then those regions will achieve the goal of promoting the progress of green production.

CONCLUSION

To build the Green Production System is a practice of green development in China, which is an important way to transform the economic development mode and to complete ecological civilization construction.

For the AHP results, it is obvious that Haidian District performs a good condition in each kind of indicators and it has reached advanced level under the current technology conditions. But what cannot be ignored is that Haidian District is facing a limitation in further developing. So it is vital to break the constraints of existing land and other resources for the future economic development of

the Haidian District. How to promote the use of technology and expand the use of various elements and resources are essential.

Acknowledgements: *This work was supported by the National Natural Science Foundation of China (Grant No. 71173006, and 71473070), the Soft Science projects of Henan Province (No. 162400410093, 162400410026), and the Soft Science Project of Henan Province Office of Education (No. 15A790016). Especially thanks to the support by Program for Innovative Research Team in Science and Technology in University of Henan Province (IRTSTHN).*

REFERENCES

1. Hall, Green index: the States' Environmental Quality Evaluation in U.S (1991-1992), M. Beijing, Normal University Press, 2001.
2. <http://energy.people.com.cn/GB/9864488.html>
3. S. De-cong, R. Ping-nan, *J.Machinery Manufacturing*, **2**, 321 (2006).
4. L. Xiao-xi. China green index annual report - a provincial comparison research, M. Beijing, Normal University Press, Beijing, 2010.
5. Beijing Haidian District Government, Haidian district development of low carbon economy "twelfth five-year" period, the transformation of the mode of economic development research, Beijing, 2010.

Experimental determination of coefficient of soil hydrodynamic dispersion

A.J. Shao^{*}, S.W. Wang, X. Chen

Hebei GEO University, Shijiazhuang, China

Received May 25, 2017; Revised July 21, 2017

The unsaturated soil hydrodynamic dispersion test was done by using unsaturated silt loam in the Yangtze River Estuary. The hydrodynamic dispersion coefficient was expressed as a linear function form in the form of mechanical dispersion coefficient. Based on the mass conservation principle, we deduced the new formulas to calculate coefficient of hydrodynamic dispersion, and calculated the hydrodynamic dispersion coefficient of unsaturated silt loam according to the soil water and salt dynamic data measured by the vertical soil column method. Based on the calculated results, the relationship between hydrodynamic dispersion coefficient and the pore velocity were established. The experimental results show that there is a linear relationship between the hydrodynamic dispersion coefficient and the average pore water velocity, and the calculated results are close to the previous ones. The method is proved to be correct and accurate, and the physical concept is clear and the formula is simple, and is more practical.

Key words: Coefficient of hydrodynamic dispersion, Solute flux, Unsaturated soil.

INTRODUCTION

With the development of society, the unreasonable discharge of industry and domestic sewage caused serious damage to the environment and caused the groundwater to be polluted to varying degrees [1]. The dispersion coefficient is the most important parameter to study the solute transport of groundwater, and the dispersion test is one of the most reliable methods to reveal the transport mechanism of solute in groundwater and to obtain the dispersion coefficient. It is indispensable for the study of groundwater pollutant transport link [2]. Dispersion test is divided into indoor tests and outdoor tests, although the outdoor test results is more in line with reality, but the actual field operation is affected by a variety of factors, and reasonable dispersion coefficient is difficult to obtain. Therefore, the laboratory tests have an important role in the study on the mechanism of the dispersion test and the influence of single factors.

In 1905 Slichter reported that solutes in the soil did not migrate at the same rate. Since then, people proposed and gradually formed the basic theory of solute transport - hydrodynamic dispersion theory. In general, the hydrodynamic dispersion is due to the thermodynamics of the particles and the mechanical mixing of the solute molecules by the fluid, that is, the diffusion of the solute in the porous medium and the convection dispersion. There are many methods to calculate the hydrodynamic dispersion coefficient in soils at home and abroad. From the initial trial algorithm, straight line diagram method, standard

curve method, point-by-point method, preferred fitting method to later linear regression method, inverse function method, microbiological method, linear regression method and so on [3, 4, 5, 6, 7]. From the whole development process, the calculation method has been from the larger hand-painted method tends to a higher degree of precision computerized, micro-processing method development [8, 9, 10, 11].

At present, the understanding of structure form in coefficient of hydrodynamic dispersion is not still unified [12]. Theoretically, the coefficient of hydrodynamic dispersion D_{sh} is the sum of molecular diffusion coefficient D_s and the mechanical dispersion coefficient D_h . With the increase of the aperture characteristic or the nonuniformity coefficient, the molecular diffusion coefficient has a small increase, the diffusion is mainly affected by concentration gradient, water content, temperature and other factors in theory [13,14]. Generally, the molecular diffusion coefficient of solute in soil is only expressed for the function of soil water content, having nothing to do with the density of solute, and it usually is shown by empirical formula [15]. Kemper et al. (1966) using the empirical formula to show the molecular diffusion coefficient D_s is as following.

$$D_s = D_0 a e^{b\theta} \quad (1)$$

Where D_s is the molecular diffusion coefficient (cm²/min), D_0 is the diffusion coefficient of solute in the free water body, θ is soil water content (cm³/cm³), a and b are the empirical constants.

According to the literature [16], while the soil water suction changes in the range of 0.3 ~ 15 atm, $b = 10$ is more suitable in the above empirical

^{*} To whom all correspondence should be sent:

E-mail: shaoaijun@sohu.com

formula, the changing range of value of a is 0.005 ~ 10.001 (silt loam to clay), the bigger the soil viscosity is, the smaller the value of a .

It is generally acknowledged, in one-dimensional flow, the mechanical dispersion coefficient D_h is in proportion to the one power of average flow velocity in soil voids [17].

$$D_h = \alpha|v| \quad (2)$$

Where D_h is the mechanical dispersion coefficient (cm²/min), v is the average porous flow velocity (cm/min), α is the dispersion degree (an empirical constant) (cm).

In the above foregoing, the dispersion coefficient D_{sh} stands for the sum of the molecular diffusion coefficient D_s and the mechanical dispersion coefficient D_h , that is,

$$D_{sh} = D_0ae^{b\theta} + \alpha|v| \quad (3)$$

When the speed of convection is quite large, the function of the mechanical dispersion will greatly exceed the molecular diffusion, so only to need to consider the mechanical dispersion function in hydrodynamic dispersion. On the contrary, when the soil solution is static, the mechanical dispersion is completely inoperative, only leaving the molecular spreading. Generally speaking, there are molecular dispersion function and mechanical dispersion function at the same time in solute transfer in soil, but it is difficult to distinguish them, so the molecular diffusion and the mechanical dispersion are referred to as hydrodynamic dispersion. In practical application, some scholars express the coefficient of hydrodynamic dispersion as the exponential function of the coefficient of molecular diffusion form. Smiles et al. believed that, in further theoretical and experimental work, the dispersion coefficient and velocity are independent of solute transport during the process of infiltration into very coarse soils [18]; Xie et al. systematically discussed the zero flux surface method, surface flux method, and proposed the positioning flux method [19]. They think longitude diffusion coefficient is not sensitive to the average flow velocity in soil voids, so D_{sh} can be alone treated as the function of the water content. However, from the literatures, many scholars express the coefficient of hydrodynamic dispersion as the linear function of the coefficient of mechanical dispersion form. They think that D_{sh} is in proportion to the one power of the average porous flow velocity. Zhang et al. obtained the calculation method of hydrodynamic dispersion parameters of adsorbed solute by experimental study on saturated and unsaturated hydrodynamic dispersion of light loam and heavy loam through indoor soil column

[20]. Shang et al. used the normal distribution function method to obtain the hydrodynamic dispersion coefficient of the disturbed soil, and the diffusion coefficient was obtained by the proportional relationship between the hydrodynamic dispersion coefficient and the average pore velocity [21]. Li et al. carried out one-dimensional soil column of hydrodynamic dispersion and diffusion experiment based on the theory of hydrodynamics dispersion, and calculate the mechanical dispersion and diffusion coefficient of soil samples according to the experimental results [22]; Li et al. identified the dispersion coefficient of one-dimensional flow and two-dimensional hydrodynamic dispersion model based on the proportional relationship between D_{sh} and mean pore velocity v by the line method of the bat algorithm, and proved the practicability of the method [23]. The coefficient of hydrodynamic dispersion is expressed as in the latter form in the paper [24]. The experimental method is the indoors upright soil column.

EXPERIMENTAL MATERIAL AND METHOD

The experimental soil was sampled from the estuary of the Changjiang River (Fig.1). The soil is silt loam, and the primitive salt content is 0.364g/kg, which is desalting soil. The soil sample used in the experiment through the natural air-drying is passed sieve mesh and mixed to well distributed. According to the actual dry density of the soil from the farmland, the soil column is filled. The degree of mineralization of supplying water in the experiment is 8g/L (close to the degree of mineralization of groundwater).

The soil column used is an upright soil column, which is made of the transparent plexiglas column, height 170cm, diameter 12.7cm. The side of the soil column is equipped with the salt sensor in order to monitor the soil salt content, and buried depth is 5, 15, 30, 45, 65, 105, 145cm, and tensiometer in the same depth to monitor the soil moisture content. Seal the bottom, open the top to evaporate. The experiment is done indoors. In order to be close to the natural environment condition, an infrared lamp is laid over the top of the column to imitate the sunlight. The bottom of soil column is equipped with Mariott bottle to control the water level and to monitor the consumption mass of water. The experiment lasted from August to October 1999, every 3 days once in the earlier and every 4 days once in the later got the observation record of soil electric conductivity, tension and the consumption mass of water. The experimental device is in Fig.2.

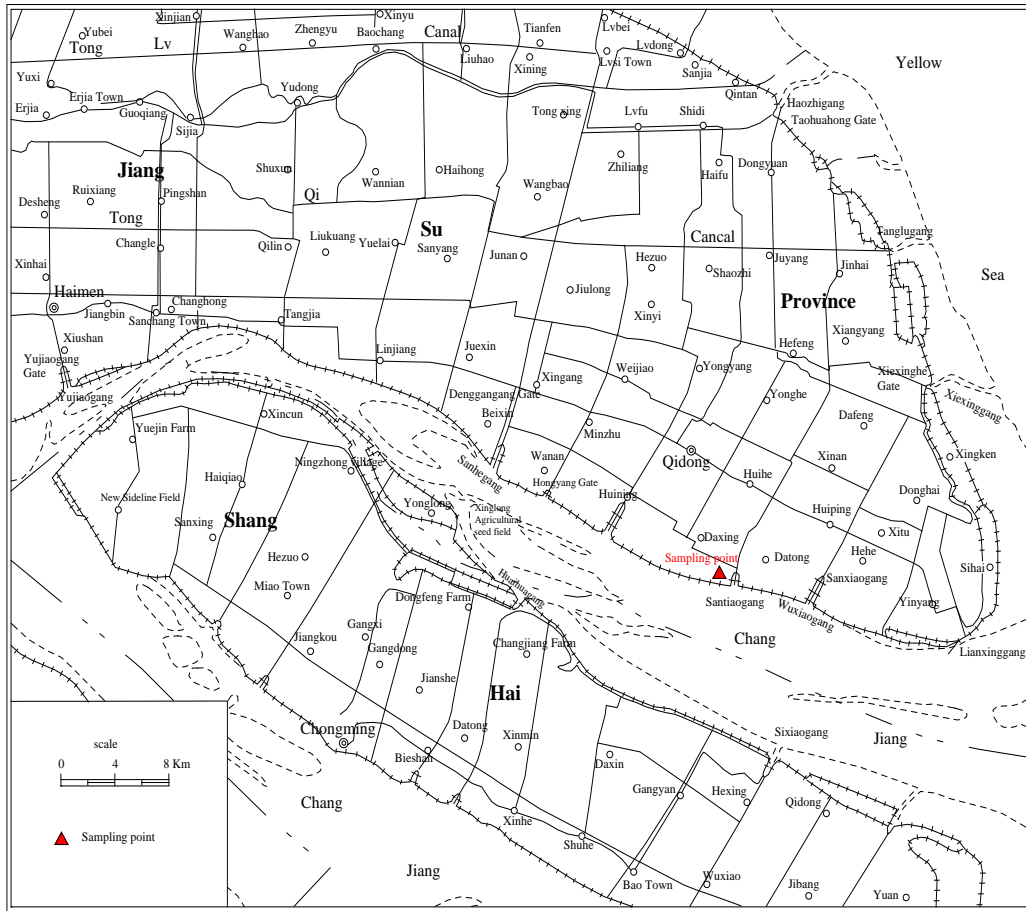


Fig. 1. Distribution of sampling points

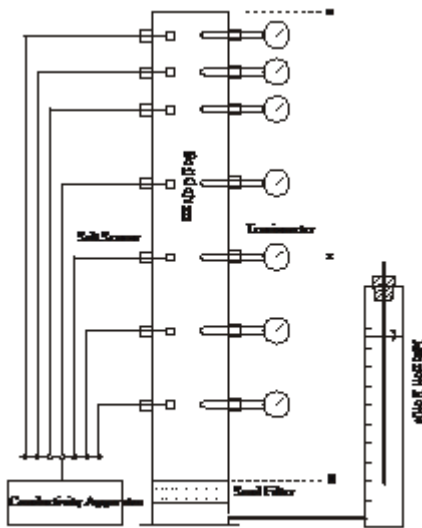


Fig.2. Schematic diagram showing experimental device

CALCULATION OF COEFFICIENT OF HYDRODYNAMIC DISPERSION

To calculate the coefficient of hydrodynamic dispersion, firstly calculate the moisture flux, and then calculate the salt flux, finally determine the

coefficient of hydrodynamic dispersion by the moisture flux and the salt flux.

Moisture flux

If both the mass of water that the solution supplied to the soil column through the bottom and the distribution of the profile water content at different moments were known, by water mass balance principle, the moisture flux q_z in any section z of the soil column can be expressed as follows.

$$q_0 - q_z = \frac{1}{\Delta t} \left[\int_0^z \theta(t_2) dz - \int_0^z \theta(t_1) dz \right] \quad (4)$$

That is

$$q_z = q_0 - \frac{1}{\Delta t} \left[\int_0^z \theta(t_2) dz - \int_0^z \theta(t_1) dz \right] \quad (5)$$

Where q_z is the moisture flux in any section of depth z (cm/d), q_0 is the mass of inflow water mass from the bottom of the soil column (cm/d), θ is the volumetric water content (cm³/cm³), $\Delta t = t_2 - t_1$ is the time interval (d).

The formula (5) is written in discrete form:

$$\begin{aligned}
& q_z^{k+1/2} \\
&= q_0^{k+1/2} - \frac{1}{\Delta t} \left[\begin{aligned} & \sum_{i=0}^{i=z} \theta_{i+1/2}^{k+1} \Delta Z \\ & - \sum_{i=0}^{i=z} \theta_{i+1/2}^k \Delta Z \end{aligned} \right] \\
&= \frac{1}{2} (q_0^{k+1} + q_0^k) - \frac{\Delta Z}{2\Delta t} \left[\begin{aligned} & \sum_{i=0}^{i=z} (\theta_{i+1}^{k+1} + \theta_i^{k+1}) \\ & - \sum_{i=0}^{i=z} (\theta_{i+1}^k + \theta_i^k) \end{aligned} \right]
\end{aligned} \quad (6)$$

Where k is the number of time intervals.

Salt flux

If both the solute flux from the bottom of the soil column and the distributions of the sectional water content and of the solute density at different moments were known, by the mass conservation law, the solute flux J_z in any section depth of z can be got:

$$J_0 - J_z = \frac{1}{\Delta t} \left[\int_0^z \theta(t_2)c(t_2)dz - \int_0^z \theta(t_1)c(t_1)dz \right] \quad (7)$$

That is,

$$J_z = J_0 - \frac{1}{\Delta t} \left[\int_0^z \theta(t_2)c(t_2)dz - \int_0^z \theta(t_1)c(t_1)dz \right] \quad (8)$$

Where J_z is the solute flux in any section depth of z ($\text{g/cm}^2 \cdot \text{d}$), J_0 is the solute flux in the bottom of the soil column ($\text{g/cm}^2 \cdot \text{d}$), c is the density of soil solution (g/cm^3), θ is the volumetric water content (cm^3/cm^3), $\Delta t = t_2 - t_1$ is the time interval (d).

The equation (8) is written in dispersed form:

$$\begin{aligned}
& J_z^{k+1/2} \\
&= J_0^{k+1/2} - \frac{1}{\Delta t} \left[\begin{aligned} & \sum_{i=0}^{i=z} \theta_{i+1/2}^{k+1} c_{i+1/2}^{k+1} \Delta Z \\ & - \sum_{i=0}^{i=z} \theta_{i+1/2}^k c_{i+1/2}^k \Delta Z \end{aligned} \right] \\
&= \frac{1}{2} (J_0^{k+1} + J_0^k) \\
&\quad - \frac{\Delta Z}{4\Delta t} \left[\begin{aligned} & \sum_{i=0}^{i=z} (\theta_{i+1}^{k+1} + \theta_i^{k+1}) (c_{i+1}^{k+1} + c_i^{k+1}) \\ & - \sum_{i=0}^{i=z} (\theta_{i+1}^k + \theta_i^k) (c_{i+1}^k + c_i^k) \end{aligned} \right]
\end{aligned} \quad (9)$$

Coefficient of Hydrodynamic Dispersion

According to the hydrodynamic dispersion principle, solute flux is equal to the sum of the

hydrodynamic dispersion flux and the convection flux, that is:

$$J = -\theta D_{sh} \frac{\partial c}{\partial z} + qc \quad (10)$$

$$D_{sh} = \frac{1}{\theta \frac{\partial c}{\partial z}} (qc - J) \quad (11)$$

Where J is the solute flux ($\text{g/cm}^2 \cdot \text{d}$), D_{sh} is the coefficient of hydrodynamic dispersion (cm^2/d), c is the density of solute (g/cm^3), θ is the volumetric water content, $\Delta t = t_2 - t_1$ is the time interval (d).

The equation (11) is written in dispersed form:

$$\begin{aligned}
(D_{sh})_z^{k+1/2} &= \frac{1}{\theta_z^{k+1/2} \frac{\Delta c}{\Delta z} \Big|_z} [(qc)_z^{k+1/2} - J_z^{k+1/2}] \\
&= \frac{1}{\frac{1}{2}(\theta_z^{k+1} + \theta_z^k) \frac{c_z^{k+1} - c_z^k}{2\Delta z}} \left[\frac{1}{2} q_z^{k+1/2} (c_z^{k+1} + c_z^k) - J_z^{k+1/2} \right] \\
&= \frac{2\Delta z}{(\theta_z^{k+1} + \theta_z^k)(c_z^{k+1} - c_z^k)} [q_z^{k+1/2} (c_z^{k+1} + c_z^k) - J_z^{k+1/2}] \quad (12)
\end{aligned}$$

Replacing the foregoing $q_z^{k+1/2}$ and $J_z^{k+1/2}$ into equation (12) can calculate the coefficient of hydrodynamic dispersion D_{sh} . If taking a series of section z, a series of D_{sh} can be calculated out. Furthermore, D_{sh} and the corresponding average pore flow velocity v in soil voids can be fitted into empirical formula.

RESULTS AND ANALYSIS

The experimental data of calculating the coefficient of hydrodynamic dispersion is shown in the following table (table 1).

Based on the experimental data of the above table, the coefficient of hydrodynamic dispersion can be calculated with the equation (12), in which the water content is calculated according to Van Genuchten model:

$$\theta = \frac{\theta_s - \theta_r}{[1 + |\alpha h|^n]^m} + \theta_r \quad (13)$$

Where, the parameters according to the actually measured data for the water characteristic curve: θ_s is 0.432, θ_r is 0.01, α is 0.006038, n is 1.9087501, m is 0.476097.

The conversion relation fitted by the experimental data between the electric conductivity and the salt content of soil is:

$$s = 2.888E_c + 0.1016 \quad (14)$$

Where s is the salt content of the soil (the salt

mass of one unit mass dry soil (g/kg)), E_c is electric conductivity (mS/cm).

Table 1. Data of hydrodynamic dispersion experiment

| Time m-d | Water volume | | | | | | | | Electric conductivity E_c (dS/m) | | | | | | |
|-------------|-----------------|-----|-----|-----|-----|-----|------|---|------------------------------------|-------|-------|-------|-------|--------|--------|
| | 5 | 15 | 30 | 45 | 65 | 105 | 145* | 5 | 15 | 30 | 45 | 65 | 105 | 145* | |
| 8-26 | 108 | 153 | 137 | 135 | 107 | 82 | 51 | 0 | 1.31 | 1.109 | 2.094 | 2.947 | 3.744 | 9.438 | 14.091 |
| 8-31 | 85 | 157 | 143 | 133 | 102 | 77 | 41 | 0 | 1.26 | 1.143 | 2.172 | 3.084 | 3.995 | 9.714 | 14.362 |
| 9-4 | 87 | 150 | 137 | 133 | 107 | 77 | 51 | 0 | 1.27 | 1.139 | 2.216 | 3.205 | 4.188 | 9.928 | 14.463 |
| 9-8 | 75 | 149 | 129 | 127 | 97 | 77 | 41 | 0 | 1.29 | 1.172 | 2.278 | 3.338 | 4.374 | 10.112 | 14.632 |
| 9-25 | 123 | 149 | 126 | 122 | 92 | 69 | 26 | 0 | 1.31 | 1.261 | 2.592 | 3.994 | 5.321 | 10.908 | 14.868 |
| 9-29 | 20 | 143 | 127 | 124 | 92 | 71 | 31 | 0 | 1.33 | 1.290 | 2.667 | 4.136 | 5.490 | 11.030 | 15.003 |
| 10-25 | 33 | 143 | 129 | 124 | 102 | 77 | 41 | 0 | 1.47 | 1.342 | 2.822 | 4.481 | 6.044 | 11.367 | 15.105 |
| 10-29 | 38 | 145 | 133 | 129 | 102 | 77 | 41 | 0 | 1.47 | 1.379 | 2.890 | 4.576 | 6.137 | 11.429 | 15.172 |

* the depth (cm)

By calculating according to the experimental data, we has got the coefficient of hydrodynamic dispersion of the unsaturated slit loam. The coefficient value is in proportion to the average flow velocity in soil voids. The fitted curve is shown in Fig.3, and the correlate coefficient $R=0.85$, that is,

$$D_{sh} = 0.35v \quad (15)$$

Where D_{sh} is the coefficient of hydrodynamic dispersion (cm^2/min), v is the average flow velocity in soil voids (cm/min).

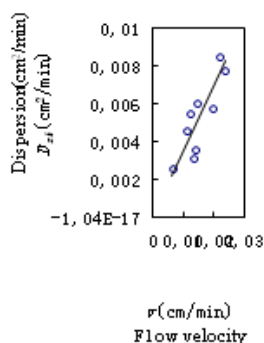


Fig. 3. $D_{sh} \sim v$ curve fitted

In the test, as sensor and moisture tensiometer are arranged in large interval, it may influence the accuracy of the calculated result in some extent. Because solute transfer law is affected by a lot of factors, such as adsorption and desorption, the physics and chemical reaction, the original salt in soil, and so on, it is much more complicated than moisture movement. From the data of fitting figure, it can be found out that the fitting points are quite scattered, but the total linear tendency is still very clear. And the calculated values of the coefficient of hydrodynamic dispersion are quite close to the

results calculated of other author, such as Yang Jinzhong, Huang Kangle, Zhang Yufang et. al. This approach is of clear physics concept and the calculated formula is simple and practical.

REFERENCES

1. G.L. Wang, *Journal of Arid Land Resources & Environment*, **18**(3), 74 (2004).
2. Y. Li, Z. Zhang, Y. Fei, Z. Wang, J. Chen, F. Zhang, Y. Qian, *Journal of Arid Land Resources & Environment*, **26**(8), 52 (2012).
3. J. Guo, *Coal Geology & Exploration*, **28**(6), 36 (2000).
4. X. Yin, *Site Investigation Science & Technology*, **22**(4), 3 (1994).
5. W. Ye, Q. Jin, Y. Huang, Y. Tang, *Journal of Hydraulic Engineering*, **36**(2), 251 (2005).
6. S. Zou, A. Parr, *Groundwater*, **132**(3), 367 (1994).
7. R. Zhao, *Site Investigation Science & Technology*, **175**(1), 24 (2012).
8. J.C. Agunwamba, *Water, Air and Soil Pollution*, **36**, 36 (1992).
9. B.X. Hu, C. He, *Mathematical Geology*, **38**(3), 327 (2006).
10. W. Liu, J. Lo, *Journal of Radio analytical and Nuclear Chemistry*, **163**(2), 373 (1992).
11. M. Rolle, D. Hochstetler, G. Chiogna, P.K. Kitanidis, P. Grathwohl, *Transport in Porous Media*, **93**(3), 347 (2012).
12. Y. Wang, Y. Hu, *Irrigation and Drainage*, **11**(1), 1 (1992).
13. Y. Du, S. Liu, *Journal of Southeast University*, **22**(1), 106 (2006).
14. X. Shi, Z. Li, R. Wang, *Bulletin of Soil & Water Conservation*, **23**(5), 15 (2003).
15. Z. Lei, S. Yang, S. Xie, *Dynamics of soil water*. Beijing: Qinghua University Press, 1988.
16. S.R. Olsen, W.D. Kemper, *Adv. Agron.*, **80**, 91 (1968).
17. J. Bear, *Dynamics of fluid in porous media*. American

- Elsevier, New York, 1972.
18. D.E. Smiles, J.R. Philip, *Soil Science Society of America Journal*, **42**(4), 537 (1978).
 19. S. Xie, Z. Lei, S. Yang, Y. Zhao, *Journal of Irrigation & Drainage*, **7**(2), 1(1988).
 20. F. Zhang, S. Kang, Y. Pan, *Journal of Hydraulic Engineering*, **3**, 84 (2002).
 21. M.T. Shang, J. Feng, P.G. Liu, Coefficient[J]. *Journal of Irrigation & Drainage*, **28**(5), 52 (2009).
 22. X. Li, W. Zhu, *Journal of Water Resources & Water Engineering*, **2**, 25 (2014).
 23. S. Li, G. Liu, L. Wang, B. Xing, Y. Ren, X. Li, *Coal Geology & Exploration*, **4**, 44 (2016).
 24. A. Shao, Numerical simulation of soil water and salt transport and dynamic forecast in Changjiang River estuarine region. Research report of post-doctor of Chinese Academy of Sciences, 2000.

Changes in blood biochemical parameters and enzyme activity of juvenile Chinese sturgeon *Acipenser sinensis* during starvation

G. Feng¹, F. Zhao¹, P. Zhuang^{1*}, X. Huang¹, T. Zhang¹, X. Shi^{2*}

¹ East China Sea Fisheries Research Institute, Chinese Academy of Fishery Sciences, Shanghai, China

² College of Hydraulic and environmental engineering, China Three Gorges University, Yichang, China

Received June 23 2017; Revised July 20, 2017

In recent years, the number of Chinese sturgeon (*Acipenser sinensis*) has decreased, due to food shortage and starvation as a result of human activity. In this study, the effects of starvation on the metabolism of juvenile sturgeon were examined by measuring their blood parameters over time to assess the utilization of energy resource and identify biomarkers of stressed sturgeon populations. Plasma was sampled every six days during 49 days of starvation. The results showed that the total protein concentration of sturgeon increased slightly during the initial period of the experiment, and then declined significantly after 25 days. It has become apparent that the concentration of albumin (ALB) declined significantly after 31 days of starvation. Glucose (GLU) concentration was decreased significantly after only 7 days of starvation, and dropped significantly again after 31 days. Triglyceride (TGL) and cholesterol (CHOL) levels were steady, until as late as 25 days after starvation. Other parameters including urea, alanine aminotransferase, aspartate aminotransferase, and lactate dehydrogenase also reduced significantly. In contrast, high-density lipoprotein cholesterol, low-density lipoprotein cholesterol, and alkaline phosphatase were less affected. The activity of alanine aminotransferase (ALT) decreased significantly after 13 and 37 days of starvation. The activity of lysozyme (LSZ) increased generally and there were significant difference between 43-day starvation group and 4 starvation groups of 1-19 days. Therefore, these results indicate that carbohydrates were metabolized preferentially in the blood of juvenile Chinese sturgeon, then proteins, and finally lipids. Furthermore, GLU, ALB, CHOL, and TGL can be used as indicators to nutritional condition. Obvious effects occurred in the blood of juvenile Chinese sturgeon after 13 days of starvation.

Key words: Chinese sturgeon, Blood, Physiology, Nutrient utilization, Starvation.

INTRODUCTION

Chinese sturgeon (*Acipenser sinensis* Gray 1835) are an anadromous species that live only in the Changjiang (Yangtze) River in China. This species is on the Red List of Threatened Species, International Union for Conservation of Nature (IUCN), and has been given Category I Protection in China [1, 2]. Since the sturgeon lifecycle includes a transition from birth in fresh water to salt water for maturity, juveniles concentrate at the river estuary from May through September annually to develop their capacity for osmoregulation by salinity challenge. At this site, the juvenile sturgeon mainly feed on demersal fish, polychaeta, amphipoda, and some small-sized benthic invertebrates including shrimp, crabs, and bivalves [3]. However, because of overfishing, water pollution, beach reclamation, and other human activity, food biomass of Chinese sturgeon in the Changjiang River estuary has declined significantly in recent years, indicating that juvenile Chinese sturgeon face scarce and starvation in the Changjiang River. Therefore, we require a non-lethal method to monitor the nutritional status of

this species for the conservation purpose.

Some types of biochemical parameters in blood have been used as the indicators of nutritional status in fishes, the relative predominance of three body constituents (carbohydrates, lipids and protein) depends on the duration of starvation, and if the temporal changes in blood biochemical parameters reflect the change in the relative predominance, the degree of nutritional stress in juvenile Chinese sturgeon may estimate more precisely. However, the nature of metabolic changes experienced during starvation largely depends on the species and duration of the fasting period. Certain fish, including goldfish, carp, rainbow trout [4], and porgy [5], preserve glycogen while metabolizing lipids and/or proteins. Other species, such as cod [6], tilapia [7], and coho salmon [8], conserve proteins and lipids while partially depleting glycogen stores. Evaluating the blood chemical parameters of fish could provide essential information on their metabolism during conditions of starvation.

Previous studies on starvation have mainly focused on teleost, which undergo natural starvation during winter months; whereas little literature is available on the effects of starvation on non-teleost species. Therefore, Chinese sturgeon

* To whom all correspondence should be sent:

E-mail: pzhuang@ecsfc.ac.cn; sxtshanghai@163.com

were used in the present study to gain a better understanding of the strategy that non-teleost fish species use to cope with starvation. The main objectives of this study were to: (1) investigate blood changes in juvenile sturgeon in response to starvation stress; (2) assess which energy resource juvenile sturgeon used preferentially during different starvation periods; (3) identify blood biochemical parameters that can potentially be used as indices of substrate utilization and nutritional state; (4) evaluate the maximum time juvenile Chinese sturgeon can suffer. These information would provide a better understanding of the metabolism of Chinese sturgeon, and could be used to further develop conservation strategies.

EXPERIMENTAL

Materials

One hundred juvenile Chinese sturgeons (7 months old) were obtained from the Chinese Sturgeon Research Institute in Yichang, China. The sturgeons were transferred to the Aquaculture Laboratory (East China Sea Fisheries Research Institute, Shanghai, China) and reared indoors in 2-m-diameter circular fiberglass tanks. Fish were stocked for 15 days under ambient light and temperature prior to experimentation in order to acclimate them to laboratory conditions. They were also fed a commercial diet (Shandong Shengsuo Feed Company, Yantai City, China) to apparent satiety 3 times per day (08:00, 14:00, and 20:00 h).

After 15 days of acclimation, 162 active juveniles (mean body length = 16.0 ± 0.8 cm, mean body weight = 21.00 ± 4.01 g) were chosen to be cultured in 3 separate tanks for the starvation experiment (54 fish per tank). The mean lengths and weights of fish did not differ among 3 groups. Water quality was measured daily during the experiment. Water temperature, pH, and dissolved oxygen levels were determined to be 19.2 ± 1.4 °C, 7.4 ± 0.3 , and 6.1 ± 0.5 mg/L, respectively. Fish were exposed to a 12 h light-dark photoperiod using overhead fluorescent lights.

Experimental treatments and sampling procedures

The study was carried out from April to May 2008. No sturgeon mortalities occurred during the experiment. Fish were fasted for 24 h prior to the first blood sampling (day 1). Thereafter, samples were taken every 6 days during total 48 days of starvation. Upon each sampling occasion, six fish were randomly selected from each tank, always at the same time of day. Juvenile sturgeon were immediately anaesthetized by immersion in tricaine methanesulphonate at 100 mg/L. Special care was taken to maintain the fish as unstressed as possible. Fish were immersed in the anaesthetic solution until they reached the stage of complete immobility. Thereafter, blood samples of each fish were taken within 2 minutes by puncturing the caudal vein with a disposable

sterilized syringe. Blood was immediately transferred into 1.5 mL Eppendorf tubes.

Analysis of samples

Blood was allowed to stand for 120 minutes at 4 °C to achieve complete clotting, then centrifuged at $10\,000 \times g$ for 10 min at 4 °C. Serum samples were then analyzed, together with the standard material, using a BS-200 Auto Chemistry Analyzer (Shenzhen Mindray Bio-Medical Electronics Co., Ltd., Shenzhen City, China). Serum glucose (GLU), total protein (TP), cholesterol (CHOL), triglyceride (TGL), alanine aminotransferase (ALT), aspartate aminotransferase (AST), alkaline phosphatase (ALP), lactate dehydrogenase (LDH), albumin (ALB), high-density lipoprotein cholesterol (HDL), low density lipoprotein cholesterol (LDL), and urea (UREA) were determined using a commercially available kit (Shenzhen Mindray Bio-Medical Electronics Co., Ltd., Shenzhen City, China) according to the manufacturer's instructions. For analytical quality control of the chemical methods used, the certified reference materials was used to ensure accuracy of the coefficient of variation for each determination method was <5%.

The levels of ALT and LSZ were determined with respective kits bought from Nanjing Jiancheng Bioengineering Institute (Jiangsu province, China), according to the manufacturer's instructions. For measurement of LSZ, serum, kit reagents, and distilled water were mixed uniformly and placed into a 37 °C water bath for 15 minutes. Subsequently, the mixtures were placed into a 0 °C ice-water bath for 3 minutes, and were further transferred into 1-cm cuvettes for analysis.

Statistical analysis

All statistical analyses were performed using one-way analysis of variance (ANOVA). Significant differences among means were determined by Duncan's multiple range test. Difference were accepted as significant when $P < 0.05$. All data were analysed with Statistics software version 6.0 (StatSoft Inc., Tulsa, OK, USA) and described as mean \pm standard deviation (SD).

RESULTS AND DISCUSSION

As shown in Table 1, chemical analysis determined that TP levels increased slightly during the initial period of starvation, and then continually declined to significantly reduced levels by day 25 ($P < 0.05$). After 25 days, TP levels remained steady, until it reached its lowest level of 5.1 g/L at the end of experiment (49 days). Similarly, ALB levels remained relatively constant with a slight decrease during the first 25 days of starvation, then decreased significantly by 31 days ($P < 0.05$).

In the experiment, GLU levels of sturgeon decreased significantly over time during starvation (Table 1). GLU concentration was significantly decreased ($P < 0.05$) after only 7 days of starvation,

and continued to decrease until it was again significantly reduced ($P < 0.05$) after 31 days.

In the experiment, the CHOL levels of sturgeon increased slightly during the first 19 days starvation, then decreased significantly by 25 days ($P < 0.05$) (Table 2). TGL levels also decreased over time during the 49 days of starvation. Its concentration was significantly reduced ($P < 0.05$) after 25 days of starvation, and again after 43 days ($P < 0.05$), and finally reached its lowest level of 5.23 mmol/L on day 49 (Table 2). Of note, the concentrations of CHOL, TGL, and UREA were all significantly decreased by day 49, compared to corresponding starting levels of each (Table 2). In addition, HDLC, LDLC and ALP levels also did not experience significant changes during 49 days of starvation (Table 3). The range of ALP, LDLC, HDLC and LDH were 93.4 ± 4.7 – 102.9 ± 19.5 , 0.20 ± 0.05 – 0.27 ± 0.10 , 0.30 ± 0.08 – 0.32 ± 0.14 , 922.0 ± 54.9 – 992.5 ± 57.8 respectively. The results of statistical tests were $P > 0.05$ for ALP, LDLC, HDLC and LDH (Table 4). The activity of alanine aminotransferase decreased significantly after 13 and 37 days of starvation. The levels ranged from 42.1 to 134.6 U/L (Figure 1). The activity of lysozyme increased generally and there were significant difference between 43-day starvation group and 4 starvation groups of 1-19 days (Figure 2). Obvious effects occurred in the blood of juvenile Chinese sturgeon after 13 days of starvation.

Evaluations of nutritional health of animals are based mainly on measurements of available energy because the quantity of energy reserves correlates with survival or the adaptive aspects of life-history variation [9, 10]. However, it has been difficult to estimate the nutritional condition of animals living in their natural conditions. Blood biochemical parameters have been used as semi-quantitative indicators of nutritional condition for some fishes [11, 12]. The lethal method is not appropriate for the conservation of Chinese sturgeon, because the fish is faced with the risk of extinction. Non-lethal blood sampling may prove particularly useful for evaluating the nutritional condition of sturgeon.

For instance, blood TP concentration provides information about fish metabolism, as it may be used as a back-up energy source during severe stress [13]. Previous studies showed that TP concentration decreased significantly after a 7-day fasting period in gilthead sea bream [14]. Friedrich et al. (2001) also found that the crude protein level of carp (*Cyprinus carpio*) significantly decreased after 12 weeks without food [15]. ALB is a major component of plasma proteins, and is a biomarker

of many diseases and other stress situations [16]. In the current study, TP concentration was determined to be increased slightly during the initial period of starvation, and then declined significantly after 25 days. And ALB concentration declined significantly after 31 days of starvation. These results suggested that during prolonged periods of starvation, sturgeon used protein as one of their energy sources.

Blood carbohydrates play an important role in the regulation of blood GLU levels. GLU is of the utmost of importance in metabolism and can be used as an indicator of stress [17]. Various patterns of change in plasma GLU levels have been described in fasting fish [14, 18]. In the current study, GLU levels of juvenile Chinese sturgeon decreased during starvation, with significant drops detected after 7 days of starvation, and again after 31 days. Similarly, plasma GLU concentrations were decreased in fasting brown trout *Salmo trutta* [19]. Generally, fish use liver glycogen for maintaining metabolic functions, thus supplying energy during short starvation [11, 20]. However, active glycogenolysis produced to counteract fasting is not enough to maintain GLU, thus the concentration of GLU is decreased again [21].

In addition, Macfarlane et al. (1990) previously found that HDLC increased significantly in striped bass (*Morone saxatilis*) during starvation [22]. However, the levels of HDLC and LDLC were fairly unaffected, and exhibited no particular pattern, during starvation of sturgeon. The discrepancy between the present study and the striped bass study may be due to species difference or the physiological statuses of fish, but this issue requires further research for clarification.

During starvation, fish rely on a few main energy resources, firstly carbohydrates, secondly lipids and finally proteins. Physiologists typically describe three phases of fasting for vertebrate animals, mainly according to their measurable changes of glucose, lipids, and proteins [23]. The specific energy source used is highly dependent on the species and duration of the fasting period used. Some fish preserve glycogen, while metabolizing lipids and/or proteins [5]. Other species conserve protein and lipids, while partially depleting glycogen [8]. In the present study, GLU concentration of juvenile Chinese sturgeon decreased significantly after 7 days of starvation, while TP, ALB, CHOL, and TGL levels decreased significantly after 25 days starvation. These data indicated that during starvation, carbohydrates were metabolized preferentially in juvenile Chinese sturgeon, followed by proteins and lipids.

Many fish species can tolerate long periods of starvation in nature. However, the starvation time different fish can sustain vary widely across species, and the overall effects of long-term starvation on different organs and tissues are also different. The neotropical fish *Hoplias malabaricus* can survive food deprivation for periods of up to 180 days, without experiencing obvious reductions in metabolism; these studies also showed perivisceral fat bodies were finally exhausted after 240 days of starvation [24]. In the present study, the concentrations of TP, ALB, GLU, CHOL, and TGL were significantly changed by ~25 or ~31 days of starvation. Therefore, Chinese sturgeon would survive at least during 49 days of starvation at 19°C.

Table 1. TP, ALB and GLU expression in serum of juvenile Chinese sturgeon during starvation.

| Starvation (days) | TP (g/L) | ALB (g/L) | GLU (mmol/L) |
|-------------------|--------------|-------------|---------------|
| 1 | 7.6 ± 0.8 a | 3.6 ± 0.5 a | 5.86 ± 0.69 a |
| 7 | 9.4 ± 1.2 b | 3.5 ± 0.4 a | 4.47 ± 0.87 b |
| 13 | 8.8 ± 1.1 ab | 3.2 ± 0.1 a | 4.38 ± 0.60 b |
| 19 | 8.9 ± 0.5 b | 3.4 ± 0.2 a | 4.14 ± 0.22 b |
| 25 | 6.0 ± 1.1 c | 3.1 ± 0.7 a | 3.89 ± 0.39 b |
| 31 | 5.5 ± 0.7 c | 2.2 ± 0.3 b | 2.34 ± 0.17 c |
| 37 | 5.6 ± 0.5 c | 2.0 ± 0.4 b | 2.73 ± 0.22 c |
| 43 | 5.4 ± 0.9 c | 2.4 ± 0.3 b | 2.38 ± 0.50 c |
| 49 | 5.1 ± 0.4 c | 2.2 ± 0.3 b | 2.11 ± 0.57 c |

Mean ± standard deviation. Values sharing same letters differ non-significantly ($P > 0.05$). The same below.

Table 2. CHOL, TGL and UREA expression in serum of juvenile Chinese sturgeon during starvation.

| Starvation (days) | CHOL (mmol/L) | TGL (mmol/L) | UREA (mmol/L) |
|-------------------|---------------|---------------|---------------|
| 1 | 2.00 ± 0.35 a | 10.42 ± 0.94 | 1.36 ± 0.21 a |
| 7 | 2.24 ± 0.45 a | 10.20 ± 0.77 | 1.47 ± 0.16 a |
| 13 | 2.12 ± 0.28 a | 11.46 ± 0.22 | 1.18 ± 0.14 |
| 19 | 2.34 ± 0.63 a | 10.40 ± 2.08 | 1.00 ± 0.30 |
| 25 | 1.17 ± 0.45 b | 7.82 ± 0.72 b | 0.96 ± 0.18 |
| 31 | 1.25 ± 0.65 b | 7.66 ± 0.59 b | 0.84 ± 0.21 c |
| 37 | 1.15 ± 0.52 b | 6.67 ± 0.49 | 0.86 ± 0.16 c |
| 43 | 1.13 ± 0.43 b | 5.92 ± 0.88 c | 0.85 ± 0.17 c |
| 49 | 1.06 ± 0.35 b | 5.23 ± 1.08 c | 0.80 ± 0.15 c |

LSZs are enzymes that damage bacterial cell walls by catalyzing the hydrolysis of 1, 4-beta-linkages. LSZ activity has previously been detected in serum, organs, and eggs of fish species [25]. Two LSZs have previously been purified and LSZ cDNA has been cloned from the head kidney of rainbow trout (*Oncorhynchus mykiss*) [26]. Furthermore, Fevolden *et al.* suggested that increases in LSZ activity could be interpreted as a response signal to stress in fish, and that the activity

change was dependent on the type and intensity of the stress [27].

Table 3. HDLC, LDLC and ALP expression in serum of juvenile Chinese sturgeon during starvation.

| Starvation (days) | HDLC (U/L) | LDLC (U/L) | ALP (U/L) |
|-------------------|---------------|---------------|----------------|
| 1 | 0.30 ± 0.08 a | 0.20 ± 0.05 a | 93.4 ± 4.7 a |
| 7 | 0.36 ± 0.05 a | 0.30 ± 0.12 a | 95.1 ± 3.0 a |
| 13 | 0.32 ± 0.07 a | 0.20 ± 0.06 a | 98.0 ± 7.4 a |
| 19 | 0.44 ± 0.06 a | 0.44 ± 0.15 a | 116.0 ± 5.6 a |
| 25 | 0.39 ± 0.11 a | 0.28 ± 0.18 a | 110.6 ± 23.7 a |
| 31 | 0.41 ± 0.06 a | 0.46 ± 0.30 a | 116.2 ± 6.2 a |
| 37 | 0.42 ± 0.06 a | 0.24 ± 0.09 a | 114.5 ± 6.8 a |
| 43 | 0.34 ± 0.15 a | 0.40 ± 0.07 a | 115.3 ± 24.7 a |
| 49 | 0.32 ± 0.14 a | 0.27 ± 0.10 a | 102.9 ± 19.5 a |

Table 4. ALT, AST and LDH expression in serum of juvenile Chinese sturgeon during starvation.

| Starvation (days) | ALT (U/L) | AST (U/L) | LDH (U/L) |
|-------------------|---------------|----------------|-----------------|
| 1 | 134.6 ± 36.6 | 387.2 ± 128.1 | 922.0 ± 54.9 ab |
| 7 | 114.0 ± 14.6 | 420.8 ± 83.4 a | 1098.2 ± 124.8 |
| 13 | 73.4 ± 10.9 b | 356.8 ± 43.1 | 1113.2 ± 113.0 |
| 19 | 76.6 ± 16.1 b | 416.8 ± 36.7 a | 1276.6 ± 40.6 |
| 25 | 54.3 ± 11.6 | 339.8 ± 20.0 | 1203.9 ± 113.6 |
| 31 | 53.2 ± 12.5 | 310.1 ± 52.4 b | 994.5 ± 74.6 c |
| 37 | 45.6 ± 6.4 c | 330.1 ± 54.8 | 1039.1 ± 135.0 |
| 43 | 45.4 ± 10.3 c | 356.8 ± 40.6 | 1021.4 ± 76.2 |
| 49 | 42.1 ± 4.1 c | 302.0 ± 10.2 b | 992.5 ± 57.8 ac |

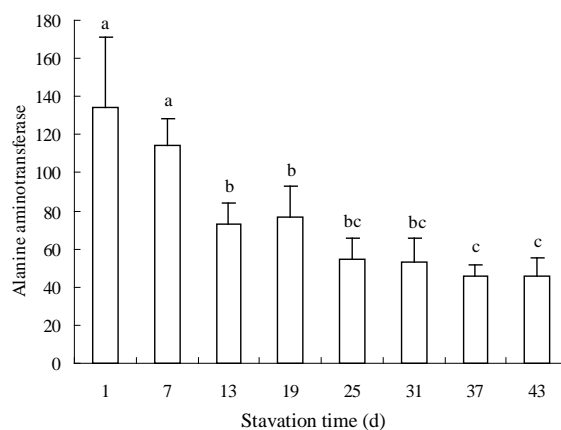


Fig. 1. Effect of starvation on activity of alanine aminotransferase in juvenile Chinese sturgeon.

In contrast, Mock *et al.* reported that chronic stress resulted in a reduced LSZ activity [28]. Therefore, it seems that the trends of LSZ activity changes may vary for different fish species, and upon different stressors. In the present study, as the starvation time increased, the LSZ activity of juvenile Chinese sturgeon generally increased. This finding suggests that the non-specific immunity of Chinese sturgeon was fairly maintained during the

starvation period. The activity of lysozyme (LSZ) increased significantly until 43-day starvation.

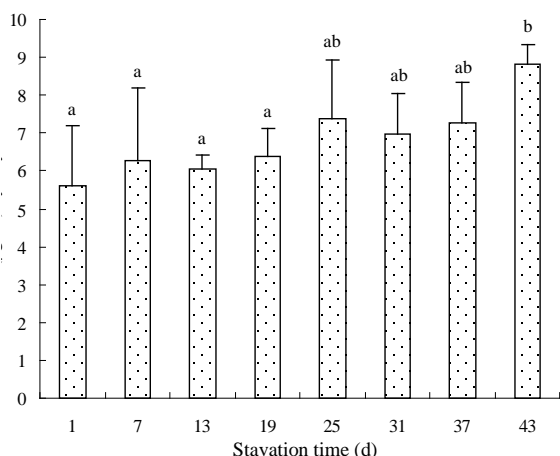


Fig. 2. Effect of starvation on activity of lysozyme in juvenile Chinese sturgeon.

CONCLUSION

Chinese sturgeon in starvation showed significant differences in many blood-chemistry levels, including: TP, ALB, GLU, CHOL, TGL, UREA, ALT, AST, and LDH. Based on our data, carbohydrates are likely metabolized preferentially in the blood of juvenile Chinese sturgeon, followed by proteins and lipids. Of note, GLU, ALB, CHOL, and TGL levels could potentially be used as indices of nutritional condition in multivariate blood-chemistry data sets. Obvious effects on activities of ALT and LSZ in the blood of juvenile Chinese sturgeon after 13 days of starvation. In addition, starvation can be suffered by juvenile Chinese sturgeon for up to 13-31 days. Taken together, the findings may reflect the evolutionary position occupied by sturgeon, as the utilization of stored metabolites during starvation appears to be intermediate to that of elasmobranchs and teleost. This information would provide a better understanding of Chinese sturgeon, and could be used to further develop conservation strategies.

Acknowledgements: The project was financially supported by the Special Research Fund for the National Non-profit Institutes of China (East China Sea Fisheries Research Institute 2011M08).

REFERENCES

1. W.E. Bemis, E.K. Findeis, L. Grande, *Environ. Biol. Fish.*, **48**, 25 (1997).

2. Q. Wei, P.L. M. Psenick, S.M. Hadi Alavi, L. Shen, J. Liu, J. Peknicova, O. Linhart, *Theriogenology*, **67**, 1269 (2007).
3. G. Luo, P. Zhuang, L. Zhang, T. Zhang, J. Liu, *J. Appl. Ecol.*, **19**(1), 144 (2008).
4. I.V. Baanante, D. Garcia, L. Bonamusa, F. Fernandez, *Comp. Biochem. Physiol.*, **100B**, 11 (1991).
5. F.M. Rueda, F.J. Martinez, S. Zamora, M. Kentouri, P. Divanach, *Aquacult. Res.*, **29**, 447 (1998).
6. G. I. Hemre, O. Lie, A. Sundby, *Fish Physiol. Biochem.*, **10**, 455 (1993).
7. S.L. Hsieh, S.Y. Shiau, *Fish. Sci.*, **66**, 32 (2000).
8. D.A. Larsen, B.R. Beckman, W.W. Dickhoff, *Gen. Comp. Endocrinol.*, **123**, 308 (2001).
9. G.T. Crossin, S.G. Hinch, A.P. Farrell, D.A. Higgs, A.G. Lotto, J.D. Oakes, M.C. Healey, *J. Fish Biol.*, **65**, 788 (2004).
10. S.M. Sogard, B.L. Olla, *J. Fish Biol.*, **56**, 1 (2000).
11. J.L. Congleton, T. Wagner, *J. Fish Biol.*, **69**, 473 (2006).
12. T. Wagner, J.L. Congleton, *Can. J. Fish. Aquat. Sci.*, **61**, 1066 (2004).
13. J.S. Almeida, P.C. Meletti, C. B. Martinez, *Comp. Biochem. Physiol.*, **140**, 356 (2005).
14. M. Sala-Rabanal, J. Sanchez, A. Ibarz, J. Fernandez-Borras, J. Blasco, M.A. Gallardo, *Fish Physiol. Biochem.*, **29**, 105 (2003).
15. M. Friedrich, K. Stepanowska, *Acta Ichthyologica et Piscatoria*, **31**(2), 29 (2001).
16. V. Gopal, S. Parvathy, P.R. Balasubramanian, *Environ. Monit. Assess.*, **48**, 117 (1997).
17. C. Pascual, A. Sanchez, E. Zenteno, G. Cuzon, G. Gabriela, R. Brito, R. Gelabert, E. Hidalgo, C. Rosas, *Aquaculture*, **251**, 416 (2006).
18. J. Blasco, J. Fernandez, J. Gutierrez, *J. Comp. Physiol.*, **162**, 539 (1992).
19. I. Navarro, J. Gutierrez, J. Planas, *Comp. Biochem. Physiol.*, **102**, 401 (1992).
20. N.D. Pedro, M.J. Delgado, B. Gancedo, M. Alonso-Bedate, *J. Comp. Physiol.*, **173**, 475 (2003).
21. J. L. Soengas, E. F. Strong, J. Fuentes, J. A. R. Veira, M. D. Andres, *Fish Physiol. Biochem.*, **15**, 491 (1996).
22. R. B. Macfarlane, H. R. Harvey, M. J. Bowers, J. S. Patton, *Can. J. Fish. Aquat. Sci.*, **47**, 739 (1990).
23. F. Hervant, J. Mathieu, J. Durand, *J. Exp. Biol.*, **204**, 269 (2001).
24. F.S. Rios, F.T. Rantin, *J. Fish Biol.*, **61**, 85 (2005).
25. R. Föngé, G. Lundblad, J. Lind, *Mar. Biol.*, **36**, 277 (1976).
26. A. Dautigny, E.M. Prager, D. Pham-Dinh, J. Jolles, F. Pakdel, B. Grinde, P. Jolles, *J. Mol. Evo.*, **32**, 87 (1991).
27. S.E. Fevolden, K. H. Roed, *J. Fish Biol.*, **43**, 919 (1993).
28. A. Mock, G. Peters, *J. Fish Biol.*, **37**, 873 (1990).

Health risk assessment of the volatile organic compounds in children's toys

S.H. Sun¹, G.Z. Huang^{1*}, Y. Wang², Q. Bi³

¹ Department of Safety Science and Engineering, School of Civil and Resource Engineering, University of Science and Technology Beijing, China

² AQSIIQ Defective Product Administrative Center, Beijing, China

³ Department of Safety Science and Engineering, School of Civil and Resource Engineering, University of Science and Technology Beijing, China

Received June 26, 2017; Revised July 20, 2017

This study focuses on a health risk assessment of volatile organic compounds (VOCs) in Children's Toys. First, the toy samples were collected and analyzed by HS-GC-MS. The geometric mean concentrations of individual VOCs obtained in all of the sampling campaign were 3.987, 6.672, 7.262, 3.756, 3.126 and 3.727 mg/kg for benzene, toluene, ethylbenzene, xylene, dichloromethane and trichloroethylene, respectively. Then, a risk assessment methodology was employed to evaluate the potential adverse health effects of the individual VOCs according to their carcinogenicities. Referring to the EU chemicals exposure model, the exposure and risk representation model were established. Finally, the USEPA model was applied to calculate the risk. The corresponding mean non-carcinogenic risks for benzene, trichloroethylene, dichloromethane, toluene, ethylbenzene and dimethylbenzene were 3.32E-06, 3.10E-06, 1.74E-06, 2.78E-07, 2.42E-07, and 6.26E-08, respectively. With respect to mean cancer risk for trichloroethylene, benzene and dichloromethane were 6.07E-05, 3.99E-05 and 6.69E-06, respectively. In addition, the total carcinogenic risk level of VOCs in toys was 1.07E-04 exceed the maximum acceptable risk level of 10⁻⁴ and the total non-carcinogenic risk was 8.75E-06 which exceeds the EPA's acceptable risk level of 10⁻⁶.

Key words: Toys; VOCs; Exposure model; Health risk assessment.

INTRODUCTION

The world's largest toy producer is China [1]. However, more and more attention has been paid to the safety of children's toys, due to toy safety hazards and recall problems, in recent years. According to the official website statistics, the U.S.CPSC (Consumer Product Safety Commission) issued a total of unsafe products recall notification 307, including 162 cases of origin in China, children's products 34, accounting for 20.99%; the European Commission issued 1585 notifications through the RAPEX system about a serious risk to health and safety of consumer goods, which children's toys 461 items, accounting for 29.1%. Chemical damage has become one of the main reasons for the recall.

Benzene, dichloromethane, trichloroethylene and other volatile organic compounds (VOCs) with different degrees of toxicity are often used as additives in the production of toys, and this has a huge impact on health when the toys are exposed to the human body. In order to guarantee the children's health and safety, countries all over the world formulated strict laws, regulations and relevant standards for the quality of toy products, which put forward corresponding requirements

regarding toxic chemical substances including organic chemical compounds in toys. [2]

There have been extensive studies on the VOCs. For example, J. Hoshi [3], H.T. Nguyen [4] et al. studied on the VOC types and concentrations in urban air. Choi E [5], Cailin Huang [6], Bin Xu [7], Liangui Bai [8], Wolkoff P. [9] et al. studied on the VOCs' health risks of indoor furniture. Some [10-15] scholars tested and evaluated the VOCs generated by the garbage disposal plant. Durmusoglu E [15] studied on the health risk assessment of BTEX emissions in the landfill environment. Xuezhong Chen [16] and Xiaohong Zeng [17] carried on the risk analysis of harmful chemicals in textiles and children's books, respectively. However, there are few studies on the health risk assessment of VOCs in children's toys.

In order to assess the risk of VOCs in toys, this paper will first analyze the scene of exposure. Afterwards, a risk assessment model of VOCs in toys will be established for quantitative calculation, which can then provide a basis for safety management of toys.

EXPERIMENTAL

Sample collection and detection

There are many methods for the determination of volatile organic compounds at home and abroad

To whom all correspondence should be sent:
E-mail: hjxhuanggz@163.com

[18-21]. After the analysis and comparison of the other areas of the determination of volatile organic matter, the method, headspace gas chromatography coupled with mass spectrometry (HS-GC-MS), was adopted to detect the residues of 8 kinds of volatile organic compounds such as benzene series in toys.

65 toy samples were collected from domestic market, 35 plastic toys and 30 plush toys. The detection results showed that 31 of the 65 samples were in the detection limit of the organic volatile matter content. The geometric mean concentration of VOCs in children's toys were 3.987, 6.672, 7.262, 3.756, 3.126 and 3.727 mg/kg for benzene, toluene, ethylbenzene, xylene, dichloromethane and trichloroethylene, respectively.

EXPOSURE ASSESSMENT

Exposure scenario

The route and level of exposure to chemicals in toys is linked to both the physico-chemical properties of the chemical and how the toy is used by the child, which can be described through exposure scenarios. These scenarios usually include environmental exposure, route of exposure, the exposed population, chemical property, absorption rate and other factors. Concentrations of chemicals can be determined by sampling and analysis of samples. When resources are limited, concentrations can be estimated by using a trend model [22]. Human behavior characteristic information can be obtained through hypothesis or survey questionnaire by selecting a part of representative populations. Some of these exposure parameters are found in the "exposure factors handbook" promulgated by the USEPA.

For the volatile organic compounds in toys, respiratory exposure and oral exposure are the main exposure pathways to human. It should be noted that mouthing behavior studies demonstrated that children place a broad range of items in their mouths, including toys [23-24]. Although the dimensions of some toys may be such that they cannot be placed in the mouth, ridges can still be sucked on. Therefore, mouthing of toys is an important exposure scenario. VOCs in toys can evaporate into the air indoor and may cause local effects in the lung, so respiratory exposure scenarios should also be considered.

Children are the main group exposed to toys. As a special group of people, they are more sensitive and vulnerable to harmful substances than adults. Exposure frequency and exposure time for toys can be different for children of different ages. Most studies have shown that mouthing of toys often

occurs in children under 6 years old. In consideration of the worst scenario, this paper mainly studied the children under this age.

Exposure model and exposure parameters

Based on the relevant exposure scenarios which have been analyzed above, the exposure to chemicals can be assessed by using the applicable mathematical formulas and the appropriate values of the variables, or exposure factors.

Oral exposure Uptake of VOCs in toys via the oral route can be calculated by the following steps:

To calculate the intake of the organic volatile compounds in toys via oral route:

$$I_{\text{oral}} = C \times \frac{S_0}{S} \times Q \times ABS \times ED \times n \quad (1)$$

Where C is the concentration of volatile organic compounds in toys, mg/kg; S_0 is the contact area with the mouth, cm^2 ; S is the toy's area, cm^2 ; Q is the toy's weight, kg; ABS is the percentage of the migration; ED is the exposure duration, d; and n is the mouthing frequency, event/d.

To calculate the daily exposure dose per unit of body weight:

$$Ex_{\text{oral}} = I_{\text{oral}} \times \frac{1}{BW \times AT} \quad (2)$$

Where BW is body weight, kg; AT is the averaging time, d.

Breathing exposure Organic volatile compounds in toys will spread in the air, which will not only affect the health of children, but also can produce toxic effects to adults to a certain extent. The dose of VOCs inhaled via the respiratory pathway can be calculated by the following steps:

To calculate the intake of the VOCs in toys via respiratory patterns:

$$I_{\text{inh}} = C \times \frac{Q}{V_m} \times F_v \times D \times IR \times ET \times ED \quad (3)$$

Where V_m is the space volume around the body, m^3 ; F_v is the volatile coefficient, unitless; D is the dilution factor, unitless; Q is the weight of the toy, kg; IR is the respiratory rate, m^3/h ; ET is the exposure time, h/d; and ED is the continuous exposure time, d.

To calculate the daily exposure dose per unit of body weight:

$$Ex_{\text{inh}} = I_{\text{inh}} \times \frac{1}{BW \times AT} \quad (4)$$

where C, Q, ED, BW and AT are the same variables as mentioned above.

Exposure parameters

Exposure parameters are key parameters in the assessment of exposure and health risk; they are critical in determining whether the assessment itself is accurate and scientific. The United States, the European Union, Japan, South Korea and other countries have issued their own exposure factors handbooks. However, due to the differences in race, living habits and other aspects, the foreign exposure parameters cannot represent the residents' exposure characteristics and behavior in China[25]. China has not yet promulgated its own exposure manual, but according to the existing research, the exposure parameters of the children's toys in China can be estimated.

The parameter values in exposure assessment are listed in Table 1.

Table 1. Parameter values in the exposure model.

| Parameters | Unit | Value |
|--|-------------------|-------|
| Toy's weight Q | kg | 1 |
| Toy's area S | cm ² | 1000 |
| Contact area with the mouth S ₀ | cm ² | 10 |
| Migration percentage ABS | - | 1 |
| Mouthing frequency n | event/d | 4 |
| Space volume around body V _m | m ³ | 225 |
| Volatile coefficient F _v | - | 1 |
| Dilution factor D | - | 1 |
| Respiratory rate IR | m ³ /h | 0.25 |
| Exposure time ET | h/d | 12 |
| Exposure duration ED | d | 365×6 |
| Average time AT | d | 2190 |
| Lifetime LT | d | 25550 |
| Average body weight BW | kg | 16 |

Dose-response

Dose-response parameters of the organic volatile compound in toys include reference dose of RfD and the slope factor of SF and both of them come from USEPA's integrated risk information system (IRIS) [26].

RISK CHARACTERIZATION

Carcinogenic risk

In consideration of the various exposure pathways of chemical carcinogen, the health risk model of carcinogenic pollutant [27-28] can be calculated as:

$$R_{ij}^c = 1 - \exp(-SF_i \times Ex_{ij}) \quad (5)$$

where R_{ij}^c is the cancer risk of its chemical carcinogen through the exposure pathways, unitless; Ex_{ij} is the daily exposure dose per unit of

body weight for its chemical carcinogen via the exposure pathways, mg/(kg·d); and SF_{ij} is the carcinogenic potency factor of its chemical carcinogen through the exposure pathways, [mg/(kg·d)]⁻¹.

The total carcinogenic risk of a variety of carcinogens via various exposure routes can be calculated as follows:

$$R^c = \sum_i \sum_j R_{ij}^c \quad (6)$$

Non-Carcinogenic risk

The health risk model of non-carcinogenic pollutant [29] can be calculated as:

$$R^{nc} = \frac{Ex}{Rfd} \times 10^{-6} \quad (7)$$

Where R^{nc} is the no-carcinogenic risk, unitless; Ex is the daily exposure dose per unit of body weight for non-carcinogenic pollutants, mg/(kg·d); and Rfd is the reference dose of the specific chemical substance, mg/(kg·d).

The total no-carcinogenic risk of a variety of no-carcinogens via various exposure routes can be calculated as:

$$R^{nc} = \sum_i \sum_j R_{ij}^{nc} \quad (8)$$

RESULTS AND DISCUSSION

Risk analysis

The non-carcinogenic risk levels of 3 non-carcinogens and 3 carcinogens were calculated using the established risk characterization model of the toys. The results are shown in Table 2.

Table 2. Non-carcinogenic risk levels of VOCs in toys for children aged 1-6.

| Exposure pathways | Toluene | Ethylbenzene | Dimethylbenzene | Benzene | Dichloromethane | Trichloroethylene |
|-------------------|----------|--------------|-----------------|----------|-----------------|-------------------|
| Oral | 2.09E-07 | 1.82E-07 | 4.70E-08 | 2.49E-06 | 1.30E-06 | 2.33E-06 |
| Inhalation | 6.95E-08 | 6.05E-08 | 1.57E-08 | 8.31E-07 | 4.34E-07 | 7.77E-07 |
| Sum | 2.78E-07 | 2.42E-07 | 6.26E-08 | 3.32E-06 | 1.74E-06 | 3.10E-06 |

Table 2 illustrates that non-carcinogenic risk ranking result of VOCs in toys is benzene>trichloroethylene > dichloromethane>toluene> ethylbenzene> dimethyl benzene and the

risk values are 3.32E-06, 3.10E-06, 1.74E-06, 2.78E-07, 2.42E-07, 6.26E-08, respectively. The risk of toluene, ethylbenzene and dimethylbenzene are less than EPA's negligible risk level of 10⁻⁶, so these three kinds of volatile organic compounds do not cause non-cancer health effects on the human body. The non-carcinogenic risk level of benzene, trichloroethylene and dichloromethane were within the USEPA's acceptable risk level of the scope of 10⁻⁴~10⁻⁶ [30] but there also have potential risk to human body.

The carcinogenic risk levels of 3 kinds of carcinogens were calculated using the established risk characterization model of the toys. The results are shown in Table 3.

Table 3. Carcinogenic risk levels of VOCs in toys for children aged 1-6.

| Exposure pathways | Benzene | Dichloromethane | Trichloroethene |
|-------------------|----------|-----------------|-----------------|
| Oral | 2.99E-05 | 5.02E-06 | 4.55E-05 |
| Inhalation | 9.97E-06 | 1.67E-06 | 1.52E-05 |
| Sum | 3.99E-05 | 6.69E-06 | 6.07E-05 |

Table 3 illustrates that the carcinogenic risk ranking result of VOCs is trichloroethylene>benzene>dichloromethane and the risk values are 6.07E-05, 3.99E-05 and 6.69E-06, respectively. The risk levels are within the scope of 10⁻⁶~10⁻⁴, which shows that there is a potential carcinogenic risk to children. In the research of Zhang Qing et al. [31], the carcinogenic risk of benzene is ranging between 1.77E-06 to 5.98E-05 range. The research conclusion of this paper, the carcinogenic risk of benzene 3.99E-05, is just in this section.

The non-carcinogenic and carcinogenic total risk values of VOCs in toys on humans are calculated and compared, and the results are 8.75E-06 and 1.07E-04, respectively. The result illustrates that Rc (carcinogenic total risk level of VOCs in toys) >Rnc (non-carcinogenic risk level of VOCs in toys) and the Rc is 12.3 times as much as Rnc, which shows that cancer risk is the main risk of VOCs in toys. In the risk management of toxic and hazardous substances in toys, the carcinogen should be the first consideration.

It should be also noticed that total carcinogenic risk level exceeds the maximum acceptable risk level of 10⁻⁴ and non-carcinogenic risk level exceeds 10⁻⁶, which may have great impact on the health of children. Relevant government departments should pay close attention to the risk of VOCs in toys.

CONCLUSION

In this paper, the individual exposure risks of 6 kinds of VOCs were evaluated. The results show that the non-carcinogenic risk ranking for VOCs in toys is benzene > trichloroethylene > dichloromethane > toluene > ethylbenzene > xylene and the risk values are 3.32E-06, 3.10E-06, 1.74E-06, 2.78E-07, 2.42E-07, 6.26E-08, respectively. On the other hand, the carcinogenic risk ranking is trichloroethylene> benzene> dichloromethane and the risk values are 6.07E-05, 3.99E-05 and 6.69E-06, respectively. The carcinogenic and non-carcinogenic risk for dichloromethane, trichloroethylene and benzene were between 10⁻⁶ and 10⁻⁴, which indicates that there is potential risk to human. The total carcinogenic risk level of VOCs in toys is larger than total non-carcinogenic risk level, and the average values are 1.07E-04 and 8.75E-06, respectively, exceed the maximum acceptable risk level of 10⁻⁴ and 10⁻⁶. This indicates that there will be great impact on the health of children. Relevant government departments should pay close attention to the risk of VOCs in toys.

It should be noted that the human health risk assessment is an iterative process having lots assumptions. Health risks may have been overestimated or underestimated due to the fact that the risks calculated based on the chemical concentrations measured in a short time were compared to specified risks developed based on the toxicological data established for exposures over a lifespan. On the other hand, the potential cumulative effects and combined effects of each volatile organic compound should be evaluated. The uncertainties in toxicological indices also contributed to overestimating or underestimating risks. We still need to make a deep study of this direction.

Acknowledgements: The author thanked the AQSIO Defective Product Administrative Center for financial and instrumental supports by the Fundamental Research Funds of China National Institute of Standardization titled *Research on Early Warning Model of Consumption Based on Risk Assessment of Defective Products* (No. 282016Y-4701).

REFERENCES

1. Y. Feng, *China Personal Protective Equipment*, **6**, 23 (2010).
2. L. Yongjian, L. Shili, *Chinese and foreign toy manufacture*, **12**, 72 (2009).

3. J. Hoshi, S. Amano, Y. Sasaki, T. Korenaga, *Environ.* **42**, 2383 (2008).
4. H.T. Nguyen, K. Kim, M. Kim, *J. Hazard. Mater.*, **161**, 163 (2009).
5. E. Choi, K. Choi, S.M. Yi, *Atmospheric Environment*, **45**, 7563 (2011).
6. C.L. Huang, J.F. Xue, Y.Q. Lin, et al. *Prevention of occupation disease harm handbook*, 194 (2004).
7. B. Xu, Y.J. Luo, F.Y. Hu. *Occupational Health and Emergency Rescue*, **23**, 22 (2005).
8. L.G. Bai. *Chinese Journal of Industrial Medicine*, **18**, 189 (2005).
9. Wolkoff P. *International Journal of Hygiene and Environmental Health*, **216**, 371 (2013).
10. M. Allen, A. Braithwaite, C. Hills, *Environ. Sci. Technol.* **31**, 1054 (1997).
11. B. Eklund, E. Anderson, B. Walker, D.B., *Environ. Sci. Technol.* **32**, 2233 (1998).
12. M. Chweigkofler, R. Hardniessner, *Environ. Sci. Technol.* **33**, 3680 (1999).
13. S.C. Zou, S.C. Lee, C.Y. Chan, K.F. Ho, X.M. Wang, L.Y. Chan, Z.X. Zhang, *Chemosphere* **51**, 1015 (2003).
14. D.A. de la Rosa, A. Velasco, A. Rosas, T. Volke-Sepulveda, *Atmos. Environ.* **40**, 2079 (2006).
15. Durmusoglu E, Taspinar F, Karademir A., *Journal of Hazardous Materials*, **176**, 870 (2010).
16. X.Z. Chen, X.L. Lin, Z.H. Zheng, et al. *Standard Science*, **1**, 60 (2013).
17. X.H. Zeng, X.Z. Chen, J. Li, et al. *Standard Science*, **7**, 37 (2015).
18. W.Y. Zhang, Y. Li, L. Liu, et al. *Chinese Journal of Analytical Chemistry*, **31**, 212 (2003).
19. Y.H. Xu, B.H. Zhu, X.H. Zhong, et al. *Chinese Journal of Chromatography*, **28**, 73 (2010).
20. Z.G. Lu, J.H. Cai, Y.H. Feng, et al. *Dyeing & Finishing*, **8**, 39 (2009).
21. H.Q. Wu, Z.X. Zhu, X.L. Huang, et al. *Journal of Instrumental Analysis*, **27**, 705 (2008).
22. US EPA, 1997. *Exposure Factors Hand Book*. Washington, D.C.
23. Smith, S.A., Norris, B., *Injury Control and Safety Promotion*, **10**, 145 (2003).
24. Tulve, N.S., Suggs, J.C., McCurdy, T., Cohen, H., Moya.J., *Expo Anal Environ Epidemiol*, **12**, 259 (2002).
25. Xiaoli, D., Nan, H., Beibei, W., *Journal of environment and health*. **29**, 99 (2012).
26. US EPA, Integrated Risk Information System (IRIS), U.S. Environmental Protection Agency (USEPA), Available at <https://www.epa.gov/iris>, 2016.
27. Yiwen, W., Tianfang, K., Zhongliang, Z., Pengna, L., Yan, Z., *Research of environmental sciences* **22**, 150 (2009).
28. Qiulian, W., Zhen, Z., Wei, L., *Research of Environmental Science*, **32**, 187 (2009).
29. Bin, Z., et al., *Geography and Geographic Information Science*, **25**, 94 (2009).
30. Chen, S.C., Liao, C.M., *The Science of Total Environment*, **366**, 112 (2006).
31. Q. Zhang, W.T. Li, H. Bai, *Journal of safety and Environment*, **13**, 254 (2013).

Study of enhancing excess sludge broken walls by alkali coupling organic solvents

J.C. Tu¹, J. Lin^{2*}, F. Wei¹, G. Cheng¹, G. Zeng², H. Wei¹

¹Nanchang Water Industry Group Co., Ltd, Nanchang, Jiangxi, PR China, 330025

²School of Chemistry & Chemical Engineering, Jingtangshan University, Ji'an Jiangxi, PR China, 343009

Received May 25, 2017; Revised July 20, 2017

Targeted at excess sludge, this paper studies the influence of different organic solvents, different addition ways and different processing time on the broken walls of excess sludge. With SCOD and SCFAs representing the effects of broken walls, the result shows that under the temperature condition of 30 °C, compared with the blank control, the pretreatment by methanol - alkali, alkali - methanol, acetone - alkali, alkali - acetone can increase the production of SCOD and SCFAs greatly, which affects the percentage composition of each monomer acid in SCFA. If the methanol treatment follows the alkali treatment (pH=10.0), the production of acetic acid reaches 90mgCOD/gVSS and it accounts for 50% of the total SCFAs, whose effect is better than that when the alkali treatment follows the methanol treatment and the propanol treatment follows the alkali treatment. Thus, when carrying out the wall-breaking on the excess sludge, the method of the methanol treatment after the alkali treatment should be adopted.

Key words: excess sludge; cell disruption; organic solvents

INTRODUCTION

Activated sludge process is widely used in the field of wastewater treatment in china, which has caused a large number of excess sludge. The problem of dealing with excess sludge has become a hot topic with much attention currently [1, 2]. It is found in the study that the protective effect of cell walls of the microorganisms in the sludge hinders the release and utilization of organics in the sludge. The pretreatment on the sludge can damage the structure of cell membranes, which releases the intracellular substance and improves the hydrolysis rate. The pretreatment mainly includes ultrasonic, pyrolysis, microwave, supercritical oxidation, adding alkaline, etc. [3-5]. This study adopts the alkali coupling organic solvents to break cell walls and uses SCOD and SCFAs to represent the effect of wall-breaking.

EXPERIMENTAL

Instrument and reagents

The dichromic acid at reference level, ferrous sulfate ($\text{FeSO}_4 \cdot 7\text{H}_2\text{O}$), ammonium ferrous sulfate [$(\text{NH}_4)_2\text{Fe}(\text{SO}_4)_2 \cdot 6\text{H}_2\text{O}$], concentrated sulfuric acid, concentrated hydrochloric acid, silver sulfate powder, phenanthroline, mercury sulfate, yeast extract, tetrahydrofuran, acetone, methanol, ethyl alcohol, petroleum ether, COD constant temperature heater, drying oven, COD digestion apparatus, ultraviolet and visible spectrophotometer, 1 gas chromatograph (Shanghai Tianmei Scientific Instruments Co., Ltd.)

and 1 constant temperature shaking table.

Experimental methods

The experiment makes use of 7 reaction bulbs (suction flasks) with an effective volume of 500 mL and the number is set as R0, R1, R2, R3, R4, R5, R6 respectively. There is a parallel experiment for all 4 different pretreatment. R0 is the blank control and the pH of the excess sludge will not be regulated artificially. For R1, methanol (1%) will first be added into the excess sludge and then add sodium hydroxide for alkaline (pH = 10.0) with each maintaining 4d. For R2, the excess sludge will first be changed to alkaline (pH = 10.0) and then add methanol (1%) with each maintaining 4d. For R3, methanol (1%) is added to the excess sludge and then maintains alkaline (pH=10.0). After 8d, acetone (1%) will be added to the excess sludge of R4 firstly and then add sodium hydroxide for alkaline (pH=10.0) with each maintaining 4d. The excess sludge of R5 will first be changed to alkaline (pH=10.0) and then add acetone (1%) with each maintaining 4d. For R6, the excess sludge will maintain alkaline (pH = 10.0) for 8d after being added acetone (1%).

Pretreatment conditions: Add 250 ml of sludge to each reaction bulb and regulate the pH of sludge with 4.0 mg L⁻¹ of NaOH and 4.0 mg L⁻¹ of HCl. The blank control will not be adjusted. During the regulation process, the pH meter will be used to evaluate the pH of the sludge. Before pH is no stable, it will be measured every 2 hours for the first day. Adjust after one measurement in order to keep the pH in the range of requirements.

Using 500 mL of the suction flask as reactor, the cork of the suction flask links the latex tubing and

* To whom all correspondence should be sent:

E-mail: 1980058159@qq.com

directly connects water-sealed equipment to make the fermentation system in the anaerobic situation, which can be shown in figure 1. The suction flask is placed in the water-bath constant temperature shaking table at 30 °C with the rotating speed of 180r/min. Shaking can make the mixture inside the bottle fully contacted. The schematic diagram of the experimental device is as follows:

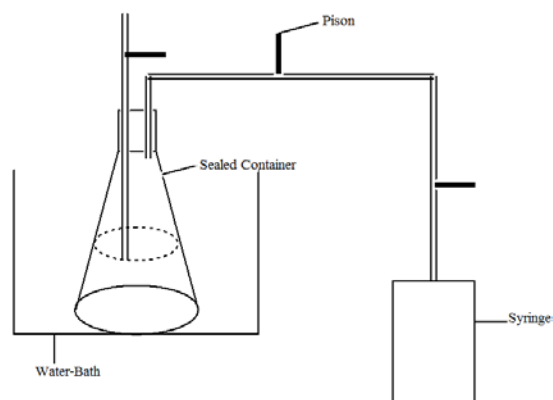


Fig. 1. Experimental device

Representation and measurement

National standard method is used to measure pH, TSS, VSS, SCOD, TCOD, PO₄³⁻-P and total nitrogen(SEPAC, 2006). Gas chromatograph GC7890II is used to measure the components of SCFAs. The carrier gas is nitrogen and the detector is FID. The chromatographic column is 30m×0.32mm×0.5mmTM-FFAP and the temperature of sample injector and detector is set at 200°C and 220°C respectively. The furnace temperature will run for 5 min at 110°C and then rise to 220°C at a speed of 5°C /min and the sample is injected 1.0 μL per time [6].

RESULTS AND DISCUSSION

Influence of different processing methods on the SCOD dissolution of excess sludge

Figure 2 reflects the SCOD concentration in each reaction bulb with the change of fermentation time when the excess sludge is under different pretreatment conditions. It can be seen from figure 2 that after 4d, it is adjusted to alkaline (PH=10.0). During the fermentation time in the first 2d, the SCOD of the excess sludge in the reaction bulb R2 and R5 grows fastest, probably because the alkaline environment leads to the rapid wall-breaking by biological microorganism extra-membrane substances and the rapid increase of SCOD concentration. It reaches around 3985 mg L⁻¹ in the 8th day. Two days ago, except the blank control of R0, the release intensity of other treatment methods is relatively bigger. The intensity of R1, R3 and R5

is basically same and then the slow-down is almost the same. The reason is that both the organic solvents and alkaline environment can lead to the rupture of membranes of biological bacteria and in the 4th day, the intensity increase of R1, R2, R3, R4, R5 and R6 is almost the same, because under different environmental conditions with alkaline sequence, the microbial cell walls in the sludge is more easily broken to release SCOD.

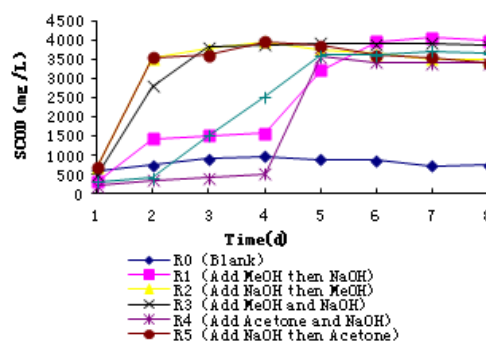


Fig. 2. Changes of dealing with SCOD by different methods

Influence of different processing methods on the content of SCFAs in the excess sludge

After the acid or alkali treatment, the SCFAs produced by the excess sludge mainly consist of fatty acids linearly chained or branched chained with 2 to 5 carbon atoms, such as acetic acid, propionic acid, isobutyric acid, n-butyric acid, isovaleric acid and n-valeric acid, etc. [7]. After being dealt with for 4d and 8d by different methods, the situation of SCFAs in the fermentation system of the sludge in the reaction bulb can be seen in figure 3 and figure 4.

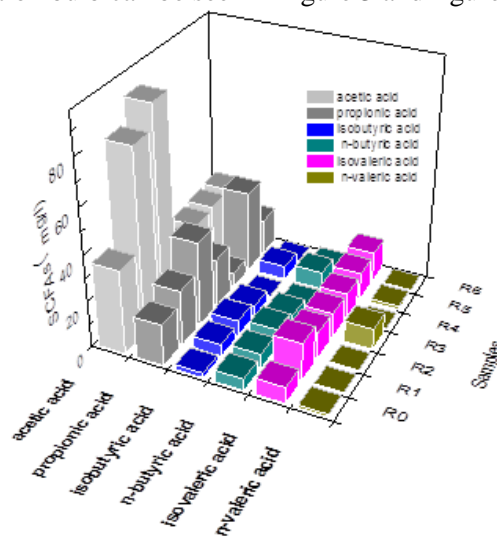


Fig. 3. Influence of different processing methods on the content of SCFAs after 4d.

As shown in figure 3, R1 and R2 produces the largest amount of acetic acid and propionic acid in the first 4d. But the rapid of breaking the microbial

cell membrane is not fast, probably because the influence of the chemical action time leads to the differences of acid production by biological fermentation.

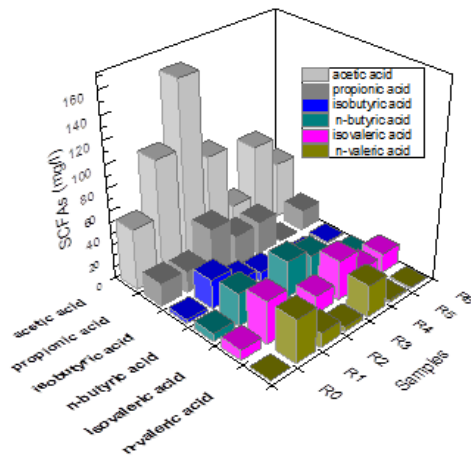


Fig. 4. Influence of different processing methods on the content of SCFAs after 8d

It can be seen from figure 4 that the production of acetic acid and propionic acid by 6 different processing methods is much bigger compared with the blank control. The productivity of acetic acid of R1 and R2 is relatively larger. In the 8th day of fermentation, the production of acetic acid of R2 reaches 160 mg L⁻¹, accounting for 67% of total acid while that of other groups has few difference. In addition, R5 and R6 hardly produce propionic acid and isobutyric acid. Obviously, within a certain period of time, adding alkali first and followed by organic solvents is more advantageous to produce acid.

Content of nitrogen and phosphorus release

During the hydrolytic acidification process of the excess sludge, the nitrogenous substances such as protein and amino acid will hydrolyze and carry out ammoniation, which generates the corresponding organic acids and release ammonia [8]. Figure 5 reflects NH⁴⁺-N concentration with the changes of hydrolysis acidification time under different processing conditions. It can be seen from figure 5 that under anaerobic conditions, in the fermentation time of 8d, the accumulated concentration of NH⁴⁺-N all increases with the time by three processing methods and blank control. By all processing methods, the NH⁴⁺-N concentration increases quickly in the first 4d and the release intensity reaches 155 mg L⁻¹ in the 6th day. It is because that both the alkaline environment and organic solvents are conducive to the biological organisms to break cell membranes and then the release amount becomes gentle. During the hydrolytic acidification

process of excess sludge, as the microbial substances of main ingredients of excess sludge, the polyphosphates in and outside its cell matrix break up and constantly release orthophosphate [9].

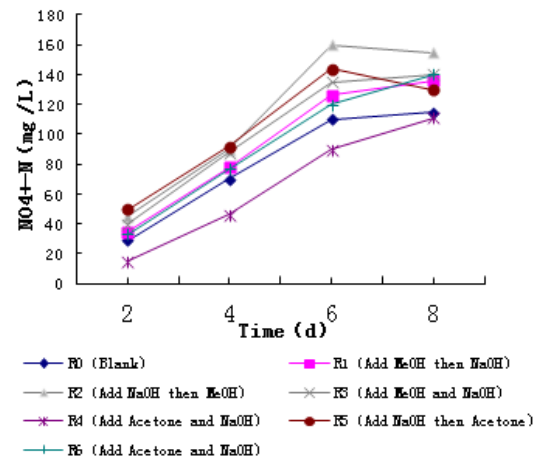


Fig. 5. Change of NH⁴⁺-N concentration with hydrolytic acidification time under different processing conditions

Figure 6 respectively reflects the PO₄³⁻-P concentration and release intensity with the change of time under different processing conditions. PO₄³⁻-P concentration in the sludge mixture by several processing methods all shows a trend of increasing over time and it is particularly significant in the first 2 days. Without the regulation of pH (blank control), the change of release intensity of phosphate is not significant.

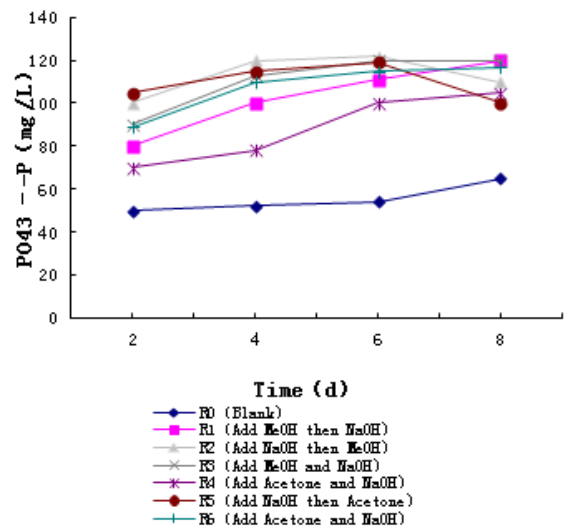


Fig. 6. Change of PO₄³⁻-P concentration with hydrolytic acidification time by different processing methods.

CONCLUSION

Under the condition of temperature 30 °C, compared with the blank control, the pretreatment by

MeOH-NaOH, NaOH-MeOH, acetone-NaOH, NaOH-acetone can increase the production of SCOD and SCFAs greatly, which affects the percentage of each monomer acid in SCFA. If the MeOH treatment follows the NaOH treatment (pH=10.0), the production of acetic acid reaches 90mg COD/gVSS and it accounts for 50% of the total SCFAs, whose effect is better than that when the NaOH treatment follows the MeOH treatment and the acetone treatment follows the NaOH treatment. Thus, when carrying out the wall-breaking on the excess sludge, the method of the MeOH treatment after the NaOH treatment should be adopted.

After 8d of pretreatment, the NH_4^+ -N and PO_4^{3-} -P concentration dissolved by NaOH-MeOH processing method is higher than that by the blank control, NaOH-acetone and MeOH-NaOH processing methods. Using magnesium ammonium phosphate (MAP) can be helpful to recycle more struvite with economic application value.

Acknowledgements: The author thanked the

Jiangxi science and Technology Department of China for financial supports (20141BBE50010, 20151BBE51026).

REFERENCES

1. K. Wang, Y. Meng, J. Zou, G. Li, *China Resources Comprehensive Utilization*, **6**, 44 (2012).
2. J. Yu, N. Tian, K. Wang, *J. Environ. Eng. China*, **1**, 82 (2007).
3. Y.C. Chiu, C.N. Chang, J.G. Lin, S.J. Huang, *Water Sci. & Technol.*, **36**, 155 (1997).
4. L. Guo, X.M. Li, X. Bo, Q. Yang, G. M. Zeng, D. X. Liao, J. J. Liu, *Bioresource. Technol.*, **99**, 3651 (2008).
5. Y. W. Wang, Y. S. Wei, J. X. Liu, *J. Hazard. Mater.*, **169**, 680 (2009).
6. S.E.P.A. China, *China Environ. Sci. Press*, **27**(2), 200 (2006).
7. H. Yuan, Y. Chen, H. Zhang, S. Jiang, Q. Zhou, G. Gu, *Environ. Sci. Technol.*, **40**, 2025 (2006).
8. H. Yuan, L. Wu, J. Yuan, S. Niu, L. Sun, *J. Environ. Eng. China*, **6**, 3287 (2012).
9. A. Spataru, R. Jain, J. W. Chung, G. Gerner, R. Krebs, P. N. L. Lens, *RSC ADV*, **6**, 104 (2016).

Research on the action mechanism of air core and experiments of separation performance inside multi-product cyclone with double vortex finders

Y.K. Zhang, P.K. Liu*, X.H. Yang, L.Y. Jiang, Y.L. Zhang, J.R. Yang

Shandong University of Science and Technology, Qingdao, China

Received June 23, 2017; Revised July 20, 2017

Narrow particle size separation is one of the principal means in boosting the efficiency and accuracy of beneficiation, with cyclone as currently the main equipment for particle classification. The traditional hydrocyclone can only obtain two products: overflow and underflow, which is not able to meet the requirements of fine classification. A new multi-product cyclone was proposed to improve the separation precision and efficiency. This multi-product cyclone was constitute of two-stage series: the primary cyclone which contains two coaxial overflow tubes with different diameters and the secondary general cyclone. Then, by utilizing the numerical simulation, the action mechanism of air column in the cyclone with two overflow tubes was researched according to a new flow field model. Finally, a “three-level-four-factor” orthogonal experiment of measuring the separation effect and the influence factors was carried out. Results show that one classification can obtain four different narrow-grade-classification products: primary underflow, primary overflow, secondary underflow, and secondary overflow. The formation and evolution process of the air core inside of two-overflow-tube cyclone is an important symbol of the stable flow field. The structural parameters and operating pressure are proven to play a significant role in the separation precise and efficiency of the multi-product cyclone. The experiments demonstrate that the proposed cyclone is effective for separation efficiency. The research results can provide a good guidance for separation performance and industrial application of multi-product cyclone separator.

Keywords: Multi-product cyclone , Numerical simulation, Orthogonal experiments.

INTRODUCTION

Narrow-grade-classification is one of the important methods in improving the efficiency and accuracy of beneficiation, with cyclone as currently the main equipment for particle classification [1]. cyclones have been widely used as particle size classification, density separation, slurry concentration and liquid clarification apparatus on solid-liquid flow in the field of mineral processing [2], coal engineering [3], chemical engineering [4], and process industries [5] because of their simple structure, absence of moving parts, high separation efficiency, large work capacity, small separation size, low investment, low maintenance costs and no environment pollution [6~8]. Plenty of parameters can affect the performance of the flow field of cyclones. Among all the parameters, structural style and structural parameters are factors having a great impact on the separation performance of cyclones [9~11]. So study of the influence of structural style and structural parameters of a cyclone on its flow field distribution and separation performance plays a deterministic role in the optimization of a cyclone's design and its normal operation [12~14]. In order to improve the separation performance of cyclones and meet the requirements of different industries, domestic and foreign scholars have designed

cyclones of various structural styles, and conducted in-depth researches on their structural parameters.

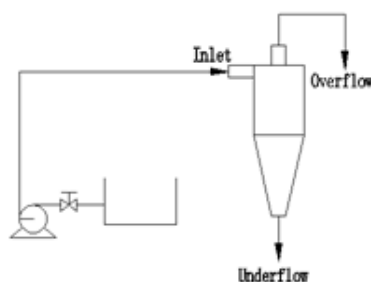


Fig. 1. Classification diagram of the traditional cyclone

From the literature research, it reveals that traditional cyclones [15~17] can only get two products from a single classification, as shown in Fig.1. Owing to its over broad definition of product particle grading range, this method was not able to meet the requirements of fine classification. To solve the problem of over broad range and obtain products with more categories of narrow particles, people usually connect several cyclones in series, as shown in Fig.2.

Although this process flow obtained four products of different sizes, it requires in addition 2 cyclones, 2 slurry pumps, which causes issues like long process flow, high investment in equipment, high energy consumption, etc. How could a cyclone obtain multiple products with narrow grading from

* To whom all correspondence should be sent:
E-mail: lpk710128@163.com

a single classification, so as to satisfy the requirement of different separation equipment on the size range of feed particles, D.P. Obeng et al. [18, 19], Mainza A. et al. [20], Ahmed et al. [21] proposed a three-product cyclone with two coaxial vortex-finder of different diameters, and three different size narrow-grade-classification products were obtained.

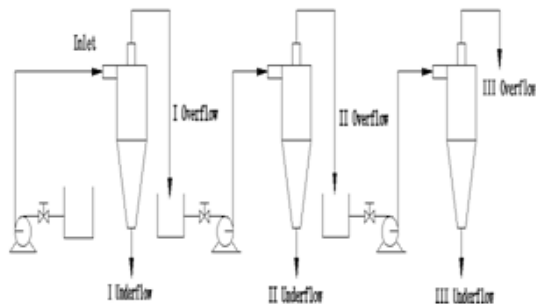


Fig. 2. Classification diagram of the three-stage multi product cyclone.

However, Investigation of a multi-product cyclone separator is seldom reported in existing literature. Structural parameters of cyclone and inlet operating pressure have a great effect on separation efficiency of the cyclone during use in power plants. All the mentioned above studies did not research the forming mechanism of the air core and did not consider the influence of structural parameters and operating pressure on the separation efficiency. Thus, improved work must be studied to examine the influence of the structural parameters and operating pressure on separation precise and classification efficiency of the cyclone with double vortex finders.

How a cyclone could obtain multiple products with narrow grading particles from the one-step classification, has become an urgent research problem. Therefore, the paper proposed a two-stage series multi-product hydrocyclone, as shown in Fig.3.

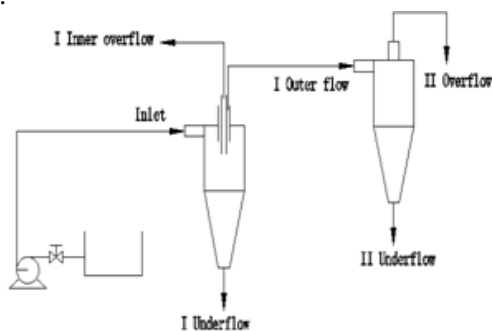


Fig. 3. Classification diagram of the multi-product cyclone.

The stage I cyclone was designed as a coaxial double vortex finders structure with different diameters. During overflow, light and fine particles exit from the inner vortex finder. The mid-size particles overflow from the outer overflow tube into the secondary cyclone. Finer classification can be obtained under the effect of residual pressure. Therefore, one-step classification can obtain four different narrow-grade-classification products: Stage I underflow, Stage I overflow, Stage II underflow, and Stage II overflow.

EXPERIMENTAL

Stage I of the cyclone is designed as a coaxial double-overflow-pipe structure, with the structural drawing sketched in Fig.4 and the structural parameters specified in Table 1.

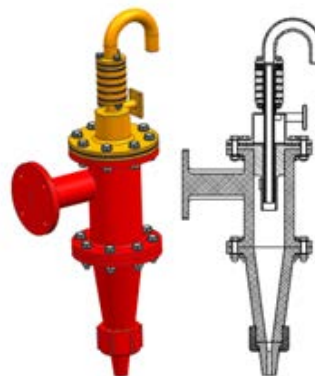


Fig. 4. Main structural parameters of the cyclone.

Table 1. Main structural parameters of the cyclone with double vortex.

| Structural parameter | Structural dimensions |
|--|-----------------------|
| Hydrocyclone diameter (mm) | 50 |
| Inner vortex finder diameter (mm) | 5, 6, 7, 9, 10 |
| Outer vortex finder diameter (mm) | 20 |
| Underflow port diameter (mm) | 6, 8, 10, 12 |
| Feed inlet equivalent diameter (mm) | 12 |
| Outer overflow pipe insertion depth (mm) | 85 |
| Inner overflow pipe insertion depth (mm) | 65, 75, 85, 95, 105 |
| Cylinder height (mm) | 116 |
| Total height (mm) | 310 |
| Cone angle of hydrocyclone (°) | 15 |



Fig. 5. The general cyclone

Fig. 6. Multi-product cyclone

Stage II of the cyclone adopts the conventional conical or cylindrical structure with a diameter of 25 mm, as shown in Fig.5. A multi-product cyclone is created by joining the two stages of cyclones, as shown in Fig. 6.

Fig.7 shows the calculation region model of double overflow pipe cyclones. The hexahedral structure grid was used in the calculation flow field, the meshing results of the cyclone were obtained as shown in Fig. 8 and total grid number was 145087 in the model of the double vortex finders cyclone.

The boundary conditions are defined as follows:

The inlet boundary condition: The inlet was set as the velocity inlet condition with a fluid velocity of 5 m/s.

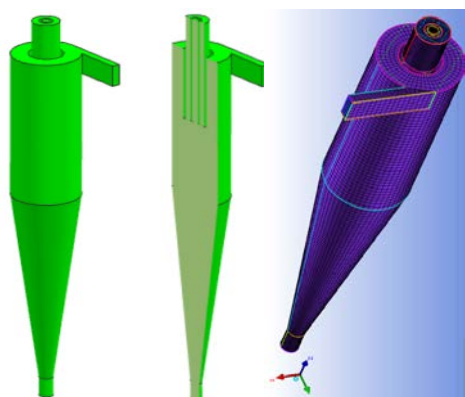


Fig. 7. The calculation flow field model

Fig. 8. Meshes of the cyclone

The outlets boundary condition: The pressure outlet boundary condition was applied for the both overflow and underflow ports boundary.

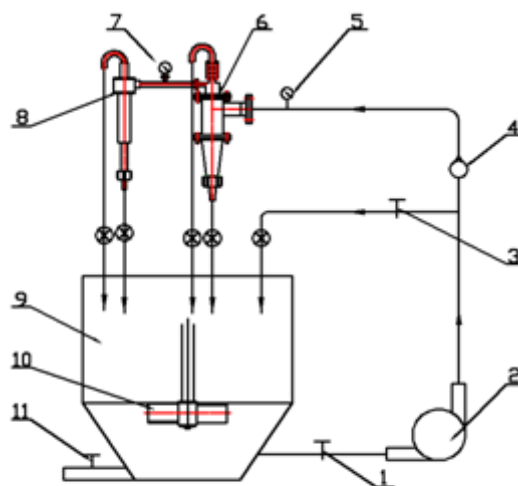
Wall modification condition: The near wall surface modification was simulated by “Standard Wall Functions”.

The discretization schemes are selected as follows:

Governing equations were solved by the finite volume method using the FLUENT software 6.3. In

the numerical simulations, the “SIMPLE” pattern was selected for the pressure-speed coupling. the pressure discretization of the governing equations were used the “PRESTO” method. The Reynolds stress discretization was solved by the first-order upwind scheme and the momentum discretization was selected the “QUICK” method. Besides, VOF (Volume of Fluid) flow model was adopted to capture the interface between air and water in the cyclone. The primary phase was set as water while the secondary phase was set as air.

Testing method



1-Valve, 2-Pump, 3-Valve, 4-Flowmeter, 5-Pressure gauge, 6-Hydrocyclone, 7-Pressure gauge, 8-Hydrocyclone, 9-Mixing tank, 10-Mixing impeller,11-Valve.

Fig. 9. Test system diagram.



Fig. 10. The test site image of the cyclone.

Fig.9 and Fig.10 is respectively the testing system sketch and local test image. The testing system consists of pumps, valves, pressure gauges, flow meters and the multi-product cyclone, etc. The slurry pump extracted the prepared fly ash slurry

from the slurry pool, through adjustment of the opening of the reflux valve and the frequency converter, stabilized the pressure at the test required inlet pressure value. After the system operated normally, we sampled at the overflow port and also at the underflow port. By using equipment like vacuum pumping and filtering system, dry box, electronic scales for test use and laser particle size analyzer, we measured the slurry concentration, particle size, flow rate, and other indices of the outputted products.

After the cyclone run stability for about 10 minutes, we sampled respectively from the underflow outlet port and overflow outlet port of the hydrocyclone, and assessed the concentration and particle size of the products. During the analysis on the collected samples, two parallel measurements were conducted on the same specimen. If the difference of the two measurements did not exceed the error tolerance of the same test, we took the arithmetic mean of them as the final results.

RESULTS AND DISCUSSION

Action mechanism of air core inside cyclone and influence of underflow diameter on the air column

The underflow port of a cyclone is one of the important factors that affect its separation index. In particular, the diameter of the underflow port has a significant effect on the cyclone's separated particle size and product distribution, which makes the study of the effect of underflow diameter on flow field especially important. In the paper, taking a double vortex finders cyclone as the research object, the study used software FLUNT6.3. A cyclone is selected with an overflow pipe diameter of 6 mm and an inserted depth of 85 mm. Five different working conditions are investigated with the underflow diameters configured to be 6 mm, 8 mm, 10 mm and 12 mm respectively. The formation mechanism of the air column in the cyclone and the effect of underflow diameter on the properties of the air column are discussed.

Fig.11(a) to Fig.11(d) demonstrate the forming and developing processes of the air column in a double-overflow-pipe cyclone corresponding to different underflow diameters of 6 mm, 8 mm, 10 mm and 12 mm. Initially the cyclone is full of air (blue area). With the development of the flow field, the internal space of the cyclone is gradually filled by liquid (red area). When negative pressure appears in the center of the cyclone, air enters the cyclone from its overflow and underflow ports, and gradually runs through the axis of the cyclone. It

can be seen from the figures that, the air column fluctuates and appears unstable when air just begins to run through; ultimately it stabilizes and becomes complete with the progress of separation process, which means that a stable flow field is generated. Regarding the formation and development mechanism of air column, researchers always hold different opinions. However, it can be concluded through the simulation done in this paper that, the overflow and underflow ports contribute in generating the air column, and the negative pressure in the cyclone is the necessary condition for the formation of air column. It can also be observed from the figures that, the axis of the air column almost coincides with the axis of the cyclone. In addition, the size and shape of the air column changes with the development of the flow field. Even after the flow field stabilizes, the air column still has different diameters at different axial positions, which shows the maximum value at the bottom of the overflow pipe. The diameter of the air column gradually becomes smaller in the overflow pipe until it reaches the junction of the pipe and cone, where obvious disorder occurs to the air column diameter. The paper attributes the variations in the size and shape of the air column to, on one hand the instability of the flow field, on the other hand the structure variation of the cyclone itself.

The formation time of air columns corresponding to cyclones with different underflow diameters is also analyzed. For underflow diameters of 6mm, 8mm, 10mm and 12mm, the formation of air column requires 1.9 s, 1.8 s, 1.65 s, and 1.6 s respectively. It indicates that a bigger underflow port requires a shorter period of time to generate the air column. From another point of view, due to the constant taper angle of the cyclone, a bigger underflow diameter implies a shorter distance between the underflow and overflow ports. So it takes a shorter time for the air column to run through between the underflow and overflow ports, and the formation of the air column becomes easier.

Orthogonal test results and discussion

The main factors affecting the performance of a multi-product cyclone are: underflow port diameter, inner overflow pipe diameter, inner overflow pipe insertion depth and feed pressure.

Such many combinations of structure parameters and operation parameters will undoubtedly require many tests and lots of work. In order to reduce the number of tests without compromising the test credibility, the paper conducted orthogonal test to comprehensively evaluate and analyze the

influential factors, to find the primary and secondary factors affecting the separation performance, and determine the best parameter combination of the hydrocyclone.

In this paper, we carried out a three-level four-factor test with the corresponding parameter values as follows: Underflow port diameter (6mm, 10mm, 14mm); Overflow pipe insertion depth (65mm, 85mm, 105mm); Overflow pipe diameter (5mm, 7mm, 9mm); Pressure (0.12MPa, 0.16MPa, 0.20MPa).

Following the testing plan of the orthogonal experiment table, we deployed Stage I underflow yield as the single evaluation indices, conducted numerical analysis on the raw data obtained from test results, and derived the processed test results shown in table 2.

Table 2 presented the orthogonal test results of a

multi-product hydrocyclone taking underflow yield as the evaluation index. By analysis, we can draw the following conclusion. The best structure parameters and inlet pressure of a multi-product hydrocyclone are: underflow pipe diameter 14mm (A3), overflow pipe insert depth 105mm (B3), overflow pipe diameter 9mm (C3), inlet pressure 0.20MPa (D3).

Comparing the average peak value R, we can see that the underflow port diameter of a hydrocyclone is the most important factor affecting Stage I underflow yield. As the underflow port diameter increased, the Stage I underflow yield also increased. Among the rest of the factors, the order of significance to Stage I underflow yield is, feed pressure followed by overflow pipe insertion depth, and the least significant factor is Stage I Inner overflow pipe diameter.

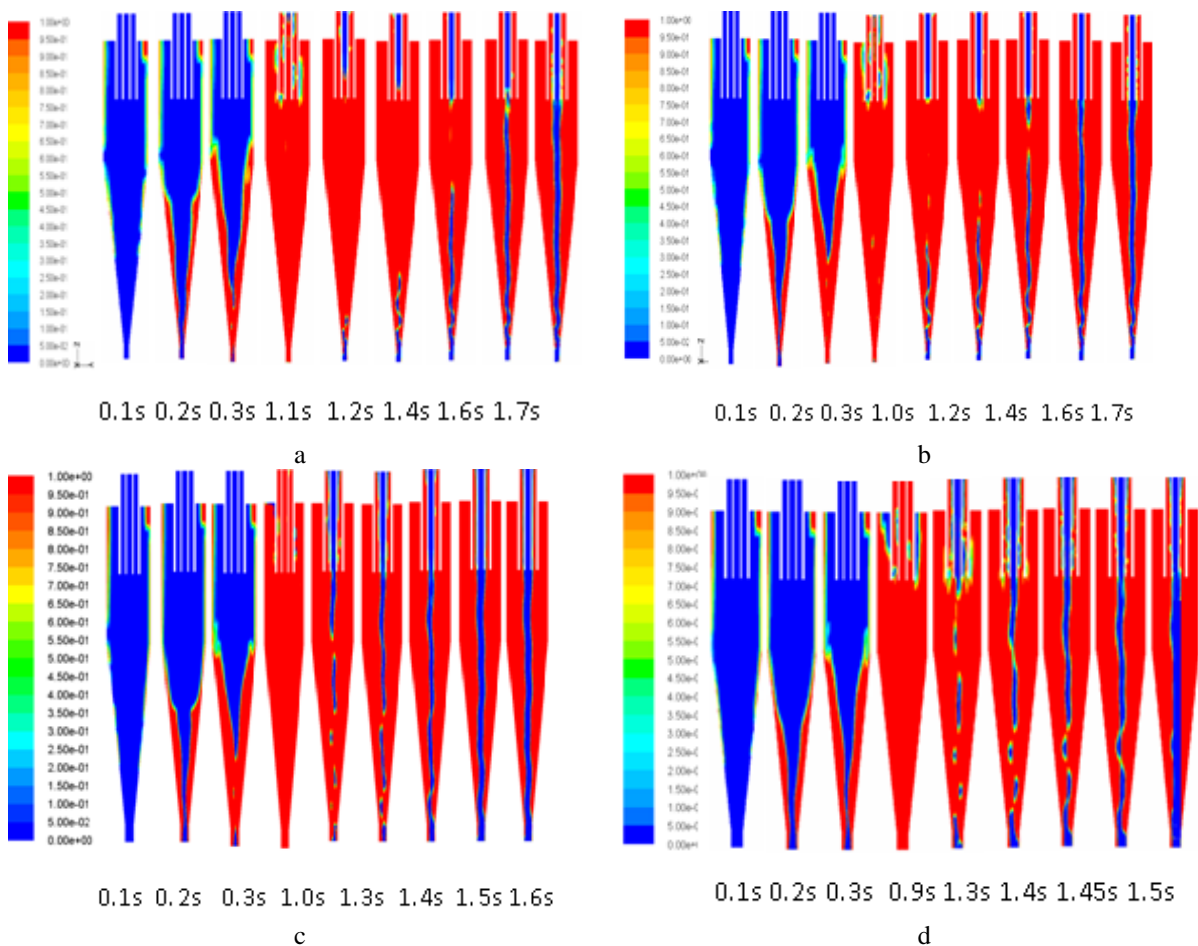


Fig. 11. The development of air column in the cyclone with diameter spigot a) 6 mm; b) 8 mm; c) 10 mm; d) 12 mm

Table 2. The orthogonal experiment of taking the first stage yield of spigot as assessment index.

| Period | Underflow port diameter (mm) | Overflow pipe insertion depth (mm) | Overflow pipe diameter (mm) | Pressure (MPa) | Stage I underflow yield (%) |
|----------------|------------------------------|------------------------------------|-----------------------------|----------------|-----------------------------|
| | A | B | C | D | |
| 1 | 1 (6) | 1 (65) | 1 (5) | 1 (0.12) | 62 |
| 2 | 1 (6) | 2 (85) | 2 (7) | 2 (0.16) | 61 |
| 3 | 1 (6) | 3 (105) | 3 (9) | 3 (0.20) | 94 |
| 4 | 2 (10) | 1 (65) | 2 (7) | 3 (0.20) | 78 |
| 5 | 2 (10) | 2 (85) | 3 (9) | 1 (0.12) | 73 |
| 6 | 2 (10) | 3 (105) | 1 (5) | 2 (0.16) | 75 |
| 7 | 3 (14) | 1 (65) | 3 (9) | 2 (0.16) | 89 |
| 8 | 3 (14) | 2 (85) | 1 (5) | 3 (0.20) | 88 |
| 9 | 3 (14) | 3 (105) | 2 (7) | 1 (0.12) | 88 |
| K_{1j} | 217 | 229 | 225 | 223 | |
| K_{2j} | 226 | 222 | 227 | 225 | |
| K_{3j} | 265 | 257 | 256 | 260 | |
| \bar{K}_{1j} | 72.33 | 76.33 | 75 | 74.33 | |
| \bar{K}_{2j} | 75.33 | 74 | 75.67 | 75 | |
| \bar{K}_{3j} | 88.33 | 85.67 | 85.33 | 86.67 | |
| R | 16 | 11.67 | 10.33 | 12.34 | |

CONCLUSION

In the paper, A new multi-product cyclone was proposed to improve the separation precision and efficiency. The multi-product cyclone can obtain multiple products with different particle grading from one-step classification.

(1) The formation and evolution process of the air column inside cyclone with double vortex finders was conducted.

(2) In the orthogonal test, we deployed Stage I underflow yield as the evaluation indices, optimized and selected the best structure design and reasonable inlet pressure for the multi-product cyclone, and found the primary and secondary factors affecting the separation performance.

(3) Comprehensive analysis revealed that the underflow port diameter had the greatest impact on Stage I underflow yield, the Stage I inner overflow

port diameter had no essential influence on Stage I underflow yield, neither the overflow pipe insertion depth nor the feed pressure is the key influential factor to Stage I underflow yield. To sum up, considering the impact of each factor, and energy consumption reduction for a multi-product cyclone, we confirmed the optimal structure parameters of the multi-product cyclone used in this paper: underflow port diameter 14mm, overflow pipe insertion depth 85mm, inner overflow pipe diameter 9mm, and feed pressure 0.16MPa.

Acknowledgements: This work was supported by the Natural Science Foundation of Shandong province (ZR2016EEM37) and key research and development project of Shangdong province(2016GSF117013).

REFERENCES

1. A. Mainza, M. Narasimha, M.S. Powell, P.N. Holtham, M. Brennan. *J. Minerals Eng.*, **19**, 1048 (2006).
2. K.T. Hsieh, K. Rajamani, *J. International Journal of Mineral Proc.*, **22**, 223 (1988).
3. S. Hore, S.K. Das, R. Singh, K.K. Bhattacharya, *J. International Journal of Coal Preparation and Utilization*, **32**(4), 193 (2012).
4. F. He, Y. Zhang, J. Wang, *J. Chem. Eng. Tech.*, **36**(11), 1935 (2013).
5. Y. Rama Murthy, K. Udaya Bhaskar, *J. Powder Tech.*, **230**, 36 (2012).
6. L. Svarovsky, Hydrocyclones, M. Holt, Rinehart and Winston, London, 1984.
7. Y. Xu, X. Song, Z. Sun, B. Tang, P. Li, J. Yu, *J. Ind. Eng. Chem. Res.*, **52**, 5470 (2013).
8. Hacifazliogluh, *J. International Journal of Coal Preparation and Utilization*, **32**(6), 290(2012).
9. K. Elsayed, C. Lacor, *J. Applied Mathematical Modelling*, **35**, 1952 (2011).
10. P.-K. Liu, L.-Y. Chu, J. Wang, Y.-F. Yu, *J. Chem. Engin. and Techno.*, **31**(3), 474 (2008).
11. M. Ghodrat, S.B. Kuang, A.B. Yu, A. Vince, G.D. Barnett, *J. Ind. Eng. Chem. Res.*, **52**, 16019 (2013).
12. Y.R. Murthy, K.U. Bhaskar, *J. Powder Technol.*, **230**, 36 (2012).
13. F.S. Kılavuz, Ö.Y. Gülsoy, *J. International Journal of Mineral Proces.*, **98**, 163 (2011).
14. Y. Xu, X. Song, Z. Sun, B. Tang, P. Li, J. Yu, *J. Ind. Eng. Chem. Res.*, **52**, 5470 (2013).
15. S.M. Mousavian, A.F. Najafi, *J. Arch Appl Mech*, **79**, 395 (2009).
16. Z. Qi, S.B. Kuang, A.B. Yu. *J. International Journal of Min. Proces.*, **9**(142), 35 (2015).
17. R.K. Dwari, M.N. Biswas, B.C. Meikap, *J. Chem. Eng. Sci.*, **2**(59), 671 (2004).
18. D.P. Obeng, S. Morrell. *J. International Journal of Mineral Proces.*, **69**(3), 129 (2003).
19. D.P. Obeng, S. Morrell, T.J. Napier-Munn, *J. International Journal of Mineral Proces.*, **76**(6), 181 (2005).
20. A. Mainza, M.S. Powell, B. Knopjes, *J. Minerals Engineering*, **17**(6), 573 (2004).
21. A. Mahmoud, M. Ibrahim, A. Galal, M.G. Farghaly, *J. International Journal of Mineral Proces.*, **91**(4), 34 (2009).

Calculation of growth process of nanostructured materials

W. Li

School of Physics and Electronic Information, Baicheng Normal University 137000 JiLin Baicheng, China

Received June 26, 2017; Revised July 20, 2017

It nanometer is today one of the hot areas of research, through electro deposition method manufacturing Orderly structure With metal and semiconductor properties, Micron from the magnitude of nanotechnology potential direct impact on the distribution of morphology, So conductive pushing the situation on the potential distribution is particularly important. This means using mathematical derivation of the potential distribution of analytical expressions, A reasonable explanation of the prospective growth of 2 dimensional nanostructures structure morphology, The theoretical analysis for the future laid the foundation.

Keywords: Nanostructural Materia, The electricity deposite, The calculator imitate, Grow head, The electricity certainly distributes

AIMS AND BACKGROUND

Preparation of mesoscopic, nano-scale of the microstructure is a concern in recent years. In the many methods used, it is one of the hot spots to study the ordered structure of micrometer to nanometer order with metal and semiconducting properties by electrodeposition. In this paper, the electrosteposition method is used to prepare the ordered array pattern of copper nanostructured material with certain microstructure in the quasi-two-dimensional electrochemical crystallization process. Therefore, the growth characteristics and the growth mechanism are analyzed Is necessary. At present, the preparation of copper nanowires under non-oscillation conditions has been very perfect, but the research on the characteristics and properties of nanostructured materials under different external conditions is relatively few. This paper is to study the growth characteristics and growth mechanism of nanostructured materials under different controlled growth conditions. Different control of growth conditions mainly refers to the input growth voltage amplitude is the same and the frequency is different. It is very meaningful to make a basic study of its vast application space[1].

EXPERIMENTAL

Mathematical model of growth mechanism in one - dimensional case

Crystal growth can be considered to be caused by stable electrical oscillation, assuming that the growth of the container length is l , voltage

is $v_0 \sin \omega t$, the problem can be described as:

$$E_{tt} - a^2 E_{xx} = 0 \quad (1)$$

$$E|_{x=0} = v_0 \sin \omega t \quad (2)$$

$$E|_{x=l} = 0 \quad (3)$$

Because the use of complex numbers to calculate more convenient, Therefore, the boundary condition $v_0 \sin \omega t$ is rewritten as $v_0 e^{i\omega t}$, that is, the imaginary part of the complex number $\text{Im}(v_0 \sin \omega t)$. When the calculation is completed, the imaginary part of the result is the solution of the equation. Since the steady oscillation is caused by the AC power supply, the cycle is the same as the AC power cycle[2]:

$$E(x, t) = X(x)e^{i\omega t} \quad (4)$$

Substituting equation (4) into the ordinary differential equation of X yields: $X'' + (\omega/a)^2 X = 0$

Solving the ordinary differential equation of X:

$$X(x) = Ae^{\frac{i\omega x}{a}} + Be^{-\frac{i\omega x}{a}}, \text{ and so:}$$

$$E(x, t) = \left[Ae^{\frac{i\omega x}{a}} + Be^{-\frac{i\omega x}{a}} \right] e^{i\omega t} \quad (5)$$

Substituting equation (5) into equation (2) yields:

$$[A + B]e^{i\omega t} = v_0 \sin \omega t \quad (6)$$

* To whom all correspondence should be sent:
E-mail: liweiliwei77@163.com

Substituting equation (5) into equation (3) yields:

$$\left[Ae^{\frac{i\omega l}{a}} + Be^{-\frac{i\omega l}{a}} \right] = 0 \quad (7)$$

The imaginary part of expression $E(x,t)$ is the final solution of the equation:

$$E(x,t) = v_0 \frac{\sin \frac{\omega(l-x)}{a} \sin \omega t}{\sin \left(\frac{\omega l}{a} \right)} \quad (8)$$

Mathematical model of growth mechanism in three-dimensional case

Assuming that there is an initial perturbation in region Ω , at time at , the region affected by this disturbance can be described as a sphere with the center of M as the radius and the sphere as the inner envelope and the outer The surface of the surface is the area where the fluctuation has been conveyed, and the outer envelope is the area where the disturbance has not yet been conveyed. The above process is described by the following equation[3]:

Wave equation:

$$E_{tt} - a^2 \Delta E = 0 \quad (9)$$

The equation is implemented by separating the variable method

$$E(r,t) = T(t)v(r) \quad (10)$$

Equation (10) is substituted into equation (9):

$$\frac{T''}{a^2 T} = \frac{\Delta v}{v}$$

Equation on the left is a function of t , the right side of the equation is a function of r , the equation to be established, must be equal to the same constant, the constant as $-k^2$, then get two equations:

$$T'' + k^2 a^2 T = 0 \quad (11)$$

$$\Delta v + k^2 v = 0 \quad (12)$$

The solution of Eq. (11) is:

$$\begin{cases} T(t) = C \cos kat + D \sin kat & (k \neq 0) \\ T(t) = C + Dt & (k = 0) \end{cases}$$

In the spherical coordinate system, the solution

of Eq. (12) is:

$$\frac{1}{r^2} \frac{\partial}{\partial r} \left(r^2 \frac{\partial v}{\partial r} \right) + \frac{1}{r^2 \sin \theta} \frac{\partial}{\partial \theta} \left(\sin \theta \frac{\partial v}{\partial \theta} \right) + \frac{1}{r^2 \sin^2 \theta} \frac{\partial^2 v}{\partial \varphi^2} + k^2 v = 0 \quad (13)$$

Separate variables on variable V :

$$v(\rho, \varphi, z) = R(\rho)Y(\theta, \varphi)$$

Substituting equation (13), Equation (13) is divided by $\left(\frac{r^2}{RY} \right)$ at both ends:

$$\frac{1}{R} \frac{d}{dr} \left(r^2 \frac{dR}{dr} \right) + k^2 r^2 = \frac{-1}{Y \sin \theta} \frac{\partial}{\partial \theta} \left(\sin \theta \frac{\partial Y}{\partial \theta} \right) - \frac{R}{Y \sin^2 \theta} \frac{\partial^2 Y}{\partial \varphi^2}$$

The left side of the equation is a function of r , and the right side of the equation is a function of θ and φ . If the equation holds, the equation needs to be equal to a constant Let the constant be $l(l+1)$:

$$\frac{1}{R} \frac{d}{dr} \left(r^2 \frac{dR}{dr} \right) = \frac{-1}{Y \sin \theta} \frac{\partial}{\partial \theta} \left(\sin \theta \frac{\partial Y}{\partial \theta} \right) - \frac{R}{Y \sin^2 \theta} \frac{\partial^2 Y}{\partial \varphi^2} = l(l+1)$$

Get two equations:

$$\frac{d}{dr} \left(r^2 \frac{dR}{dr} \right) + [k^2 r^2 - l(l+1)] R = 0 \quad (14)$$

$$\frac{1}{\sin \theta} \frac{\partial}{\partial \theta} \left(\sin \theta \frac{\partial Y}{\partial \theta} \right) + \frac{1}{\sin^2 \theta} \frac{\partial^2 Y}{\partial \varphi^2} + l(l+1) Y = 0 \quad (15)$$

Equation (14) is not a standard Bessel equation, and the equation (14) is transformed so that: $x = kr$, Substituting equation (14)

$$x^2 R'' + 2xR' + [x^2 - l(l+1)] R = 0$$

Let $R = \frac{\omega}{\sqrt{x}}$, substitute equation (14)

$$x^2 \omega'' + x\omega' + \left[x^2 - \left(l + \frac{1}{2} \right)^2 \right] \omega = 0$$

Let $v = \left(l + \frac{1}{2} \right)$, substitute equation (14)

$$x^2 y'' + xy' + (x^2 - v^2)y = 0 \quad (16)$$

$x_0 = 0$ is the first order pole of $p(x) = (1/x)$, the second order pole of $q(x) = (1 - v^2/x^2)$, so: $x_0 = 0$ is the regular singularity of the equation

Determine the equation: $s(s-1) + s - v^2 = 0$

Determine the two roots of the equation: $s_1 = v, s_2 = -v$; ($s_1 - s_2 = 2$ or v is an

integer)

$$y(x) = a_0x^s + a_1x^{s+1} + a_2x^{s+2} + \dots + a_kx^{s+k} \dots (a_0 \neq 0)$$

The recursive formula for the coefficients

$$\text{is: } \left[(s+k)^2 - v^2 \right] a_k + a_{k-2} = 0$$

$$a_k = \frac{-a_{k-2}}{(s+k)^2 - v^2} = \frac{-a_{k-2}}{(s+k+v)(s+k-v) - v^2}$$

The general solution of the equation is:

$$y(x) = \sum_{k=0}^{\infty} \frac{(-1)^k}{\Gamma(v+k+1)} \left(\frac{x}{2}\right)^{v+2k} + \sum_{k=0}^{\infty} \frac{(-1)^k}{\Gamma(-v+k+1)} \left(\frac{x}{2}\right)^{-v+2k} \quad (19)$$

The other party said finishing

$$\frac{\sin \theta}{\Theta} \frac{d}{d\theta} \left(\sin \theta \frac{d\Theta}{d\theta} \right) + l(l+1) \sin^2 \theta = \frac{-1}{\Phi} \frac{d^2 \Phi}{d\varphi^2}$$

The left side of the equation is a function of θ , and the right side of the equation is a function of φ [4]. If the equation is to be established, it should be equal to a constant λ :

$$\Phi'' + \lambda \Phi = 0 \quad (20)$$

$$\sin \theta \frac{d}{d\theta} \left(\sin \theta \frac{d\Theta}{d\theta} \right) + [l(l+1) \sin^2 \theta - \lambda] \Theta = 0 \quad (21)$$

Eigenvalue problem of solution

$$\text{equation: } \lambda = m^2 \quad (m = 0, 1, 2, \dots)$$

Eigenfunction:

$$\Phi(\varphi) = A \cos m\varphi + B \sin m\varphi \quad (22)$$

Substituting $\lambda = m^2$ into equation (21):

$$\frac{1}{\sin \theta} \frac{d}{d\theta} \left(\sin \theta \frac{d\Theta}{d\theta} \right) + \left[l(l+1) - \frac{m^2}{\sin^2 \theta} \right] \Theta = 0 \quad (23)$$

Let $\begin{cases} \theta = \arccos x \\ x = \cos \theta \end{cases}$, replace θ with

$$\text{x: } \frac{d\Theta}{d\theta} = \frac{d\Theta}{d\theta} \frac{dx}{d\theta} = -(\sin \theta) \frac{d\Theta}{dx}$$

so:

$$\frac{1}{\sin \theta} \frac{d}{d\theta} \left(\sin \theta \frac{d\Theta}{d\theta} \right) = \frac{1}{\sin \theta} \frac{dx}{d\theta} \frac{d}{dx} \left(-\sin^2 \theta \frac{d\Theta}{dx} \right) = \frac{d}{dx} \left[(1-x^2) \frac{d\Theta}{dx} \right]$$

Equation (23) can be organized as:

$$\frac{d}{dx} \left[(1-x^2) \frac{d\Theta}{dx} \right] + \left[l(l+1) - \frac{m^2}{1-x^2} \right] \Theta = 0 \quad (24)$$

To be further organized as:

$$(1-x^2) \frac{d^2 \Theta}{dx^2} - 2x \frac{d\Theta}{dx} + \left[l(l+1) - \frac{m^2}{1-x^2} \right] \Theta = 0 \quad (25)$$

It is difficult to solve equations by conventional methods (25), Next, we discuss the relationship between equation (25) and equation (26):

$$(1-x^2) y'' - 2xy' + l(l+1)y = 0 \quad (26)$$

According to Leibniz formula:

$$\frac{d^n}{dx^n} [A(x)B(x)] = \sum_{k=0}^n \frac{n!}{(n-k)!k!} \frac{d^{n-k}}{dx^{n-k}} [A(x)] \frac{d^k}{dx^k} [B(x)]$$

m times the equation (26), we can get:

$$(1-x^2)u'' - 2x(m+1)u' + (l-m)(l+m+1)u = 0 \quad (27)$$

It can be seen that the equation (25) is obtained by the differential equation (26), if the general solution of the equation (26)

$$y(x) = d_0 y_0 + d_1 y_1$$

Then the general solution of equation (25) is:

$$y(x) = c_0 y_0^m + c_1 y_1^m$$

among them:

$$\begin{cases} y_0^m = (1-x^2)^{\frac{m}{2}} \frac{d^m}{dx^m} y_0 \\ y_1^m = (1-x^2)^{\frac{m}{2}} \frac{d^m}{dx^m} y_1 \end{cases}$$

Next, the series solution is used to solve the equation (26) in the neighborhood of $x_0 = 0$,

$$y'' - \left(\frac{2x}{1-x^2} \right) y' + \left[\frac{l(l+1)}{1-x^2} \right] y = 0$$

among them:

$$p(x) = \left(\frac{-2x}{1-x^2} \right), q(x) = \frac{l(l+1)}{1-x^2}$$

The solution of the equation is[5]:

$$y(x) = a_0 + a_1 x + a_2 x^2 + \dots + a_k x^k + \dots$$

Further recursion can be:

$$y'(x) = a_1 + 2a_2 x + 3a_3 x^2 + \dots + (k+1)a_{k+1} x^k + \dots$$

$$y''(x) = 2a_2 + 3 \cdot 2a_3 x + 4 \cdot 3a_4 x^2 + \dots + (k+2)(k+1)a_{k+2} x^k + \dots$$

Put these expressions into the equation, the power of the same project merger, you can get:

$$\begin{cases} 2 \cdot 1 a_2 + l(l+1)a_0 = 0 & 3 \cdot 2 a_2 + (l^2 + l - 2)a_1 = 0 \\ 4 \cdot 3 a_4 + (l^2 + l - 6)a_2 = 0 & 5 \cdot 4 a_5 + (l^2 + l - 12)a_3 = 0 \\ \dots & \dots \\ (k+2)(k+1)a_{k+2} + (l^2 + l - k^2 - k)a_k = 0 \end{cases}$$

Recursive formula for the induction coefficient[6]:

$$a_{k+2} = \frac{(k^2 + k - l^2 - l)}{(k+2)(k+1)} a_k = \frac{(k-l)(k+l+1)}{(k+2)(k+1)} a_k$$

and so:

$$\begin{cases} y_0(x) = 1 + \frac{(-l)(l+1)}{2!} x^2 + \frac{(2-l)(-l)(l+1)(l+3)}{4!} x^4 + \dots \\ \frac{(2k-2-l)(2k-4-l)\dots(2-l)(-l)(l+1)\dots(l+2k-1)}{(2k)!} x^{2k} + \dots \\ y_1(x) = x + \frac{(1-l)(l+2)}{3!} x^3 + \frac{(3-l)(1-l)(l+2)(l+4)}{5!} x^5 + \dots \\ \frac{(2k-1-l)(2k-3-l)\dots(1-l)(l+2)\dots(l+2k)}{(2k+1)!} x^{2k+1} + \dots \end{cases}$$

The general solution of equation (26) is: $y(x) = d_0 y_0(x) + d_1 y_1(x)$.

The general solution of equation (25)

is: $y(x) = c_0 y_0^m + c_1 y_1^m$

In summary, the potential distribution in the

whole space is: $E = \{T \cdot R \cdot \Theta \cdot \Phi\}$

$$(1) T(t) = C \cos kat + D \sin kat \quad (k = 0, 1, 2, \dots)$$

$$(2) R = \begin{cases} \sum_{k=0}^{\infty} \frac{(-1)^k}{\Gamma(v+k+1)} \left(\frac{r}{2}\right)^{v+2k} + \sum_{k=0}^{\infty} \frac{(-1)^k}{\Gamma(-v+k+1)} \left(\frac{r}{2}\right)^{-v+2k} & (v \neq \text{Integer}) \\ \left[\frac{2}{\pi} \left(\ln \frac{r}{2} + 0.577216 \right) + 1 \right] \sum_{k=0}^{\infty} \frac{(-1)^k}{k!(v+k)!} \left(\frac{r}{2}\right)^{v+2k} & (v = \text{Integer}) \end{cases}$$

$$(3) \Theta = c_0 y_0^m + c_1 y_1^m$$

The solution of the equation is:

$$\begin{cases} y_0(x) = 1 + \frac{(-l)(l+1)}{2!} x^2 + \frac{(2-l)(-l)(l+1)(l+3)}{4!} x^4 + \dots \\ \frac{(2k-2-l)(2k-4-l)\dots(2-l)(-l)(l+1)\dots(l+2k-1)}{(2k)!} x^{2k} + \dots \\ y_1(x) = x + \frac{(1-l)(l+2)}{3!} x^3 + \frac{(3-l)(1-l)(l+2)(l+4)}{5!} x^5 + \dots \\ \frac{(2k-1-l)(2k-3-l)\dots(1-l)(l+2)\dots(l+2k)}{(2k+1)!} x^{2k+1} + \dots \end{cases}$$

Where: c_0, c_1, l are constants, and $k = 0, 1, 2, \dots$

$$(4) \Phi(\varphi) = \cos m\varphi + \sin m\varphi \quad (m = 0, 1, 2, \dots)$$

RESULTS AND DISCUSSION

The MATLAB language is the most influential and dynamic software in the world today. It is based on matrix operations and has evolved into a

highly integrated computer language. It provides powerful scientific computing, flexible programming flow, high-quality graphical visualization and interface design. The following uses MATLAB 6.0, the third chapter of the mathematical formula derived in the specific boundary conditions were simulated, the following computer simulation and experimental data comparison:

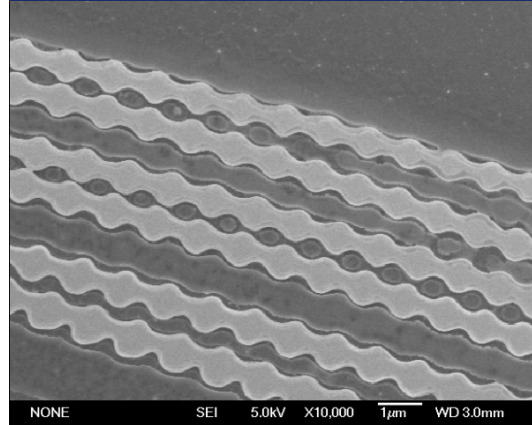


Fig. 1. Water bath temperature: -4.15°C, PH:4.444(Survey temperature: 18.7°C), Density: 50mmol/l CuSO4 Input voltage oscillation amplitude: 0.72V, Frequency: 0.8 Hz growth appearance.

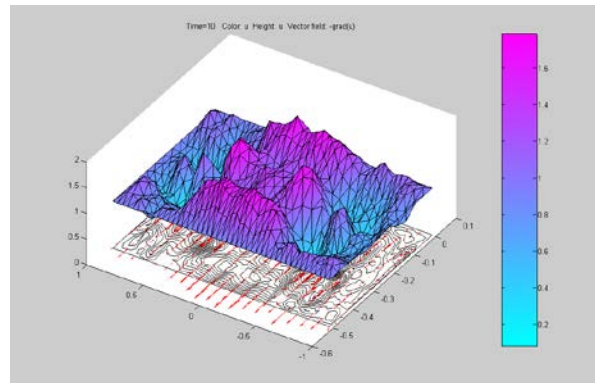


Fig. 2. The potential distribution of the growth front is simulated by MATLAB

The simulation results show that the image is consistent with the crystal growth morphology in the experiment, which verifies the correctness of the mathematical formula. In this paper, the physical model of the nanostructured materials grown by electro deposition was established. Some basic work has been done to study the growth of nanostructured materials[7].

CONCLUSIONS

This text more and completely introduced research general situation, making method and

token method of the Na rice structure material[8]. The making mechanism which counteracts to aim at the structure material of the electricity deposition method making Na rice carried on mathematics to deduce with the emulation of calculator. Make use of the accurate control of the in addition growth electricity power in the quasi- two-dimensional electricity crystallize the process, the making submits to have must the copper Na rice structure material of microstructural have the preface array the pattern, and to grow a characteristics and grew a mechanism to carry on analysis[9]. Finally put forward signal and crystal of the in addition electric voltage to grow the mathematical formula that the sophisticated electricity certainly distributes, counteracted Matlab to carry on emulation to play to show, mainly include a contents:

1. Under the one dimensional circumstance:

$$E(x,t) = v_0 \frac{\sin \frac{\omega(l-x)}{a} \sin \omega t}{\sin \left(\frac{\omega l}{a} \right)}$$

2. Under the one dimensional circumstance, the distribute of electricity power satisfies

$$E = \{T \cdot R \cdot \Theta \cdot \Phi\}$$

Detailed contents:

$$(1) T(t) = C \cos kat + D \sin kat \quad (k = 0, 1, 2, \dots)$$

$$(2) R = \begin{cases} \sum_{k=0}^{\infty} \frac{(-1)^k}{\Gamma(v+k+1)} \left(\frac{r}{2}\right)^{v+2k} + \sum_{k=0}^{\infty} \frac{(-1)^k}{\Gamma(-v+k+1)} \left(\frac{r}{2}\right)^{-v+2k} & (v \neq \text{Integral}) \\ \left[\frac{2}{\pi} \left(\ln \frac{r}{2} + 0.577216 \right) + 1 \right] \sum_{k=0}^{\infty} \frac{(-1)^k}{k!(v+k)!} \left(\frac{r}{2}\right)^{v+2k} & (v = \text{Integral}) \end{cases}$$

$$(3) \Theta = c_0 y_0^m + c_1 y_1^m$$

The continuation is the definition of y_0^m and y_1^m :

$$\begin{cases} y_0^m = (1-x^2)^{\frac{m}{2}} \frac{d^m}{dx^m} y_0 \\ y_1^m = (1-x^2)^{\frac{m}{2}} \frac{d^m}{dx^m} y_1 \end{cases}$$

$$\begin{cases} y_0(x) = 1 + \frac{(-l)(l+1)}{2!} x^2 + \frac{(2-l)(-l)(l+1)(l+3)}{4!} x^4 + \dots \\ \frac{(2k-2-l)(2k-4-l)\dots(2-l)(-l)(l+1)\dots(l+2k-1)}{(2k)!} x^{2k} + \dots \\ y_1(x) = x + \frac{(1-l)(l+2)}{3!} x^3 + \frac{(3-l)(1-l)(l+2)(l+4)}{5!} x^5 + \dots \\ \frac{(2k-1-l)(2k-3-l)\dots(1-l)(l+2)\dots(l+2k)}{(2k+1)!} x^{2k+1} + \dots \end{cases}$$

c_0, c_1 and l is constants, $k = 0, 1, 2, \dots$

$$(4) \Phi(\varphi) = \cos m\varphi + \sin m\varphi \quad (m = 0, 1, 2, \dots)$$

3. The usage Matlab carried on emulation to play to show, crystal growth in its picture and experiment the facial look be basic to fit together and verified the accuracy that the mathematical formula deduce thus and further[10].

Comprehensive say, this text built up an electricity deposition a method a growth the Na rice structure material of physical model. Did some foundation a work for the growth that the research controls the Na rice structure material.

REFERENCES

1. D. Nan: *Solid State Electronics*, **86**(17), 3827 (2015).
2. M.Z. Zhang: *Applied Physics*, **49**(4), 226 (2011).
3. K. Ming, K.D. Jiang: *Applied Physics*, **67**(6), 264 (2013).
4. M. Jiang, T. Sun, R.W. Zhang: *Applied Physics*, **24**(2), 125 (2004).
5. I. En, A. Jiang, R. Pan: *Organic Electronics*, **86**(17), 527 (2015).
6. S. Li, F. Liu, T.M. Zhang: *Materials Letters*, **82**(15), 206 (2015).
7. Q.J. Yang, D. Wu: *J of The Physical Condens Matter*, **75**(11), 176 (2014).
8. S. Zhang, M. Wu, X.B. Yang: *J Of The Physical Society Of Japan*, **70**(6), 1452 (2001).
9. F. Xu, D. Min, Y. Sun, T. Li: *J of Physical C*, **82**(15), 206 (2015).
10. S. Zhong, Y. Wang, M. Wang, *Physical Review E*, **67**(6), (2003).

Calculation and applied analysis of natural gas hydrate saturation based on experimental data

J. Zhao^{1*}, Y. L. Wu¹, Y.Q. Ji¹

¹ School of Geoscience and Technology, Southwest Petroleum University, Chengdu, China

Received June 26, 2017; Revised July 20, 2017

The saturation is a very important parameter to evaluate natural gas hydrate. In order to accurately calculate the natural gas hydrate saturation during the synthesis process and analyses the relationship between resistivity and saturation in hydrate deposits, the resistivity and pressure values during the synthesis of natural gas hydrate were measured. Based on the instrument calibration and gas equation of state, the calculation model of natural gas hydrate saturation is established. The relationship between the saturation value of natural gas hydrate and the resistivity is discussed under different particle size, compaction and shale content. The results show that there is a certain exponential relationship between the saturation of gas hydrate and resistivity and a nonlinear relationship between gas hydrate saturation and resistivity index. There are some differences from the relationship in Archie's formula. Therefore, the Archie formula is not suitable for the calculation of hydrate saturation in sediment by logging data. Through the application analysis, it is concluded that the experimental model of gas hydrate saturation has the advantages of high accuracy and applicability.

Keywords: Gas hydrate Saturation; Rock physical experiment; P-V-T equilibrium equation; Resistivity Index

INTRODUCTION

Gas hydrate is the cage-type crystalline compounds formed under high pressure by water and natural gas in low temperature; the interaction between water molecules makes the stable solid lattice and gas molecules occupy the body cavity of lattice [1, 2]. Gas hydrate of nature is mainly distributed in the Marine sediments of the continental slope and the frozen continent; it is estimated that the organic carbon content in gas hydrate is twice as the other traditional resources all over the world such as a recoverable natural gas and oil [3, 4]. Gas hydrate is praised as new types of potential energy which is clean, efficient and rich reserves because of widely distributed, rich reserves, high density, etc [5]. And it also has been given high attention and researched in many countries [6, 7].

Archie formula, Dual water model and some other formulas like these have been used to calculate the gas hydrate saturation [8-12]. Tinivella estimated gas hydrate saturation according to the longitudinal wave with the theory of application of double phase medium [13]; Lee pointed out that weighted of three-phase time average equation and the three-phase Wood equation can be used to estimate deep sea sediment velocity of hydrate[14,15]; Wang Xiujuan estimated gas hydrate saturation with the application of P-wave velocity thermal elastic theory and considered the influence of the thermodynamic

properties to saturation estimation results, which is effective[16]; Mo Xiuwen, on the basic of previous studies, put forward the method that is using of logging interpretation of chloride ion mass concentration to calculate the hydrate saturation[17]; Chen Yufeng studied the relationship between the hydrate saturation and resistivity with the using of natural gas hydrate resistivity measurement system. And the results showed that increase resistivity index and water saturation are not like linear relationship which is described by Archie formula, it considered that the resistivity calculated saturation requires correction [18, 19].

This article uses SHW-III acoustic power test device of gas hydrate which is with high visualization degree, complete measurement data and real-time data monitoring, and uses the method of continuous supply of natural gas in stages to the greatest extent on the synthesis of gas hydrate. Using P-V-T equilibrium equation calibrate the related parameters of the hydrate instrument in the first place, and then deduced the theory of calculation of natural gas hydrate saturation equation, to achieve the purpose of accurate calculation of natural gas hydrate saturation finally. Verification and analysis the calculation method of gas hydrate saturation through the experimental data.

SATURATION CALCULATION

Natural gas hydrate is mainly formed by continuous supplication of natural gas in stages, so

* To whom all correspondence should be sent:
E-mail: zhaojun_70@126.com

the volume of measuring room and pipeline in experimental device will have a greater impact on the calculation result. Therefore, it is necessary to calibrate the volume of the measuring room V_1 and pipeline V_s , the schematic diagram of experimental device shown in Fig. 1.

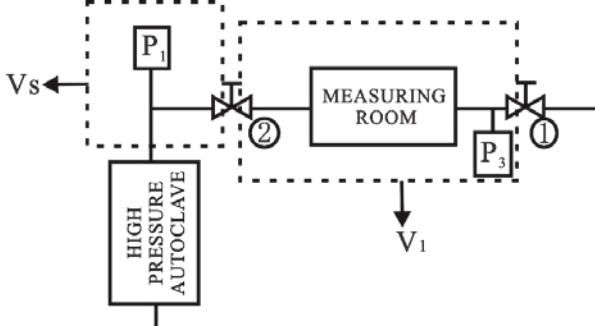


Fig. 1. Experimental device schematic diagram

Calibrate the volume of the measuring room V_1 and pipeline V_s : Firstly, put the solid stainless steel module into autoclave, fill with a certain pressure of gas in the system, and then close the valve ② and open the valve ①. Next, empty the gas of measuring room and record the initial stable pressure P_{1A} ; And then close the valve ①, open the valve ② and record the pressure for a steady state P_{1B} . At this point establish the P-V-T equation in balance state:

$$\frac{P_{1A} V_s}{Z_{1A}} = \frac{P_{1B} (V_s + V_1)}{Z_{1B}}$$

Where P_{1A} is the initial stable pressure, P_{1B} is the steady state pressure, Z_{1A} is the compression factor of gas in the pressure P_{1A} for conditions, Z_{1B} is the compression factor of gas in the pressure P_{1B} for conditions.

Put a module with known volume V_2 into measuring room and repeat the above steps. Record the steady state pressure P_{2A} and P_{2B} when the valve ② closing and opening. Meanwhile establish the P-V-T equation in balance state:

$$\frac{P_{2A} V_s}{Z_{2A}} = \frac{P_{2B} (V_s + V_1 - V_2)}{Z_{2B}}$$

Where P_{2A} is the initial stable pressure, P_{2B} is the steady state pressure, Z_{2A} is the compression factor of gas in the pressure P_{2A} for conditions, Z_{2B} is the compression factor of gas in the pressure P_{2B} for conditions.

By the above two P-V-T equilibrium equation of state the measuring room volume V_1 and volume of pipeline V_s can be obtained. In order to improve the accuracy, changing different volume of modules load to measuring room and repeat the processes can get more P-V-T equilibrium equations under the condition of constant temperature, with the

simultaneous Formula 1 multiple of the measuring room volume V_1 and the volume of pipeline V_s can be calculated, and final averaged.

The formation of gas hydrate is mainly adopts the method of continuous supplication of natural gas in stages which has the following steps: firstly, instead of certain water put amount of gas into porous medium filled with water, to make a suitable space for the formation of hydrate; Then continuing in stages to pass into the gas in porous media, synthesis of hydrate and calculation of water saturation and gas hydrate saturation at equilibrium under appropriate conditions, repeating the above process until the water in the porous media is completely consumed. Assuming V_{e_i} , V_{w_i} , V_{c_i} respectively the volumes of gas, residual water and hydrate in porous media for i time at the start of the reaction synthesis. And the synthetic process of natural gas hydrate can be expressed in Fig. 2.

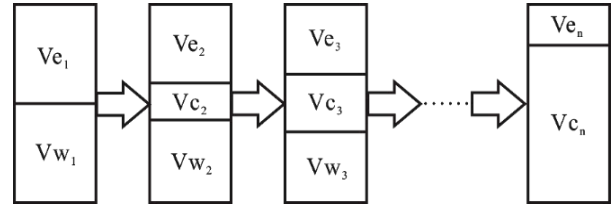


Fig. 2. The synthetic process diagram of natural gas hydrate

As take the first natural gas hydrate synthesis process as an example: at the start of the reaction, the inner pressure of the autoclave is P_{1a} and the corresponding compression factor is Z_{1a} , P-V-T equilibrium equation can be established when system for the amount of substance n_{1a} gas filled the space of autoclave V_{e_1} and the volume of pipeline V_s .

$$P_{1a} (V_{e_1} + V_s) = Z_{1a} n_{1a} RT$$

At the end of the reaction, the pressure in the autoclave is P_{1b} and the corresponding compression factor is Z_{1b} , P-V-T equilibrium equation can be set up when system for the amount of substance n_{1b} as filled the space of autoclave V_{e_2} and the volume of pipeline V_s .

$$P_{1b} (V_{e_2} + V_s) = Z_{1b} n_{1b} RT$$

The consumption of natural gas amount of substance in the synthesis reaction process of natural gas hydrates of the first time is:

$$\Delta n_1 = n_{1a} - n_{1b} = \frac{P_{1a} (V_{e_1} + V_s)}{Z_{1a} RT} - \frac{P_{1b} (V_{e_2} + V_s)}{Z_{1b} RT}$$

The volume of natural gas Ve_1 in autoclave can be calculated by the water discharged at the first time. And Ve_2 can be calculated by the following processes:

Put the amount of substance n_3 in the measuring room so that the stable pressure is P_3 and the corresponding compression factor is Z_3 . At the same time, P-V-T equilibrium equation 6 can be established.

$$P_3V_1 = Z_3n_3RT$$

P-V-T equilibrium equation can be established after opening valve ② so that the part of the natural gas spread into autoclave and expanded rapidly to reach equilibrium. Meanwhile, the pressure becomes P_{2a} and corresponding to the compression factor becomes Z_{2a} .

$$P_{2a}(Ve_2 + V_s + V_1) = Z_{2a}(n_{1b} + n_3)RT$$

By the above two P-V-T equilibrium equations, we can get the expression of Ve_2 :

$$Ve_2 = \left[\frac{P_{2a}(V_s + V_1)}{Z_{2a}} - \frac{P_{1b}V_s}{Z_{1b}} - \frac{P_3V_1}{Z_3} \right] \left/ \left[\frac{P_{1b}}{Z_{1b}} - \frac{P_{2a}}{Z_{2a}} \right] \right.$$

The use of the above formula can be calculated natural gas consumption Δn_1 , and according to natural gas hydrate formation reaction equation calculates the corresponding water consumption of natural gas consumed Δn_1 moles, as expressed by volume ΔVw_1 . At this point the remaining water volume in the autoclave is:

$$Vw_2 = Vw_1 - \Delta Vw_1$$

Where can be obtained based on the calculation of quality of the first water discharged. Thus, when the end of the first synthesis gas hydrates, water saturation of the porous medium is:

$$S_w = \frac{Vw_2}{V_\phi}$$

Gas hydrate saturation is:

$$S_c = \frac{Vc_2}{V_\phi} = \frac{V_\phi - Vw_2 - Ve_2}{V_\phi}$$

According to the above steps, the water saturation and the hydrate saturation value in the porous medium at the end of the hydrate formation at each stage can be obtained.

LITHO-ELECTRIC RELATION ANALYSIS

According to the records of experimental parameters and combining with the theory on the calculation formula, water saturation, gas saturation, hydrate saturation and resistivity and resistivity index and so on in natural gas hydrate formation in porous medium in the autoclave are all obtained with the condition of reaction temperature is 1°C .

Under the experimental condition that the reaction temperature is for 1°C , the relationship between resistivity and the hydrate saturation in different particle size、different axial compressive and different shale content of porous medium to form natural gas hydrate in autoclave as shown in Figure 3、Figure 4 and Figure 5. Under the condition of three different particle size、three different axial compressive and three different shale content of rock sample text, the calculations obtained hydrate saturation (S_c) and resistivity (R) in linear coordinates show a certain exponential relationship from Fig. 3、Fig. 4 and Fig. 5; With the larger grain size, lowered cementation degree and decreasing the shale content, the resistivity increase when containing the same natural gas hydrate saturation.

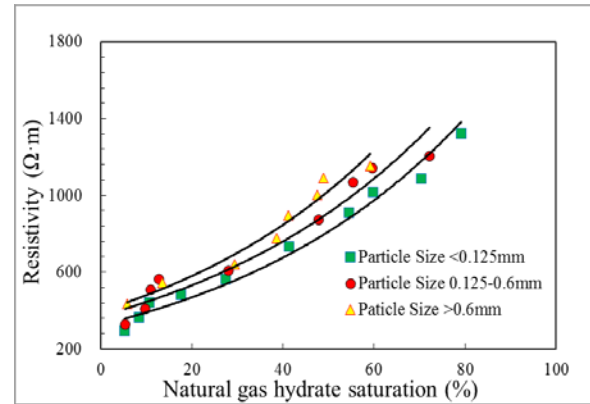


Fig. 3. The relationship between hydrate saturation and resistivity in different particle size experimental conditions

The relationship between resistivity index (I) and water saturation (S_w) in the natural gas hydrate formation process in porous media with the condition of reaction temperature is 1°C in the autoclave as shown in Fig. 6、Fig. 7 and Fig. 8. The figures show that in the linear coordinates the relationship of resistivity index (I) and water saturation (S_w) from three different particle size、three different axial compressive and three different shale content of sample test is not a line (but there exists similarities of change trend). It means

that under the experimental conditions, hydrate sediments have the phenomenon of Non-Archie.

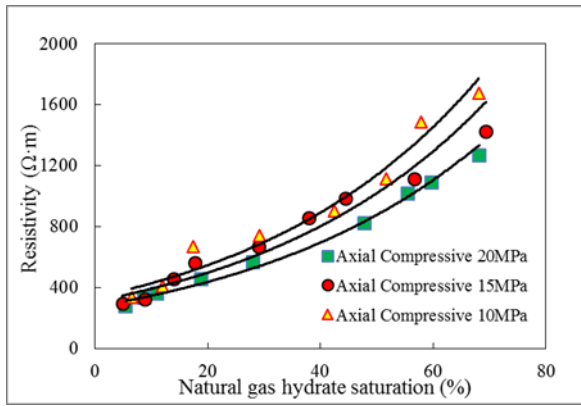


Fig. 4. The relationship between hydrate saturation and resistivity in different axial compressive experimental conditions

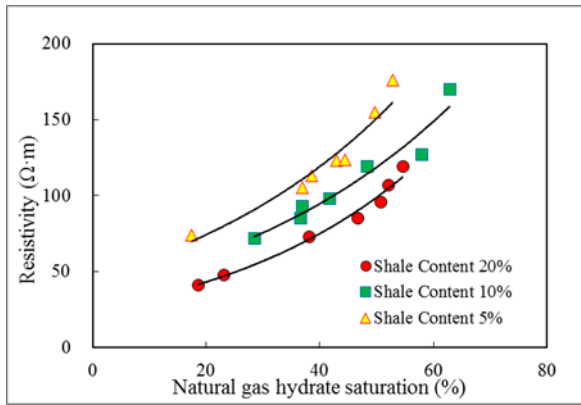


Fig. 5. The relationship between hydrate saturation and resistivity in different shale content experimental conditions

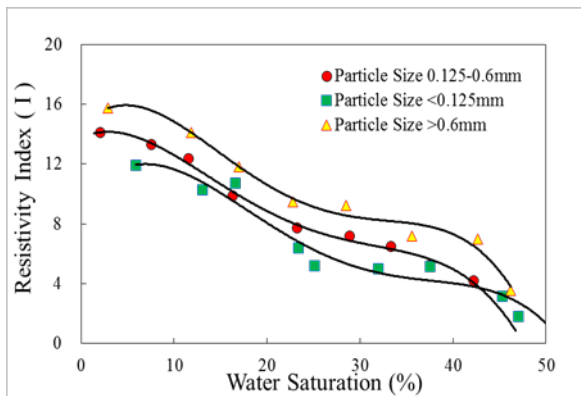


Fig. 6. The relationship comparison chart of resistivity index and water saturation in different particle size experimental conditions.

That because Archie formula is only suitable for pure sandstone. We change the state of pure sandstone and size of original pore after the synthesis of natural gas hydrate in porous media so that there is Non-Archie phenomenon existing between resistivity index (I) and water saturation

(S_w). It is the same with the conclusion from Yufeng Chen in the research of the relationship between sediment gas hydrate saturation and resistivity [11].

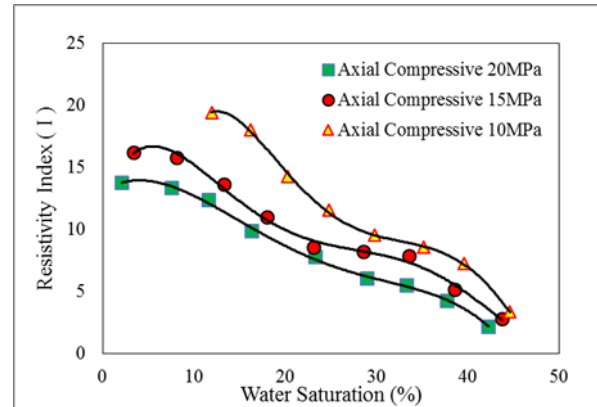


Fig. 7. The relationship comparison chart of resistivity index and water saturation in different axial compressive experimental conditions

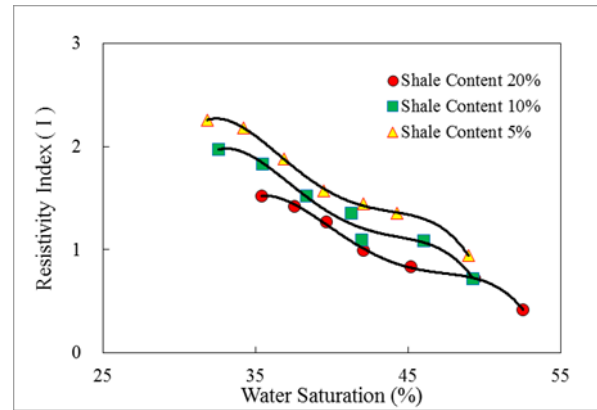


Fig. 8. The relationship comparison chart of resistivity index and water saturation in different shale content experimental conditions

CONCLUSION

1. Through this experiment, we formed a new natural gas hydrate synthesis method, a set of instrument-related parameters calibration method and a set of synthetic gas hydrate process of natural gas hydrate saturation computational model.

2. The data analysis results show that: the saturation of natural gas hydrate (S_c) and the resistivity(R) shows a certain exponential relationship, the water saturation (S_w) and the resistivity index (I) did not show the linear relationship (have the phenomenon of Non-Archie); With the larger grain size, lowered cementation degree and decreasing the shale content, the resistivity increase when containing the same natural gas hydrate saturation.

3. The results of comparative analysis show that: The result of this experiment accord to the objective phenomena and laws of rock physics experiments, so

the method adopted to synthesize the natural gas hydrate and the computational model is correct in the experiment, which put forward a new idea computing the saturation of natural gas hydrate.

Acknowledgements: This paper is funded by the National Key R & D Plan (2016YFC0304008), the views expressed are authors' alone.

REFERENCES

1. S. Li, X. Xia, J. Xuan, Y. Liu, Q. Li, *Chinese Journal of Chemical Engineering*, **1**(8), 39 (2010).
2. W. Hao, J. Wang, S. Fan, W. Hao., *Energy conversion and management*, **49**(10), 2546 (2008).
3. S. Li, X. Xu, R. Zheng, Y. Chen, J. Hou, *Fuel*, **160**, 117 (2015).
4. H. Lu, T. Kawasaki, T. Ukita, I. Moudrakovski, T. Fujii, S. Noguchi, *Marine & Petroleum Geology*, **28**(10), 1801 (2011).
5. Z.R. Chong, S.H.B. Yang, P. Babu, P. Linga, X. S. Li, *Applied Energy*, **162**, 1633 (2016).
6. A. Pavlenko, H. Koshlak, O. Vytyaz, C. Rybicki, *Technology Analysis & Strategic Management*, **23**(8), 851 (2015).
7. D. Zhang, Z. Li, J. Chen, *Scientia Geologica Sinica*, **47**(2), 561 (2012).
8. U. Shankar, M. Riedel, *Marine & Petroleum Geology*, **28**(10), 1768 (2011).
9. U. Shankar, M. Riedel, *Marine & Petroleum Geology*, **58**, 265 (2014).
10. G.Y. Kim, *Geophysics and Geophysical Exploration*, **15**(2), 102 (2012).
11. F. Chen, Y. Zhou, X. Su, G. Liu, H. Lu, J. Wang, *Marine Geology & Quaternary Geology*, **31**(5), 95 (2011).
12. Y. Chen, K.J. Dunn, X. Liu, M. Du, X. Lei, *Geophysics*, **79**(5), 11 (2014).
13. U. Tinivella, *Bollettino di Geofisica Teorica ed Applicata*, **40**(1), 19 (1999).
14. M.W. Lee, D.R. Hutchinson, W.P. Dillon, J. J. Miller, W. F. Agena, B.A. Swift, *Marine and Petroleum Geology*, **10**(5), 493 (1993).
15. M.W. Lee, D.R. Hutchinson, T.S. Collett., W. P. Dillon, *Journal of Geophysical Research: Solid Earth*, **101**(B9), 20347 (1996).
16. X. Wang, *Geophysical Prospecting for Petrole*, **44**(6), 545 (2005).
17. X.W. Mo, J.A. Lu, Z.B. Sha, *Journal of Jilin University*, **42**(4), 921 (2012).
18. Y. Chen, D. Li, D. Liang, J. Du, N. Wu, *Progress in Geophysics*, **28**(2), 1041 (2013).
19. Y. Chen, D. Li, D. Liang, X. Zhou, N. Wu, *Editorial Office of Acta Petrolei Sinica*, **34**(3), 507 (2013).

Analgesic effect of vinegar-processed myrrh and the processing technology research

W.Q. Song^{1,2,3,4}, X.Q. Wang¹, Y. Qi^{1,2,3,4}, J. Meng^{1,3,4}, X.G. Hu¹, S.M. Wang^{1,2,3,4}, S.W. Liang^{1,2,3,4,*}

¹College of Traditional Chinese Medicine, Guangdong Pharmaceutical University, Guangzhou 510006, China,

²Key Laboratory of Digital Quality Evaluation of Chinese Materia Medica, Guangzhou 510006, China

³Engineering & Technology Research Center for Chinese Materia Medica Quality of the Universities of Guangdong Province, Guangzhou 510006, China

⁴Engineering & Technology Research Center for Chinese Materia Medica Quality of Guangdong Province, Guangzhou 510006, China

Received June 27, 2017; Revised July 20, 2017

The aim of the experiment was to optimize the processing technology of myrrh by orthogonal test, and to make a preliminary pharmacological study on the difference of analgesic effect before and after the processing of myrrh. The method is based on beta-elemene, volatile content and extract oil as the evaluation index, the stir frying temperature, heating time and heating time after the vinegar processed were investigated, the best vinegar processing of myrrh was optimized by testing the comprehensive score of orthogonal optimization, analgesic experiment was performed with the writhing, To investigate whether the analgesic effect were increased after the myrrh processed. Our result is the effect of frying temperature was statistically significant, the best processing of vinegar is preferred to take the net amount of raw myrrh in hot pot, heat gently fry to smoke, 6min, surface micro melting, uniform spraying 5% vinegar, then heated 2min and stir fry until surface light, quickly remove, stand open and cool (every 100kg myrrh, vinegar 5kg), myrrh and vinegar-processed myrrh have analgesic effect, enhance the analgesic effect of vinegar processing, with statistical significance. We can determine the processing parameters of vinegar -processed myrrh, and make it clear that the analgesic effect of vinegar-processed myrrh will be enhanced.

Keywords: myrrh, processing technology, orthogonal test, analgesic effect.

INTRODUCTION

Myrrh is dry resin of Olive plant, it divided into natural myrrh and gum opoponax [5]. Myrrh was found in "medicinal theory". Myrrh is mild, bitter and acrid. Heart liver and spleen meridians, it has good effect for promoting blood circulation to relieve pain, detumescence and promoting granulation. Myrrh mainly contain volatile oil, resin and other ingredients [1]. The study on components of myrrh are mostly concentrated on isolation and identification. Now the main methods of processing of myrrh have stir-baking with vinegar, stir-bake to yellowish and so on. Due to the clinical use of pungent odor, have certain stimulation to the stomach, easy to cause vomiting and nausea. Now the study on the myrrh is more concentrate on volatile oil, including the study on extraction technology and the chemical composition [7]. Myrrh contain volatile oil and resin are effective components[4], and the volatile oil is stimulating, processed with the purpose of eliminating part of volatile oil, reduce the stimulation[3]. But at the same time, reduce the side effects of drugs, whether

reduce the effects of analgesic efficacy. How to reduce the loss of myrrh in the course of processing, improve product yield, how to optimize the processing technology of myrrh with efficacy and toxicity experiments, these problems need to be further studied, so as to explore the best processing technology of myrrh, to ensure the safety and effect of clinical application.

MATERIALS AND METHODS

Instrument

Waters 2695 Highly Effective Liquid Chromatography, 2998 PDA; Luna 5 C18 column (4.6 x 250 mm, 5 μm); Smart SensorAR550 infrared thermometer (Hongkong SigMa company); KQ-500E ultrasonic cleaner (Kunshan Ultrasonic Instrument Co. Ltd.); Sartorius BP211D 1/10 000 electronic balance, GZX-B40 MBE electric constant temperature drying oven (Shanghai Boxun Industrial Co. Ltd. medical equipment factory); TC-15 constant temperature electric heating jacket (Haining Huaxing instrument factory); RE-52A rotary evaporator (Shanghai Yarong biochemical instrument factory); volatile oil tester.

* To whom all correspondence should be sent:
E-mail: swliang371@126.com

Reagent

Mobile phase: orthophosphoric acid (AR), methanol (chromatographic pure), acetonitrile (chromatographic pure), water is distilled water; other reagents methanol and ethanol (analytical pure); indometacin Enteric-coated Tablets (batch number: 140101, Guangdong Southern China Pharmaceutical Group Co. Ltd, approval number: Chinese medicine H44020701), acetic acid solution (0.75%); saline, sodium chloride injection (Chinese medicine H13022576, batch number: A14080706); ethanol (medical), glacial acetic acid and other reagents as the pure analysis, β -elemene as reference (National Institute for the control of Pharmaceutical and Biological Products, batch number: 100268-200401). Rice vinegar (purchased from FoShan Haitian seasoning food Limited by Share Ltd, Food production license No: QS 440603023486); Myrrh was purchased from Guangzhou Qingping medicine market, by Professor Li Shuyuan of the Guangdong Pharmaceutical University for the identification of dry resin for the olive branch plant of *Commiphora myrrha* Engl or *Commiphora molmol* Engl.

Animals

Kunming mice, both male and female weight 18 ~ 22g, SPF level, provided by experimental animal center of Guangzhou University of Chinese Medicine (Animal license No.: SYXK Guangdong 2014-0081).

Prepare control solution

Precision weighing β -elemene control sample (10.25mg) in 10mL flask. Dissolve and dilute with methanol, shake, as the mother reserved. To learn the 2ml liquor to a 10mL volumetric flask. Dissolve and dilute with methanol to the scale, shake, as control solution.

Prepare test solution

Take 0.2mL volatile oil under the "determination of volatile oil content". In 10mL flask, dissolved and diluted with methanol to the scale, shake. Over 0.45 m microporous membrane, take proper amount of the filtrate.

METHODS

Orthogonal factor level design

According to preliminary test results, vinegar moxibustion for frying temperature (80°C、100°C、120°C), heating time (6min, 8min, 10min) and heating time after adding vinegar (2min, 3min,

4min) as main influencing factors of processing. Each factor takes 3 levels, L9 (3⁴) orthogonal test was used to design the experiment. The myrrh after election and removal, weighing 9 samples, each of the 200g, according to L9 (3⁴) orthogonal experiment method to carry out processing, remove, crush and sift.

Determination of volatile oil content

Take processed product 20g, according to the method of determination of volatile oil to determine volatile oil (Appendix D X B method), results are shown in table.

Measure content of β -elemene

Chromatographic condition

Chromatographic column: Luna 5u C18 column (250 x 4.6 mm, 5 m); the mobile phase: acetonitrile-water (90:10); temperature of column: 30°C wavelength of detection: 210nm; flow rate: 1mL/min; sample size: 10L.

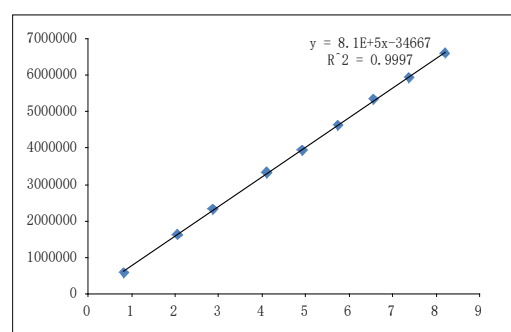


Fig.1. β -elemene standard curve.

Investigate linear relation

Take a amount of β -elemene reference solution under the "Prepare control solution". Samples were 2, 5, 7, 10, 12, 14, 16, 18, 20 L, according to the above conditions to determine, to determine the peak area, the peak area integral value(Y) as the ordinate. With the standard β -elemene injection volume(X) as abscissa. Respectively for linear regression, regression equation: $Y=8.1E+5x-34667$, $R^2=0.9997$. The results showed that β -elemene in 0.82~8.2g range showed a good linear relationship.

Test the precision

Precision take 10L from β -elemene reference solution. According to the chromatographic conditions (under "chromatographic condition") for sampling 6 times. The calculated RSD value of measured β -elemene peak area was 0.36%. Indicates the instrument has good precision.

Table 1. Results of precision.

| Times of sampling | The peak area of β -elemene |
|-------------------|-----------------------------------|
| 1 | 3366826 |
| 2 | 3347631 |
| 3 | 3349192 |
| 4 | 3348580 |
| 5 | 3373500 |
| 6 | 3371823 |
| RSD (%) | 0.36 |

Test the stability

Take 20g of myrrh powder, precision weighing. Preparation under the "Prepare test solution". In 0, 2, 4, 8, 12, 24 h each injection 10L, with the peak area (A) of β -elemene measured as the index. Calculated relative standard deviation (RSD), To investigate the stability of the sample solution. Obtain β -elemene RSD is 1.81%.The results showed that the sample solution was stable within 24h

Table 2. Results of samples' stability.

| Inject time/h | peak area of β -elemene |
|---------------|-------------------------------|
| 0 | 4486596 |
| 2 | 4457576 |
| 4 | 4447117 |
| 8 | 4465825 |
| 12 | 4418967 |
| 24 | 4559992 |
| RSD (%) | 1.81 |

Test the repeatability

Precision weighing the same batch of myrrh powder and divided into 6 parts. Each one is 20g. Preparation under the "chromatographic condition", injection was 10L, with peak area (A) of β -elemene measured as the index, calculated the relative standard deviation (RSD), to investigate the repeatability of the method. To obtain β -elemene RSD = 2.20%.

Table 3. The results of repeatability.

| Number | Sample weight/g | peak area A of β -elemene |
|---------|-----------------|---------------------------------|
| 1 | 20.0052 | 2417445 |
| 2 | 20.0015 | 2441171 |
| 3 | 20.0051 | 2317036 |
| 4 | 20.0045 | 24467291 |
| 5 | 20.0042 | 2364141 |
| 6 | 20.0026 | 2438017 |
| RSD (%) | --- | 2.20 |

Sample recovery

Precision take an amount of control product of β -elemene. Chromatography methanol was added to 0.9533mg/mL as reference solution. Precision

weighing known content of myrrh crude 10g, divided into 6 parts. Precisely add the β -elemene control reference solution 3mL. Prepared by the method under the "Prepare test solution ", under "chromatographic condition "measured the chromatographic conditions. The experimental results of β -elemene average recovery rate was 100.07%, RSD was 2.47%.

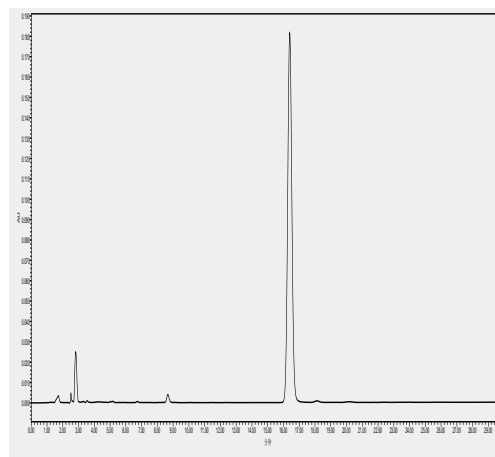


Fig. 2. HPLC diagram of β -elemene of reference substance

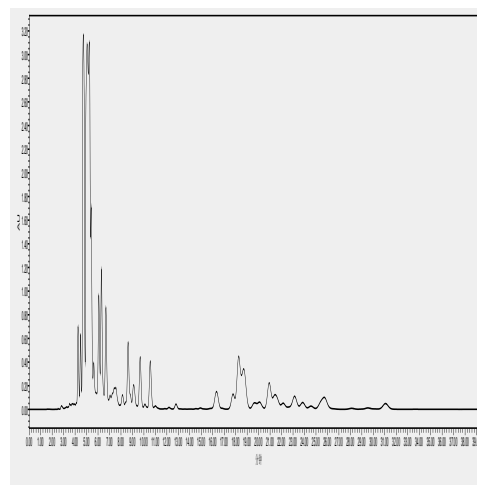


Fig. 3. HPLC diagram of the vinegar-processed myrrh samples.

Measure sample content

Precisely draw control solution and sample solution 10 μ L. Inject into Liquid chromatograph. Determined by the chromatographic conditions under "chromatographic condition". To calculate the content of β -elemene of each dry sample, the results was shown in Figure 3.

RESEARCH THE SOLVENT OF EXTRACTION

The extract is the index of the dissolution of the pieces, ethanol concentration affects dissolution of active ingredient in vinegar-processed myrrh. Therefore solvent of extraction of the

vinegar-processed myrrh need examined. This study selected 95% ethanol, 75% ethanol, 50% ethanol, 25% ethanol and water as solvent. According to hot-maceration method of 2010 version of Chinese Pharmacopoeia (Appendix X A) [8] to determine. To calculate content of extract after drying.

Table 4. The selection of solvent for extract.

| solvent | Content /% |
|------------|------------|
| 95%ethanol | 40.00 |
| 75%ethanol | 43.13 |
| 50%ethanol | 37.79 |
| 25%ethanol | 33.62 |
| water | 34.57 |

As can be seen from table 4, the extracted content of 75% alcohol was the highest. Therefore, using 75% ethanol to extract the extraction of vinegar-processed myrrh.

THE ANALGESIC EFFECTS OF MYRRH AFTER PROCESSING

Prepare samples

The raw products: Take the net amount of myrrh and add 75% ethanol, reflux extracted for 2 times, each time micro boiling for 1hours, cooling for 30min, filtering, merging the filtrate for 2 times, rotary evaporation to recover ethanol. Be condensed liquid medicine which containing crude drug, until the concentration of 65mg/ml, spare.

Vinegar processed products: The processing of vinegar moxibustion has been optimized processing(in the hot pot, heat gently 6min, fry to smoke, surface micro melting, spraying 5% vinegar, then heated 2min, stir fry until surface light). As the concentration of 65mg/ml that liquid medicine containing crude drug and vinegar liquid, spare.

Indomethacin was mixed with normal saline until concentration was 0.325mg/ml.

GROUPING AND ADMINISTRATION

Grouping: 48 mice, free feeding, drink. After 1weeks, meet were randomly and divided into myrrh group, vinegar processed myrrh group, normal saline group, positive control group, 4 groups, and 12 rats in each group, marked with picric acid. Observe and record the writhing times of mice in 15min. Results see table 7.

Drug delivery: fed with myrrh, vinegar processed myrrh and equal volume normal saline, once a day, dose was 20ml/kg. Continuous administration 5days.No drug was given 4 days before the experiment in the indomethacin group.

Intraperitoneal injection was given on the fifth day. Each group was treated with alleviating pain test after 1hours of the last administration, that is, intraperitoneal injection of 0.1ml/10g acetic acid (0.75%).

THE INDEX OF ANALGESIC EFFECT OF MYRRH AFTER PROCESSING

By intraperitoneal injection of chemical drugs to mice, the acute peritonitis caused by prolonged pain stimulation, the lethal mice produced writhing response. Because myrrh has the function of promoting blood circulation and relieving pain, can reduce reaction in mice. According to the number of writhing, can judge the analgesic effect of myrrh after processing.

RESULTS

The weighted average method was used to evaluate the processing of vinegar processed myrrh.(the evaluation indicator weighted as follows: β -elemene content evaluation score =the content of β -elemene in each sample x highest content of β -elemene in 40/9 samples; volatile oil content evaluation score= the content of volatile oil in each sample x the highest content of volatile oil in 40/9 samples; alcohol extract content evaluation score = alcohol extract in each sample x the highest content of alcohol extract in 20/9 samples; comprehensive score = β -elemene content evaluation score + alcohol extract content evaluation score —volatile oil content evaluation core). The result is as follows:

Table 5. Results of orthogonal test design

| Test number | A | B | C | D |
|-------------|--------|--------|--------|--------|
| 1 | 1 | 1 | 1 | 1 |
| 2 | 1 | 2 | 2 | 2 |
| 3 | 1 | 3 | 3 | 3 |
| 4 | 2 | 1 | 2 | 3 |
| 5 | 2 | 2 | 3 | 1 |
| 6 | 2 | 3 | 1 | 2 |
| 7 | 3 | 1 | 3 | 2 |
| 8 | 3 | 2 | 1 | 3 |
| 9 | 3 | 3 | 2 | 1 |
| K_1 | 17.050 | 13.773 | 12.793 | 12.703 |
| K_2 | 11.007 | 10.653 | 9.470 | 11.497 |
| K_3 | 6.903 | 10.533 | 12.697 | 10.760 |
| R | 10.147 | 3.240 | 3.323 | 1.943 |

* $F_{0.05(2,2)}=19.000$

Table 6. Results of orthogonal design test

| Test number | β -elemene /% | Volatile oil content /% | Alcohol extract /% | Comprehensive score |
|-------------|---------------------|-------------------------|--------------------|---------------------|
| 1 | 0.4172 | 3.64 | 41.33 | 21.36 |
| 2 | 0.3303 | 3.60 | 41.86 | 13.71 |
| 3 | 0.3846 | 3.79 | 40.17 | 16.08 |
| 4 | 0.2140 | 2.84 | 40.85 | 10.05 |
| 5 | 0.1937 | 2.50 | 41.57 | 12.10 |
| 6 | 0.2580 | 3.19 | 41.41 | 10.87 |
| 7 | 0.1781 | 2.55 | 41.40 | 9.91 |
| 8 | 0.1599 | 2.75 | 41.42 | 6.15 |
| 9 | 0.2035 | 3.25 | 40.62 | 4.65 |

* $F_{0.05(2,2)}=19.000$ **Table 7.** The analgesic effect of processed myrrh

| Group | Number of animals | Writhing times | The inhibition ratio |
|--|-------------------|----------------|----------------------|
| Normal saline group (negative control) | 12 | 24.00±21.51 | 53.21% |
| Myrrh processed group | 12 | 11.23±9.21 | 77.88% * |
| 100°C vinegar processed myrrh group | 12 | 5.15±9.59 | 78.53% * |
| Indomethacin group (positive control) | 12 | 2.23±3.87 | 90.71% ** |

Note: t test, compared with physiological saline, * show $P<0.05$, ** show $P<0.01$ (If the value of P is less than 0.05, it is significant difference).

From the above analysis of variance showed, the primary and secondary order of the influencing factors of vinegar processed myrrh A (frying temperature) > C (heating time after add vinegar) > B (heating time), and the effect of frying temperature was statistically significant. After comprehensive consideration, in accordance with the provisions of the national pharmacopoeia stipulates that vinegar dosage is 5%. Therefore, the optimal processing technology of vinegar processed myrrh was identified as A1B1C1, that is, to take the net amount of raw myrrh, in hot pot, heat gently 6min, fry to smoke, surface micro melting, uniform spraying 5% vinegar, then heated 2min, stir fry until surface light, quickly remove, cool open (each 100kg myrrh with vinegar 5kg).

The analgesic effect of myrrh after processing

According to the results of t test, we can see that the vinegar processed myrrh and myrrh have

analgesic effect, analgesic effect of vinegar processed myrrh were enhanced, with statistical significance.

DISCUSSION

At present, research on the processing technology of myrrh is mostly take the content of volatile oil and appearance as the index [6]. But by consulting a large number of documents, it is not clear whether the content of processed myrrh volatile oil significantly reduced and whether it is the effective components [2]. When appearance as the index, due to the lack of objective standard, does not accurately reflect the quality of processed products, but can be used as a reference index. Volatile oil, β -elemene and extracts as 3 indicators for the evaluation of the comprehensive weighted score. By orthogonal test, we can optimum the best processing technology of vinegar processed myrrh. As a reference, the appearance character provides the basis for its quality control. This study belongs to the laboratory experiment, in order to further determine standardized processing of myrrh, the optimization of the experimental process need the pilot test and to be enlarged.

Myrrh has analgesic effect, but vinegar processed products are better, it has statistical difference between the crude, probably because accessories vinegar also has an analgesic effect, it improve the dissolution rate of other components which have analgesic effect., The reason for the strengthening of vinegar processed myrrh analgesic effect, need to be further studied.

REFERENCE

1. T.B. Ruan, *Journal of Chinese Materia Medica*, **20**(8), 466 (1995).
2. W.H. Li, L. Yang, *Jilin Journal of Traditional Chinese Medicine*, **23**(4), 45 (2003).
3. N.F. Jiao, *Shandong J Tradit Chin Med*, **20**(9), 531 (2001).
4. Y.Q. Sun, G. Wei, L.L. Zhou, *Traditional Chinese medicinal materials*, **24**(8), 566 (2001).
5. R.Q. Hou, *Journal of Shenyang Pharmaceutical University*, **14**(3), 157 (1997).
6. W.H. Chen, *Formulation and technology*, **7**(7), 45 (2010).
7. J.F. Zhao; C.L. Zhou; L. Han. *China Pharmacy*, **22**(7), 661 (2011).
8. Chinese Pharmacopoeia Commission. *Pharmacopoeia of People's Republic of China: 2010 Edition* [M]. Beijing: The Medicine Science and Technology Press of China, Beijing, 2010, app. X A62.

Comparative experimental study of hydrogen and methane with coal cogeneration system and methane of single-phase production

D.P. Xia^{1,2,3}, H. Nan^{1,*}, X.B. Su^{1,2,3}, Y. Bai¹, X. Chen¹

¹School of Energy Science and Engineering, Henan Polytechnic University, Jiaozuo 454000, China

²Collaborative Innovation Center of Coalbed Methane and Shale Gas for Central Plains Economic Region, Henan Province, 454000, China

³College of Resource and Environment, Henan Polytechnic University, Jiaozuo, 454000, China

Received June 26, 2017; Revised July 20, 2017

With low coal rank lignite as bio-gas production substrate, characteristics of single phase methane production in coal seam and cogeneration of hydrogen and methane gas at 35 °C were studied, with liquid phase and solid phase product during reaction analyzed for comparative mechanism study of single-phase and two-phase gas. The results showed that: (1) In single-phase and two-phase gas production with coal as substrate, single-phase methane production rate is 22.86ml / g, cogeneration production rate is 26.24ml / g, second-phase methane concentration ratio is 7.9% higher than single-phase. (2) Single-phase methane fermentation featured ethanol fermentation, while cogeneration featured butyric acid type and acetic acid type fermentation. (2)C and O contents of coal after cogeneration and single-phase production of methane declined, but H content increased. Lignin, cellulose, hemicellulose consumption rates of co-produced coal were respectively 15.2%, 18.1% and 16.6%; XRD results show that crystalline structure damage of coal was more obvious after cogeneration. (3) Single-phase production mechanism of methane gas featured carbon dioxide reduction, while cogeneration experimental hydrogen production featured hydrolysis and decomposition of macromolecules, methanogenic phase featured acetic acid fermentation. Experimental results show obvious biological effects of cogeneration of bio-hydrogen and methane, which can significantly improve the utilization of residual coal.

Keywords: cogeneration of hydrogen and methane, VFA change, coal degradation, mechanism

INTRODUCTION

Seam biogas in the United States have achieved commercial exploitation. Recently, research group [1-6] study confirmed that if there is proper control of the reaction conditions, in first period of seam biogas production, bio-hydrogen will be generated, which is consistent with traditional four-stage fermentation theory.

Coal is degraded by white rot fungi into cellulose, lignin material that can be used, which can be degraded into small molecules of acid and alcohol [7-15] by hydrolytic bacteria and syntrophic acetogenic bacteria. Hydrogen will be produced in the process which combines with carbon dioxide and produces methane under the role of methanogens. Hydrogen is a cleaner energy than methane, with yield and substrate utilization rate lower than the methane. If cogeneration of the two is realized, maximal recycling of resources can be achieved with biological residual coal mining realized[16]. Early tests confirmed feasibility of hydrogen and methane production with two-phase anaerobic fermentation. In this study, with independent methane production experiment, cogeneration experiment of hydrogen and methane

as the basis, reaction conditions were adjusted before the end of the second set of experiments, methane was produced by changing the pH and adding nutrients, and analysis was done from gas production rate, fermentation period, VFA change, coal structural parameters in order to define the reaction mechanism.

MATERIALS AND METHODS

Preparation of Coal Sample

Place low rank coal sample into the crusher to be grinded into pulverized coal of 0.25mm or so. Then screen out 400g of coal sample into autoclave sterilization pot for 30min sterilization at 120 °C to reduce side effects of microorganism outside. Then, transfer coal sample to a sample bag, and finally place the coal sample into 60 °C oven to be dried to constant weight for standby application.

White Rot Fungi Liquid Enrichment

Enrich white rot fungi, inoculate appropriate amount of white rot fungi into medium after sterilization and cooling of white rot fungi enriched medium. Shock and mix for 2min in a fast mixer, so that thallus is dispersed. Then culture 2d in 35°C constant temperature shaking chamber.

* To whom all correspondence should be sent:
E-mail: 7784257712qq.com

Mine Water Bacterial Liquid Enrichment

Prepare hydrogenogens-rich liquid 1000ml respectively with mine water and hydrogenogens medium, and prepare hydrogenogens-rich liquid 1000ml with mine water and methanogens medium for standby application.

EXPERIMENTAL PROGRAM

Methanogenesis Experiment

20g pulverized coal + 20ml white rot fungi liquid+ 200ml methanogens mine water enrichment nutrient solution, set three parallel samples to be placed in 35 °C incubator, adjust p H = 7, gas production time at 35 days, and ultimately take the average value for calculation.

3.2. Cogeneration of Hydrogen and Methane

Hydrogen production stage: 20g coal + 20ml white rot fungi liquid + 200ml enriched hydrogenogens liquid, adjust the initial pH value of the sample at about 6.8 which then receives anaerobic fermentation for about 10 days at 35 °C. Methanogenic stage: Similarly, supplement 1 mol / L NaOH solution to hydrogen production reaction flask at anaerobic work station, adjust the pH to about 7, add methanogens nutrient solution and add a small amount of trace elements. The total gas production time is 50 days. Set three parallel samples and ultimately take the average value for calculation. Record total gas production, gas concentration of two set of experiments. Carry out pH value detection and VFA analysis of reaction liquid, perform element and XRD analysis of coal before and after the reaction, calculate lignin and cellulose, hemicellulose consumption in order to carry out comparative analysis of the two gas production mechanisms.

EXPERIMENTAL RESULTS

Analysis of Gas Production

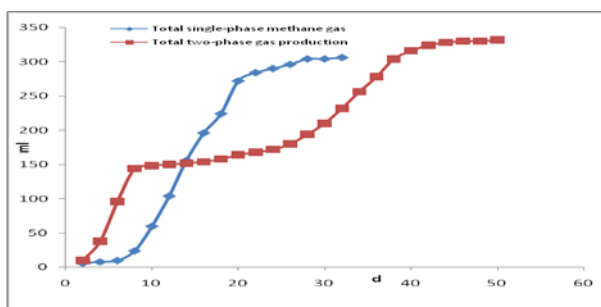


Fig. 1. Cumulative production output of methane and hydrogen.

Gas production changes show that single-phase production of CH₄ lasted 36 days, with a total CH₄

volume of 306ml; two-phase hydrogen and methane gas production time was 52 days, total first-phase hydrogen production volume was 114ml, total second-phase production volume was 264ml, with total gas production at 398ml. Two-phase situation is 18.1% more than single phase.

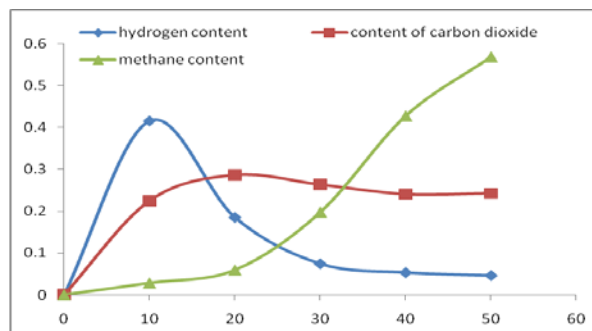


Fig. 2a. Two-phase system gas concentration variation diagram.

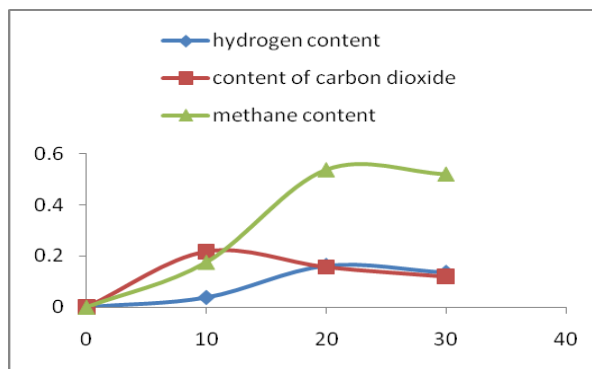


Fig. 2b. Single-phase methane gas concentration variation diagram.

Changes in gas concentrations show that in single-phase production of CH₄ system, H₂ concentration peaked at 16.3%, remaining low, while CO₂ concentration decreased after growth, reaching 21.7% on the tenth day and then reducing to 11.9%, CH₄ concentration kept growing to 50.6% at end of the experiment; cogeneration experiment shows that, H₂ content and concentration peaked at 40.6% on the tenth day, the highest value of hydrogenogens metabolic activity, and then plummeted afterwards, CO₂ concentration peaked at 28.7% on 22rd day and then maintained at around 25%. Obviously, CH₄ gas production and concentration of two-phase gas production are higher than that of single phase in gas production effect.

As can be seen from the figure, gas production lag phase of independent methane production lasted 8 days, which was because methanogens is with longer growth cycle which needs some time from growth delay to metabolism bloom phase. Hydrogenogens at hydrogen production stage in

cogeneration experiment was with shorter growing cycle, and hydrogen production basically ended after about 10 days. Second-phase methanogenesis had a delay of about 10 days, delaying about two days compared with independent methanogenesis. It is mainly because low pH value growth environment of methanogens. After adding alkali solution, methanogens needed an adjustment period, and therefore methanogens lag phase of cogeneration experiment was longer than independent methanogenesis. But seen from the figure, average production rate of cogeneration system is 32% higher than average production rate of independent methanogenesis, with average methane content also increased by 7.3%, indicating that gas production performance of cogeneration hydrogen and methane is better than single-phase system.

Effect on Liquid Fermentation Products

Effect on pH

During single-phase fermentation of methanogenesis, pH value decreased to some extent, until the minimal point 6.21 throughout the reaction on the 16th day or so, but continued to increase to 7.82 afterwards. Two-phase hydrogen production and methanogenesis reached the lowest value 5.25 on the twelfth day before stabilizing at 8.25. As is apparent, lowest pH value of two phase is much lower than that of single phase with final pH higher than that of single phase.

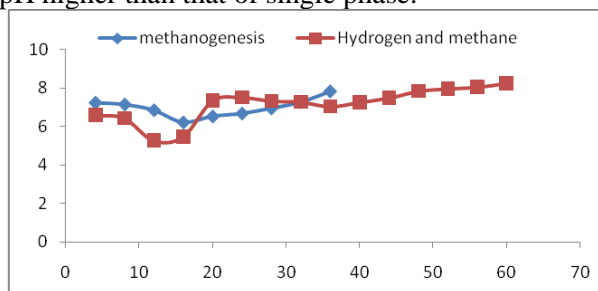


Fig. 3. pH value changing curve of single-phase and two-phase gas production.

As is seen from Figure 5, during single-phase methanogenesis fermentation, substrate degradation featured ethanol type fermentation. Peak occurred on the 18th day, about 0.35mmol / L, while acetic acid, butyric acid peaked on the 15th day, respectively 3.15mmol / L and 2.85mmol / L, whose concentration bottomed out to 0.35mmol / L and 0.21mmol / L after fermentation on the 26th day. The degradation rate of ethanol was very low throughout the experiment. After reaching the peak on the 10th day, ethanol concentration stopped significant change with only slight decrease in the later period, indicating that the acid generated

thereafter was rapidly degraded and no longer accumulated in fermentation liquid.

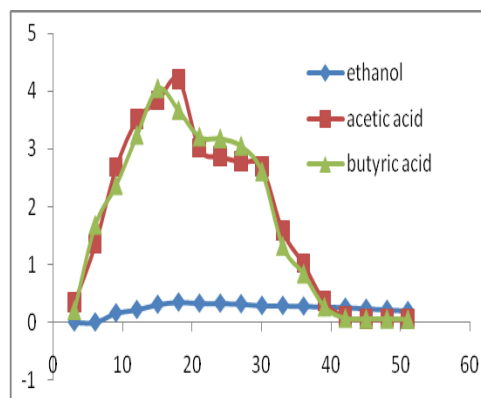


Fig. 4a. Variation of two-phase system of small molecule acid.

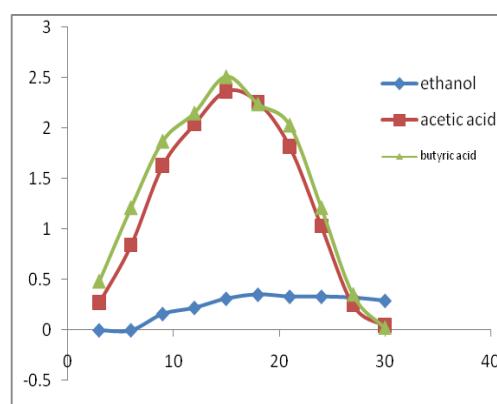


Fig. 4b. Variation of single-phase system of small molecule acid.

As is seen from the figure, first-phase substrate degradation in two-phase anaerobic fermentation featured butyric acid type fermentation. In production of butyric acid, a large amount of hydrogen was produced. At the end of hydrogen reaction, residual concentration of acetic acid was 4.21mmol / L, that of butyric acid was 3.67mmol / L, while that of ethanol was only 0.17mol / L or so. However, in the second phase, after methanogens recovered activity after 6d lag phase, butyric acid and acetic acid began to be used by methanogens. At the end of the reaction, acetic acid and butyric acid in the solution were substantially reduced to zero. From this, it can be concluded that concentration of acetic acid and butyric acid produced in two-phase and single-phase system are greatly different from each other, but final two-phase decomposition is more thorough. In analysis of the reasons, due to action of syntrophic acetogenic bacteria and fermentation bacteria, in cogeneration hydrogen production stage, more volatile fatty acids will be produced, which also provide fermentation substrate for

methanogenesis. After pH adjustment and physiological lag phase of bacteria, methanogens's VFA consumption accelerated. Judging from that final acetic acid and butyric acid concentration is zero, reaction of the stage features acetic acid decomposition.

Degradation of Coal

Degradation of Coal Elements

Comparative change of coal sample elements before and after aerogenesis is shown in the following table. As can be seen from the table, C content in coal suffered from varying degrees of decline after aerogenesis, decreased most after cogeneration to final amount of 73.5%. Gas experiment mainly studied organic carbon in microbial degradable coal. In cogeneration test, it was secondary aerogenesis with large consumption of C element, and therefore degree of degradation was more thorough. H element content increased, especially after hydrogen production when H content increased to 6.37%, 22.3% over that of raw coal sample. It was mainly because hydrolysis reaction occurred during hydrogen production, microbial enzymes substance decomposed macromolecules in coal and generated water-soluble small molecule compounds, aromatic ring fractured and induced active functional group with higher hydrogen content. Therefore, H element content increased, and after methanogenesis, hydrogen elements were broken down into water-soluble small molecules acid. So after methanogenesis, H element content decreased compared with hydrogen generation. O element increase was mainly a result of hydrolysis of macromolecules in coal in hydrogen production stage.

Table 1. Analysis of elemental changes of coal.

| Sample | C (%) | H (%) | O (%) |
|---------------------------------------|-------|-------|-------|
| Raw coal sample | 81.35 | 4.96 | 15.72 |
| Coal sample after methanogenesis | 76.35 | 5.45 | 13.64 |
| Coal sample after hydrogen production | 80.2 | 6.07 | 16.74 |
| Coal sample after cogeneration | 73.5 | 5.39 | 14.13 |

Coal Lignin, Cellulose, Hemicellulose Decomposition

As can be seen from the table, compared to single-phase methanogenesis system, cellulose, hemicellulose and lignin consumption rates of two-phase system were respectively increased by 3.6%, 5.8% and 6%, so degradation of two-phase system was definitely more thorough. Lignin,

cellulose, hemicellulose are more easily decomposed organic compounds in low rank coals. Under the action of primary enzymes such as laccase and manganese peroxidase, lignin and cellulose-based substances were hydrolyzed to high-molecular polymers such as polysaccharide protein and fat, which were further broken down into monose, amino acid and fatty acid. As is apparent from the table, in cogeneration system, after hydrogen production, acidic environment of the system is more conducive to degradation and use of cellulose, hemicellulose, lignin and other substances in the coal. Coal degradation rate was increased, availability of intermediate products including ethanol, acetic acid, propionic acid, butyric acid and other small molecules increased correspondingly, and therefore aerogenesis efficiency of hydrogen production and methanogenesis in co-fermentation was also improved.

Table 2. Decomposition of main chemical substances in coal.

| | Cellulose | Hemi-cellulose | Lignin |
|-------------------------------------|-----------|----------------|--------|
| Single-phase methanogenesis | 12.3% | 10.6% | 11.6% |
| Two-phase hydrogen production phase | 10.5% | 10.4% | 9.7% |
| Two-phase methanogenic phase | 7.6% | 6.2% | 5.5% |
| Two-phase system | 18.1% | 16.6% | 15.2% |

XRD Analysis of Coal Structure

Table 3. XRD structural parameters of coal.

| | d ₀₀₂ (10 ⁻¹ nm) | La (10 ⁻¹ nm) | Lc (10 ⁻¹ nm) |
|---------------------------------------|---|-----------------------------|-----------------------------|
| Raw coal sample | 3.694 | 2.517 | 0.896 |
| Coal sample after methanogenesis | 3.876 | 2.426 | 0.862 |
| Coal sample after hydrogen production | 3.945 | 2.503 | 0.877 |
| Coal sample after cogeneration | 3.936 | 2.368 | 0.833 |

In cogeneration experiment, after acid production in hydrogen production stage, three-dimensional molecular structure of coal was oxidized, benzene ring was gradually opened to introduce oxygen-containing groups such as

carboxyl, hydroxyl at open place, resulting in weakened bond energy, larger bond length and greater interlayer distance d_{002} . In addition, order degree of orientation was also reduced after hydrogen production. As a result, number of plies of condensed ring aromatic layer was decreased to some extent, also height, extension and diameter of aromatic layer were obviously less than those of independent methanogenesis, and loose degree of coal structure was larger than that of independent methanogenesis, which explained why coal structure degradation of two-phase hydrogen production and methanogenesis experiment was stronger than that of independent methanogenesis experiment.

Mechanism Analysis

Based on the above gas, liquid and solid phase change results, let us explore difference in aerogenesis mechanism of single-phase methane production and cogeneration of hydrogen and methane. In single-phase methanogenesis process, various types of oxygen-containing functional groups such as methyl, etc. were degraded by microorganism and dissolved in the reaction liquid after falling off, forming small molecule compounds; pH of reaction liquid lowered, concentration of fermentation substrate such as methyl etc. in this stage first increased and then decreased. CO_2 was the main production gas, and as the reaction proceeded, acetic acid content in the fermentation liquid continuously declined. pH value kept growing, and methane concentration during the stage continued to increase, reaching a peak at 53.68%, while CO_2 continued to reduce, indicating that CO_2 was consumed. CO_2 reduction pathway for CH_4 output appeared, with $\text{CO}_2 + 4\text{H}_2 \rightarrow \text{CH}_4 + 2\text{H}_2\text{O}$ as the representative reaction. The stage was for main output pathway of methane. In cogeneration of hydrogen and methane, under action of syntrophic acetogenic bacteria, a large amount of H_2 and CO_2 plus many small molecule acid were generated. Methane concentration was low at this time, but after re-adjusting pH and adding nutrients, various VFA began to be degraded and utilized by methanogens. However, due to adaptation period, methanogens's utilization of degradation intermediates was lagged. After fermentation to 36d, VFA concentration was only slightly reduced and methane concentration was very low at this time. After 36d, methanogens activity increased, use rate of small molecule acid was greatly increased, concentration of various acids decreased rapidly, causing gradual increase in pH value. After reaction proceeded to about 60d,

pH value of test fermentation liquid increased to 8.28, and in the process CO_2 concentration remained high, indicating that second phase methanogenesis process featured acetic acid substance fermentation, with reaction equation as $\text{CH}_3\text{COOH} \rightarrow \text{CH}_4 + \text{CO}_2$.

CONCLUSION

(1) In the case of single-phase fermentation of methanogenesis, average content of methane in gas was about 48.6%, with gas production rate at 18.7ml / g; in the case of cogeneration of aerogenesis, average content of pre-gas hydrogen reached 42.3%, with gas production rate at 9.6 ml / g, methane content in second-phase aerogenesis reached 53.6%, with gas production rate at 23.7 ml / g, respectively improving by 8.15% compared with single-phase fermentation.

(2) Degradation of substrate during single-phase methanogenesis featured ethanol type fermentation; degradation of substrate in two-phase anaerobic fermentation of hydrogen production phase featured butyric acid type fermentation, and second phase also featured ethanol type fermentation. Although higher concentrations of butyric acid and acetic acid were generated in hydrogen production phase fermentation, after pH adjustment, most of the acetic acid and butyric acid were utilized by methanogens, generating methane and carbon dioxide, which made methane amount gas produced in methanogenesis phase increased compared with hydrogen production phase.

(3) In independent methanogenesis, main elements of coal, lignin and cellulose degradation rate, aromatic parameter were lower than those of cogeneration system at the end of aerogenesis, which proved that degradation of coal in cogeneration experiment was more thorough with higher utilization of residual coal.

Acknowledgements: This work was financially supported by the National Natural Science of Foundation of China (Grants 41472127, 41472129 and 41502158) and the 2014 Shanxi Provincial Programme for Tackling Key Problems of Coal-based Science and Technology (MQ2014-01) and Coal Seam Gas Joint Foundation of Shanxi (Grant 2013012004).

REFERENCES

1. S. Zahedi, R. Solera, F. Micolucci, C. Cavinato, D. Bolzonella, *Waste management*, **49**, 6 (2016).
2. M. Abo-Hashesh, R. Wang, P.C. Hallenbeck, *Bioresour. Technol.*, **102**, 8414 (2011).
3. F. Abouelenien, W. Fujiwara, Y. Namba, M. Kosseva,

- N. Nishio, Y. Nakashimada, *Bioresour. Technol.*, **101**, 6368 (2010).
4. C. Cavinato, D. BolzoneUa, F. Fatone, P. Pavan, *Bioresour Technol*, **102**(18), 8605 (2011).
5. Y.F. Zhao, X.L. Liu, S.Z. Li, W.Q. Ruan, J.S. Liu, M. Tian, *Transactions of the Chinese Society of Agricultural Engineering*, **27**, 255 (2011).
6. D. Li, Z.H. Yuan, Y.M. Sun, L. Ma, L. Li, *Chinese J Appl Environ Biol*, **15**, 250 (2009).
7. K.S. Lee, Y.S. Lo, Y.C. Lo, P.J. Lin, J.S. Chang, *Biotechnology Letters*, **25**, 133 (2003).
8. B.F. Xie, Mechanism Study of cogeneration of hydrogen and methane with starch / cellulose biomass fermentation, Hangzhou: Zhejiang University, 2009.
9. J. Xiong, H.R. Yuan, K.S. Wang, *Environmental Science & Technology*, **13**, 25 (2012).
10. D.W. Liu, D.P. Liu, J.Z. Raymond, I. Angelidaki, *Water Research*, **40**(11), 2230 (2006).
11. S. Liu, W.Z. Li, *Transactions of the Chinese Society of Agricultural Engineering*, **16**, 197 (2012).
12. S. Liu, W.Z. Li, C.Y. Wang, G.X. Zheng, Z.D. Liu, *Chinese Journal of Environmental Engineering*, **03**, 700 (2010).
13. A.R. Scott, W.R. Kaise, W.B. Ayers, *AAPG Bulletin*, **78**(8), 1186 (1994).
14. D. Li, Z.H. Yuan, Y.M. Sun, L.L. Ma, *Transactions of the Chinese Society of Agricultural Engineering*, **25**(1), 59 (2009).

Study on the wet inside filtration theory of fiber layer for dust particles based on equivalent analogy hypothesis

X.S. Chen, Y.L. Zhang *

Environmental and Municipal Engineering College of Qingdao University of Technology, Qingdao, 266520

Received May 30, 2017; Revised August 28, 2017

Article is intended for the process of wet fiber layer which was the combination of fiber filtration mechanism and washing mechanism, the hypothesis of the cleaning fluid in the fiber layer evenly distributed on the surface of the fiber filament is introduced by adopting the equivalent analogy, thereby establishing the theoretical model of purification efficiency, and achieving the theoretical analysis of filtration process of wet fiber layer for the dust particle. Meanwhile, the semi-theoretical and semi-empirical purification efficiency formula for dust purification and its correction method are obtained through dimensionless correction of the theoretical formula by means of the experiments carried out, which facilitates the theoretical study of the wet fiber layer for dust purification and is of guiding significance to practical application.

Keywords: dust particles, fiber filter layer, wet filter, equivalent analogy, filter efficiency

INTRODUCTION

The wet fiber filtration is an efficient method for dust purification combining fiber layer filtration with spray washing and the purification process of wet fiber layer for dust particles is the combination of fiber filtration mechanism and washing mechanism [1]. This combination process which has the high effect of the dust filtration of fiber filter layer, in addition to the cleaning effect of the fluid on the dust deposit within the fiber filter layer. Compared to the dry fiber layer for dust filtration and purification, it features advantages such as long service life of fiber filter material, no reentrainment of dust, high efficiency of dust capture, etc. especially significant in the trapping of fine dust and widely used for industrial dust collection.

In the filtration process of wet fiber layer, due to the extremely complex distribution of washing fluid in the fiber filter layer, it is impossible to make theoretical analysis, currently there is no perfect theoretical formula to describe the purification theory of wet fiber layer for dust filtration [2-4]. In this paper, the in-depth research on the purification mechanism of wet fiber layer for dust filtration was carried out on the basis of the assumption of equivalent analogy, avoiding the complex fluid distribution in the fiber filter layer, serves as the bridge for theoretical and quantitative description of filling rate of the fluid in the fiber filter layer, thereby obtaining the theoretical formula of filtration efficiency, while with the help of experiments and the dimensionless correction

method, a semi-theoretical semi-empirical formula of the filtration and purification efficiency of the wet fiber layer was given, which accomplished an access to a relatively perfect semi-theoretical semi-empirical formula for filtration efficiency of the wet fiber layer and provides a theoretical explanation for the filtration and purification method of wet fiber layer for dust particles.

Analysis of filtration efficiency of the wet fiber layer

Equivalent analogy analysis

In order to avoid the distribution complexity of washing fluid in the fiber filter layer in the whole analytical process, so that the wet filtration process can be described theoretically, under the premise of the equal filling rate of the fluid in the fiber filter layer, based on the assumption of the previous dry fiber layer filtration [5-6], the following assumption of equivalent analog was proposed.

1) The filament in the filter material has a circular cross-section and the dust particles are spherical;

2) The dusty air flows perpendicular to the filament

3) the flushing fluid that flew into the inside of fiber filter layer flows uniformly and attached to the surface layer of the filaments under the action of the air flow, forming a composite trap with the static fiber and dynamic flushing fluid for dust particle collection;

4) Once the dust particle is filtered, it will be taken away by the flowing cleaning fluid, having no influence on the subsequent purification process

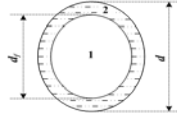
5) Dust particle filtration process is taking place in the spatial volume occupied by the fiber filter

* To whom all correspondence should be sent:
E-mail: zhyoliang@163.com

material, which is defined as the dust collection space.

Composite trap and the equivalent diameter d

After the analog equivalent assumption, the cleaning fluid and filaments formed the composite trap, as shown in Fig. 1, the equivalent diameter of the composite trap should consist of the diameter of filaments and the flowing cleaning fluid film attached to the surface of the filaments.



1 -filaments; 2 - flowing cleaning fluid film

Fig. 1. The cross-section of composite trap

The annular cross-sectional area of the flowing cleaning fluid film formed in the composite trap should be:

$$\frac{\pi}{4}(d^2 - d_f^2) = \frac{V \cdot \beta_1}{l_f}$$

Where: V – the volume of space occupied by wet fiber filter layer (m^3); β_1 - Dynamic filling rate of the cleaning fluid (%); l_f – the overall length of the filament (m), $l_f = 4\beta_f V / (\pi d_f^2)$ where, β_f - static filling rate of the filament (%).

The total length of the filaments is substituted into the above formula, and the expression for equivalent diameter of the composite trap can be drawn:

$$d = d_f \sqrt{1 + \frac{\beta_1}{\beta_f}} \tag{1}$$

The relationship between the equivalent diameter d of the composite trap and the dynamic filling rate of the fluid β_1 and the fiber filament d_f was established in formula (1), which serves as the bridge for theoretical analysis of filtration and purification of the wet fiber layer.

The filling rate β of the composite filter

In the filtration and purification process of the wet fiber layer, the internal composite trap contains the cleaning fluid film in a flowing state in addition to the filaments, so the total filling rate in the wet filter trapping space should include the static filling rate β_f of the filaments and the dynamic filling rate β_1 of the cleaning fluid, that is:

$$\beta = \beta_f + \beta_1 \tag{2}$$

Wherein, the static filling rate β_f of the fiber was given when the product manufactured, the dynamic filling rate β_1 of the cleaning fluid and the wet filtration purification process depend on the

amount of water spray, experiments show that when the filling rate of filaments in the fiber layer is less than 3%, it should be the ratio of spray amount per unit time and the volume of filter material in the fiber layer being sprayed (dust collecting space), i.e.:

$$\beta_1 = \frac{q}{A \cdot H} \tag{3}$$

Where: q is the spray volume received on the surface of filaments in the fiber layer per unit time (m^3/s); A is the sprayed area of the fiber filter layer surface (m^2); H is the thickness (m) of the fiber filter layer.

Theoretical analysis of the wet fiber layer filtration efficiency

Theoretical analysis

The filtration and purification model of dust-laden air flowing through the wet fiber layer is shown in Figure 2, due to the spherical spray section, the circular filtration model is given in Fig. 2.

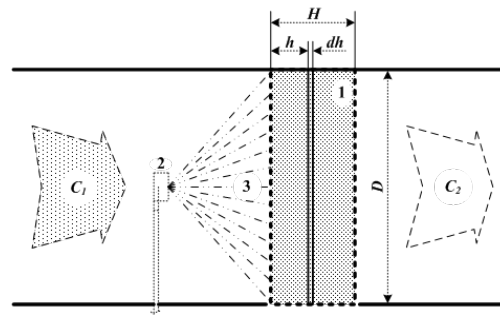


Fig. 2. Filtration model

Provided that the air volume flowing through the wet fiber layer is Q , the flow rate of air flow before filtration is u , the dust concentration in the air flow before filtration and after filtration is C_1 , and C_2 , the thickness of the wet filter layer is H , the frontal area (also the sprayed wet area) is A , the filling rate of the composite trap in the fiber filter layer is β , then the filtration velocity of the air flow in the wet filter layer should be:

$$u_x = \frac{u}{(1 - \beta)} = \frac{Q}{A(1 - \beta)} \tag{4}$$

As shown in Fig. 3, infinitesimal sheet taken from the wet filter layer is used for analysis. The volume of infinitesimal sheet should be $dV = A \cdot dx$. The concentration of dust particles in the air entering the infinitesimal sheet is C_x . In the infinitesimal sheet, the mass of dust particles under the captured per unit time in the composite trap per unit length should be $C_x \cdot u_x \cdot E$, wherein, E is the dust collecting efficiency of the composite trap per unit length.

Provided that the length of composite trap in the infinitesimal sheet is set as dl , after the air flows through the infinitesimal sheet dV , the concentration of dust particles reduced by $-Q \cdot dC_x$, and the mass of dust particles trapped in this infinitesimal sheet is $C_x \cdot u_x \cdot E \cdot dl$, the two should be equal, namely:

$$-Q \cdot dC_x = C_x \cdot u_x \cdot E \cdot dl$$

The length of the composite trap in infinitesimal sheet can be written as $dl = \frac{4 \cdot \beta \cdot A \cdot dx}{\pi \cdot d^2}$, where d is the

equivalent diameter of the composite trap, the dl and u_x in formula (3) are substituted into the above formula and the analyzed differential expression can be obtained as follows:

$$-\frac{dC_x}{C_x} = \frac{4 \cdot \beta \cdot E}{(1-\beta) \cdot \pi \cdot d} dx$$

Taking the integral for both ends of the equal sign, the following formula is obtained:

$$\int_{C_1}^{C_2} -\frac{dC_x}{C_x} = \int_0^H \frac{4 \cdot \beta \cdot E}{(1-\beta) \cdot \pi \cdot d} dx$$

The ratio of dust concentration after and before the airflow filtration obtained by integrating:

$$\frac{C_2}{C_1} = \exp\left[-\frac{4 \cdot \beta \cdot H \cdot E}{\pi \cdot (1-\beta) \cdot d}\right]$$

The stage purification efficiency η_d of wet filtration should be:

$$\eta_d = 1 - \frac{C_2}{C_1} = \frac{C_1 - C_2}{C_1} = 1 - \exp\left[-\frac{4 \cdot \beta \cdot H \cdot E}{\pi \cdot (1-\beta) \cdot d}\right] \quad (5)$$

The theoretical formula of stage efficiency based on the deduced hypothesis of equivalent analogy has been obtained through theoretical analysis, where d represents the equivalent diameter of the composite trap in the wet filtration and purification process; β indicates the sum of the dynamic filling rate of the cleaning fluid and the static filling rate of filaments in the dust collecting space.

The foregoing expression of the equivalent diameter (1) and the total filling rate expression (2) are substituted into formula (5), the derived theoretical formula of stage efficiency of wet filtration and purification based on the equivalent analogy hypothesis can be obtained:

$$\eta_d = 1 - \exp\left\{-\frac{4 \cdot \sqrt{\beta_f \cdot (\beta_1 + \beta_f)} \cdot H \cdot E}{\pi \cdot (1 - (\beta_1 + \beta_f)) \cdot d_f}\right\} \quad (6)$$

The formula (6) comprises the filling rate of the cleaning fluid, allowing the theoretical analysis of the wet filtration process to be achieved, furthermore, the equivalent diameter of the composite trap formed by the cleaning fluid and filaments is introduced into the E value in formula (6), reflecting the co-trapping effect of filaments and flushing fluid for dust particles.

The dust purification efficiency of singly rooted

composite trap

The E in formula (6) represents the dust filtration and purification efficiency of the dust-laden air flowing round the single composite trap per unit length in the wet filtration and purification process. Research shows that when the dust air flows around the single cylindrical trap, although the trapping of dust particles is the result of multiple mechanism of the entrapment, collision, diffusion and coagulation etc, the major effect of the entrapment by the cylindrical trap and the inertia separation of the dust particles as well as the diffusion of fine particles lead to the result ($d_p < 1\mu\text{m}$), therefore, the purification efficiency of the single composite trap can be calculated according to the following formula:

$$E = 1 - (1 - \eta_R)(1 - \eta_I)(1 - \eta_D) \quad (7)$$

The entrapment effect and efficiency

η_R in formula (6) is the efficiency of the dust particles trapped when the dust air flows around the single composite trap per unit length, expressed as follows^[5]:

$$\eta_R = 1 + \frac{d_p}{d} - \frac{1}{1 + d_p/d}$$

Where: $R = d_p/d$ is called interception parameter, d_p is diameter (m) of dust particles; d is the equivalent diameter (m) of the composite trap, which is to be calculated by formula (1).

Inertia effect and efficiency

η_I in formula (6) represents the efficiency of the dust particle trapped due to the separation from the flow line and collision on the composite trap as the result of its own inertia when the dust air flows around the single composite trap per unit length, expressed as follows

$$\eta_I = \frac{S_{ik}^3}{S_{ik}^3 + 0.77S_{ik}^2 + 0.22}$$

Where: $S_{ik} = \rho_p d_p^2 u_x / 9\mu d$ is named the Stokes dimensionless number.

Diffusion effect and efficiency

η_D in formula (6) indicates the efficiency of diffusion of fine dust particles ($d_p < 1\mu\text{m}$) in the dust-laden air towards the cylindrical composite trap, expressed as follows

$$\eta_D = \sqrt{\frac{8}{u_x d / D}}$$

Where: $D = k_B T C_u / 3\pi\mu d_p$ is called the diffusion coefficient; $k_B = 1.38 \times 10^{-23}$ (J/K), is called the Boltzmann constant; $C_u = 1 + 0.165/d_p$ is referred to as Cunningham correction factor, the unit for dust particle diameter d_p is set as μm .

EXPERIMENTAL TESTS OF THEORETICAL FORMULA

Experimental conditions

The theoretical formula (6) was tested through laboratory analogue experiment and the experiment system is shown in Fig. 3.

The microbead-like silicon powder was used as the specimen for dust particles, and water as the flushing fluid in the experiment. Basic parameters used in the experiment are as shown in Table 1.

Comparison and analysis of the experimental results and theoretical calculation

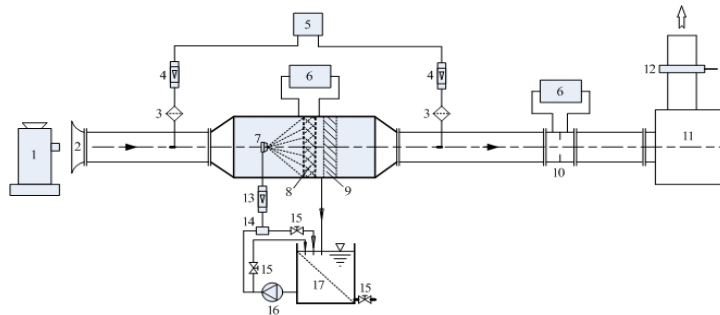
The experimental curve of stage purification efficiency was obtained through analogue experiments with the parameters in Table 1, while the theoretical curve of the stage purification efficiency was calculated with the parameters in Table 1 according to theoretical equations (6) and (7). The resulting two curves are plotted in Fig. 4.

As can be seen from Fig. 4, the curve trend of the calculation by theoretical equation (6) and the measured one in the analogue experiments are basically consistent, adequately revealing the law of the wet filtration and purification, especially for the dust particles larger than 10µm, the theoretical calculations and experimental results are

consistent, while for the dust particles below 10µm, there is certain deviation between the results, the smaller the dust particle size is, the greater the deviation, the theoretically calculated purification efficiency of fine dust particles is higher than the experiment measured one.

The main reason lies in the surface tension of the cleaning fluid (water), and the trapping of fine dust mainly relies on diffusion effect, so fine dust particles can hardly break through the fluid (water) surface to be moistened and trapped, while in theory it is simply assumed that as long as the dust particles come into contact with the fluid surface, they will be moistened and trapped, the effect of surface tension is not taken into account.

Despite the gap between the theoretical and the measured results of the fine dust particles, the result of theoretical analysis has fully reflected the basic law of the filtration process. Meanwhile, the analysis of analogue experimental curve shows that in the wet filtration and purification process, the purification efficiency of the fine dust will be improved by sufficiently reducing the surface tension of the cleaning fluid, and the actual experiment result will be closer to the calculated result by theoretical formula (6), which instructs the way to further improve the purification efficiency of the fine dust.

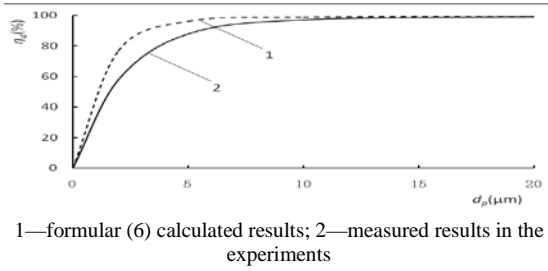


1 - dust emitter; 2 - collector; 3 - sampling head; 4 - gas flowmeter; 5 - sampler; 6 - micro-manometer; 7 - atomizing nozzle; 8 - fibrous filter layer; 9 - fluid exhaustion unit; 10 - orifice flowmeter; 11 - blower and control cabinet; 12 - gate valve; 13 - fluid flow meter; 14 - filter; 15 - valves; 16 - feed liquid pump; 17 - fluid storage tank.

Fig. 3. The analogue experiment system

Table 1. Analogue experiment parameters

| Air flow parameters | | | Fiber filter parameters | | | | Dust parameters | Spray parameters | |
|--|--|---|--|-----------------------------|--|--------------------------------|---|--|--------------------------------|
| Dynamic viscosity $\mu / \text{N} \cdot \text{s} \cdot \text{m}^{-2}$ | Absolute temperature $T / ^\circ\text{K}$ | Filtration velocity $u_x / \text{m} \cdot \text{s}^{-1}$ | Filament diameter $d_f / \mu\text{m}$ | Thickness H / m | Area of fluid received A / m^2 | Filling rate $\beta_f / \%$ | true density of dust specimen $\rho_p / \text{kg} \cdot \text{m}^{-3}$ | Quantity of fluid supplied $Q / \text{L} \cdot \text{h}^{-1}$ | Filling rate $\beta_1 / \%$ |
| 1.81×10^{-5} | 290 | 1.39 | 133 | 0.04 | 0.11 | 1.01 | 2750 | 72 | 0.45 |



1—formular (6) calculated results; 2—measured results in the experiments

Fig. 4. Comparison between the calculated results using formula (6) and measured results

Correction of theoretical formula

In practical applications, to get the calculated result of theoretical formula (6) closer to the actual one, the experimental data obtained are applied for its dimensionless correction.

The exponential term in theoretical formula (6) is set with a correction factor ζ , the equation becomes the following one:

$$\eta_d = 1 - \exp \left\{ -\zeta \cdot \frac{4}{\pi} \cdot \frac{\sqrt{\beta_f \cdot (\beta_1 + \beta_f)} \cdot H}{1 - (\beta_1 + \beta_f)} \cdot \frac{H}{d_f} \cdot E \right\} \quad (8)$$

Taking the natural logarithm for both ends of the equal sign after the deformation of the formula, the following one is obtained:

$$\ln \frac{1}{1 - \eta_d} = \zeta \cdot \frac{4H}{\pi \cdot d_f} \cdot \frac{\sqrt{\beta_f \cdot (\beta_1 + \beta_f)}}{1 - (\beta_1 + \beta_f)} \cdot E$$

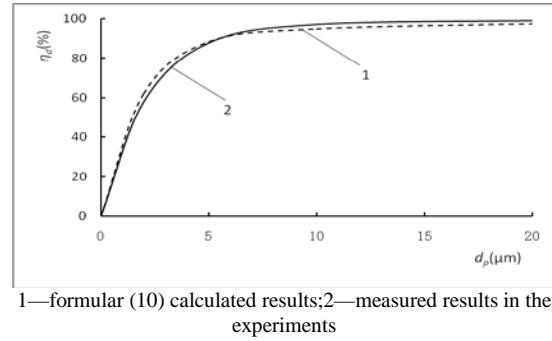
Provided that $Y = \ln \frac{1}{1 - \eta_d}$ and $X = \frac{4H}{\pi \cdot d_f} \cdot \frac{\sqrt{\beta_f \cdot (\beta_1 + \beta_f)}}{1 - (\beta_1 + \beta_f)} \cdot E$, the following linear equation is obtained:

$$Y = \zeta \cdot X \quad (9)$$

The relevant values of different particle sizes are calculated with experimental data and the parameters in Table 1 and substituted to determine the scatter plot of X corresponding to Y , as per the form of formula (9) for linear equation regression, the slope $\zeta = 0.97$ of the linear equation is obtained, which is substituted into formula (8) and the corrected formal of the theoretical formula is obtained:

$$\eta_d = 1 - \exp \left\{ -0.97 \cdot \frac{4}{\pi} \cdot \frac{\sqrt{\beta_f \cdot (\beta_1 + \beta_f)} \cdot H}{1 - (\beta_1 + \beta_f)} \cdot \frac{H}{d_f} \cdot E \right\} \quad (10)$$

Formula (10) is a semi-theoretical and semi-empirical formula for stage efficiency of the wet fiber layer for dust filtration and purification after the dimensionless correction. The stage efficiency curve of the wet fiber layer filtration and purification calculated with this formula compared with the measured result is as shown in Fig. 5.



1—formular (10) calculated results; 2—measured results in the experiments

Fig. 5. Comparison between the calculated result based on formula (10) and the measured result

It can be seen from Fig. 5 that the two curves are very close, indicating formula (10) can accurately reflect the actual situation of the wet fiber layer filtration and purification, which can be used to guide the practical application.

CONCLUSIONS

For the wet filtration and purification technology combining the fiber layer with spray for dust particles, the equivalent relationship has been established between the system fluid amount and the filling rate inside the fiber layer by means of the equivalent analogy hypothesis, enabling the complex problems to be described theoretically.

The derived purification efficiency formula for wet filtration and purification process of dust particle reflects the functions and influences of physical parameters in the process of wet filtration, which can be used to guide actual wet filtration and purification process. The semi-empirical and semi-theoretical efficiency formula obtained through dimensionless correction of the theoretical formula reflects the actual situation more accurately. For other specific cases, the correction method mentioned in this article may be used to obtain accurate semi-empirical and semi-theoretical calculation formula for practical application.

The theoretical calculations and experimental results in Figure 4 show that the surface tension of the cleaning fluid is an important factor affecting the purification effect of the fine dust, it is just because the surface tension of the cleaning fluid that hinders the cleaning fluid from moistening and trapping the fine dust particles, as a result, the surface tension of the cleaning fluid reduced as much as possible will be of significance to purification of fine dust particles.

Acknowledgements: Fund program: The project funded by the National Natural Science Fund (51274127, 51204100)

REFERENCES

- 1.G.Y. Sun, Filtering performance and mechanism research of wet fiber, *Master's thesis, Northeastern University*, **10**, 126 (1987).
- 2.Y.L. Zhang, Tang M.K., *Metal Mine*, **9**, 91 (2010).
- 3.X.S. Chen, Y. Li, *Environmental Engineering*, **6**, 38 (2005).
- 4.C.S. Rao, *Environmental Pollution Control Engineering*, New York: John Wiley & Sons, **8**, 25 1991.
- 5.X.D. Xiang, *Modern dust collection theory and technology*, Metallurgical Industry Press, **8**, 108 (2002).
- 6.G.Q. Zhang, *Aerosol mechanics-theoretical basis for dust collection and purification*, Beijing: China Environmental Science Press, **12**, 53 (1987).

Effect of key parameters on the secondary combustion efficiency of boron - containing gas

Z. He¹, X.Y. Sun^{1*}, X. Gu¹, J. He¹

¹ College of Aerospace and Civil Engineering, Harbin Engineering University, Harbin, China

Received June 23, 2017; Revised August 28, 2017

The key factors influencing the secondary combustion of solid rocket ramjet engine were summarized. The secondary combustion chamber model with front and rear inlet was established. The influence of the particle diameter and gas injection angle on the effect of cold mixing and secondary combustion was studied by numerical simulation. The results show that the smaller the particle diameter is, the more favorable the blending efficiency is and the higher the combustion efficiency is. The larger fuel injection angle is more favorable for blending, and the combustion efficiency can be improved remarkably. Increasing the air-fuel ratio can increase the gas and particle combustion efficiency. The influencing factors of working process of secondary combustion chamber are verified by numerical simulation of cold mixing and combustion process of the secondary combustion chamber. The phenomenon is explained theoretically.

Keywords: Solid Rocket Ramjet, Intake, Supplementary Combustion Chamber, Cold Flow Blending; Combustion Efficiency.

INTRODUCTION

The SIMPLE method was used by Vanka [1] to calculate the flow of the ramjet under cold flow conditions, and the vortex and backflow observed by the water flow test were reproduced [1, 2]. Chen and Tao based on the two-dimensional axisymmetric solid rocket engine model [3]. The results show that the blending and combustion process influent on the engine performance, and put forward appropriate to reduce the inlet length, reduce air-fuel ratio and reduce the Airway angles benefiting to improve blending and combustion thereby improving engine performance. Hong studied the combustion process in a two-dimensional re-combustion chamber [4]. The results show that the larger the intake angle is, the smaller the area of the back burner chamber is. At the same time, the recovery coefficient of total pressure will be lower. T.M. Liou et al. [5] showed the complexity of the flow in the secondary combustion chamber in the case of cold flow, and revealed the structure of the three-dimensional vortex in the flow field [5, 6, 7]. The concept of vortex intensity is introduced to quantitatively describe the motion of vortices, and the results reveal the movement of the vortex in the combustion chamber. Foelsche studied the effects of temperature, oxygen mole fraction, temperature and other parameters on the boron combustion process in the crystal state [8]. The results show that the burning time of boron particles will be shortened with increasing pressure.

EXPERIMENTAL

METHODS

The King model and Williams model are the most representative of the ignition model of boron particles, and the King ignition model is used to calculate the reaction flow field in the afterburner chamber as follows:

$$d_p = d_B + 2\delta \quad (1)$$

$$\frac{dd_B}{dt} = -\frac{2R_B M_B}{\pi d_B^2} \quad (2)$$

$$\frac{d\delta}{dt} = -\frac{(R_B/2 - R_E - R_H) M_{B_2O_3}}{\pi d_B^2 \rho_{B_2O_3}} \quad (3)$$

$$\frac{dT_p}{dt} = \frac{Q}{(\pi d_B^2 / 6) c_{pBL} \rho_{BL} + \pi d_B^2 \delta c_{pB_2O_3}} \quad (4)$$

$$(T_p > 2450K)$$

$$\frac{dT_p}{dt} = \frac{Q}{(\pi d_B^2 / 6) c_{pB} \rho_B + \pi d_B^2 \delta c_{pB_2O_3}} \quad (5)$$

$$\frac{d\delta}{dt} = \frac{Q}{(\pi d_B^2 / 6) \rho_B \Delta H_M} \quad (6)$$

$$(T = 2450K)$$

$$R_B = f(d_p, T_p, p_{O_2}, \delta) \quad (7)$$

$$R_E = f(d_p, T_p, p) \quad (8)$$

$$R_H = f(d_p, T_p, p_{H_2O}) \quad (9)$$

* To whom all correspondence should be sent:

E-mail:sunxiaoyu520634@163.com

For the boron particle size, for the oxide layer thickness, for the melting fraction, for the particle temperature; for the boron grain consumption rate, the rate of B_2O_3 evaporation, B_2O_3 and water reaction rate, the meaning of other symbols reference [9]. The total combustion reaction of boron particles is: $2B(s) + O_2(g) \rightarrow B_2O_2 + 110kcal/mol$. The burning rate is: where is the reaction rate constant.

MODELS

The physical model is shown in Figure 1. The overall mesh is shown in Figure 2. The boundary conditions were as follows: air inlet total temperature 573K, air inlet flow rate were equal, respectively, 2kg/s, four air inlet pressure 6atm. Rich gas flow 0.17kg/s. The gas inlet temperature was 1831 K and the gas generator pressure was 5 atm. There are six gas components: CO, H_2 , HCl, $AlCl_3$, CO_2 and H_2O , and their mass fractions are 0.45, 0.2, 0.05, 0.15, 0.1 and 0.05 respectively. Assuming boron particles accounted for 60% of the gas, particle diameter of 2, particle temperature and velocity and gas in the same gas phase values.

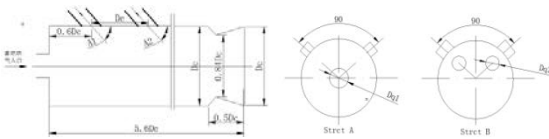


Fig. 1. Schematic diagram of the supplementary chamber



Fig. 2. Model building and meshing

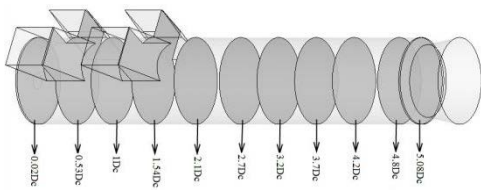


Fig. 3. Location of the cross section of the supplementary chamber

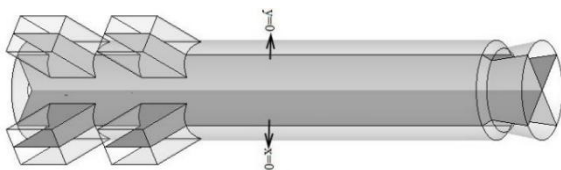


Fig. 4. Axial section of the post-combustion chamber.

When the blending degree and the dimensionless particle concentration are calculated, the cross section of the afterburner is taken as the reference, and the cross section is taken to analyze the blending degree (Figure 7 and Figure 8). The non-dimensional isobaric concentration cloud diagram, the oxygen-fuel ratio, the oxygen and particle blending degree cloud diagram are given.

RESULTS AND DISCUSSION

SIMULATION

The simulation results show that the inlet angle is 90° , the gas injection angle is 90° , the other parameters are not changed, and the particle diameter is $2\mu m$, $5\mu m$ and $10\mu m$ respectively.

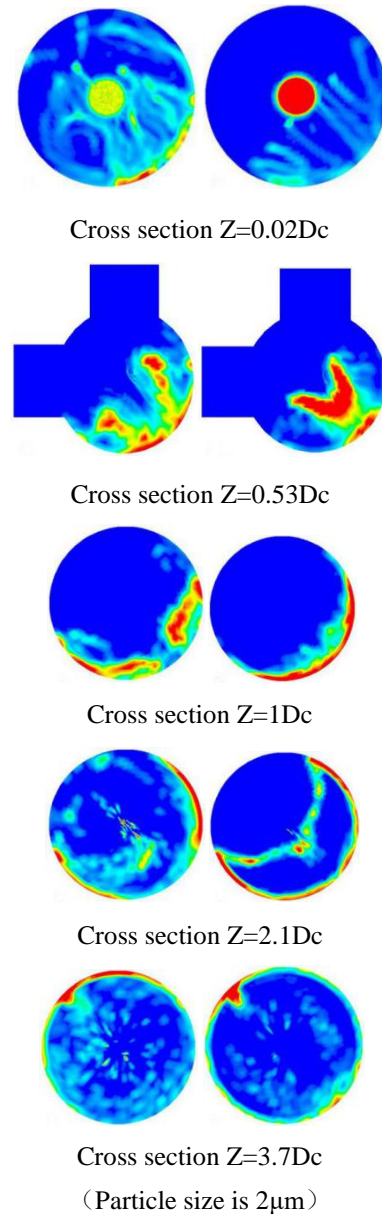


Fig. 5. Unequal particles on different cross-section concentration cloud (left particle size of 5, the right particle size of 10).

From Figure 5, With the increase of the boron particle diameter, the agglomeration phenomenon will increase, and the influence of the vortex movement on the particle agglomeration area will be weakened. Figure 6 shows that the larger the particle diameter, the worse the blending effect. From the blending curve, it can be concluded that the particle diameter is consistent with the particle trajectory, and the diameter of the small particle is better than that of the large particle diameter in the whole flow field.

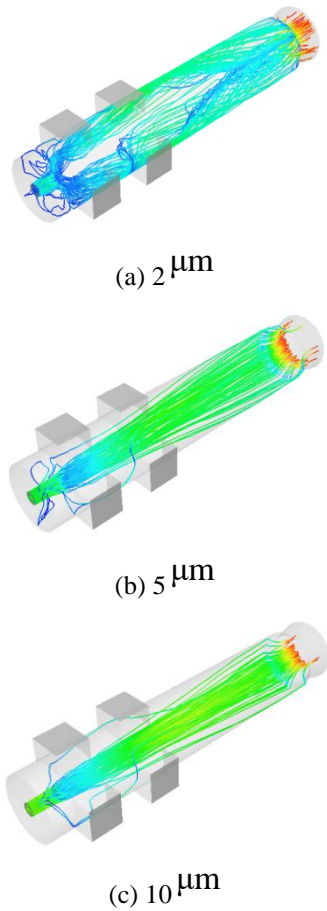


Fig. 6. Particle distribution in secondary combustion chamber with different particle diameters

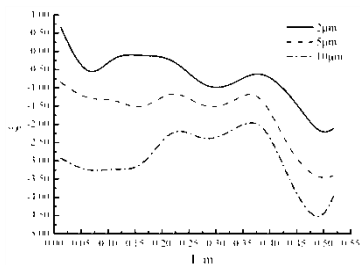


Fig. 7. Blending curves for different particle diameters

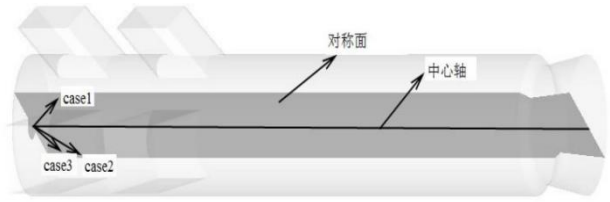


Fig. 8. Gas injection angle and the central axis angle diagram.

Effect of Gas Injection Angle on Gas Particle Blending

In this section, the inlet angle is 90° , the particle diameter is taken as $2 \mu\text{m}$, and the other parameters are unchanged. The injection angle of fuel gas is 0° , 45° , -30° , -45° from the central axis of the secondary chamber, corresponding to case0, case1, case2, case3.

Figure 9 shows that the gas angle changes in the secondary combustion chamber head flow field impact. Figure 10 shows that the best blending effect in the head of the afterburner is case3, followed by case2, with the most severe case of particle aggregation, so that a large amount of gas enters the supplementary chamber and then flows back to the front of the supplementary chamber due to the vortex effect, thus prolonging the residence time of gas and particles in the supplementary chamber.

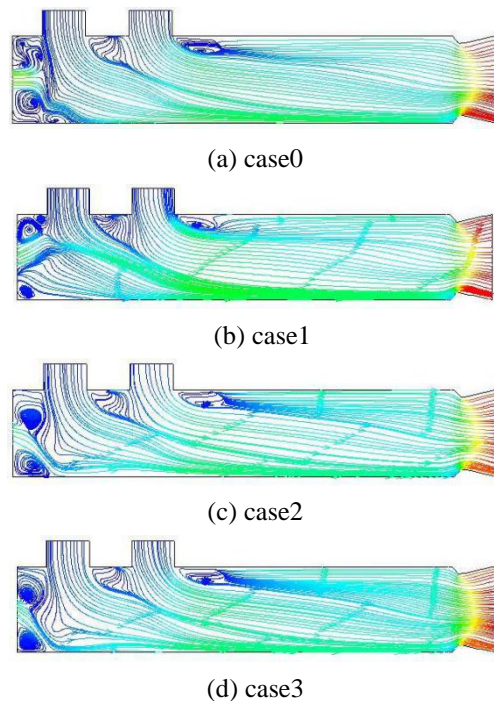


Fig. 9. Streamline of $x = 0$ axial section with different gas injection angles.

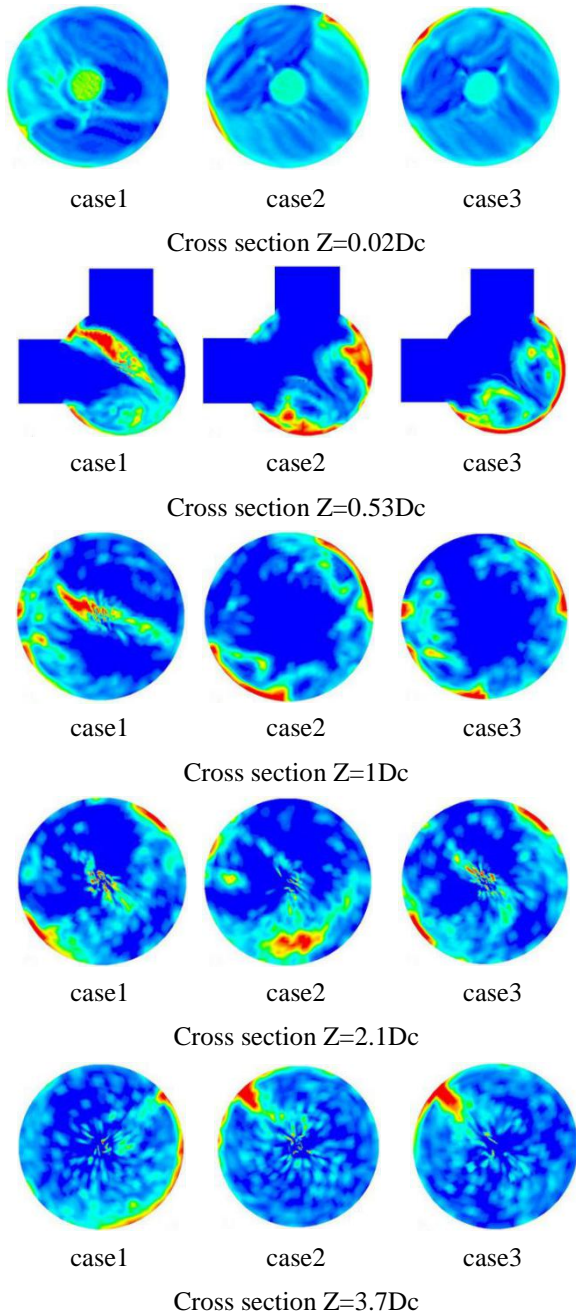


Fig.10. Dimensionless isotonic cloud plot at different cross-sections for different gas incidence angles

As can be seen from Figure 11, This shows that the gas injection angle will affect the mixing of gas particles, and the upward jet is not conducive to blending, the downward spray is conducive to blending, the 45° angle of the blending is better than 30°.

According to the blending curve of Figure 12, it can be seen that the best case of gas blending is case3, which indicates that the larger the angle of gas injection is, the more favorable the gas blending is. However, according to the study [10], when the gas injection angle exceeds a certain range, it is not conducive to reducing the primary combustion residue of the gas generator, and will affect the

injection efficiency. Therefore, in the design of fuel injection angle, it should be a comprehensive study of its combustion efficiency and the impact of jet efficiency. The influence of air inlet angle on secondary combustion was investigated experimentally

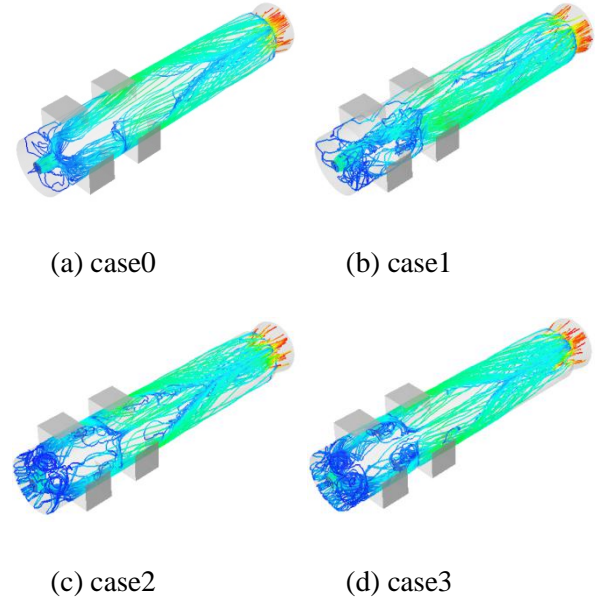


Fig. 11. Distribution of particle trajectories at different angles of incidence of gas

EXPERIMENT

The experimental design of the engine uses a modular design, can easily adjust the nozzle structure, inlet angle, head distance and length of the combustion chamber and other parameters, dual lower two-way intake, gas generator filled with boron-rich propellant short grain, Working time 10s. The simulation flight height $H = 10\text{km}$, the Mach number $Ma = 2.8$, the angle of attack $\alpha = 0^\circ$, the side slip angle $\beta = 0^\circ$ (Figure 13) .

Different air inlet angles lead to different radial velocity components of the intake air, affecting the head reflow and downstream vortex intensity and the gas and air mixing effect, thus affecting the secondary combustion efficiency. In this paper, the inlet angle of 30° and 45° is adopted, and the nozzle of the gas generator is 5 nozzles. The experimental results are shown in Table 1.

The experimental results show that the incident angle is increased, the blending effect is enhanced, and the specific impulse is increased. It is concluded that the tangential impact of the large gas inlet angle on the fuel gas is enhanced, and the area of the gas and air is relatively increased in the area of the sidewall area where the gas is forced to the relatively weak air flow, which enhances the airflow Blending, to improve the combustion efficiency. When the

small angle of the inlet, gas and air interaction is weak, the two air flow into non-interfering two-tier flow, gas gathering in the supplementary chamber below, while the air is gathered in the top, the contact area of the two Small, the combustion is not sufficient, the combustion efficiency drops.

Table 1 different air intake angle combustion chamber combustion performance

| | | |
|-------------------------------------|-------|-------|
| Intake angle | 30 | 45 |
| Average air - fuel ratio | 18784 | 17597 |
| Burning rate | 6911 | 7406 |
| Theoretical characteristic velocity | 91480 | 97670 |
| Theoretical impulse | 10438 | 10438 |
| Calculate flight specific impulse | 6709 | 8033 |
| Specific impulse efficiency | 6428 | 7696 |

CONCLUSIONS

The effects of different particle diameters and fuel gas injection angles on the mixing of particles and gas flow in the solid rocket ramjet engine were studied by mixing the boron particles and the gas in the cold flow. , And the blending of particles was quantitatively analyzed by blending, dimensionless particle cloud and oxygen-fuel ratio. The results show that:

1. the smaller the particle diameter is more conducive to blending, particle diameter is relatively small, with the flow is better, the particles with the return area of fluid movement. As the particle diameter becomes larger, the particle itself does not move with the fluid in the recirculation zone due to the high velocity of the particle itself, and the particles tend to collect towards the axis, the middle region, Mixing is not good, combustion efficiency will decline.

2. It is favorable for the blending of gas and gas when the angle of fuel gas injection is changed. The angle between the gas entrance angle and the

centerline of the axial plane is more favorable for blending. When the gas injection angle is too large, it is disadvantageous for lowering the primary combustion residue of the gas generator, and the ejection efficiency is affected. Therefore, in the design of fuel-rich fuel injection point of view, it should be a comprehensive study of its combustion efficiency and the impact of jet efficiency.

3. The experimental results show that the specific impulse efficiency of 45 ° inlet is higher and the specific impinging efficiency of 30 ° inlet is lower, but the angle of incidence increases, which aggravates the deposition of combustion products in the supplementary combustion chamber.

Acknowledgements: This work is supported financially by the National Natural Science Foundation of China (No. 11602066) and the National Science Foundation of Heilongjiang Province of China (QC2015058 and 42400621-1-15047), the Foundation Research Funds for the Central Universities.

REFERENCES

- 1.S.P. Vanka, R.R. Craig, F.D. Stull, *AIAA*, **85**, 1271 (1985).
- 2.D.L.Cherng, V. Yang, K.K. Kuo, *Journal of propulsion*, **5**, 1989.
- 3.L. Chen, C.C. Tao, *AIAA*, **84**, 1378 (1984).
- 4.Z.C. Hong, J.L. Pan, C. Lin, *Chinese Society. Mech. Engineers. J.*, **7**(1), 1 (1986).
- 5.T.M. Liou, Y.H. Hwang, Y.H. Hung, *AIAA*, **88**, 3010 (1988).
- 6.T.M. Liou, S.M. Wu, *Propulsion. Power. J.*, **4**(1), 53 (1988).
- 7.T.M. Liou, Y.H. Hwang, Y.H. Hung, *Propulsion. Power. J.*, **5**(6), 686 (1989).
- 8.R.O. Foelsche, R.L. Burton, H. Krier, *AIAA*, **97**, 0127 (1997).
- 9.M.K King, *Boca Raton: CRC*, **1**, 80 (1993).
10. W. Bao, W.Y. Niu, L.Q. Chen, *Solid Rocket Tech. J.*, **28**(4), 433 (2007).

Optimization for adsorption separation process of simulated moving bed based on moving asymptotes algorithm

Y.H. Yang, X.B. Chen*, C.Y. Jiang

School of Electronics and Information Engineering, University of Science and Technology Liaoning, Liaoning, Anshan, China

Received May 24 2017; Revised July 21, 2017

The Simulated Moving Bed (SMB) is a continuous multi-column chromatographic process that has become an attractive technology for complex separation tasks that are regularly encountered in the areas of pharmaceuticals, fine chemicals and biotechnology. This paper focuses on the implementation of the control concept to SMBs operating. Based on moving asymptotes algorithm, the optimizing strategy is carried out for improvements of the extract and raffinate purity, the productivity and the solvent consumption. The feasibility of the moving asymptotes is verified by the triangle theory. The simulation results illustrate that the moving asymptotes method is fast in convergence and the optimal solutions are distributed uniformly.

Key words: Adsorption separation process, Simulated moving bed, Equilibrium diffusion model, Moving asymptotes, Optimizing strategy

INTRODUCTION

The Simulated Moving Bed (SMB) separation technology is a kind of continuous chromatographic separation technique for scale production, which is with the advantages of strong separation ability, small appearance and low operation costs. It has a large range of applications in the areas of the petroleum chemical industry, fine chemical industry and sugar industry [1,2]. Recently, due to the strong coupling and the mechanism complexity in the SMB separation process, many researches carried out the modeling, the model solving and optimizing of SMB separation process in order to give the theoretical guidance for the product development, the process of industrialization and the application range can be expanded accordingly. The commonly used SMB chromatography models[3] are General Rate Model (GRM), Lumped Pore Diffusion Model (PORM), Ideal Model (IM), Equilibrium Dispersive Model (EDM) and Transport Dispersive Model (TDM). Comparing with other models, EDM has higher practicability. During the simulation process, EDM ignores the influence of mass transfer resistance, whose calculation speed is faster than GRM and PORM, the considered factors of which are more comprehensive than IM. Therefore, it has a large range of applications[4]. By using EDM, the influence of changing feed flow rate on SMB separation technology was researched[5]. On the other hand, SMB model is very difficult to be solved for its style of partial differential equations.

Therefore, the general solution method is to transfer the partial differential equations to ordinary differential equations by using discrete methods, such as orthogonal collocation finite element method, Galerkin method and CE/SE method[6]. In reference [7], the adsorption isotherm model was simulated by using CE/SE method; the advantages and disadvantages of the finite difference method and orthogonal collocation finite element method were discussed. By comparing with other methods, the orthogonal collocation finite element method is not only convenient and fast, but also flexible and accurate in the processing of stiff problems. There are many operation conditions that affect the chromatographic separation performance in SMB process, such as switching time, flow rate of the area, and the size of the column. Therefore, the optimization analysis of SMB is a hot research topic in this area. Marco Mazzotti firstly proposed the triangle theory[8] which is under the ideal status, hence the axial dispersion and mass transfer resistance were not considered and there must be accuracy problem in real applications. In recent years, the genetic algorithm or particle swarm optimization is used for SMB process design[9, 10]. The genetic algorithm needs copy, crossover and mutation operations in the process, thus its efficiency must be affected. And the particle swarm optimization algorithm is with shortcomings like easily falling into local optimal solution, being prone to unstable and slow in convergence in the actual operation of the process.

In this paper, the equilibrium diffusion model of SMB chromatographic separation process is firstly solved by using orthogonal collocation finite

* To whom all correspondence should be sent:
E-mail: yangyh2636688@163.com

element method. Then, the optimization strategy is proposed based on the method of moving asymptotes [11]. Finally, the simulation is carried out in the operation optimization of SMB chromatographic separation process. The simulation results show that the proposed optimization method can improve the economic benefits of SMB operation and guide the process operation.

BASIC PRINCIPLE OF SMB

SMB is composed by a plurality of chromatographic columns with the valves and the pipelines in series, principle of which is to simulate the movement direction of the solid phase to achieve the solid phase and fluid phase countercurrent motion by periodically opening and closing the valve to switch import and export positions [12-14]. Fig. 1 shows the operation process of SMB in which the solid arrow indicates the location of imports and exports for current cycle, the dotted arrow indicates that for the next cycle. SMB chromatographic separation process can be divided into four zones, as shown in Fig 1. The feed solution and the elution are imported between zone 2 and 3, zone 1 and 4, respectively. The extraction and raffinate are collected between zone 1 and 2, zone 3 and 4 respectively. The function of zone 1 is mainly to realize the regeneration of the adsorbent, and the strong absorption component is desorbed from the solid phase. The effect of zone 2 is to desorb the weak adsorption components and adsorb the strong adsorption components, the purpose is to make the extract contain only strong absorption components, and do not contain weak adsorption components. Zone 3 is opposite to zone 2, so that the liquid contains only the weak absorption of components, and does not contain strong absorption component. The effect of zone 4 is the regeneration of the elution solution, the weak adsorption components are desorbed from the fluid phase [15]. By selecting the reasonable design parameters, the type of adsorbent, elution solution and operating parameters, the raffinate contains only the weak adsorption component B, the extract contains only the strong adsorption component A, so as to achieve the purpose of continuous separation.

EQUILIBRIUM DIFFUSION MODEL OF SMB CHROMATOGRAPHIC SEPARATION

The mathematical model of SMB chromatographic separation is coupled by a series

of single chromatographic column model and node model [16].

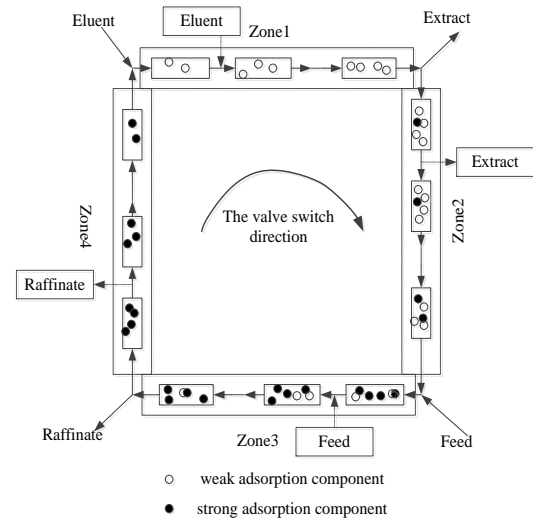


Fig.1.Operation schematic diagram of SMB

Because EDM has a higher practicability, and the computer simulation speed of which is fast, therefore, the EDM single column chromatographic model is adopted in this paper. There are two assumptions as follows [17]: (1) The flow and the solid phase reach the equilibrium state instantaneously. (2) The effect of axial diffusion and non equilibrium is integrated into the axial diffusion coefficient. The effect of molecular diffusion, eddy diffusion and mass transfer resistance on the model is considered, the influence of interphase mass transfer resistance is ignored. The diffusion of the fluid phase and solid phase is instant and reach an equilibrium state, thus its influence is not considered.

The mathematical description of EDM is as follows:

$$\frac{\partial c_i}{\partial t} + F_a \frac{\partial q_i}{\partial t} + u \frac{\partial c_i}{\partial x} = D_a \frac{\partial^2 c_i}{\partial x^2} \quad (1)$$

Initial condition is:

$$c_i(x, 0) = q_i(x, 0) = 0 \quad (2)$$

Boundary condition is:

$$1) \quad c_i(t, 0) = \psi_i(t) \quad (3)$$

$$2) \quad uc_i(t, 0) + D \frac{\partial c_i}{\partial x} \Big|_{0,l} = uc_k(t) \quad (4)$$

$$\frac{\partial c_i}{\partial x} \Big|_{x=L} = 0 \quad (5)$$

where $\psi_i(t)$ is inlet concentration of the i th chromatographic column, $c_k(t)$ is known.

Adsorption isotherm equation is:

$$q_i(x, t) = f[c(x, t)] \quad (6)$$

The equilibrium relationship between the nodes can be obtained by the mass conservation relation:

$$Q_4 + Q_D = Q_1, c_{i,4}^{out} Q_4 = c_{i,1}^{in} Q_1 \quad (7)$$

$$Q_1 - Q_E = Q_2, c_{i,1}^{out} = c_{i,2}^{in} \quad (8)$$

$$Q_2 - Q_F = Q_3, c_{i,2}^{out} Q_2 + c_{i,F} Q_F = c_{i,3}^{in} Q_3 \quad (9)$$

$$Q_3 - Q_R = Q_4, c_{i,3}^{out} = c_{i,4}^{in} \quad (10)$$

OPTIMIZATION STRATEGY OF SMB

Principle of moving asymptotes

Moving Asymptotes (MA) is an optimization method based on convex function. In 1987, Svanberg firstly proposed the method, which uses the sub problem with convex functions and separable variables to approximate the original problem [11]. For this algorithm, the selection principle of the approximate function is that the private function is replaced by the first order derivative of the current iteration point. The method of moving asymptotes is used to optimize the multi-objective problem and the implicit problem is converted into a convex approximation sub problem. The optimization model is as follows:

Considering the optimization problem P,

$$\text{MIN } f_0(X) \quad X \in R^n \quad (11)$$

$$\text{S.T. } f_i(X) \leq f_i^* \quad i=1, \dots, m \quad (12)$$

$$x_{ja} \leq x_j \leq x_{jb} \quad j=1, \dots, n \quad (13)$$

where $f_0(X)$ is the objective function, $X = (x_1, \dots, x_n)^T$ is the design variable, $f_i(X) \leq f_i^*$ is behaviour constraint, and $x_{ja} \leq x_j \leq x_{jb}$ is technical constraint.

The method to solve the problem P is to construct the sub problem. The solution of the original problem is approximated by the sub problem. The detailed algorithm procedure is as follows:

Step 1: Choose the initial point x^0 , let $k = 0$.

Step 2: Give the iteration point x^k , and calculate $f_i(x^k)$ and $\nabla f_i(x^k)$, $i=1, \dots, m$.

Step 3: The established sub problem is used to approximate the original problem, which means that $f_i(x)$ is replaced by $f_i^k(x)$, and the establishment of sub problem $f_i^k(x)$ needs the data calculated in step 2.

Step 4: Solve sub problem. The optimal solution of the sub problem is taken as the next iterative point, i.e. $k=k+1$, and return to step 2.

Construction of sub problem

In the process of using moving asymptotes algorithm for solving optimization problem, the key point is to construct and solve sub problem. In the k th iterative of the algorithm, the sub problem is constructed as follows:

$$\text{MIN } f_0^k(X) \quad X \in R^n \quad (14)$$

$$\text{S.T. } f_i^k(X) \leq f_i^* \quad i=1, \dots, m \quad (15)$$

$$x_j^\alpha \leq x_j \leq x_j^\beta \quad j=1, \dots, n \quad (16)$$

where $i=0, 1, \dots, m$.

$$f_i^k(X) = r_i^k + \sum_{j=1}^n \left(\frac{p_{ij}^k}{U_j^k - x_j^k} + \frac{q_{ij}^k}{x_j^k - L_j^k} \right) \quad (17)$$

$$r_i^k = f_i(X^k) - \sum_{j=1}^n \left(\frac{p_{ij}^k}{U_j^k - x_j^k} + \frac{q_{ij}^k}{x_j^k - L_j^k} \right) \quad (18)$$

$$p_{ij}^k = \begin{cases} (U_j^k - x_j^k) \frac{\partial f_i(X)}{\partial x_j} & \frac{\partial f_i(X)}{\partial x_j} > 0 \\ 0 & \frac{\partial f_i(X)}{\partial x_j} \leq 0 \end{cases} \quad (19)$$

$$q_{ij}^k = \begin{cases} -(x_j^k - L_j^k) \frac{\partial f_i(X)}{\partial x_j} & \frac{\partial f_i(X)}{\partial x_j} < 0 \\ 0 & \frac{\partial f_i(X)}{\partial x_j} \geq 0 \end{cases} \quad (20)$$

where $\frac{\partial f_i^k(X)}{\partial x_j}$ is the value at $X = X^k$, which is a variable changing with the iteration point x_j^k , and satisfies $L_j^k < x_j^k < U_j^k$. At $x = x^k$, there is

$$f_i^k(x^k) = f_i(x^k) \quad (21)$$

$$\frac{\partial f_i^k}{\partial x_j} = \frac{\partial f_i}{\partial x_j} \quad i=1, \dots, m, j=1, \dots, n \quad (22)$$

In the sub problem, if x_j^k is close to L_j^k or U_j^k , the value of f_i^k will increase sharply. Therefore, $x_j^k = L_j^k$ or $x_j^k = U_j^k$ is the asymptote. The solution after each iteration is maintained between L_j^k and U_j^k , the values of which are changed between the iterations, it is equivalent to the movement of asymptote, thus L_j^k and U_j^k are called moving asymptotes.

The second partial derivative of f_i^k at $X = X^k$ is:

$$\frac{\partial^2 f_i^k}{\partial (x_j)^2} = \frac{2p_{ij}^k}{(u_j^k - x_j)^3} + \frac{2q_{ij}^k}{(x_j - l_j^k)^3} \quad (23)$$

Simplify the equation (23), we obtain

$$\frac{\partial^2 f_i^k}{\partial (x_j)^2} = \begin{cases} \frac{2\partial f_i / \partial x_j}{u_j^k - x_j} & \partial f_i / \partial x_j > 0 \\ 0 & \partial f_i / \partial x_j > 0 \\ \frac{-2\partial f_i / \partial x_j}{x_j - l_j^k} & \partial f_i / \partial x_j > 0 \end{cases} \quad (24)$$

It is easy to see that the function f_i^k is a convex function. In addition, the next iterative point always exists between the lower bound of L_j^k and upper bound of U_j^k . In view of this situation, it is able to obtain a good effect of approximation by regulating

the boundary values during the running process of the algorithm. By comparing the method of moving asymptotes with other optimization algorithms, its advantages are very obvious, sub problem is constructed with convexity and separable independent variable.

Solution of sub problem

In the method of moving asymptotes, sub problem we constructed needs to be solved by an algorithm, here Lagrange function is selected.

For equations (14) - (16), the number of iterations is omitted by k , and the simplified form is as follows:

$$\text{MIN } r_0 + \sum_{j=1}^n \left(\frac{p_{0j}}{U_j - x_j} + \frac{q_{0j}}{x_j - L_j} \right) \quad (25)$$

$$\text{S. T } \sum_{j=1}^n \left(\frac{p_{ij}}{U_j - x_j} + \frac{q_{ij}}{x_j - L_j} \right) \leq b_i \quad i = 1, \dots, m \quad (26)$$

$$\alpha_j \leq x_j \leq \beta_j \quad j = 1, \dots, n \quad (27)$$

Where $\alpha_j = \max\{x_j^\alpha, \alpha_j\}$, $\beta_j = \min\{x_j^\beta, \beta_j\}$, $L_j < \alpha_j \leq \beta_j < U_j$, and $b_i = f_i^* - r_i$.

The sub problem is a variable separable convex function, and the dual method can be used to solve the problem. The sub problem is constructed as a Lagrange function, which is:

$$l(x, y) = f_0^k(X) + \sum_{i=1}^m y_i f_i^k(X) \quad (28)$$

Substitute sub problem (25) into (28), we have

$$l(x, y) = r_0 - Y^T B + \sum_{j=1}^n \left(\frac{p_{0j} + Y^T P_j}{U_j - x_j} + \frac{q_{0j} + Y^T Q_j}{x_j - L_j} \right) \quad (29)$$

The following equation can be obtained by simplifying the equation (29).

$$l(x, y) = r_0 - Y^T B + \sum_{j=1}^n l_j(x_j, Y) \quad (30)$$

$B = (b_1, \dots, b_m)^T$, $P_j = (P_{1j}, \dots, P_{mj})^T$, $Q_j = (Q_{1j}, \dots, Q_{mj})^T$ and $Y = (y_1, \dots, y_m)^T$.

where Y is the multiplier of Lagrange's function.

$$l_j(x_j, y) = \frac{p_{0j} + Y^T P_j}{U_j - x_j} + \frac{q_{0j} + Y^T Q_j}{x_j - L_j} \quad (31)$$

If $y_i \geq 0$, the dual objective function can be constructed as:

$$w(Y) = r_0 - Y^T B + \sum_{j=1}^n w_j(Y) \quad (32)$$

Where,

$$w_j(Y) = \min_{x_j} \{l_j(x_j, Y); \alpha_j \leq x_j \leq \beta_j\} \quad (33)$$

The minimum value of x_j is determined by Y , it can be expressed as $x_j(Y)$. If $y_i \geq 0$, then $p_{0j} + Y^T P_j \geq 0$ and $q_{0j} + Y^T Q_j \geq 0$. Hence, $l_j(x_j, Y)$ is convex function.

Therefore, assume that there is at least one positive term in $p_{0j} + Y^T P_j$ and $q_{0j} + Y^T Q_j$, and the first order derivative of $l_j(x_j, Y)$ on x_j is:

$$l_j'(x_j, Y) = \frac{p_{0j} + Y^T P_j}{(U_j - x_j)^2} - \frac{q_{0j} + Y^T Q_j}{(x_j - L_j)^2} \quad (34)$$

The second order derivative of $l_j(x_j, Y)$ on x_j is:

$$l_j''(x_j, Y) = \frac{2(p_{0j} + Y^T P_j)}{(U_j - x_j)^3} + \frac{2(q_{0j} + Y^T Q_j)}{(x_j - L_j)^3} \quad (35)$$

The second order derivative of $l_j(x_j, Y)$ on x_j is positive, so the first order derivative of $l_j(x_j, Y)$ on x_j is increasing function. The conclusion about the minimum value of $x_j(Y)$ can be gotten as follows:

(1) If $l_j'(\alpha_j, Y) \geq 0$, then $x_j(Y) = \alpha_j$;

(2) If $l_j'(\beta_j, Y) \leq 0$, then $x_j(Y) = \beta_j$;

(3) If $l_j'(\alpha_j, Y) < 0$ and $l_j'(\beta_j, Y) > 0$, then $x_j(Y)$

has a unique solution. The form of the solution is shown in the following form:

$$x_j(Y) = \frac{(p_{0j} + Y^T P_j)^{1/2} L_j + (q_{0j} + Y^T Q_j)^{1/2} U_j}{(p_{0j} + Y^T P_j)^{1/2} + (q_{0j} + Y^T Q_j)^{1/2}} \quad (36)$$

Substitute $x_j(Y)$ into the following function $w(Y)$, we have:

$$w(Y) = r_0 - Y^T B + \sum_{j=1}^n \left(\frac{p_{0j} + Y^T P_j}{U_j - x_j(Y)} + \frac{q_{0j} + Y^T Q_j}{x_j(Y) - L_j} \right) \quad (37)$$

Hence, the first order partial derivative of $w(Y)$ on y_i is obtained:

$$\frac{\partial w}{\partial y_i} = -b_i + \sum_{j=1}^n \left(\frac{p_{ij}}{U_j - x_j(Y)} + \frac{q_{ij}}{x_j(Y) - L_j} \right) \quad (38)$$

Then, the dual problem of the sub problem is equivalent to the maximum value of the dual function $w(Y)$ when $y_i \geq 0$.

SMB optimization strategy

Maximizing extraction and raffinate purity

In the separation of SMB, the high purity of product is the most basic requirement in the process. In this optimization problem, the feed flow rate Q_F and the elution flow rate Q_D are fixed values. Based On this basis, the concentration of the extraction and raffinate reach to maximum.

In this paper, the flow rate of zone 2 is taken as one of the control variables, and another one is the switching time t^* . The mathematical model of the optimization problem is:

$$\text{Max } P_1 = X_E(Q_{11}, t^*) \quad (39)$$

$$\text{Max } P_2 = X_R(Q_{11}, t^*) \quad (40)$$

The optimization problem also ensures that the purity of the product reaches a certain constraint, such as

$$X_A \geq 98\% \quad (41)$$

$$X_B \geq 98\% \quad (42)$$

Decision variables are as follows:

$$2min \leq t^* \leq 4min \quad (43)$$

$$30mL/min \leq Q_{II} \leq 45mL/min \quad (44)$$

$$Q_F = 3.64mL/min \quad (45)$$

$$Q_D = 21.15mL/min \quad (46)$$

$$Q_1 = 56.83mL/min \quad (47)$$

The optimization is carried out by using the method of moving asymptotes, the distribution of Pareto optimal solution set is shown in figure 2. The simulation results show that the moving asymptotes algorithm converges to Pareto solution set, which has better dispersion degree and more uniform distribution.

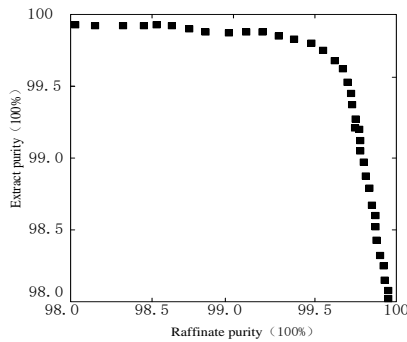


Fig. 2. Optimal solution distribution of MA

In order to ensure the accuracy of the algorithm of moving asymptotes in SMB optimization, the triangle theory is used to verify the algorithm. Based on the balance theory, m_2 and m_3 are fixed values under ideal conditions. However, due to the existence of the diffusion coefficient and mass transfer resistance in the separation process of actual production, m_2 and m_3 is moving from high to low with the Pareto optimal solution.

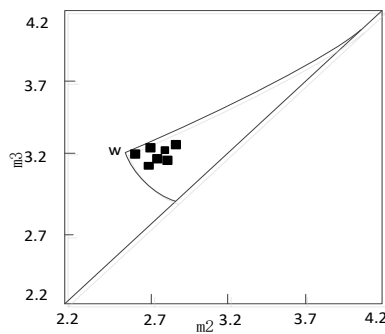


Fig. 3. m_2 - m_3 plane of MA

The corresponding positions of operation points of SMB after optimization on $m_2 - m_3$ plane are

shown in figure 3. It can be seen from the figure that the optimization results of proposed algorithm remain in complete separation region, and the calculation results meet the triangle theory.

Maximizing productivity and minimizing solvent consumption

From an economic point of view, SMB solvent consumption and productivity are important economic indicators. In this paper, the flow rate of feed Q_F and the flow rate of zone 1 Q_1 are fixed values to minimize the solvent consumption and maximize the productivity. Because the flow rate of feed Q_F and the flow rate of zone 1 Q_1 are given, therefore, according to the relationships between the flow rate in each zone, three of the operation parameters Q_D , Q_R , Q_E , Q_2 , Q_3 and Q_4 are independent, Q_D , Q_R , Q_E and t^* are taken as control variables. Therefore, the mathematical description of this optimization is as follows:

$$\text{Max } P_1 = P_r(Q_D, Q_R, Q_E, t^*) \quad (48)$$

$$\text{Min } P_2 = SC(Q_D, Q_R, Q_E, t^*) \quad (49)$$

The optimization problem also ensures that the purity of the product reaches a certain constraint, which is:

$$X_A \geq 98\% \quad (50)$$

$$X_B \geq 98\% \quad (51)$$

Decision variables and fixed parameters:

$$2min \leq t^* \leq 4min \quad (52)$$

$$10mL/min \leq Q_D \leq 40mL/min \quad (53)$$

$$5mL/min \leq Q_R \leq 20mL/min \quad (54)$$

$$10mL/min \leq Q_E \leq 30mL/min \quad (55)$$

$$Q_F = 3.64mL/min \quad (56)$$

$$Q_1 = 56.83mL/min \quad (57)$$

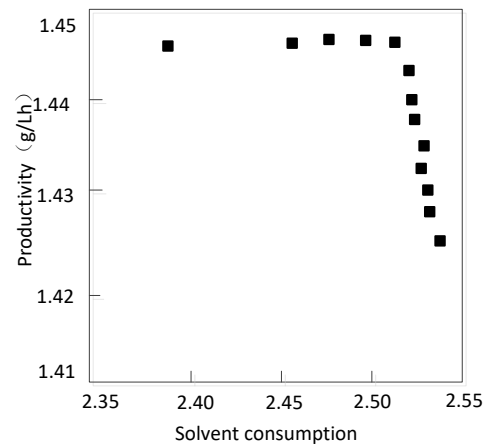


Fig. 4. Optimal solution distribution of MA

Moving asymptotes algorithm is used to solve this problem, figure 4 shows the Pareto optimal solution set distribution. We can get that when the solvent consumption is increased, the productivity will be reduced accordingly.

Figure 5 shows the position of optimized operating point in the $m_2 - m_3$ plane, the optimization results maintain complete separation region. The decision variables distribution diagram of moving asymptotes method is shown in figure 6, the control solutions of variables are uniformly distributed, and the number of optimal solutions are satisfied.

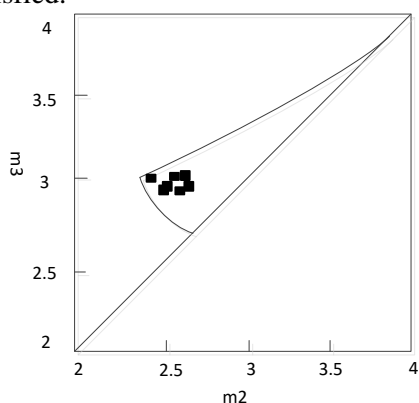


Fig. 5. m_2 - m_3 plane of MA

CONCLUSION

In this paper, According to moving asymptotes algorithm, extract purity, raffinate purity, productivity and solvent consumption are optimized and simulated. The feasibility is verified by triangle theory. The simulation results show that the algorithm has a fast convergence speed, and the optimal solutions are well-distributed. The SMB optimization strategy can be used for SMB separation process design and operation guidance.

The limitation of this study is that it is based on the separation of the two components, and the

algorithm has some space to improve. Our future work will continue to improve the optimization algorithm to realize the online optimization control of the various modified simulated moving bed.

Acknowledgements: The author thanked the Chromatographic Separation Center of University of Science and Technology Liaoning for instrumental supports.

Symbol description:

- c_i : Concentration of component i in fluid phase
- q_i : Concentration of component i in solid phase
- u : Superficial velocity
- ε : Column porosity
- h : Space step
- A : Strong adsorption component
- B : Weak adsorption component
- D_a : Axial diffusion coefficient
- F_a : Phase rate
- H_i : Henry's constant of component i
- L : Column length
- Q : Flow rate

Subscripts

- 1,2,3,4: denote zone 1,2,3 and 4 respectively
- i : Component

- E: Extraction
- F: Feed
- R: Raffinate
- D: Elution

Superscripts

- *: Equilibrium value
- in: Entry value
- out: Export value

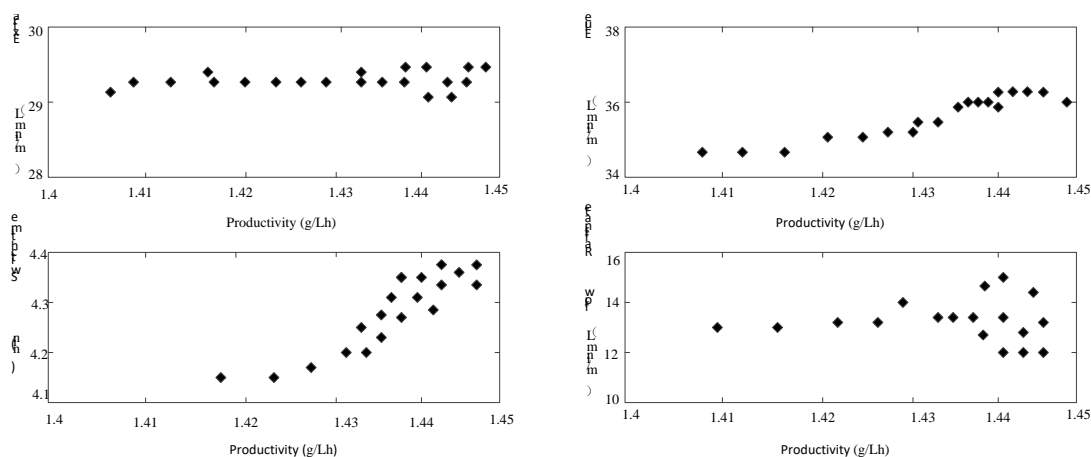


Fig. 6. Control variable distribution of MA

REFERENCES

1. S. Qamar, N. Abbasi, S. Javeed, *Chem. Engin. Sci.*, **107**(14), 192 (2014).
2. J.Y. Song, K.M. Kim, C.H. Lee, *J. Chromatography. A.*, **1471**, 102 (2016).
3. L.F. Gomes, F. Augier, D. Leinekugel-Le-Cocq, *Chem. Engin. Sci.*, **153**, 188 (2016).
4. H. Schramm, M. Kaspereit, A. Kienle, *J. Chromatography. A.*, **1006**(1-2), 77 (2003).
5. H. Schramm, A. Kienle, M. Kaspereit, *Chem. Engin. Sci.*, **58**(23-24), 5217 (2003).
6. B.C. Lin, Simulated moving bed chromatography, Chemical Industry Press, Beijing, China, 2007.
7. M. Wang, Y.J. Chai, W.B. Xu, *Comput. Engin. Des.*, **31**(2), 388 (2010).
8. M. Mazzotti, G. Storti, M. Morbidelli, *J. Chromatography. A.*, **769**(1), 3 (1997).
9. A.S.A. Neto, A.R. Secchi, M.B.S. Jr, *J. Chromatography. A.*, **1470**, 42 (2016).
10. J.P.S. Aniceto, S.P. Cardoso, C.M.Silva, *Comput. Chem. Eng.*, **90**, 161 (2016).
11. K. Svanberg, *Int. J. Numer. Methods. Eng.*, **24**(12), 359 (1987).
12. S. Abel, G. Erdemb, M. Mazzotti, *J. Chromatography. A.*, **1033**(2), 229 (2004).
13. M. Amanullah, C. Grossmann, M. Mazzotti, *J. Chromatography. A.*, **1165**(1-2), 100 (2007).
14. C. Park, H.G. Nam, S.H. Jo, *J. Chromatography. A.*, **1435**, 39 (2016).
15. P.S. Gomes, A.E. Rodrigues, *Chem. Eng. Technol.*, **35**(1), 17 (2012).
16. M. Rezazadeh, M.S. Esfahani, A. Rahimi, *Chem. Eng. Technol.*, **38**(5), 759 (2015).
17. K. Horvath, J.N. Fairchild, K. Kaczmarski, *J. Chromatography. A.*, **1217**(52), 8127 (2010).

Investigation of the process and performance of a molding wood substitute packaging material

H. Sun^{1, 2, 3, *}, Y.F. Cao¹, X.L. Yang¹, L.Q. Wang^{1, 2}, X.C. Zhang^{1, 2}

¹ Jiangnan University, Wu Xi 214122, China;

² State Key Laboratory of Pulp and Paper Engineering, South China University of Technology, Guangzhou

³ Jiangsu Key Laboratory of Advanced Food Manufacturing Equipment and Technology, Wuxi, China

Received May 25, 2017; Revised July 21, 2017

A molded wood substitute packaging material was obtained through the breaking, molding and drying of the wood processing residues. The samples of different wood substitute packaging material were prepared through the orthogonal design method and the influence of different process parameters on wood substitute material's physical and mechanical properties was analyzed via a range of analytic techniques. Wood substitute packaging material with better properties can be afforded via the process of hot-pressing for 10min at the conditions of 120~125°C under 10MPa pressure with sizing amount of 20%. The resultant wood residues packaging products can meet the requirements of national standard (GB/T 4897-92D) and also the standards of green packaging materials.

Keywords: wood substitute packaging material, mold pressing, process parameters, physical and mechanical properties

INTRODUCTION

With a worldwide shortage of forest resources, global supply of wood raw material is becoming increasingly tense [1]. As in China, the forest resources are scarce and the supply and demand of timber is imbalanced [2]. At present, the annual timber gap is about $7 \times 10^7 \text{m}^3$. Meanwhile, the full use of processing residua and waste wood from the consumption of industries and human life will greatly ease the supply and demand of China's timber [3].

The poplar plantation has some processing shortages, such as uneven distribution, low-density, the prone to shrinkage deformation and veneer peeling raising [4]. All these bring a lot of difficulties to development and utilization [5]. However, high moisture content and soft material simplify the manufacturing board technology and lower the production cost [6]. For the time being, poplar material is one of the main raw materials of the wood-based panel production [7].

This paper aims at further using orthogonal test method to analyze the influences of hot - pressing temperature, hot-pressing time and hot-pressing pressure sizing amount. on the physical and mechanical properties followed by formulation and optimization of its molding process parameters [8].

EXPERIMENTAL

Materials

Poplar fiber: Processing fast-growing poplar's branches into cells with the diameter of 3~4cm by chipping machine. Dry and ground them after cooking and softening, then make them into poplar fiber with moisture content of 15%~20%.

Melamine modified urea - formaldehyde resin adhesive as the resource. Its solid content is 50~55%, viscosity is (20°C) 26~30cps and curing time is 90~120s.

The pretreatment agent for the poplar fiber is NaOH solution, the mass fraction of 1.5% according to the mass ratio of 1: 100 between NaOH (AR) and poplar. The solution must be used right after it is ready.

Curing agent: choose NH₄Cl (AR) as the curing agent.

Instrument

Three-point bending experiment was conducted on RXPlus Universal electronic testing machine made in Lloyd company and the accuracy is 0.5%, span is 100mm. The force was applied at the rate of 60mm/min. Experiments were conducted in packaging products quality supervision and inspection center of China.

Methods

Preparation of wood residues packaging products

According to related documents, there are several factors have a great impact on plates: sizing

* To whom all correspondence should be sent:

E-mail: sunhao@jiangnan.edu.cn

amount, hot - pressing temperature, hot-pressing time and hot-pressing pressure. This study adopts Orthogonal Test Method and chooses L9(34) to research the above four factors' influence on physical and mechanical properties. According to early study and practice, select three levels of each factor [9] (see Table 1).

Table 1. Orthogonal Factors Table.

| Level | A Sizing amount(%) | B Temperature (°C) | C Time (min) | D Pressure (MPa) |
|-------|-----------------------|-----------------------|-----------------|---------------------|
| 1 | 10 | 100~105 | 5 | 5 |
| 2 | 15 | 120~125 | 10 | 8 |
| 3 | 20 | 140~145 | 15 | 10 |

Weighing and paving fibers into mold cavity in size of 250mm×50mm×14mm and then forming a single slab of particle board with density of 0.75g/cm³. After about 30~60s' manual preloading, press the slab without too much pressure. Discharge the water vapor inside to prevent the packaging products from bumps and stratification [10].

The prepared key issues of the wood residues packaging products

The high rate of residues is due to the serious phenomenon of stratification and bumps. There are two solutions: First, the hot-pressing temperature cannot be higher than 180°C. And the time should be at least 8.5min; second, after the clamping of the upper and lower mold, the pressure is adjusted to maximum of the testing design for about 60s. Then the pressure reduced to zero quickly and split up mold, making the rapid discharge of water inside the mold then adjust the pressure to the designed value.

Physical and mechanical property testing

The physical and mechanical property testing conducted in accordance with the GB/T

17657-1999 [11]. The testing includes MOR, MOE, IB, TS, density and so on.

RESULTS AND DISCUSSION

The physical and mechanical property testing of wood substitute packaging materials conducted in accordance with the GB/T 17657-1999. The testing includes MOR, MOE, IB, TS, density and so on. The testing results are shown in Table 2.

Factors analysis to packaging products' MOR

MOR is the determinants of the maximum capacity packaging products resisting bending forces without being destroyed [12]. According to the orthogonal testing results, the range result of the hot-pressing parameters' impact on the MOR is shown in Table 3.

Influence analysis of hot-pressing temperature on MOR

In hot-pressing parameters, temperature has a great impact on mechanical property [13]. First, when the moisture content is certain, the fiber's plasticity can be significantly improved by raising temperature. Then it will be easier to control the plate's thickness and density. Second, raising temperature can make adhesive cure rapidly, and shorten hot-pressing time. Meanwhile, it can increase the fluidity of the adhesive so that the

Table 3. Analysis of the range of MOR

| | Temperature (°C) | Time (min) | Pressure (MPa) | Sizing amount (%) |
|-----------|------------------|------------|----------------|-------------------|
| MOR (MPa) | 1 51.3 | 55.1 | 46.8 | 38.7 |
| | 2 55.7 | 58.7 | 53.8 | 73.9 |
| | 3 57.1 | 50.3 | 63.5 | 51.5 |
| R | 5.8 | 8.4 | 16.7 | 35.2 |

Table 2. Orthogonal Test Results

| Testing number | Sizing amount(%) | Factor Temperature (°C) | Time (min) | Pressure (MPa) | Physical and mechanical property | | | |
|----------------|------------------|-------------------------|------------|----------------|----------------------------------|----------|--------|------------------------------|
| | | | | | MOR (MPa) | IB (MPa) | TS (%) | Density (g/cm ³) |
| 1 | 10 | 100~105 | 5 | 5 | 11.2 | 1.43 | 7.3 | 0.682 |
| 2 | 10 | 120~125 | 10 | 8 | 12.8 | 1.51 | 7.1 | 0.689 |
| 3 | 10 | 140~145 | 15 | 10 | 14.7 | 1.57 | 6.8 | 0.758 |
| 4 | 15 | 100~105 | 10 | 10 | 29.7 | 1.72 | 4.2 | 0.681 |
| 5 | 15 | 120~125 | 15 | 5 | 19.4 | 1.64 | 5.6 | 0.723 |
| 6 | 15 | 140~145 | 5 | 8 | 24.8 | 1.83 | 4.8 | 0.902 |
| 7 | 20 | 100~105 | 15 | 8 | 16.2 | 1.69 | 5.4 | 0.777 |
| 8 | 20 | 120~125 | 5 | 10 | 19.1 | 1.74 | 5.3 | 0.725 |
| 9 | 20 | 140~145 | 10 | 5 | 16.2 | 1.68 | 6.9 | 0.961 |

distribution will be more evenly. When temperature is too high, the outer glue is already going to solidify

is too high, the outer glue is already going to solidify

before reaching the preset pressure value, so this layer's strength will be low and high temperature will make fiber's adhesive degrade, reducing its strength [14]. On the contrary, when the temperature is too low, the lignin inside the poplar fiber cannot be fully melted and cannot play the role of gluing. So low temperature is difficult to improve packaging products' MOR [15].

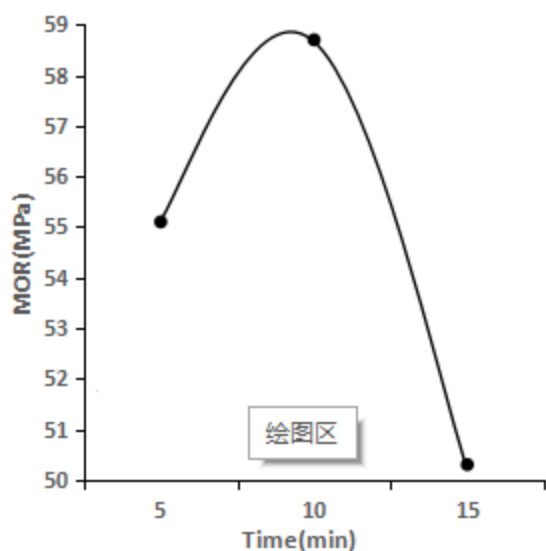


Fig. 1. Hot-pressing temperature's influence on MOR

The hot-pressing temperature's influence on MOR is shown in Fig. 1. We can know from the Fig. 1: as the temperature rises, the MOR increases and the change of MOR is larger in the range of 100~125°C. But when in 125~145°C, the change of MOR become relatively slow. It indicates that too high temperature will reduce packaging products' MOR. From the comprehensive consideration of energy saving and packaging products' MOR, the best temperature for hot - pressing is 120~125°C.

Influence analysis of hot-pressing time on MOR

The overall moisture content of slab is over 15%~20%, that will produce a large amount of water vapor, and leads to the phenomenon of bumps and stratification in the surface. In addition, high moisture content will extend the curing time of adhesive. In order to solve it, the time should be extended properly. However, extending the pressing time directly influences the production cycle. The influence of pressing time on MOR is shown in Fig. 2.

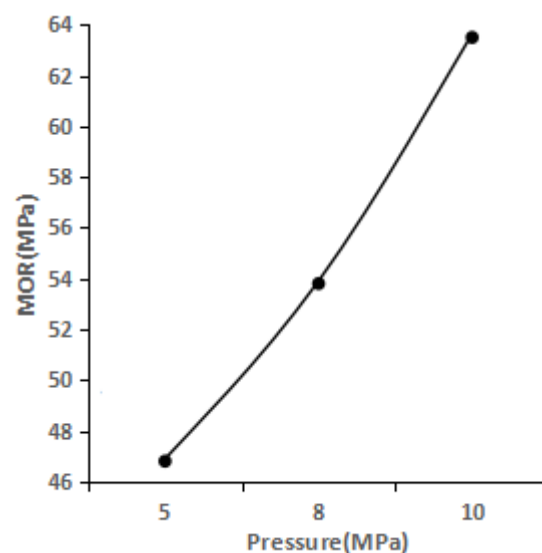


Fig. 2. Hot-pressing time's influence on MOR

From Fig. 2, we can know that: within a certain range, the MOR will increase along with the extension of time. But when higher than the range, the MOR will reduce. At the same temperature, the longer the time is, the more obvious the coking phenomenon and the degradation and catalysis of the adhesive, leading to the decrease of the MOR. When the pressing time is short, the slab inside will not reach the required temperature and the lignin will not be fully fused, which will cause the decrease of the MOR. From the comprehensive consideration of energy saving and the MOR, the most proper time is 10min.

Influence analysis of hot-pressing pressure on MOR

During the process of hot-pressing, exerting some pressure is mainly in order to discharge part of the air inside the slab, so that the poplar fiber can be bonded together in close contact to achieve higher bonding strength. Increasing the pressing pressure at the beginning can increase the core layer's density and gradient and improve its MOR. And also can narrow the gap between poplar fibers and increase the gluing area, which is good for the gluing of the poplar fiber. Nevertheless, too much pressure will crush the packaging products and reduce MOR.

The influence of hot-pressing pressure on MOR is shown in Fig. 3. We can know from the Fig. 3: as the pressure increases, the packaging products' MOR is also on the rise. Mainly because the increasing pressure makes the gap between poplar fiber smaller and the gluing area increases, thereby increasing the MOR. Taking all factors into consideration, the best pressure during the process of hot - pressing is 10MPa.

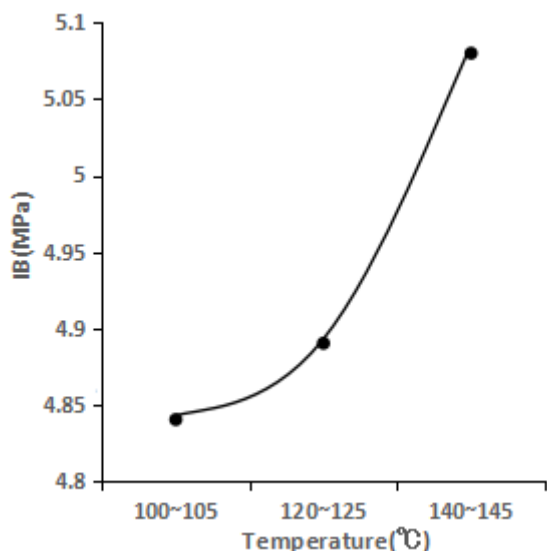


Fig. 3. Hot-pressing pressure's influence on MOR

Based on the analysis of various factors on MOR, we can know that the value of range in size order is sizing amount, hot-pressing pressure, hot-pressing time and hot-pressing temperature. Therefore, the best formula for MOR is when the hot-pressing temperature is 120~125°C, hot-pressing time is 10min, hot-pressing pressure is 10MPa and the sizing amount is 20%.

Factors analysis to packaging products' IB

IB means the bonding strength between the poplar fibers inside the packaging products. The larger IB is, the greater ability the packaging products possess to resist the bending due to the changing temperature. The range results the hot - pressing parameters have on the packaging products' IB during the pressing process is shown in Table 4.

Table 4. Analysis of the range of IB

| | Temperature(°C) | Time(min) | Pressure(MPa) | Sizing amount(%) | |
|-------|-----------------|-----------|---------------|------------------|------|
| 1 | 4.84 | 4.90 | 4.75 | 4.51 | |
| IB | 2 | 4.89 | 4.99 | 5.13 | 5.19 |
| (MPa) | 3 | 5.08 | 5.01 | 5.03 | 5.11 |
| R | 0.24 | 0.11 | 0.38 | 0.68 | |

Influence analysis of hot-pressing temperature on IB

The IB is mainly determined by two factors: one is the level of pressing temperature and the other is the binding capacity between poplar fibers. Among them, too high pressing temperature will make the surface solidify rapidly, even have the coking phenomenon. But the temperature inside does not increase rapidly, the filled adhesive does not play a role. Meanwhile, high temperature may make the adhesive itself contains degrade and the IB decrease.

When the pressing temperature is too low, the pressing cycle will be extended. The temperature inside cannot reach the requirement for the purpose of material gluing and lead to the decrease of IB.

The influence of hot-pressing temperature on IB is shown in Fig. 4. We can know from the Fig. 4: as the pressing temperature increases, the IB is also on the rise. Mainly because the increase of pressing temperature make the temperature inside the slab increase and the adhesive the poplar fiber itself contains produce gluing effect, thereby increasing the IB. But the bonding strength in the surface will decrease. Because of the high temperature, the phenomenon of coking and adhesive degradation is appeared in the surface. Therefore, the best hot-pressing temperature is 120~125°C.

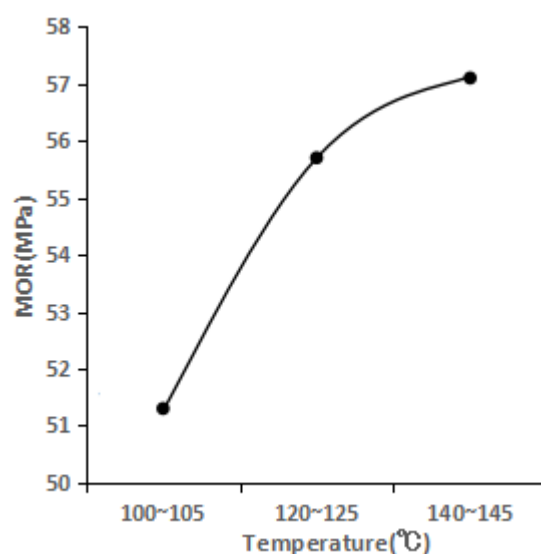


Fig. 4. Hot-pressing temperature's influence on IB

Analysis of the influence of hot-pressing time on IB

The influence of hot-pressing time on IB is shown in Figure 5. We can know from the Figure 5: the influence of hot - pressing time is relatively small. In a short time, pressing temperature cannot sufficiently spread into the inside of the slab so that it won't have a good bonding and combination between poplar fibers. Therefore, the IB is relatively low in 5minutes. But the strength of IB between 10min and 15min has no big difference. For IB of packaging products, the best time for hot - pressing time is 10min.

Influence analysis of hot-pressing pressure on IB

During the process of hot-pressing, the pressure is of great significance to control the resilience of the slab. Larger hot-pressing pressure can make the density of packaging products greater and strengthen the bonding and combination between the poplar fibers inside the packaging products. But too much

pressure will make the slab crushed and increase the MOR and IB. Therefore, a reasonable choice of hot-pressing pressure is important. The influence of hot-pressing pressure on IB is shown in Figure 6. We can know from the Fig. 6: within a certain range, as the pressure increases, the packaging product' IB will increase. But if the pressure is too large, the IB will decrease. So for IB, the optimal hot-pressing pressure is 8MPa during the process of hot-pressing.

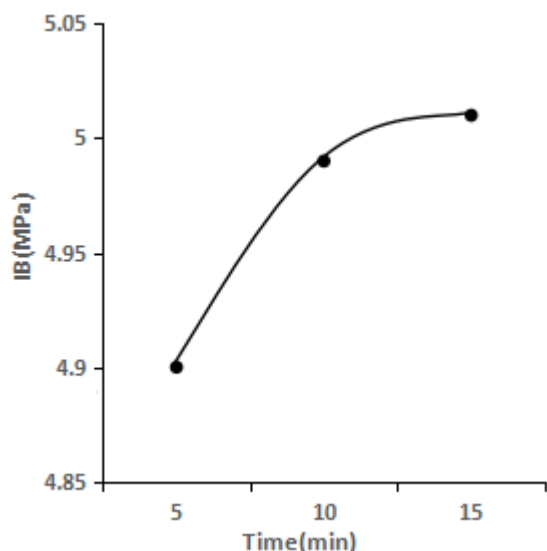


Fig. 5. Hot-pressing time's influence on IB

Influence analysis of hot-pressing pressure on IB

During the hot-pressing process, the pressure is of great significance to control the resilience of the slab. Larger hot-pressing pressure can make the density of packaging products greater and strengthen the bonding and combination between the poplar fibers inside the packaging products. But too much pressure will make the slab crushed and increase the MOR and IB. Therefore, a reasonable choice of hot-pressing pressure is important. The influence of hot-pressing pressure on IB is shown in Fig. 6. We can know from the Fig. 6: within a certain range, as the pressure increases, the packaging product' IB will increase. But if the pressure is too large, the IB will decrease. For IB, the optimal hot-pressing pressure is 8MPa during hot - pressing process of. Based on the analysis of various factors on IB, we can know that the order is sizing amount, hot-pressing temperature, hot-pressing pressure and hot - pressing time. Sizing amount has the greatest impact on IB while the hot-pressing time is the least. Therefore, the best formula for IB is that the hot-pressing temperature is 120~125°C, hot-pressing time is 10min, hot-pressing pressure is 8MPa and sizing amount is 20%.

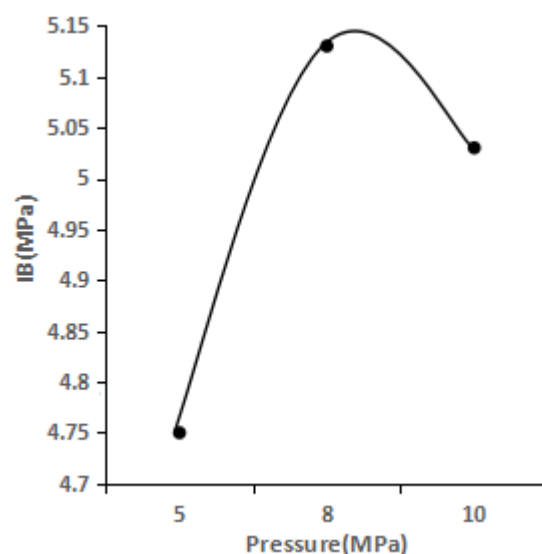


Fig. 6. Hot-pressing pressure's influence on IB

Factors analysis to packaging products' TS

TS means the ratio of the packaging products' thickness before absorbing and after absorbing in a certain time. The larger TS is, the quicker the thickness decreases after the absorbing and the greater the degree of bending deformation. The range results the hot-pressing parameters have influence on the TS during the pressing process is shown in Table 5.

Table 5. Analysis of the range of TS.

| | Temperature (°C) | Time (min) | Pressure (MPa) | Sizing amount (%) | |
|--------|------------------|------------|----------------|-------------------|------|
| TS (%) | 1 | 18.0 | 19.3 | 17.3 | 20.2 |
| | 2 | 16.9 | 18.1 | 19.8 | 15.6 |
| | 3 | 18.5 | 17.4 | 16.3 | 17.6 |
| | R | 1.6 | 1.9 | 3.5 | 4.6 |

Influence analysis of hot-pressing temperature on TS

Too high temperature will lead to the phenomenon of coking and increase the absorbing capacity, thereby increasing the TS. Proper pressing temperature will increase the TS by forming the pre-cured layer in the surface. When the hot-pressing temperature is low, the surface of packaging products is not fully cured and the poplar fiber inside the slab does not bond and combine greatly. It leads to the larger thickness and then the absorbing capacity increases and the TS increases. The influence of hot-pressing temperature on TS is shown in Fig. 7. We can know from the Fig. 7: within a certain range of temperature, the thickness decreases. But when the pressing temperature is too high, the TS increases rapidly. Taking all these factors, for TS, the optimal temperature in the process of hot pressing is 120 ~ 125°C.

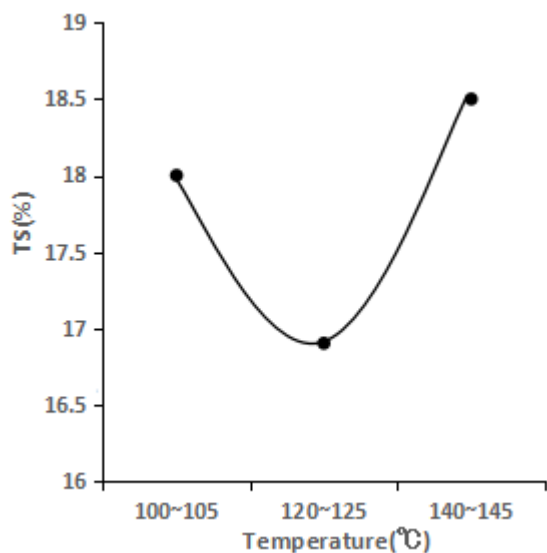


Fig. 7. Hot-pressing temperature's influence on TS

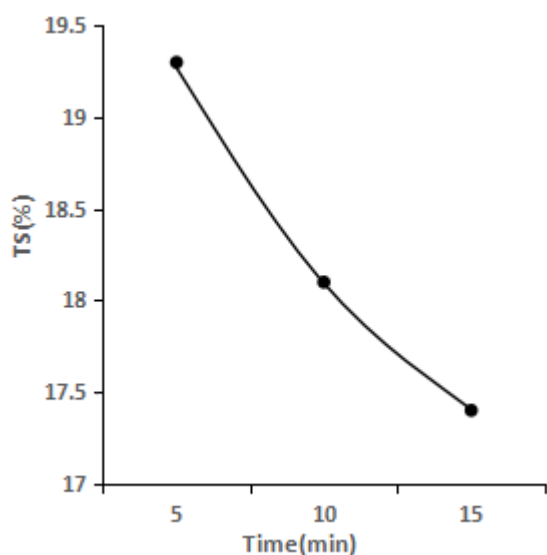


Fig. 8. Hot-pressing time's influence on TS

Influence analysis of hot - pressing time on TS

With the extension of pressing time, the adhesive is fully cured. It will be very hard for moisture to permeate into the fiber, so the TS of packaging products decreases. Therefore, during the process of hot pressing, packaging products which require low TS should extend the pressing time properly. The influence of pressing time on TS is shown in Fig. 8. We can know from the Fig. 8: with the extension of pressing time, packaging products' TS decreases rapidly. Taking all these factors, for TS, the optimal time for hot pressing is 15min.

Influence analysis of hot-pressing pressure on TS

Hot-pressing pressure has a great impact on TS. Certain pressure can make the fibers more closely combine and increase the liquidity of adhesive. The influence of hot-pressing pressure on TS is shown in

Fig. 9. We can know from the Fig. 9: with the increase of hot-pressing pressure, packaging products' TS increases first, and then decreases. As pressure increases, the slab is crushed and the combination between the poplar fibers become more closely, which make the TS decrease. Taking all factors, for TS, the optimal pressure for hot pressing during the process of pressing is 10MPa.

Based on the analysis of various factors on packaging products' TS, we can know that the value of range in size order is sizing amount, hot-pressing temperature, hot-pressing time and hot - pressing temperature. That is, sizing amount has the greatest impact on IB while the hot-pressing temperature is the least. Therefore, the best formula for TS is when the hot-pressing temperature is 120~125°C, hot-pressing time is 15min, hot-pressing pressure is 10MPa and the sizing amount is 20%.

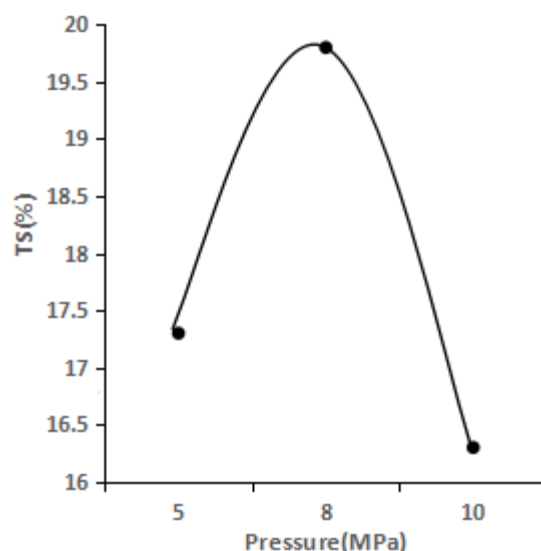


Fig. 9. Hot-pressing pressure's influence on TS

CONCLUSION

Based on the analysis of the physical and mechanical properties of packaging products and combining some features and requirements in the process of hot-pressing, we can draw a conclusion of a better molding process parameters, which are the hot-pressing temperature at 120~125°C, the hot-pressing time with 10min, the hot-pressing pressure of 10MPa and the sizing amount of 20%.

During the process of hot-pressing, the temperature, the time and the pressure are closely related and mutually restrained. Properly increasing temperature or pressure can shorten the pressing time and save energy.

The physical and mechanical properties of packaging products made from the above hot - pressing process parameters meet the requirement of

national standard (GB/T 4897-92D) [16].

In order to reduce the phenomenon of stratification and bumps, the moisture content of poplar fiber should be controlled between 15%~20% during the hotpressing. The process takes the way of secondary pressure and the slab should be preloaded before the real hot-pressing.

Acknowledgements: This work was supported by State Key Laboratory of Pulp and Paper Engineering (Project Number 2015-14- SKLPPE). This work is supported by Fundamental Research Funds for the Central Universities (Grant Number JUSRP 11209).

REFERENCES

1. K. MacDicken, G. Reams, J. de Freitas, *Forest Ecology & Management*, **352**, 1 (2015).
2. H.T. Yildirim, Z. Candan, *C. T. & F.*, **16**, 175 (2014).
3. M. Yan, N. Guo, H. Ren, X. Zhang, G. Zhou, *Forest Ecology & Management*, **337**, 119 (2015).
4. Isabelle M, Henry, Matthew S, Zinkgraf, Andrew T, Groover, L. Comai, *The Plant cell*, **27**, 2370 (2015).
5. H. Wang, J. He, *Forestry Machinery & Woodworking Equipment*, **10**, 13 (2008).
6. E.N. Yargicoglu, B.Y. Sadasivam, K.R. Reddy, K. Spokas, *Waste management*, **36**, 256 (2015).
7. E. Ergül, N. Ayrilmis, *Science Direct*, **61**, 66 (2014).
8. F. Zhang, L. Yu. *Packaging Journal*, **8**, 14 (2016)
9. Z. Y. Zhang, B. Li, H. Yan, H. Sun, L. Q. Wang, Y. Qian, X.C. Zhang. *Packaging Engineering*, **37**, 72 (2016)
10. Z. Zhou, J.C. Cao, P. Z. Tang. *Packaging Engineering*, **22**, 15 (2001).
11. GB/T 17657-1999, "Test methods of evaluating the properties of wood-based panels and surface decorated wood-based panels".
12. M. X. Wu, C. H. Zhang. *Technological Sciences*, **8**, 284, (2015)
13. C.T. Mei, *European Journal of Wood & Wood Products*, 94. (2012).
14. J. Y. Gu, Y. C. Hu, *Chemical Industry Press*, 249. (2009).
15. S.L. Xiag, Y. X. Li, *China Forest Products Industry*, **3**, 5 (1995).
16. GB/T 4897-92D, "Wood-based panels-Particalboard".

Seed germination of *Vicia hirsuta* (Linn.) S.F.Gray

X.J. Yang *, L.D. Duan

Department of urban construction, Shaoyang University, Hunnan Province-422004, China

Received February xx 2016, Revised May 24rd 2017

In order to study the germination characteristics of *Vicia hirsuta* (Linn.)S.F.Gray seeds, a series experiments had been done: after the seeds which coats were cut by scalpel were cultivated in 5°C, 10°C, 15°C, 20°C, 25°C, 30°C separately, the results showed that 25°C was the optimal germination temperature for the seeds; the imbibition process of vetch seeds were studied under the optimum temperature; the seeds were germinated with different concentrations (1, 10, 100, 1000 µmol/l) of GA3 and 6-BA solution; the seeds were germinated with the different temperature (30°C/10°C; 25°C/15°C); the seeds were laminated with the wet river sand in the incubator. The experimental results showed: the germination of the seeds which coats were cut by scalpel were 100% in 25°C for 24h; the seed germination next to 3% when the seeds were nursed with the 30-day's different temperature, the 30-day's treatment GA3 and 6-BA under 25°C, and the 60-day's lamination with river sand. The dormancy type of the *Vicia hirsute* (Linn.)S.F.Gray seeds which coat obstacle as water barrier were physical dormancy.

Keywords: *Vicia hirsuta* (Linn.)S.F.Gray; Optimum temperature; Seed coat damage; Seed dormancy

INTRODUCTION

The seed germination and dormancy, the two very important stages in the seed life, trended to the totally opposite condition through the seed life activities. They were also important things of the higher plant individual development, which concerned to the survival, reproduction and distribution of the plant community. The seed germination and dormancy had been studied for a long time, but till now a little knowledge had been get about in the seed biological field. Physical dormancy (or hard seed) was wildly found in the legume seed because the seed coat or the skin was impermeable (Hu Xiaowen 2009). In addition to the inherent factors of seed itself, the seed germination and dormancy also affected by the following factors: the temperature or temperature fluctuation in the process of system development, humidity or soil moisture, light and plant growth regulators, soil fertility, gas exchange, animal feed and etc. [1~2].

In order to improve the seed low germination rate, many scholars in and aboard had done a lot of research on the seed germination of various plants.

We found that different seed germination were related to the fluctuating temperature according to the following researches: Study on 22 Species of Perennial Grasses Seed by Yan song, Li-hua (2012) [3]; Research on Wild Rose *Rhodiola* Seeds by Liu Cai-fu, Zhao Wenhua.(2012) [4]; Study on the Tibet *Inula* Root Seeds by Bao Fugui (2011) [5~6]; and Study on the Seeds of the Castor Bean by Jiang

Xiaojun and Wen Xiangduo;

The seed germination rate was improved obviously after the seed coat was cut with the mechanical method based on the related researches as the following: Treated the Seed Coat of Aohan alfalfa Seed with Frosted Quartz by Wang Li and etc. (2009) [7] Dealt the *Sophora flavescens* Seeds with Sandpaper Grinding by Wang Lei and etc.. (2010) [8]

The seed germinating potential, percentage, and vigor index were improved after the seed treated with different concentrations of GA3 solution. The results got from the following studies: Research on the Seeds of *Cercis gigantean* by SHAO Bei-bei (2010) [9], and Physical dormancy in seeds of *Dodonaea viscosa* (Sapindales, Sapindaceae) from Hawaii, Baskin J M, Davis B H, Baskin C C, Gleason S M, CordelS. (2004) [10]

All of the above studies, the *Vicia hirsuta* (Linn.)S.F.Gray Seeds were selected as the research object according to some relevant information about other several kinds of the legume *Vicia* genus seeds and the low germinating seed under the natural conditions[11~12]. Till now, the *Vicia hirsuta* Seeds germinating characteristics had not yet been found. The ornamental value and garden use of the *Vicia hirsuta* had not been excavated. It was only regarded as weeds in many places.

Seed germination of the *Vicia hirsuta* (Linn.)S.F.Gray had been studied with the following methods: fluctuating temperature treatment; seed imbibition process; different concentrations of plant hormone treatment; treatment of lamination with river sand. The researchers attempted to discover the tiny vetch germination characteristics in-depth and to provide

* To whom all correspondence should be sent:
E-mail: yxj0008@163.com.

reference for exploitation, protection and cultivation of tiny vetch.

Vicia hirsuta (Linn.)S.F.Gray is annual herbaceous of vicia L. species. The stems are thin and soft, angled, nearly glabrous, trailing or climbing; paripinnate leaves, tendril branched; stipules linear, base with 2-3 cracked tooth; 4-8 pairs leaflets, linear or narrowly oblong, 0.5-1.5 cm long, apex truncate, with short pointed, base ministry gradually narrow, glabrous; Racemes is shorter than leaves obviously, 2-4 (-7) flowers; Calyx campanulate, calyx teeth lanceolate, about 2 mm; corolla length of 3-5 mm, white, light blue, green or purple white, thin pink, upper petal elliptic, about 5 mm, apex truncate or slightly concave, different petals nearly spoon shaped, the length equal to the upper petal, keel shorter; Ovary sessile, densely brown hirsute, with 2 ovules, the surrounding of the upper part is glabrous; The pod shaped oblong, 0.5-1 cm long, densely brown hirsute; 2 Seeds, obovate-spheroid, two sides protruding; Flower and fruit of 2-7 months [13]; it widely introduced and naturalized in wheat fields or hill slopes in Jiangsu, Zhejiang, Sichuan, Shanxi, Taiwan and etc. The *Vicia hirsuta* has strong adaptability and barren resistance, but it's good in the sandy loam with loose and fecund, good drainage as well.

The *Vicia hirsuta* (Linn.)S.F.Gray is applied to garden greening as the new plant for the groundcover and vertical greening. It has good ornamental value with its foliage green and beautiful shape. In addition, it is also used as the green manure and feed because the animal likes to eat it. The whole plant is used as the medicine for it is good for promoting blood circulation, stomach-calming, eyesight and anti-inflammatory and etc. [14].

MATERIAL AND METHOD

Experimental material, reagent, instrument

Experimental material

The *Vicia hirsuta* (Linn.)S.F.Gray seed(collected at the square of Qiliping Campus of Shaoyang University from 2014.10 to 2014.11

River sand(buy at market), filter paper(buy at market)

Experimental reagent

Potassium Permanganate KMnO₄ (AR): Tianjin bodi chemicals co.;

GA3 (analysis of pure): National Pharmaceutical Group Chemical Reagent Co., ltd.;

6-BA (analysis of pure): the Chemical Reagent Co., Ltd.

Distilled water (made)

Experimental instrument

CXZ intelligent seed germination box (Ningbo Jiangnan instrument factory);

AYU220 type electronic balance (SHIMADZU): a sense of 0.0001g;

A 100 ml volumetric flask, 1000ml volumetric flask, beaker, glass rod, cylinder, test tubes, filter paper and washed ear ball, thermometer, plastic head dropper, tweezers, a Petri dish.

EXPERIMENTAL METHOD

Treatment of the experimental material

The *Vicia hirsuta* (Linn.)S.F.Gray seeds: The *Vicia hirsuta* (Linn.)S.F.Gray fruits were treated by rubbing, shelling, washing, rinsing in water, natural drying and then preserved in a cool and dry place.

River sand: The sand was gone through 10 meshes screen, disinfected with 0.5% KMnO₄ solution, immersed for half an hour, cleaned with water and drained.

Determination of the weight of 1000 seeds

The natural dried *Vicia hirsuta* (Linn.)S.F.Gray seeds were divided into 12 parts with the four –way division. One thousand grain seeds were randomly selected from each part, weighted with a sense of volume to 0.0001g electronic analytical balance. This process was repeated three times, and the average value was calculated.

Test of seed water imbibition

300 grain *Vicia hirsuta* seeds randomly selected were divided into two parts, each part including 150 grains, one of them including 150 grain seeds which coats were cut. The two part seeds were equal divided into 3 groups respectively (1, 2, 3; cut 1, cut 2, cut 3). The seeds were weighted first and then recorded o hour. The seeds were immersed in the clean water and imbibed water. The weight of each group were measured and recorded down at 1h, 2h, 3h, 4h, 6h, 8h, 10h, 12h, 16h, 20h, 24h, 30h, 36h, 48h, 60h, 72h respectively.

Reagent preparation 0.50 % KMnO₄

To prepare 1000ml KMnO₄ solution with concentration of 0.50%, 5.000g KMnO₄ (which was accurately weighted by an electronic balance) was needed. The KMnO₄ were purred into the beaker, we added water and stirred until the solution fully dissolved and injected into volumetric flask with the capacity of 1000 ml along the glass rod. The beaker wall was washed with distilled water, and then each wash solution was

injected into a volumetric flask [15~18]. Distilled water was injected slowly into the volumetric flask, when surface near the volumetric flask scale 1 ~ 2cm stop. The glue dropper was used to add, and eyes with the surface of the concave surface at the bottom of the flat, when the solution titrated to scale line stop dropping. The volumetric flask was capped and shaken upside down till the solution well.

Configuration the GA3 and 6BA solution of 1000 μ mol/L, 100 μ mol/L, 10 μ mol/L, 1 μ mol/L

100mL GA3 and 6BA with different concentration (1 μ mol/L, 10 μ mol/L, 100 μ mol/L, 1000 μ mol/L) were Prepared respectively. Firstly, 100mL GA3 and 6BA solution with concentration of 1000 μ mol/L were configured: firstly, quantitative 6-BA and GA3 were weighted and put into a clean beaker respectively, dissolved with appropriate sodium hydroxide solution. Secondly, until completely dissolved, the solution was neutralized with hydrochloric acid; a proper amount of distilled water was added into the solution and the solution was injected into a 100 ml volumetric flask along the glass rod. Thirdly, the inside of the beaker was cleaned several times with a small amount of distilled water till no residue and each washing solution was purred into a volumetric flask [15~18]. The distilled water was added to a volumetric flask, when the surface near capacity graduated bottle 1cm to 2cm stop. The glue dropper was used to head dropping, and eyes with the surface of the concave surface at the bottom of the flat, when the solution titrated to scale line stop dropping. The volumetric flask was capped and shaken upside down till the solution well. Fourthly, with this method, the solution was diluted according to the concentration gradient. 100mL solution with concentration of the 100 mmol / L, 10 mmol / L, 1 mmol / L were prepared respectively.

The optimum temperature of seed germination

18 Petri dishes (diameter 9cm, high 2cm) were picked out, cleaned, and labeled with A1-A4, B1-B4, C1-C4, D1-D4, E1-E4. Eighteen part of the *Vicia hirsuta* (Linn.)S.F.Gray seeds (each 50 grains) which had been winnowed were randomly selected. The seeds were get out after immersed in KMnO4 solution with concentration of 0.5% for 30 minutes, rinsed with distilled water for 3 - 4 times until no disinfectant residual in the seed. The seeds which coat was cut were placed in 18 culture dishes (4 culture dishes as a group). The dishes were put into the incubators with temperature at 5°C, 10°C, 15°C, 20°C, 25°C, 30°C and nursed for one month.(Table 1)

Table 1. The optimum temperature of seed germination

| Test | The temperature (°C) |
|-------|----------------------|
| A1-A4 | 5 |
| B1-B4 | 10 |
| C1-C4 | 15 |
| D1-D4 | 20 |
| E1-E4 | 25 |
| F1-F4 | 30 |

Seed imbibition test

6 Petri dishes (diameter 9cm, high 2cm) were picked out and cleaned. 6 part of the *Vicia hirsuta* (Linn.)S.F.Gray seeds (each 50 grains) which had been winnowed were randomly selected. Three of them were pierced the seed coat with a blade (be careful not to row to the embryo), and divided into F1 to F3 group (parallel experiment) and cultured in the optimum temperature for 72h.(Table 2)

Table 2. The germination of seed which coat was broken.

| Number | The way of deal |
|-------------|------------------|
| F1, F2, F3, | Cut or the whole |

Breaking the seed dormancy by GA3 and cytokinins 30 petri dishes were picked out (diameter 9cm, high 2cm) and cleaned. 30 part of the *Vicia hirsuta* (Linn.)S.F.Gray seeds (each 50 grains) which had been winnowed were randomly selected, divided into five groups G, h, I, J, K(n = 3, parallel experiments) , added different concentrations (0,1, 10, 100, 1000 μ mol/l) of GA3, cultured in optimum temperature for a month.(Table 3)

Table 3. To break the seed dormancy by GA3

| Number | Concentration (μ mol/L) |
|----------------|------------------------------|
| G1, G2, G3, G4 | 0 |
| H1, H2, H3, H4 | 1 |
| I1, I2, I3, I4 | 10 |
| J1, J2, J3, J4 | 100 |
| K1, K2, K3, K4 | 1000 |

Lamination treatment on the seed germination

Four beakers with the capacity of 100ml were picked out and cleaned. Four part of the *Vicia hirsuta* (Linn.)S.F.Gray seeds (each 50 grains) which had been winnowed were randomly selected. The seeds were wrapped with disinfect clean nylon gauze, divided into A to L group (n = 4, parallel experiments), put into the clean river sand, and nursed in optimum temperature for one to two months (Table 4)

Table 4. The seed germination of seed lamination

| Number | Material of lamination |
|----------------|------------------------|
| L1, L2, L3, L4 | River sand |

RESULTS

Basic information of the seed

The seeds were randomly selected and weighted with the four - way division. Average 1000 seeds were weighted for 5.1638g; the maximum differences of 1000 seed weight for each group were below 0.05. In this way, we ensured that the used seed quality, particle size and seed germination activity were almost the same.

In order to test the seed water content, firstly, the sample boxes were dried, cooled, weighted, and then marked. Secondly, three parts of the seeds (each part are 100 grain) were chosen, put into the boxes we had prepared, weighted (accurate to 0.0001g), and put into the oven with temperature 80°C for 48h. The box was covered with crucible tongs (the box sealed). Thirdly, the boxes which contained the sample seeds were picked out, put into the dryer, cooled to room temperature, weighted in 30-40 minutes later. After calculating, we found that the water contents of the sample tiny vetch seeds were 9.3%.

Table 5. The basic information of seed

| Species | Harvest year | Collection site | Life form | 1000Weight (g) | Moisture content (%) | Viability (%) |
|--|--------------|-----------------|-----------|----------------|----------------------|---------------|
| <i>Vicia hirsuta</i> (Linn.) S.F.Gray. | 2014 | Shaoyang, Hunan | Annual | 5.1638 | 9.3 | 99 |

Referred to international rules for seed testing, the seed viability was determined with TTC (2, 3, 5-Triphenyl Tetrazolium Chloride, TTC)staining method. The prepared seeds which coats were cut were randomly selected, invaded into Tetrazole solution (concentration of 1%) for 4 hours under the temperature 20°C. This proceeding was repeated for 3 times, and each time 50 grain seeds were used. As a result, the percentage of the seed viability was 99% after the seeds were treated and silted. (See Table 2.1)(Table 5)(Fig. 1)

The seed imbibitions test

As shown from Fig. 1, we knew that the water absorption rate of the seed which coat was cut was 97.12%, while the whole seed water absorption rate was 14.98% during 0 to 6 hours. After 12 hours the water absorption of the whole seed no longer increased, and the water absorption of the seeds which coat were cut still increased. As a result, the seed coat of the small vetch was a barrier for the seed water absorption.

The consequence and analysis of the optimum temperature for seed germination (Table 6)

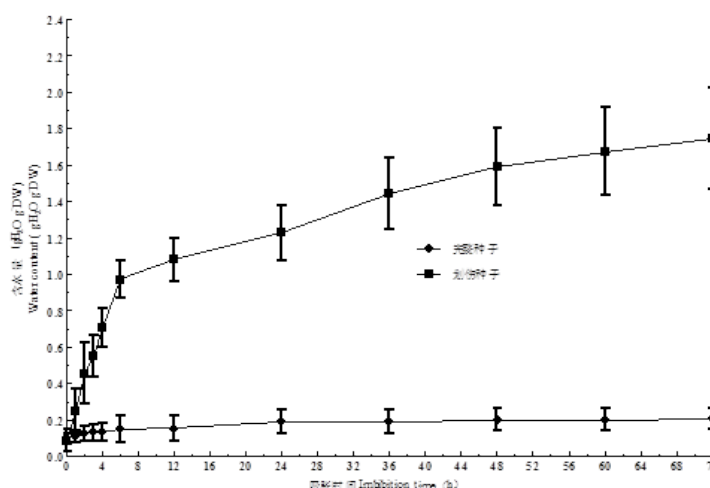


Fig. 1. The curve of whole seeds and the seeds which coats were cut

Table 6. The germination of seed under different temperature

| Temperature (°C) | Number | Germination (%) |
|------------------|--------|-----------------|
| 5 | 0 | 0c |
| 10 | 0 | 0c |
| 15 | 0 | 0c |
| 20 | 38 | 76b |
| 25 | 47 | 94a |
| 30 | 34 | 68b |

Note: values in same column the different small letters indicate significantly different at P 0.05, the below is same.

As shown from Table 6, we found that the seed germination rate of the tiny vetch which coat was cut was zero after 30 hours nurturing under the temperature 5 to 15 degrees Celsius, while under the temperature 25 degrees Celsius, the seed germination rate reached to 94%. As a consequence, the optimum temperature for the seed germination of the tiny vetch was 25 degrees Celsius

The consequences and analysis of the seed germination by plant hormones or by fluctuating temperatures (Table 7)(Table 8)(Table 9)

Table 7. To break the seed dormancy by GA3

| Concentration (μmol/L) | Number | Germination (%) |
|------------------------|--------|-----------------|
| 0 | 0 | 0 |
| 1 | 4 | 8 |
| 10 | 3 | 6 |
| 100 | 3 | 6 |
| 1000 | 2 | 4 |

As shown from Table 7~9, it was seen that when the seeds were soaked in different concentrations of GA3 and 6-BA solution and cultivated in variety temperature, the 3 groups of *Vicia hirsuta* (Linn.)S.F.Gray seed germination rate were very low (the average germination rate was 3.2%), which indicated that plant hormones and different cultivating temperature hadn't promote the tiny vetch seed germination.

Consequence and analysis of the seed germination of seed lamination(Table 10)

Table 8. To break the seed dormancy by 6-BA

| Concentration (μmol/L) | Number | Germination (%) |
|------------------------|--------|-----------------|
| 0 | 0 | 0 |
| 1 | 3 | 6 |
| 10 | 2 | 4 |
| 100 | 3 | 6 |
| 1000 | 0 | 0 |

Table 9. To break the seed dormancy by changing temperature

| Temperature (°C) | Number | Germination (%) |
|------------------|--------|-----------------|
| 25/15 | 4 | 8 |
| 30/10 | 3 | 6 |

Table 10. The seed germination of seed lamination

| Experiment time (d) | Number | Germination (%) |
|---------------------|--------|-----------------|
| 30 | 1 | 2 |
| 40 | 2 | 4 |
| 50 | 2 | 4 |
| 60 | 2 | 4 |

As shown from Table 10, it was seen that the seed germination percentage was 3.5% after the seed lamination with river sand in optimum temperature. Seed lamination hadn't helped the seed germination.

DISCUSSION

During experiment, the seeds we select for the test are freshly collected in October, 2014 because the proportion of hard seeds are 42.5% at early stage and the seed coats permeability are relatively good. With the time going, although the seed coats haven't obviously dehydration, the water inside the seeds evaporates and the seed water entrance decrease gradually. The proportion of hard seeds increases from early 42.5% to 93% in experiment in June, 2015.

After the seed coat is cut, the seed imbibition rate of the *Vicia hirsuta* (Linn.)S.F.Gray seeds reaches to 100% in 5°C, 10°C, 15°C, 20°C, 25°C, 30°C after 24 hours. The seed germination rate reaches to 94% after the seeds are nurtured in 25 degrees Celsius for 30 hours. The germination rate reaches 76% and 68% in 20°C and 30°C while the germination rate is zero in 5°C, 10°C and 15°C. All above, the optimum temperature for the *Vicia hirsuta* seeds is 25 °C.

The germination rate of the tiny vetch seeds is 3.2% with 30 day's treatment by plant hormones and fluctuating temperature. The seed germination rate is just 3.5% with the 60-day's lamination treatment with river sand. The plant hormones and lamination treatment have no help for the seed germination. The water absorption barrier of the seeds has great impact on the seed germination. The *Vicia hirsuta* seeds have the physical dormancy, so to break the seed physical dormancy is an effective way to improve the seed germination rate.

Acknowledgements : We extend our sincerely appreciation to Song Songquan (the researcher of Institute of botany, Chinese academy of sciences)

and the members of group for their helps.

Foundation item: Project (2016JJ6135) supported by National Natural Science Foundation of Hunan

REFERENCES

1. F.G. Bao, S.L. He, *Guangdong Agricultural Science*, **07**, 48 (2011).
2. J.M. Baskin, B.H. Davis, C.C. Baskin, S.M. Gleason, S. Cordel, *Seed Science Research* a, **4**(I), 81 (2004).
3. W. Bolingue, L.V. Benoit, O. Leprince, J. Buitink, *Seed Science Research*, **20**(2), 97 (2010).
4. J.M Baskin, B.H Davis, C.C Baskin, S.M Gleason, S. Cordel, *Seed Science Research* a, **4**(I), 81 (2004).
5. W. Bolingue, L.V. Benoit, O. Leprince, J. Buitink, *Seed Science Research*, **20**(2), 97 (2010).
6. N.J Chung, N.C Paek, *Agronomy Journal*, **95**(1), 184 (2003).
7. F. Gubler, A.A. Millar, J.V. Jacobsen, *Plant Biology*, **8**(2), 183 (2005).
8. J.M. Herranz, P. Ferrandis, E. Martinez-Duro, *Plant Ecology*, **211**, 89 (2010).
9. C.F. Liu, W.H. Zhao, *Liaoning Forestry Science and Technology*, **04**, 12 (2012).
10. Y.J. Qiu, T. Yong, S.M. Wang, P. Li, Y.H. Cheng, *Anhui Agricultural Sciences*, **02**, 474 (2009).
11. K. Ronnenberg, K. Wesche, I. Hensen, *Plant Ecology*, **196**, 269 (2008).
12. L.H. Song, B. Cao, *Seed*, **05**, 62 (2012).
13. B.B. Shao, *Practical Forestry Technology*, **02**, 4 (2010).
14. J.A. Van Assche, F. Vandeloos, *Seed Science Research*, **20**, 237 (2010).
15. R.D. Van-Klinken, B. Lukitsch, C. Cook, *Annals of Botany*, **102**(2), 255 (2008).
16. J.A. Wang, S.I. Shi, *Grassland and Turf*, **02**, 41 (2011).
17. L. Wang, Q.C. Liu, K.L. Wang, Q.H. Liu, *Acta Agriculturae Jiangxi*, **02**, 16 (2009).
18. L. Wang, Y.H. Zhou, X.L. Guan, H. Zhang, S.Q. Chen, *Seed*, **03**, 44 (2010).
19. C.W. Weekley, J. Tucker, S. Valligny, E. S. Menges, *Cas-tanea*, **73**, 235 (2008).
20. S.X. Yin, *Anhui Agricultural Science Bulletin*, **03**, 43 (2012).

Research on vegetation spatial heterogeneity in longitudinal range-gorge region of Yunnan province, China

C.Y. Xu, C.Y. Hao*

College of Surveying & Land Information Engineering, Hennan Polytechnic University, Jiaozuo City, China

Received June 26 2017; Revised July 20, 2017

In the southwest of Yunnan Province of China, there are Mt. Laobie, Mt. Bangma, Mt. Wuliang and Mt. Ailao, which influenced its climate and vegetation. It may be one of the main issues of mountain ecology in China. In this paper, Moran Coefficient was adopted to calculate the spatial autocorrelation degree, and semivariance function was used for spatial variability and spatial heterogeneity analysis. The results indicate that the spatial differentiation patterns of main climatic factors have been consistent with the trend of mountains, showed higher autocorrelation in south-north direction and lower in west-east direction. And all these reveal that the barrier function was remarkable in the orientation of the mountains while the topographic corridor effect was rather obvious in the extension direction. The barrier function was stronger with more complicated structure resulted from directivity for Mt. Ailao and Mt. Laobie while it was weaker for Mt. Bangma and Mt. Wuliang. All in all, the corridor-barrier functions of vertical mountains were closely related to the trend and scale of each mountain.

Key words: Enhanced vegetation index, spatial variability, anisotropism, corridor-barrier functions, Mt. Ailao.

INTRODUCTION

Spatial heterogeneity is an important concept in landscape ecology, and is also one of the main properties of ecosystem. In most current researches, the understanding of spatial variability only stays on qualitative or semi-quantitative level, and more importantly, those results cannot explain how the overall pattern forms. So it is not still used in generalization of pattern [1, 2]. It is well known that the quantitative analysis of spatial heterogeneity can be considered from two aspects: spatial characteristics and spatial comparison. And both can be quantified by mathematical statistics methods, allowing the spatial variability analysis to be carried out on different scales [3]. Quantitative description of landscape pattern is the premise for understanding the dynamic states and ecological processes of landscape heterogeneity pattern, as well as their interactions. Only after we figure out the patterns, can it be possible to find out the reasons for pattern formation [4]. Therefore, in this paper, we focus on the study area with complex terrain - the Longitudinal Range-gorge Region in Yunnan, China, and used three statistical indicators, spatial autocorrelation, spatial variability and anisotropy, together with the enhanced vegetation index (*EVI*) and its ecological factors like water, temperature and heat, to show the spatial heterogeneity of vegetation and the reasons for its formation.

EXPERIMENTAL

Study area

The Longitudinal Range-gorge Region is located in Yunnan Province, China, which includes Hengduan Mountains that is directly associated with the uplift of Qinghai-Tibetan Plateau, and the adjacent mountain valley area in south-north direction. The Longitudinal Range-gorge Region is a set of range/gorge groups that are approximately distributed in north-south direction and aligned in west-east way. From west to east, they are Mt. Laobie / R. Nanding, Mt. Bangma / R. Lancang, Mt. Wuliang / R. Amo, and Mt. Ailao / R. Yuan. These four pairs of range / gorge terrain unit have maximal high relief amplitude, all of which are above 1200m; and they are at the altitude between 2000m and 4000m, belonging to high- and mid-altitude mountains [5]. Among those mountains, Mt. Ailao has the highest elevation, with magnificent overlapping peaks and towering momentum. The unique microhabitats formed by such a kind of combination of complicated topography and warm-humid air current, which cause a great diversity in river hydrology, soil type, and vegetation species. So in this study area, it is very significant of the spatial heterogeneity of vegetation landscape [6].

Data acquisition

The relationship between vegetation and its climate factors is a traditional research subject in ecology, geography and climatology [7]. The plant ecological studies have shown that the main climate

* To whom all correspondence should be sent:
E-mail: haocy@hpu.edu.cn

factors that determine vegetation coverage changes are radiation, temperature, water, and their combinations [8, 9]. And terrain conditions can indirectly affect vegetation in specific regions by changing the redistribution of main climate factors [10, 11]. Therefore, this study used enhanced vegetation index (EVI) and total solar radiation, mean minimum temperature, mean maximum temperature, and mean annual precipitation as the quantitative indicators for vegetation and its climate factors.

EVI based on MODIS

Based on the monitoring methods, the ways to measure vegetation coverage can be divided into two categories, field reconnaissance and remote sensing retrieval [12]. Studies have shown that the vegetation index method in remote sensing retrieval is easy to conduct and doesn't depend on experimental data, which was widely used in macro vegetation ecology studies [13]. In vegetation ecology, MODIS data from United States of American (USA) is more widely used, which mainly has two categories of indexes, normalized differential vegetation index (NDVI) and enhanced vegetation index (EVI). Compared to NDVI, EVI has many improvements, for example, it has increased sensitivity to high biomass areas by revising the surface reflectance, and it has enhanced vegetation monitoring accuracy via coupling the leaf canopy background signal and reducing the atmosphere effect [14, 15]. Therefore, this study used the annual average EVI in 2014 as vegetation index to explore the spatial heterogeneity of vegetation in high biomass areas - Yunnan tropical rainforest in China, with the spatial resolution of 1 km.

Temperature and precipitation based on PRISM

Parameter elevation Regressions on Independent Slopes Model (PRISM) is a climate map based on the geographical spatial characteristic and regression statistical methods, developed by Spatial Climate Analysis Service of Oregon State University of USA. It used Digital Elevation Model (DEM) as the platform, integrated Geographical Information System (GIS) spatial interpolation technology, and considered the effects on temperature and precipitation from elevation, gradient, slope aspect, distance, land and sea locations, vapor sources, etc., to get the spatialization of meteorological elements through windowing technology and linear interpolation [16]. Long term (1961—1990) monthly mean values for minimum and maximum temperature and

monthly precipitation at 0.041 decimal degrees spatial resolution in China were got by applying PRISM technology based on observation data of 2450 meteorological stations in China and its surrounding countries. And they have been proved to be very reliable. As to eighteen ecological research stations of Chinese Ecosystem Research Network independent of the national meteorology station network, the average relative errors rates of monthly mean values for minimum temperature, maximum temperature and monthly precipitation are 6.9%, 13.3% and 19.3% respectively, which are better spatial simulation results of both temperature and precipitation in mountainous area under the existing conditions of the distribution pattern of the meteorological stations [17].

Total solar radiation based on model simulation

We combined Angstrom and Bristow-Campbell climatological models for total solar radiation computing, and used DEM, monthly mean temperature and mean percentage of sunshine as the basic data, to achieve the spatialization of monthly total solar radiation, and thereby obtained the annual total solar radiation in this study area. After tested by the measured data, the results generated by this method showed high accuracy: the mean error rate was only 3.69% [18].

Main methods

In geosciences field, the geostatistics methods are used frequently to analyze the spatial patterns and variation rules of different natural variables. Most importantly, these methods have been proved to be effective for studying the spatial patterns and spatial comparisons of vegetation landscape [19, 20].

Spatial autocorrelation

Spatial autocorrelation is used to determine whether a variable correlates with distance and the degree of correlation [21]. Spatial autocorrelation coefficients are used to quantitatively describe the dependency of variables on space. If a variable becomes closer and closer as the measuring distance decreases, then it has a positive correlation with space; if it gets more and more different, then it is negatively; if it doesn't show space dependency, then this variable is spatially uncorrelated. Moran coefficient (MC) is one of the most commonly used indicators for measuring spatial autocorrelation [22].

Semivariogram

By definition, semivariogram can reveal the variation patterns of spatial variables within a certain region. After calculating for the measured data from samples, we can use several theoretical models to fit the data and get four important parameters, range, sill, nugget and fractal dimension, which are very critical for explaining the ecological significance of semivariogram. It mainly has two aspects of meanings.

Anisotropy

For spatial variables, semivariogram is not only related to measuring distance, but also associated with location and directions. When a variation function is constructed along one particular direction, it is called anisotropic variogram. Apparently, anisotropy is an important part of spatial heterogeneity. Higher anisotropy means higher degree of spatial heterogeneity. Studies have shown that the anisotropy and spatial variability, caused by terrain, water and other ecological factors, are more significant [23].

Spatial heterogeneity

Among the four parameters of semivariogram, except for range that only indicates the size of intervals, all the other parameters, including sill, nugget and fractal dimension, can describe the spatial heterogeneity. In practical applications, sill ($C0+C$) and fractal dimension (D) are more common. Sill represents system properties or the maximum variation of regionalized variables, in which the greater it is for the same variable in different regions, the higher the spatial heterogeneity will be. However, when comparing different regionalized variables, sill is not valid because it's largely affected by its own definition and measurement units. Since the fractal dimension represents the curvature of semivariogram curve, the greater it is, the higher the spatial heterogeneity caused by spatial autocorrelation will be. Fractal dimension is dimensionless, so that it is possible to determine the degree of spatial heterogeneity by comparing the fractal dimension of different variables.

RESULTS AND DISCUSSION

After considering the central locations of every longitudinal mountain, we chose 23°39'30"-23°58'0"N as the cross-section in latitudinal direction. By way of moving window control, we confirmed that each sample region has 36×36 valid data points, with a total of 1296.

Spatial autocorrelation

MCs of major climate factors from each sample area are listed in (Figure 1 to Figure 4), calculated by a classical statistical method. From the figures, we can see that the spatial autocorrelation is not only different for different indicators, but also distinct for the same indicator in different directions, on which is an important aspect we want to emphasize in this study.

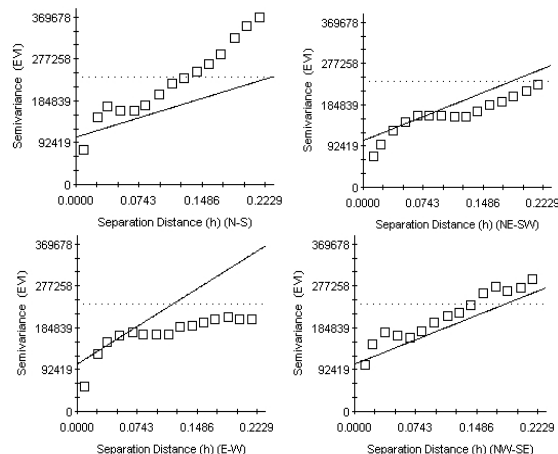


Fig. 1. Semivariogram of EVI in Mt. Laobie.

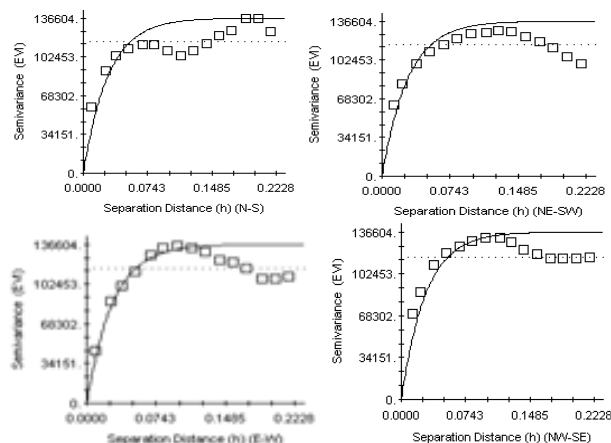


Fig. 2. Semivariogram of EVI in Mt. Bangma.

The major influencing factors of vegetation include annual precipitation, mean minimum temperature, mean minimum temperature, total solar radiation, etc. Most of them showed negative spatial correlation in isotropy; the directions of their maximum anisotropic positive correlation values are consistent with the orientation of mountain ranges, and the directions of their maximum negative correlation values are perpendicular to the mountain trends. Specifically, in Mt. Laobie and Mt. Bangma, which are in northeast-southwest direction, these climate factors have the maximum positive spatial autocorrelation in northeast-southwest direction, except for annual precipitation of Mt. Laobie, whose maximum value of positive

spatial autocorrelation is in west-east direction. For negative correlation, most of the factors have maximum values in northwest-southeast direction, such as total solar radiation, mean minimum and maximum temperature. In the north-south trending Mt. Wuliang, the maximum values of positive spatial autocorrelation show south-north direction, especially the mean maximum temperature whose *MC* is up to 0.7481, while the negative correlation stands out in the west-east direction, especially the mean minimum temperature whose *MC* is up to -0.8799.

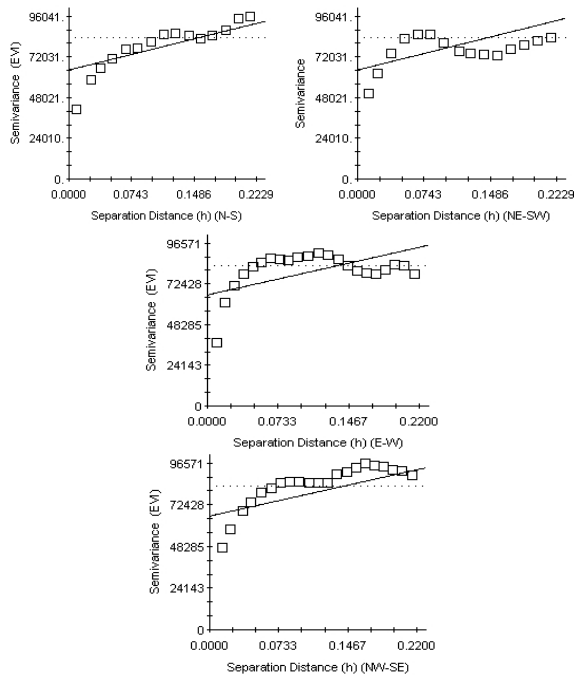


Fig. 3. Semivariogram of EVI in Mt. Wuliang

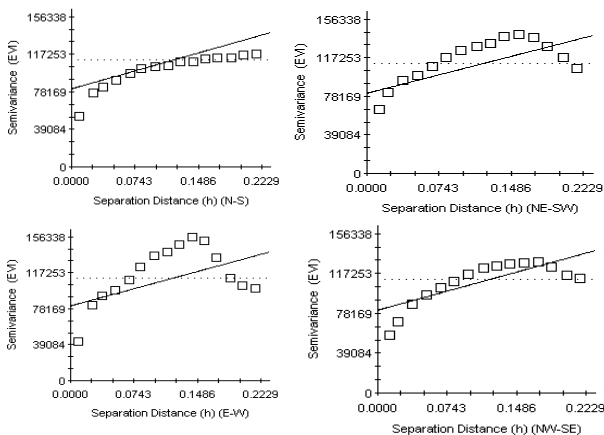


Fig. 4. Semivariogram of EVI in Mt. Ailao

In Mt. Ailao which is in northwest-southeast direction, the maximum positive correlation values of *MC* are also in northwest-southeast direction, and the maximum negative correlation values are more significant in both northeast-southwest direction and west-east direction: the *MC* of annual

precipitation and mean maximum temperature have the biggest absolute value in west-east direction, while mean minimum temperature and total solar radiation have the maximum *MC* value in northwest-southeast direction. These results demonstrate that the trend of mountain barrier effect is closely related to the mountain trend: the maximum barrier effect of each mountain is perpendicular to the mountain trend, and the maximum corridor effect of every valley is in the same direction as valley trend.

Spatial variability

We used GS+ 7.0 to analyze the spatial variability of *EVI* and its climate factors, and the results are shown in these figures. This study mainly compared *C0+C* and *D* values of the four sample areas in order to analyze their spatial heterogeneity, because these two values can illustrate the spatial variability and distribution features of vegetation from different aspects.

From the figures, we can see that the five variables, *EVI*, annual precipitation, mean minimum temperature, mean maximum temperature and total solar radiation, have the comparing orders of 2, 1, 1, 2, 1 in Mt. Ailao, with an average of 1.4; for Mt. Laobie, Mt. Bangma and Mt. Wuliang, the average comparing orders of the five variables are 1.8, 2.8 and 4 respectively. Therefore, the overall ranking of these four mountains from big to small is Mt. Ailao, Mt. Laobie, Mt. Bangma and Mt. Wuliang, which reflects the order of barrier effect of these mountains. This result is related to the mountain height, mountain trend, and the angle of main airflows. Among these mountains, Mt. Ailao is the most magnificent one, whose northwest-southeast direction is almost perpendicular to the most influencing airflow in the study area - southwest summer monsoon, so that *EVI* and its major climate factors have the most significant spatial heterogeneity. In contrast, Mt. Wuliang has more gentle topography with the direction of north-south, so its interception to southwest summer monsoon is not significant, and the spatial heterogeneity is ranked last.

From the figures, we can also see that the *D* values of *EVI* and its major climate factors within the study area are all between 1.116 and 1.906. By comparison, the *D* values of *EVI* and total solar radiation are both higher than 1.817, indicating that their spatial variability caused by random factors is high, and the spatial distribution is more complex; the *D* values of annual precipitation, mean minimum temperature and mean maximum

temperature are all lower than 1.577, suggesting that they have low levels of spatial variability caused by random factors, and their spatial autocorrelation is more significant.

In a word, from the spatial heterogeneity comparison of each longitudinal mountain, we find that Mt. Ailao and Mt. Laobie have bigger barrier effect and more complex spatial heterogeneity, while Mt. Bangma and Mt. Wuliang have smaller barrier effect and more regular spatial distribution. From the spatial heterogeneity comparison of *EVI* and its climate factors, we come to a decision that *EVI* and total solar radiation have high fractal dimension and more complex spatial distribution, while annual precipitation, mean minimum temperature and mean maximum temperature have small fractal dimension and stronger spatial autocorrelation.

Anisotropy

To further explore the spatial variability of vegetation on different directions, we used GS+7.0 to plot the *EVI* variability of each longitudinal mountain along four directions, south-north, northeast-southwest, east-west and northwest-southeast (Figure 1 to Figure 4). From the plot we can see that the *EVI* of each mountain has different anisotropy. The *EVI* anisotropy features of Mt. Laobie and Mt. Bangma are very similar: they have more variations on south-north direction, followed by east-west direction, and have smaller variations on northeast-southwest and northwest-southeast directions. This is mainly because the directions of these two mountains are both northeast-southwest. The *EVI* spatial pattern of Mt. Wuliang in south-north direction shows higher variation on east-west and northeast-southwest directions, but lower variation on northwest-southeast direction; the *EVI* anisotropy of Mt. Ailao is higher in east-west and southeast-northwest directions, but lower in south-north and northwest-southeast directions, which is closely related to its north-west to south-east direction.

In summary, affected by the main airflow – southwest summer monsoon, the *EVI* variation of each longitudinal mountain has larger or largest values on the east-west direction, indicating that the east-west direction of study area should be the dominant direction of barrier effect; the maximum *EVI* variation direction is perpendicular to the mountain direction, also suggesting that the *EVI* anisotropy is formed by mountain barrier effect. Oppositely, the terrain effect of each longitudinal mountain on south-north direction should be the main direction of corridor effect. Therefore, we

arrive at a conclusion that the different *EVI* anisotropy of each mountain is controlled by mountain trending and the major airflow movement from west to east.

CONCLUSION

Firstly, the *EVI* of major influencing climate factors mostly have negative spatial autocorrelation, indicating that the terrain influence is mainly based on barrier effect; the maximum positive autocorrelation value of *MC* is in the same direction as mountain trend, the maximum negative autocorrelation value is perpendicular to the mountain direction, suggesting that the barrier effects of different mountains are strictly related to mountain trends.

Secondly, water, temperature and heat of Mt. Ailao have complex spatial heterogeneity and large barrier effect, while these factors have more regular spatial distribution and smaller barrier effect for Mt. Bangma and Mt. Wuliang.

Thirdly, the *EVI* values of longitudinal mountains have different anisotropy, and are strictly related to mountain directions. Its formation is controlled by both the north-south direction of mountains and the main airflow movement from west to east.

Fourthly, for vegetation parameter *EVI* and water, temperature, heat, both the statistical anisotropy characteristics and spatial variability are consistent with the terrain scale and direction of these mountains, indicating that the topographic features have constraint effects on vegetation and its ecological factors.

Acknowledgements: The authors thanked the project of No. 41371105 supported by the National Natural Science Foundation of China.

REFERENCES

1. J.F. Knowles, P.D. Blanken, M.W. Williams, *Biogeochemistry*, **125**(2), 185 (2015).
2. C. Xu, S. Sheng, T. Chi, X.J. Yang, S.Q. An, M.S. Liu, *Landsc. & Ecol. Eng.*, **10**(2), 295 (2013).
3. K.P. Overmars, G.H.J. Koning, A. Veldkap, *Ecol. Modell.*, **164**(2-3), 257 (2003).
4. J. Wu, D.E. Jelinski, M. Luck, *Geographic Inf. Syst.*, **6**(1), 6 (2000).
5. C.Y. Hao, E.F. Dai, S.H. Wu, C.H. Zhou, H. Wang, T. Pan, *Chin. Sci. Bull.*, **51**(S), 143 (2006).
6. T. Pan, E.F. Dai, S.H. Wu, *J. Mount. Sci.*, **7**(1), 176 (2010).
7. M.L. Liang, Z.H. Xie, *Climatic & Environ. Res.*, **11**(5), 582 (2006).
8. Q. Huo, Q. Feng, Y.H. Su, *J. Mount. Sci.*, **12**(1), 166 (2015).

9. D. Leber, F. Holawe, H. Hausler, *Geo-Journal*, **37**(4), 451 (1995).
10. A.L. Marcelo, R.H. Jorge, P.G. Edward, Z.A. Francisco, W.F. Karl, *Wetlands*, **35**(4), 783 (2015).
11. B.W. Qiu, C.Y. Zeng, Z.H. Tang, W. J. Li, H. Aaron, *J. Mount. Sci.*, **10**(4), 541 (2013).
12. A. Vrieling, K.M. Beurs, M.E. Brown, *Climatic Change*, **109**(3), 455 (2011).
13. L.L. Golubyatnikov, E.A. Denisenko, *Izv., Atmos. & Ocean. Phy.*, **42**(4), 584 (2006).
14. E.P. Glenn, P.L. Nagler, A.R. Huete, *Srvy. Geophys.*, **31**(6), 531 (2010).
15. J.D. Kalma, T.R. Mcvicar, M.F. McCabe, *Srvy. Geophys.*, **29**(4), 421 (2008).
16. C. Daly, W.P. Gilson, G.H. Taylor, G.L. Johnson, P. Pasteris, *Clim. Res.*, **22**(2), 99 (2002).
17. H.Z. Zhu, T.X. Luo, C. Daly, *Geog. Res.*, **22**(3), 351 (2003).
18. C.Y. Hao, C.Y. Xu, S.H. Wu, *Resour. Sci.*, **31**(6), 1031 (2009).
19. D.A. Dick, F.S. Gilliam, *Wetlands*, **27**(4), 951 (2007).
20. D.M. Lambert, L.D. James, B. Rodolfo, *Precis. Agric.*, **5**(6), 579 (2004).
21. A. Dounavi, N. Koutsias, M. Ziehe, H.H. Hattemer, *J. Forest Res.*, **129**(6), 1191 (2010).
22. F. Csillag, S. Kabos, T.K. Rimmel, *Environ. & Eco l. Stat.*, **15**(4), 385 (2008).
23. B. Kozar, R. Lawrence, D.S. Long, *Precis. Agric.*, **3**(4), 407 (2002).

Study on the computing methods of mixed layer depth and gradation based on sand wave motion

M.J. Zhang, Y.H. Yang *, H.Q. Zhang

Key Laboratory of Engineering Sediment of Ministry of Transport, Tianjin Research Institute for Water Transport Engineering, Tianjin, China

Received September 20, 2016; Revised January 14, 2017

As for non-uniform sand mathematical models, the determination of mixed layer depth and gradation is of extremely important significance and will directly decide the reliability and accuracy of corresponding computing results. On the basis of sufficient indoor and outdoor data, the relation curve between relative wave height and relative velocity is represented, with curve parameters being matched; besides, based on the physical meanings of mixed layer depth and its relation with sand wave height, the sand wave motion-based computing method of mixed layer depth is derived out. Starting from the concept of mixed layer, it is assumed that the original bed material gradation will be uniform along depth, the porosity remains unchanged before and after scouring and silting, blending layer depth is a constant in the computing period, scoured sediment will be substituted equivalently by original bed materials below blending layer's lower boundary, deposited sediment will lead to equivalent ascending and descending of blending layer's upper and lower boundaries, the mixing will be uniform in the process, and the estimation methods of the sand wave bed's mixed layer under three models are derived out and obtained, including the pure deposition model, the pure scouring model and the coarse-deposition fine-scouring model.

Keywords: Sand wave, mixed layer, depth, gradation

INTRODUCTION

Mixed layer, also known as turbulent layer, exchange layer and mobile layer, refers to the bed layer under mobile or quasi-mobile state during the constant exchange with the mobile sediment in water flow within the scope below the bed surface during scouring. As for non-uniform sand mathematical models, the determination of mixed layer depth and gradation is of extremely important significance [1,2]. Firstly, from the aspect of starting conditions, the starting of non-uniform sand will not only be based on water flow conditions and the physical features of sediment particles, but will receive the effect of bed material's composition. Under different bed material composition, the difference of resistance features nearby the bed surface will lead to the difference of bed surface's velocity and shear force, while the difference of near-wall flow structure will result in the difference of concealing and exposure among coarse and fine particles, thus affecting the starting conditions of non-uniform sands. As a result, mixed layer gradation will greatly influence the starting situations of non-uniform sand, thus determining scoured strength of sediments with different particle sizes. Secondly, mixed layer depth directly determines the quantities of sediments participated in scour and exchange within the computing period, restrict the maximum scouring quantity in unit time

and thus affect the scour velocity of the entire computing period. Thirdly, as mixed layer depth will determine the quantity of sediments participated in scouring and silting and exchange, with fixed scouring quantity or deposition quantity, mixed layer depth will directly affect the adjustment of bed material gradation of the entire mixed layer, further affecting sediment's starting and scouring strength. Finally, mixed layer depth will also determine the size of riverbed's extreme scouring quantity, as when the sediments within the entire mixed layer cannot be started or totally transformed into bed load, riverbed scouring will terminate or transform into the adjustment phase dominated by bed load motion. At the time, mixed layer depth will determine the quantity of sediments unable be started and under certain initial bed material gradation, the depth will also decide watercourse's final scouring quantity.

With respect to mixed layer depth, Chien N. [3] put forward in the coarsening study of Yellow River's downstream riverbed that the movable layer depth of a riverbed is about 2.5-3.5m. Zhao L. J. [4] also starting from the perspective of sand wave motion, divided the mixed layer into two parts, respectively as the direct exchange layer and the bed material adjustment layer. The probability method of the protection layer is on the basis of mixed layer's physical meanings, believes that the lower interface the mixed layer is the just bed surface elevation free of water flow influence and from the perspective of protection layer's generation, indirectly obtains

* To whom all correspondence should be sent:
E-mail: yyh200@163.com

mixed layer depth. The study of Broah [5] is representative as for this method. Li Y. T. [6] under given bed material composition and hydraulic conditions, analyzed the determination of the mixed mobile layer's lower interface under different sediment conditions and scouring time or scouring depth. Wang S. Q. [7] studied the adjustment of mixed mobile layer's bed material gradation during riverbed scouring and silting; research indicated that it was closely related with the mixing velocity, scale and other factors of mixed mobile layer's bed material; but the majority of existing computing methods cannot reflect the effects of mixed mobile layer's internal kinetic factors on the change of bed material gradation, thus greatly affecting the computing of unbalanced sediment of suspended load. In order to reflect the influence of mixed mobile layer's kinetic features on the change of bed material gradation, Liu J. M. [8] introduced the concept of "bed material's exchange velocity" related with the features of sand wave motion and set up corresponding computing models, and the introduction of this concept deepened the understanding about mixed mobile layer's mechanism. The mixed mobile layer equation set up by Armanini [9] considered the vertical mixing resulted from sand wave's cyclical fluctuations.

As an important riverbed form, sand wave will move in accompany with the exchange of bed materials and its motion can be regarded as a physical background for mixed layer computing. Considering from the physical background of sand wave motion, this paper has derived out the computing methods of mixed layer depth and gradation.

Sandwavemotion-based computing of mixed layer depth

Take sand wave motion as an example, during scouring, certain sediments in the mixed layer will be scoured away, while others will remain on the bed surface to maintain sand wave motion, which will continue to absorb the original bed material under static state on the original bed surface - all above constitute to the entire phenomena in the mixed layer.

With respect to sandy riverbed, the upper boundary of the mixed layer is the bed surface contacting with water flow, while the lower boundary is the static riverbed free of water flow turbulence. Actually, only the bed surface will be under the direct turbulence of water flow, which, however, will disturb the bottom of a wave trough by sand wave motion and in a wave cycle, the sediments on bed surface and those on the trough bottom will roll in turn within the range of one wave length. As a result, Karim and Kennedy proposed that mixed layer depth is the half of wave height, that is to say average wave

height equals:

$$E_m = \frac{1}{2}h_s \quad (1)$$

Wherein: h_s is the wave height.

In the process of the flume experiment, Zhong D. Y. added dyed tracer sediments with the same specific gravity and the same gradation as that of bed materials into water flow and observed their mixing in bed material's exchange layer. Fig. 1 is the relationship between the maximum depth that tracer sediment in the riverbed and the sediment height. Judging from the figure, the mixing scale of bed material is related with sand wave height and can be expressed as

$$H_s = 0.7h_s \quad (2)$$

That is to say, the sediment depth H_s is generally lower than h_s . The maximum value can be equal to h_s and mixed layer's average depth E_m is taken as the half of wave height, that is to say Equation (2) is suitable.

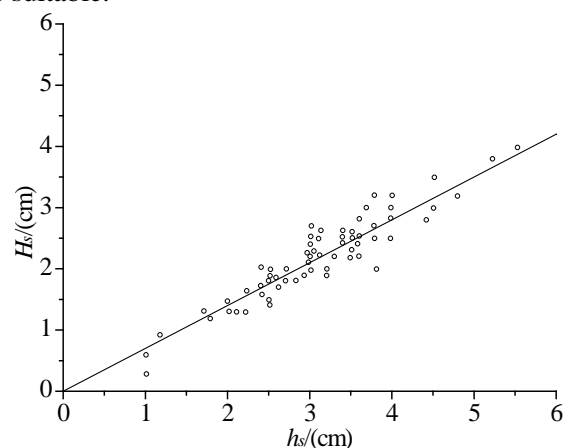


Fig. 1. Relationship Between Sediment depth and Sand Wave Height.

Bed materials of sandy riverbed are basically movable and the coarsening layer is formed due to the repeated turbulence and repeated selective scouring of sediments in the mixed layer and is generally thicker than the mixed layer depth.

Fig. 2 and Fig. 3 are respectively the profiles and plans of sand wave height and coarsening layer depth on the bed surface observed in clean water scouring flume experiments. Judging from these figures:

$$E = \eta h_s > E_m \quad (3)$$

Wherein η is the proportionality coefficient, $\eta=1.07-1.16$ and the average value can be determined as 1.1.

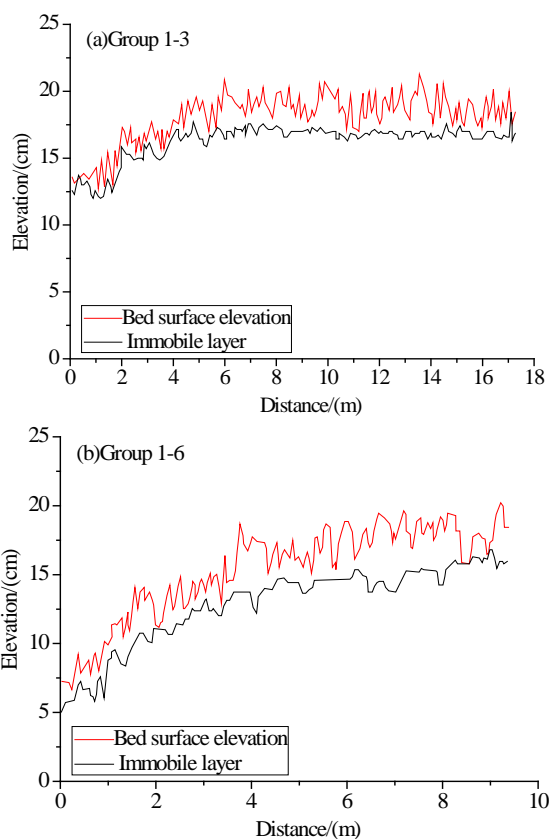


Fig. 2. Change of Coarsening Layer Depth at the Time of Experiment Ending.

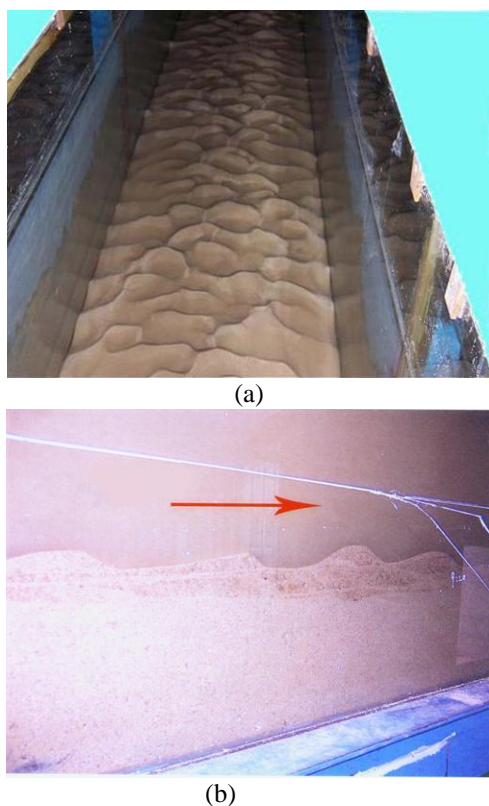


Fig. 3. Plan and Profile Pictures of a Sand Wave. (a) Plan, (b) Profile.

Yin X. L. [10] had put forward the idea that the

coarsening layer depth formed due to fine-sand riverbed scouring was slightly larger than sand wave height as early as 1963 based on the measured materials concerning the downstream of Guanting Reservoir along the Yongding River and relevant flume experiments.

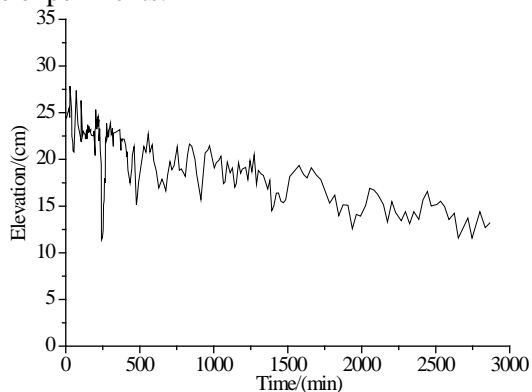


Fig. 4. Changing Process of Riverbed Elevation at the Same Position.

The reason that coarsening layer depth is larger than the sand wave height is that the water flow higher than sand peak will directly rush at sand wave's upstream face in the downstream along extremely unstable separation boundary and thus result in strong undermining on the upstream face; the sediments washed up will partially be rolled back to last sand wave's wave trough and partially led to the downstream by vertical water flow along the slope surface, leaving deep holes locally. With the downwards motion of sand waves on the upstream, these deep holes will be gradually filled up by the coarse particles rolled down from the peak top and the subsequent sand wave will then crawl thereon and generally will not disturb the hole bottom. Fig. 4 shows the change of certain fixed point's riverbed elevation under clean water scouring and the high point therein is the bed surface elevation at the time of wave peak, while the low point is that during wave trough; a 12cm deep hole will occur after 4 hours of scouring and then the sand wave will keep moving upwards and will not disturb the hole bottom; and until 45 hours of scouring when the accumulated undercut depth reaches 11cm, the trough bottom will be close to the hole bottom. This is why coarsening layer depth is larger than wave height, signifying that coarsening layer depth is generally larger than the mixed layer depth.

Sand wave height changes unstably with time, is extremely non-uniform in space and greatly different in plan, and cannot be easily measured, with limited study up to now. Earlier studies included the relationship between sand wave's relative height (h_s/h) and water flow's Froude

number set up by Zhang R. J. [11] based on measured data concerning the Yangtze River. Afterwards, Reju [12] established the relationship between relative wave height (h_s/D) and bed load's sediment transport rate. Allen built up the relationship between sand wave's relative height (h_s/h) and non-dimensional shear stress. And Wang S. Q. [7] put forward the relationship between relative wave height (h_s/D_{50}) and effective scale-free shear force.

Karim and Kennedy suggested to compute the value of h_s by the Allen equation, i.e.

$$h_s/h = b_0 + b_1 \frac{\theta}{3} + b_2 \left(\frac{\theta}{3}\right)^2 + b_3 \left(\frac{\theta}{3}\right)^3 + b_4 \left(\frac{\theta}{3}\right)^4 \quad (4)$$

Based on measured values, $b_0=0.079865$, $b_1=2.23897$, $b_2=-18.1264$, $b_3=70.9001$ and $b_4=-88.3283$ and it is suitable to $0.25 \leq \theta \leq 1.5$.

The Zhang R. J. equation is as follows:

$$\frac{h_s}{h} = 0.086 \frac{U}{\sqrt{gh}} \left(\frac{h}{d}\right)^{\frac{1}{4}} \quad (5)$$

Substituting into the Somov equation, it will obtain:

$$\frac{h_s}{h} = 0.126 \frac{U}{U_c} \left(\frac{d}{h}\right)^{\frac{1}{12}} \quad (6)$$

Recently, Zhan Y. Z. [13] obtained the following wave height equation in combination with certain theoretical analysis based on the analysis results about the Yangtze River by Zhang B. N..

$$\frac{h_s}{h} = A - B \left(\frac{U}{U_c} - C\right)^2 \frac{h_s}{h} = 0.126 \frac{U}{U_c} \left(\frac{d}{h}\right)^{\frac{1}{12}} \quad (7)$$

Wherein U_c is the starting velocity of sediment. $A=0.53$, $B=0.1352$ and $C=3.0$.

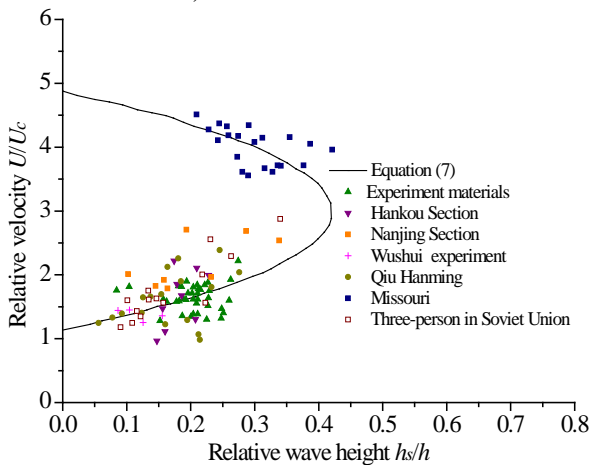


Fig. 5. Relationship Between Relative Wave Height and Relative Velocity.

Based on Equation (6) and (7), sand wave's relative height is mainly the function of water flow's relative strength U/U_c . Equation (7) signifies that: when water flow's relative strength is low, the

relative wave height will increase with the increase of water flow's relative strength; while when water flow's relative strength is large, the relative wave height will decrease with the increase of water flow's relative strength, which accurately reflects the principles related with sand wave growth and decline and water flow strength. More extensive indoor and outdoor materials have been collected under this research, and the relation curve between relative wave height and relative velocity is drawn, as shown in Fig. 5. Results show that it would be more appropriate to describe relative wave height by Equation (7). Wherein $A=0.42$, $B=0.12$ and $C=3.0$ and compared with the coefficients obtained by Zhan Y. Z., A and B are slightly different, while C is the same. The point-based trends in the figure are reasonable. The relatively scattered phenomenon is probably resulted from measurement accuracy or the non-corresponding between sand wave scale and water flow conditions, which will lead to certain lagging behind.

Estimation of sand wave-free bed's blending layer gradation

Yue P. J. [14,15] assumed that the distribution of original bed material gradation along depth is constant and that the porosity remains unchanged before and after scouring and silting, and also divided bed material gradation into three categories based on riverbed's scouring and silting features, i.e.

One-way deposition

$$p_i = \Delta h_i' / \Delta h'' \quad (8)$$

One-way scouring

$$p_i = \frac{p_{0i}(T + \Delta T) - p_i'' \Delta h''}{T + \Delta T - \Delta h''} \quad (9)$$

Coarse-deposition fine-scouring

$$p_i = \frac{p_{0i}(T + \Delta T) + p_i' \Delta h' - p_i'' \Delta h''}{T + \Delta T + \Delta h' - \Delta h''} \quad (10)$$

Wherein T is the initial blending layer depth at the first time period; p_{0i} is original bed material gradation, while p' and p'' are respectively the gradation of the deposit and the scoured material; ΔT is the depth of the turbulent layer to be substituted from former period's riverbed in the next time period and to ensure that no negative value will occur concerning the turbulent layer gradation in the period of scouring, it needs to satisfy:

$$p_{0i} T - p_i'' \Delta h'' \geq 0 \quad (11)$$

Equation (8) - (10) are only appropriate to sand wave-free beds. For sand wave bed, Equation (8) and (9) are both inaccurate and while the other equations can satisfy the sediment balance requirements, the

denominator therein should be E_m .

Estimation of sand wave bed's blending layer gradation

Regarding the concept of blending layer, it is assumed that original bed material gradation p_{0i} is uniformly distributed along depth; the porosity remains unchanged before and after scouring and silting; the blending layer depth is a constant in the computing period; scoured sediment will be substituted equivalently by original bed materials below blending layer's lower boundary; deposited sediment will lead to equivalent ascending and descending of blending layer's upper and lower boundaries; the mixing will be uniform in the process, etc. Under above conditions,

(1) Pure deposition

Pure deposition is as shown in Fig. 6 and the equation of sediment balance in the blending layer is:

$$p_i(n-1)(E_m - \Delta h'(n)) + p_i'(n)\Delta h'(n) = p_i(n)E_m \quad (12)$$

Namely:

$$p_i(n) = p_i(n-1) - [p_i(n-1) - p_i'(n)] \frac{\Delta h'(n)}{E_m} \quad (13)$$

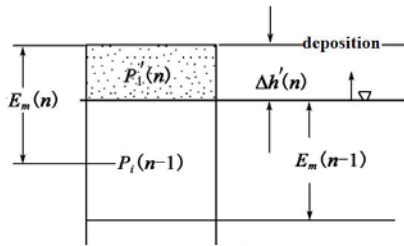


Fig. 6. Schematic Columnar Profile of Pre Deposition.

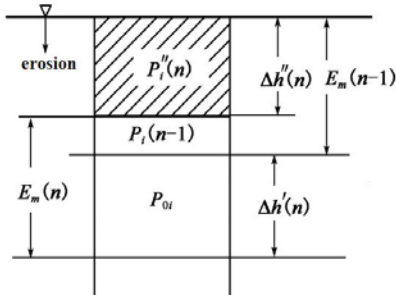


Fig. 7. Schematic Columnar Profile of Pure Scouring.

The time step taken in computing is not proper to be over large and it needs to make sure $\Delta h'(n)/E_m < 1$, otherwise, the bed material gradation will be distorted.

(2) Pure scouring

Pure scouring is as shown in Fig. 7 and the equation of sediment balance in the blending layer is:

$$E_m p_i(n-1) - p_i''(n)\Delta h''(n) + p_{0i}\Delta h''(n) = E_m p_i(n) \quad (14)$$

Based on Equation (14), it could obtain that

$$p_i(n) = p_i(n-1) + [p_{0i} - p_i''(n)] \frac{\Delta h''(n)}{E_m} \quad (15)$$

(3) Coarse-deposition fine-scouring

Coarse-deposition fine-scouring is generally found on the downstream away from the dam, the sediments recovered by upstream riverbed are relatively coarser and those bed materials downstream finer; in the process of sediment exchange, the coarse-deposition fine-scouring model occurs. Under the limitation of sediment carrying ability and the suspension probability, the deposition quantity of coarse sands $\Delta h'$ is always less than the fine sands exchanged out $\Delta h''$, while the riverbed will still undercut ($\Delta h'' - \Delta h'$). As shown in Fig. 8, the equation of sediment balance in the blending layer is:

$$E_m p_i(n-1) - p_i''(n)\Delta h''(n) + p_i'(n)\Delta h'(n) + p_{0i}[\Delta h''(n) - \Delta h'(n)] = E_m p_i(n) \quad (16)$$

Namely

$$p_i(n) = p_i(n-1) + [p_{0i} - p_i''(n)] \frac{\Delta h''(n)}{E_m} - [p_{0i} - p_i'(n)] \frac{\Delta h'(n)}{E_m} \quad (17)$$

In Equation (17), when $\Delta h'=0$, it will obtain Equation (15); while when $\Delta h''=0$, it will obtain the Equation (13) and as it is deposit, the p_{0i} here shall be substituted by $p_{i(n-1)}$.

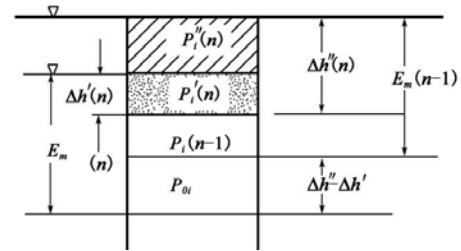


Fig. 8. Schematic Columnar Profile of Coarse-deposition Fine-scouring.

CONCLUSION

As for non-uniform sand mathematical models, the determination of mixed layer depth and gradation is of extremely important significance and will directly decide the reliability and accuracy of corresponding computing results. On the basis of sand wave motion, the computing of mixed layer depth and gradation are studied in this paper.

(1) On the basis of sufficient indoor and outdoor data, in combination with relevant flume experiment data, the relation curve between relative wave height and relative velocity is represented in this paper, with curve parameters being matched; besides, the principles related with sand wave growth & decline and water flow strength are exposed.

(2) Regarding the motion of bed surface's sand wave as a physical background for mixed layer

computing and on the basis mixed layer depth's physical meanings and its relation with sand wave height, the sand wave motion-based computing method of mixed layer depth is derived out.

(3) Starting from the concept of mixed layer, it is assumed that the original bed material gradation will be uniform along depth, the porosity remains unchanged before and after scouring and silting, blending layer depth is a constant in the computing period, scoured sediment will be substituted equivalently by original bed materials below blending layer's lower boundary, deposited sediment will lead to equivalent ascending and descending of blending layer's upper and lower boundaries, the mixing will be uniform in the process, etc., and the estimation methods of the sand wave bed's mixed layer under three models are derived out and obtained, including the pure deposition model, the pure scouring model and the coarse-deposition fine-scouring model.

Acknowledgements: This study is subsidized by National Natural Science Foundation of China (51579123, 51209112), the key Research and Development Program of China(2016YFC0402100), the key Research and Development Program of Tianjin(16YFXTSF00280), Tianjin Natural Science Foundation (15JCYBJC21900, 15JCQNJC07900), and by Central Public Research Institutes Fundamental Research(TKS160103, TKS170228).

REFERENCES

- 1.M.F. Karim, M.H. Forrest, *Journal of Hydraulic Engineering*, **112**(8), 705 (1985).
- 2.D.Y. Zhong, H.W. Zhang (eds.), *Journal of Hydraulic Engineering*, **9**, 24 (2004).
- 3.N. Chien, *Journal of Sediment Research*, **1**, 16 (1959).
- 4.L.J. Zhao, H.W. Zhang (eds.), *Journal of Sediment Research*, **4**, 49 (1994).
- 5.J.P. Broah, C.V. Alonso (eds.), *Journal of the Hydraulics Division*, **108**(12), 1486 (1982).
- 6.H. Hu, Y.T. Li, *Journal of the Hydraulics Division*, **12**, 69 (1982).
- 7.S.Q. Wang, *Journal of Sediment Research*, **4**, 14 (1992).
- 8.J.M. Liu, S.Q. Wang (eds.), *Journal of Hydraulic Engineering*, **2**, 47 (2002).
- 9.A. Armanini, *Journal of Hydraulic Research*, **33**(5), 611 (1996).
- 10.X.L. Yin, *Journal of Hydraulic Engineering*, **1**, 15 (1963).
- 11.R.J. Zhang, Sand Wave Motion and Bed Load's Sediment Transport Rate. –Paper Collections of Zhang R J, China's Water Conservancy and Power Press, Beijing, 1996, 37.
- 12.K.G. Reju, J.P. Soni, *Journal of Hydraulic Research*, **14**, 241 (1976).
- 13.Y.Z. Zhan, M.H. Yu (eds.), *Engineering Journal of Wuhan University*, **39**(6), 10 (2006).
- 14.P.J. Yue, *Journal of Waterway and Harbor*, **2**, 30 (1997).
- 15.Y.H. Wang, X.B. Cheng (eds.), *Journal of Waterway and Harbor*, **3**, 14 (2013).

Development of traditional and herbal Chinese medicine (chemical and biochemical perspectives) with emphasis on legal systems

J. Zhang¹, A. Chen¹, M. Babae², L. Wang³, Y. Qiao^{1,*}

¹ School of Chinese Materia Medica, Beijing University of Chinese Medicine, Bei San Huan East Road, Beijing, China

² Department of Law, Jouybar branch, Islamic Azad University, Jouybar, Iran.

³ Dongfang Hospital, Beijing University of Chinese Medicine, Fengtai District, Beijing, 100078, China

Received September 20, 2016; Revised January 14, 2017

Many chemical and biochemical mechanisms from herbal plants have been well known in China for example anti-oxidant or anti- cancer effects but lacking in legal construction of herbal or Traditional Chinese Medicine (TCM) is obvious in compared with its significance in Chinese public health care. Legislation and implementation of Traditional Chinese Medicine Law can accelerate greatly the construction of TCM legal system. At present, the legislative body is proactively bringing forward the legislation of TCM Law. TCM legal construction will be progressed to a great extent to form TCM legal system. Systematic construction is the basic development trend in China's TCM legislation. Current laws and regulations along with TCM Law (Draft) under review by legislative body, have exhibited several principles and basic content units for future construction of TCM legal system. With rapid growth of medical and pharmaceutical of herbal plants, It is need to legislate proper rules for achieve to effective applications and also more bio-ethics.

Keywords: Medicinal plants, Traditional Chinese Medicine (TCM), Chemical and Biochemical perspectives, Law, Development Trend

INTRODUCTION

TCM is representative of the great traditional Chinese culture, which impacted significantly over thousands of years on the procreation and development of Chinese people. As a part of public health care, TCM is also on the track of legalization little by little^[1-8]. A comprehensive legal system is required for the development of TCM cause, and it is a compulsory historical mission for Chinese legislators and academia. In recent years, TCM legal system is developing at a increasingly rapid pace.

As a basic law for TCM industry, TCM Law can lead the construction of TCM legal system after enforced. It is indispensable to study further the fundamental issues on construction of TCM legal system. In this text, Traditional Chinese Medicine Law of the People's Republic of China (Draft) is to be interpreted, and current TCM-related laws and regulations are to be organized and analyzed, whereby to form an analysis on the development trend of TCM legal system construction, and therefore to give more advice on the improvement of legal system.

Review on Current TCM legislation

In a society of rule of law, any social business is not regulated by a single law, but a relatively comprehensive system comprising multiple laws, regulations and normative documents. China has not

yet formulated TCM legal system, but some legal norms for TCM industry development. It is by the relatively loose combination between these legal norms that TCM industry is regulated lawfully.

Organization of Relevant Current Laws

As per retrieval and collection of public network and government sector websites, it can be concluded that TCM-related laws and regulations have reached a considerable scale, and formed a basis for the construction of legal system intended to regulate the entire TCM industry.

MATERIALS AND METHODS

The materials studied in this paper are derived from the laws enacted by State Legislative Branch as well as the normative documents published in the official website of National Health and Family Planning Commission of PRC (<http://www.nhfpc.gov.cn/>), China Food and Drug Administration (<http://www.sda.gov.cn/> / WS01 / CL0001 /), State Administration of Traditional Chinese Medicine (<http://www.satcm.gov.cn/>) and other government departments. Find out the development tendency of traditional Chinese medicine legislation by analyzing laws of regulations and normative documents.

By the end of 2015, the construction of TCM legal system is in the following basic condition:

Laws Promulgated and Enforced by National Legislative Body:

* To whom all correspondence should be sent:

E-mail: yjqiao@263.net

12 laws are directly associated with TCM industry (two of them) :

| No. | Name of Law | Date of Promulgation |
|-----|--|----------------------|
| 1 | Law of the People's Republic of China on Medical Practitioners | Jun 26, 1998 |
| 2 | Drug Administration Law of the People's Republic of China | Sept 20, 1984 |

19 laws are partially associated with TCM industry (two of them):

| No. | Name of Law | Date of Promulgation |
|-----|---|----------------------|
| 1 | Constitution of the People's Republic of China | Dec 4, 1982 |
| 2 | Standardization Law of the People's Republic of China | Dec 29, 1988 |

Administrative Regulations Promulgated by the State Council:

2 regulations are special ones on TCM:

| No. | Name of Administrative Regulation | Date of Promulgation |
|-----|---|----------------------|
| 1 | Regulations of the People's Republic of China on Traditional Chinese Medicine | Apr 7, 2003 |
| 2 | Regulations on Species and Varieties of Traditional Chinese Medicine Drugs | Oct 14, 1992 |

26 administrative regulations are closely relative to TCM industry(three of them):

| No. | Name of Administrative Regulation | Date of Promulgation |
|-----|---|----------------------|
| 1 | Measures of the People's Republic of China for Health Supervision at Frontier Ports | Dec 30, 1981 |
| 2 | Regulations on the Administration of Sanitation at Public Places | Apr 1, 1987 |
| 3 | Regulations of the People's Republic of China on Prevention and Treatment of Pneumoconiosis | Dec 3, 1987 |

26 Local Regulations Formulated by Local Governments

In addition to the above laws and regulations, up

to 200 departmental rules regarding TCM industry have been promulgated successively by competent authorities such as National Health and Family Planning Commission, State Administration of Traditional Chinese Medicine, and China Food and Drug Administration, etc.

RESULTS AND DISCUSSION

Characteristics of Current TCM Legal System

Firstly, in respect of the contents, current TCM laws and regulations have involved treatment, healthcare, research, education, industry, culture, etc.^[5-8], showing an embryo TCM legal system to regulate the industry.

Secondly, in respect of legal level, there were three distinct levels, i.e., law, administrative regulation, local regulation, which are also the three levels of Chinese law.

Thirdly, in respect of the progression of legal construction, from 21st century, the construction of TCM legal system is apparently speeding.

Deficiency of Current TCM Legal System

Incomplete System

A complete legal system is to be based on constitution and to consist of laws, administrative regulations, local regulations, rules and other normative documents, wherein laws is positioned as the core. From the statistics aforementioned, it can be inferred that relevant issues on TCM industry have been provided in other laws, but not in a "Traditional Chinese Medicine Law" or "Traditional Medicine Law". Since there has always been a lack of a law specifically regulating traditional medicine industry, there is no "basic law" on TCM industry.

Negligence of TCM Industry Features

TCM has its own principle of development, which shall be observed, and only by the actual situation of TCM should laws be made to propel TCM into rapid healthy development^{[2][4]}. Large numbers of current laws and regulations, on the contrary, are based on criteria and standards of modern medicine, which provide TCM related issues sparsely in other special laws or regulations. Consequently, current legislation is inadequate to the fulfillment of promotion and protection of TCM industry, even on some level inhibit its development^[6].

Indistinct Definition of Regulatory Scope

On the grounds that administrative regulation and departmental rules are more intended to standardize and regulate concrete issues, not to analyze or bound fundamental concepts or scopes in the industry, some basic issues have not yet been clarified in terms of

TCM. By way of illustration, no laws have provided the scope of "TCM" in the concrete.

Systematic Construction as the Development Trend of TCM Legislation

In the context of extensive construction of a society of rule of law, no industry can be completely covered or regulated merely by a single law or several regulations, which entails a whole legal system, as is the case with TCM industry.

Factual Basis of TCM Legal System

Social demand is the primary basis and also an indispensable incentive for legal construction. Since the founding of PRC, there has been a progress in service, healthcare, education, research, culture and industry, etc. of TCM. An unprecedented opportunity offered for TCM development especially during the implementation of 12th and 13th five-year plan, where TCM received full recognition from society. The full development of TCM industry has brought forth unprecedented demand which laid the social foundation for TCM legal system construction.

Leading Role of "Basic Law" Enforced In the Industry

Law is the core of a legal system for an industry. China is striving for TCM Law, which is intended to be promulgated and enforced recently. TCM Law will immediately fill the gap in "basic law" in TCM legal system. Such a TCM Law is to be a radical implication for the foundation of whole legal system, whereby other regulations are amended and modified to make a compatible "Set of Laws and Regulations" premised thereon, so that an embryo of TCM legal system is brought in.

Promotion of Legal System Construction by Academic Research

Academic research is the prerequisite and basis for legislation, which deserves more attention than it had always received. Over the last decade, the formulation of TCM Law by legislature brought TCM legal construction to more attention from academia. TCM and legal academia are increasingly progressing the joint study on TCM legal construction, a discernible boom is arising in legislative and statute study.

Three Principles of TCM Legislation

Based on "TCM Law (Draft)" and implementation of administrative and local regulations concerning TCM over recent years, three fundamental principles could be drawn. In the meantime, these are the major ideology of Chinese TCM legislation in a future period. And we can have these principles ready to

hand when deciding the trend of TCM legislation.

Functional Position of Legal System as Support and Promotion

For any industry, the legal system regulates, restricts, ensures and boosts it. The emphases of legislative values will differ according to industries and the specific stages in their development. From the status quo, it can be inferred that the emphases of legislative values of TCM will remain ensuring and promoting development of TCM industry. TCM Law (Draft) under review by national legislature reflects this principle.

More Clear Definition of TCM

From the academic perspective of medicine, traditional medicine in China comprises traditional Chinese medicine and minority medicine. There are meanwhile several minority medicines besides TCM, such as Tibetan medicine, Mongolian medicine, Uighur medicine, Dai medicine, Zhuang medicine, etc., which are collectively referred to as ethnic medicine or minority medicine. Notwithstanding TCM is not yet clearly defined from a legal perspective. In general, laws in effect presently do not adopt "TCM" as a term, but instead "traditional medicine", "traditional physic", etc. (Note: e.g. the Constitution of the People's Republic of China provides in Article 21, "China supports medicine and hygiene, along with modern medicine and traditional medicine..."; Drug Administration Law of the People's Republic of China provides in Article 3, "China supports modern drugs and traditional drugs...".) On the contrary, the industrial administrative regulations, i.e. Regulations of the People's Republic of China on Traditional Chinese Medicine adopted distinctly "TCM" as a term, which is defined almost the same way as "TCM" in medical academia; Therein are adopted "TCM.

Legal Promotion of TCM Modernization

As always, TCM is perceived as traditional medicine, which is more inherited than reformed by the masses who is even suspicious of the hybrid of modern technology and TCM. It has to be understood that TCM is not only traditional but also modern. Legal system construction shall ensure healthier development of TCM in modern society^[7].

Basic Modules of TCM Legislation

TCM cause involves medicine, healthcare, education, scientific research, culture, industry, etc. In respect of the contents, the law shall contain some aspects as basic modules, which are to be intertwined to form the skeleton contents of TCM legal system. In regard to TCM Law (Draft) under review by

legislature, these modules are gradually discernible, namely TCM medical service, TCM drug, TCM education, TCM scientific research, TCM inheritance and culture diffusion.

TCM Medical Service

Medical service represents TCM cause to the most significant extent, and is the core of TCM legal contents. As far as legal construction is concerned, provisions in relation to TCM medical service shall comprise three major aspects:

Firstly, clarify the position of TCM medical service. TCM medical service are carried out and constantly progressing on the fundamental basis of definite legal position. Secondly, construct TCM medical institution. China will encourage and support social powers to found TCM medical institution, which is largely benefit to the development of TCM medical institution. Thirdly, quicken the qualification of TCM service provider. In addition to qualification by medical licensing examination, people with TCM inheritance from mentor and actual skill are entitled more specifically in law to take examinations on practical skill and efficacy, by which to qualify as medical practitioner.

TCM Drug Protection and Development

As the most important means of treatment, TCM drug is inseparable from TCM. The law is in particular more protective of the quality of TCM drugs and the planting of TCM drugs. Moreover, evaluation system of genuine regional drug is to be established, where the market repute and value is maintained by encouraging use of geographical marks etc. for genuine regional drug of good quality. The distribution system of TCM drugs will be set up subject to more specific requirements^[4].

In reference to the two traditional administration method, i.e., TCM decoction pieces and in-house TCM formulation by medical institution, China will set forth more systematic way of management. The law is to allow distinctly for reprocessing of TCM decoction pieces by medical institution. It is unambiguously specified that TCM medical institution can commission drug manufacturer to produce in-house TCM formulations. Such provisions will empower TCM medical institution to use more flexibly and widely TCM decoction pieces and in-house TCM formulations.

Considering the contents of TCM Law (Draft), it has been more clarified that research and development and manufacture of TCM investigational new drug is encouraged and supported on a national basis. Apart from the protection of traditional technique and craft for TCM drug

processing, as well as the promotion of manufacture of TCM patient drug in traditional dosage form, it is encouraged that TCM patient drug be researched and developed by modern science and technology.

TCM Education

Perfect TCM education system lays the prerequisite and foundation for nurturing TCM experts. TCM education is an integral part of national educational cause, which is on a fundamental basis regulated by education-related laws and regulations. Thus TCM-related provision in TCM legislation is not intended to provide a systematic and comprehensive solution for problems in educational fields. TCM legal construction is mainly focused on two issues about TCM education: Firstly, broaden the paths for talent training. Secondly, emphasize the TCM involvement in TCM education.

TCM Scientific Research

TCM scientific research concerns two aspects: one is the inheritance of classical TCM; the other is the innovation of TCM in the context of modern science and technology. Meanwhile, China has inspired researchers in law to use modern science and technology to study TCM, and to progress innovation of TCM knowledge and technology.

TCM Culture Inheritance and Diffusion

TCM is typical of Chinese great traditional culture with clinical values and immense cultural values in addition. It will be a long time of construction and refinement before TCM legal system achieves maturity. TCM legal system construction will be propelled substantially by the formulation and implementation of TCM Law. It is anticipated that in about 5 years after the implementation of TCM Law, there is bound to be an extensive construction and amendment of TCM-related laws and regulations, gradually forming a relatively complete legal system. This legal system will be indispensable as regards its promotion and consolidation of the full development of TCM industry.

CONCLUSION

By analyzing the current situation of Chinese medicine legislation, we can draw the following two basic conclusions: First, it will play a leading role in the Fundamental Law by the promulgation and implementation of Chinese Medicine Law. China will gradually build a "regulations group" to guarantee traditional Chinese medicinal development based on the Chinese Medicine Law, and then forming a juristic guarantee system of traditional Chinese medicine development. Second, traditional Chinese

medicine will develop more rapidly and more standardized in the protection of legal system, then gradually become a new economic growth point and a competitive national soft power carrier.

Acknowledgement: *This research was supported by the Build of Legal System Framework of Chinese Medicine hold by State Administration of Traditional Chinese Medicine.*

REFERENCES

1. B.B. Cao, *Chinese Journal of Integrative Medicine* , **21**(3), 66 (2015).
2. M.L. Coghlan, J. Haile, J. Houston, *Plos Genetics*, **8**(4), 436 (2012).
3. Y. Liu, Z. Yang, C. Jing, *Frontiers of Medicine*, 1 (2016):
4. L. Lu, Y. Fang, X. Wang, *Cellular & Molecular Neurobiology* , **28**(4), 479 (2008).
5. A. Ma, Study on Local Legislation of Traditional Chinese Medicine Development Policy in Gansu Province, *Medicine & Society*, 2014.
6. F. Snyder, L. Yi, G. Yazdani, *Social Science Electronic Publishing*, **2**(1), 129 (2014).
7. K. Tian, *Journal of Nanjing University of Traditional Chinese Medicine*, 10(3),166 (2009).
8. V.T. Wong, F. Pang, *Healthcare Management Forum*, **19**(1), 21 (2006).

The factor analysis of climatic change on water resource: a case study in Haihe river basin of Hebei province

A.J. Shao, L.Y. Zhao, S.W. Wang

Hebei GEO University, Shijiazhuang, China

Received May 25, 2017; Revised July 20, 2017

Hebei is a province of north China. According to the data of climate and runoff from 68 weather stations and 105 hydrologic stations in Hebei province between 1956 and 2000, the change of climatic essential factors and runoff are analyzed. Since the 1960s, the average annual temperature in Hebei province has been increasing gradually. Compared with the 1960s, the average temperature in the 1990s has risen 0.9°C. From the age, the average annual evaporation in Hebei province has appeared a tendency of decline. And it descends 62 mm every ten years on average. The average year's precipitation has gradually diminished year by year. The precipitation in the 1990s has decreased 60 mm compared with the 1950s. The average year's runoff of the whole province, which declines 19.4×10^8 m³ every ten years on average, emerging a gradually decreasing trend from the 1950s to the 1990s, is 120.2×10^8 m³. With the decrease of the precipitation and the rise of the temperature, the runoff declines. The models of climatic essential factors and the runoff established by utilizing the multiple regression analysis are logarithmic non-linear functions. Obviously, the impact of precipitation variety on the runoff is more than the effect of the temperature or the evaporation change on the runoff by the sensitivity analysis. According to the prediction of the future climatic change with regard to the runoff, the whole province runoff will alter from 114.36 to 138.24×10^8 m³ in 2030. Similarly, the runoff will vary from 106.8 to 137.8×10^8 m³ in 2050.

Keywords: climatic change, runoff, water resources, sensitivity, analysis, prediction

INTRODUCTION

Hebei, a province of north China, is a severely resource-based water-deficient area. The amount of water resources per capita or acre of the whole province is respectively 1/7 and 1/9 of the national average, far below internationally recognized severe water shortage cordon. The mean annual runoff of the whole province is 120.8×10^8 m³, which is 58.5% of the total amount of water resources. The surface runoff takes an important position in the constitution of water resources.

The change of water resources is closely connected with climatic conditions, and climate change has a direct influence on runoff. Internationally the research into climate change impacts on runoff is carried out based on hydrologic model of basin and water resources assessment model [1]. The commonly used hydrological models such as SLURP model, HBV model, macroPDM model and so on, have already gradually developed and applied to the research of the prediction of climate change impacts on water resources [2]. For the moment, domestic and overseas scholars are doing research based on distributed hydrologic model coupled between GIS/RS and climatic model. And they have made certain progress. The

distributed hydrologic model has already not only become important means of currently multi-target hydrologic investigation oriented, but also is the trend or direction of the development of modern hydrologic model[3-6]. However, there are not so many models on influence of climatic factor for the runoff in a large scale, furthermore, the complexity and uncertainty of climate factors make all the GCM climatic models should be enhanced further.

This article mainly studies the effects of changes of meteorological factors on surface runoff. According to the data of climate and assessment of surface water resources from 68 weather stations and 105 hydrological stations in Hebei province from 1956 to 2000, the change of climatic factors and runoff are analyzed. Because of the nonlinear relations between runoff and climatic elements, we establish a logarithmic non-linear statistical model by multiple regression analysis, referring to documents written by domestic and overseas scholars [7-11]. We take meteorological elements such as precipitation, evaporation and temperature into consideration. Then, we carry on sensitivity analysis of the effects of changes of climatic elements on runoff using different climatic situations, and we predict surface runoff according to future climate change.

* To whom all correspondence should be sent:
E-mail: shaoajun@sohu.com

CHARACTERISTICS OF CLIMATE CHANGE

Temperature

Temperature is one of the significant meteorological elements. A great deal of domestic and international researches indicates that, in the last hundred years, the earth weather system is undergoing a marked change, the center of which is global warming. The temperature in China has gone up by 0.4 to 0.5°C, so the recent twenty years is the warmest periods of the 20th century. The lowest of mean annual temperature in Hebei province is 9.8°C in 1960s, rising gradually later. The highest temperature is 10.7°C in 1990s, which is 0.9°C higher than that in 1960s. And the temperature rises 0.3°C during every decade [12, 13] (Table 1). According to the age, the mean annual temperature in Hebei province, going up 0.3 to 0.4°C during every decade, is on the rise in general. The temperature rises by a large margin, above 1°C in most areas of the Eastern Hebei Plains, Yanshan hilly areas, parts of the Northern Hebei Plateaus and local regions of Taihang Mountains Plains.

Table 1 The average temperature in every ten years in the 20th century in Hebei province (°C).

| | 1950 s | 1960 s | 1970 s | 1980 s | 1990 s |
|----------------|-----------|-----------|-----------|-----------|-----------|
| Mountain area | 7.8 | 8.6 | 8.7 | 8.8 | 9.3 |
| Plain area | 11.9 | 12.2 | 12.2 | 12.3 | 12.9 |
| Whole province | 9.9 | 9.8 | 9.9 | 10.1 | 10.7 |

Evaporation

Evaporation is not only one of the important segments of water circulation, but also the major meteorological element. On the basis of observed data by 20 cm caliber evaporation pan, the maximum of mean annual evaporation in Hebei province is 1881 mm in 1960s, then falling gradually later. According to the age, the mean annual evaporation in Hebei province, diminishing 62 mm during every decade, shown a declined trend totally. The evaporation falls by a large margin, over 220 mm among western of the Eastern Hebei Plains, middle of Taihang Mountains and eastern of Taihang Mountains Plains. People may think that climate warming may increase evaporation from terrestrial water surface, but the result is opposite. According to the research, there is an obviously positive interrelationship between the main cause for evaporation decline and the decrease in average wind velocity [14] (Table 2).

Table 2 The average evaporation in every ten years in the 20th century in Hebei province (mm)

| | 1950s | 1960s | 1970s | 1980s | 1990s |
|----------------|-------|-------|-------|-------|-------|
| Mountain area | 1739 | 1798 | 1771 | 1674 | 1648 |
| Plain area | 1996 | 2048 | 1932 | 1764 | 1707 |
| Whole province | 1860 | 1881 | 1816 | 1705 | 1695 |

Precipitation

Atmospheric precipitation, the important segments of water circulation and one of the most significant meteorological element, is the main source of forming surface runoff. In a word, the general tendency is that the precipitation in Hebei province has become gradually less by age. Besides, the range of reduction of the mountainous regions is more than that of the plain areas [15] (Table 3).

Table 3 The average precipitation in every ten years in the 20th century in Hebei province (mm)

| | 1950 s | 1960 s | 1970 s | 1980 s | 1990 s |
|----------------|-----------|-----------|-----------|-----------|-----------|
| Mountain area | 590 | 545 | 541 | 510 | 522 |
| Plain area | 560 | 582 | 551 | 526 | 507 |
| Whole province | 576 | 561 | 545 | 517 | 516 |

IMPACT OF CLIMATE CHANGE ON SURFACE RUNOFF

Surface runoff is expressed by river runoff. According to a series of hydro-meteorological data from 1956 to 2000, the maximum of the surface runoff of the whole province is 294×108 m³(in 1959), besides the minimum is 45.3×108 m³ (in 1999) and the extremum ratio is 6.5. The variation for overyear is rather big.

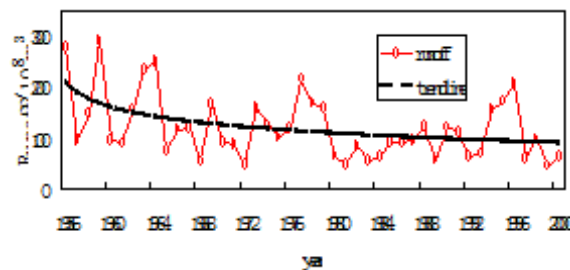


Fig 1. The runoff and the trend line

The runoff fluctuates a lot during 1950s, 1960s and 1970s, especially in 1956, 1959 and 1963. On the contrary, it fluctuates a little in 1980s. The range of change in runoff increases in 1990s particularly in 1996, which is related to the great floods in 1996.

The general tendency is that the runoff has become less by age (Figure 1).

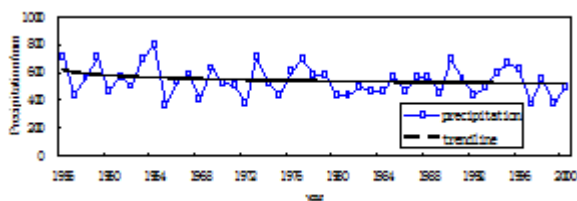


Fig 2. The precipitation and the trendline

The maximum of the annual precipitation of the whole province is 795.2 mm (in 1964), and the minimum is 366.3 mm (in 1965). The whole tendency is that the precipitation is dropping year by year (Figure 2). The tendency of runoff is in accordance with that of precipitation, and the change of runoff is obviously under the control of precipitation. That is to say, the runoff increases with the rise of precipitation, and it decreases with the reducing of precipitation. The peak or crest value of precipitation curve is in accordance with that of runoff curve completely. The maximum of the annual evaporation of the whole province is 2104.4 mm (in 1972), and the minimum is 1465.2 mm(in 1956).

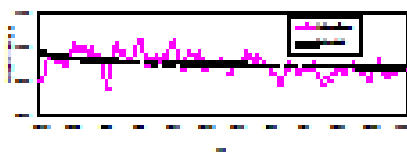


Fig 3. The evaporation and the trendline

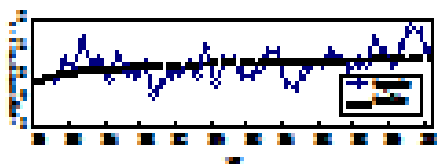


Fig 4. The temperature and the trendline.

The general tendency is that the evaporation has become less year by year, which is in accordance with the tendency of runoff (Figure 3). The maximum of the temperature of the whole province is 11.6°C (in 1998), and the minimum is 7.9°C (in 1956). The whole tendency is that the temperature has been rising year by year, which is opposite to the tendency of runoff. That is to say, the runoff decreases with the rise of temperature (Figure 4).

The tendency of surface runoff of the whole province nearly keeps in step with that of precipitation, and it decreases with the reducing of precipitation. The tendency of surface runoff is

Table 4. The response of the runoff to the climatic changes

opposite to that of temperature, and it decreases with the rise of temperature. In accordance with the hydro-meteorological observed data of the whole province from 1956 to 2000, we establish a statistical model, which indicates the relationship among the surface runoff y ($108\text{m}^3/\text{a}$), precipitation x_1 (mm/a), temperature x_2 ($^{\circ}\text{C}/\text{a}$) and evaporation x_3 (mm/a), by statistical software—Eviews. The statistical model is as follows:

$$\text{Model one: } \ln y = -10.2 + 2.14 \ln x_1 - 0.74 \ln x_2 \quad (1)$$

$$\text{Model two: } \ln y = -26.5 + 2.45 \ln x_1 + 1.05 \ln x_3 \quad (2)$$

Through statistical examination, we can see that in the Model One, the calculated value $F=69.4$, the value referred to table $F_{\alpha}=3.21(\alpha=0.05)$, it is markedly interrelated because of $F>F_{\alpha}$. In the Model Two, the calculated value $F=76.1$, the value referred to table $F_{\alpha}=3.21(\alpha=0.05)$, it is also markedly interrelated owing to $F>F_{\alpha}$. Consequently, we can carry out the related forecast using the model established.

From the model mentioned above, we can see that precipitation is in positive correlation with runoff, and it is in negative correlation with temperature, namely, runoff increases with the rise of precipitation and it decreases with the rise of temperature. In addition, according to the observed data, a positive correlation is found between evaporation and runoff, and both of them show a downward tendency with the passage of time.

From the model mentioned above, according to the change of meteorological factor, we can analyze the change in runoff. The method is known as sensitivity analysis of change in climatic elements on runoff. Precipitation ranges from -20% to $+20\%$, which is the same as evaporation, and the temperature ranges from 0 to $+3^{\circ}\text{C}$. We can obtain the response of runoff to different kinds of changes in climatic elements by calculation (Table 4).

From Table 4 we can see that the temperature rises and the runoff decreases at constant precipitation. Both the precipitation and the runoff rise at constant temperature. The less the precipitation is, the higher the temperature is and the less the runoff is. The response to runoff is more distinct during high or low flow year. Obviously, the impact of precipitation on runoff is more than the effect of change in temperature or evaporation on runoff. At present, the decreasing precipitation is one of the major causes for the reducing of runoff.

| | | | | | | |
|--------------------------|------|--------|--------|--------|-------|-------|
| Changes in precipitation | | -20% | -10% | 0 | +10% | +20% |
| | 0°C | -38% | -20.1% | 0 | 22.6% | 47.7% |
| Changes in temperature | +1°C | -42.6% | -24.7% | -4.6% | 18% | 43.1% |
| | +2°C | -46.7% | -28.8% | -8.7% | 13.9% | 39% |
| | +3°C | -50.4% | -32.5% | -12.4% | 10.2% | 35.3% |
| Changes in evaporation | -20% | -65.5% | -44.9% | -20.9% | 5.4% | 35.4% |
| | -10% | -55.5% | -34.5% | -10.5% | 15.8% | 45.8% |
| | 0 | -45% | -24% | 0 | 26.3% | 56.3% |
| | +10% | -34.5% | -13.5% | 10.5% | 36.8% | 66.8% |
| | +20% | -24% | -3% | 21% | 47.3% | 77.3% |

IMPACT OF FUTURE CLIMATE CHANGE on SURFACE RUNOFF

Prediction of Future Climate Change in Hebei Province

The United Nations Intergovernmental Panel on Climate Change (IPCC), which is jointly established by World Meteorological Organization (WMO) and the UN Environment Programme (UNEP) in 1988, is an intergovernmental organization.

The third assessment by IPCC shows that the global average surface temperature has been rising continually since 1861. The added value of the 20th century is 0.6±0.2°C. In accordance with the prediction using the global weather patterns of IPCC opened in 2002 by Chinese academics, they make tendency forecast for climate change of the 20th century in Mainland China. Besides, they present the change of average annual temperature and annual precipitation in 2030 and 2050 in Hebei province according to analog results of regional weather patterns provided by National Climate Center. These will serve as a basis. They predict the surface runoff in 2030 and 2050 in Hebei province on the basis of the statistical assessment model of impacts of climate change on surface runoff in Hebei province in recent 50 years.

The prediction of future climate change shows that, in 2030, the average annual temperature of Hebei province will rise over 1°C, as compared with 1.3 to 1.4°C in the northern part of Zhangjiakou, Chengde, Qinhuangdao and the northeastern part of Tangshan, 1.2 to 1.3°C in the southern part of Zhangjiakou, Langfang and the southwestern part of Tangshan, and 1.1 to 1.2°C in the south-central part of the region. In addition, the annual precipitation will be widespread increase. The annual precipitation will go up 3% to 5% in the northern part of Zhangjiakou, Chengde, and part of the city of Langfang, as compared with 9% to 13% on the east coast of Tangshan, in part of Qinhuangdao, Cangzhou, the southern part of Shijiazhuang, Xingtai and Handan, and 5% to 9% in other regions. In 2050, the average annual temperature of Hebei province will still be rising continuously.

Prediction of Surface Runoff in Hebei Province in 2030 and 2050

According to the statistical assessment model of impacts of climate change on surface runoff in Hebei in recent 50 years, the multivariate statistical method mentioned above reflects the response of runoff to climate change, namely, the sensitivity of climate change towards the effect of runoff. Runoff is the most sensitivity to climate change in variables of water resources. Combining with the prediction of future climate change provided by National Climate Center, this section makes a prediction for change in water resources under the circumstance of future climate change in Hebei province in the aspect of runoff on the basis of these models, which is used as a reference in plan for utilization of water resources in Hebei province in the future.

Table 5 and 6 are the response of surface runoff in Hebei province on climate condition predicted in 2030 and 2050 respectively. The temperature in Hebei province in 2030 is on the high side, ranging from 1.1 to 1.4°C, and the annual precipitation will rise ranging from 4% to 12%.

The established mathematical models indicate the relationship of climatic condition by runoff, temperature and precipitation in the past 50 years. It also reflects the response of surface runoff in Hebei to changes in climatic element without analyzing the effects of artificial factors, such as reservoir filling cutoff of mountainous areas, the groundwater over-extracted in plain regions, the lowering of the groundwater table and so on. Therefore, the prediction based on these mathematical models has a great deal of uncertainty. The conclusion we may have would be preliminary, and it can only reflect the impacts of changes in temperature and precipitation on surface runoff in the present circumstances.

Table 5. The prediction of the runoff in Hebei province in 2030 (108m³).

| | | | | | |
|--------------------------|--------|-------|--------|--------|--------|
| Changes in precipitation | +4% | +6% | +8% | +10% | +12% |
| Changes in +1.1°C | 117.24 | 122.4 | 127.56 | 132.84 | 138.24 |

| | | | | | | |
|-------------|--------|--------|--------|--------|--------|--------|
| temperature | +1.2°C | 116.28 | 121.44 | 126.6 | 131.88 | 137.28 |
| | +1.3°C | 115.2 | 120.36 | 125.52 | 130.8 | 136.2 |
| | +1.4°C | 114.36 | 119.52 | 124.56 | 129.96 | 135.36 |

Table 6. The prediction of the runoff in Hebei province in 2050 (108m³).

| Changes in precipitation | +4% | +6% | +8% | +10% | +12% | +14% |
|--------------------------|--------|-------|-------|-------|-------|-------|
| +1.7°C | 111.3 | 116.5 | 121.6 | 126.9 | 132.3 | 137.8 |
| +1.8°C | 110. | 115.5 | 120.7 | 126 | 131.4 | 136.9 |
| +1.9°C | 109.4 | 114.6 | 119.7 | 125.0 | 130.4 | 135.9 |
| Changes in temperature | +2.0°C | 108.6 | 113.4 | 118.9 | 124.2 | 129.6 |
| | +2.1°C | 107.6 | 112.8 | 117.9 | 123.2 | 128.6 |
| | +2.2°C | 106.8 | 111.9 | 117.1 | 122.4 | 127.8 |

CONCLUSION

(1) According to the analysis of the data of climate and assessment of surface water resources from 68 weather stations and 105 hydrological stations in Hebei province in recent 50 years — from 1956 to 2000, the lowest of the average annual temperature in Hebei is in 1960s, rising gradually later. And the highest is in 1990s, 0.9°C increase over that of 1960s. The average annual temperature rises 0.3 to 0.4°C during every decade. According to the age, the mean annual evaporation in Hebei province, diminishing 62mm during every decade, shown a declined trend on the whole. The general tendency is that the precipitation of the whole province has become gradually less by age. The average annual precipitation of the whole province in 1990s decreases 60mm comparing to that in 1950s. There is 15mm decline during every decade. Besides, the range of reduction of the mountainous regions is more than that of the plain areas.

(2) The average annual surface runoff of the whole province is 120.2×10⁸ m³, and the mountainous areas is 102×10⁸ m³, as compared with 18.2×10⁸ m³ of the plain regions. The mean annual runoff has shown a trend of decrease since from 1950s to 1990s. The mean annual runoff declines 19.4×10⁸ m³ during every decade. One of the major causes for the decrease is the general reduction of precipitation. The large amount of precipitation in 1996 is the chief reason for runoff rising a bit in 1990s. Runoff decreases with the reduction of precipitation and it increases with the decline of temperature. Their relationship is nonlinear logarithm. The sensitivity analysis shows that the

impact of precipitation on runoff is more than the effect of change in temperature or evaporation on runoff.

(3) On the basis of the prediction of future climate change of surface runoff in Hebei, the surface runoff of the whole province in 2030 ranges from 114.36 to 138.24×10⁸ m³, as compared with ranging from 106.8 to 137.8×10⁸ m³ in 2050. The factors that influence change in runoff are complicated, including both climatic and artificial elements. Hence, the conclusion we may have would be preliminary, and it can only reflect the impacts of changes in climatic factors on runoff in the present circumstances.

REFERENCES

1. Working Group of IPCC, Technical Guidelines for Assessing Climate Change Impacts and Adapting [R], 1994.
2. C. Lingfei, W. Hongya, *Resources Science*, **26**(6), 62 (2004).
3. R.A. Freeze, R.L. Harlan, *Journal of Hydrology*, **9**, 237 (1969).
4. K.J. Beven, M.J. Kirkby, *Hydrological Sciences Bulletin*, **24**(1), 43 (1979).
5. B. Storm, K.H. Jensen, *Nordic Hydrology*, **15**, 283 (1984).
6. D. Yang, S. Herath, K. MMusiaka, *Hydrological Processes*, **11**, 2085 (2001).
7. Liu Changming, Fu Guobin. Some analyses of climate change impacts on hydrological regimes in China [A]. ZHANG Yi (chief editor). *Climate Changes and Their Impacts* [C]. Beijing: Meteorology Press, 1993.
8. Xu C, Chen Y, Yang Y, Hao X, Shen Y. *Journal of Geographical Sciences*, **20**(4), 599 (2010).
9. X. Zhang, Cao, Guo. *International Journal of Sediment Research*, **25**(3), 283 (2010).
10. H. Wang, Y. Chen, W. Li, H. Deng. *Chinese Geographical Science*, **23**(3), 286 (2013).
11. Y. Songcai, *Quaternary Sciences*, **22**(2), 148 (2002).
12. L. Xuefeng, R. Xin, L. Yuanhua, *Scientia Meteorologica Sinica*, **25**(6), 638 (2005).
13. L. Yuanhua, C. Shaojing, *Chinese Journal of Agrometeorology*, **26**(4), 224 (2005).
14. A. Yuegai, L. Yuanhua, *Journal of Arid Land Resources and Environment*, **19**(4), 159 (2005).
15. S. Aijun, H. Chunsheng, *China Rural Water and Hydropower*, **10**, 38 (2002).

The strategy choice of company in environmental research with government imposing carbon tax

Fan Zhang

Department of Economics, School of Economics and Finance, Xi'an Jiaotong University, , No.74, Yanta west Rd., Yanta Dist., Xi'anCity,710049,Shannxi, China

Received June 26, 2016; Revised July 21, 2017

In order to find the optimal uniform carbon tax imposed by government to pursue social welfare maximization and how carbon tax would affect the stock price of Duopoly companies, this paper studies some scenarios where spillover effect is considered by utilizing game theory tool. Based on the complete information hypothesis, optimal quantity, emission reduction and carbon tax are solved. Further, it is found that, by numerical calculation and under same carbon tax, social welfare, company profit, emission reduction and stock price under scenario where companies adopt environmental research joint venture strategy are all higher than that of environmental cartel, that of scenario with competitive R&D activity and that of scenario without spillover effect considered, respectively. And, differences in terms of social welfare, profit and stock prices among these scenarios tend to widen with carbon tax increasing. In this sense, duopoly companies have the incentive to fully share information and cooperate in R&D activity (namely, they would adopt “environmental research joint venture” strategy) to benefit from the highest profit, highest stock price as well as emitting least pollution under the uniform carbon tax set by government.

Key words: environmental research joint venture, game analysis, welfare, stock, spillover

INTRODUCTION

In recent decades, climate change has caused adverse impacts on natural and human systems on all continents and across the oceans, and the cause of such unpleasant change is evidently due to anthropogenic greenhouse gas (GHG) emission [1]. With its overwhelming destruction power to the earth, greenhouse gas emission has gained considerable attention from both academic world and policymakers' offices. Compared with traditional method such as technology advancement and official mandate, market could also lower emission by price signal to accommodate behaviors and decisions of producer and consumer. And the market tool discussed here is carbon tax.

Carbon tax, one kind of environmental tax in essence, internalizes the loss caused by polluting companies into the cost function and manufacturing price, and is adopted by many countries such as Finland, Demark, Norway, Italy and Sweden [2]. Usually speaking, different scholars show quite opposite opinions about effect of carbon tax to the economy. Recently, game theory tool has become a powerful analytic tool for studying interactions between different parties emitting CO₂ to see their optimal choice. Many works with game theory about pollution or greenhouse gas emission have sprang up in terms of considering emission trading permits [3], non-cooperative or cooperative R&D

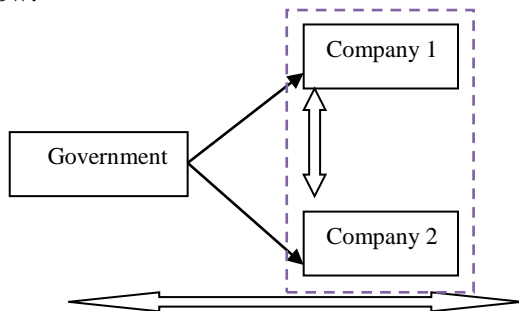
[4], green supply chain scenario game model [5], choice and effects of imposing uniform or differential carbon tax [6].

It is not hard to conclude that carbon tax is widely discussed nowadays in many aspects, such as its socio-economic effects (such as welfare, Gini coefficient, income effect) at different regions, countries or sectors, effects with carbon emission trading combined [7] and game analysis. However, few people further study how the stockholder wealth would change due to carbon emission reduction R&D activity since some scholars started to pay attention to the environmental R&D cartel. Generally speaking, terminology “R&D” could be traced by Kamien et al. [8] who provided a classification of different R&D organizational forms to obtain cost-reducing R&D but he failed to consider the pollution aspect. Later, Poyago-Theotoky [4] took into account the pollution effects and developed it into “environmental R&D” or abatement activities where firms engages in R&D activity so as to develop new processes to reduce unneeded emissions. In his paper, Poyago-Theotoky [4] mainly discussed two kinds of environmental R&D activities: namely, (1) environmental competition R&D, (2) environmental cooperation R&D (hereinafter “environmental cartel” or “ERC”) but only talked little and did none numerical experiment about the third environmental R&D activities: “environmental research joint venture” (hereinafter “ERJV”). In definition, it is quite easy to understand environmental competition

* To whom all correspondence should be sent:
E-mail: zhf808@163.com

R&D as companies do not cooperate in emission reduction and they only care about their own profit function. Poyago-Theotoky [4] confirmed that ERC is an activity that “firms coordinate their R&D but do not share information fully” while ERJV refers to the situation where firms would share information completely (mathematically, the spillover effect parameter would be one).

This paper aims to study scenarios where both Duopoly companies are dedicated to reducing their carbon emissions, so uniform carbon tax makes sense for analysis that follows. Based on pioneering works of Poyago-Theotoky [4] and Sun [9], effect of uniform carbon tax under framework of welfare by adopting game theory analytic tool is tested with further research on “environmental research joint venture” which is neglected by Poyago-Theotoky [4]. Specifically, this paper, combining with the total social utility which contains the carbon tax revenue to return, constructs a three-stage Duopoly model: the first stage shows the optimal uniform carbon tax set by administrative institution on the corporations in order to get maximum social utility, followed by the second stage demonstrating how hard these two companies would be dedicated to reducing carbon emission and the third stage presenting the optimal quantity decision made by these two participants to chase maximum profit in goods market. In essence, the first stage is a Stackelberg model, the second one is a cooperative or non-cooperative game and the third stage is a typical Duopoly model. Overall, the technological route for this three-stage game model for duopoly market under government's regulation is showed below:



First stage, Stackelberg model: government sets carbon tax and companies decide how to react to it, such as adopting cleaner production process
 Second stage: emission reduction activity
 Third stage, Cournot model: how companies compete in the goods market to get maximum profit with full knowledge of carbon tax

Fig. 1. Technology route of duopoly model

MODELING

Assumptions

Assumption 1: There are only two companies in the market and these two companies produce

homogeneous goods to satisfy market need. Market quantity shares linear relationship with market price: $P = \alpha - \beta Q$. For convenience, let beta be one. And each company owns same unit cost c , releasing one unit emission per product [4].

Assumption 2: Spillover effect is considered here. That is, companies influence each other in terms of reduction technologies to some degree: u ranges from 0 to 1. In detail, if u equals 0, then no spillover effect exists, otherwise, companies would reduce emissions by just using the other company's existing green technology. Specifically, if company 1 releases total emission e_1 , then company 2 could reduce pollution by amount of $u_1 e_1$ without any investment in R&D, therefore, actually total emission is $w_i = q_i - e_i - u_j e_j$, $i, j=1, 2$ and $i \neq j$. (see J.A. Poyago, 2007[4]; Sun, 2014[9]). Moreover, as J.A. Poyago-Theotoky (2007) suggested, when u equals 1, then it means two Duopoly companies adopt environmental research joint venture strategy.

Assumption 3: carbon emission reduction cost (R&D cost function) is a convex function, $\frac{re_i^2}{2}$: appearing in the form of quadratic function $\frac{re_i^2}{2}$: and $r > 0$. Here, r refers to the cost parameter of R&D and larger r means lower research efficiency or higher investment in reduction technology.

Assumption 4: complete information hypothesis holds and government levies uniform carbon tax on these two companies to pursue the harmonization of economy, society and environment. Here, society aspect contains collected carbon emission transferred to the consumer as well as consumer surplus.

Social welfare functions building

Concerning utility, this paper follows logic of Wang [10] that government considers harmonization of economy, society and environment. In detail, the total social utility function would contain profits of companies, consumer surplus and tax revenue, and pollution caused. In quantitative terms and for convenience, pollution part is captured via a linear function with pollution damage parameter d ($d > 0$) from Poyago-Theotoky [4]:

$$U_{pollution} = d(w_1 + w_2)$$

Therefore, total utility function appears in the following form:

$$U_{total} = \Phi_1 + \Phi_2 + U_{consumer} + U_{tax} - U_{pollution}$$

Where sum of Φ_1 and Φ_2 denotes economic part, sum of U_{consumer} and U_{tax} donates society part, and $U_{\text{pollution}}$ denotes environment part.

Table 1. optimal result of carbon tax, reduction and quantity

| Item | Spillover effect exists | | | No spillover effect $u_1 = u_2 = 0$ |
|------------|----------------------------------|--|--|---|
| | Competitive strategy | Cooperative strategy | | |
| | $0 < u_1, u_2 < 1$ | $0 < u_1, u_2 < 1$ | $u_1 = u_2 = 1$ | |
| | | Environment R&D cartel | Environment research joint venture (ERJV) | |
| | | (ERC) | (ERJV) | |
| Carbon tax | $t^* = \frac{6dr + 9d(u_1)}{4r}$ | $t^{**} = \frac{9d(2 + 2u_1 + 2u_2) + 9d(u_1)}{4r + 9(1 + u_1)^2 +}$ | $t^{***} = \frac{3dr + 36d - Ar}{2r + 36}$ | $t^{****} = \frac{3dr + 9d - Ar}{2r + 9}$ |
| Reduction | t^*/r | $t^{**}(1 + u_1)/r$ | $2t^{***}/r$ | t^{****}/r |
| Quantity | $(A - t^*)/3$ | $(A - t^{**})/3$ | $(A - t^{***})/3$ | $(A - t^{****})/3$ |

Functions solving

Under complete information hypothesis, use reverse calculation methodology to solve the third stage:

max

$$\Pi_i = (\alpha - (q_i + q_j))q_i - cq_i - t(q_i - e_i - u_j e_j) - re_i^2/2$$

Companies with carbon tax constraints compete in the goods market and decide the optimal output to chase the maximum profit, therefore, take the partial derivatives of profit function to the independent variable “quantity” and set them to zero. Solve simultaneous equations about quantities to obtain:

$$q_1 = q_2 = (A - t)/3, \text{ where } A = \alpha - c$$

Then, companies plan carbon emission reduction strategy and during the second stage, still calculate the partial derivatives of profit function to emission reduction amount. Note that, cooperative R&D situations (“ERC” where $0 < u_1, u_2 < 1$ and “ERJV” where $u_1 = u_2 = 1$) ask that total profit of two companies reaches the top while competitive R&D situation (where $0 < u_1, u_2 < 1$) means that each company cares only about its profit maximum. Final results are displayed in table 1. Note that, in the no spillover effect scenario, profit would not be influenced by the spillover effect parameters (as $u_1 = u_2 = 0$), so the results for competitive strategy and cooperative strategy are the same.

When it comes to the first stage, take results containing key variables “carbon tax” from stage 3

and stage 2 into the total social utility functions and get the partial derivatives of social functions to the carbon tax to get the optimal uniform carbon tax rate as showed in table 1.

Judging from table 1, under same tax scenarios and regardless of government optimizing total utility, environment research joint venture ($u_1 = u_2 = 1$) reduces more than any other strategy, even all of these scenarios would produce same quantities.

Further, it can be proved that $t^{***} > t^{**} > t^* > t^{****}$ with respect to d given other parameters in optimal carbon tax formula remain unchanged. That is to say, optimal carbon tax under environment research joint venture is higher than that of environment R&D cartel, that of competitive strategy with spillover effect considered and that of no spillover effect scenario, respectively. And again, it could be confirmed that environment research joint venture would reduce much more pollution than any other three strategy.

CONCLUSIONS

This paper studies the optimal uniform carbon tax imposed by government in Duopoly companies in order to pursue total social utility under four scenarios, namely, scenario where duopoly companies compete in both product market and emission reduction R&D, scenarios where duopoly companies only compete in product market and collaborate in emission reduction (if they do not fully share information, then it is “environmental cartel”; otherwise, it is “environmental research joint venture”) and scenario where no spillover effect exists. Observing the quantity, emission reduction and total social welfare, it is concluded that environmental research joint venture dominates the other three under same carbon tax. Furthermore, this paper studies the stock price of duopoly companies and finds a negative relationship between carbon tax and stock price. Compared with other three scenarios, companies adopt environmental research joint venture strategy enjoys the highest stock price (i.e. the highest personal wealth for stockholders), and the stock prices of other two scenarios, scenario where companies competes in R&D with spillover effect considered and scenario with no spillover effect, are somewhat identical.

However, some questions should also be paid attention when carbon tax is imposed in reality. First, as discussed above, China has a strong wish to impose carbon tax but now has not yet conducted such action, so the inverse demand presented

function and other parameters here are just used to analyze, true parameters should be studied in careful manner to get satisfactory result to make government policy more powerful and useful. Also, note that collaboration in R&D (environmental research joint venture then environmental cartel) is always good for duopoly companies to conduct; however, companies would more likely tend to take part in seeking rent rather than collaboration in R&D (see Fig 2, take environmental cartel scenario for example).

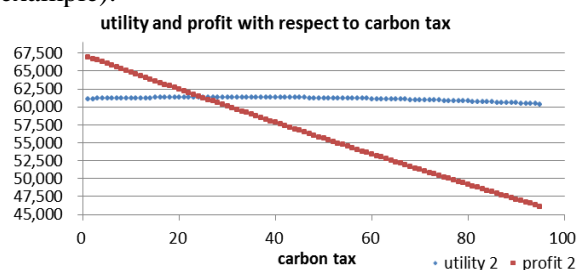


Fig. 2. Rent-seeking problems

As discussed above, quantity and profit would decrease with increased carbon tax and the highest quantity and corresponding profit lie in the point that no carbon tax is imposed, so the duopoly companies may use their market power or other means to persuade, bribe or even threaten the government to set lower carbon tax far from the optimal one. Therefore, even the collaboration strategy (that is “environmental research joint venture”) dominates other strategies, how to make sure such strategy to come into reality or conduct effectively really matters.

Acknowledgements: This work is supported by National Social Science Fund(Grant No.14BJL002),The Ministry of education of Humanities and Social Science project (Grant No.11YJA790204) and the Fundamental Research Funds for the Central Universities.

REFERENCES

- 1.PCC, R.K. Pachauri, L.A. Meyer (eds.), in: Climate Change 2014: Synthesis Report. Contribution of Working Groups I, II and III to the Fifth Assessment Report of the Intergovernmental Panel on Climate Change, IPCC, Geneva, Switzerland, 2014, p. 151.
- 2.J.C. Zhang, W.Z. Zhong, *China population, resources and environment*, , **25**(5), 53 (2015).
- 3.X. J. Wen, Y. Zhao, Y. F. Luo, C. Y. Yue, *System engineering theory and practice*, **4**, 27(2003).
- 4.J.A. Poyago-Theotoky, *Journal of Economic Behavior & Organization*, **62**, 63 (2007).
- 5.Q.H. Zhu, Y.J. Dou, *Journal of management sciences in China*, **14**(6), 86 (2011).
- 6.W.S. Yu, Z.Y. Zhang, *China population, resources and environment*, **23**(6), 8 (2013).
- 7.K. Zhang, Q. Wang, Q.M. Liang, H. Chen, *Renewable and sustainable energy reviews*, **58**, 297 (2016).
- 8.M.I. Kamien, E. Muller, I. Zang, *American Economic Review*, **82**, 1293 (1992).
- 9.S. Ya-nan, *China population, resources and environment*, **24**(3), 32-40 (2014).
- 10.W. Kun, Optimal decision of enterprise production and emission reduction with carbon tax policy considered, Tian Jin: department of management and economics of Tian Jin University, (2013).

BULGARIAN CHEMICAL COMMUNICATIONS

Instructions about Preparation of Manuscripts

General remarks: Manuscripts are submitted in English by e-mail or by mail (in duplicate). The text must be typed double-spaced, on A4 format paper using Times New Roman font size 12, normal character spacing. The manuscript should not exceed 15 pages (about 3500 words), including photographs, tables, drawings, formulae, etc. Authors are requested to use margins of 3 cm on all sides. For mail submission hard copies, made by a clearly legible duplication process, are requested. Manuscripts should be subdivided into labelled sections, e.g. **Introduction, Experimental, Results and Discussion**, etc.

The title page comprises headline, author's names and affiliations, abstract and key words.

Attention is drawn to the following:

a) **The title** of the manuscript should reflect concisely the purpose and findings of the work. Abbreviations, symbols, chemical formulas, references and footnotes should be avoided. If indispensable, abbreviations and formulas should be given in parentheses immediately after the respective full form.

b) **The author's** first and middle name initials, and family name in full should be given, followed by the address (or addresses) of the contributing laboratory (laboratories). **The affiliation** of the author(s) should be listed in detail (no abbreviations!). The author to whom correspondence and/or inquiries should be sent should be indicated by asterisk (*).

The abstract should be self-explanatory and intelligible without any references to the text and containing not more than 250 words. It should be followed by key words (not more than six).

References should be numbered sequentially in the order, in which they are cited in the text. The numbers in the text should be enclosed in brackets [2], [5, 6], [9–12], etc., set on the text line. References, typed with double spacing, are to be listed in numerical order on a separate sheet. All references are to be given in Latin letters. The names of the authors are given without inversion. Titles of journals must be abbreviated according to Chemical Abstracts and given in italics, the volume is typed in bold, the initial page is given and the year in parentheses. Attention is drawn to the following conventions:

a) The names of all authors of a certain publications should be given. The use of “*et al.*” in

the list of references is not acceptable.

b) Only the initials of the first and middle names should be given.

In the manuscripts, the reference to author(s) of cited works should be made without giving initials, e.g. “Bush and Smith [7] pioneered...”. If the reference carries the names of three or more authors it should be quoted as “Bush *et al.* [7]”, if Bush is the first author, or as “Bush and co-workers [7]”, if Bush is the senior author.

Footnotes should be reduced to a minimum. Each footnote should be typed double-spaced at the bottom of the page, on which its subject is first mentioned.

Tables are numbered with Arabic numerals on the left-hand top. Each table should be referred to in the text. Column headings should be as short as possible but they must define units unambiguously. The units are to be separated from the preceding symbols by a comma or brackets.

Note: The following format should be used when figures, equations, etc. are referred to the text (followed by the respective numbers): Fig., Eqns., Table, Scheme.

Schemes and figures. Each manuscript (hard copy) should contain or be accompanied by the respective illustrative material as well as by the respective figure captions in a separate file (sheet). As far as presentation of units is concerned, SI units are to be used. However, some non-SI units are also acceptable, such as °C, ml, l, etc.

The author(s) name(s), the title of the manuscript, the number of drawings, photographs, diagrams, etc., should be written in black pencil on the back of the illustrative material (hard copies) in accordance with the list enclosed. Avoid using more than 6 (12 for reviews, respectively) figures in the manuscript. Since most of the illustrative materials are to be presented as 8-cm wide pictures, attention should be paid that all axis titles, numerals, legend(s) and texts are legible.

The authors are asked to submit **the final text** (after the manuscript has been accepted for publication) in electronic form either by e-mail or mail on a 3.5” diskette (CD) using a PC Word-processor. The main text, list of references, tables and figure captions should be saved in separate files (as *.rtf or *.doc) with clearly identifiable file names. It is essential that the name and version of

the word-processing program and the format of the text files is clearly indicated. It is recommended that the pictures are presented in *.tif, *.jpg, *.cdr or *.bmp format, the equations are written using "Equation Editor" and chemical reaction schemes are written using ISIS Draw or ChemDraw programme.

The authors are required to submit the final text with a list of three individuals and their e-mail addresses that can be considered by the Editors as potential reviewers. Please, note that the reviewers should be outside the authors' own institution or organization. The Editorial Board of the journal is not obliged to accept these proposals.

EXAMPLES FOR PRESENTATION OF REFERENCES

REFERENCES

1. D. S. Newsome, *Catal. Rev.–Sci. Eng.*, **21**, 275 (1980).
2. C.-H. Lin, C.-Y. Hsu, *J. Chem. Soc. Chem. Commun.*, 1479 (1992).
3. R. G. Parr, W. Yang, *Density Functional Theory of Atoms and Molecules*, Oxford Univ. Press, New York, 1989.
4. V. Ponec, G. C. Bond, *Catalysis by Metals and Alloys* (Stud. Surf. Sci. Catal., vol. 95), Elsevier, Amsterdam, 1995.
5. G. Kadinov, S. Todorova, A. Palazov, in: *New Frontiers in Catalysis* (Proc. 10th Int. Congr. Catal., Budapest, 1992), L. Guzzi, F. Solymosi, P. Tetenyi (eds.), Akademiai Kiado, Budapest, 1993, Part C, p. 2817.
6. G. L. C. Maire, F. Garin, in: *Catalysis. Science and Technology*, J. R. Anderson, M. Boudart (eds), vol. 6, Springer-Verlag, Berlin, 1984, p. 161.
7. D. Pocknell, *GB Patent 2 207 355* (1949).
8. G. Angelov, PhD Thesis, UCTM, Sofia, 2001.
9. JCPDS International Center for Diffraction Data, Power Diffraction File, Swarthmore, PA, 1991.
10. *CA* **127**, 184 762q (1998).
11. P. Hou, H. Wise, *J. Catal.*, in press.
12. M. Sinev, private communication.
13. <http://www.chemweb.com/alchem/articles/1051611477211.html>.

CONTENTS

| | |
|--|-----|
| <i>T. Shen, X.J. Li, D.P. Wang, M.L. Yao</i> , Research on infrared interference performance of carbon smoke | 5 |
| <i>A.J. Shao, Z.G. Li, S.W. Wang</i> , The factor analysis of environment changes on groundwater | 9 |
| <i>C.G. Zhang, G.L. Zhang, M.H. Zhang, J.G. Chen</i> , Distribution and magnetic features of igneous rocks in the Gaize-Nima area of Tibet plateau based on magnetic data | 14 |
| <i>B. Bai, S. Jiang</i> , Thermally induced pore pressure and consolidation volumetric strain for saturated soils | 19 |
| <i>Z.J. Dai, S.X. Chen, J. Li</i> , The water storage capability and hydraulic conductivity of different expansive soils | 25 |
| <i>Q.W. Yu, L. Zhang</i> , Financial crisis early-warning model for listed company in china energy industry based on logistic regression | 31 |
| <i>L.L. Tan, X.M. Tian, H. Fan, F. H. Zhang, H.J. Wang, Y.B. Li, C. Fei, K.Y. Wang</i> , Effect of polymer compounds on base ions of salinized soil | 37 |
| <i>M.-Y. Chen, Y.-S. Perng</i> , Application of the bootstrap panel method an empirical study of the granger causality between carbon dioxide emissions and economic growth in emerging countries | 42 |
| <i>Z.Z. Li, J.Q. Su</i> , Evaluating air quality through aerial demand function and an application evaluating air quality .. | 47 |
| <i>H.G. Zheng, F.R. Qiao, Y.Q. Li , J.S. Zhang, L.J. Liao, D.J. Wang, J.X. Yu</i> , The evaluation of the sustainability of land consolidation and remediation in Funing County | 53 |
| <i>H.D. Wen, J. Dai</i> , CO ₂ emissions and economic growth nexus in China: A cointegration analysis of the four-stage environmental Kuznets Curve | 59 |
| <i>X. Yu, X. Rui, D. Zhang, S. Yao, Y. Song, W. Sun, L. Zhu, L. Wu</i> , Extraction and tracking method of drop zone of storm cells based on modified SCIT algorithms | 64 |
| <i>S.L. Lin, J.M. Hu, R.Guo, Y. Lin, L.L. Liu, B.K. Tan, S.X. Zeng</i> , Potential dietary toxicity assessment of alum-processed jellyfish | 70 |
| <i>P. Sun, R.-J. Li, O. Igwe, H. Luo</i> , A new formula of loess earth pressures based on the joint strength theory | 78 |
| <i>J.C. Cao, H. Zhou, S. Chen , L. Shi, J. Zhou</i> , Influence of Cu-Fe alloy on the transient thermal characteristics of IMCCR under two special operating conditions | 83 |
| <i>T.R. Zhao</i> , Empirical study of effect of financial capital on sustainable economic development in western rural China | 90 |
| <i>L.J. Li, Y.L. Li, X.Y. Li</i> , On coordinated development of BTH urban agglomeration subjected to atmospheric environmental capacity | 95 |
| <i>Q.L. Chang, W.J. Tang, H.Q. Zhou, J.B. Bai</i> , Study and application of repeated mining with paste backfill to recover remaining strip pillars | 101 |
| <i>J.K. Li, J. Zhang, Z. H. Gao, Q. Chen, Z. X. Liu</i> , An evaluation system of ecology-safe and environment-friendly society - green production system | 107 |
| <i>A.J. Shao, S.W. Wang, X. Chen</i> , Experimental determination of coefficient of soil hydrodynamic dispersion | 113 |
| <i>G. Feng, F. Zhao, P. Zhuang, X. Huang, T. Zhang, X. Shi</i> , Changes in blood biochemical parameters and enzyme activity of juvenile Chinese sturgeon <i>Acipenser sinensis</i> during starvation | 119 |
| <i>S.H. Sun, G.Z. Huang, Y. Wang, Q. Bi</i> , Health risk assessment of the volatile organic compounds in children's toys | 124 |
| <i>J.C. Tu, J. Lin, F. Wei, G. Cheng, G. Zeng, H. Wei</i> , Study of enhancing excess sludge broken walls by alkali coupling organic solvents | 129 |
| <i>Y.K. Zhang, P.K. Liu, X.H. Yang, L.Y. Jiang, Y.L. Zhang, J.R. Yang</i> , Research on the action mechanism of air core and experiments of separation performance inside multi-product cyclone with double vortex finders catalyst..... | 133 |
| <i>W. Li</i> , Calculation of growth process of nanostructured materials | 140 |
| <i>J. Zhao, Y. L. Wu, Y.Q. Ji</i> , Calculation and applied analysis of natural gas hydrate saturation based on experimental data | 145 |
| <i>W.Q. Song, X.Q. Wang, Y. Qi, J. Meng, X.G. Hu, S.M. Wang, S.W. Liang</i> , Analgesic effect of vinegar-processed myrrh and the processing technology research | 150 |
| <i>D.P. Xia, H. Nan, X.B. Su, Y. Bai, X. Chen</i> , Comparative experimental study of hydrogen and methane with coal cogeneration system and methane of single-phase production | 155 |
| <i>X.S. Chen, Y.L. Zhang</i> , Study on the wet inside filtration theory of fiber layer for dust particles based on equivalent analogy hypothesis algorithm | 161 |
| <i>Z. He, X.Y. Sun, X. Gu, J. He</i> , Effect of key parameters on the secondary combustion efficiency of boron - containing gas | 167 |
| <i>Y.H. Yang, X.B. Chen, C.Y. Jiang</i> , Optimization for adsorption separation process of simulated moving bed based on moving asymptotes algorithm | 172 |
| <i>H. Sun, Y.F. Cao, X.L. Yang, L.Q. Wang, X.C.Zhang</i> , Investigation of the process and performance of a molding wood substitute packaging material | 179 |
| <i>X.J. Yang, L.D. Duan</i> , Seed germination of <i>Vicia hirsuta</i> (Linn.) S.F.Gray | 186 |

| | |
|--|-----|
| <i>C.Y. Xu, C.Y. Hao</i> , Research on vegetation spatial heterogeneity in longitudinal range-gorge region of Yunnan province, China | 192 |
| <i>M.J. Zhang, Y.H. Yang, H.Q. Zhang</i> , Study on the computing methods of mixed layer depth and gradation based on sand wave motion | 198 |
| <i>J. Zhang, A. Chen, M. Babae, L. Wang, Y. Qiao</i> , Development of traditional and herbal Chinese medicine (chemical and biochemical perspectives) with emphasis on legal systems | 204 |
| <i>A.J. Shao, L.Y. Zhao, S.W. Wang</i> , The factor analysis of climatic change on water resource: a case study in Haihe river basin of Hebei province | 209 |
| <i>F. Zhang</i> , The strategy choice of company in environmental research with government imposing carbon tax | 214 |
| <i>INSTRUCTIONS TO THE AUTHORS</i> | 219 |